OXIDE AND OXIDE FLUORIDES OF XENON(IV) AND NEW DEVELOPMENTS IN XENON(II), AND KRYPTON(II) CHEMISTRY

OXIDE AND OXIDE FLUORIDES OF XENON(IV) AND NEW DEVELOPMENTS IN XENON(II), AND KRYPTON(II) CHEMISTRY

By

DAVID S. BROCK

A Thesis
Submitted to the School of Graduate Studies
in Partial Fulfillment of the Requirements
for the Degree
Doctor of Philosophy

McMaster University

DOCTOR OF PHILOSOPHY McMaster University

(Chemistry) Hamilton, Ontario

TITLE: OXIDE AND OXIDE FLUORIDES OF XENON(IV) AND NEW DEVELOPMENTS IN XENON(II), AND KRYPTON(II) CHEMISTRY

AUTHOR: David S. Brock, B. Sc. (McMaster University)

SUPERVISOR: Professor Gary J. Schrobilgen

NUMBER OF PAGES: 409, xxviii

ABSTRACT

This Thesis extends the fundamental chemistry of the noble-gas elements, namely, xenon and krypton. More specifically, the chemistry of Xe(IV) has been extended by the synthesis and characterization of Xe(IV) oxide and oxide fluoride derivatives. The syntheses of $XeOF_2$, $F_2OXeN{\equiv}CCH_3$, and $XeOF_2{\cdot}n$HF and their structural characterizations are described. All three compounds are endothermic and explosive at temperatures approaching 0 °C. Although $XeOF_2$ had been previously reported, it had not been isolated as a pure compound. Xenon oxide difluoride has now been characterized in CH_3CN solution by ^{19}F, ^{17}O, and ^{129}Xe NMR spectroscopy and $XeOF_2$, $F_2OXeN{\equiv}CCH_3$, and $XeOF_2{\cdot}n$HF have been characterized in the solid-state by Raman spectroscopy. The low-temperature X-ray crystal structure of $F_2OXeN{\equiv}CCH_3$ reveals a long Xe–N bond trans to the Xe–O bond and a geometrical arrangement about xenon in which the atoms directly bonded to xenon are coplanar and $CH_3C{\equiv}N$ acts as a fourth ligand in the equatorial plane. The geometry about xenon is consistent with an AX_2YZE_2 VSEPR arrangement of bond pairs and electron lone pairs and represents a rare example of a Xe(IV)–N bond.

The missing Xe(IV) oxide, XeO_2, has been synthesized at 0 °C by hydrolysis of XeF_4 in water and 2.00 M $H_2SO_{4(aq)}$ and characterized by low-temperature Raman Spectroscopy. The Raman spectra of XeO_2 amend prior vibrational assignments of xenon doped SiO_2 and are in accordance with prior speculation that xenon depletion from the Earth's atmosphere could occur by xenon insertion at high temperatures and high pressures into SiO_2 in the Earth's crust.

The $XeOF_3^-$ anion has been synthesized as its Cs^+ and $N(CH_3)_4^+$ salts, and structurally characterized in the solid state by low-temperature Raman spectroscopy. The calculated anion geometry is based on a square planar AX_3YE_2 VSEPR arrangement with the longest Xe–F bond trans to the oxygen atom. The F–Xe–F angle is bent away from the oxygen atom to accommodate the greater spatial requirement of the oxygen double bond domain. The $XeOF_3^-$ anion of the Cs^+ salt is fluorine-bridged in the solid-state, whereas the anion of the $N(CH_3)_4^+$ salt approximates the gas-phase anion.

The $[H(OXeF_2)_n][AsF_6]$ and $[FXe^{II}(OXe^{IV}F_2)_n][AsF_6]$ (n = 1, 2) salts have been synthesized and structurally characterized in the solid state by low-temperature Raman spectroscopy. The chain length of each cation is limited to one or two $OXeF_2$ subunits, which are oxygen-bridged and are strongly ion-paired with the AsF_6^- anion. The reaction of $XeOF_2{\cdot}x HF$ in superacidic HF/SbF_5 solvent mixtures resulted in a mixture of $([XeF_3{\cdot}HF][Sb_2F_{11}])_2{\cdot}[H_5F_4][SbF_6]$, $[XeF_3{\cdot}HF][Sb_2F_{11}]$, and $[XeF_3][SbF_6]$. The XeF_3^+ cations in each structure are very similar, displaying T-shaped coordination of three fluorine atoms, and a short contact to the fluorine atom of HF, in $([XeF_3{\cdot}HF][Sb_2F_{11}])_2{\cdot}[H_5F_4][SbF_6]$ and $[XeF_3{\cdot}HF][Sb_2F_{11}]$, or to a fluorine atom of SbF_6^- in $[XeF_3][SbF_6]$.

Vibrational frequency assignments for the aforementioned compounds were aided by comparison with frequencies derived from quantum-chemical calculations, by ^{18}O enrichment, and, where appropriate, by ^{2}H enrichment.

The syntheses and structural characterizations of $[XOF_2][AsF_6]$ (X = Cl, Br), the XeF_2 adduct-salts, $[BrOF_2][AsF_6]{\cdot}n XeF_2$ (n = 1, 2), and the KrF_2 adduct-salt,

$[BrOF_2][AsF_6]\cdot 2KrF_2$, are also described. The crystal structure of $[BrOF_2][AsF_6]$ shows a positional disorder among the oxygen atom and the fluorine atoms. The low-temperature Raman spectra of $[XOF_2][AsF_6]$, the complex cation salts, $[BrOF_2][AsF_6]\cdot n XeF_2$ (n = 1, 2), and $[BrOF_2][AsF_6]\cdot 2KrF_2$ have been assigned on the basis of the crystal structures and with the aid of quantum-chemical calculations. The low-temperature (−173 °C) X-ray crystal structure of $[BrOF_2][AsF_6]\cdot 2KrF_2$ consists of isolated molecular units and represents an example of KrF_2 coordinated to a main-group atom. The contact distances between bromine and fluorine atom of NgF_2 (Ng = Kr, Xe) is shorter in $[BrOF_2][AsF_6]\cdot 2XeF_2$ than in the KrF_2 analogue, which is attributed to the more polar nature of the Xe–F bonds. The ELF and QTAIM analyses of $[BrOF_2][AsF_6]_3^{2-}$ and $[BrOF_2][AsF_6]\cdot 2XeF_2$ were carried out and are compared with those of free $BrOF_2^+$ and $[BrOF_2][AsF_6]\cdot 2KrF_2$ to better understand the effect of Br(V) coordination number on the localization domain of the Br(V) valence electron lone pair.

The syntheses of $FXeON^{16}O_2$ and $FXeON(^{18}OO)$ has shed light on the mechanism leading to the formation of $FXeONO_2$. Raman spectroscopy indicated the absence of $^{16/18}O$ isotopic scrambling among the oxygen sites of $FXeONO_2$ which was confirmed by factor-group analyses of the 16 isotopomeric crystallographic unit cells that result from *syn-/anti*-isomerization, $FXe^{16}ON(^{16}O_A{}^{18}O_S)/FXe^{16}ON(^{16}O_S{}^{18}O_A)$, among the four $FXeONO_2$ molecules of the unit cell. The intermediate oxide fluoride, $O(XeF)_2$, was observed in the synthesis of $FXeONO_2$, providing valuable insight into the reaction pathway. A reinterpretation of the solid-state ^{16}O- and ^{18}O-enriched Raman spectra of $O(XeF)_2$ was also carried out.

ACKNOWLEDGEMENTS

I wish to sincerely thank Professor Gary J. Schrobilgen as my primary mentor in learning the day-to-day operations of the laboratory, for providing me with interesting and exciting avenues of research, as well as for his insight, guidance, enthusiasm, patience, and confidence in me both inside and outside of the laboratory.

I would also like to thank the other members of my supervisory committee, Dr. Raman Chirakal, Dr. Ronald J. Gillespie and Dr. Robert G. Syvret, for their support, useful discussions, and interest in my research projects.

A heartfelt thanks to Dr. Hélène P. A. Mercier for her expertise, advice, encouragement, and friendship throughout the course of this work, as well as for the numerous hours spent in helping solve various crystal structures and writing contributions for our publications together.

A special thanks to Dr. Bernard Silvi for his collaboration in several studies involving ELF and QTAIM analyses. His expertise and explanations were most pleasant and enlightening.

I am also very grateful to Dr. Matthew D. B. Moran, Dr. Bernard E. Pointner and Dr. John F. Lehmann for their expertise, advice, and support during my first years of graduate school.

Thanks also to other past and present members of the Schrobilgen research group, namely Dr. Michael Hughes, Dr. Gregory Smith, Dr. Kazuhiko Matumoto, Dr. Vural Bilir, Jonathan J. Casalis de Pury, Babak Behnam-Azad, Maria Ivanova, Rezwan Ashique, Jonathan Paxon, Dr. Karsten Koppe, and Saurabh S. Chitnis for all of their help and encouragement. I am also grateful to Dr. Jennilee Gavina, Erik Youngson, Dr. Bonnie Leung, Dr. Jason Traer, Dr. Heather Cuthbert and Rev. Dieter Reda for useful discussions, good times, and for their friendship.

For their help in their respective fields, I would like to thank Dr. Jim Britten (X-ray crystallographic facilities), Dr. Steve Kornic (NMR and Spectroscopy facilities), and Michael Palme (Chemistry Glassblowing Shop).

I would like to acknowledge the Ontario Ministry of Education and Training - Ontario Graduate Scholarships in Science & Technology program (OGSST), the McMaster University Internal Prestige "Ontario Graduate Fellowships" Program, the James A. Morrison Memorial Scholarship program, and the McMaster University Department of Chemistry for financial support in the form of bursaries and scholarships over the years.

Finally, I would like to thank my wife and inspiration, Lindsey, for her unwavering love, endless understanding, amazing support, and full confidence in my abilities. As well, special thanks to my parents, Tom and Connie, my grandparents Tom and Bubs Brock, and Russ and Eve Baer, my brother and sister-in-law, Iain and Christie, my brother Michael, and my "adopted" family Paul, Francine, Matthew, and Sarah Askett for all of their financial and emotional support throughout my post-secondary education.

PREFACE

The following Chapters have been published, in part or in whole, by the American Chemical Society (ACS). All experimental and computational work was conducted by the author.

Chapter 3: Brock, D. S.; Bilir, V.; Mercier, H. P. A.; Schrobilgen, G. J. *J. Am. Chem. Soc.* **2007**, *129*, 3598–3611.

Chapter 4: Brock, D. S.; Schrobilgen, G. J. *J. Am. Chem. Soc.* **2011**, accepted.

Chapter 5: Brock, D. S.; Mercier, H. P. A.; Schrobilgen, G. J. *J. Am. Chem. Soc.* **2010**, *132*, 10935–10943.

Chapter 6: Brock, D. S.; Mercier, H. P. A.; Schrobilgen, G. J. submitted.

Chapter 7: Brock, D. S.; Casalis de Pury, J. J.; Mercier, H. P. A.; Schrobilgen, G. J.; Silvi, B. *J. Am. Chem. Soc.*, **2010**, *132*, 3533–3542.

Chapter 8: Brock, D. S.; Casalis de Pury, J. J.; Mercier, H. P. A.; Schrobilgen, G. J.; Silvi, B. *Inorg. Chem.*, **2010**, *49*, 6673–6689.

Chapter 9: Moran, M. D.; Brock, D. S.; Mercier, H. P. A.; Schrobilgen, G. J. *J. Am. Chem. Soc.*, **2010**, *132*, 13823–13839.

LIST OF ABBREVIATIONS AND SYMBOLS

General

BDH	British Drug Houses
SAE	Society of Automotive Engineers
ax	axial
eq	equatorial
CCD	charge-coupled device
FT	Fourier transform
FEP	perfluoroethylene/perfluoropropylene copolymer
IR	infrared
Kel-F	chlorotrifluoroethylene polymer
PTFE	tetrafluoroethylene polymer
VSEPR	valence shell electron pair repulsion
N.A.	natural abundance (isotopic)
aHF	anhydrous HF

Raman Spectroscopy

$\Delta\nu$	frequency
cm^{-1}	wavenumber
ν	stretching mode
δ	bending mode
ρ_w	wagging mode

ρ_r	rocking mode
ρ_t	twisting mode
o.o.p.	out-of-plane
i.p.	in-plane

Nuclear Magnetic Resonance Spectroscopy

NMR	nuclear magnetic resonance
ppm	parts per million
δ	chemical shift
I	nuclear spin quantum number
J	scalar coupling constant, in Hz
Hz	Hertz, or cycles per second
FID	free induction decay
SF	spectral frequency
SW	sweep width
TD	time domain
PW	pulse width
$\Delta\nu_{1/2}$	line width at half height
WF	width factor

X-ray Crystallography

a, b, c, α, β, γ	unit cell parameters

V	unit cell volume
λ	wavelength
Z	molecules per unit cell
mol. wt.	molecular weight
ρ	density
μ	absorption coefficient
F	structure factor
R_1	conventional agreement index
wR_2	weighted agreement index

Computational and Thermochemical

DFT	density functional theory
MP2	Møller-Plesset, second order perturbation
HF	Hartree-Fock
RLC	relative large core
NBO	natural bond orbital
NPA	natural population analysis
ΔH^{o}	standard enthalpy of reaction
ΔH_f^{o}	standard enthalpy of formation

TABLE OF CONTENTS

page

CHAPTER 1: INTRODUCTION

CHAPTER 2: EXPERIMENTAL SECTION

CHAPTER 3: $XeOF_2$, $F_2OXeN{\equiv}CCH_3$, AND $XeOF_2{\cdot}n$HF; RARE EXAMPLES OF XE(IV) OXIDE FLUORIDES

CHAPTER 4: SYNTHESIS OF THE MISSING OXIDE OF XENON, XeO_2, AND ITS IMPLICATIONS FOR EARTH'S MISSING XENON

CHAPTER 5: $XeOF_3^-$, AN EXAMPLE OF AN AX_3YE_2 VSEPR ARRANGEMENT; SYNTHESES AND STRUCTURAL CHARACTERIZATIONS OF [M][$XeOF_3$] (M = Cs, $N(CH_3)_4$)

CHAPTER 6: [$H(OXeF_2)_n$][AsF_6] and [$FXe^{II}(OXe^{IV}F_2)_n$][AsF_6] (n = 1, 2): Examples of Xenon(IV) Hydroxy and Oxide Fluoride Cations; and the Crystal Structures of [$XeF_3{\cdot}HF$][Sb_2F_{11}] and ([$XeF_3{\cdot}HF$][Sb_2F_{11}])$_2{\cdot}$[H_5F_4][SbF_6]

CHAPTER 7: A RARE EXAMPLE OF A KRYPTON DIFLUORIDE COORDINATION COMPOUND; $[BrOF_2][AsF_6]\cdot 2KrF_2$

CHAPTER 8: XeF_2 COORDINATION TO A HALOGEN CENTER; RAMAN SPECTRA (n = 1, 2) AND X-RAY CRYSTAL STRUCTURES (n = 1) OF $[BrOF_2][AsF_6]\cdot n XeF_2$ AND $[XOF_2][AsF_6]$ (X = Cl, Br)

CHAPTER 9: $Xe_3OF_3^+$, a Precursor to a Noble-Gas Nitrate and the First Neutral Oxide Fluoride of Xe(II); Syntheses and Structural Characterizations of $FXeONO_2$ and $O(XeF)_2$

CHAPTER 10: CONCLUSIONS AND DIRECTIONS FOR FUTURE WORK

LIST OF TABLES

LIST OF FIGURES

CHAPTER 1

Introduction

1.1. Introduction to Noble-Gas Reactivity

This Thesis has as its primary focus, the chemistry of xenon(IV). Thus, the present Chapter is mainly concerned with the status of xenon(IV) chemistry prior to the onset of the present Thesis research.

The events leading up to the discovery of noble-gas reactivity have been chronicled previously in a number of excellent review articles[1–12] as well as historical reviews that include experiments preceding the discovery and span over 100 years.[13,14]

In 1895, Henri Moissan attempted the reaction of newly discovered noble-gas, argon, with fluorine gas at room temperature and under the action of an induction spark, without success.[15] Attempts were also made in 1933 to induce reactivity between krypton and bromine,[16] krypton and chlorine,[16] and xenon and fluorine,[17] however, all failed. These failures, especially the attempted reaction of xenon and fluorine,[17] led to the noble-gases being regarded as chemically inert for the next three decades, and entrenched the so-called octet rule.[13,14] The first credible report of noble gases reactivity was made in 1962 by Neil Bartlett when he reacted deep red-brown PtF_6 vapor with xenon gas at room temperature. The product was a yellow-orange solid, then formulated as $[Xe][PtF_6]$.[18] The product has since been reformulated as a XeF^+ salt, $[XeF][PtF_6]$, in admixture with PtF_5 which, when warmed to $\leq$60 °C, gave $[XeF][Pt_2F_{11}]$.[19,20] This discovery was reported just a few months before the synthesis of XeF_4[21] and an erroneous report of XeF_2,[22] although the latter was definitivly synthesized in 1963.[22]

Since the discovery of noble-gas reactivity, numerous other noble-gas compounds have been synthesized and structurally characterized, and are described in several reviews.[1–12] Among these compounds, the chemistry of xenon is the most diverse, forming compounds in the +½, +2, +4, +6, and +8 oxidation states. In contrast, krypton is only known to form compounds in the +2 oxidation state.[12] Radon compounds also exist but have only been obtained at the radiotracer level and their oxidation states are uncertain.[23–25] There are also several reports in the literature of matrix-isolated argon compounds,[26–30] however, no argon compound has been synthesized to date in macroscopic amounts.

Xenon in the +2 oxidation state has been shown to form bonds with F, Cl, O, N, and C.[1–11] Consequently, numerous compounds of Xe(II) have been synthesized and characterized. Rather fewer Xe(VI) species are known because of the higher oxidative potential of Xe(VI) relative to Xe(II) and the greater likelihood of Xe(VI) oxidizing N- or C-coordinating ligands rather than forming bonds. The number and diversity of Xe(IV) compounds, prior to the present work, is even more sparse and largely restricted to well-characterized fluoride species. The factors that contribute to the paucity of Xe(IV) compounds are discussed below.

1.2. Xe(IV) Chemistry

1.2.1. Xe(IV) Fluorides

The first Xe(IV) compound, discovered mere months after Bartlett's discovery of noble-gas reactivity, was synthesized by the reaction of Xe and F_2 in a 1:5 molar ratio at 400 °C (~2 to 3 atm.; eq 1.1).[31] The product, XeF_4, is stable indefinitely at room

$$Xe + 2F_2 \xrightarrow{400\ ^\circ C} XeF_4 \tag{1.1}$$

temperature under anhydrous conditions and is the synthetic precursor for all other Xe(IV) species. The crystal structure,[32–34] Raman spectrum,[35–37] and NMR spectra[37–40] show that XeF_4 is consistent with an AX_4E_2 VSEPR[41] arrangement of bond pairs and valence electron lone pairs, giving it a square-planar geometry (Figure 1.1) with Xe–F bond lengths of 1.953(2) Å.[32] An example in which XeF_4 functions as a ligand to a metal center, $[Mg(XeF_2)(XeF_4)][AsF_6]_2$,[42] has recently been reported. The salt was characterized by X-ray crystallography and by Raman spectroscopy and is also novel because it is the only known example in which XeF_2 and XeF_4 are simultaneously coordinated to the same metal center.

The fluoride ion donor and acceptor properties of XeF_4 have been studied, resulting in the formation of XeF_3^+ and XeF_5^- salts. When compared with XeF_2, XeF_4 is a weaker fluoride ion donor[43] and requires a stronger fluoride-ion acceptor to form the corresponding cation. In contrast with XeF_2, which donates a fluoride ion to AsF_5,[44,45] XeF_4 forms a weak adduct with AsF_5 that is only stable at low-temperatures (< −78 °C).[46] In the presence of a stronger Lewis acid such as SbF_5, XeF_4 has been shown to form stable $[XeF_3][SbF_6]$ and $[XeF_3][Sb_2F_{11}]$ salts.

The direct interaction of XeF_4 and SbF_5 results in yellow $[XeF_3][Sb_2F_{11}]$ (eq 1.2) when an excess of SbF_5 is allowed to react with XeF_4 at room temperature and yellow *α*-

$$XeF_4 + SbF_{5\,(excess)} \xrightarrow{RT} [XeF_3][Sb_2F_{11}] \tag{1.2}$$

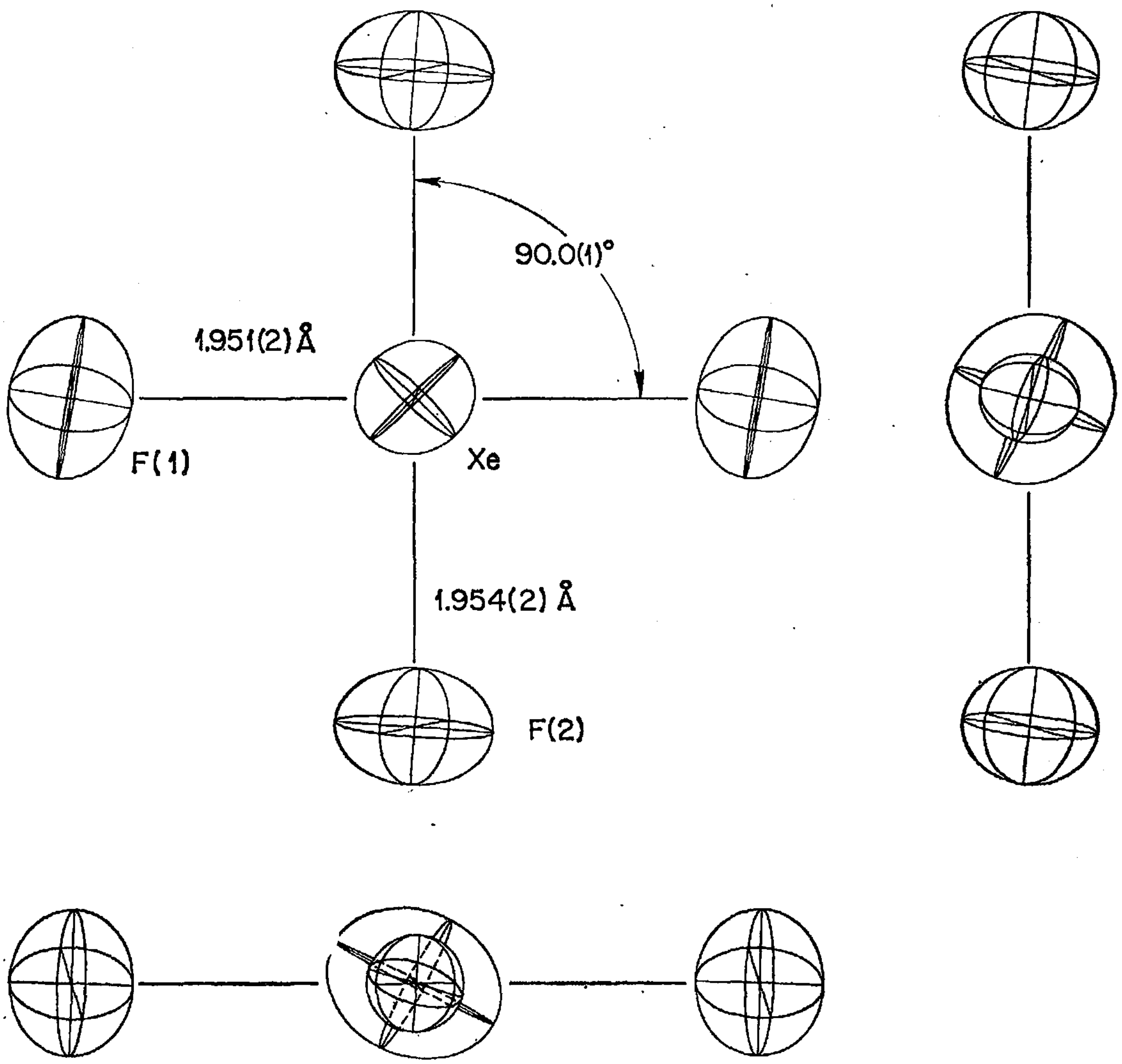

Figure 1.1. Geometry and thermal motion of the XeF_4 molecule. From ref 32.

$[XeF_3][SbF_6]$ is formed when $[XeF_3][Sb_2F_{11}]$ is fused with an excess of XeF_4 at 80 °C (eq 1.3).[47] A low-temperature phase of $[XeF_3][SbF_6]$ has been synthesized by the reaction of a stoichimoetric excess of XeF_4 with SbF_5 in HF solvent at room temperature (eq 1.4) and has been designated as β-$[XeF_3][SbF_6]$.[46] The XeF_3^+ cation has been fully characterized

$$[XeF_3][Sb_2F_{11}] + XeF_{4\,(excess)} \xrightarrow{80\,^{\circ}C} 2\,\alpha\text{-}[XeF_3][SbF_6] \qquad (1.3)$$

$$XeF_{4\,(excess)} + SbF_5 \xrightarrow[RT]{HF} \beta\text{-}[XeF_3][SbF_6] \qquad (1.4)$$

in SbF_5 solution by ^{19}F and ^{129}Xe NMR spectroscopy.[47–49] The ^{19}F spectrum consists of a doublet and triplet centered at 39.7 and 23.0 ppm, respectively, in SbF_5 solvent with ^{129}Xe satellites and $^{1}J(^{19}F–^{129}Xe)$ couplings of 2620 and 2440 Hz, respectively, and a $^{2}J(^{19}F–^{19}F)$ coupling of 174 Hz. The ^{129}Xe spectrum consists of a single resonance centered at 595 ppm which is split into a doublet of triplets as a result of coupling to the equatorial and two axial fluorine atoms, consistent with a T-shaped geometry. The cation geometry was confirmed for $[XeF_3][Sb_2F_{11}]$ and α- and β-$[XeF_3][SbF_6]$ by Raman spectroscopy[46,50] and by the X-ray crystal structure of β-$[XeF_3][SbF_6]$.[45,51,52] The primary coordination sphere of xenon in XeF_3^+ consists of a T-shaped arrangement of fluorine ligands in accordance with an AX_3E_2 VSEPR[41] arrangement of three bonding electron pairs and two valence electron lone pairs (Figure 1.2). The mutually trans Xe–F bond lengths for $[XeF_3][Sb_2F_{11}]$ (1.88(1), 1.89(1) Å;[51] 1.883(4), 1.908(4) Å[45]) and β-$[XeF_3][SbF_6]$ (1.906(13), 1.907(15) Å)[52] are elongated relative to the cis Xe–F bond length (1.83(1);[51] 1.832(4)[45] and 1.835(10) Å,[52] respectively) but the corresponding bond lengths are equal to within ±3σ when the two structures are compared. In both structures, two relatively short secondary contacts (SbF_6^-, 2.485(10) and 2.715(13) Å;[52]

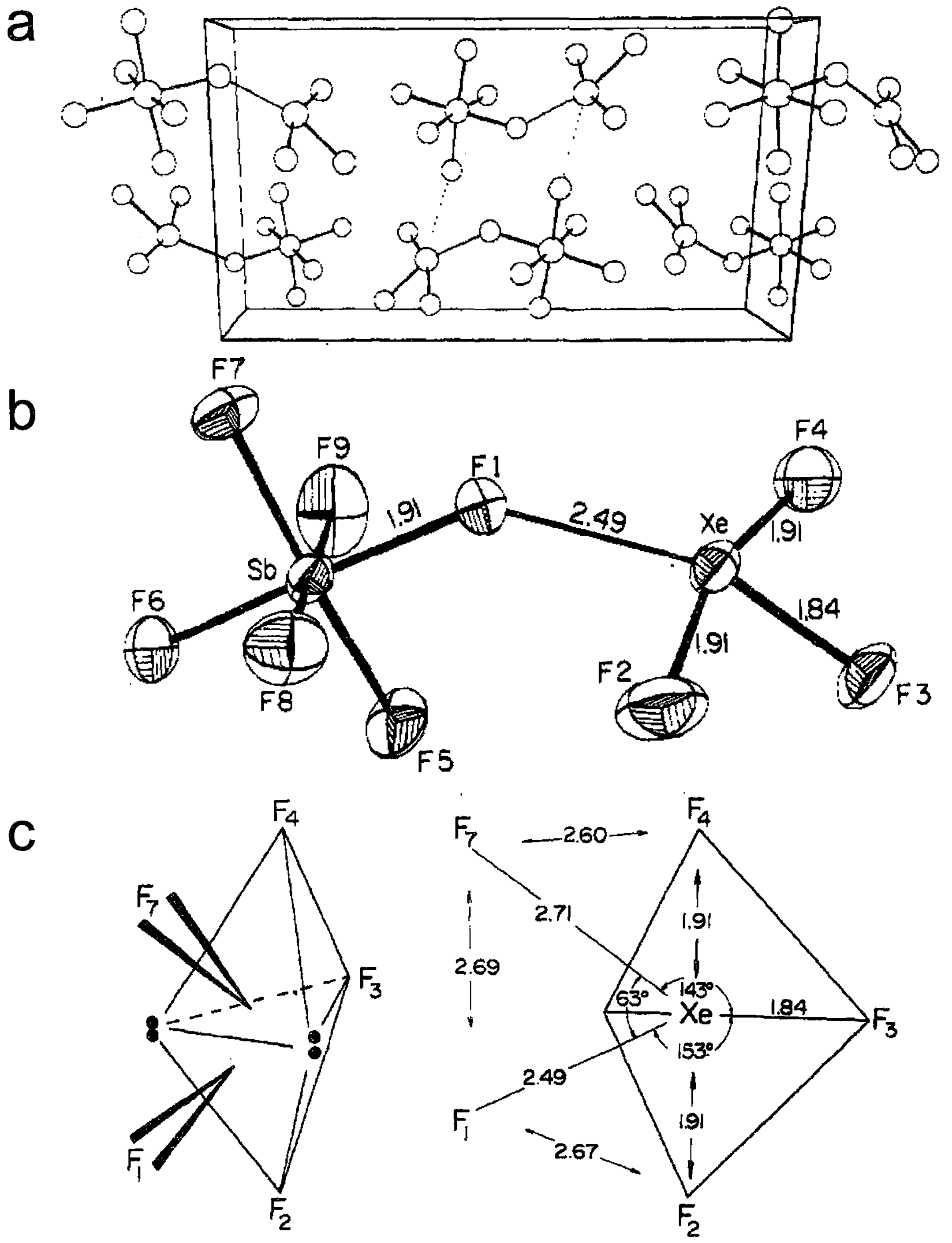

Figure 1.2. A perspective view (a) of the packing of the $[XeF_3][SbF_6]$ units within the unit cell as viewed down the *a*-axis and (b) of the $[XeF_3][SbF_6]$ structural unit with the atoms as 50% probability thermal ellipsoids. Interatomic distances are in angstroms. (c) An approximate model for the fluorine bridging in $[XeF_3][SbF_6]$. From ref 52.

$Sb_2F_{11}^-$, 2.50(1) and 2.94(1) Å;[51] 2.490(4)[45]) occur with the anions. These contacts are situated in the XeF_3^+ molecular plane and form an irregular pentagonal planar arrangement around xenon (Figure 1.2.b).

The XeF_5^- anion forms a regular pentagonal planar (D_{5h}) arrangement[53] around xenon in accordance with an AX_5E_2 VSEPR[41] arrangement of five bonding electron pairs and two lone valence electron lone pairs (Figure 1.3). The XeF_5^- anion has been synthesized (eq 1.5) as the $N(CH_3)_4^+$, Cs^+, Rb^+, K^+, and Na^+ salts and has been

$$XeF_4 + MF \xrightarrow[14h]{190\ ^\circ C} [M][XeF_5] \quad (M = N(CH_3)_4, Cs, Rb, K, Na) \qquad (1.5)$$

characterized by Raman and infrared spectroscopy, by ^{19}F and ^{129}Xe NMR spectroscopy, and by an X-ray crystal structure determination of the $N(CH_3)_4^+$ salt.[53] The ^{129}Xe NMR spectrum of $[N(CH_3)_4][XeF_5]$ dissolved in CH_3CN and containing a one molar excess of $[N(CH_3)_4][F]$ displayed a well-resolved binomial sextet, consistent with the coupling of the ^{129}Xe nucleus to five chemically equivalent ^{19}F nuclei in the XeF_5^- anion [$\delta(^{129}Xe)$, −527.0 ppm from $XeOF_4$; $^1J(^{19}F–^{129}Xe)$, 3400 Hz]. The ^{19}F NMR spectrum showed a narrow singlet flanked by ^{129}Xe satellites [$\delta(^{19}F)$, 38.1 ppm $^1J(^{19}F–^{129}Xe)$, 3398 Hz].

In the crystal structure, the average Xe–F bond length of the anion (2.012(2) Å) is elongated relative to that of XeF_4 (1.953(2) Å[32]). The XeF_5^- anion represents the first example of a pentagonal planar geometry. This contrasts with the equatorial fluorine atoms of IF_7, which are puckered by 7.5°.[54] The reason why XeF_5^- apparently does not exhibit puckering is attributed to the presence of the two axial electron lone pairs which exert greater repulsive forces than the two axial fluorines in the IF_7 molecule, thus forcing the XeF_5^- anion to be planar.[53] However, the planar arrangement imparts

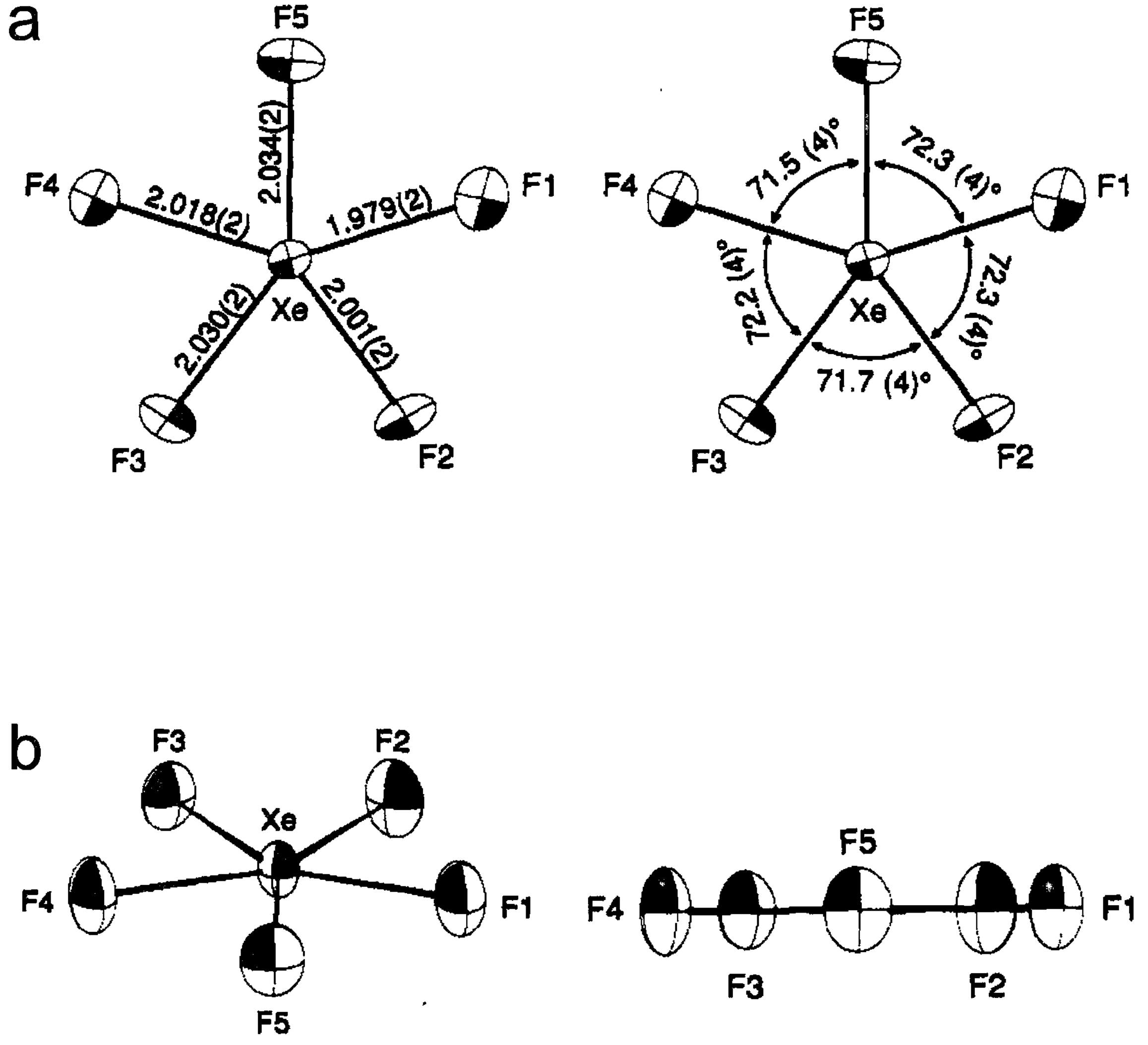

Figure 1.3. (a) Bond lengths (Å) and angles (deg) for XeF_5^- at −86 °C in $[N(CH_3)_4][XeF_5]$. Projection of the XeF_5^- anion on (111). Esds are given in parentheses; thermal ellipsoids are shown at the 50% probability level. (b) Projections of the XeF_5^- anion on (130) (left) and (010) (right). Thermal ellipsoids are shown at the 50% probability level. From ref 53.

congestion to the fluorine atoms where the intramolecular F···F distances range from 2.35 to 2.38 Å,[53] which are significantly less than twice the van der Waals radius for fluorine (2.94 Å [55]).

1.2.2. $OTeF_5$ Derivatives of Xe(IV)

The chemistry of Xe(IV) has also been extended by the use of the pentafluoroorthotellurate ligand, $OTeF_5$. The $OTeF_5$ group has an electronegativity of 3.87[56] which is comparable to that of fluorine, 3.98.[57] The most efficient synthesis of $Xe(OTeF_5)_4$ has been accomplished by the reaction of XeF_4 with $B(OTeF_5)_3$ (eq 1.6).[58]

$$3XeF_4 + 4B(OTeF_5)_3 \xrightarrow{\text{Freon-113}} 3Xe(OTeF_5)_4 + 4BF_3 \qquad (1.6)$$

The $Xe(OTeF_5)_4$ molecule has been characterized in the solid state by Raman[38,59] and X-ray crystallography.[60] Both methods of characterization show the local environment around Xe is square-planar but the crystal structure (Figure 1.4) shows that the TeF_5 groups are bent out-of-plane, as a result of the steric requirements of the valence electron lone pairs on oxygen, and bend with two groups up and two groups down to minimize steric interactions between the bulky $OTeF_5$ ligands.[60]

The ^{19}F and ^{129}Xe NMR spectra of $Xe(OTeF_5)_4$ have been recorded in $CFCl_3$[38,56] and $C_4F_9SO_2F$[58] solvents and show that the four $OTeF_5$ groups are equivalent. The mixed compounds, $Xe(OTeF_5)_{4-x}F_x$ (x = 0–3), have also been synthesized, by ligand exchange between XeF_4 and $Xe(OTeF_5)_4$, and the characterizations of the resulting species by ^{19}F and ^{129}Xe NMR spectroscopy.[38] The ^{129}Xe chemical shifts of the compounds increase linearly when the $OTeF_5$ groups are replaced by fluorine (211 ppm/$OTeF_5$ group). The

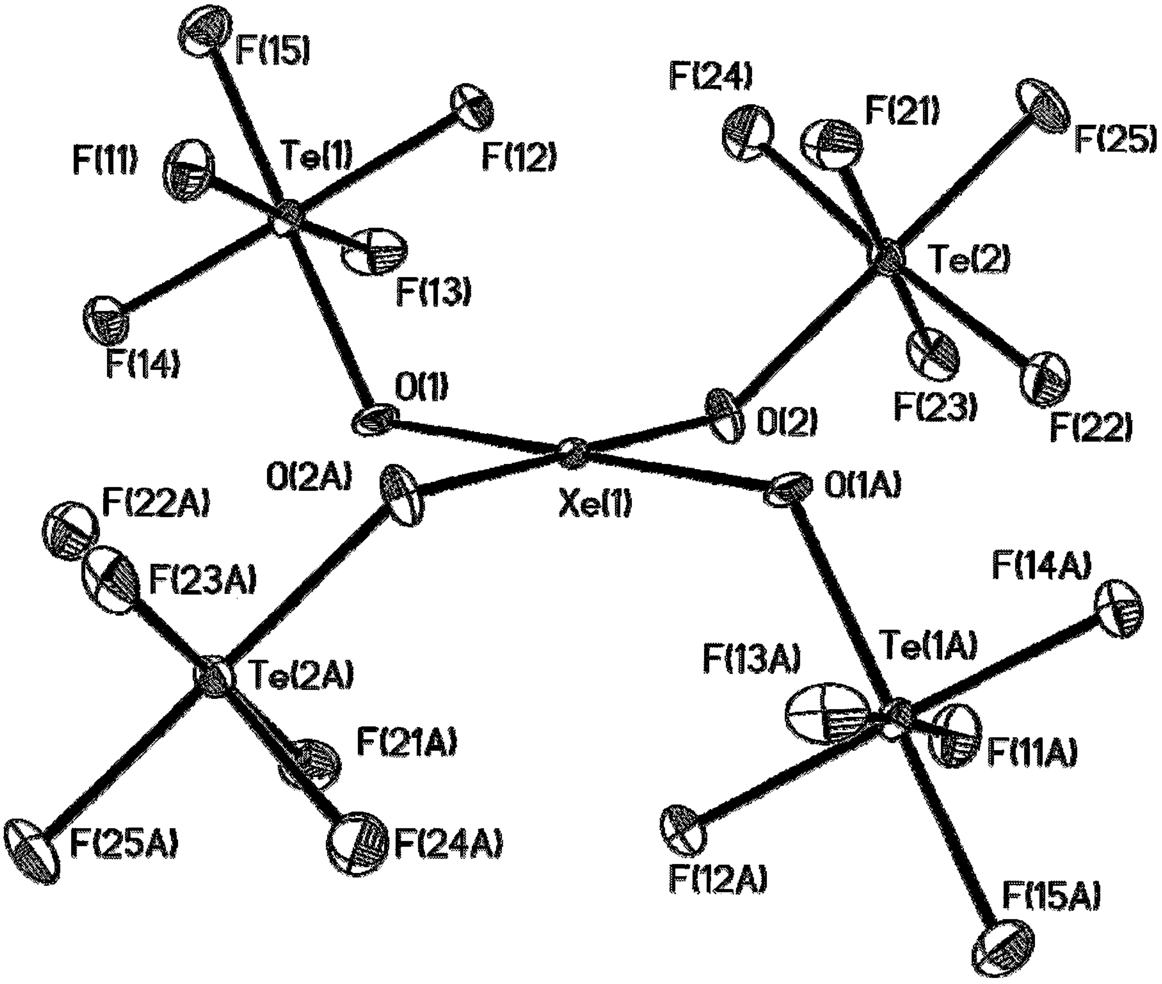

Figure 1.4. The X-ray crystal structure of $Xe(OTeF_5)_4$. Thermal ellipsoids are shown at the 50% probability level. From ref 60.

low-frequency shift with decreasing numbers of fluorine ligands reflect the higher effective electronegativity of fluorine compared to that of the $OTeF_5$ group[38] and is a consistent trend that has been observed for other $OTeF_5$ derivatives of Xe.[56] A similar trend is also observed in the ^{129}Xe NMR spectrum of the related family of cations, $F_xXe(OTeF_5)_{3-x}^+$ (x = 0–2), but the difference is 182 ppm/$OTeF_5$ group.[61] The cations were synthesized by the reaction of $Xe(OTeF_5)_4$ in excess SbF_5. Antimony pentafluoride acts as a Lewis acid as well as a source of fluoride ions which scramble with the $OTeF_5$ groups giving rise to the mixed cation series, $F_xXe(OTeF_5)_{3-x}^+$.

Although the entire family of cations was observed in solution, none have been isolated or characterized in the solid state. The difficulty lies in the reluctance of Xe(IV) to act as a ligand donor. As noted above, XeF_4 will only donate a fluoride ion in the presence of an exceptionally strong Lewis base, such as SbF_5. However, with fluorine atoms present, the ligands scramble to give a random distribution of all possible mixed cations, XeF_3^+, $XeF_2(OTeF_5)^+$, $XeF(OTeF_5)_2^+$, and $Xe(OTeF_5)_3^+$. A possible solution that the authors proposed was to use the corresponding $OTeF_5$ analogue of SbF_5, $Sb(OTeF_5)_5$.[61] Unfortunately, the latter molecule is unstable, decomposing to $Sb(OTeF_5)_3$ and $F_5TeOOTeF_5$ and therefore must be synthesized in situ at low temperatures. A solution of "$Sb(OTeF_5)_5$" in SO_2ClF was prepared by adding an equimolar amount of $Xe(OTeF_5)_2$ to $Sb(OTeF_5)_3$ (eq 1.7) and was shown to contain an equimolar mixture of $[XeOTeF_5][Sb(OTeF_5)_6]$ and $Sb(OTeF_5)_3$ which behaves as though it were $Sb(OTeF_5)_5$ (eq 1.8).[61] Such a reaction has been successful in forming the $O{=}Xe(OTeF_5)_3^+$ cation

$$2Xe(OTeF_5)_2 + 2Sb(OTeF_5)_3 \xrightarrow{SO_2ClF} [XeOTeF_5][Sb(OTeF_5)_6] + Sb(OTeF_5)_3 + Xe \quad (1.7)$$

$$[XeOTeF_5][Sb(OTeF_5)_6] + Sb(OTeF_5)_3 \xrightarrow{SO_2ClF} \text{“}Sb(OTeF_5)_5\text{”} + Xe \tag{1.8}$$

from neutral $O{=}Xe(OTeF_5)_4$ (eq 1.9) but similar attempts to form the $Xe(OTeF_5)_3^+$ cation from neutral $Xe(OTeF_5)_4$ were unsuccessful.[61] Therefore, to date, no $OTeF_5$ ligated

$$\text{“}Sb(OTeF_5)_5\text{”} + O{=}Xe(OTeF_4)_4 \xrightarrow{SO_2ClF} [O{=}Xe(OTeF_5)_3][Sb(OTeF_5)_6] \tag{1.9}$$

cation of Xe(IV) has been isolated or characterized in the solid state.

1.2.3. C_6F_5 and OIO_4 Derivatives of Xe(IV)

The only example of a C–Xe(IV) bond that is presently known is the $C_6F_5XeF_2^+$ cation. The BF_4^- salt was obtained by the reaction of stoichiometric amounts of $C_6F_5BF_2$ and XeF_4 in CH_2Cl_2 at –55 °C and the product, $[C_6F_5XeF_2][BF_4]$, was precipitated as a pale yellow solid (eq 1.10).[62] Pure, solid $[C_6F_5XeF_2][BF_4]$ was found to be very shock

$$XeF_4 + C_6F_5BF_2 \xrightarrow[-55\ ^\circ C]{CH_2Cl_2} [C_6F_5XeF_2][BF_4] \tag{1.10}$$

sensitive. The crystal structure shows a pentagonal planar arrangement around Xe (Figure 1.5) when the short contacts to the anion are also considered. The longer contacts are puckered out of the molecular plane presumably to alleviate steric congestion within the plane.[63] This salt was also characterized by solution ^{19}F, ^{11}B, and ^{129}Xe NMR spectroscopy in CH_3CN at –40 °C and aHF at –40 and –80 °C to provide a complete interpretation of the NMR spectra. In solution, CH_3CN molecules coordinate to xenon, forming the adduct cation, $[C_6F_5XeF_2{\cdot}(NCCH_3)_n]^+$. Crystallization from CH_3CN yielded $[C_6F_5XeF_2{\cdot}1.5(NCCH_3)][BF_4]$ in which three crystallographically independent structural units were observed. In one case, a single CH_3CN ligand is N-coordinated to xenon giving a square planar coordination around xenon (Figure 1.6.a). In each of the other

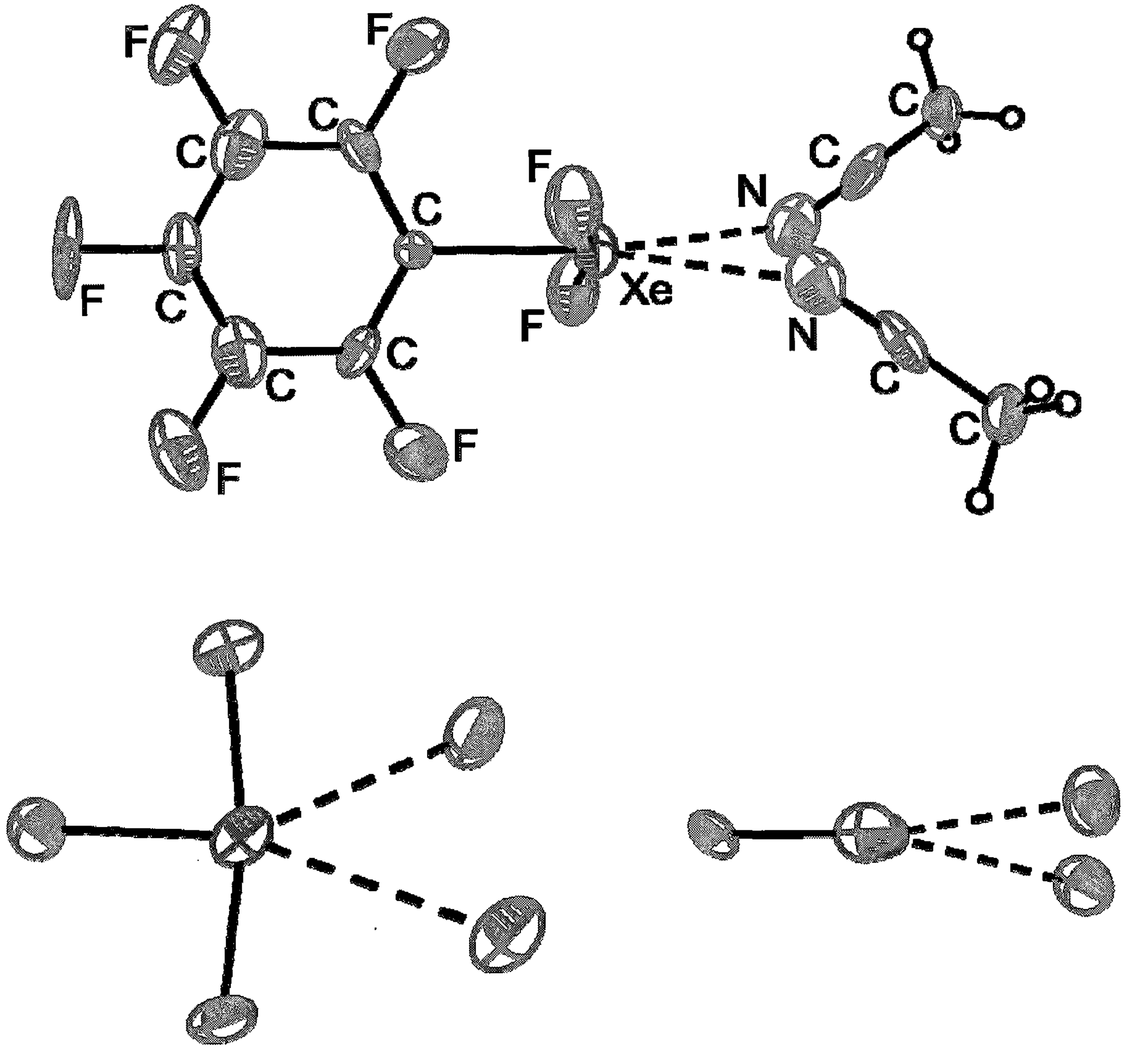

Figure 1.5. Pentagonal-planar geometry around xenon in $[C_6F_5XeF_2][BF_4]$. Thermal ellipsoids are shown at the 50% probability level. From ref 63.

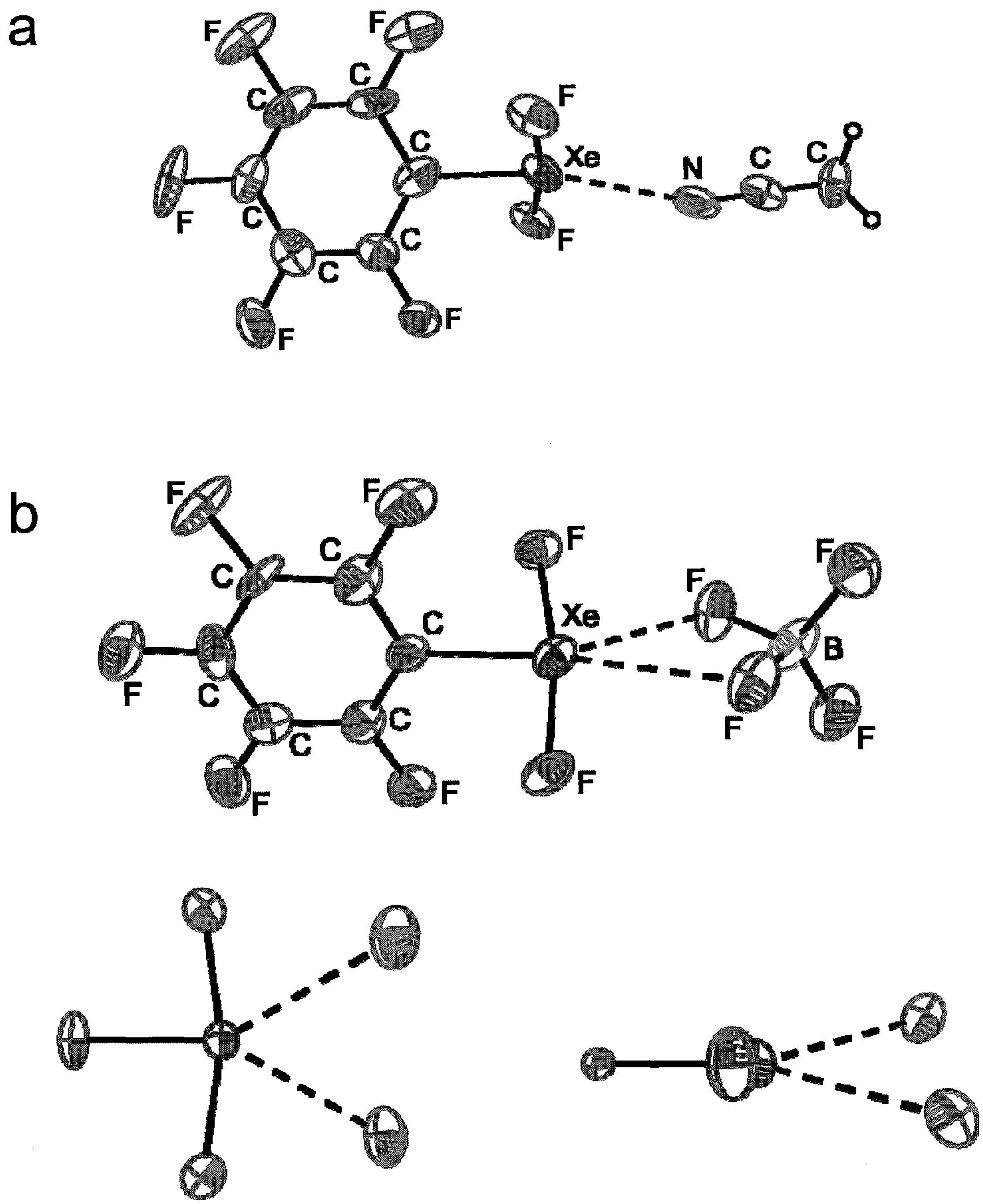

Figure 1.6. (a) Square-planar and (b) pentagonal-planar geometries and thermal motion around xenon in the three crystallographically independent molecules in $[C_6F_5XeF_2{\cdot}1.5(NCCH_3)][BF_4]$. Thermal ellipsoids are shown at the 50% probability level. From ref 63.

independent structural units, two CH_3CN ligands are N-coordinated to xenon giving rise to a pentagonal-planar arrangement around xenon (Figure 1.6.b,c). In each of the latter cases, the steric requirements in the molecular plane distort the longer contacts to CH_3CN out of the plane and to a greater extent than was observed for $[C_6F_5XeF_2][BF_4]$.[63]

A preliminary study of a mono-substituted $OIOF_4$ derivative, $F_3XeOIOF_4$, has been reported.[64] The ^{19}F and ^{129}Xe NMR study of $F_3XeOIOF_4$ (eq 1.11) indicates that $OIOF_4$ group is slightly more electronegative than the $OTeF_5$ group based on the ^{129}Xe

$$XeF_4 + (IO_2F_3)_2 \xrightarrow{CFCl_3} F_3XeOIOF_4 + IOF_3 + \tfrac{1}{2}O_2 \qquad (1.11)$$

chemical shift of 24.4 ppm for monosubstituted $F_3XeOIOF_4$ relative to −25.5 ppm for $F_3XeOTeF_5$, suggesting that the $OIOF_4$ group the most highly electronegative ligand known next to fluorine itself.[64] The study also indicated that $F_3XeOIOF_4$ has a square planar arrangement around xenon, similar to XeF_4, but with one of the fluorine ligands replaced by the $OIOF_4$ group. To date, there has been no characterization of a Xe(IV) compound containing the $OIOF_4$ group in the solid state.

1.2.4. Oxide Fluoride Species of Xe(IV)

In contrast with the Xe(IV) fluoro-species, XeF_4, XeF_3^+, and XeF_5^-, which have been extensively characterized in solution and in the solid state (see Section 1.2.1), knowledge of Xe(IV) oxide fluoride species is much more limited. This stems from several issues including a reliable, high-yield synthesis for $XeOF_2$.

While there are previous reports of $XeOF_2$[65–67] and $XeOF_3^-$ [67] in the literature, which will be elaborated on in Section 3.1, none have proven to be definitive. Although inconclusive, these studies clearly show that the oxides and oxide fluorides of Xe(IV) are inherently unstable and decompose either explosively by redox elimination of O_2 (eq 1.12) or by disproportionation to Xe(VI) and Xe(II) (eq. 1.13 and 1.14).[67] A related disproportionation is also encountered when XeF_4 hydrolyzes in water to form XeO_3, HF, Xe, and O_2 (eq 1.15).[68,69]

$$XeOF_2 \longrightarrow XeF_2 + \tfrac{1}{2}O_2 \qquad (1.12)$$

$$2XeOF_2 \longrightarrow XeO_2F_2 + XeF_2 \qquad (1.13)$$

$$2[Cs][XeOF_3] \longrightarrow [Cs][XeO_2F_3] + XeF_2 + CsF \qquad (1.14)$$

$$2XeF_4 + 4H_2O_{(excess)} \xrightarrow{H_2O} XeO_3 + 8HF + Xe + \tfrac{1}{2}O_2 \qquad (1.15)$$

1.3. Recent Aspects of Xenon(II) Chemistry

1.3.1. Xenon(II) Oxide-Fluorides, $Xe_3OF_3^+$ and $O(XeF)_2$

With a relative abundance of known Xe(II) compounds, it is somewhat surprising that there have been no definitive reports of a neutral oxide, or oxide-fluoride, of Xe(II). Xenon(II) oxide, XeO, which has been shown to have an unstable $^3\Pi$ ground state is therefore unlikely to exist as a monomer in the solid-state.[70] The first oxide-fluoride of Xe(II), $Xe_3OF_3^+$, has recently been synthesized by the reaction of XeF_2 with $[H_3O][PnF_6]$ in HF solvent (Pn = As, Sb; eq 1.16).[71] The resulting salts have been characterized in the solid state by Raman spectroscopy and single-crystal X-ray diffraction. Subsequently, $O(XeF)_2$ has been synthesized by the neat reaction of $[Xe_3OF_3][AsF_6]$ with NOF (eq 1.17).[72] The ^{19}F and ^{129}Xe NMR spectra of $O(XeF)_2$, in conjunction with the ^{16}O-, ^{17}O-,

$$3XeF_2 + [H_3O][PnF_6] \xrightarrow[-50\ ^\circ C]{HF} [Xe_3OF_3][PnF_6] + 3HF \qquad (1.16)$$

$$[Xe_3OF_3][AsF_6] + NOF \xrightarrow{\text{neat}} O(XeF)_2 + XeF_2 + [NO][AsF_6] \qquad (1.17)$$

and ^{18}O-enriched Raman spectra, and calculated vibrational frequencies,[72] indicate that the structure is analogous to that of the isoelectronic $F(XeF)_2^+$ cation.[19,71,73–79] However, the previous Raman spectra were wrongly assigned and incorrectly assigned bands to a non-existent $(XeO)_n$ cyclic polymer.[72]

1.3.2. Xenon(II) Nitrates

The $O(XeF)_2$ molecule has played a role in the synthesis of the first nitrate of xenon, $FXeONO_2$. The mono-nitrate has been previously postulated as an intermediate formed by HF displacement of XeF_2 by anhydrous HNO_3 solvent.[80,81] These results were reexamined when $FXeONO_2$ was successfully synthesized by the reaction of $[Xe_3OF_3][AsF_6]$ with O_2NF (eq 1.18).[72] The crystal structure of $FXeONO_2$ was

$$[Xe_3OF_3][AsF_6] + 2NO_2F \xrightarrow{\text{neat}} FXeONO_2 + 2XeF_2 + [NO_2][AsF_6] \quad (1.18)$$

determined and $FXeONO_2$ was also characterized in SO_2ClF and CH_3CN solvents by ^{14}N, ^{19}F, and ^{129}Xe NMR spectroscopy.[72] However, the interpretations of the solid-state ^{16}O- and ^{18}O-enriched Raman spectra were over-simplified.[72] As a result, the proposed mechanism was incorrect and the possible intermediacy of $O(XeF)_2$ was also missed.

1.3.3. XeF_2 as a Ligand

Another important category of Xe(II) compounds are XeF_2 coordination complexes with metal cation centers, which have been synthesized according to eq 1.19.[82,83] A list of XeF_2 coordination complexes with metal cation centers is given in

$$[M^{n+}][PnF_6^-]_n + mXeF_2 \xrightarrow{HF} [M(XeF_2)_p^{n+}][PnF_6^-]_n + (m-p)XeF_2 \quad (1.19)$$

Table 1.1 in addition to the aforementioned XeF_4 adduct, $[Mg(XeF_2)(XeF_4)][AsF_6]_2$[42] (Section 1.2.1).

The number of XeF_2 molecules coordinated to the metal center ranges from one to nine, with only an example of a seven-coordinate complex missing.[82,83] In these complexes, XeF_2 coordinates to a metal cation center either as a terminal ligand (Figure 1.7.a) or as a bridging molecule between two metal centers (Figure 1.7.b). If the XeF_2 molecule coordinates as a terminal ligand, a single fluorine atom coordinates to the Lewis acidic metal center and results in a lengthening of the bridging Xe–F bond and a shortening of the terminal Xe–F bond. In contrast, when XeF_2 bridges between two metal centers, both Xe–F bond lengths typically increase.[82,83] Some requirements that should be fulfilled in order to obtain homoleptic compounds include an electron affinity of 15 eV for the cation, a weakly basic anion (e.g., SbF_6^-) and the coordination number of the cation should be 6. The latter gives rise to an optimum arrangement with regards to repulsions between the negative F-ligands of the coordinating XeF_2 molecule and their more positive xenon domains.[82] It has also noted that it is difficult, or even impossible, to predict what kind of structure a newly isolated coordination compound will adopt.[82]

The Raman spectra of the aforementioned XeF_2 coordination compounds display intense Xe–F stretching modes while the A–F (A = B, P, As, Sb) and M–F vibrations are usually far less intense.[82,83] When XeF_2 coordinates to one or two metal centers, there is a transfer of electron density from the ligand to the metal center, rendering Xe more electropositive and shifting ν(Xe–F) to higher frequency relative to the symmetric

Table 1.1. Coordination Complexes Involving XeF_2 as a Ligand [a]

M^+	M^{2+}(alkaline earth metal)	M^{2+}(transition or main-group metal)	M^{3+}(lanthanide metal)
$[Li(XeF_2)_3][AsF_6]$	$[Mg(XeF_2)_4][AsF_6]_2$	$[Cu(XeF_2)_6][SbF_6]_2$	$[La(XeF_2)_{2.5}][AsF_6]_3$
$[Ag(XeF_2)_2][AsF_6]$	$[Mg(XeF_2)_2][AsF_6]_2$	$[Zn(XeF_2)_6][SbF_6]_2$	$[Nd(XeF_2)_{2.5}][AsF_6]_3$
$[Ag(XeF_2)_2][PF_6]$	$[Mg(XeF_2)_2][SbF_6]_2$	$[Cd(XeF_2)][BF_4]_2$	$[Nd(XeF_2)_3][SbF_6]_3$
	$[Ca(XeF_2)_5][PF_6]_2$	$[Cd(XeF_2)_5][PF_6]_2$	
	$[Ca_2(XeF_2)_9][AsF_6]_4$	$[Cd(XeF_2)_4][AsF_6]_2$	
	$[Ca_2(XeF_2)_4][AsF_6]_2$	$[Cd_2(XeF_2)_{10}][SbF_6]_4$	
	$[Ca(XeF_2)_{2.5}][AsF_6]_2$	$[Cd_2(XeF_2)_6][SbF_6]_4$	
	$[Sr(XeF_2)_3][PF_6]_2$	$[Cd_3(XeF_2)_4][SbF_6]_6$	
	$[Sr(XeF_2)_3][AsF_6]_2$	$[Pb_3(XeF_2)_{11}][PF_6]_6$	
	$[Ba(XeF_2)_4][PF_6]_2$	$[Pb(XeF_2)_3][PF_6]_2$	
	$[Ba(XeF_2)_5][AsF_6]_2$	$[Pb(XeF_2)_3][AsF_6]_2$	
	$[Ba(XeF_2)_5][SbF_6]_2$		

[a] From ref 82.

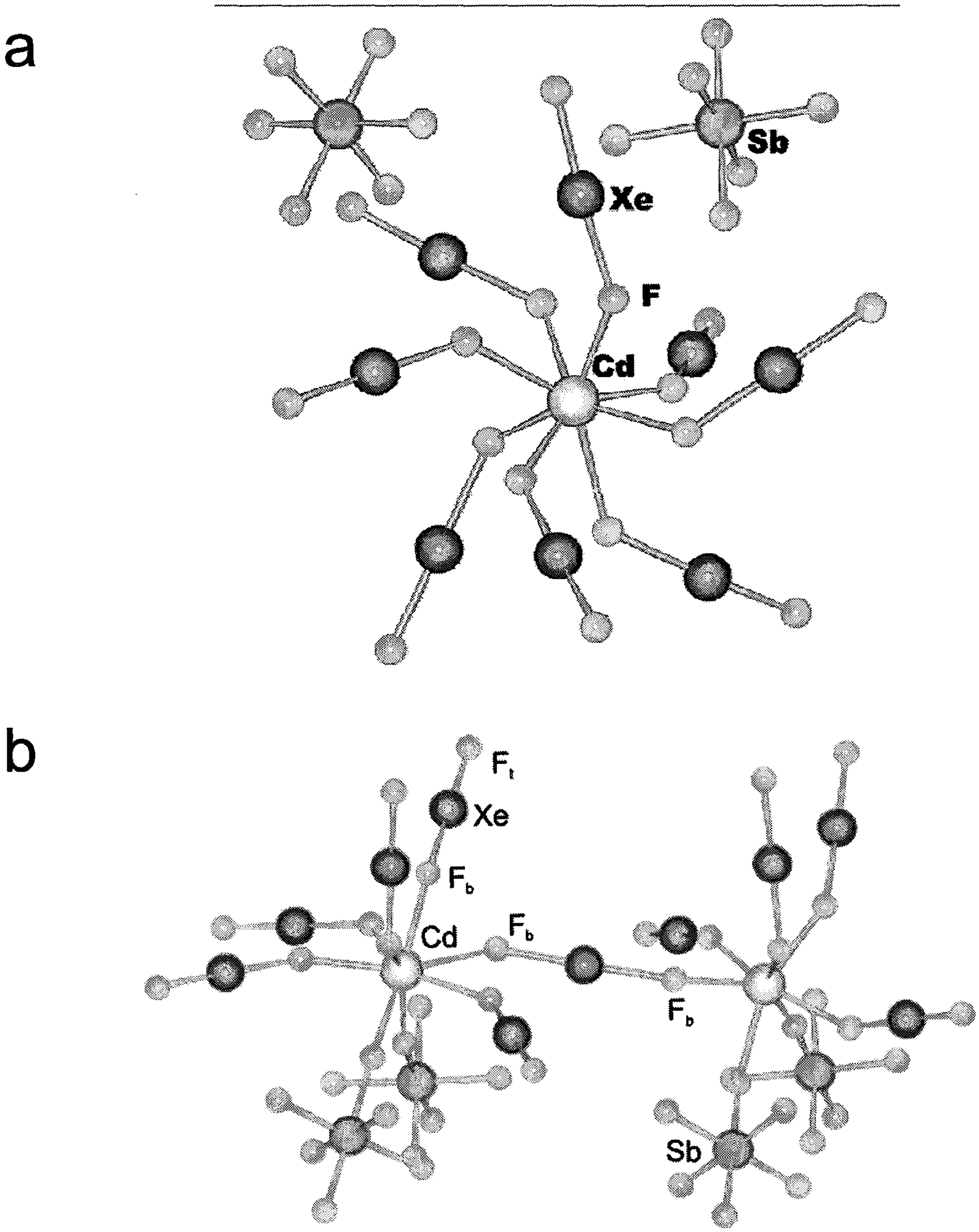

Figure 1.7. Crystal structures of (a) $[Cd(XeF_2)_8][SbF_6]_2$ and (b) $[Cd_2(XeF_2)_{10}][SbF_6]_4$ showing XeF_2 coordinated to metal cations as terminal and bridging ligands, respectively. From ref 84.

stretching band of free XeF_2 at 497 cm^{-1}. When XeF_2 is terminally coordinated, the band corresponding to XeF_2 is replaced by two bands: the band at higher frequency corresponds to the terminal vibration ν(Xe–F) and occurs between 544 and 584 cm^{-1}. The band at lower frequency, occurring between 411 and 479 cm^{-1}, corresponds to the stretching vibration of the Xe---F brindge bond, ν(Xe---F).[82,83] Typically for a bridging XeF_2 molecule, a single ν(XeF_2) band is observed and occurs in the range from 500 to 535 cm^{-1}.[82,83] It is interesting to note that no mention was made or inferred that would indicate whether or not the ν(Xe–F) stretching modes are in any way coupled, either intra- or intermolecularly.

1.4. Krypton(II) Chemistry

Krypton is the only noble gas other than xenon to form isolable compounds in macroscopic amounts.[12] The chemistry of krypton is limited because the only stable oxidation states known are 0 and +2, although there was an early spurious report of KrF_4[85] that was subsequently disproven.[86] Krypton difluoride was the first krypton compound to be synthesized and represents the starting point for all other krypton chemistry. Unlike XeF_2, KrF_2 cannot be synthesized using high-temperature, high-pressure methods because KrF_2 is an endothermic compound ($\Delta H_f = 60.2$ kJ mol^{-1}, gas at 93 °C).[87,88] Macroscopic quantities of KrF_2 can be synthesized by using high-energy particle beams (e^-, protons, α),[89,90] electric discharges,[86,91,92] UV irradiation,[93–97] or hot wire reactors[97–99] as means to generate fluorine atoms at low temperatures (eq 1.20). The latter two methods are currently preferred. In all cases, highly reactive fluorine radicals react with solid krypton at low temperatures to form the metastable KrF· radical (eq 1.21) which then likely reacts according to eqs 1.22–1.24 to form KrF_2.

$$F_2 \longrightarrow 2F\cdot \tag{1.20}$$

$$F\cdot + Kr \longrightarrow KrF\cdot \tag{1.21}$$

$$KrF\cdot + F_2 \longrightarrow KrF_2 + F\cdot \tag{1.22}$$

$$KrF\cdot + KrF\cdot \longrightarrow KrF_2 + Kr \tag{1.23}$$

$$KrF\cdot + F\cdot \longrightarrow KrF_2 \tag{1.24}$$

In the solid state, KrF_2 is dimorphic with a high-temperature β-phase that was obtained at −80 °C (Figure 1.8.a) that reversibly converts to a low-temperature α-phase (Figure 1.8.b) upon cooling to −125 °C.[99,100] The Kr-F bond length in α-KrF_2 is 1.894(5) Å[99] and is in excellent agreement with that determined for β-KrF_2 (1.89(2) Å, −80 °C) by X-ray diffraction[101] and for gaseous KrF_2 by electron diffraction (1.889(10) Å, −40 °C).[102] The dimorphism is also apparent in the Raman spectra where α-KrF_2 possesses a single ν(KrF_2) stretching band and β-KrF_2 is factor-group split into two ν(KrF_2) stretching bands.[99,100]

Like XeF_2, KrF_2 has been reacted with strong Lewis acid pentafluorides in order to synthesize salts having the formulations [KrF][MF_6] (eq 1.25 and 1.26) and [Kr_2F_3][MF_6] (eq 1.27) where M = Nb, Ta, Ru, Pt, As, Sb, V, Rh, Pt, Au, and/or Bi.[12] In the crystal structures of [KrF][AsF_6], [KrF][SbF_6], and [KrF][BiF_6] (Figure 1.9)[99] the

$$KrF_2 + 2MF_5 \longrightarrow [KrF][Pn_2F_{11}] \qquad (Pn = As, Sb, Bi) \tag{1.25}$$

$$KrF_2 + PnF_5 \longrightarrow [KrF][PnF_6] \tag{1.26}$$

$$2KrF_2 + PnF_5 \longrightarrow [Kr_2F_3][PnF_6] \tag{1.27}$$

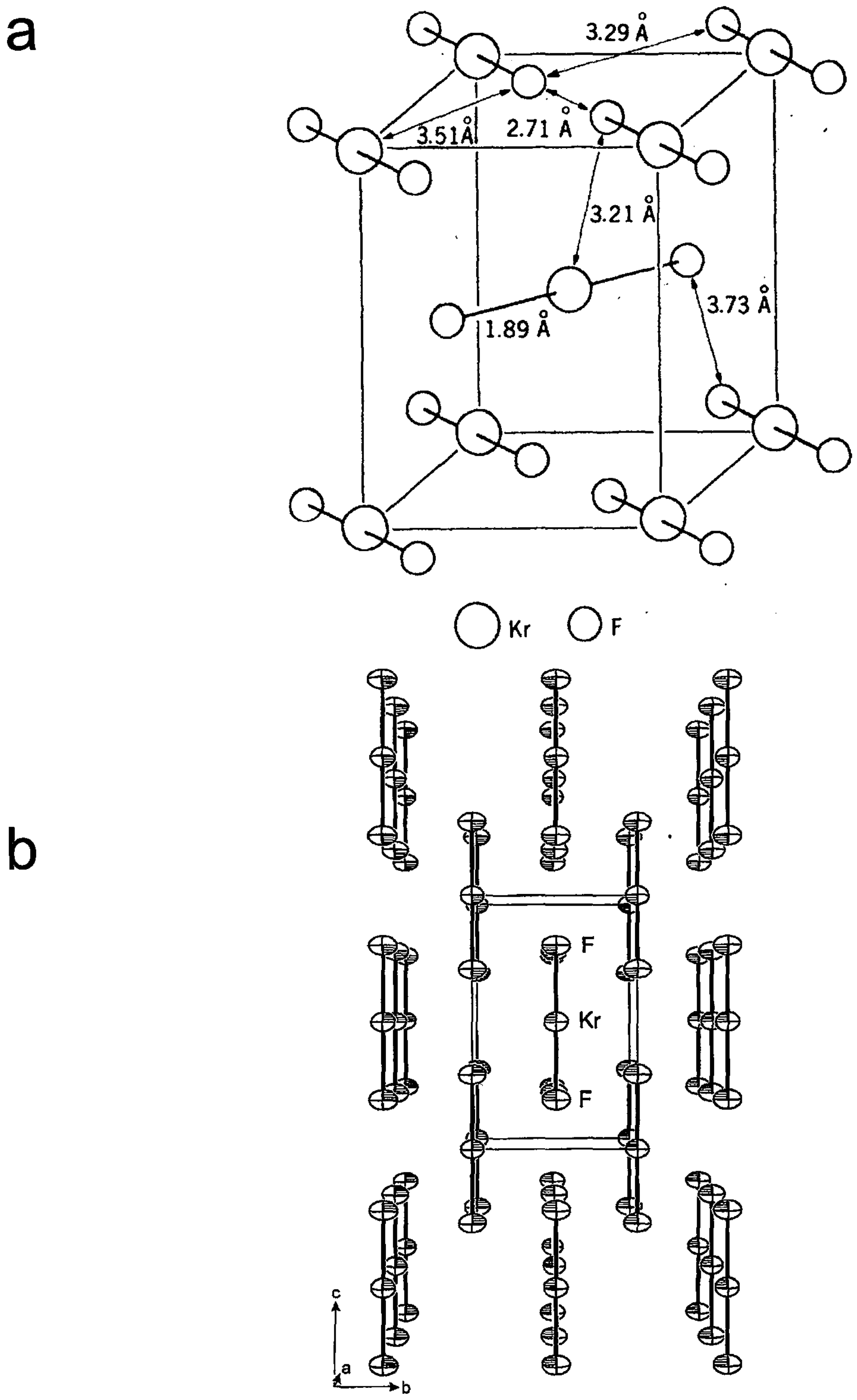

Figure 1.8. Packing diagrams for (a) β-KrF$_2$ (ref 101) and (b) α-KrF$_2$ viewed along the *a*-axis (ref 99).

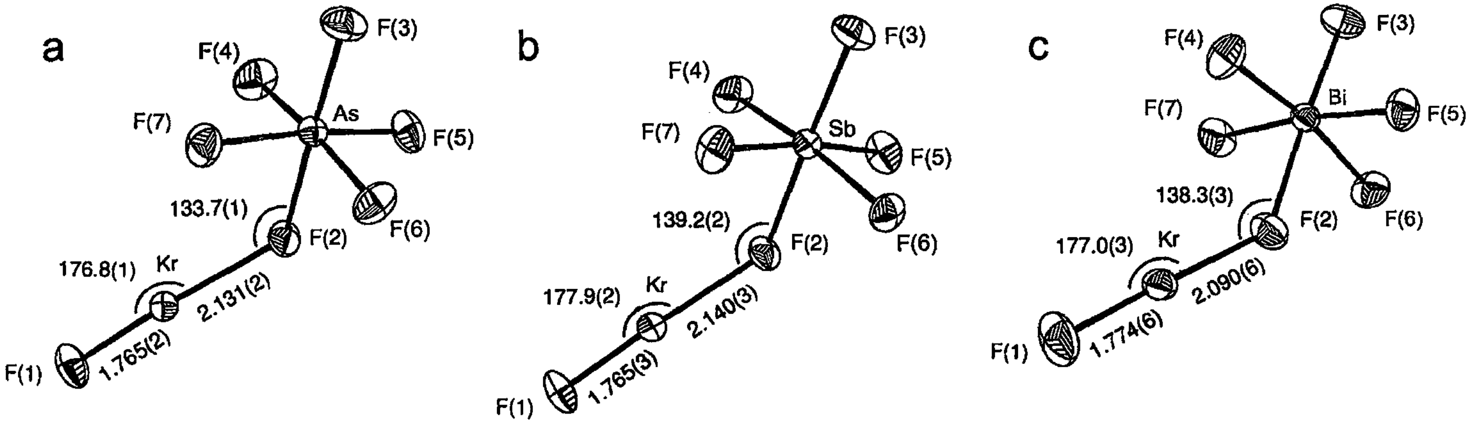

Figure 1.9. Structures of (a) [KrF][AsF_6], (b) [KrF][SbF_6], and (c) [KrF][BiF_6]; thermal ellipsoids are shown at the 50% probability level.From ref 99.

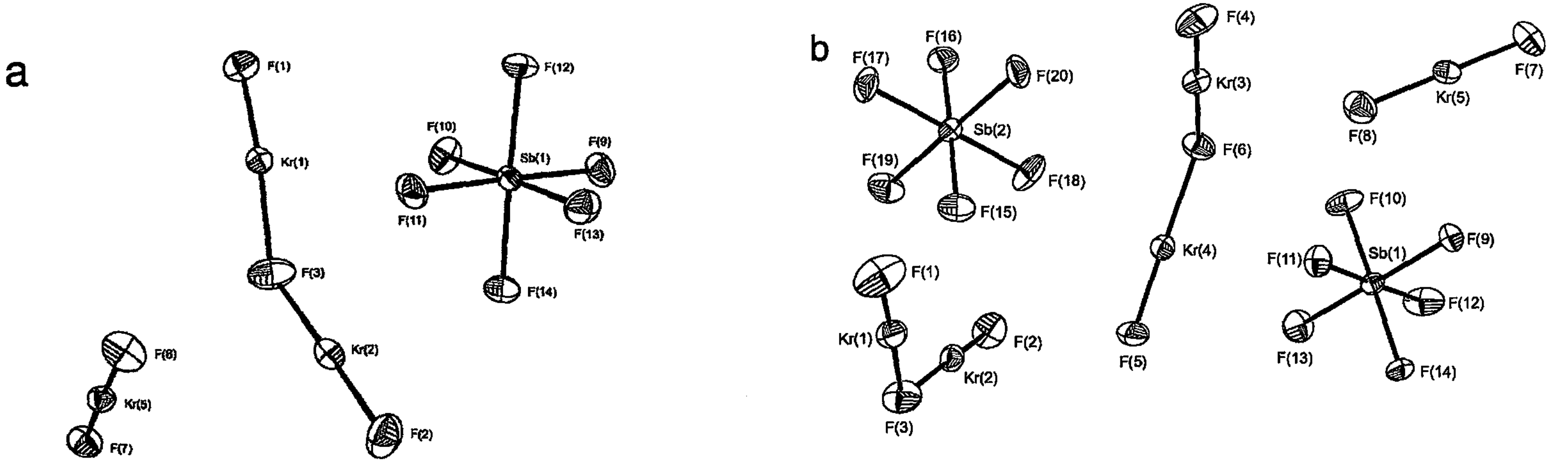

Figure 1.10. Structures of (a) [Kr_2F_3][SbF_6]·KrF_2 and (b) [Kr_2F_3]$_2$[SbF_6]$_2$·KrF_2; thermal ellipsoids are shown at the 50% probability level.From ref 99.

KrF^+ bond lengths (1.765(2)–1.774(6) Å) are significantly shorter than in free KrF_2 (1.89(2) Å,[101] 1.889(10) Å[99]) and, while the cation in each case is ion paired to the anion, the Kr---F_b bond lengths are sufficiently long (2.090(6)–2.140(3) Å) to be considered contacts and not adducted. The crystal structures of $[Kr_2F_3][SbF_6]\cdot KrF_2$ and $[Kr_2F_3]_2[SbF_6]_2\cdot KrF_2$ (Figure 1.10)[99] show that the $Kr_2F_3^+$ cations are more isolated than KrF^+ cations in their salts. In both cases, as with the $Xe_2F_3^+$ cations in their salts,[73,78,79] the cation is bent at the bridging fluorine to give a V-shaped cation. The bent angle is a consequence of the steric requirements of the valence electron lone pairs on fluorine.

Several other Kr(II) derivatives have been synthesized, including the only oxygen bonded species, $Kr(OTeF_5)_2$, which has been synthesized at low-temperature by the reaction of KrF_2 and $B(OTeF_5)_3$ (eq 1.28).[103] A family of nitrogen bonded cations R_FCNKrF^+ (R_F = CF_3, C_2F_5, n-C_3F_7) has also been synthesized (eq. 1.29)[104] as has $HCNKrF^+$ (eq. 1.30).[105] All of the aforementioned species have Xe(II) analogues and

$$3KrF_2 + 2B(OTeF_5)_3 \xrightarrow[-90\text{ to }-120\ ^\circ C]{SO_2ClF} 3Kr(OTeF_5)_2 + 2BF_3 \qquad (1.28)$$

$$KrF_2 + R_FCNAsF_5 \xrightarrow[-60\ ^\circ C]{BrF_5} [R_FCNKrF][AsF_6] \qquad (1.29)$$

$$KrF_2 + [HCNH][AsF_5] \xrightarrow[-60\ ^\circ C]{HF} [HCNKrF][AsF_6] + HF \qquad (1.30)$$

have been characterized by low-temperature NMR spectroscopy.[103–105] At present, no crystal structure has been determined for either a Kr–O or Kr–N bonded species because they are only somewhat stable in solution at low temperature and decompose rapidly when warmed to −78 °C and −50 to −60 °C, respectively.

In contrast to the large number of XeF_2 adducts with metal centers that are known, KrF_2 has only been shown to form Lewis acid-base adducts with group 6 d^0

transition metal centers, namely $MOF_4{\cdot}KrF_2$ (M = Cr,[106] Mo,[107] W[107]). The structural characterizations of these adducts were limited to solution ^{19}F NMR[107] and solid-state Raman spectroscopy[106,107] and indicate that the adducts result from weak coordination of KrF_2 through a fluorine bridge to the metal atom. In the absence of X-ray crystal structures, an assessment of the degree of coordination, based on the relative bond lengths of terminal and bridge Kr–F bonds cannot be presently made. In addition, there are no examples known in which KrF_2 acts as an adduct to a main-group center.

1.5. Purpose and Scope of the Present Research

The overall goal of this Thesis is to extend and deepen our knowledge of the fundamental chemistry of the noble-gas elements, namely, xenon and krypton. More specifically, a major focus of the research is to extend the chemistry of Xe(IV) by the synthesis and characterization of Xe(IV) oxide and oxide fluoride derivatives. A reliable synthetic route to bulk amounts of the precursor oxide fluoride, $XeOF_2$, and a thorough characterization of the compound was lacking in the literature. The development of a reliable synthetic protocol would offer the possibility to extend Xe(IV) oxide fluoride chemistry by studying the Lewis donor and acceptor properties of $XeOF_2$. Reaction of $XeOF_2$ with fluoride ion sources such as CsF or the so-called "naked fluoride ion source," $[N(CH_3)_4][F]$, are expected to yield the corresponding anion, $XeOF_3^-$, while the reaction of $XeOF_2$ with an oxidatively resistant nitrogen base, such as CH_3CN, might be expected to yield the first example of a Xe(IV)–N bond. The electron-pair donor abilities of $XeOF_2$ towards Lewis acids such as $[XeF][AsF_6]$ and in superacidic media such as

HF/AsF_5 are also of interest because significant electron density should exist on the oxygen atom of $XeOF_2$ rendering it moderately basic. The aforementioned focus on Lewis donor and acceptor properties of $XeOF_2$ is of interest because of the anticipated instability of the Xe(IV) oxide-fluorides relative to their Xe(VI) analogues.

In related noble-gas adduct chemistry, another facet of the research is the syntheses and characterization of XeF_2 adducts with non-metal main-group centers such as Br(V) and Cl(V) with an emphasis on their characterization by single-crystal X-ray diffraction. The chemistry may also be expected to be extendable to the more reactive KrF_2 molecule, thereby providing the first KrF_2 adducts to non-metal main-group center. In addition, studies of these systems are expected to shed light on the stereochemical activity of the valence electron lone pair of Br(V) and how it is affected by coordination (steric crowding).

The final area of study in this Thesis is a more complete characterization of the only example of a xenon nitrate, $FXeONO_2$. The syntheses of $FXeON^{16}O_2$ and $FXeON(^{18}OO)$ require a fuller reinvestigation by vibrational spectroscopy and the resulting solid-state ^{16}O- and ^{18}O-enriched Raman spectra require reinterpretation. The intermediate oxide fluoride, $O(XeF)_2$, was expected to play a role in the reaction and therefore also required reinterpretation of its solid-state ^{16}O- and ^{18}O-enriched Raman spectra.

CHAPTER 2

EXPERIMENTAL SECTION

2.1. Standard Techniques

2.1.1. Dry Box and Vacuum Line Techniques

The compounds used and prepared during the course of this work were moisture- and temperature-sensitive, and were handled under rigorously anhydrous conditions on glass and metal vacuum line systems or in an inert atmosphere (N_2 gas) dry box (Vacuum Atmospheres Model DLX, oxygen and moisture <0.1 ppm) equipped with a glass cryowell for low-temperature work. Preparative work inside the dry box requiring low temperatures was accomplished using a metal Dewar filled with 4.5 mm copper-plated spheres (air rifle BBs) that had previously been cooled to ca. –140 °C in the glass cryowell (–196 °C) of the dry box.

Preparative work involving volatile fluorides that attack glass (e.g., HF) were carried out on metal vacuum lines constructed primarily from 316 stainless steel and nickel and fitted with 316 stainless steel valves (Autoclave Engineers, Inc., Figure 2.1). Pressures were measured at ambient temperatures using MKS Model PDR-5B pressure transducers having wetted surfaces constructed of Inconel. The pressure transducer possessed a range of 0–1150 Torr, which was accurate to ±0.5 Torr.

Reactions that did not involve transfer of materials that attack glass were carried out on Pyrex glass vacuum lines equipped with grease-free 6-mm J. Young glass stopcocks outfitted with PTFE barrels (Figure 2.2). Pressures inside the glass manifold

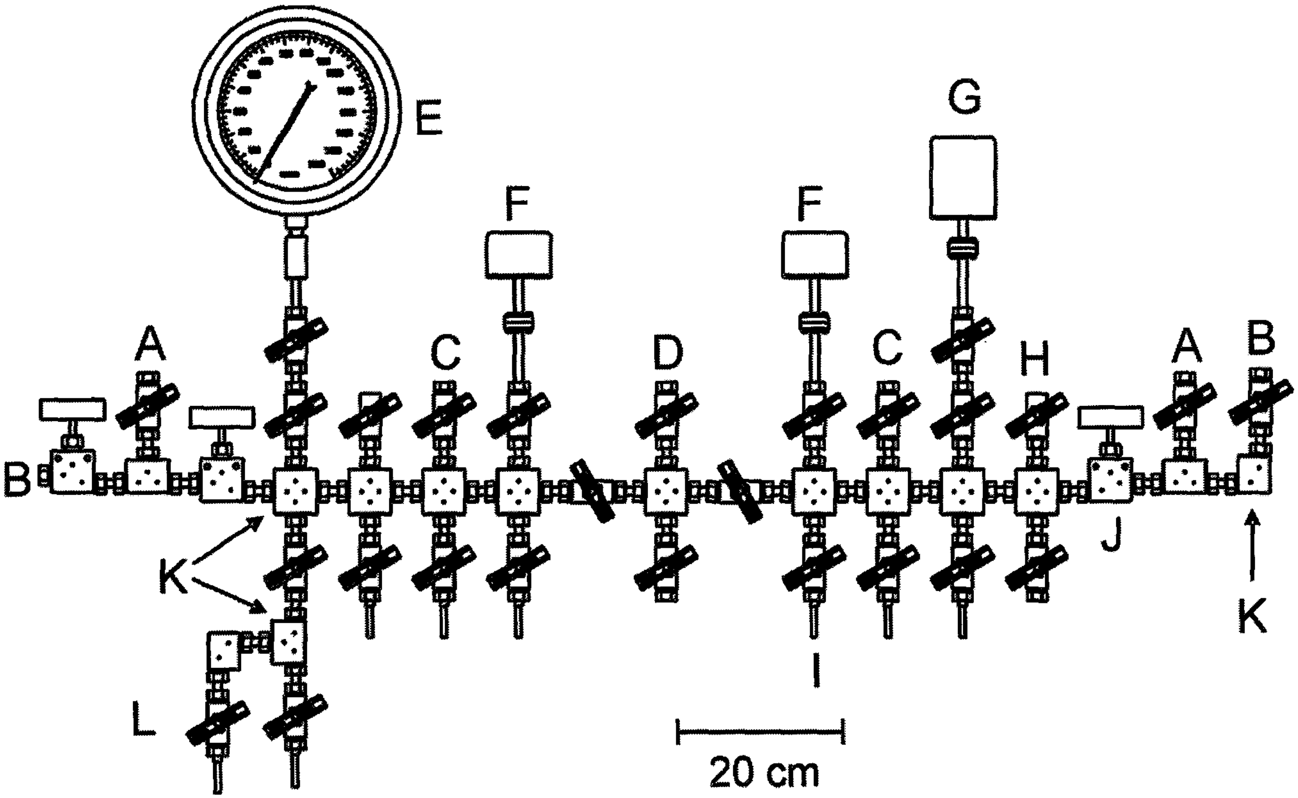

Figure 2.1. The metal vacuum line used for the manipulation of corrosive materials. (A) Outlet to liquid nitrogen and soda lime traps followed by a two-stage direct-drive rotary vacuum pump (Edwards E2M8) – roughing vacuum. (B) Outlet to soda lime and liquid nitrogen traps followed by a two-stage direct-drive rotary vacuum pump (Edwards E2M8) – high vacuum. (C) Dry N_2 inlets. (D) F_2 inlet. (E) Bourdon pressure gauge (0–1500 Torr). (F) MKS Model PDR-5B pressure transducers (0–1000 Torr). (G) MKS Model PDR-5B pressure transducer (0–10 Torr). (H) Ultra-high purity argon inlet. (I) ¼-in. o.d. ($^{1}/_{8}$-in. i.d.) nickel reaction vessel port. (J) High-pressure stainless steel valve (Autoclave Engineers). (K) 316 stainless steel X-, T-, and L-connections employing $^{3}/_{8}$-in. o.d. ($^{1}/_{8}$-in. i.d.) threaded nickel tubing. (L) Submanifold. From ref 108.

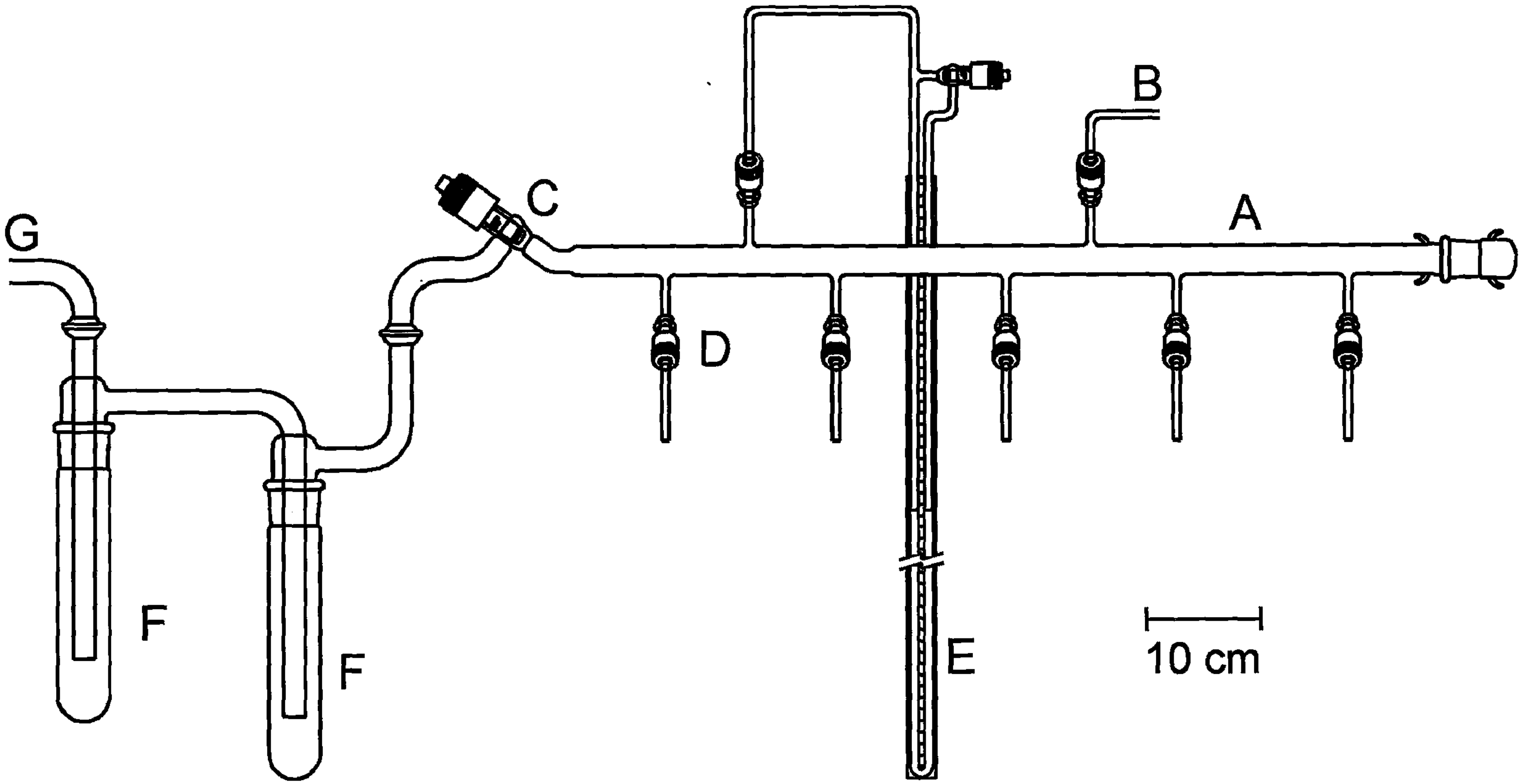

Figure 2.2. Glass vacuum line used for the manipulation of non-corrosive volatile materials. (A) Main vacuum manifold. (B) Dry N_2 inlet. (C) 15-mm greaseless glass J. Young stopcock with PTFE barrel. (D) 6-mm greaseless J. Young stopcock with PTFE barrel. (E) Mercury manometer. (F) Liquid N_2 cold trap. (G) Outlet to vacuum pump. From ref 108.

were monitored using a mercury manometer.

Vacuum on the glass vacuum lines (ca. 10^{-3}–10^{-4} Torr) was accomplished using Edwards two-stage internal vane E2M8 direct-drive vacuum pumps. Vacuum was maintained on the metal line using two E2M8 vacuum pumps; the first, a roughing pump, was used primarily for the removal of volatile fluoride and oxide fluoride compounds. The rough pump was used to pump reactive, volatile fluorine compounds through a fluoride/fluorine trap consisting of a stainless steel tube (ca. 60 cm, 15 cm dia.) packed with soda lime absorbent (Fisher Scientific, 4–8 mesh), followed by a final trapping procedure, utilizing a glass liquid nitrogen trap to remove CO_2 and water formed by reaction of fluoride materials with soda lime and other volatile materials that were unreactive towards soda lime. The second vacuum pump provided the high vacuum (ca. 10^{-4} Torr) source for the manifold and was fitted with a glass liquid nitrogen trap.

2.1.2. Preparative Apparatus and Sample Vessels

All synthetic work was carried out in reactors constructed from lengths of ¼-in. o.d. FEP tubing which were heat-sealed at one end and heat-flared (45° SAE) at the other. The tubing was connected to Kel-F valves, encased in aluminum housings, using brass flare fittings. All vessels were then connected to a glass vacuum line using ¼-in. stainless steel Swagelok Ultratorr unions and were rigorously dried by pumping (a minimum of 6 h) under dynamic vacuum. Vessels were then connected to the metal vacuum line using a ¼-in. PTFE Swagelok union and passivated with ca. 1000 Torr of F_2 for ca. 12 h. Once passivated, vessels were evacuated under dynamic vacuum to remove all volatile impurities and back-filled with dry N_2 (ca. 1000 Torr) prior to use. Similarly, connections made to a metal vacuum line were dried under dynamic vacuum and passivated with F_2 gas overnight. Connections made to a glass vacuum line were dried under dynamic vacuum overnight. The glass vessels used were dried under dynamic vacuum for a minimum of 8 hr and were periodically heated with a Bunsen burner.

Nuclear magnetic resonance spectra were acquired using sample tubes prepared from lengths of ¼-in. o.d. FEP tubing. One end of each tube was heat-sealed using the end of a heated thin-walled 10-mm o.d. glass NMR tube, while the other end was fused to ca. 5 cm of ¼-in. o.d. thick wall tubing. The remaining end of the thick wall was heat-flared (45° SAE) for connection to a Kel-F valve. Prior to acquisition of the NMR data, the sample tubes were heat-sealed under dynamic vacuum using a nichrome wire resistance furnace of appropriate diameter. Otherwise, NMR samples were prepared in 5-mm o.d. thin wall precision glass NMR tubes (Wilmad) fused to ¼-in. o.d. lengths of glass tubing which were, in turn, attached to 4-mm J. Young PTFE/glass stopcocks by use of ¼-in. stainless steel Swagelok Ultratorr unions fitted with Viton O-rings. The NMR tubes were then vacuum-dried for 8–12 h before use, and once sample and solvent were added, the tubes were heat-sealed under dynamic vacuum.

Low-temperature Raman spectra of solids (ca. –160 °C) were recorded on samples prepared in thin-walled ¼-in. FEP tubing as well as 5-mm o.d. glass tubes fused to ¼-in. o.d. lengths of glass tubing which were in turn attached to 4-mm J. Young PTFE/glass stopcocks by use of ¼-in. stainless steel Swagelok Ultratorr unions fitted with Viton O-rings. The Raman sample tubes were then vacuum-dried for 8–12 h before use, and once the sample was added, the tube was heat-sealed under dynamic vacuum.

All connections to vacuum lines were made using thick-walled ¼-in. FEP tubing in conjunction with either a ¼-in. PTFE Swagelok connector outfitted with PTFE compression fittings (front and back ferrules) or ¼-in. stainless steel Swagelok Ultra-Torr connectors outfitted with stainless steel compression fittings and Viton rubber O-rings.

2.2. Preparation and Purification of Starting Materials

2.2.1. Sources and Purification of Gasses; N_2, Ar, F_2, Xe, and Kr

House nitrogen gas was generated by boiling off liquid nitrogen (Air Liquide) and was further dried through a freshly regenerated bed of type 4Å molecular sieves. High purity argon gas (VitalAire), also employed for the back pressuring of reaction vessels, was used without further purification. Technical grade fluorine gas (Air Products) and ultra-high purity Xe (Air Products, 99.995%) and Kr (Air Products, 99.995%) were used without further purification.

2.2.2. Purification of Solvents; Anhydrous HF, BrF_5, SO_2ClF, CH_3CN, SO_2, $XeOF_4$, $H_2{}^{16}O$, $H_2{}^{18}O$, and $D_2{}^{16}O$.

HF. Anhydrous hydrogen fluoride, HF (Harshaw Chemical Co.), was purified by addition of ca. 5 atm of fluorine gas to a commercial HF sample contained in a nickel can for a period of approximately one month prior to use, converting residual water to HF and O_2. The HF was then distilled into a Kel-F storage vessel equipped with a Kel-F valve and stored at room temperature for future use. Transfer of HF was accomplished by vacuum distillation from the Kel-F storage vessel, on a metal vacuum line, through connections constructed from FEP, as shown in Figure 2.3.

BrF_5. Bromine pentafluoride (Ozark-Mahoning Co.) was purified in an FEP vessel equipped with a Kel-F valve and loaded with 20 g of KF (to complex HF as $[K][HF_2{\cdot}nHF]$). Bromine and BrF_3 impurities were eliminated by the direct fluorination of these species to BrF_5 at ambient temperature as previously described.[109] The product was stored in the purification vessel under 1000 Torr of a 2:1 mixture of N_2 and F_2 at –78 °C and transferred under dynamic vacuum when required.

SO_2ClF. Sulfuryl chloride fluoride (Allied Chemical Co., Baker and Adams Division, >90%, ca. 100 g crude material) was purified by fractional distillation through two FEP U-tube traps cooled to –78 and –90 °C, respectively, effectively removing the inert impurity SO_2F_2. The remaining SO_2ClF was then condensed into an FEP U-tube containing ca. 80 g of SbF_5 at –78 °C and slowly warmed to room temperature with vigorous mixing to remove SO_2, which is known to rapidly reduce xenon(II) species. The purified SO_2ClF was then transferred to an FEP U-tube cooled to –78 °C and containing dried KF. Again, the mixture was slowly warmed to room temperature with vigorous mixing and allowed to stand with periodic mixing at room temperature for ca. 2 h to remove any residual HF. The sample was again cooled to –78 °C and condensed into a 1.25-in. FEP reaction vessel containing XeF_2 (1.7 g) for 24 h to ensure all impurities with reducing properties (i.e., SO_2) were removed. Finally, the liquid was distilled by dynamic pumping at –78 °C into a glass vessel, outfitted with a 6-mm J. Young all glass stopcock,

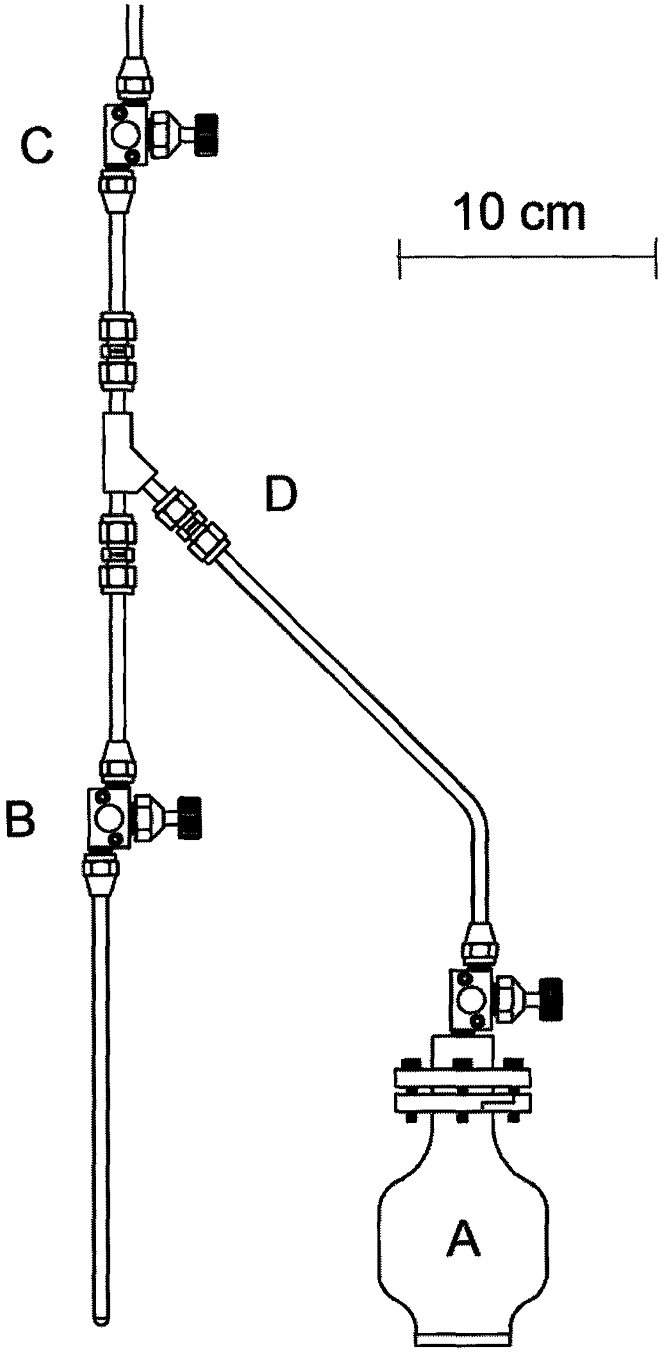

Figure 2.3. Hydrogen fluoride distillation apparatus. (A) Kel-F storage vessel containing HF. (B) FEP reaction vessel fitted with a Kel-F valve. (C) Kel-F valve connected to vacuum manifold. (D) Kel-F Y-connection with ¼-in. PTFE Swagelok unions. From ref 108.

over a bed of dry KF. The purity of the sample was assessed by ^1H, ^{17}O, and ^{19}F NMR spectroscopy of a neat sample recorded at –80 °C, in which only trace amounts of SO_2F_2 (2.2%) were found. Transfers were performed using a glass vacuum line by vacuum distillation of SO_2ClF through a sub-manifold comprised of a Y-shaped glass connection to the reaction vessel (Figure 2.4). The sample was stored at room temperature until used.

CH_3CN. Acetonitrile (Caledon, HPLC Grade) was purified according to the literature method,[110] stored over molecular sieves in a glass vessel outfitted with a grease-free 6-mm J. Young glass/PTFE stopcock, and was transferred under vacuum using a glass vacuum line and a glass Y-piece into a smaller glass dispensing vessel outfitted with a grease-free 6-mm J. Young glass/PTFE stopcock. Acetonitrile was then dispensed under vacuum using a glass vacuum line and a glass Y-piece into individual reaction vessels. (Figure 2.5).

SO_2. Sulfur dioxide (Aldrich) was stored over P_4O_{10} in a glass vessel, outfitted with a grease-free 6-mm J. Young PTFE/glass stopcock. Transfers were performed under vacuum using a glass vacuum line and a glass Y-piece.

$XeOF_4$. Xenon oxide tetrafluoride was prepared and purified according to the literature method by the hydrolysis of XeF_6.[38]

$H_2{}^{16/17/18}O$ and D_2O. Both H_2O (Caledon, HPLC grade) and $H_2{}^{18}O$ (Isotec, 98.6 atom % ^{18}O) were used without further purification and were also used to prepare 2.00 M $H_2{}^{16/18}O$ solutions in CH_3CN. An ^{17}O-enriched sample of H_2O (Office de Rayonnements Ionisants, Saclay, France; 35.4% ^{16}O, 21.9% ^{17}O, 42.7% ^{18}O) and D_2O (MSD Isotopes, 99.8 atom% D) were also used without further purification.

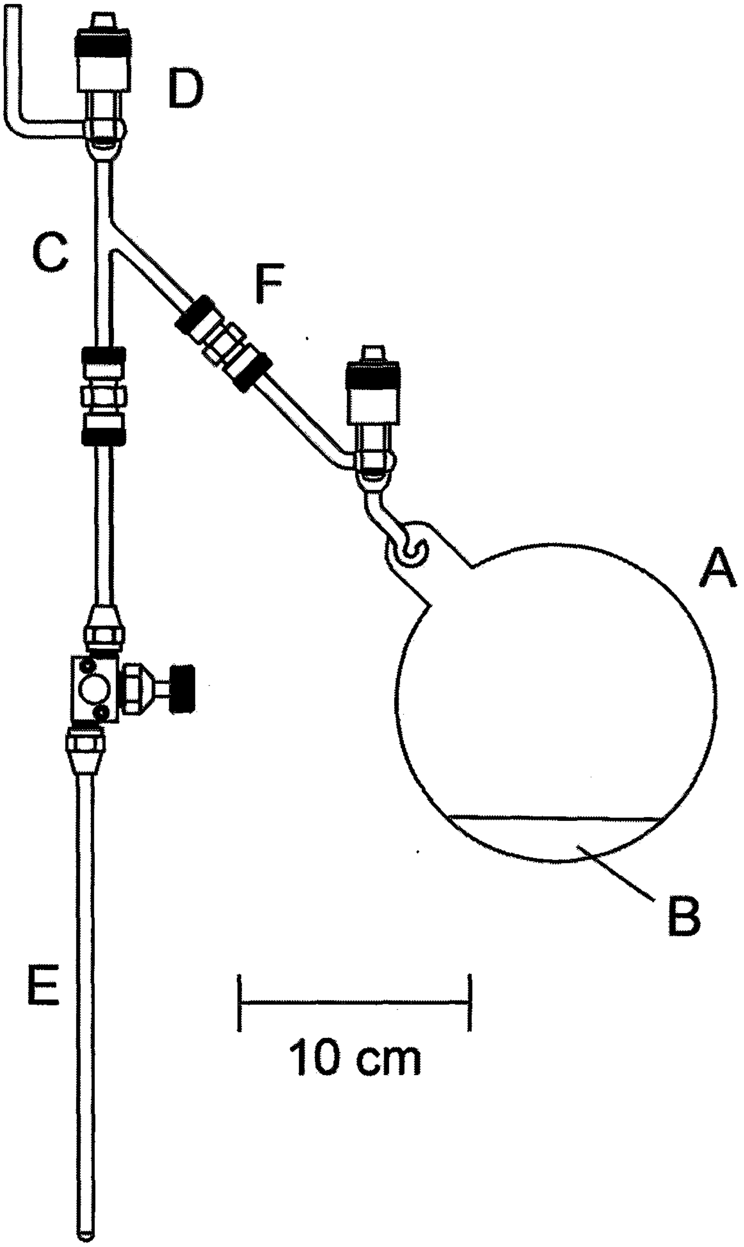

Figure 2.4. Apparatus used for the vacuum transfer of SO_2ClF solvent. (A) 250-mL glass vessel equipped with a grease-free 6-mm J. Young PTFE/glass stopcock outfitted with PTFE barrel. (B) Bed of dry, powdered KF. (C) Glass Y-connector. (D) 6-mm J. Young PTFE/glass valve. (E) FEP reaction vessel fitted with a Kel-F valve. (F) Stainless steel Swagelok Ultratorr Union. From ref 108.

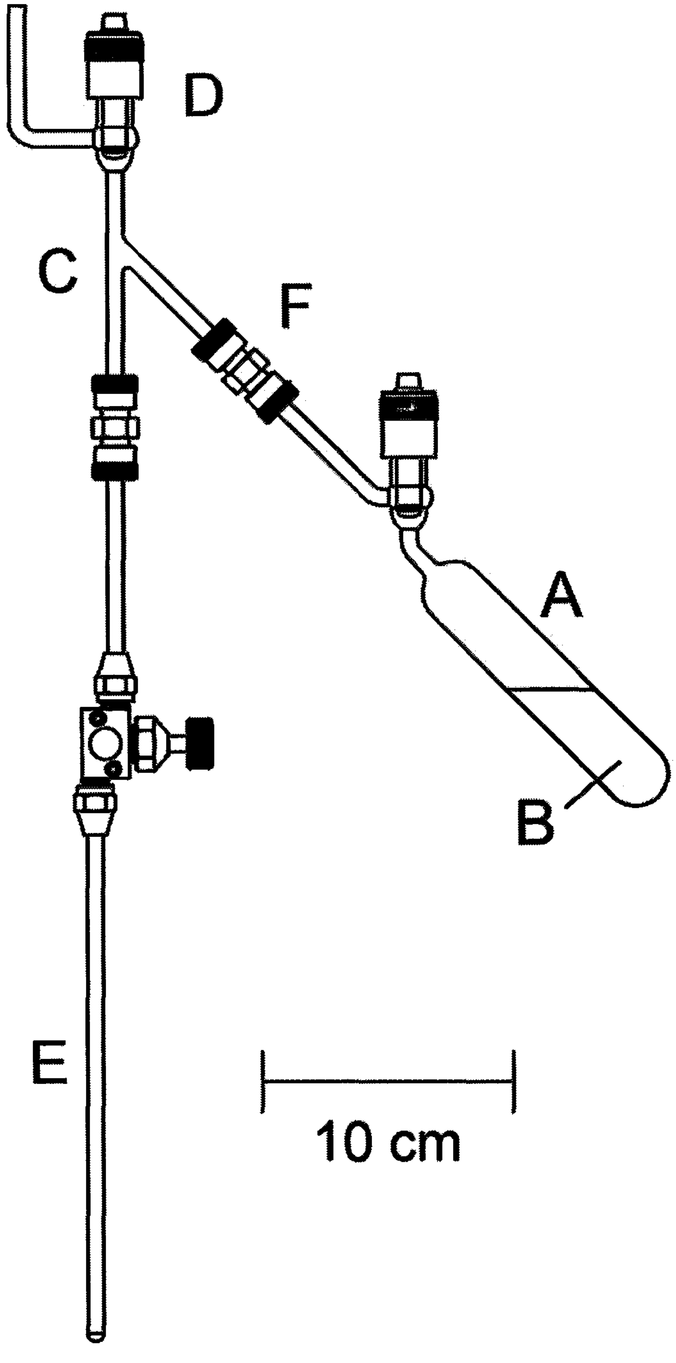

Figure 2.5. Apparatus used for the vacuum transfer of CH_3CN solvent. (A) 200-mL glass vessel equipped with a grease-free 6-mm J. Young PTFE/glass stopcock outfitted with PTFE barrel. (B) CH_3CN. (C) Glass Y-connector. (D) 6-mm J. Young PTFE/glass valve. (E) FEP reaction vessel fitted with a Kel-F valve. (F) Stainless steel Swagelok Ultratorr Union. From ref 108.

2.2.3. Preparation and Purification of Starting Materials; CsF, $[N(CH_3)_4][F]$, CaF_2, D_2SO_4, XeF_2, XeF_4, PnF_5, $[XeF][PnF_6]$, $[H_3{}^{16/18}O][PnF_6]$, and $[Xe_3{}^{16/18}OF_3][PnF_6]$ (Pn = As, Sb)

CsF and $[N(CH_3)_4][F]$. Cesium fluoride (CsF, ICN-KCK Laboratories Inc., 99.9%) was dried by fusion in a platinum crucible, followed by immediate transfer of the melt to a drybox port which was immediately evacuated. Upon transferring to a nitrogen atmosphere drybox, the sample was ground to a fine powder and stored in a PFA container inside the drybox until used. The naked fluoride ion source, $[N(CH_3)_4][F]$, was prepared according to the literature method[111] and was stored in an FEP tube inside a drybox until used.

CaF_2. Calcium fluoride powder (J.T. Baker, 98.2%) was dried in a glass vessel under dynamic vacuum at 200–250 °C for 24 h and stored in a drybox until used. Sulfuric acid-*d*$_2$ (Aldrich, 99.5 atom % ^{2}H) was used without further purification.

AsF_5. Arsenic pentafluoride was prepared as previously described[112,113] by direct fluorination of purified AsF_3 with purified F_2 (see Syntheses of O_2NF and ONF) in a nickel can. The AsF_5 was used from the reaction can without further purification.

SbF_5. Antimony pentafluoride (Ozark Mahoning) was purified by vacuum distillation as previously described[61] and stored in a glass vessel inside a desiccator until used. Subsequent transfers of SbF_5 were performed by use of a dry all-glass syringe in the inert atmosphere of a glove bag which had previously been purged with dry nitrogen for at least 12 h.

XeF_2 and XeF_4. Xenon difluoride[112] and XeF_4[31] were prepared according to the literature methods and stored in a Kel-F tube inside a dry box until needed.

[XeF][PnF_6]. The salts, [XeF][PnF_6], were prepared by the reaction of XeF_2 with PnF_5. In a typical preparation for [XeF][AsF_6],[74] anhydrous HF was condensed into an FEP vessel containing a pre-weighed amount of XeF_2 (2.7798 g, 16.42 mmol). A stoichiometric excess of AsF_5 (18.95 mmol, ca. 15% excess) was condensed into the vessel and the contents were warmed to ambient temperature and thoroughly mixed. On cooling the sample to –78 °C, a large amount of pale yellow solid precipitated from the HF solution. The solvent, and residual AsF_5, were then removed by evacuating the sample at –78 °C through an FEP U-tube cooled to –196 °C. The HF free sample was then back pressured to ca. 1 atm with dry nitrogen and stored inside a drybox. For [XeF][SbF_6], aHF was condensed into an FEP vessel containing a pre-weighed amount of SbF_5 (1.0463g, 4.8274 mmol). Inside a drybox, the sample was frozen at –145 °C and a stoichiometric amount of XeF_2 (0.81737 g, 4.8283 mmol) was added to the vessel. The reactor was removed from the drybox and the contents were warmed to ambient temperature and thoroughly mixed. On cooling the sample to –78 °C a large amount of yellow solid precipitated from the HF solution. The HF solvent was then removed by evacuating the sample at –78 °C through an FEP U-tube cooled to –196 °C. The HF free sample was then back pressured to ca. 1 atm with dry nitrogen and stored inside a drybox. The purities of the [XeF][PnF_6] samples were verified by FT-Raman spectroscopy and all subsequent transfers of [XeF][PnF_6] were carried out in the drybox.

$[H_3{}^{16/18}O][PnF_6]$. Literature methods were used for the syntheses of $[H_3{}^{16/18}O][AsF_6]$,[114] and $[H_3{}^{16/18}O][SbF_6]$[114] by the reaction of $H_2{}^{16}O$ or $H_2{}^{18}O$ with AsF_5 or SbF_5, respectively, in HF solvent.

$[Xe_3{}^{16/18}OF_3][PnF_6]$. The syntheses of high-purity $[Xe_3{}^{16/18}OF_3][PnF_6]$ involved dissolution at −50 °C of near-equimolar amounts of $[H_3{}^{16/18}O][PnF_6]$ and XeF_2 (up to ca. 20 mol % excess XeF_2) at ca. 0.2–3 M H_3O^+ in a 0.25-in. FEP reactor which had a side arm fused to it. The solution was rapidly warmed to −35 °C for ca. 30 s and immediately cooled to −50 °C. After 5 min at −50 °C, a voluminous deep red-orange microcrystalline precipitate of $[Xe_3{}^{16/18}OF_3][PnF_6]$ formed. The reaction mixture was maintained at −50 °C for an additional 20–30 min to ensure the reaction was complete. Unreacted XeF_2 and/or $[H_3{}^{16/18}O$ $O][PnF_6]$, as well as $[Xe_2F_3][PnF_6]$ byproduct, were soluble and were decanted from the settled precipitate at −50 °C into the side arm of the reactor at −78 °C. The product, $[Xe_3{}^{16/18}OF_3][PnF_6]$, decomposed under HF above −30 °C with Xe gas evolution.

2.2.4. Preparation of KrF_2

Krypton difluoride was prepared by use of a 316 stainless steel hot-wire reactor (Figure 2.6) equipped with a nickel filament, similar to that originally described[98] and subsequently modified.[97] The filament was fabricated from a $^1/_{16}$-in. dia. nickel wire tightly wound about a second length of $^1/_{16}$-in. nickel wire that was, in turn, coiled and stretched into a helix. In a typical preparation, the hot-wire reactor was pressurized with 1000 Torr (50 mmol) of krypton and then cooled to −196 °C in a 20-L Dewar. After

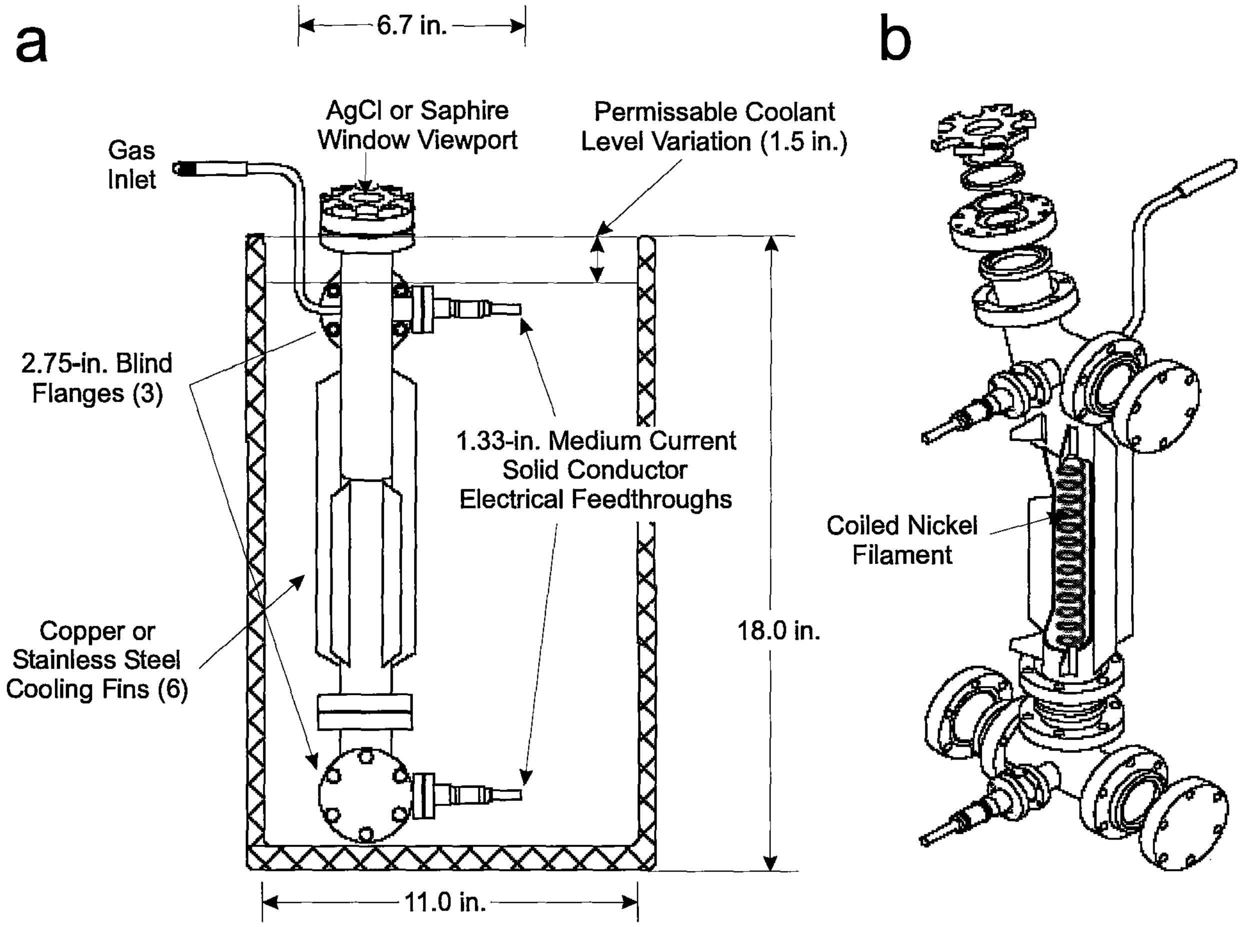

Figure 2.6. The stainless steel hot-wire reactor used for the preparation of KrF_2. (a) External view and dimensions of a hot-wire reactor submerged in a liquid nitrogen coolant bath. (b) A perspective drawing of the hot-wire reactor showing the flange assembly and nickel filament (cut away region). Reproduced with permission from ref 115.

reaching thermal equilibrium, the reactor was pressurized with 25 Torr of F_2 and the DC power supply for the nickel filament was adjusted to ca. 6 V and 30 A (the filament was dull red in color under these conditions). The F_2 pressure increased to ca. 45 Torr after the power supply was turned on and was regulated between 25 and 45 Torr by the periodic addition of F_2 during the synthesis. The decreasing F_2 pressure was used to qualitatively monitor the production of KrF_2, and additional Kr (1.0 to 2.0 mmol) was condensed into the reactor when the rate of KrF_2 production slowed or ceased. Upon completion of the reaction (*ca.* 12 h), excess F_2 was removed under dynamic vacuum at –196 °C. The excess Kr and crude KrF_2 were recovered as a pink solid (the coloration arises from chromium oxide fluoride contamination) by allowing the reactor to slowly warm to room temperature while dynamically pumping the volatile contents through a ½-in. o.d. FEP U-trap (–196 °C). The Kr/KrF_2 mixture was then warmed to –78 °C under dynamic vacuum to remove the unreacted Kr. The crude KrF_2 was purified by briefly warming the sample to 0 °C and flash distilling off the more volatile chromium oxide fluorides. The remaining colorless KrF_2 was finally warmed to room temperature and rapidly sublimed into a $^3/_8$-in. o.d. FEP tube equipped with a Kel-F valve, where it was stored under 1000 Torr of N_2 or Ar at –78 °C until used. This synthesis is highly reproducible and typically yields 2.5 to 3.0 g of purified KrF_2 over a 12 h period.

2.2.5. Synthesis of High-Purity Deuterium Fluoride

Deuterium fluoride was prepared by the reaction of 25.59 g (0.2556 mol) of D_2SO_4 with 20.09 g (0.3400 mol) of CaF_2 powder. The reaction was carried out in a ¾-in.

o.d. FEP reaction vessel fitted with a Kel-F valve. The DF was initially vacuum distilled from the reaction slurry at room temperature into a –196 °C cold trap comprised of a U-tube constructed from ½-in. o.d. FEP tubing and equipped with Kel-F valves.

Throughout, the reaction vessel was periodically agitated until the slurry solidified, whereupon the reaction vessel was incrementally heated to no more than 105 °C in a silicone oil bath over a period of 2 h and the DF was collected in the U-tube until DF evolution ceased. The crude DF was then statically distilled at room temperature into an FEP vessel containing 1.06 g of XeF_2 at –196 °C. Upon warming to room temperature, XeF_2 dissolved and any D_2O that had transferred or SO_2 that formed in the course of the acid displacement reaction was converted to DF and O_2, and SO_2F_2, respectively. After standing at room temperature for 1 h, the mixture was cooled to –78 °C and DF was distilled under dynamic vacuum into a second FEP U-tube at –196 °C. The sample was warmed to room temperature and a portion was condensed into a 4-mm o.d. FEP NMR tube at –196 °C. The room temperature ^{19}F NMR spectrum revealed a small amount (1.3 mole %) of SO_2F_2 ($\delta(^{19}F)$, 29.3 ppm; $^{1}\Delta^{19}F(^{34/32}S)$, –0.0482 ppm) but no fluorine containing species other than DF could be detected under high-gain conditions. The remaining DF was stored by condensing it into a Kel-F vessel containing 0.140 g of resublimed BiF_5 (Ozark Mahoning Co.) to remove trace amounts of D_2O that may still be present. The yield of pure anhydrous DF was 8.93 g (83.1% based on D_2SO_4 as the limiting reagent). Transfer of DF was accomplished by vacuum distillation from the Kel-F storage vessel, on a metal vacuum line, through connections constructed of FEP.

2.2.6. Syntheses of Nitryl Fluoride, O_2NF, and Nitrosyl Fluoride, ONF

O_2NF. The syntheses of O_2NF[116] and ONF[117] are based on the published methods using more rigorously purified starting materials. In a typical preparation, NO_2 (0.1005 mmol) was allowed to expand into a metal vacuum line manifold and ballast can (total volume 2.062 L) pre-passivated with NO_2, and then condensed into a nickel reactor (ca. 65 mL) at –196 °C. Fluorine gas was then used to passivate the vacuum manifold and ballast can, followed by removal under dynamic vacuum. The manifold was repressurized with F_2, which was condensed into the measuring can at –196 °C (0.0961 mmol). After the line was evacuated, the measuring can was warmed to –183 °C using a liquid O_2 bath, and F_2 gas, free of non-volatile contaminants such as HF, was allowed to expand into the manifold and condensed into the reactor containing NO_2 at –196 °C (0.05473 mmol; 8.9 mol % excess). The reaction vessel was then warmed to –78 °C for 4–5 h, followed by warming to room temperature and was allowed to stand overnight. Second additions of NO_2 (0.1049 mmol) and F_2 (0.0551 mmol; 5.1 mol % excess) were made to the reaction vessel at –196 °C and allowed to react in the same manner. Excess F_2 gas was removed under dynamic vacuum at –196 °C. The ^{19}F NMR spectrum of the neat liquid product at –80 °C showed a small amount of ONF as the only fluorine-containing impurity (2.5 % by integration).

ONF. Nitrosyl fluoride, ONF, was prepared in a manner similar to that used for the preparation of O_2NF. Twice reacting NO (0.0905 mol) and F_2 (0.0417 mol) in a nickel reactor (65 mL) gave a combined yield of 8.63 g (0.176 mol) of ONF. Trace amounts of

O_2NF (0.22%) and ONF_3 (0.85%) found in the sample were estimated by recording the ^{19}F NMR spectrum of a sample of the neat liquid product at −80 °C.

Transfers of ONF and O_2NF were carried out using a fluorine-passivated FEP submanifold (dedicated to this use) that was passivated once with the corresponding fluoride (ONF or O_2NF) prior to transfer to an intermediate FEP vessel. This served to verify passivation of the submanifold was complete in the case of ONF. In the event of incomplete passivation, a distinct blue to light blue color appeared in the intermediate vessel that resulted from reaction of ONF with residual moisture and/or unpassivated metal surfaces, giving intense blue N_2O_3. This procedure also allowed a controlled amount of ONF/O_2NF to be metered into the reaction vessel.

2.2.7. Preparation of $FXeOTeF_5$ and $[XeOTeF_5][AsF_6]$

The mixed $FXe(OTeF_5)$ species was synthesized according to the literature method.[118] In the drybox, 1.697 g (2.789 mmol) $Xe(OTeF_5)_2$ was added to a ½-in. FEP reaction vessel followed by the addition of 0.4721g (2.822 mmol) of XeF_2. The reactor was removed from the drybox and slightly warmed by hand whereupon the solids melted and formed a pale yellow solution. The reactor was allowed to sit for two days at room temperature with periodic mixing to ensure complete reaction.

The $XeOTeF_5^+$ was synthesized by the reaction of $FXeOTeF_5$ with AsF_5 according to the literature method.[119] A ½-in. FEP reaction vessel containing 2.169 g (5.578 mmol) $FXeOTeF_5$ was cooled to −196 °C and approximately 7.00 mmol of AsF_5 was condensed into the reaction vessel. The reactor was warmed and mixed at −50 °C for several hours and allowed to react at −78 °C for three days to ensure the reaction was complete. The excess AsF_5 was removed under dynamic vacuum at −78 °C and the reactor containing $[XeOTeF_5][AsF_6]$ was transferred and stored in the drybox.

2.2.8. Preparation of $[ClOF_2][AsF_6]$ Precursors; ClF, $ClONO_2$, $ClOF_3$

2.2.8.1. ClF

Chlorine monofluoride was synthesized according to the literature method.[120] Chlorine gas (Air Liquide) was dried and purified by bubbling the gas through concentrated H_2SO_4 and collecting it in a glass trap maintained at −78 °C. Chlorine trifluoride (40.0 mmol) was condensed into a 70 mL nickel vessel followed by condensing 38.0 mmol Cl_2 into the reaction vessel. The reaction vessel was warmed to −78 °C for ca. 20 min. followed by warming the vessel to room temperature for ca. 20 min. and finally warmed to 200 °C for 15 h. The ClF was isolated and impurities were removed by passing the contents of the reaction vessel (maintained at −78 °C) through a pair of FEP U-tubes, the first cooled between −130 and −140 °C to remove unreacted ClF_3 and the second cooled to −196 °C to recover ClF.

2.2.8.2. $ClONO_2$

Chlorine nitrate was synthesized according to the literature method[121] by the reaction of ClF with $Pb(NO_3)_2$. Lead nitrate (BDH) was dried under dynamic vacuum for 72 h at 100 °C. In the drybox, 6.80 g (20.5 mmol) of $Pb(NO_3)_2$ was added to a 40 mL steel reaction vessel. Approximately 1.76 g (32.3 mmol) of ClF was condensed into the reaction vessel at −196 °C. The reaction vessel was warmed stepwise to −78 °C and then to 0 °C. The resulting $ClONO_2$ was isolated and purified by passing the contents of the reaction vessel through a pair of FEP U-tubes, the first cooled to −120 °C to collect $ClONO_2$ and the second cooled to −196 °C to collect unreacted ClF.

2.2.8.3 $ClOF_3$

Direct fluorination of $ClONO_2$ according to the literature method[122] was used to synthesize $ClOF_3$. Approximately 0.110 mol of $ClONO_2$ was condensed into a 70 mL nickel vessel, followed by condensing 0.110 mol of F_2. The reaction vessel was warmed to −35 to −40 °C for 4 h. The non-condensables were first removed from the vessel at −196 °C followed by warming the vessel stepwise to −78 °C and then to room temperature while collecting the products in a pair of FEP U-tubes, the first cooled to between –95 and −100 °C to collect $ClOF_3$ and the second cooled to −196 °C to collect the remaining products, FNO_2, Cl_2, ClO_2F.

2.2.9. Synthesis of $[ClOF_2][AsF_6]$

The title salt, $[ClOF_2][AsF_6]$, was synthesized according to the literature method[123,124] by the reaction of $ClOF_3$ with AsF_5. Approximately 1.353 g (12.48 mmol) of $ClOF_3$ was condensed into a ½-in. FEP reactor followed by condensing in 2.121 g (15.6 mmol, 25% excess) AsF_5. The reactor was warmed to –55 to −60 °C for several minutes. The reaction did not appear to be complete so the reactor was maintained at –78

°C for 2 days. The excess AsF_5 was removed at –78 °C under dynamic vacuum and the reactor was transferred and stored in the drybox.

2.3. Syntheses of $XeOF_2$, $F_2OXeN{\equiv}CCH_3$, and $XeOF_2{\cdot}n HF$

2.3.1. Preparation of $F_2OXeN{\equiv}CCH_3$

In a typical synthesis, 60.6 mg of XeF_4 was added, inside a drybox, to a ¼-o.d. FEP reaction tube attached to a ¼-in. stainless steel Swagelok Ultra-Torr union fitted with Viton O-rings which was, in turn, attached to a Kel-F valve through a short length of thick-wall ¼-in. o.d. FEP tubing that was compression fitted to the valve. The reactor was disassembled outside the drybox at the union and quickly replaced with a Kel-F plug having two $^1/_{16}$-in. holes drilled through its top which opened into the reaction vessel. A $^1/_{16}$-in. o.d. Teflon tube, with a slow stream of dry argon passing through it, was threaded through one hole and positioned well above the XeF_4. This permitted nitrogen in the reaction vessel to be displaced by argon through the second hole in the Kel-F plug. The vessel was cooled to −78 °C while maintaining the argon flow. The argon flow was halted and 150 μL of 2.00 M solution of $H_2{}^{16/18}O$ in CH_3CN was syringed into the reactor through the argon outlet hole and frozen onto the walls of the reaction vessel to give a 3–5% stoichiometric excess of $H_2{}^{16/18}O$. The argon flow was recommenced and the solution was melted onto the XeF_4 at −42 °C and thoroughly mixed, resulting in the immediate formation of a yellow solution and precipitate. The solution was cooled to −45 °C whereupon more yellow solid precipitated. The union and valve assembly was reconnected and the solvent was immediately removed at −45 to −42 °C under dynamic vacuum, leaving a pale yellow microcrystalline powder. Completeness of solvent removal was monitored by Raman spectroscopy (Table 3.6).

2.3.2. Preparation of $Xe^{16/18}OF_2$

A 66.1 mg sample of $F_2{}^{16/18}OXeN{\equiv}CCH_3$ was pumped under dynamic vacuum for 5 h with frequent agitation while maintaining the sample between –45 to –42 °C. This resulted in a bright yellow powder corresponding to $Xe^{16/18}OF_2$, which was shown to be free of coordinated CH_3CN by Raman spectroscopy (–150 °C). The compound is stable indefinitely when stored at –78 °C.

A solution of ^{17}O-enriched $XeOF_2$ in CH_3CN was prepared for ^{17}O NMR spectroscopy by in situ hydrolysis of XeF_4 (0.0219 g, 0.106 mmol) with ^{17}O-enriched H_2O (2.0 µL, 0.10 mmol) at –45 °C in a 4-mm o.d. FEP NMR tube.

2.3.3. Preparation of $Xe^{16/18}OF_2{\cdot}n^{1/2}HF$

Approximately 0.3 mL of anhydrous $^{1/2}HF$ was distilled into an evacuated reactor containing 54.1 mg of freshly prepared $Xe^{16/18}OF_2$ and frozen on the vessel walls at –196 °C. **Caution:** *If condensation is too rapid and liquid HF condenses directly onto $XeOF_2$, rapid, decomposition/detonation is likely to occur.* The $^{1/2}HF$ was melted onto the $Xe^{16/18}OF_2$ sample at –78 °C and was frequently mixed, over a 12–72 h period, by suspending the entire sample in $^{1/2}HF$ at this temperature and periodically monitored by recording the Raman spectrum of $Xe^{16/18}OF_2$/ $Xe^{16/18}OF_2{\cdot}n^{1/2}HF$ under a frozen layer of

$^{1/2}$HF. Once solvation was complete, the resulting very pale yellow powder was isolated by removal of the $^{1/2}$HF solvent under dynamic vacuum at –78 °C.

2.3.4. Crystal Growth of $F_2OXeN{\equiv}CCH_3$

Crystals of $F_2OXeN{\equiv}CCH_3$ were grown as described in Section 2.10.1 by slow cooling of a CH_3CN solution of $XeOF_2$, previously saturated at ca. –35 °C, from –35 to –45 °C over the course of 5 h in a ¼-in. o.d. FEP reactor as described in the synthesis of $F_2OXeN{\equiv}CCH_3$. When crystal growth was deemed complete, the reactor was maintained at –45 °C and was disassembled at the Swagelok Ultra-Torr union and quickly replaced with a Kel-F plug and $^1/_{16}$-in. o.d. Teflon tubing which had a slow stream of argon slowly passing through it (see Section 2.3.1). A second length $^1/_{16}$-in. o.d. Teflon tubing was inserted through the outlet hole of the Kel-F cap while maintaining the argon flow. Lowering the outlet tube into the solution expelled the yellow supernatant through it into a second ¼-in. o.d. FEP tube cooled to –78 °C. The union and valve assembly were replaced and the crystals were dried under dynamic vacuum at –45 to –42 °C and stored at –78 °C until a suitable crystal could be selected and mounted on the diffractometer. In addition to having a propensity to twin, the crystalline adduct proved difficult to handle because dry samples exploded at temperatures approaching 0 °C and had a tendency to slowly loose CH_3CN under dynamic vacuum at –45 °C (see Syntheses and Properties of $XeOF_2$, $F_2OXeN{\equiv}CCH_3$, and $XeOF_2{\cdot}n$HF). Crystalline $F_2OXeN{\equiv}CCH_3$ and its solutions were handled under low lighting conditions throughout crystal growth, crystal mounting, and data collection to minimize photodecomposition.

2.4. Synthesis of XeO_2

2.4.1. Aqueous Preparation of XeO_2

Under a head of high-purity Ar, 0.400 mL of $H_2{}^{16}O$ ($H_2{}^{18}O$; $H_2{}^{16}O$/ $H_2{}^{18}O$; D_2O) was syringed into a ¼-in. FEP reactor, which was plugged with a Teflon cap, and cooled to 0 °C in an ice/water bath. Once cooled, the cap was briefly removed and 40–50 mg of crystalline XeF_4 was added to the reactor, a few crystals at a time. **NOTE:** *When water was added directly to solid XeF_4, or XeF_4 crystals were added too rapidly, heat generated by the reaction could not be adequately dissipated, resulting in extensive decomposition of XeO_2 to Xe and O_2 which ejected the remaining water and product from the reactor.* A bright, yellow-orange suspension immediately formed upon contact, but upon mixing for ca. 20 s at 0 °C, the color of the suspension changed to yellow. The yellow solid was found to be XeO_2 (see Section 4.2) while the yellow-orange product was possibly a mixture of molecular XeO_2 and/or lower molecular weight polymorphs resulting from incomplete polymerization. The reactor containing the yellow solid was then placed in an ice/water bath in a centrifuge and centrifuged for 10 s at 7000 rpm at a radial distance of 13 cm. The sample was removed and immediately quenched at −78 °C and the Raman spectrum was recorded at −160 °C.

2.4.2. Synthesis of XeO_2 in Non-aqueous Media

A 46.6 mg (0.225 mmol) [56.0 mg (0.270 mmol)] sample of $XeOF_2$[125] ([Cs][$XeOF_3$])[126] was synthesized as previously described (using finely divided CsF for [Cs][$XeOF_3$]). A 115 μL (135 μL) aliquot of 2.00 M H_2O in CH_3CN was syringed into an

FEP reactor as described above (see Section 2.3.1), freezing it onto the walls at −78 °C. The solution was melted onto the solid at −42 °C and thoroughly mixed. In the case of $XeOF_2$, a yellow suspension resulted that, upon pumping at −42 °C under dynamic vacuum, began to bump leaving droplets of the suspension on the vessel walls that evaporated to thin films of pale-yellow solid. The latter subsequently detonated with the emission of blue light. The sample was quenched at −78 °C and its stability under CH_3CN was confirmed by quenching at −196 °C and recording its Raman spectrum at −150 °C. The spectrum confirmed that small amounts of XeO_2 were present along with large amounts of $F_2OXeNCCH_3$ and CH_3CN. In the case of the $[Cs][XeOF_3]$ hydrolysis, a yellow solid also formed that remained suspended in CH_3CN; however, unlike the $XeOF_2$ reaction, it was possible to remove CH_3CN at −42 °C under dynamic vacuum. The Raman spectrum of the dry solid, recorded at −150 °C, showed an appreciable quantity of XeO_2. The Raman band at 570 cm^{-1} arising from XeO_2 is in agreement with that recorded in aqueous media (Table 4.1).

2.5. Synthesis and Characterization of the $XeOF_3^-$ Anion

2.5.1. Syntheses of $[M][Xe^{16/18}OF_3]$ ($M = N(CH_3)_4$, Cs)

In typical syntheses, a ¼-in. o.d. FEP reactor containing 0.306 mmol ($N(CH_3)_4^+$ salt) or 0.166 mmol (Cs^+ salt) of $Xe^{16/18}OF_2$ was cooled to −196 °C, and sufficient CH_3CN was condensed onto the walls of the reactor so that upon warming to −42 °C the solvent thawed, contacting, without detonation, and dissolving $Xe^{16/18}OF_2$. Alternatively, CH_3CN was syringed into the reactor in a manner identical to that used for the synthesis of $XeOF_2$ (see Section 2.3.1) Note: *In the event that the amount of CH_3CN added is insufficient to dissolve $XeOF_2$, the former method requires refreezing the sample at −196 °C, which often leads to sample detonation.* The latter method is far less likely to result in detonation and is preferred because CH_3CN is added at a higher temperature (−78 °C). The solution was quickly frozen at −78 °C and introduced into a drybox through a cold port, and 0.319 mmol of $[N(CH_3)_4][F]$ (0.171 mmol of CsF) was added while maintaining the reactor below −78 °C. The cold reactor was removed from the drybox and warmed to −42 °C, and the contents were thoroughly mixed, whereupon a pale yellow solid precipitated from solution. The solvent was removed under dynamic vacuum while maintaining the sample between −45 and −42 °C. The completeness of solvent removal was monitored by Raman spectroscopy and required several hours for the last traces of CH_3CN to be removed, resulting in pale yellow Cs^+ and $N(CH_3)_4^+$ salts.

2.5.2. Attempted Syntheses of $[M'][XeOF_3]$ (M' = NO, NO_2)

Approximately 0.2 mL of ONF or O_2NF was condensed into an evacuated sample tube containing $XeOF_2$ (43.3 mg for the ONF reaction; 49.7 mg for the O_2NF reaction) and frozen onto the vessel walls at −196 °C. The ONF or O_2NF was melted onto $XeOF_2$ at −78 °C. In the case of ONF reaction, an immediate explosion ensued upon contact with $XeOF_2$. In the case of the O_2NF reaction, the solid immediately changed from yellow to white upon contact with liquid O_2NF (see Section 5.2.3).

2.5.3. Reactivities of [M][$XeOF_3$] with SO_2 and $XeOF_4$

In an effort to solubilize [$N(CH_3)_4$][$XeOF_3$], ca. 0.2 mL of SO_2 was distilled into an evacuated sample tube containing 72.1 mg of [$N(CH_3)_4$][$XeOF_3$] by freezing the condensate onto the walls of the reaction vessel at −196 °C. Upon warming the sample to −78 °C, contact of SO_2 vapor with the [$N(CH_3)_4$][$XeOF_3$] resulted in an immediate explosion. In a second attempt, ca. 0.2 mL of $XeOF_4$ was frozen onto the upper walls of an evacuated 4-mm o.d. FEP sample tube containing 11.9 mg (0.0353 mmol) of [Cs][$XeOF_3$] at −196 °C. The $XeOF_4$ was melted onto [Cs][$XeOF_3$] at ca. 20 °C, and upon contact the solid rapidly turned from yellow to white. The $XeOF_4$ was removed under dynamic vacuum at ca. 20 °C, and a Raman spectrum of the white powder was recorded, revealing it to be a mixture of XeF_4, XeO_2F_2, and [Cs][$F(XeOF_4)_m$].[127]

2.6. Syntheses of New Xe(IV) Cations

2.6.1. Preparation of [$^{1/2}H^{16/18}OXeF_2$][AsF_6]

In a typical synthesis, 25.4 mg (0.124 mmol) of $Xe^{16/18}OF_2{\cdot}n^{1/2}HF$ was prepared in situ according to the literature method[125] and was suspended in approximately 0.3 mL of anhydrous $^{1/2}HF$ in a ¼-in. o.d. FEP T-reactor that was joined to a Kel-F valve by means of compression fittings. The suspension was frozen at −196 °C and 0.140 mmol of AsF_5 was condensed into the reactor. The reaction mixture was then warmed to −78 °C and mixed and allowed to stand at −78 °C for 12 h to ensure complete reaction. The solvent was then removed under dynamic vacuum at −78 °C, leaving behind a white microcrystalline powder that was stable for at least four weeks when stored at −78 °C in the absence of moisture. It is important to ensure that $XeOF_2$ was fully solvolyzed to $XeOF_2{\cdot}n$HF prior to the addition of AsF_5, otherwise extensive decomposition to $[XeF][AsF_6]$ is observed.

2.6.2. Preparation of $[^{1/2}H^{16/18}OXe(F)_2{}^{16/18}OXeF_2][AsF_6]$

The most efficient synthesis of the title compound was achieved by initially suspending 33.1 mg (0.161 mmol) of $Xe^{16/18}OF_2{\cdot}n^{1/2}HF$, prepared in situ, in ca. 0.3 mL of anhydrous $^{1/2}$HF in a ¼-in. o.d. FEP T-reactor that had been connected to a Kel-F valve by means of compression fittings. The sample was introduced into the drybox without allowing the sample to warm above –78 °C, whereupon the $^{1/2}$HF was frozen in a cryowell (−120 °C), the sample was opened and 16.8 mg (0.0805 mmol) of $[^{1/2}H_3{}^{16/18}O][AsF_6]$ was added. The sample was resealed and removed cold from the drybox. The sample was warmed to –78 °C and the reagents were thoroughly mixed and allowed to react for 12 h. Within minutes, the yellow color of the sample began to intensify and after the reaction was complete, the color had intensified to bright yellow. Removal of the solvent under dynamic vacuum at –78 °C resulted in a yellow powder. The attempted synthesis of the SbF_6^- analogue using the same procedure resulted in decomposition within several minutes to $[Xe_3OF_3][SbF_6]$ salt with no evidence for $HOXe(F)_2OXeF_2^+$.

2.6.3. Preparation of [FXe$^{16/18}$OXeF$_2$][PnF$_6$] (Pn = As, Sb)

A ¼-in. o.d. FEP T-reactor was connected to a Kel-F valve and 46.3 mg (0.226 mmol) of Xe$^{16/18}$OF$_2$·nHF was prepared in situ in ca. 0.3 mL of aHF. The sample was transferred cold into the drybox and was maintained at ca. −120 °C in a cryowell. To a reactor, 86.0 mg (0.253 mmol) [93.4 mg (0.242 mmol) for the Sb salt] of [XeF][PnF$_6$] was added and the reactor was removed from the drybox cold. The reactor was warmed to −78 °C and over the course of 5−10 min, the color of the undissolved solid began to intensify to bright yellow. The reaction required approximately one week, with periodic agitation, to reach go to completion and resulted in a bright yellow solid under HF. In contrast, samples containing ^{18}O required up to one month to go to completion. Removal of the solvent under dynamic vacuum at −78 °C resulted in yellow powders.

2.6.4. Preparation of [FXe$^{16/18}$OXe(F)$_2$$^{16/18}$OXeF$_2$][AsF$_6$]

The synthesis of [FXe$^{16/18}$OXe(F)$_2$$^{16/18}$OXeF$_2$][AsF$_6$] is analogous to that of [FXe$^{16/18}$OXeF$_2$][AsF$_6$], however, in a typical synthesis 60.5 mg (0.295 mmol) of Xe$^{16/18}$OF$_2$·nHF, was allowed to react with 26.5 mg (0.0782 mmol) of [XeF][AsF$_6$]. Unlike [FXe^{16}OXeF$_2$][AsF$_6$], [FXe^{16}OXe(F)$_2$^{16}OXeF$_2$][AsF$_6$] required two weeks to go to completion with periodic agitation, while ^{18}O-enriched samples required at least one month. In each case, removal of the solvent under dynamic vacuum at −78 °C resulted in yellow powders. Attempts to synthesize the analogous SbF$_6^-$ salts using [XeF][SbF$_6$] proved unsuccessful, resulting in a mixture of [FXeOXeF$_2$][SbF$_6$] and XeOF$_2$·nHF.

2.6.3. Crystal Growth of ([XeF_3·HF][Sb_2F_{11}])$_2$·[H_5F_4][SbF_6], [XeF_3·HF][Sb_2F_{11}] and [XeF_3][SbF_6]

Crystals of ([XeF_3·HF][Sb_2F_{11}])$_2$·[H_5F_4][SbF_6], [XeF_3·HF][Sb_2F_{11}], and [XeF_3][SbF_6] were grown in ¼-in. o.d. FEP T-shaped reaction vessels. Approximately 0.15 mL (~17 mol %) of SbF_5 in HF was cooled to −78 °C and poured through a ¼-in. Teflon Swagelok union onto frozen HF (0.15 mL; −196 °C) containing 11.7 mg (0.0569 mmol) of $XeOF_2$·*n*HF. The sample was warmed to −78 °C and well mixed before warming to −50 °C to dissolve the solid. The solution was cooled to −78 °C and over the course of 24 h, colorless crystals formed. The reaction vessel was maintained at −78 °C, while the supernatant was decanted into the side arm of the reaction vessel, which was also maintained at −78 °C. The side arm containing the supernatant was then cooled to −196 °C and heat-sealed under dynamic vacuum. The remaining crystals were dried under dynamic vacuum at −78 °C and stored at −78 °C until a suitable crystal could be selected and mounted on the X-ray diffractometer.

2.7. Synthesis and Characterization of [$BrOF_2$][AsF_6]·2KrF_2

2.7.1. Preparation of [$BrOF_2$][AsF_6]

In a typical synthesis, 62.1 mg (0.126 mmol) of [$BrOF_2$][AsF_6]·XeF_2 that had been prepared in a ¼-in. o.d. FEP reaction tube was pumped under dynamic vacuum for 12−18 h at 0 °C. The resulting white powder was shown to be [$BrOF_2$][AsF_6] by low-temperature Raman spectroscopy[128] and, in contrast with a previous report,[128] was stable for at least 12 h at room temperature with no signs of decomposition.

2.7.2. Preparation of $[BrOF_2][AsF_6]{\cdot}2KrF_2$

Approximately 0.3 mL of aHF was condensed into an evacuated ¼-in. o.d. FEP reaction tube containing 40.7 mg (0.126 mmol) of freshly prepared $[BrOF_2][AsF_6]$ at −196 °C. The frozen HF was melted onto the $[BrOF_2][AsF_6]$ sample at −78 °C and was then refrozen at −196 °C. Krypton difluoride (45.0 mg, 0.369) was sublimed into the reactor at −196 °C, followed by warming to −78 °C, whereupon KrF_2 immediately reacted as evidenced by the increased volume of the white solid that had remained undissolved at −78 °C. The reactants were well mixed, and the product was isolated after 2 h by removal of the HF solvent under dynamic vacuum at −78 °C.

2.7.3. Crystal Growth of $[BrOF_2][AsF_6]{\cdot}2KrF_2$

Crystals of $[BrOF_2][AsF_6]{\cdot}2KrF_2$ were grown by the general crystal growth procedure described in Section 2.10.1 and entailed slow cooling of an HF solution of $[BrOF_2][AsF_6]{\cdot}2KrF_2$, previously saturated at ca. −40 °C, from −51 to −55 °C over the course of 5 h in a ¼-in. o.d. FEP reactor equipped with a side arm. When crystal growth had ceased, the reactor was maintained at −55 °C, and the supernatant was decanted into the side arm cooled to −78 °C. Once the majority of the supernatant had been decanted, the contents of the side arm were frozen at −196 °C, and the side arm was heat sealed off under dynamic vacuum. The crystals were dried under dynamic vacuum at −60 °C and stored at −78 °C until a suitable crystal could be selected and mounted at low temperature on the diffractometer.

2.8. Syntheses of $[BrOF_2][AsF_6]\cdot nXeF_2$ ($n = 1, 2$) and $[XOF_2][AsF_6]$ (X = Cl, Br)

2.8.1. Preparation of $[BrOF_2][AsF_6]\cdot XeF_2$

In a typical synthesis, 70.5 mg (0.126 mmol) of $[XeOTeF_5][AsF_6]$ was added, inside a drybox, to a ¼-in. o.d. FEP reactor that was fitted to a Kel-F valve by means of a compression fitting. The solid was dissolved in ca. 0.3 mL of BrF_5 at −52 °C and warmed to room temperature as previously described.[129] The solution was cooled to −52 °C, and the solvent was immediately removed between −52 and −50 °C under dynamic vacuum, leaving behind a white microcrystalline powder that contained adducted BrF_5. Completeness of solvent removal was monitored by Raman spectroscopy (see Table 8.1). The solid was pumped under a dynamic vacuum for 12 h with frequent agitation while maintaining the sample at −52 to −50 °C. This resulted in a fine white powder corresponding to $[BrOF_2][AsF_6]\cdot XeF_2$, which was shown by Raman spectroscopy to be free of coordinated BrF_5. The compound was stable indefinitely when stored under anhydrous conditions at −78 °C.

2.8.2. Preparation of $[BrOF_2][AsF_6]\cdot 2XeF_2$

In a typical synthesis, 45.6 mg (0.269 mmol) of XeF_2 was added, inside a drybox, to a ¼-in. o.d. FEP reactor containing 0.130 g (0.265 mmol) of $[BrOF_2][AsF_6]\cdot XeF_2$. The solids were dissolved in ca. 0.3 mL of aHF at −20 °C. Upon cooling the solution to −78 °C, a white microcrystalline powder, corresponding to $[BrOF_2][AsF_6]\cdot 2XeF_2$, precipitated from solution and was isolated by removal of the HF under a dynamic vacuum at −78 °C.

2.8.3. Preparation of $[BrOF_2][AsF_6]$

Crystals of $[BrOF_2][AsF_6]$ were isolated from a solution of $[BrOF_2][AsF_6]{\cdot}XeF_2$ in BrF_5 solvent (see Section 2.8.5). In a typical synthesis, a 60.1 mg sample of $[BrOF_2][AsF_6]{\cdot}XeF_2$ was pumped under dynamic vacuum for 20 h while maintaining the sample at 0 °C. This resulted in a fine, white powder corresponding to $[BrOF_2][AsF_6]$, which was shown to be free of coordinated XeF_2 by Raman spectroscopy. The compound was stable indefinitely when stored at −78 °C.

2.8.4. Crystal Growth of $[BrOF_2][AsF_6]{\cdot}2XeF_2$

Crystals of $[BrOF_2][AsF_6]{\cdot}2XeF_2$ were grown by the general crystal growth procedure described in Section 2.10.1 using a ¼-in. o.d. FEP T-shaped reaction vessel. A 124 mg (0.252 mmol) sample of $[BrOF_2][AsF_6]{\cdot}XeF_2$ was dissolved at ca. −18 °C in ca. 0.3 mL of HF. The solution was cooled from −28 to −32 °C over the course of 12 h, yielding crystals of $[BrOF_2][AsF_6]{\cdot}2XeF_2$. When crystal growth was deemed complete, the reaction vessel was adjusted to and maintained at −35 °C, while the supernatant was decanted into the side arm of the reaction vessel, which was maintained at −78 °C. The side arm containing the supernatant was then cooled to −196 °C and heat-sealed under dynamic vacuum. The remaining crystals were dried under dynamic vacuum at −35 °C and stored at −78 °C until a suitable crystal could be selected and mounted on the X-ray diffractometer.

2.8.5. Crystal Growth of $[BrOF_2][AsF_6]$

The attempted growth of $[BrOF_2][AsF_6]\cdot XeF_2$ crystals by the general crystal growth procedure described in Section 2.10.1 yielded crystalline $[BrOF_2][AsF_6]$ instead. A solution (0.1 mL) of BrF_5 containing 67.0 mg (0.136 mmol) $[BrOF_2][AsF_6]\cdot XeF_2$ was slowly pumped under a dynamic vacuum at −60 °C. Small, clear, needle-shaped crystals of $[BrOF_2][AsF_6]$ grew over a period of 2 h and were isolated by rapidly pumping the remaining solvent off under a dynamic vacuum at −35 °C. The crystals were stored at −78 °C until a suitable crystal could be selected and mounted on the X-ray diffractometer.

2.8.6. Crystal Growth of $[ClOF_2][AsF_6]$

Attempts to grow crystals of a XeF_2 adduct with $[ClOF_2][AsF_6]$ by the general crystal growth procedure described in Section 2.10.1 resulted in the growth of $[ClOF_2][AsF_6]$ and $[Xe_2F_3][AsF_6]$ crystals instead. A ¼-in. o.d. FEP T-shaped reaction vessel containing 0.3 mL of HF, 33.2 mg (0.115 mmol) of $[ClOF_2][AsF_6]$, and 19.5 mg (0.122 mmol) of XeF_2 was warmed to ca. 25 °C in order to dissolve the solids. Slow cooling of the solution from −59 and −62 °C resulted in the formation of block-shaped crystals over the course of 4 h, which were found to be $[Xe_2F_3][AsF_6]$ (trigonal phase,[73] vide infra). When crystal growth was deemed complete, most of the supernatant (−62 °C) was decanted into the side arm of the reaction vessel (−78 °C), and the side arm was frozen at −196 °C and sealed off under dynamic vacuum. When the residual solvent surrounding the $[Xe_2F_3]$ $[AsF_6]$ crystals was removed under dynamic vacuum at −65 °C, numerous thin, brittle, plate-shaped crystals corresponding to $[ClOF_2][AsF_6]$ (vide infra) instantly grew in admixture with crystalline $[Xe_2F_3][AsF_6]$. The crystals were stored at −78 °C until suitable crystals could be selected and mounted on the diffractometer. The block-shaped crystals had a unit cell consistent with the trigonal phase of $[Xe_2F_3][AsF_6]$,[73] whereas the thin plates were shown to be $[ClOF_2][AsF_6]$.

2.9. Synthesis of Xe(II) Derivatives

2.9.1. Preparation of $FXeONO_2$ and $FXe^{16}ON(^{16}O^{18}O)$

In a typical synthesis, ca. 100 mg of $[Xe_3OF_3][AsF_6]$ ($[Xe_3{}^{18}OF_3][AsF_6]$) was synthesized (vide supra) in a ¼-in. o.d. FEP reaction vessel outfitted with a Kel-F valve. The reaction vessel also had a section of ¼-in. o.d. FEP tubing fused to it, forming a side arm that was bent to form an h-shaped reactor. The h-shaped reactor and a ¼-in. o.d. FEP transfer vessel fitted with a Kel-F valve were connected by means of 45° SAE compression fittings to a three-way FEP connector. A nickel vessel outfitted with a 316 stainless steel valve and containing NO_2F was connected to the remaining port of the three-way connector by means of a ¼-in. stainless steel Swagelok Ultratorr union fitted with Viton O-rings. All connections and the FEP reaction vessels were passivated with F_2 for several hours prior to use. The nickel NO_2F sample vessel was cooled to −78 °C, and a portion of NO_2F was condensed into a second ¼-in. o.d. FEP vessel at −196 °C, followed by warming to −78 °C to control the amount of NO_2F added to $[Xe_3OF_3][AsF_6]$. The NO_2F in the auxiliary vessel (−78 °C) was then condensed onto $[Xe_3OF_3][AsF_6]$ at −196 °C, followed by warming the reaction mixture to −50 °C, where, after 5 h, the solid slowly changed from a magenta or red-orange color to a white suspension in excess liquid NO_2F. Excess NO_2F was removed under vacuum at −110 °C to yield a white, microcrystalline, solid mixture of $FXeONO_2$, XeF_2, and $[NO_2][AsF_6]$. Sulfuryl chloride fluoride (ca. 0.75 mL) was then condensed onto the mixture at −196 °C. The solution was warmed to −30 °C and agitated for several seconds to effect dissolution of $FXeONO_2$ and XeF_2. The solid was allowed to settle (ca. 1 min), and the supernatant was then decanted into the side arm of the reaction vessel at −78 °C. After the solid had settled to the bottom of the side arm, the supernatant was decanted into the main tube of the reactor, and the process was repeated. Longer extraction times (ca. 5−10 min) and/or more agitation in attempts to improve product yield resulted in partial $[NO_2][AsF_6]$ extraction, thereby contaminating the final product. The main portion of the reactor, containing $[NO_2][AsF_6]$, was removed by heat-sealing it off under dynamic vacuum, and the $FXeONO_2/XeF_2$ mixture was dried under dynamic vacuum at −78 °C and stored at that temperature until studied by Raman spectroscopy.

2.9.2. Preparation of $O(XeF)_2$

A sample of ca. 100 mg of $[Xe_3OF_3][AsF_6]$ in a ¼-in o.d. FEP tube fitted with a Kel-F valve was connected to a metal vacuum line through an h-shaped FEP connection that was in turn connected to an empty ¼-in o.d. FEP tube fitted with a Kel-F valve. Nitrosyl fluoride was condensed into the empty tube at –196 °C. The solid NOF was white in color, confirming the high purity of the compound. A small amount of NOF was then condensed into the top of the reaction vessel at –196 °C. The solid NOF was warmed to –78 °C whereupon it melted, contacting and reacting with $[Xe_3OF_3][AsF_6]$ to form a bright yellow solid over the red-orange solid precipitate. The sample was titrated with NOF at −78 °C until no red color persisted, resulting in a faint aqua-coloured solid-liquid mixture. Excess NOF was then removed under dynamic vacuum at −78 °C, yielding a pale yellow solid.

The ^{18}O-enriched samples of $O(XeF)_2$ were prepared from $[Xe_3{}^{18}OF_3][AsF_6]$ in a manner similar to that used for the preparation of $^{16}O(XeF)_2$.

2.9.3. Attempted Crystal Growth of $O(XeF)_2$

Numerous attempts were made to grow crystals of $O(XeF)_2$ from CH_3CN solution at low temperature. However, complete dissolution could only be achieved at temperatures ranging from –15 to –25 °C. Prolonged times at this temperature (ca. 2–3 hours) failed to crystallize any material, and further cooling failed to produce any solid material, indicative of decomposition which is commensurate with the solid-state decomposition temperature. When the solution was quickly cooled to temperatures at or below –30 °C, crystals immediately formed, but detonated after drying at –42 °C, emitting blue light. Attempts to mount crystals grown quickly at –35 °C and slightly wet with CH_3CN gave a diffraction pattern, but no unit cell could be determined, and was likely because the fast crystal growth yielded multiple crystals rather than single crystals.

2.10. X-ray Crystallography

2.10.1. Crystal Growth

Unless otherwise noted, crystals for structure determination by single crystal X-ray diffraction were grown in the low-temperature crystal growing apparatus depicted in Figure 2.7. The following procedure summarizes the general approach used to grow crystals from solutions using the temperature gradient method.

Solvent (ca. 1 mL) was condensed onto the compound (ca. 0.3 mmol) at –196 °C that had been synthesized in situ in one arm of a ¼-in o.d. FEP T-shaped reactor fitted with a Kel-F valve. The reactor was warmed so as to just effect dissolution, and while maintained at that temperature, the reactor was attached to a vacuum line and pressurized to ca. 1 atm with dry nitrogen. The arm containing the solution was inclined at ca. 5° from the horizontal inside the glass dewar of a crystal growing apparatus[99] that had been previously adjusted to the same temperature. The temperature was then lowered over a period of time, usually several hours, whereupon crystals began to grow on the walls of the FEP vessel. The reactor was then held for a further period of time to allow for more complete crystallization. Crystals were isolated by decanting the solvent under dry nitrogen into the side arm of the FEP vessel which was immersed in liquid nitrogen, followed by evacuation and vacuum drying of the crystalline product under dynamic vacuum at –80 °C before the side-arm containing the supernatant was heat-sealed off. A crystal having dimensions less than 0.35 x 0.35 x 0.35 mm^3 was selected at –104 ±2 °C for low-temperature X-ray structure determination and was mounted in a cold stream (–173 °C) on a goniometer head as described in the next section.[130]

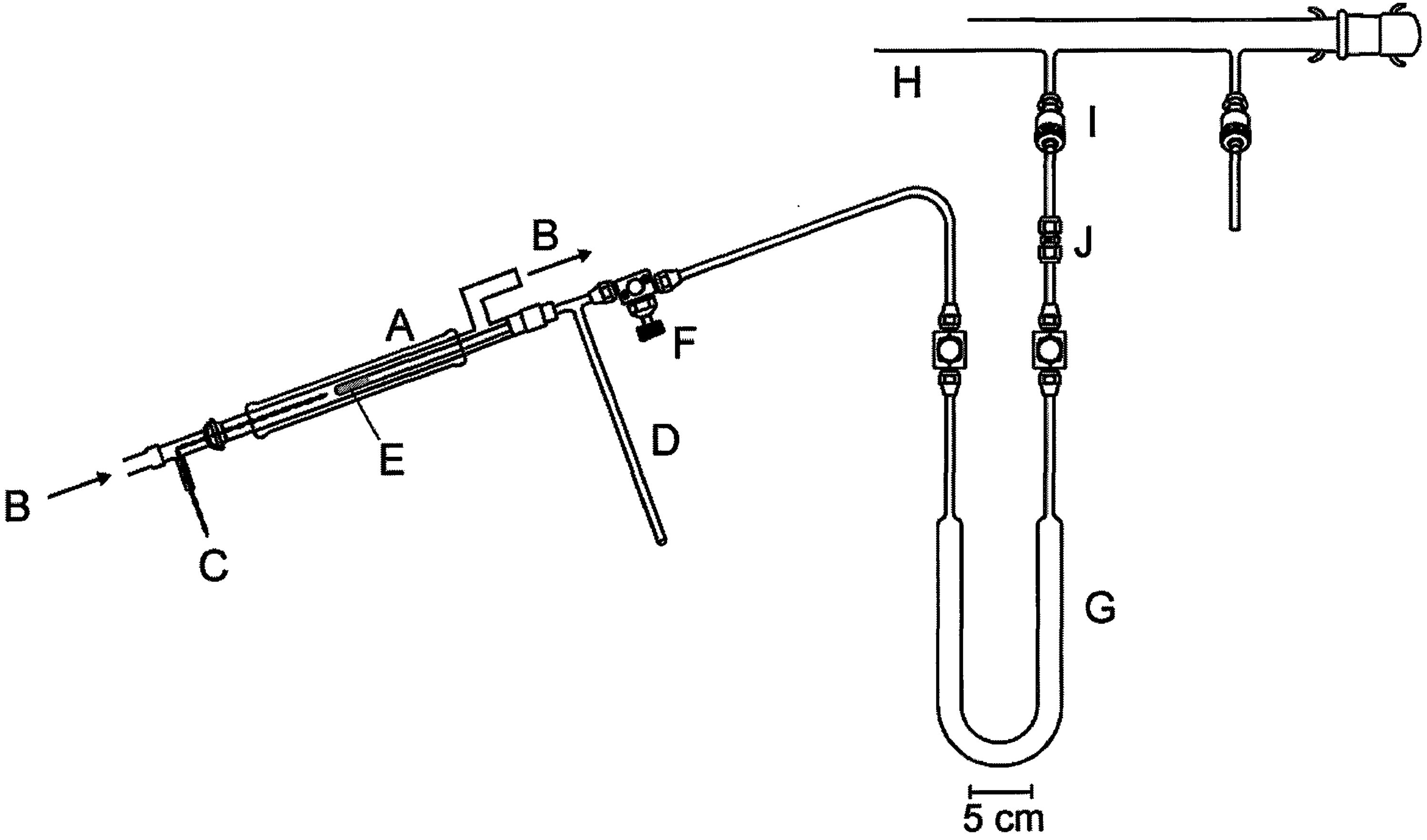

Figure 2.7. Low-temperature crystal growing apparatus. (A) Glass-jacketed dewar. (B) Nitrogen cold flow. (C) Thermocouple lead. (D) T-shaped FEP reaction vessel with side arm. (E) Sample region. (F) Kel-F valve. (G) FEP U-trap. (H) Vacuum manifold. (I) Greaseless J-Young valve with PTFE barrel. (J) ¼″ PTFE Swagelok or ¼-in. stainless steel Swagelok Ultra-Torr connector. From ref 108.

2.10.2. Low-Temperature Crystal Mounting

Because most of the samples investigated in this work were thermally unstable and/or moisture sensitive, all of the samples investigated were mounted at low temperature using the apparatus depicted in Figures 2.8 and 2.9. The reaction vessels containing the samples were first cut open below the Kel-F valve under a flow of dry argon gas, using an inverted glass funnel, while maintaining the sample at –78 °C. The sample was then quickly dumped into to the aluminum trough of the crystal mounting apparatus under a stream of dry argon, precooled (–104 ±2 °C) by the regulated passage of dry nitrogen gas flow through a 5-L dewar filled with liquid N_2 (Figure 2.8). The temperature inside the trough was measured using a copper-constantan thermocouple positioned in the sample region of the trough. Using an additional glass sleeve, which was fitted into a concentric position around the silvered cold-flow dewar, an ambient nitrogen gas flow was slowly passed through the sleeve in order to maintain a laminar flow, thereby reducing atmospheric moisture build up in the trough. Crystals were then selected using a stereo-zoom microscope and mounted on a glass fibre (0.05 to 0.1-mm o.d.) using perfluorinated polyether oil (Ausimont Inc., Fomblin Z15 or Z25) which served as an adhesive upon freezing at low temperature. The glass fibre was previously mounted with epoxy cement to a copper pin fitted to a magnetic base and affixed to the end of a magnetic wand (Hampton Research). The magnetic wand could be fastened to an adjustable support stage such that samples could be inspected under the stereo-zoom microscope once affixed to the glass fibre. The mounted crystal and magnetic pin were quickly (ca. 5 s) transferred from the crystal mounting apparatus to the magnetic mount

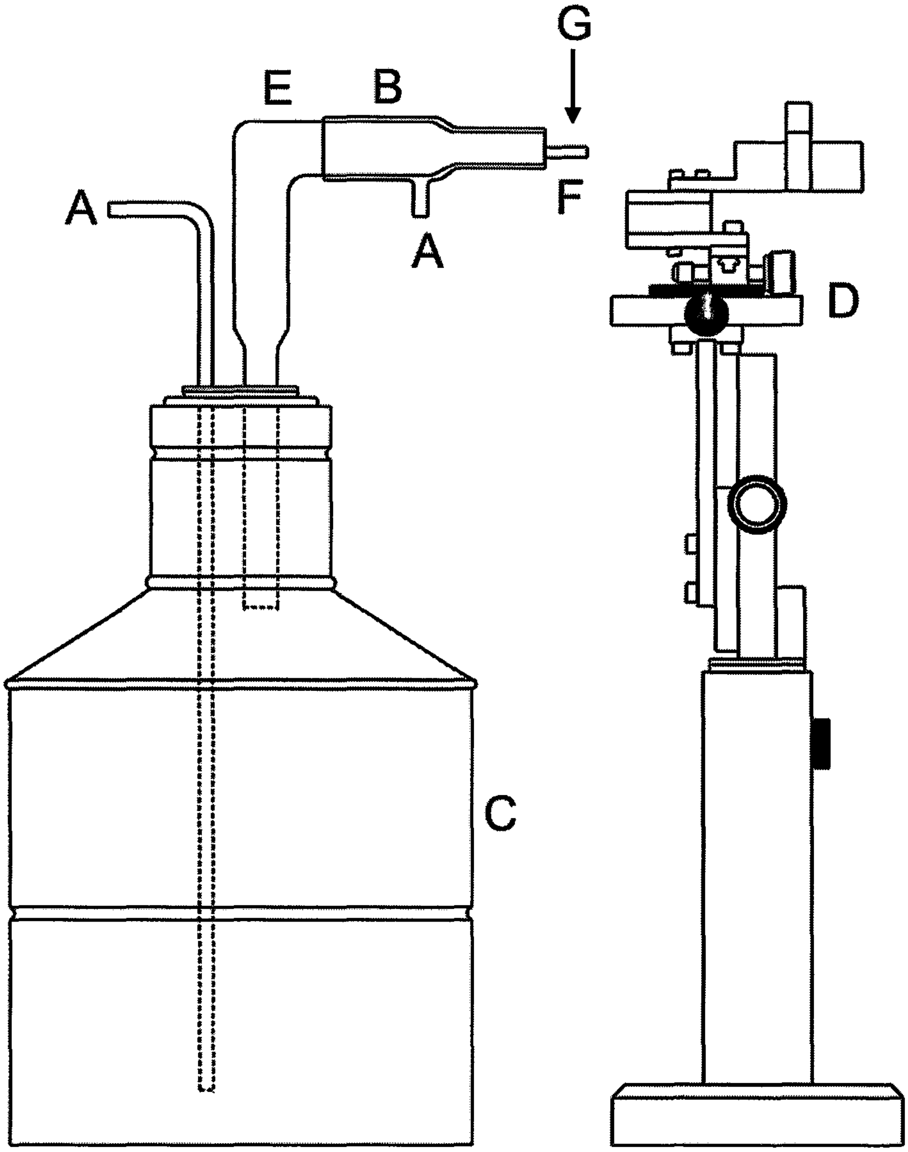

Figure 2.8. Low-temperature crystal mounting apparatus. (A) Nitrogen inlet. (B) Glass sleeve for ambient nitrogen flow. (C) Liquid N_2 dewar. (D) Adjustable support stage. (E) Silvered dewar (glass). (F) Aluminum trough. (G) Stereo-zoom microscope. From ref 108.

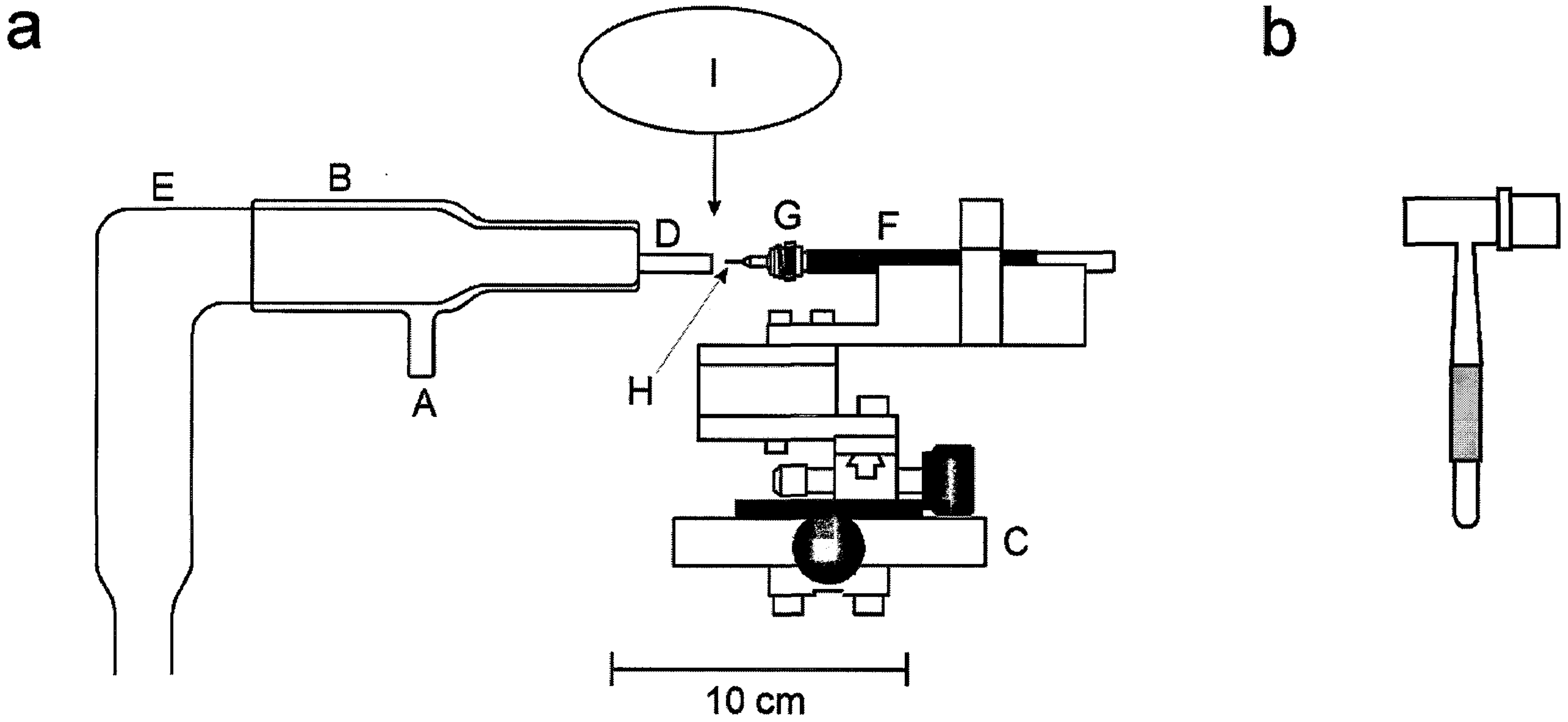

Figure 2.9. (a) Enlarged view of the crystal mounting apparatus; (A) Ambient nitrogen gas flow inlet. (B) Glass sleeve for ambient nitrogen gas flow. (C) Adjustable support stage. (D) Aluminum trough. (E) Silvered glass jacketed dewar. (F) Magnetic-tipped wand affixed to (G) the magnetic-based copper pin-fibre assembly. (H) Glass fibre. (I) Stereo-zoom microscope. (b) A set of cryotongs employed in the transfer of the copper pin-fibre assembly with adhered crystal from the support stage to the goniometer head. From ref 108.

of the goniometer by means of cryotongs (Hampton Research) which were precooled in liquid N_2 prior to use. The crystals were maintained at low temperature on the goniometer head by a cold N_2 gas flow provided by a Oxford Cryosystems low-temperature cryostream accessory.

2.10.3. Data Collections

The crystallographic data acquired during the course of this Thesis were collected using two different diffractometers, which are each described in detail in the subsequent sections. Both instruments were equipped with a Oxford Cryosystems low-temperature cryostream accessory that provided a stream of cold, gaseous N_2 for low-temperature data collection. Both molybdenum instruments were controlled by a Cryostream Controller 700 (Oxford Cryosystems).

2.10.3.1. Siemens P4 diffractometer.

The Siemens diffractometer was equipped with a Siemens 1K CCD area detector controlled by SMART[131] and a rotating anode (molybdenum) emitting Kα radiation monochromated (λ = 0.71073 Å) by a graphite crystal. Diffraction data collection (–173 °C) consisted of a full φ-rotation at $\chi = 0^\circ$ using 0.3° (1040 + 30) frames, followed by a series of short (80 frames) ω scans at various φ and χ settings to fill the gaps. The crystal-to-detector distance was 4.994 cm, and the data collection was carried out in a 512 × 512 pixel mode using 2 × 2 pixel binning. Processing of the raw data was completed using

SAINT+,[132] which applied Lorentz and polarization corrections to three-dimensionally integrated diffraction spots.

2.10.3.2. Bruker SMART APEX II diffractometer.

The Bruker SMART APEX II diffractometer was equipped with an APEX II 4K CCD area detector and a 3-axis goniometer, controlled by the APEX2 Graphical Use Interface (GUI) software,[133] and a sealed tube X-ray source (Mo target) emitting Kα radiation monochromated (λ = 0.71073 Å) by a graphite crystal. Diffraction data collection was typically done at –173 °C and consisted of a full ϕ-rotation at a fixed χ = 54.74° with 0.36° (1010) frames, followed by a series of short (250 frames) ω scans at various φ settings to fill the gaps. The crystal-to-detector distance was 4.959–4.989 cm, and the data collection was carried out in a 512 × 512 pixel mode using 2 × 2 pixel binning. Processing of the raw data was completed using the APEX2 GUI software,[133] which applied Lorentz and polarization corrections to three-dimensionally integrated diffraction spots.

2.10.4. Solution and Refinement of Structures

The program SADABS[132] was used for the scaling of diffraction data, the application of a decay correction, and an empirical absorption correction based on the intensity ratios of redundant reflections. The XPREP program was used to confirm the unit cell dimensions and the crystal lattices. The final refinements were obtained by introducing anisotropic parameters for all the atoms except hydrogen, an extinction parameter, and the recommended weight factor. The maximum electron densities in the final difference Fourier maps were located around the heavy atoms. All calculations were performed using the SHELXTL package for the structure determination, refinement, and molecular graphics.[134,135] Structure solutions were obtained by direct methods which located the As, Br, Kr, Sb and/or Xe atoms. Successive difference Fourier syntheses revealed the positions of the carbon, nitrogen, oxygen, and fluorine atoms. The PLATON[136] program could not suggest additional or alternative symmetries. For $F_2OXeN{\equiv}CCH_3$, the positions of the hydrogen atoms were calculated and a relatively satisfactory model could be obtained, however, the refinement as a single-crystal remained at an overall agreement factor of about 32%, with unsatisfactory behaviour for some parameters. With the introduction of the twin matrix $(1010\bar{1}000\bar{1})$ characteristic of a pseudomerohedral twin, the refinement converged. The volume fractions of the twin individuals are $t_{\mathrm{I}} = 0.87$ and $t_{\mathrm{II}} = 0.13$. A positional disorder arises for the $BrOF_2^+$ cation in $[BrOF_2][AsF_6]$ in which the oxygen and fluorine atoms could not be distinguished from one another.

2.11. Raman Spectroscopy

All Raman spectra were recorded on a Bruker RFS 100 Fourier transform Raman spectrometer employing a quartz beam splitter and a liquid-nitrogen cooled Ge diode detector. The 1064-nm line of a Nd-YAG laser was used for excitation with a laser spot of <0.1 mm at the sample and configured such that only the 180°-backscattered radiation was detected. The scanner velocity was 5 kHz and the wavelength range was 5894 to

10394 cm^{-1} relative to the laser line at 9394 cm^{-1}, resulting in a spectral range of 3501 to –999 cm^{-1}. Fourier transformations were processed using a Blackman Harris 4-term apodization and a zero-filling factor of 2. Typical acquisitions used 1.0 cm^{-1} resolution, 300–350 mW power, and involved 600 scans for strongly scattering samples and 1200–1600 scans for weakly scattering samples. Low-temperature spectra were acquired using a Bruker I0121 low-temperature accessory which provided temperatures ranging from –150 to –160 °C for routine samples, with an estimated error of ±1 °C.

2.12. Nuclear Magnetic Resonance Spectroscopy

High-field nuclear magnetic resonance spectra were recorded unlocked (field drift < 0.1 Hz h^{-1}) on a Bruker DRX-500 (11.744 T) spectrometer using XWINNMR. The spectrometer was equipped with a Bruker 5-mm combination ^{1}H/^{19}F probe, or a Bruker 5-mm broad band inverse probe. Low-temperature spectra were acquired using a cold nitrogen gas flow and a variable temperature controller (BV-T 3000). The ^{19}F and ^{129}Xe spectra were referenced externally at 30 °C using neat samples of $CFCl_3$ and $XeOF_4$, respectively. The chemical shift convention used is that a positive (negative) sign indicates a chemical shift to high (low) frequency of the reference compound. A summary of typical spectroscopic parameters used for the spectra acquired for this Thesis are provided in Table 2.1. Spectra in the present study often used Gaussian multiplication to enhance spectral resolution.

Table 2.1. Summary of Parameters Typically Used for NMR Data Acquisition

Acquisition Parameter[a]	^{19}F	^{129}Xe
B_o = 11.744 T		
SF (MHz)	470.593	139.051
TD (K)	32	16
SW (kHz)	25	20
Hz/pt	0.76	2.44
PW (μs)	1.00	18.0
RD (s)	0	0.1
NS	200	1,000

[a] The abbreviations denote: B_o, applied magnetic field; SF, spectral frequency; TD, time domain; SW, sweep width; PW, pulse width; RD, relaxation delay; NS, number of scans

2.13. Quantum-Chemical Calculations

All calculations were performed using the Gaussian 03[137] or Gaussian 09[138] software packages. Geometries were fully optimized using density functional theory (SVWN, SVWN5, BP86, B3LYP, B3PW91, MPW1PW91, and/or PBE1PBE) and Møller-Plesset (MP2) methods using (SDB-)cc-pVTZ, aug-cc-pVDZ(-PP), and/or aug-cc-pVTZ(-PP) basis sets. The standard all-electron cc-pVTZ, aug-cc-pVDZ, or aug-cc-pVTZ basis sets, as implemented in the Gaussian program, were utilized for all elements except Kr, Br, Xe and As, for which the semirelativistic large core (RLC) pseudopotential basis set SDB-cc-pVTZ (with cc-pVTZ), aug-cc-pVDZ-PP (with aug-cc-pVDZ), or aug-cc-pVTZ-PP (with aug-cc-pVTZ) were used.[139] The combined uses described are indicated by (SDB-)cc-pVTZ, aug-cc-pVDZ(-PP), and aug-cc-pVTZ(-PP), respectively.

Basis sets were obtained online from the EMSL Basis Set Exchange (https://bse.pnl.gov/bse/portal).[140,141] Fundamental vibrational frequencies were calculated along with Raman intensities, and Natural Bond Orbital (NBO) analyeses were obtained for the optimized local minima. The program GaussView[142] was used to visualize the vibrational displacements that form the basis of the vibrational mode descriptions presented.

CHAPTER 3

$XeOF_2$, $F_2OXeN{\equiv}CCH_3$, and $XeOF_2{\cdot}n$HF; Rare Examples of Xe(IV) Oxide Fluorides

3.1. Introduction

Among the principal formal oxidation states of xenon, +2, +4, +6, and +8, the +4 oxidation state has been little studied and is presently limited to XeF_5^-,[53] XeF_4,[32,35,38] $Xe(OTeF_5)_4$,[38,58,60] $Xe(OTeF_5)_{4-x}F_x$ (x = 0–3),[38] several XeF_3^+ salts,[48,51,52] and $[C_6F_5XeF_2][BF_4]$,[62] and to preliminary reports of F_3XeOIO_4,[64] $F_xXe(OTeF_5)_{3-x}^+$ (x = 0–2),[61] $XeOF_2$,[65–67] and $XeOF_3^-$.[67] The modest and slow progress that has been made in the syntheses and structural investigations of xenon(IV) oxide fluoride species contrasts with that of xenon(VI)[5,143] and stems from the explosive nature of the synthetic precursor, $XeOF_2$, and the need to find a reliable, high-yield synthesis for $XeOF_2$.

Although vibrational spectroscopic evidence for $XeOF_2$ has been communicated on three prior occasions, none of these studies resulted in the unambiguous characterization or the isolation of pure $XeOF_2$. In two studies, $XeOF_2$ was reported as the product of the co-condensation of H_2O and XeF_4 vapors at low temperatures. Co-deposited thin films were characterized by infrared spectroscopy,[65,66] yielding infrared spectra that were in good agreement with each other. In one of these studies, samples were also prepared by a bulk co-condensation procedure and characterized by Raman spectroscopy.[66] Both the bulk co-condensation product[66] and the infrared spectra obtained from thin films[65,66] are shown by the present work to be mixtures of $XeOF_2$ and

$XeOF_2{\cdot}n$HF. One of the components in the latter studies, $XeOF_2{\cdot}n$HF, was subsequently synthesized as the sole product by the hydrolysis of finely divided XeF_4 in HF but was erroneously attributed to $XeOF_2$.[67]

The inconsistencies related to the vibrational spectra of the reaction products of XeF_4 and H_2O in the prior published work, the lack of corroborating structural evidence for the products obtained in these early studies, and the absence of a facile synthesis of synthetically useful amounts of pure $XeOF_2$ motivated the present study, which describes reproducible high-yield and high-purity routes to $XeOF_2$, $F_2OXeN{\equiv}CCH_3$, and $XeOF_2{\cdot}n$HF and their structure determinations, offering the potential to extend the range of oxo-derivatives of xenon(IV).

3.2. Results and Discussion

3.2.1. Syntheses and Properties of $XeOF_2$, $F_2OXeN{\equiv}CCH_3$, and $XeOF_2{\cdot}n$HF. Reaction progress and the purities of all products were routinely monitored by recording the low-temperature Raman spectra (–150 °C) of the solids which were isolated as their natural abundance, ^{18}O-enriched (98.6 atom %), and ^{2}H-enriched (99.5 atom %) isotopomers.

Xenon oxide difluoride was initially obtained as the CH_3CN adduct by low-temperature hydrolysis of XeF_4 in CH_3CN solution containing 2.00 M H_2O according to eq 3.1. Water was added in ca. 3–5% stoichiometric excess to avoid unreacted XeF_4

$$XeF_4 + H_2O + CH_3CN \xrightarrow[-45\text{ to }-42\ ^{\circ}\mathrm{C}]{CH_3CN} F_2OXeN{\equiv}CCH_3 + 2HF \qquad (3.1)$$

contaminant in the product. A 2-fold stoichiometric excess of H_2O yielded only $XeOF_2$ and did not result in the formation of other xenon-containing products such as $OXe(OH)F$, $OXe(OH)_2$, or XeO_2. Although HF resulting from the hydrolysis of XeF_4 forms an adduct with CH_3CN (see 3.2.4, Raman Spectroscopy), it could be removed under dynamic vacuum along with the solvent at –45 to –42 °C. The $F_2OXeN{\equiv}CCH_3$ adduct crystallized as pale yellow blades at –35 to –45 °C which were isolated by removal of the bulk solvent under dynamic vacuum at –45 to –42 °C while periodically monitoring its removal by low-temperature Raman spectroscopy.

Further pumping on polycrystalline $F_2OXeN{\equiv}CCH_3$ for several hours at –45 to –42 °C, resulted in slow removal of adducted CH_3CN (eq 3.2), with the time depending on the sample size, leaving behind $XeOF_2$ as a bright yellow amorphous powder. Neither $F_2OXeN{\equiv}CCH_3$ nor $XeOF_2$ were soluble in SO_2ClF up to –78 °C and were recovered unchanged upon removal of SO_2ClF under vacuum at –78 °C.

$$F_2OXeN{\equiv}CCH_3 \xrightarrow[\text{-45 to -42 °C}]{\text{dynamic vac.}} XeOF_2 + CH_3CN \qquad (3.2)$$

Addition of anhydrous HF to $XeOF_2$ at –78 °C resulted in a very pale yellow and insoluble powder having a new Raman spectrum in which several bands were sensitive to $^{1/2}H$ isotopic substitution (see 3.2.4, Raman Spectroscopy). The results indicated that $XeOF_2{\cdot}n HF$ was formed according to eq 3.3. When $XeOF_2{\cdot}n HF$ was pumped under dynamic vacuum at –78 °C, with frequent agitation, bound HF was slowly removed over

$$XeOF_{2\,(s)} + n HF \xrightarrow[\text{12 h @ -78 °C}]{\text{HF}} XeOF_2{\cdot}n HF \qquad (3.3)$$

a period of several hours, regenerating unsolvated $XeOF_2$.

All three compounds, $F_2OXeN{\equiv}CCH_3$, $XeOF_2$, and $XeOF_2{\cdot}n$HF, are kinetically stable at –78 °C for indefinite periods of time, but decompose rapidly to explosively with emission of blue light upon warming to 0 °C. The major gas-phase decomposition pathway is O_2 elimination according to eq 3.4 while the minor pathway is disproportionation to Xe(II) and Xe(VI) according to eq 3.5. Both decomposition pathways have been observed in CH_3CN solutions of $XeOF_2$ and inferred from the

$$XeOF_{2\,(g)} \longrightarrow XeF_{2(g)} + \tfrac{1}{2}\,O_{2(g)} \qquad (3.4)$$

$$\Delta H^{o}_{rxn} = -245.8\ \mathrm{kJ\ mol^{-1}} \qquad \Delta G^{o}_{rxn} = -259.3\ \mathrm{kJ\ mol^{-1}} \qquad \mathrm{MP2/(SDB\text{-})cc\text{-}pVTZ}$$

$$2XeOF_{2\,(g)} \longrightarrow XeF_{2(g)} + XeO_2F_{2(g)} \qquad (3.5)$$

$$\Delta H^{o}_{rxn} = -98.8\ \mathrm{kJ\ mol^{-1}} \qquad \Delta G^{o}_{rxn} = -86.9\ \mathrm{kJ\ mol^{-1}} \qquad \mathrm{MP2/(SDB\text{-})cc\text{-}pVTZ}$$

formation of small, but unequal, molar amounts of XeF_2 and XeO_2F_2 (see 3.2.2, NMR Spectroscopy).

3.2.2. ^{129}Xe, ^{19}F, and ^{17}O NMR Spectroscopy. In contrast with HF, $XeOF_2$ has appreciable solubility in CH_3CN, allowing the low temperature (–42 °C) ^{19}F, ^{17}O, and ^{129}Xe NMR spectra to be recorded.

The ^{19}F NMR spectrum of a solution of $XeOF_2$ prepared by the hydrolysis of XeF_4 in CH_3CN consisted of a singlet (–48.8 ppm) with accompanying ^{129}Xe ($I = \frac{1}{2}$, 26.44%) satellites corresponding to $^{1}J(^{19}\mathrm{F}–^{129}\mathrm{Xe}) = 3446$ Hz (Figure 3.1a). In addition, a weak singlet (–179.2 ppm) corresponding to XeF_2 (~2% or less) with accompanying ^{129}Xe ($I = \frac{1}{2}$, 26.44%) satellites ($^{1}J(^{129}\mathrm{Xe}–^{19}\mathrm{F}) = 5641$ Hz), a second weaker singlet (83.2 ppm) corresponding to XeO_2F_2 (~1% or less) with accompanying ^{129}Xe satellites

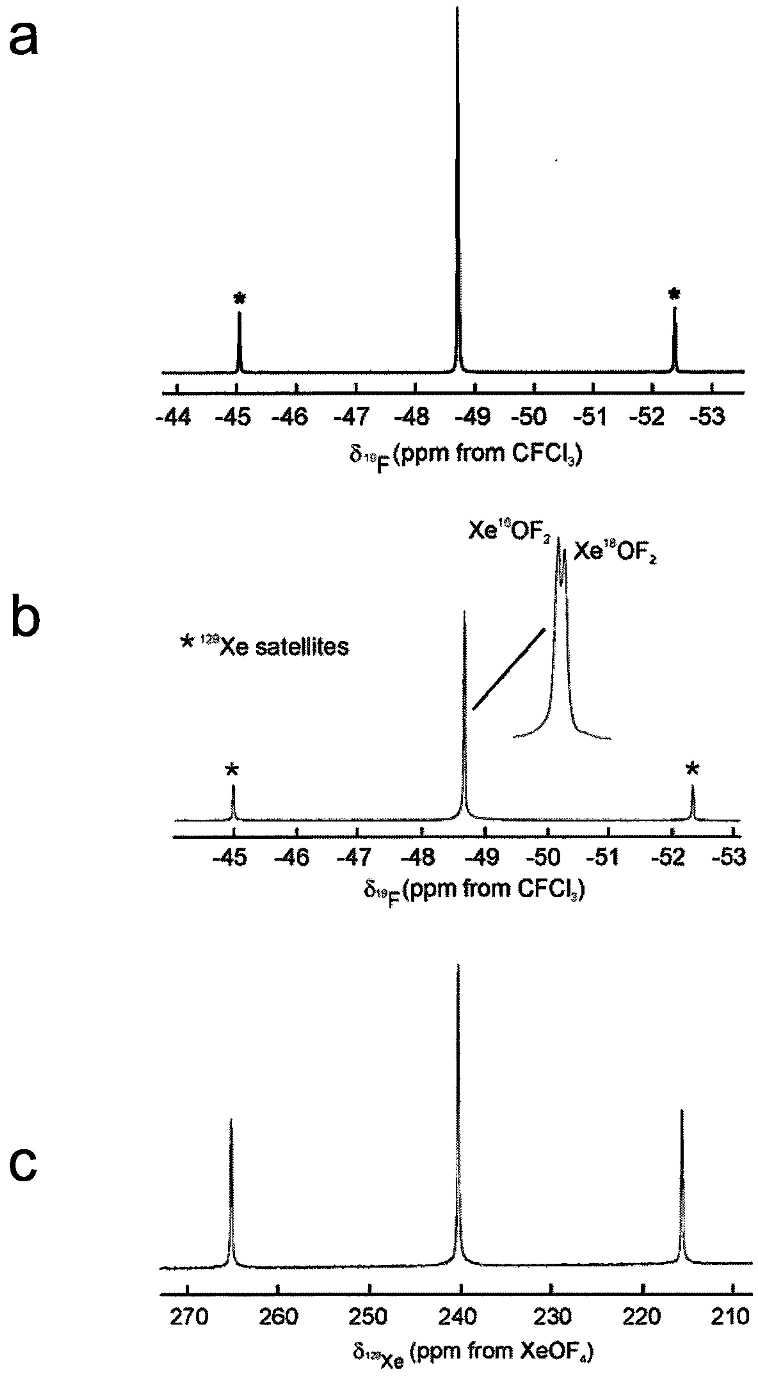

Figure 3.1. The ^{19}F NMR spectrum (470.599 MHz) of (a) Xe^{16}OF$_2$ and (b) Xe^{16,18}OF$_2$, and (c) the ^{129}Xe NMR spectrum (138.339 MHz) of Xe^{16}OF$_2$. Spectra were recorded in CH$_3$CN at –45 °C.

($^1J(^{129}\text{Xe}–^{19}\text{F})$ = 1320 Hz), and an intense singlet corresponding to HF ($\delta(^{19}\text{F})$, –179.8 ppm,[144] $\Delta\nu_{½}$ = 83 Hz) were observed. The ^{129}Xe NMR spectrum of $XeOF_2$ in CH_3CN consisted of a triplet ($\delta(^{129}\text{Xe})$, 242.3 ppm) arising from $^1J(^{129}\text{Xe}–^{19}\text{F})$ = 3447 Hz (Figure 3.1c). Weak XeF_2 [$\delta(^{129}\text{Xe})$, –1779.0 ppm, $^1J(^{19}\text{F}–^{129}\text{Xe})$ = 5648 Hz] and XeO_2F_2 [$\delta(^{129}\text{Xe})$, 227.4 ppm, $^1J(^{19}\text{F}–^{129}\text{Xe})$ = 1324 Hz] resonances were also visible as triplets in the ^{129}Xe NMR spectrum. In several preparations, small amounts (ca. 0.01 %) of unreacted XeF_4 [$\delta(^{19}\text{F})$, –20.5 ppm; $\delta(^{129}\text{Xe})$, 336.7 ppm; $^1J(^{129}\text{Xe}–^{19}\text{F})$ = 3911 Hz] were also observed. The increased shielding (lower frequency) of the ^{129}Xe resonance of $XeOF_2$ relative to that of XeF_4 is opposite to the decreased shielding (high-frequency shift) that occurs upon increasing oxygen substitution observed for Xe(VI): XeF_6, $XeOF_4$, XeO_2F_2, XeO_3 and for Xe(VIII): XeO_3F_2, XeO_4.[7] The trend reversal may arise because one or more CH_3CN molecules are nitrogen coordinated to the Lewis acidic xenon center of $XeOF_2$ (see 3.2.3, X-ray Crystal Structure of $F_2OXeN{\equiv}CCH_3$), contributing added shielding to ^{129}Xe and ^{19}F. Upon donation of nitrogen electron lone pair electron density into the xenon valence shell, the ^{129}Xe nuclear shielding is enhanced and the effective electronegativity of Xe(IV) is decreased, resulting in increased ^{19}F shielding relative to that of XeF_4. Failure to observe separate resonances for bound and free CH_3CN in the low-temperature ^{1}H and ^{14}N NMR spectra of $XeOF_2$ solutions in CH_3CN indicates that the Xe-N donor-acceptor interaction(s) is (are) labile under these conditions.

A solution of $XeOF_2$ in CH_3CN was also prepared by the reaction of XeF_4 with ^{17}O-enriched water (35.4%, ^{16}O; 21.9%, ^{17}O; 42.77%, ^{18}O) dissolved in CH_3CN at –45 °C. The central line and the ^{129}Xe satellites of the ^{19}F resonance [$\delta(^{19}\text{F})$, –48.6 ppm;

${}^{1}J({}^{129}\mathrm{Xe}–{}^{19}\mathrm{F})$ = 3448 Hz] were split as a result of the secondary isotope shift [${}^{2}\Delta{}^{19}\mathrm{F}({}^{18/16}\mathrm{O})$ = –0.0136 ppm] between $\mathrm{Xe}^{16}\mathrm{OF}_2$ and $\mathrm{Xe}^{18}\mathrm{OF}_2$ (Figure 3.1b). The observation of the isotope shift confirms the assignment of the singlet and its satellites to XeOF_2 and represents the only two-bond isotope shift that has been observed for a xenon compound. The ^{17}O NMR spectrum showed an intense broad resonance at $\delta({}^{17}\mathrm{O})$ = 209 ppm ($\Delta\nu_{½}$ = 1300 Hz), assigned to XeOF_2, but was too broad, owing to quadrupolar relaxation, to show ${}^{2}J({}^{19}\mathrm{F}–{}^{17}\mathrm{O})$ coupling or ^{129}Xe satellites arising from ${}^{1}J({}^{129}\mathrm{Xe}–{}^{17}\mathrm{O})$ coupling. These couplings also were not visible in the ^{129}Xe [δ = 240.1 ppm; ${}^{1}J({}^{129}\mathrm{Xe}–{}^{19}\mathrm{F})$ = 3448 Hz] and the ^{19}F NMR spectra because quadrupolar relaxation by the ^{17}O, and its attendant broadening, made it impossible to distinguish the equi-intense components of the anticipated sextets ($I = {}^{5}/_{2}$) from the spectral baselines. A weak, broad resonance at $\delta({}^{17}\mathrm{O})$ = 3.4 ppm, which likely arises from excess $\mathrm{H_3O^+}$, and a weak, but very sharp resonance at $\delta({}^{17}\mathrm{O})$ = 77.7 ppm ($\Delta\nu_{½} \approx$ 10 Hz) were also observed in the ^{17}O NMR spectrum. The latter resonance likely results from the decomposition of XeOF_2 in $\mathrm{CH_3CN}$ at –45 °C. Although XeOF_2 was shown to decompose according to eq 3.6 in $\mathrm{CH_3CN}$ solvent, it may also act as a source of atomic oxygen (eq 3.7) which is expected to react

$$\mathrm{XeOF_2} \xrightarrow[-45\ ^{\circ}\mathrm{C}]{\mathrm{CH_3CN}} \mathrm{XeF_2} + ½\mathrm{O_2} \tag{3.6}$$

$$\mathrm{XeOF_2} \xrightarrow[-45\ ^{\circ}\mathrm{C}]{\mathrm{CH_3CN}} \mathrm{XeF_2} + [\mathrm{O}] \tag{3.7}$$

$$\mathrm{CH_3C{\equiv}N} + [\mathrm{O}] \xrightarrow[-45\ ^{\circ}\mathrm{C}]{\mathrm{CH_3CN}} \mathrm{CH_3C{\equiv}N^{+}{-}O^{-}} \tag{3.8}$$

with $\mathrm{CH_3CN}$ to give acetonitrile *N*-oxide according to eq 3.8. The reaction of $\mathrm{CH_3CN}$ with atomic oxygen, $\mathrm{O}({}^{3}\mathrm{P})$, generated by laser flash photolysis of pyridine *N*-oxide in

CH_3CN solvent, has been previously documented.[145,146] The narrow ^{17}O line width is consistent with the axial symmetry of $CH_3C{\equiv}N^+{-}O^-$.

3.2.3. X-ray Crystal Structure of $F_2OXeN{\equiv}CCH_3$.

A summary of the refinement results and other crystallographic information are given in Table 3.1. Important bond lengths, bond angles, and contacts are listed in Table 3.2.

The structure of $F_2OXeN{\equiv}CCH_3$ consists of $XeOF_2$ molecules and CH_3CN ligands that interact by means of short Xe···N contacts (Figures 3.2 and 3.3). Two crystallographically independent adduct conformations define the asymmetric unit in which four molecules of each conformer comprise the contents of the unit cell. The Xe–N–C angles are bent in both conformers with the CH_3CN ligand lying in the $XeOF_2$ plane for one conformer and out of the $XeOF_2$ plane for the other conformer.

The primary coordination of the $XeOF_2$ moiety is a planar, T-shaped arrangement of two valence electron lone pairs and an oxygen double bond domain in the equatorial plane and two mutually *trans*-fluorine atoms perpendicular to that plane. The nitrogen electron pair donor atom of CH_3CN is coordinated trans to the oxygen atom and is coplanar with the $XeOF_2$ moiety in both conformers so that the geometry of the F_2OXeN moiety is consistent with an AX_2YZE_2 VSEPR[41] arrangement of three single bond domains (X and Z), one double bond domain (Y), and two electron lone pair domains (E), placing the valence electron lone pairs trans to one another.

Table 3.1. Summary of Crystal Data and Refinement Results for $F_2OXeN{\equiv}CCH_3$

space group	$P2_1/c$ (No. 14)
a (Å)	8.7819(4)
b (Å)	13.9862(6)
c (Å)	11.0182(6)
β (deg.)	128.476(2)
V (Å^3)	1059.47(1)
Z (molecules/unit cell)	8
mol. wt. (g mol^{-1})	1810.83
ρ_{calc} (g cm^{-3})	2.838
T (°C)	–173
μ (mm^{-1})	6.43
λ (Å)	0.71073
R_1	0.0299
wR_2	0.0675

R_1 is defined as $= \Sigma\|F_o| - |F_c\|/\Sigma|F_o|$ for $I > 2\sigma(I)$; wR_2 is defined as $[\Sigma[w(F_o^2)^2 - (F_c^2)^2]/\Sigma w(F_o^2)^2]^{1/2}$ for $I > 2\sigma(I)$.

Table 3.2. Experimental and Calculated (C_1) Geometrical Parameters for $F_2OXeN{\equiv}CCH_3$

exptl[a]					SVWN[b]	MP2[b]
Bond Lengths (Å)						
bent in-plane structure[a]		bent out-of-plane structure[a]				
Xe(1)–O(1)	1.778(4)	Xe(2)–O(2)	1.782(4)	Xe(1)–O(1)	1.813	1.774
Xe(1)–F(1)	1.958(3)	Xe(2)–F(3)	1.975(3)	Xe(1)–F(1)	2.013	1.993
Xe(1)–F(2)	1.952(3)	Xe(2)–F(4)	1.981(3)	Xe(1)–F(2)	2.013	1.993
Xe(1)—N(1)	2.808(5)	Xe(2)—N(2)	2.752(5)	Xe(1)---N(1)	2.702	2.883
N(1)–C(10)	1.142(7)	N(2)–C(20)	1.127(7)	N(1)–C(1)	1.152	1.167
C(10)–C(11)	1.448(8)	C(20)–C(21)	1.453(8)	C(1)–C(2)	1.428	1.455
				C(2)–H	1.099	1.087
Bond Angles (deg)						
F(1)–Xe(1)–F(2)	174.2(2)	F(3)–Xe(2)–F(4)	171.9(1)	F(1)–Xe(1)–F(2)	167.6	168.9
F(1)–Xe(1)–O(1)	92.4(2)	F(3)–Xe(2)–O(2)	94.1(2)	F(1)–Xe(1)–O(1)	96.2	95.6
F(2)–Xe(1)–O(1)	93.4(2)	F(4)–Xe(2)–O(2)	94.0(2)	F(2)–Xe(1)–O(1)	96.2	95.6
F(1)–Xe(1)—N(1)	90.1(2)	F(3)–Xe(2)---N(2)	84.5(1)	F(1)–Xe(1)---N(1)	83.7	84.4
F(2)–Xe(1)—N(1)	84.1(2)	F(4)–Xe(2)---N(2)	87.3(1)	F(2)–Xe(1)---N(1)	83.8	84.4
Xe(1)—N(1)–C(10)	164.9(4)	Xe(2)---N(2)–C(20)	134.6(4)	Xe(1)---N(1)–C(1)	179.2	179.4
N(1)–C(10)–C(11)	178.9(6)	N(2)–C(20)–C(21)	178.4(6)	N(1)–C(1)–C(2)	179.9	179.9
Long Contacts (Å)						
		Xe(2)—N(1)	3.635(5)			
		Xe(2)—N(1A)	3.526(5)			

[a] Bent in-plane and out-of-plane structures and their labeling schemes are given in Figure 3.3. [b] (SDB-)cc-pVTZ basis set. The labeling scheme corresponds to that used in Figure 3.5b.

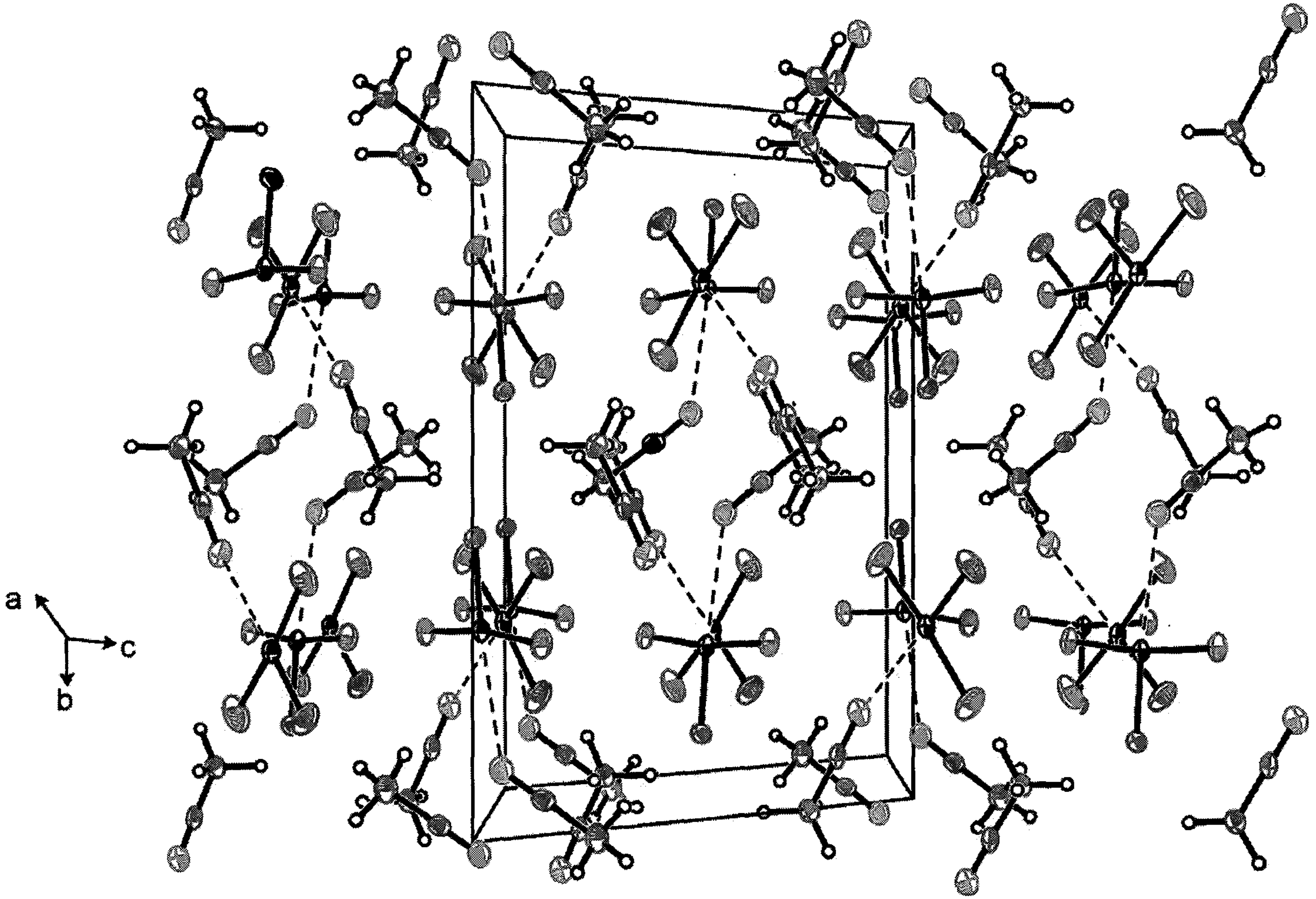

Figure 3.2. Crystal packing for $F_2OXeN{\equiv}CCH_3$ viewed along the *a*-axis; thermal ellipsoids are shown at the 50% probability level.

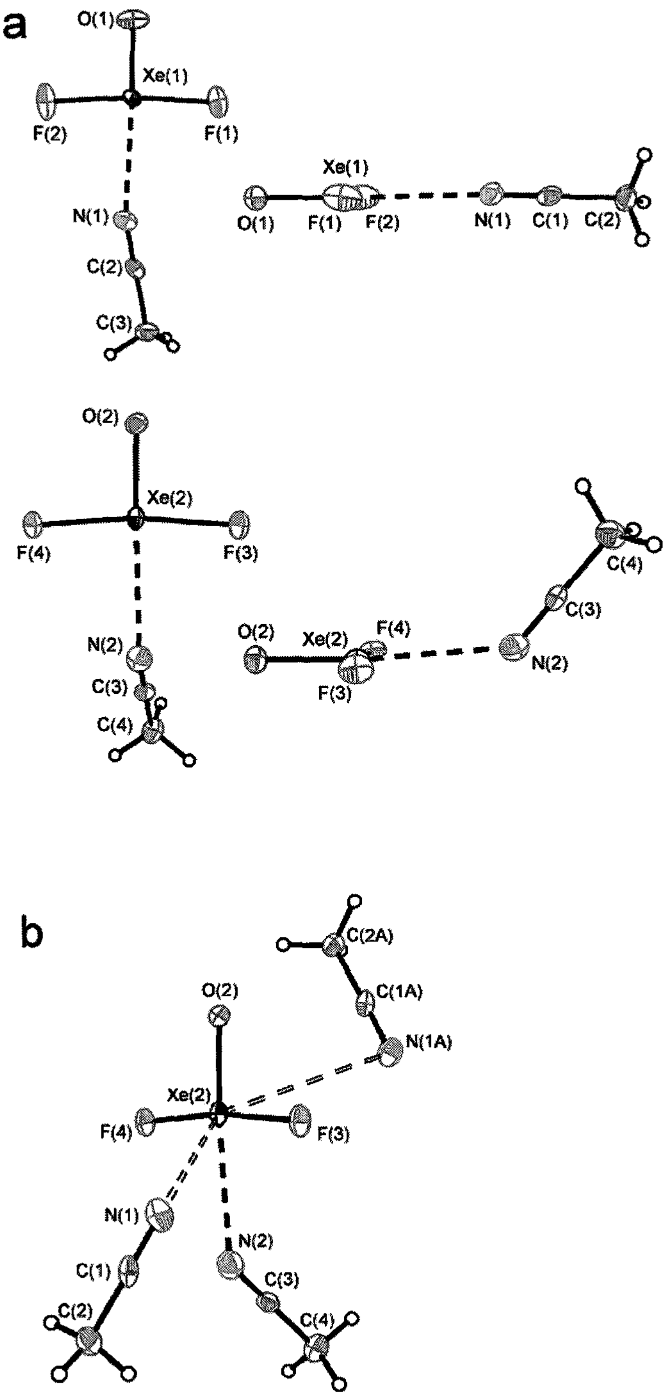

Figure 3.3. The X-ray crystal structure of $F_2OXeN{\equiv}CCH_3$ showing (a) two independent structural units and (b) the long contacts to Xe(2); thermal ellipsoids are shown at the 50% probability level.

The Xe–O bond lengths of both conformers are equal, within 3σ (1.778(4), 1.782(4) Å) and are somewhat longer than those observed in the neutral Xe(VI) and Xe(VIII) oxides and oxide fluorides $\mathrm{XeOF_4}$ (1.713(3) Å),[147] $\mathrm{XeO_2F_2}$ (1.714(4),[148] 1.734(9)[149] Å), $\mathrm{XeO_3}$ (1.74(3)–1.77(3) Å),[33] and $\mathrm{XeO_4}$ (1.736(2) Å).[150] Overall, the Xe–F bond lengths of $\mathrm{F_2OXeN{\equiv}CCH_3}$ are comparable to those in $\mathrm{XeF_4}$ (1.953(2) Å).[32] The Xe-F bond lengths of those of the in-plane conformer (1.952(3), 1.958(3) Å), where the longer Xe–F bond lengths correspond to the shorter Xe–N bond in the out-of-plane conformer. The equatorial F–Xe–F angles (171.9(1)°, out-of-plane; 174.2(2)°, in-plane) are slightly bent away from the Xe–O the out-of-plane conformer (1.975(3), 1.981(3) Å) are slightly longer when compared with double bond domain towards the Xe–N bond, in accord with the greater steric requirement of the double bond domain relative to that of a single bond domain. This angle is reproduced in the calculated structure (see 3.2.5, Computational Results).

The in-plane conformer (Figure 3.3a) has a Xe(1)–N(1) distance of 2.808(5) Å and a Xe(1)–N(1)–C(10) angle of 164.9(4)°. The xenon atom of this conformer has no additional long contacts that are at, or less than the sum of the van der Waals radii of Xe and F (3.63 Å)[55] or Xe and N (3.71 Å).[55] In the case of the out-of-plane conformer (Figure 3.3a), the nitrogen atom lies out of the $\mathrm{XeOF_2}$ plane by 0.23 Å. The NCC moiety is rotated 57.8° out of the $\mathrm{XeOF_2}$ plane and subtends an angle of 11.1° with the OXeN-axis. This conformer has a slightly shorter Xe(2)–N(2) distance (2.752(5) Å) and a smaller Xe(2)–N(2)–C(20) angle (134.6(4)°) than the in-plane conformer. The xenon atom of this conformer has two additional longer Xe(2)···N contacts, 3.526(5) [Xe(2)···N(1A)], and 3.635(5) [Xe(2)···N(1)] Å (Figure 3.3b), which are close to the sum of the Xe and N van der Waals radii and occur on opposite sides of the F_2OXeN plane with dihedral angles of 63.6° and 117.4°, respectively. The shorter Xe(IV)–N distances in the present adducts are significantly less than the sum of the Xe and N van der Waals radii (3.71 Å),[55] but are significantly longer than all known Xe(II)–N bond lengths, namely, $[Xe(N(SO_2F)_2][Sb_3F_{16}]$ (2.02(1) Å),[151] $[F_5TeN(H)Xe][AsF_6]$ (2.044(4) Å),[152] $FXeN(SO_2F)_2$ (2.200(3) Å),[153] $[F_3S{\equiv}NXeF][AsF_6]$ (2.236(4) Å),[154] and $[C_6F_5XeN{\equiv}CCH_3][AsF_6]{\cdot}CH_3CN$ (2.681(8) Å).[155] Although the primary coordination of Xe(IV) in $XeOF_2$ is unsaturated and is expected to exhibit significant Lewis acidity, the Xe(IV)–N bond of $F_2OXeN{\equiv}CCH_3$ is significantly longer and weaker than the Xe(II)–N bonds of $F_3S{\equiv}NXeF^+$ and $C_6F_5XeN{\equiv}CCH_3^+$.

3.2.4. Raman Spectroscopy. The low-temperature Raman spectra of solid $Xe^{16/18}OF_2$, $F_2{}^{16/18}OXeN{\equiv}CCH_3$, and $Xe^{16/18}OF_2{\cdot}n\mathrm{HF}$ are shown in Figure 3.4. The observed and calculated frequencies and their assignments are listed in Tables 3.3–3.6. The modes associated with coordinated CH_3CN in $F_2{}^{16/18}OXeN{\equiv}CCH_3$ differ slightly from those of the free ligand, but could be easily identified (Tables 3.4, 3.6, A1.1 and A1.2).

The spectral assignments for $Xe^{16/18}OF_2$, $F_2{}^{16/18}OXeN{\equiv}CCH_3$, and $Xe^{16/18}OF_2{\cdot}n^{1/2}\mathrm{HF}$ were made by comparison with the calculated frequencies and Raman intensities (Tables 3.3–3.5 and A1.3–A1.10) of the energy-minimized geometries (Figure 3.5), and in the case of CH_3CN modes, by comparison with those of the free ligand and other CH_3CN adducts. The spectra of CH_3CN and $CH_3CN{\cdot}m\mathrm{HF}$, prepared from a 2:1 molar ratio of HF and CH_3CN (no free CH_3CN was observed; also see 3.2.2, NMR

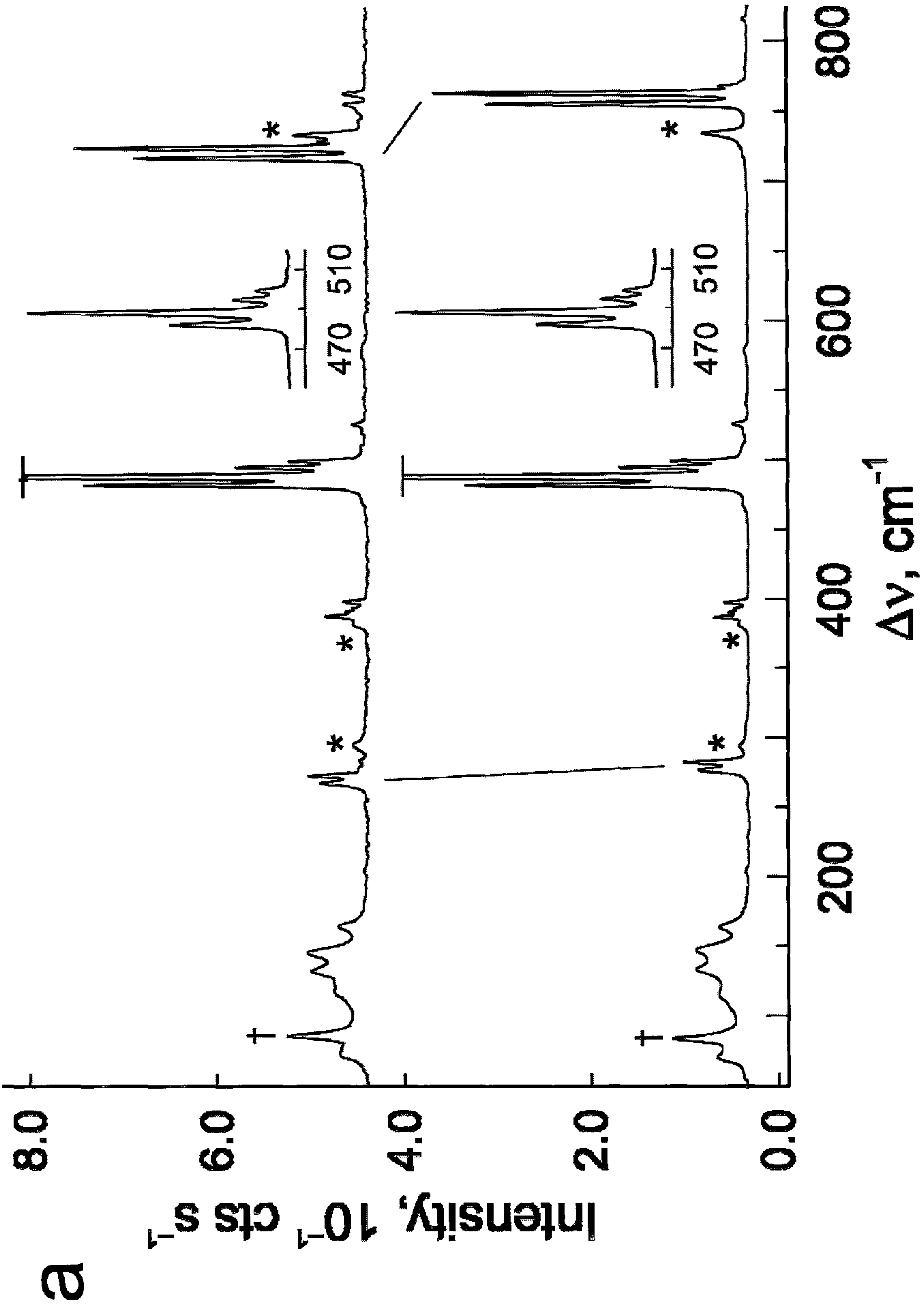
a
Intensity, 10⁻¹ cts s⁻¹
8.0
6.0
4.0
2.0
0.0
Δν, cm⁻¹
200
400
600
800
470
510
†
*

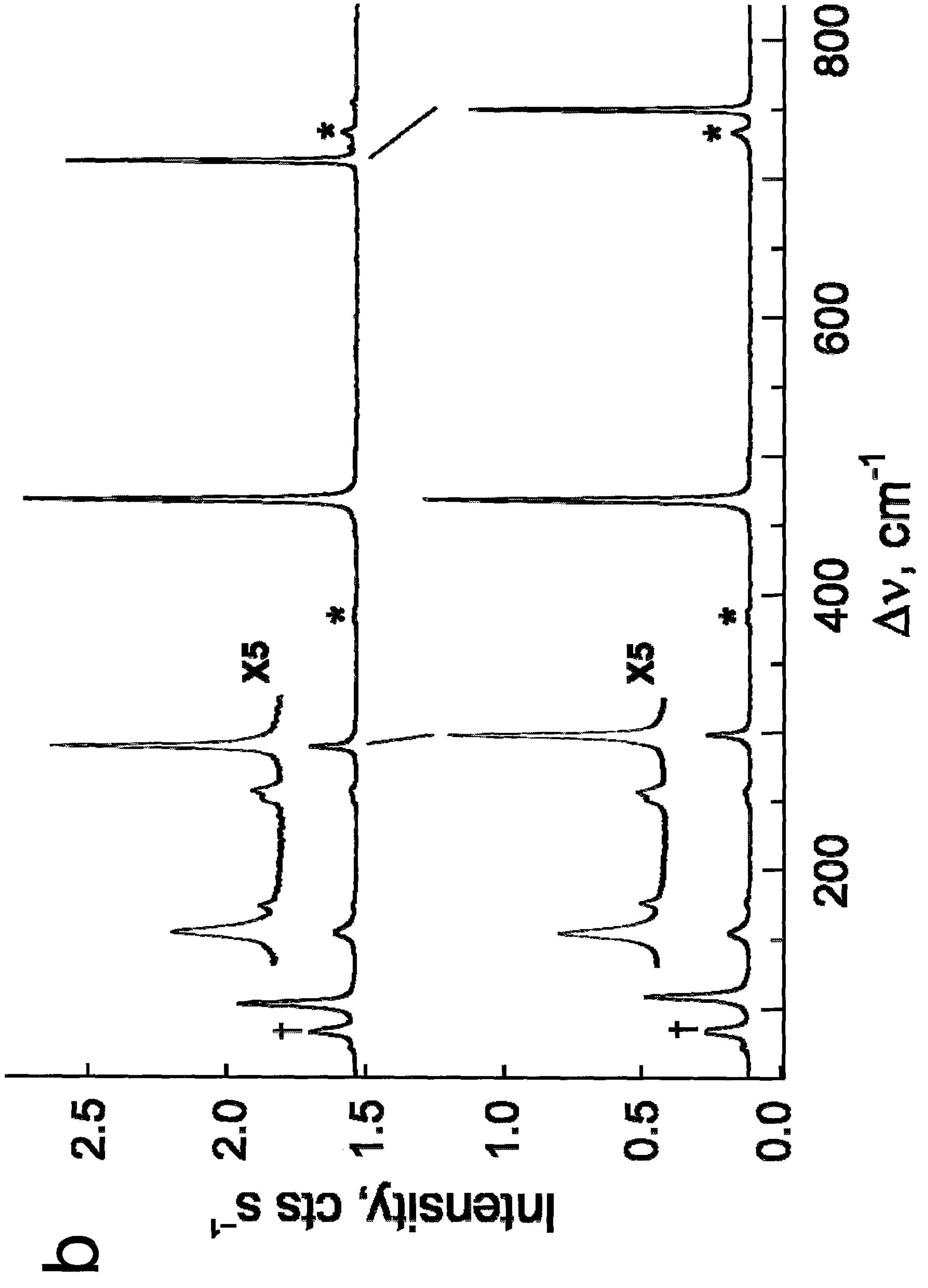
b
Intensity, cts s^{-1}
0.0
0.5
1.0
1.5
2.0
2.5
200
400
600
800
Δν, cm^{-1}
X5
X5
*
*
*
*
†
†

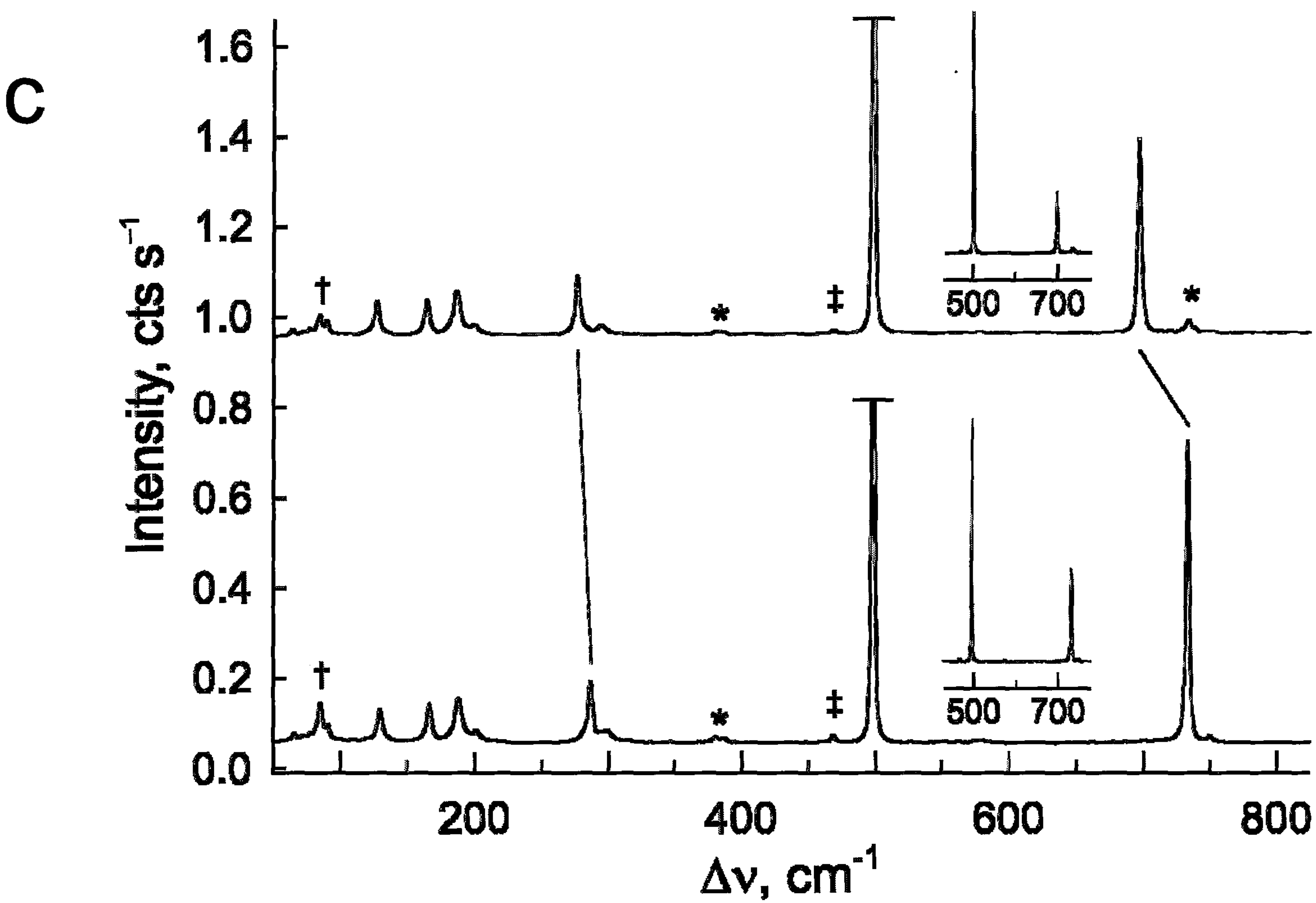

Figure 3.4. Raman spectra recorded at –150 °C using 1064-nm excitation for natural abundance (lower trace) and 98.6% ^{18}O-enriched (upper trace): (a) $XeOF_2$, (b) $F_2OXeN{\equiv}CCH_3$, and (c) $XeOF_2{\cdot}n$HF. Symbols denote FEP sample tube lines (*), instrumental artifact (†), and $XeOF_2$ (‡).

Table 3.3. Experimental and Calculated Vibrational Frequencies[a] for $Xe^{16/18}OF_2$

exptl[b]		calcd[c]				assgnts[f]
		SVWN[d]		MP2[e]		
$Xe^{16}OF_2$	$Xe^{18}OF_2$	$Xe^{16}O F_2$	$Xe^{18}OF_2$	$Xe^{16}OF_2$	$Xe^{18}OF_2$	(C_{2v}) symmetry
749.9(83)	712.8(84)	795.4(16)[22]	756.2(14)[21]	939.1(9)[60]	892.5(9)[55]	ν(XeO)
n.o.	n.o.	572.3(<<1)[213]	573.8(<<1)[214]	582.5(<<1)[252]	583.8(<1)[253]	$\nu_{as}(XeF_2)$
467.8(100)	467.8(100)	505.3(25)[7]	505.3(25)[7]	509.1(37)[7]	508.9(37)[7]	$\nu_s(XeF_2)$
298.1(13)	289.0(14)	244.4(4)[3]	235.1(4)[3]	283.0(4)[3]	272.1(4)[3]	$\rho_{rock}(XeOF_2)$ ip
256.2(2) 251.4(1)	256.2(2) 251.8(1)	200.0(<<1)[21]	200.3(<<1)[20]	217.7(<<1)[25]	218.1(<<1)[25]	$\delta(XeF_2)$ oop
175.7(1) 154.0(6)	172.8(1) 153.5(7)	154.9(<1)[14]	154.9(<1)[14]	176.1(<1)[19]	176.1(<1)[19]	$\delta(XeF_2)$ ip
108.2(32)	102.4(35)					lattice mode

[a] Frequencies are given in cm^{-1}. The abbreviation denotes not observed (n.o.). [b] The Raman spectrum of $Xe^{16/18}OF_2$ was recorded in an FEP sample tube at −150 °C using 1064-nm excitation. Values in parentheses are relative Raman intensities. [c] Values in parentheses are Raman intensities ($Å^4$ amu^{-1}) and values in square brackets denote infrared intensities (km mol^{-1}). [d] SVWN/(SDB-)cc-pVTZ. [e] MP2/(SDB-)cc-pVTZ. [f] Abbreviations denote symmetric (s), asymmetric (as), stretch (ν), bend (δ), rock (ρ_{rock}), in-plane bend (i.p.), and out-of-plane bend (o.o.p.). The in-plane and out-of-plane mode descriptions are relative to the $XeOF_2$ plane.

Table 3.4. Experimental and Calculated Vibrational Frequencies[a] for $F_2{}^{16/18}OXeN{\equiv}CCH_3$

expt[b]		calc[c]				assgnts[f]
		SVWN[d]		MP2[e]		
$F_2{}^{16}OXeNCCH_3$	$F_2{}^{18}OXeNCCH_3$	$F_2{}^{16}OXe{\cdot}NCCH_3$	$F_2{}^{18}OXeNCCH_3$	$F_2{}^{16}OXeNCCH_3$	$F_2{}^{18}OXeNCCH_3$	(C_1) symmetry
3009.1(10) 2999.0(10)	3008.7(10) 2999.0(11)	3067.6(78)[4] 3066.7(79)[4]	3067.6(78)[4] 3066.6(79)[4]	3198.7(60)[<1] 3198.2(60)[<1]	3198.7(60)[<1] 3198.2(60)[<1]	$\nu_{as}(CH_3)$
2937.8(59)	2937.8(60)	2983.7(266)[3]	2983.6(266)[3]	3101.9(185)[<<1]	3101.9(185)[<<1]	$\nu_s(CH_3)$
2726.1(1)	2726.1(1)					g
2297.1(2) 2287.0(7)	2297.1(2) 2287.0(6)					h
2253.7(51)	2254.1(51)	2347.2(287)[68]	2347.5(286)[67]	2234.7(96)[8]	2234.7(96)[8]	$\nu(C{\equiv}N)$
1437.4(1), br 1406.6(1), br	1436.0(2), br 1409.9(1), br	1383.5(9)[15] 1383.4(9)[15]	1383.5(9)[15] 1383.4(9)[15]	1491.1(7)[11] 1491.1(7)[11]	1491.1(7)[11] 1491.1(7)[11]	$\delta_{as}(CH_3)$
1370.4(5) 1356.9(6)	1370.4(6) 1357.1(6)	1333.5(14)[8]	1333.4(14)[8]	1416.6(4)[1]	1416.6(4)[1]	$\delta_s(CH_3)$
1034.3(1)	1034.0(1)	995.7(<1)[7] 995.6(<1)[7]	995.7(<1)[7] 995.7(<1)[7]	1065.5(<1)[2] 1065.4(<<1)[2]	1065.5(<1)[2] 1065.4(<1)[2]	$\rho_{rock}(CH_3)$
926.3(5) 924.0(9)	925.9(5) 924.0(8)	974.1(15)[5]	973.7(15)[5]	942.7(10)[6]	942.7(10)[7]	$\nu(C{-}C)$
766.8(5) 762.4(51) 754.7(43)	728.6(8) 724.1(47) 717.1(38)	795.9(54)[64]	756.7(49)[61]	938.4(19)[100]	892.0(17)[92]	$\nu(XeO)$
525.2(2)	525.0(2)	549.0(<<1)[214]	550.4(<<1)[214]	565.0(<<1)[250]	566.5(<<1)[251]	$\nu_{as}(XeF_2)$
499.1(12) 494.4(21) 488.1(100) 481.8(46)	498.7(13) 494.5(21) 488.1(100) 481.8(46)	486.3(24)[3]	486.3(24)[3]	493.1(37)[5]	493.1(37)[5]	$\nu_s(XeF_2)$

Table 3.4. (continued ...)

397.4(4) 392.6(2) 390.2(3)	397.2(4) 392.6(3) 389.7(4)	387.0(2)[1] 384.8(2)[~0]	386.7(2)[<1] 384.7(2)[~0]	374.0(2)[1] 372.6(2)[<1]	374.0(2)[1] 372.6(2)[<1]	δ(CCN)
283.2(11) 277.4(8)	272.3(10) 267.0(8)	242.7(4)[20]	233.3(3)[2]	282.0(4)[3]	271.2(4)[2]	ρ_{rock}(XeOF$_2$) ip
n.o.	n.o.	215.5(<1)[26]	214.9(<1)[26]	226.9(<1)[29]	226.8(<1)[28]	δ(OXeF$_2$N) oop
164.1(5) 147.9(9)	162.9(5) 144.3(10)	177.7(~0)[28]	177.6(~0)[28]	187.7(<1)[30]	187.9(<1)[30]	ν(XeN) + δ(XeF$_2$) ip
133.7(9) 116.4(5)	130.4(9) 117.1(6)	119.6(2)[<1]	119.4(2)[~0]	101.1(1)[1]	101.1(1)[1]	ν(XeN) − δ(XeF$_2$) ip
		108.8(2)[2]	106.7(2)[2]	97.2(2)[5]	95.0(2)[5]	δ(OXeN) ip + minor δ(XeF$_2$) oop
		83.6(<<1)[4]	83.9(<1)[4]	81.4(<1)[4]	81.3(<1)[4]	δ(XeNC) ip
		31.0(<<1)[2] 14.9(<1)[~0] 6.0(2)[2]	30.5(<<1)[2] 21.3(<<1)[<1] 7.9(2)[2]	34.4(<<1)[1] 16.6(2)[1] 8.9(<<1)[<<1]	33.7(<<1)[1] 16.4(2)[1] 8.9(<<1)[<<1]	coupled deformations

---

[a] Frequencies are given in cm^{-1}. The abbreviation denote broad (br), and not observed (n.o.). Additional abbreviations are given in footnote f of Table 3.3. [b] The Raman spectrum of F$_2{}^{16/18}$OXeN≡CCH$_3$ was recorded in an FEP sample tube at −150 °C using 1064-nm excitation. Values in parentheses are relative Raman intensities. [c] Values in parentheses are Raman intensities (Å^4 amu^{-1}), and values in square brackets are infrared intensities (km mol^{-1}). [d] SVWN/(SDB-)cc-pVTZ. [e] MP2/(SDB-)cc-pVTZ. [f] Bond elongations and angle openings are denoted by plus (+) signs and bond contractions and angle closings are denoted by minus (–) signs. [g] Overtone corresponding to 2 x 1357 cm^{-1}. [h] Combination bands corresponding to 1370 + 926 and 1357 + 924 cm^{-1}.

Table 3.5. Experimental Vibrational Frequencies[a] for $F_2Xe^{16/18}O{\cdot}n$HF and $F_2Xe^{16/18}O{\cdot}n$DF

expt[b]				assgnts (C_1)	
$Xe^{16}OF_2{\cdot}n$HF	$Xe^{18}O\ F_2{\cdot}n$HF	$Xe^{16}OF_2{\cdot}n$DF	$Xe^{18}OF_2{\cdot}n$DF		
2854(<1), br	2854(<1), br	2164(1), br	2165(1), br	ν_1	ν(H[D]F) + minor ν(O---H[D]–F)
n.o.	n.o.	n.o.	n.o.	ν_2	δ(O---H[D]–F)
733.5(34)	696.4(25)	734.0(46)	697.3(27)	ν_3	ν(XeO)
n.o.	n.o.	n.o.	n.o.	ν_4	HF o.o.p. wag
n.o.	n.o.	n.o.	n.o.	ν_5	$\nu_{as}(XeF_2)$ + minor H[D]F o.o.p. wag
498.2(100)	497.7(100)	497.7(100)	497.7(100)	ν_6	$\nu_s(XeF_2)$
299.1(2)	294.8(1)	293.8(2)	289.8(2)	ν_7	$\delta(F_{H[D]}XeO)$
286.6(8)	276.4(8)	285.1(10)	275.9(8)	ν_8	$\rho_{rock}(XeOF_2)$ i.p. + minor H[D]F o.o.p. wag
200.2(2)	199.8(2)	201.2(2)	199.8(2)	ν_9	$\delta(XeF_2)$ o.o.p.
187.2(6)	186.3(6)	187.2(7)	186.3(7)		
166.0(5)	164.6(5)	165.5(6)	164.1(6)	ν_{10}	$\delta(XeF_2)$ i.p.
129.4(4)	127.0(11)	127.5(5) 119.3, sh	125.6(6)	ν_{11}	$\rho_{rock}(XeOF_2)$ o.o.p. + ν(H[D]F---Xe)
89.9(2)	89.8(2)[c]				
65.3(1)	64.3(1)				
n.o.	n.o.	n.o.	n.o.	ν_{12}	XeF_2 torsion about Xe–O bond

[a] Frequencies are given in cm^{-1}. Abbreviations are given in footnote f and a of Table 3.3 and 3.4, respectively. [b] Raman spectra of $F_2Xe^{16/18}O{\cdot}n$HF and $F_2Xe^{16/18}O{\cdot}n$DF were recorded in an FEP sample tube at –150 °C using 1064-nm excitation. Values in parentheses denote relative Raman intensities. [c] Lattice modes and/or instrumental artifacts.

Table 3.6. Experimental Raman frequencies for $XeOF_2$, $F_2OXeN{\equiv}CCH_3$, $F_2OXeN{\equiv}CCH_3/CH_3CN/CH_3CN{\cdot}m HF$ mixtures and $XeOF_2/F_2OXeN{\equiv}CCH_3$ mixtures [a]

$F_2OXeN{\equiv}CCH_3$ $CH_3CN.m HF$ CH_3CN	$F_2OXeN{\equiv}CCH_3$	$F_2OXeN{\equiv}CCH_3$ $XeOF_2$	$XeOF_2$	assgnts [b]	
3018.1(3)				$\nu_{as}(CH_3)$	$CH_3CN{\cdot}m HF$
2949.0(9)				$\nu_s(CH_3)$	
2309.6(2)				$\nu(C{\equiv}N)$	
2282.1(6)					
1451.9(2)				CH_3 def. as	
1361.7(3)				CH_3 def. s	
932.5(2)				$\nu(C\text{-}C)$	CH_3CN
2247.4(2)				$\nu(C{\equiv}N)$	
1457.0sh				CH_3 def. as	
1375.8(1)				CH_3 def. s	
3009.1(8)	3009.0(7)	3008.9(7)		$\nu_{as}(CH_3)$	$F_2OXeNCCH_3$
2998.8(8)	2999.3(7)	2999.1(7)			
2937.5(44)	2937.6(40)	2937.7(43)		$\nu_s(CH_3)$	
2726.2(1)	2726.2(2)	2726.1(1)			
2297.1(2)	2297.1(2)	2296.6(2)		$\nu(C{\equiv}N)$	
2286.1(5)	2286.9(5)	2286.9(6)			
2254.3(39)	2254.2(39)	2254.2(42)		$\nu(C{\equiv}N)$	
1438.0(1)	1438.8(2)	1438.3(1)		CH_3 def. as	
1407.3(1)	1409.4(2)	1407.0(1)			
1370.6(5)	1370.3(5)	1370.3(5)		CH_3 def. s	
1356.9(6)	1356.9(5)	1357.0(5)			
1034.6(2)	1034.4(2)	1034.1(1)		$\rho_{rock}(CH_3)$	
926.6sh	926.6(sh)	926.2(sh)		$\nu(C\text{-}C)$	
923.9(8)	923.7(8)	923.7(8)			
767.0(4)	767.0(4)	767.0(5)		$\nu(XeO)$	
762.3(46)	762.3(45)	762.3(47)			
754.4(41)	754.4(41)	754.5(45)			
525.2(2)	525.2(3)	525.3(2)		$\nu_{as}(XeF_2)$	
498.8(12)				$\nu_s(XeF_2)$	
494.5(21)	498.8(12)	498.8(12)			
487.6(100)	494.6(20)	494.5(20)			
481.8(44)	487.6(100)	487.8(100)			
	481.8(49)	481.8(52)			
397.4(5)	397.4(4)	397.4(4)		$\delta(CCN)$	
392.8(3)	392.8(3)	392.6(2)			
390.2(4)	390.2(4)	390.0(4)			

Table 3.6. (continued ...)

283.0(11)	283.0(11)	283.1(11)			$F_2OXeNCCH_3$
277.2(8)	277.2(9)	277.4(8)		$\rho_{rock}(XeOF_2)$ i.p.	
164.7(5)	164.7(4)	164(4)			
148.9(9)	148.9(7)	148.6(8)		$\nu(XeN) + \delta(XeF_2)$ i.p.	
133.8(9)	133.8(7)	133.8(6)		$\nu(XeN) - \delta(XeF_2)$ i.p.	
	116.4(3)			$\nu(XeN) - \delta(XeF_2)$ i.p.	
71.5(6)	71.5(5)			lattice modes	
		750.2(42)	750.0(60)	$\nu(XeO)$	$XeOF_2$
		468.0(57)	468.0(100)	$\nu_s(XeF_2)$	
		297.8(8)	297.8(11)	$\rho_{rock}(XeOF_2)$ i.p.	
			256.1(1)	$\delta(XeF_2)$o.o.p.	
		253.2(1)	251.6(sh)	$\delta(XeF_2)$o.o.p.	
		174.6(1)	175.5(1)	$\delta(XeF_2)$ i.p.	
			153.3(6)	$\delta(XeF_2)$ i.p.	
		108.1(15)	108(22)	lattice modes	

---

[a] Frequencies are given in cm^{-1}. The abbreviation denotes broad (br) and shoulder (sh). [b] The original sample was a mixture consisting of $F_2OXeN\equiv CCH_3$, CH_3CN and $CH_3CN\cdot m HF$ (column 1). Slow removal of uncoordinated CH_3CN and $CH_3CN\cdot m HF$ under dynamic vacuum gave $F_2OXeN\equiv CCH_3$ (column 2). Gradual pumping of $F_2OXeN\equiv CCH_3$ first gave a mixture of $F_2OXeN\equiv CCH_3$ and $XeOF_2$ (column 3) while prolonged pumping resulted in unsolvated $XeOF_2$ (column 4). [b] The abbreviations denote symmetric (s), asymmetric (as), stretch (ν), bend (δ), rock (ρ_{rock}), in-plane bend (i.p.), and out-of-plane bend (o.o.p.). The in-plane and out-of-plane mode descriptions are relative to the $XeOF_2$ plane.

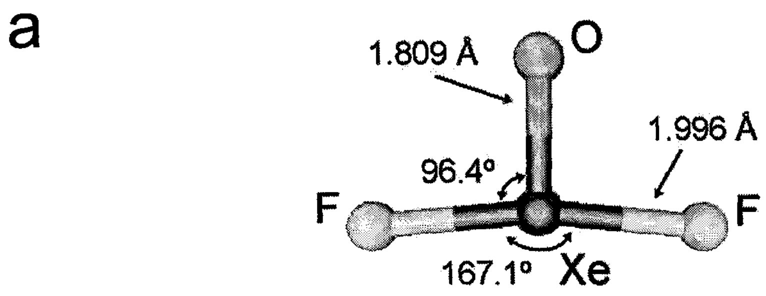
a
1.809 Å
O
1.996 Å
96.4°
F
F
167.1°
Xe

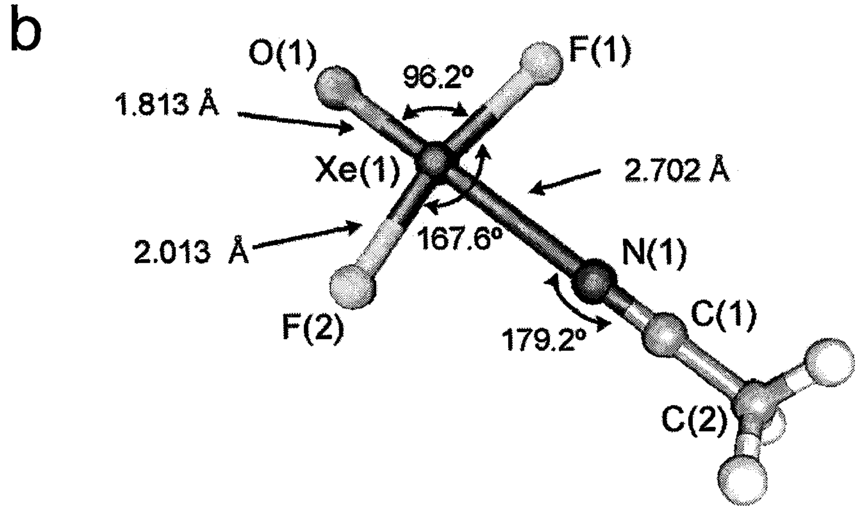
b
O(1)
96.2°
F(1)
1.813 Å
Xe(1)
2.702 Å
2.013 Å
167.6°
N(1)
F(2)
179.2°
C(1)
C(2)

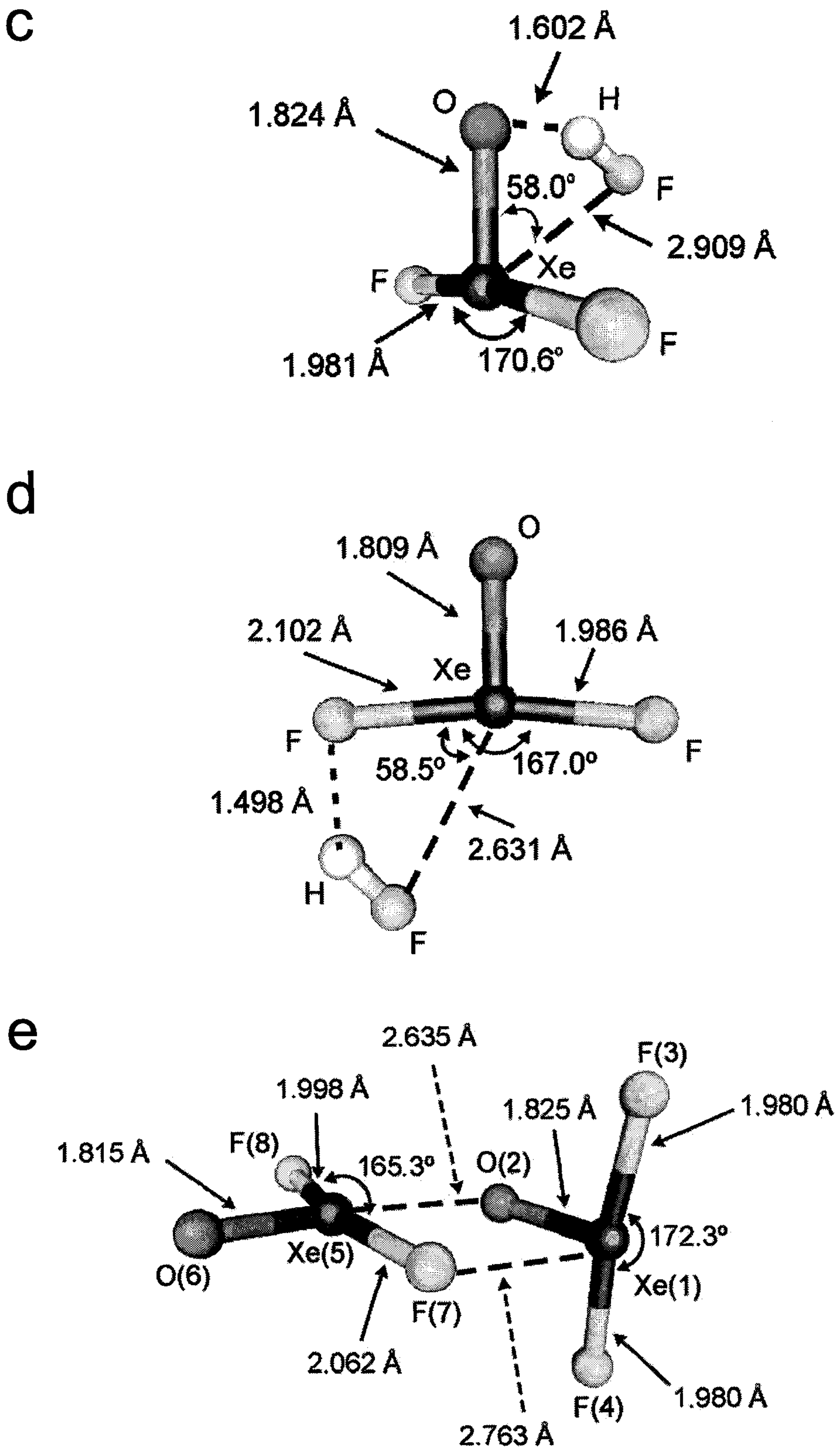
c
1.602 Å
1.824 Å
O
H
58.0°
F
2.909 Å
Xe
F
F
1.981 Å
170.6°
d
O
1.809 Å
2.102 Å
1.986 Å
Xe
F
F
58.5°
167.0°
1.498 Å
2.631 Å
H
F
e
2.635 Å
F(3)
1.998 Å
1.825 Å
1.980 Å
1.815 Å
F(8)
165.3°
O(2)
172.3°
O(6)
Xe(5)
Xe(1)
F(7)
2.062 Å
F(4)
1.980 Å
2.763 Å

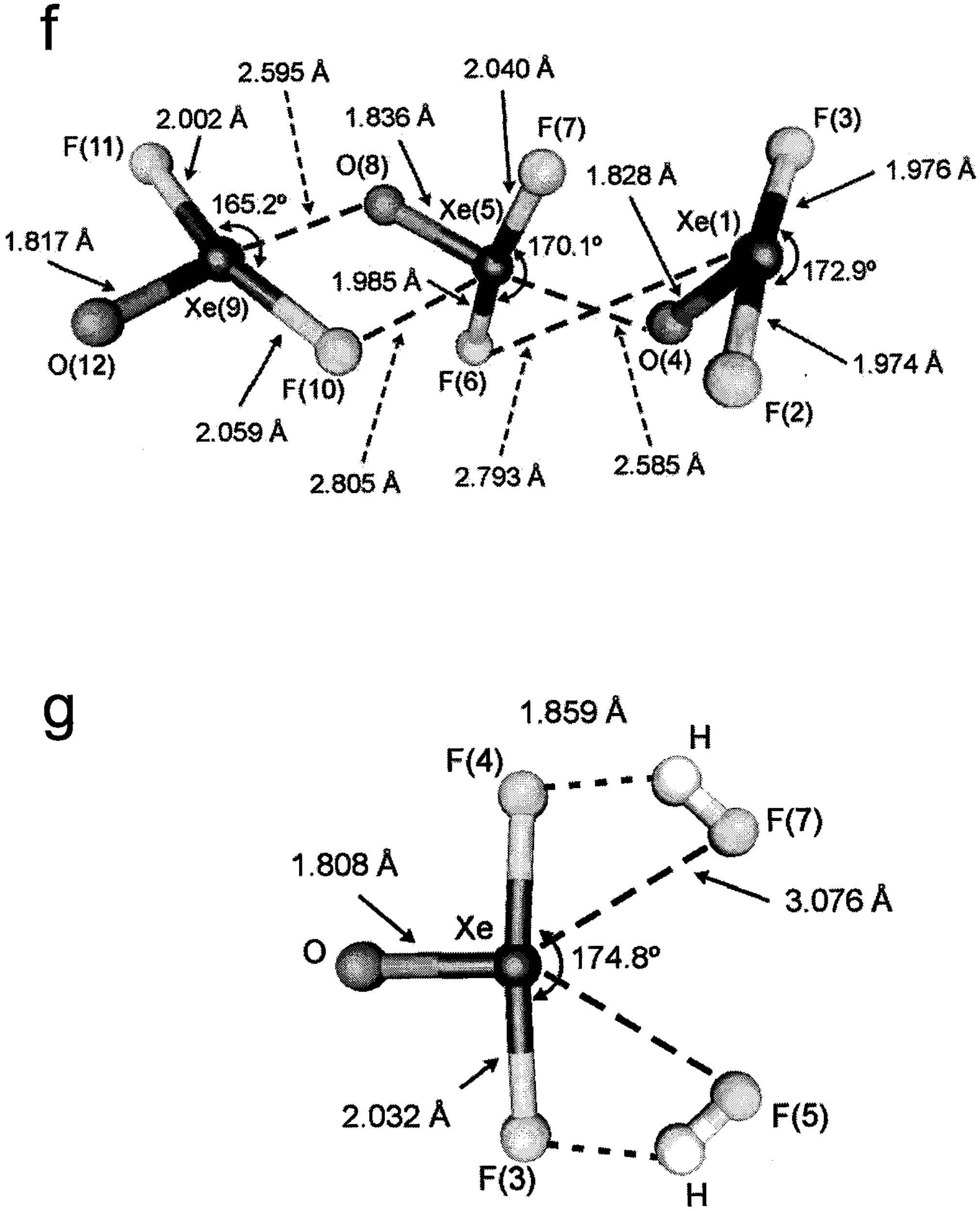

Figure 3.5. Calculated geometries (SVWN/(SDB-)cc-pVTZ) of (a) $XeOF_2$, (b) $F_2OXeN{\equiv}CCH_3$, (c) $XeOF_2{\cdot}HF$, O···H coordinated, (d) $XeOF_2{\cdot}HF$, F···H coordinated, (e) $(XeOF_2)_2$, (f) $(XeOF_2)_3$, and (g) $XeOF_2{\cdot}2HF$.

Spectroscopy), were also recorded at –150 °C and assigned (Tables A1.1 and A1.2) for comparison with those of $F_2{}^{16/18}OXeN{\equiv}CCH_3$. Assignments of modes involving the oxygen and hydrogen atoms were also supported by experimental and calculated $^{16/18}O$ and $^{1/2}H$ isotopic shifts. Vibrational frequencies calculated at both the MP2 (values in parentheses in the present discussion and throughout) and SVWN levels of theory reproduced the observed frequency trends across the series of compounds.

3.2.4.1. $XeOF_2$. The $XeOF_2$ molecule (C_{2v}) possesses six fundamental vibrational modes belonging to the irreducible representations $3A_1 + 2B_1 + B_2$ (the *xy*-plane is the molecular plane) that are Raman and infrared active. Although, there is overall good agreement between the observed and calculated frequency trends for $XeOF_2$, the stretching frequencies are overestimated whereas those of the deformation modes are slightly underestimated. Discrepancies are expected to arise, in part, because the low coordination number and large valence shell of xenon in $XeOF_2$ are conducive to association in the solid state.

The highest frequency mode at 749.9 cm^{-1} is assigned to the ν(Xe-O) stretch, and displays a substantial low-frequency shift (37.1 cm^{-1} or 4.95%) upon substitution of ^{18}O and is in good agreement with the calculated percentage $^{16/18}O$ isotope shift [39.2 (46.6) cm^{-1} or 4.93 (4.96)%]. The mode at 298.1 cm^{-1} displays a smaller $^{16/18}O$ isotope shift of 9.1 cm^{-1} (3.05%) [calculated 9.3 (10.9) cm^{-1} or 3.81 (3.85)%] and is assigned to the in-plane $\rho_{rock}(XeOF_2)$ mode. Similar isotope shifts were observed and calculated for the $Xe^{16/18}OF_2{\cdot}n^{1/2}HF$ and $F_2{}^{16/18}OXeN{\equiv}CCH_3$ adducts (vide infra). It is clear from the high frequency of ν(Xe-O) that the formal Xe-O bond order is close to two, ruling out the polymeric infinite chain structure, [-O–Xe(F_2)-]$_n$, predicted by Gillespie.[156] However, the calculated ν(Xe-O) and $\nu_s(XeF_2)$ frequencies of $XeOF_2$ are significantly higher than the experimental values, and the experimental frequencies are 9 and 20 cm^{-1}, respectively, lower than those of $F_2OXeN{\equiv}CCH_3$ (vide infra), suggesting that weak oxygen and/or fluorine coordination to adjacent xenon atoms occurs in the solid (cf. gas-phase dimer and trimer in the Computational Results).

As predicted from the calculated Raman intensities, the $\nu_s(XeF_2)$ stretch at 467.8 cm^{-1} is the most intense mode in the Raman spectrum. Because the XeF_2 moiety is near linear and near centro-symmetric, mutual exclusion applies. Thus, $\nu_{as}(XeF_2)$ is expected to be very weak and was not observed, but is predicted to occur at 572.3 (582.5) cm^{-1} compared to $\nu_{as}(XeF_4)$ of XeF_4 (586 cm^{-1}, infrared spectrum).[35] The weak modes at 251.4 and 256.2 cm^{-1} are assigned to the out-of-plane XeF_2 bending mode, and the modes at 154.0 and 175.7 cm^{-1} are assigned to the in-plane XeF_2 bending mode.

3.2.4.2. $F_2OXeN{\equiv}CCH_3$. A solution sample of $F_2OXeN{\equiv}CCH_3$, generated in CH_3CN according to eq 3.1, was pumped under dynamic vacuum at –45 to –42 °C until a slurry of $F_2OXeN{\equiv}CCH_3$ wetted with CH_3CN had formed. Removal of the remaining CH_3CN and HF was then monitored by low-temperature Raman spectroscopy after every 5−10 min pumping interval. This permitted distinction and unambiguous assignment of the CH_3CN modes associated with the solvent, $F_2OXeN{\equiv}CCH_3$, and $CH_3CN{\cdot}m$HF [$\nu_{as}(CH_3)$, 3018.1; $\nu_s(CH_3)$, 2949.0; ν(CN), 2282.1, 2309.6; $\delta_{as}(CH_3)$, 1451.9; $\delta_s(CH_3)$, 1361.7; ν(CC), 932.5 cm^{-1}; also see Tables 3.6, A1.1 and A1.2].

All vibrational modes (24 A) of $F_2OXeN{\equiv}CCH_3$ (C_1) are predicted to be Raman and infrared active. The $\nu_s(CH_3)$, $\nu_{as}(CH_3)$, $\nu(CN)$, $\delta_{as}(CH_3)$, $\delta_s(CH_3)$, $\nu(XeO)$, $\nu_s(XeF_2)$, $\delta(CCN)$, and $\delta_{rock}(XeOF_2)$ ip bands are split into two to four components (Table 3.4). To account for these splittings, a factor-group analysis was performed based on the single crystal X-ray structure. The analysis reveals that each Raman and infrared band is split, as a result of coupling within the unit cell, into a maximum of four components, $2A_g + 2B_g$ in the Raman spectrum and $2A_u + 2B_u$ in the infrared spectrum (Table 3.7).

The frequencies associated with the $XeOF_2$ moiety have been assigned by analogy with those of $XeOF_2$ as discussed above, and require no further commentary except to note that the $\nu_s(XeF_2)$ stretching frequency is shifted to higher frequency when compared with that of $XeOF_2$, which is also observed for the HF adduct (vide infra).

Table 3.4 shows that the $XeOF_2$ group modes are affected by the adduct formation, with both the ν(Xe-O) and $\nu_s(XeF_2)$ modes being shifted to higher frequencies by 9 and 20 cm^{-1}, respectively. In contrast, the calculated frequencies indicate that $\nu_s(XeF_2)$ should decrease [19 (16) cm^{-1}] and that ν(Xe-O) should remain unchanged when adduct formation takes place in the gas phase. The discrepancy may result from $XeOF_2$ association in the solid state which likely occurs by means of asymmetric oxygen bridges (vide supra). Formation of the CH_3CN adduct presumably disrupts solid state association, forming discrete monomers, as shown in its crystal structure, resulting in increases in Xe–O bond order and $\nu(XeO)$.

In contrast with $XeOF_2$ and $XeOF_2{\cdot}n$HF, the low symmetries of the two conformations observed for $F_2OXeN{\equiv}CCH_3$ in its crystal structure allow the $\nu_{as}(XeF_2)$

Table 3.7. Factor-Group Analysis for $F_2OXeN{\equiv}CCH_3$

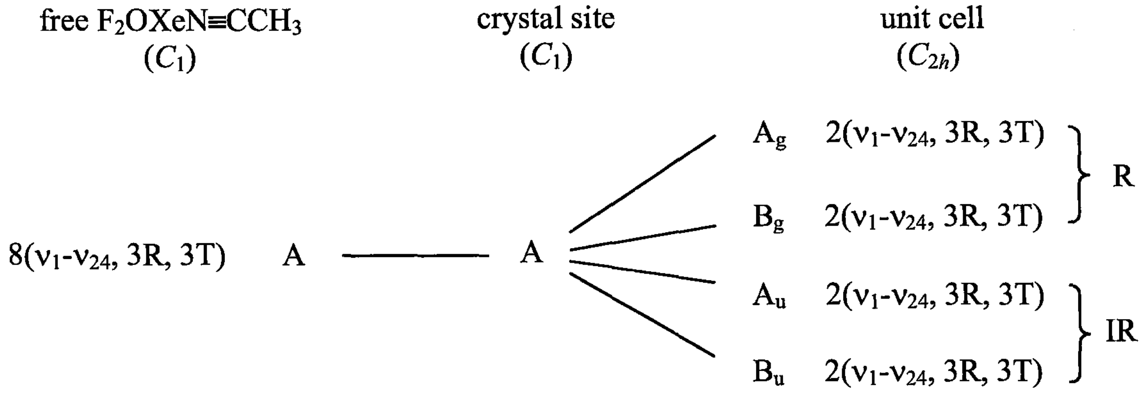

There are two crystallographically unique $F_2OXeN{\equiv}CCH_3$ molecules in the asymmetric unit of the unit cell, both having C_1 site symmetry. Each structure type is distinguished by its non-linear Xe-N-C angle which lies either in or out of the $XeOF_2$ plane. The present factor-group analysis correlates the gas-phase molecular symmetry of both conformations (C_1) to their site symmetries (C_1) which, in turn, are correlated to the unit cell symmetry (C_{2h}) for a total of 8 molecules per unit cell. The present analysis has been simplified by assuming a single adduct conformation. Consequently, no provision has been made for coupling between different conformers. The analysis reveals that each Raman and infrared band will be split, as a result of coupling within the unit cell, into a maximum of four components, $2A_g + 2B_g$ in the Raman spectrum and $2A_u + 2B_u$ in the infrared spectrum.

mode to be observed as a weak line at 525.2 cm^{-1}. The in-plane δ(XeF_2) deformation mode is symmetrically and anti-symmetrically coupled to the ν(XeN) stretch, occurring at 147.9, 164.1 cm^{-1} [ν(XeN) + ν(XeF_2) i.p.] and 116.4, 133.7 cm^{-1} [ν(XeN) – ν(XeF_2) i.p.].

All frequencies associated with coordinated CH_3CN were readily assigned by comparison with those of the free base. The modes at 2253.7 and at 390.2, 392.6, and 397.4 cm^{-1} are assigned to the ν(CN) stretch and the δ(NCC) bend, respectively, and are shifted to higher frequencies when compared with those of the free ligand. The experimental ν(CN) (5.3 cm^{-1}) and δ(NCC) (2.1 cm^{-1}, average) complexation shifts are much smaller than those associated with other Lewis acid adducts of CH_3CN (CH_3CNSbF_5, 80 and 36 cm^{-1};[157] CH_3CNBF_3, 114 and 58 cm^{-1};[158] and CH_3CNBCl_3, 118 and 80 cm^{-1},[159] respectively), and are indicative of a comparatively weak donor–acceptor bond in $F_2OXeN{\equiv}CCH_3$. While the calculated ν(CN) [15.2 (16.7) cm^{-1}] and δ(NCC) [8.9 (9.8) cm^{-1}) complexation shifts are much less, the ratios of the stretching to bending complexation shifts are similar.

3.2.4.3. $XeOF_2{\cdot}n$HF. When HF was added to $XeOF_2$ at –78 °C, a Raman spectrum that was more complex than that of $XeOF_2$ resulted, which was identical to that previously reported for, and erroneously assigned to $XeOF_2$.[67] In an attempt to more fully understand the nature of the interaction between HF and $XeOF_2$, the deuterium substituted $^{16/18}O$ isotopomers were also synthesized.

When the Raman spectra of all four isotopomers are considered (Table 3.5), only one of the eight $XeOF_2{\cdot}n HF$ modes that could be observed exhibited both $^{16/18}O$ and $^{1/2}H$ dependencies that were > 2 cm^{-1}. In addition, three modes exhibited only $^{16/18}O$ dependence, one mode exhibited only $^{1/2}H$ dependence (this mode is very broad, ~100 cm^{-1}, and is not expected to exhibit a discernable $^{16/18}O$ isotope shift), and three were unshifted. In order to account for the isotopic dependencies of the experimental vibrational frequencies and to determine the manner in which HF is coordinated in $XeOF_2{\cdot}n HF$, several simplified models were calculated (see 3.2.5, Computational Results).

The vibrational assignments for $Xe^{16/18}OF_2{\cdot}n^{1/2}HF$ were based upon a comparison of two energy-minimized structures in which a single HF molecule coordinates to $XeOF_2$. In one case, the HF molecule occupies a plane perpendicular to the $XeOF_2$ plane and is coordinated to xenon through fluorine and is cis to the oxygen atom so that HF is hydrogen-bonded to oxygen (Figure 3.5c). The second energy-minimized model (Figure 3.5d) in which HF is also fluorine-coordinated to xenon differs in that HF is hydrogen-bonded to the fluorine on xenon and lays in the $XeOF_2$ plane. The latter structure is favored by 7.8 (1.6) kJ mol^{-1} over the O···H bonded structure in Figure 3.5c.

The O···H bonded model, in which bicoordinate HF increases the xenon coordination number by bonding through fluorine, gives twelve modes: five $^{16/18}O$- and $^{1/2}H$-dependent modes (ν_1, ν_2, ν_4, ν_7, ν_8), one $^{16/18}O$-dependent mode (ν_3), one $^{1/2}H$-dependent modes (ν_5), and five unshifted modes (ν_6, ν_9–ν_{12}). In contrast, the F···H bonded structure gives one $^{16/18}O$- and $^{1/2}H$-dependent mode (ν_1), two $^{16/18}O$-dependent modes (ν_3, ν_8), three $^{1/2}$H-dependent mode (ν_2, ν_4, ν_7), and six (ν_5, ν_6, ν_9–ν_{12}) unshifted modes. Overall, the calculated vibrational frequencies derived from the slightly less stable O···H-bonded structure, when compared with the calculated $XeOF_2$ and $F_2OXeN{\equiv}CCH_3$ frequencies, best reproduces the experimental frequency trends and isotopic shifts patterns. Consequently, the ensuing vibrational assignments and descriptions (Table 3.5) are based on this structure.

The modes at 2854 and 2164 cm^{-1} are readily assigned to ν(HF) and ν(DF), where their lower frequencies relative to those in a neon matrix (HF 3992; DF 2924 cm^{-1})[160] and in the solid phase (HF 3056, 3408; DF 2284, 2524 cm^{-1})[161,162] are consistent with coordinated HF and DF. The ν(XeO) stretching frequency of $XeOF_2{\cdot}n$HF (733.5 cm^{-1}) shows the expected $^{16/18}$O isotopic dependence and is shifted to lower frequency relative to that of $XeOF_2$ (749.9 cm^{-1}). The most intense mode at 498.2 cm^{-1} corresponds to $\nu_s(XeF_2)$, which is comparable to that in $F_2OXeN{\equiv}CCH_3$ (481.8, 488.1, 494.4, 499.1 cm^{-1}) but higher than in $XeOF_2$ (467.8 cm^{-1}). The asymmetric mode $\nu_{as}(XeF_2)$ is again expected to be very weak and was not observed. Upon ^{18}O enrichment, the modes at 286.6 and 299.1 cm^{-1} shift to 276.4 and 294.8 cm^{-1}, respectively. Upon ^{2}H enrichment, these modes shift to even lower frequencies, and are assigned to $\rho_{rock}(XeOF_2)$ i.p. + minor HF o.o.p. wag and $\delta(F_HXeO)$, respectively. The in-plane XeF_2 (166.0 cm^{-1}) and the out-of-plane XeF_2 (187.2, 200.2 cm^{-1}) bends are shifted to higher and lower frequency, respectively, when compared with those of $XeOF_2$ and show only small (< 2 cm^{-1}) $^{16/18}$O isotopic dependencies. The mode at 129.4 cm^{-1} shifts to lower frequency upon ^{2}H and ^{18}O enrichment and is assigned to a coupled mode involving the coordinated HF molecule, $\rho_{rock}(XeOF_2)$ oop + ν(HF···Xe).

An energy-minimized structure for $XeOF_2 \cdot 2HF$ was also obtained, but provided vibrational frequencies that were in poor agreement with the experimental values (see 3.2.5, Computational Results).

3.2.5. Computational Results. The electronic structures of $(Xe^{16/18}OF_2)_n$ (n = 1-3), $F_2{}^{16/18}OXeN{\equiv}CCH_3$ and $Xe^{16/18}OF_2{\cdot}n^{1/2}HF$ (n = 1, 2) were optimized starting from C_1 symmetries and resulted in stationary points with all frequencies being real. Only the SVWN/(SDB-)cc-pVTZ and MP2/(SDB-)cc-pVTZ (MP2 values in the present discussion are given in parentheses) results are reported in this paper (Tables 3.2–3.4, Figure 3.5 and Tables A1.3–A1.11; also see Chapter 2, Experimental Section). Xenon tetrafluoride was used to benchmark calculations (Table A1.12).

3.2.5.1. Geometries. (i) $(XeOF_2)_n$ (n = 1-3). The geometry of $XeOF_2$ optimized to C_{2v} symmetry with an Xe–O bond length of 1.809 (1.770) Å and Xe–F bond length of 1.996 (1.980) Å, compared to 1.971 (1.960) Å in XeF_4 and its experimental bond length, 1.953(2) Å.[32] The fluorine atoms are bent away from the oxygen atom, with an O–Xe–F angle of 96.4 (96.0) ° and an F–Xe–F angle of 167.1 (168.2)°. The calculated structure is in accord with that predicted by the VSEPR model of molecular geometry (see 3.2.4 Raman Spectroscopy).

The geometries of $(XeOF_2)_2$ and $(XeOF_2)_3$ were also calculated (Tables A1.9 and A1.10) to study the effects of oligomerization on the vibrational frequencies and to assess the relative merits of $XeOF_2$ association in the solid state. In both cases, two starting models were used with all Xe–O bonds collinear: one with all $XeOF_2$ groups coplanar, as originally proposed by Gillespie,[156] and one with the $XeOF_2$ planes alternating so that they subtend dihedral angles of 90°. All systems converged to a single twisted dimer (Figure 3.5e) and open-chain, twisted trimer (Figure 3.5f). Both the dimer and trimer possess Xe···O and Xe···F contacts that are significantly less than the sum of the van der Waals radii (3.68 and 3.63 Å, respectively).[55] The formal Xe-O double bond involved in the contact elongates, allowing the F–Xe–F angle to open up. As well, the Xe–F bonds elongate and both $\nu(XeO)$ and $\nu_s(XeF_2)$ decrease significantly relative to those of the calculated monomer.

(ii) $F_2OXeN{\equiv}CCH_3$. The geometry of $F_2OXeN{\equiv}CCH_3$ optimized to C_1 symmetry in which the NCC moiety lay in the $XeOF_2$ plane and the Xe–N–C angle is nearly linear. Overall there is a good agreement between the observed and the calculated Xe–O and Xe–F bond lengths as well as the F–Xe–F and O–Xe–F bond angles (Table 3.2). The most notable differences occur between the observed and calculated Xe–N–C bond angle and Xe–N bond length. The Xe–N bond length, which is slightly underestimated by the SVWN calculation, has a calculated value of 2.702 (2.884) Å when compared with 2.752(5) (out-of-plane conformer) and 2.808(5) (in-plane conformer) Å in the crystal structure. Unlike the experimental Xe–N–C bond angles (164.9(4)°, in-plane conformer; and 134.6(4)°, out-of-plane conformer), the calculated Xe–N–C angle is essentially linear [179.2 (179.4)]. The energies of the two experimental adduct conformations were calculated at the MP2 level and are 78.2 (out-of-plane) and 86.9 (in-plane) kJ mol^{-1}

higher in energy than the energy-minimized geometry. The conformational differences are likely a consequence of solid state packing.

Upon adduct formation, the calculated Xe–O bond length (1.809 to 1.813 Å) and ν(XeO) remain essentially unchanged. The Xe–F bond lengths are elongated (1.996 to 2.013 Å) and the ν(XeF) decreases accordingly. In contrast, the experimental ν(XeO) and ν(XeF) frequencies increase (Tables 3.3 and 3.4).

(iii) $XeOF_2{\cdot}n$HF. Because an experimental structure for $XeOF_2{\cdot}n$HF is unavailable, it was not possible to directly establish the number of HF molecules coordinated to $XeOF_2$. Energy-minimized structures and their vibrational frequencies were calculated in order to better comprehend how HF interacts with $XeOF_2$. It was decided to limit the models to a $XeOF_2$ monomer interacting with only one or two HF molecules. These results are given in Tables A1.3 to A1.8.

Four starting geometries were used in which a single HF molecule, H-bonded to either oxygen or fluorine, lay either in the $XeOF_2$ plane and collinear with the Xe–O bond, or perpendicular to the $XeOF_2$ plane. A single energy-minimized structure was found for each pair of O···H–F and F···H–F bonded starting geometries. In both minimized geometries, the fluorine of HF is coordinated to xenon. In the F···H–F---Xe structure, the HF molecule lies in the $XeOF_2$ plane (Figure 3.5d), and in the O···H–F---Xe structure, it occupies the plane perpendicular to the $XeOF_2$ plane (Figure 3.5c). Although the F···H–F···Xe structure is 7.8 (1.6) kJ mol^{-1} more stable than the O···H–F···Xe structure, the calculated frequencies of the latter are in better agreement with the experimental frequencies (see 3.2.4, Raman Spectroscopy). In the O···H structure, both the Xe–O bond length and F–Xe–F axial bond angle increase when compared with those of $XeOF_2$, whereas the Xe–F bond lengths decrease. In the F···H structure, both the Xe–O bond length and the F–Xe–F bond angle remain unchanged, whereas the Xe–F bond involved in the F···H contact increases and the other Xe–F bond decreases. In both cases, the O···H and F···H distances are significantly shorter than the sum of their respective van der Waals radii.

Initial geometries in which two HF molecules were orientated in or out of the $XeOF_2$ plane and were H···O or H···F coordinated or had mixed H···O/H···F coordination for both orientations were used. Of these ten initial geometries, only one energy-minimized geometry having non-imaginary frequencies was obtained. This geometry has two F···H–F and two Xe···F–H interactions that lie in the $XeOF_2$ plane (Figure 3.5g). Both the Xe–F distance and F–Xe–F angle have increased relative to that of $XeOF_2$ whereas Xe–O has decreased. The Xe···F and F···H contact distances are significantly longer than those in the calculated structure containing one coordinated HF molecule (Figure 3.5d). The geometry calculated for $XeOF_2{\cdot}2HF$, however, provided vibrational frequencies that were in poor agreement with the experimental values (Tables A1.7 and A1.8).

3.2.5.2. Natural Bond Orbital (NBO) Analyses. The NBO[163–166] analyses were carried out for the MP2- and SVWN-optimized gas-phase geometries of $XeOF_2$, $F_2OXeN{\equiv}CCH_3$, and CH_3CN. The NBO results are given in Table 3.8. The MP2 and SVWN results are similar; only the MP2 results are referred to in the ensuing discussion.

Table 3.8. NBO Valencies, Bond Orders, and Charges (NPA) for $XeOF_2$, $F_2OXeN\equiv CCH_3$ and CH_3CN

Charges [Valencies]	$XeOF_2$				$F_2OXeN\equiv CCH_3$				CH_3CN			
	SVWN		MP2		SVWN		MP2		SVWN		MP2	
Xe(1)	1.971	[1.478]	2.112	[1.473]	2.011	[1.437]	2.065	[1.450]				
O(1)	-0.807	[0.777]	-0.897	[0.782]	-0.853	[0.722]	-0.887	[0.754]				
F(1)	-0.582	[0.317]	-0.608	[0.304]	-0.598	[0.277]	-0.599	[0.286]				
F(2)	-0.582	[0.317]	-0.608	[0.304]	-0.598	[0.277]	-0.599	[0.286]				
N(1)					-0.410	[2.035]	-0.405	[1.988]	-0.310	[1.958]	-0.313	[1.892]
C(1)					0.374	[3.014]	0.359	[2.979]	0.271	[3.014]	0.283	[2.879]
C(2)					-0.791	[3.295]	-0.781	[3.288]	-0.786	[3.299]	-0.678	[3.290]
H					0.288	[0.786]	0.283	[0.791]	0.275	[0.788]	0.236	[0.805]
Bond Orders												
Xe(1)-O(1)	0.812		0.825		0.752		0.789					
Xe(1)-F(1)	0.333		0.324		0.290		0.301					
Xe(1)-F(2)	0.333		0.324		0.290		0.301					
O(1)---F(1)	-0.017		-0.021		-0.015		-0.017					
Xe(1)---N(1)					0.099		0.059					
N(1)-C(1)					1.926		1.924		1.951		1.882	
C(1)-C(2)					1.024		1.000		1.012		0.951	
C(2)-H					0.753		0.760		0.758		0.775	

Single point calculations were carried out for geometries that were constrained to those of the experimental conformers and reveal that the NBO analyses (Table 3.7) are very similar to that of the fully optimized C_1 structure and insensitive to the Xe–N–C bond angle.

The NBO analysis gives natural charges of 2.11 and 2.06 for Xe in $XeOF_2$ and $F_2OXeN{\equiv}CCH_3$, respectively. These charges, which are approximately the average of the formal charge 0 (covalent model) and formal oxidation number 4 (ionic model) for Xe in both molecules, are in accord with the natural charges for O (–0.90, –0.89) and F (–0.61, –0.60) in $XeOF_2$ and $F_2OXeN{\equiv}CCH_3$, respectively. In both cases, the charges are also about half of their respective oxidation numbers, and indicate that the bonds in free and adducted $XeOF_2$ are polar covalent. Among the plausible valence structures I–IV for

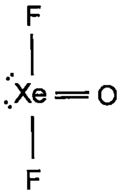

I

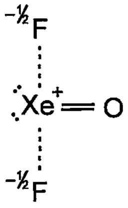

II

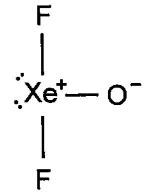

III

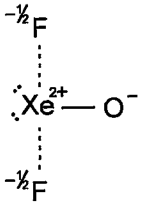

IV

$XeOF_2$, the calculated charges are best represented by structure IV, where the near linear XeF_2 moiety can be described as a 3 center-4 electron bond.[167] The Xe–O/Xe–F bond order ratio (2.55) and Xe/O/F valencies (1.47/0.78/0.30) are in overall agreement with this localized description of polar covalent bonding in $XeOF_2$.

Upon adduct formation with CH_3CN, the nitrogen electron pair density donated into the xenon valence shell results in essentially no change in the O and F ligand charges but small decreases in their bond orders and valencies, whereas Xe maintains its positive charge very close to 2. Thus, the Xe–O and Xe–F bonds are only slightly more ionic in $F_2OXeN{\equiv}CCH_3$. The charge distribution of the CN group is polarized toward the positive xenon center, with 0.10 e charge shifting from carbon to nitrogen upon coordination with a corresponding polarization charge on the CH_3 group towards the positively charged carbon atom of the CN group.

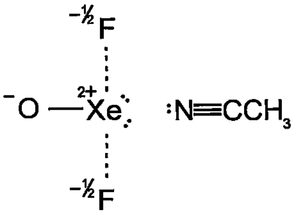

V

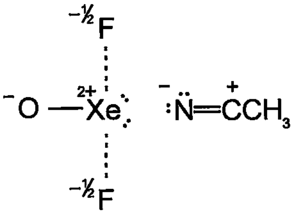

VI

The most plausible valence bond contributions that contribute to a description of $F_2OXeN{\equiv}CCH_3$ are those that retain the charge distribution and Xe-O and Xe-F bond orders of structure IV and also account for the very low Xe-N bond order (0.05) and polarization of the CH_3CN ligand to give an enhanced negative charge on nitrogen. These criteria are met by valence structures V and VI, where structure V is dominant and yields a picture of adduct formation between $XeOF_2$ and CH_3CN that is similar to that of XeF^+ and HCN.[168] In this depiction, mutual penetration of outer diffuse non-bonded densities of the Xe and N atoms occurs which, unlike a covalent interaction, produces no substantial shared density as reflected in the very low Xe–N bond order and small changes in Xe and N valencies.

The calculated gas-phase xenon-ligand dissociation energy for $F_2OXeN{\equiv}CCH_3$ at the MP2 level of theory is 41.8 kJ mol^{-1}, which is significantly less than the donor-acceptor adduct dissociation energies of $F_3S{\equiv}NXeF^+$ (157.2 kJ mol^{-1}) and $HC{\equiv}NXeF^+$ (157.1 kJ mol^{-1}).[154] The $F_2OXeN{\equiv}CCH_3$ donor-acceptor interaction is in better agreement with those calculated for $HC{\equiv}NAsF_5$ (38.6 kJ mol^{-1}) and $F_3S{\equiv}NAsF_5$ (27.8 kJ mol^{-1}).[154] These findings also support a valence bond description of $F_2OXeN{\equiv}CCH_3$ that is dominated by the nonbonded structures V and VI and a bonding description in which the $CH_3C{\equiv}N$ is weakly coordinated to $XeOF_2$.

3.3. Conclusion

Long-standing discrepancies among the published vibrational assignments ascribed to $XeOF_2$ are now accounted for and the synthesis of pure $XeOF_2$ in synthetically useful quantities has been achieved. Comparisons of the present experimental frequencies for $XeOF_2$ and $XeOF_2{\cdot}n$HF with those assigned to $XeOF_2$ in the previous three early communications[65–67] show that the spectra obtained from H_2O/XeF_4 co-condensation experiments[65,66] arose from mixtures of $XeOF_2{\cdot}n$HF and $XeOF_2$ while the product described in the latter report[67] consisted of only $XeOF_2{\cdot}n$HF. In these accounts, HF produced in the co-condensation reactions either coordinated to $XeOF_2$ or was pumped off, yielding mixtures of $XeOF_2{\cdot}n$HF and $XeOF_2$ that were erroneously ascribed to a single component, $XeOF_2$.

The solid state vibrational spectrum of $XeOF_2$ and the calculated energy-minimized dimer and trimer geometries, and their vibrational frequencies, point to an extended structure in which neighboring $XeOF_2$ molecules weakly interact by means of asymmetric oxygen-xenon-oxygen bridges and Xe···F contacts.

The Lewis acid properties of $XeOF_2$ are demonstrated by the syntheses of $F_2OXeN{\equiv}CCH_3$ and $XeOF_2{\cdot}n$HF. The crystal structure of $F_2OXeN{\equiv}CCH_3$ provides a rare example of a Xe(IV)–N bond which is among the weakest Xe–N bonds known. It has been shown by calculation of energy-minimized structures of $XeOF_2{\cdot}HF$ and $XeOF_2{\cdot}2HF$, in combination with calculated and experimental vibrational frequencies resulting from $^{16/18}O$ and $^{1/2}H$ isotopic substitution, that most likely $n = 1$, and that HF, in this instance, is coordinated to $XeOF_2$ by means of weak O···H and Xe···F bonds.

The present syntheses of $XeOF_2$ and its HF and CH_3CN adducts, along with their detailed structural characterizations, represent a significant extension of Xe(IV) chemistry and account for most of what is presently known about the oxide fluoride chemistry of Xe(IV). The present findings may be expected to facilitate the extension of Xe(IV) oxide fluoride chemistry into areas such as the fluoride ion donor-acceptor properties of $XeOF_2$ and derivatives with other highly electronegative ligands, as well as offer the possibility to synthesize presently unknown XeO_2.

CHAPTER 4

Synthesis of the Missing Oxide of Xenon, XeO_2, and Its Implications for Earth's Missing Xenon

4.1. Introduction

Atmospheric studies of Earth and Mars have shown that xenon is depleted by a factor of approximately 20 relative to the lighter noble gases (Ne, Ar, Kr).[169] More recent studies have found that as much as 90% of the Earth's primordial xenon is absent from its atmosphere,[170] and that more than 99% of xenon has been degassed from the Earth's mantle.[171] It has also been shown that the Earth's core is unlikely to function as a xenon reservoir.[172,173] These findings have aroused the curiosity of researchers from across a broad range of disciplines spanning planetary, mineralogical, geological, nuclear, and other physical sciences as well as theoretical and computational sciences who have attempted to account for atmospheric xenon depletion. Among the explanations that have been advanced to account for xenon depletion are entrapment in ices,[174] water clathrates,[175] sediments,[176] and early escape from the atmosphere;[177] however, all four hypotheses have been shown to be untenable.[174–177] It has also been proposed that xenon displaces silicon from quartz (SiO_2) at the high pressures (0.7–5 GPa) and temperatures (500–1500 K) that are encountered in the continental crust, with the implication that xenon may be retained within silicate minerals and SiO_2 as XeO_2.[78] The high abundance of SiO_2 would make it a significant and readily available reservoir for xenon.

In addition to offering a potential explanation for the Earth's missing xenon, the possible formation of XeO_2 in the Earth's crust is of fundamental chemical interest because XeO_2 represents the missing oxide of xenon. Shortly after the discovery of noble-gas reactivity,[18] solid, colorless XeO_3 was synthesized by hydrolysis of XeF_6 (eq 4.1)[179,33] and was followed shortly thereafter by the discovery of XeO_4, a pale yellow, volatile solid (eq 4.2 and 4.3).[180,181] Both oxides are highly endothermic and shock

$$XeF_6 + 3H_2O \longrightarrow XeO_3 + 6HF \tag{4.1}$$

$$2XeF_6 + 10NaOH \xrightarrow{NaOH_{(aq)}} [Na]_4[XeO_6] + Xe + O_2 + 2H_2O + 6[Na][HF_2] \tag{4.2}$$

$$[Na]_4[XeO_6] + 2H_2SO_4 \xrightarrow{H_2SO_{4(conc)}} XeO_4 + 2[Na]_2[SO_4] + 2H_2O \tag{4.3}$$

sensitive (ΔH_f XeO_3, 402 kJ mol^{-1}; XeO_4, 643 kJ mol^{-1}).[182] In contrast, xenon monoxide, XeO, has not been synthesized and has been shown by gas-phase quantum-chemical calculations to have an unstable $^3\Pi$ ground state and, therefore, is unlikely to exist as a monomer.[70] It was initially postulated that the hydrolysis product of XeF_4 was either $Xe(OH)_4$ or $XeO_2{\cdot}2H_2O$,[183] but subsequent studies showed the final product to be XeO_3, which arose from the redox disproportionation given in eq 4.4.[68,69] Another early study

$$4XeF_4 + 8H_2O \xrightarrow{H_2O} 2XeO_3 + 2Xe + O_2 + 16HF \tag{4.4}$$

reported the hydrolysis of XeF_4 and the formation of a transient yellow solid at 0 °C. The reaction conditions, which influenced the stability of this species, were optimized by adjusting the acidity of the aqueous medium, but the yellow product was never isolated or characterized.[184] A subsequent study in which XeF_4 and H_2O were co-condensed at −80 °C yielded a pale-yellow product that was incorrectly equated with the aforementioned transient yellow species, and purported to be $XeOF_2$.[65] This proposal was subsequently refuted when $XeOF_2$ was synthesized and unambigously characterized, showing the pale-yellow co-condensed product to be a mixture of $XeOF_2$ and $XeOF_2{\cdot}n\mathrm{HF}$,[125] and by the current study which shows the transient yellow species possesses a Raman spectrum that does not correspond to that of either $XeOF_2$ or $XeOF_2{\cdot}n\mathrm{HF}$.

4.2. Results and Discussion

4.2.1. Synthesis of XeO_2. In the present study, the aforementioned transient yellow solid was synthesized at 0 °C by the addition of crystalline XeF_4 to either water or 2.00 M $H_2SO_{4(aq)}$. In both cases, intense, yellow-orange suspensions initially formed which, upon mixing for ca. 20 s at 0 °C, produced bright yellow suspensions. The "aged" bright yellow solids are consistent with macromolecular XeO_2 (vide infra) while the initial yellow-orange products are possibly a mixture of molecular XeO_2 and/or lower molecular weight polymorphs resulting from incomplete polymerization (eq 4.5). The products were

$$n\mathrm{XeF_4} + 2n\mathrm{H_2O} \longrightarrow [n\mathrm{XeO_2}\ \text{and/or}\ {}^{n}/m(\mathrm{XeO_2})_m] + 4n\mathrm{HF} \longrightarrow (\mathrm{XeO_2})_n + 4n\mathrm{HF} \qquad (n>m) \quad (4.5)$$

precipitated by briefly centrifuging the reaction mixture at 0 °C followed by immediate quenching at −78 °C and recording the Raman spectrum in situ at −150 °C. At no time were the supernatants discoloured, indicating that the yellow products are insoluble in acidified aqueous media. The Raman spectra of the products formed in water and 2.00 M $H_2SO_{4(aq)}$ were identical, indicating that HSO_4^- is not involved in the product.

The yellow product is kinetically stabilized at low-temperatures but decomposes rapidly near ambient temperature. At the reaction temperature, 0 °C, the yellow color persisted for ca. 2 min, whereas samples that had been quenched and stored at −78 °C were stable for considerably longer periods with most decomposition occurring over the first 72 h as evidenced by fading of the original color to pale yellow, with a very faint yellow color persisting after 1 week. In each case, Raman spectra of partially decomposed samples revealed only mixtures of the yellow product and small amounts of XeO_3[185] (i.e., the totally symmetric XeO_3 stretch, A_1, was observed as a weak, broad band at 780 cm^{-1}).

4.2.2. Hydrolyses of [Cs][XeOF₃] and XeOF₂

Hydrolysis of $[Cs][XeOF_3]$ or $XeOF_2$ in CH_3CN solvent also led to XeO_2 formation, albeit in smaller amounts than afforded by the direct hydrolysis of XeF_4 in aqueous media. It has been previously noted that hydrolysis of $[Cs][XeOF_3]$ in CH_3CN solvent in the presence of an excess of CsF resulted in a complex product that could not be definitively identified, but which included Raman bands attributable to XeO_3 modes.[185] It has now been shown that when $[Cs][XeOF_3]$ is synthesized by the reaction of stoichiometric amounts of $XeOF_2$ and CsF (eq 4.6) and subsequently hydrolyzed in CH_3CN with a stoichiometric amount of H_2O, a significant amount of XeO_2 is formed (eq 4.7). As a non-metallic oxide, XeO_2 is acidic and insoluble under acidic conditions, but

$$XeOF_2 + CsF \xrightarrow{CH_3CN} [Cs][XeOF_3] \qquad (4.6)$$

$$[Cs][XeOF_3] + H_2O \xrightarrow{CH_3CN} XeO_2 + [Cs][F(HF)_2] \qquad (4.7)$$

under basic conditions, it rapidly decomposes to Xe and O_2. This is in accordance with the stabilization of the yellow solid under acidic conditions in an earlier hydrolysis study,[184] and likely accounts for the absence of XeO_2 under the fluoro-basic conditions that result from the use of excess fluoride in the synthesis of $XeOF_3^-$.[32] The HF produced in the stoichiometric reaction (eq 4.6 and 4.7) would undoubtedly react with CsF to form $[Cs][F(HF)_x]$, thereby decreasing the basicity of the solution and preventing HF from back reacting with XeO_2.

It has been previously noted that reaction of XeF_4 with two equivalents of H_2O in CH_3CN produced only $XeOF_2$.[125] While this observation is correct, it has been shown in the present work that when $XeOF_2$ is isolated and then reacted with one equivalent of H_2O in CH_3CN, the bulk precipitated sample had a Raman spectrum that showed only a weak XeO_2 band at 570 cm^{-1}. The difference between the two sets of results likely arises from an equilibrium between $XeOF_2$ and XeO_2 (eq 4.8) that favours the left side of eq 4.8 unless the HF formed in the reaction is removed.

$$F_2OXeNCCH_3 + H_2O \xrightleftharpoons{CH_3CN} XeO_2 + 2HF + CH_3CN \qquad (4.8)$$

4.3. Raman spectroscopy. The yellow species was identified and structurally characterized by Raman spectroscopy using ^{18}O and D isotopic enrichment. Reaction of XeF_4 with $H_2{}^{18}O$ resulted in a Raman spectrum that was similar to that obtained from the reaction of XeF_4 with $H_2{}^{16}O$ (Figure 4.1); however, all vibrational bands were shifted to lower frequencies (Table 4.1). The presence of a single, intense band in the Xe–O/Xe–F stretching region, and the absence of unshifted modes, indicates there are no Xe–F bonds in the compound and that the compound is an oxide and/or hydroxy derivative of Xe(IV).[187] When XeF_4 was allowed to react with $D_2{}^{16}O$, the Raman spectrum of the product was identical to that of $H_2{}^{16}O$ reaction product, and devoid of any bands that

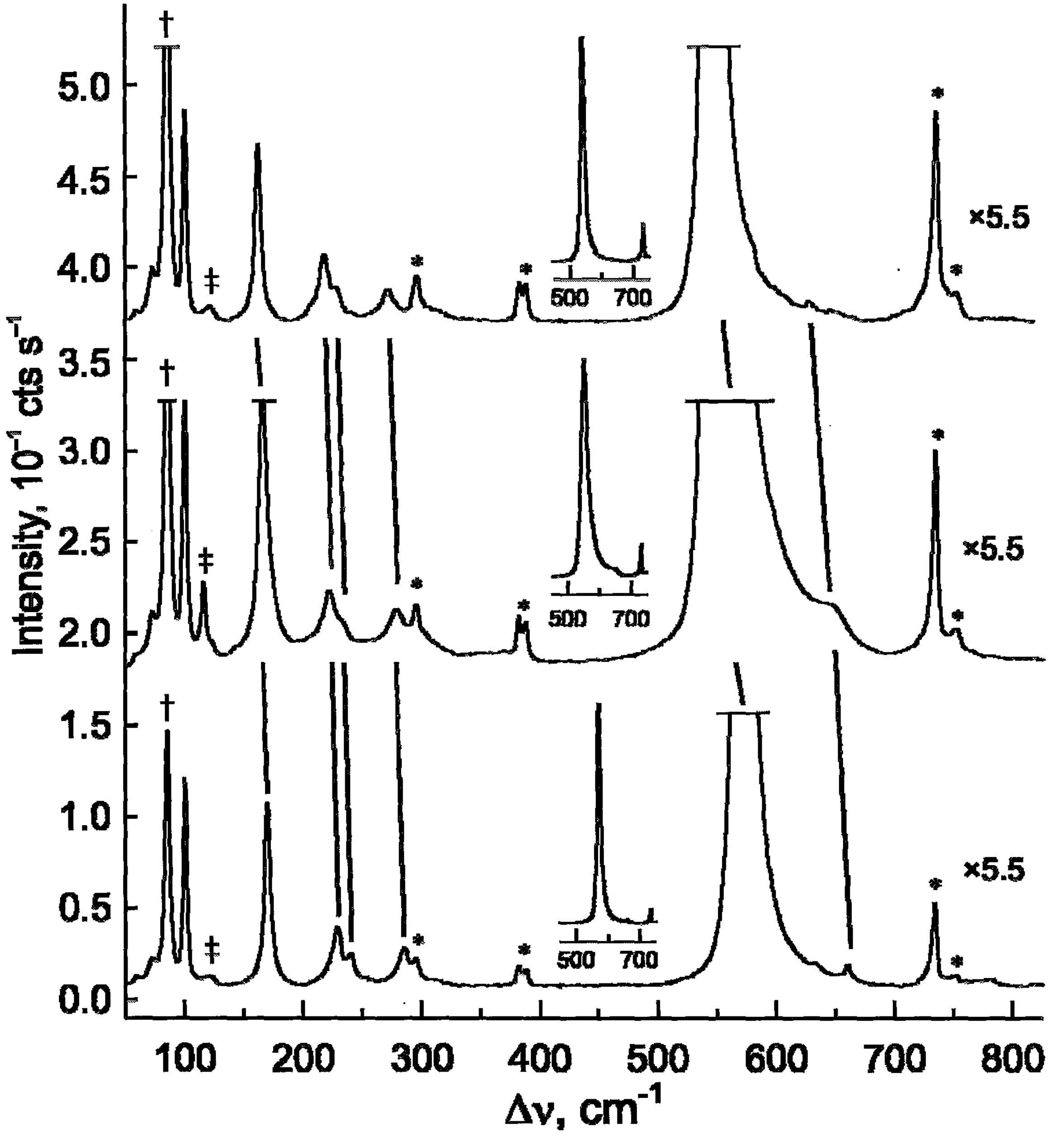

Figure 4.1. Raman spectra of natural abundance (lower trace), 50% (middle trace) and 97.8% ^{18}O-enriched (upper trace) XeO_2 recorded under frozen water at –150 °C using 1064-nm excitation. Symbols denote FEP sample tube lines (*), instrumental artifact (†), and minor, incompletely polymerized (yellow-orange) product(s) (‡).

Table 4.1. Vibrational Frequencies for XeF_4, $Xe^{16}O_2$, $Xe^{16/18}O_2$, and $Xe^{18}O_2$ [a]

XeF_4 [b]		$Xe^{16}O_2$ [c]	$Xe^{16/18}O_2$ [c,d]	$Xe^{18}O_2$ [c]	D_{2d} [e]	assgnts (L = F, O) [f]
586	ν_6, $\nu(E_u)$	632.3(1)	626.5sh	625.8(1)	$\nu(E)$	$\nu_{as}(XeL_t - XeL_t)$
554	ν_1, $\nu(A_{1g})$	570.3(100)	550.9(100)	542.6(100)	$\nu(A_1)$	$\nu_s(XeL_4)$
524	ν_4, $\nu(B_{2g})$				$\nu(B_2)$	$\nu_{as}(XeL_{2t} - XeL_{2t})$
291	ν_3, $\nu(A_{2u})$	283.9(3)	276.9(2)	270.0(3)	$\nu(B_2)$	$\delta(XeL_4)$ o.o.p., umbrella mode
218	ν_2, $\nu(B_{1g})$	239.1(2)	231sh	226.6(2)	$\nu(B_1)$	$\delta(XeL_{2c} + XeL_{2c})$
		227.9(4)	221.3(4)	216.9(6)		
n.o.	ν_5, $\nu(B_{2u})$	n.o.	n.o.	n.o.	$\nu(A_2)$	$\delta(XeL_{2t})$ o.o.p. – $\delta(XeL_{2t})$ o.o.p.
161	ν_7, $\nu(E_u)$ [g]	168.9(13)	165.0(19)	161.1(13)	$\nu(E)$	$\delta(XeL_{2t})$ i.p.
		99.5(14)	99.3(17)	99.5(15)		lattice mode

[a] Frequencies are given in cm^{-1}. [b] From ref 186. The symmetries refer to the D_{4h} point symmetry of XeF_4. [c] Values in parentheses denote Raman intensities. [d] The sample was prepared by hydrolysis of XeF_4 in an equimolar mixture of $H_2{}^{16}O$ and $H_2{}^{18}O$. [e] The symmetries refer to the local D_{2d} point symmetry of the XeO_4 units in the extended structure of XeO_2. [f] The abbreviations denote trans (t), cis (c), symmetric (s), asymmetric (as), stretch (ν), bend (δ), in-plane bend (i.p.), and out-of-plane bend (o.o.p.). The in-plane and out-of-plane mode descriptions are relative to the molecular planes of XeF_4 and the XeO_4-unit. [g] This mode was not directly observed. The frequency was obtained from the $2\nu_7$ overtone at 322 cm^{-1}.

displayed H/D isotopic dependencies, ruling out a hydroxy compound. The most intense band in the spectrum (570.3 cm^{-1}) is assigned to a symmetric stretching mode that is too low to be associated with the symmetric stretch of XeO_3 (780 cm^{-1})[185] but too high for a Xe(II) oxide fluoride or oxide.[188] The spectrum is therefore most consistent with the formation of the Xe(IV) oxide, XeO_2. Moreover, monomeric XeO_2 is predicted to have a bent geometry based on an AX_2E_2 (X = bond pair, E = valence electron lone pair) VSEPR[41] arrangement of bond pairs and lone pairs (structure I) and would consequently

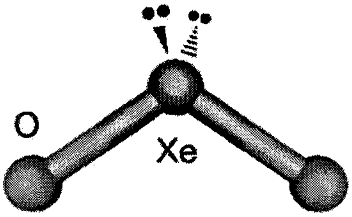

I

be a polar molecule. This expectation contrasts with the insolubility of this material in aqueous media, suggesting that XeO_2 likely has an extended (chain or network) structure.

The Raman spectra of $Xe^{16}O_2$ and $Xe^{18}O_2$ (Figure 4.1) also support extended structures. The vibrational frequencies of gas-phase monomeric XeO_2 have been calculated at the CCSD(T) level of theory using the 6-311 g* and aug-cc-PVTZ basis set for oxygen, giving three Raman-active modes at 647 (668), 205 (206), and 703 (716) cm^{-1}, where the aug-cc-PVTZ values are given in parentheses.[189] The bands in the experimental Raman spectra of XeO_2 number six and are broad ($\Delta\nu_{½} \approx 20$ cm^{-1}), which is consistent with vibrational coupling and bridge-bonding in an extended structure. A 1:1

molar mixture of $H_2{}^{16}O$ and $H_2{}^{18}O$ was also used to synthesize XeO_2, as described above, in an attempt to resolve the independent spectra corresponding to the $^{16/18}O$ isotopomers of monomeric XeO_2, namely, $Xe^{16}O_2$, $Xe^{16/18}O_2$, and $Xe^{18}O_2$. Instead of three discrete overlapping isotopomeric spectra, the Raman spectrum was comprised of broadened bands that occurred at frequencies that were intermediate with respect to the spectra of $Xe^{16}O_2$ and $Xe^{18}O_2$ (Figure 4.1 and Table 4.1). This result is also in accordance with an extended XeO_2 structure in which vibrational coupling extends beyond the primary coordination sphere of xenon. The aforementioned behavior of XeO_2 is not unlike SiO_2, which forms discrete monomeric units with double bonds to oxygen in the gas phase, and extended networks in the solid state which display extensive vibrational coupling.[190]

There is a notable similarity between the Raman frequencies of XeO_2 and those of XeF_4 (Table 4.1), which are in closest agreement for $Xe^{18}O_2$, where the atomic mass of ^{18}O is closest to that of ^{19}F. This leads to the conclusion that the extended XeO_2 structure has a local square-planar geometry around xenon (structure II). The square-planar structural unit is consistent with the VSEPR model of molecular geometry,[41] which is an AX_4E_2 arrangement of four bond pairs and two valence electron lone pairs. This is in

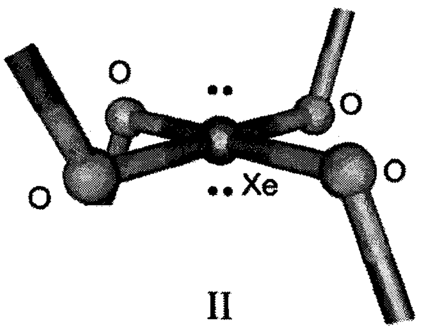

II

accordance with other Xe(IV) compounds which have square-planar (XeF_4,[32] $F_2OXeNCCH_3$,[125] $XeOF_2$,[125] $XeOF_3^-$,[126] $Xe(OTeF_5)_4$[60]) or pentagonal-planar (XeF_5^-,[53] $[XeF_3][SbF_6]$,[52] $[XeF_3][Sb_2F_{11}]$[51]) xenon coordination spheres in the solid state when short secondary contacts are taken into account. However, the bent angles at the oxygen atoms in the extended structure of XeO_2 result in reduction of the local D_{4h} symmetry at xenon and three additional vibrations that are otherwise associated with rotation of the free molecule[191] (see Table 4.2). The observed bands in the Raman spectrum are most consistent with symmetry lowering to D_{2d} symmetry where the planar XeO_4 moiety is predicted to give rise to nine vibrational bands belonging to the irreducible representations $A_1 + 2A_2 + B_1 + 2B_2 + 3E$, where modes of A_1, B_1, B_2, and E symmetry are Raman active (seven bands); those of B_1, B_2, and E symmetry are infrared active (six bands); and those of A_2 symmetry are Raman and infrared inactive. The vibrational assignments for XeO_2 are therefore made by analogy with the square-planar D_{4h} symmetry of XeF_4 with the understanding that the vibrational mode descriptions under local D_{2d} symmetry will be very similar

The most intense Raman band of XeO_2 occurs at 570.3 cm^{-1} and displays an ^{18}O-isotopic shift of -27.7 cm^{-1}. The band occurs at a frequency that is much lower than the symmetric and asymmetric Xe–O stretches predicted for the gas-phase molecule.[189] This is consistent with coordination of the oxygen atoms to neighboring xenon atoms, which imparts single bond character to the Xe–O bonds and lowers the frequencies of the Xe–O stretching modes. A similar trend has been observed for $XeOF_2$.[125] The 570.3 cm^{-1} band is assigned to the combined $\nu_s(XeO_4)$ and $\nu_{as}(XeO_{2t} - XeO_{2t})$ modes, where t represents

Table 4.2. Site Symmetry Analyses for the XeO_4 Moiety in the Polymeric Structure of XeO_2 [a]

Xe^{18}O$_2$ [b]	XeF$_4$ [c]	D_{4h}	D_4	$D_{2d}(C_2')$	$D_{2d}(C_2'')$	C_{4v}	C_{4h}	$D_{2h}(C_2')$	$D_{2h}(C_2'')$	C_4	S_4	$D_2(C_2')$	$D_2(C_2'')$	$C_{2v}(C_2, \sigma_v)$
625.8	586	**E_u (IR)**	E (R,IR)	E (R,IR)	E (R,IR)	E (R,IR)	**E_u (IR)**	**B_{2u} (IR) + B_{3u} (IR)**	**B_{2u} (IR) + B_{3u} (IR)**	E (R,IR)	E (R,IR)	**B_2 (R,IR) + B_3 (R,IR)**	**B_2 (R,IR) + B_3 (R,IR)**	**B_1 (R,IR) + B_2 (R,IR)**
542.6	554	A_{1g} (R)	A_1 (R)	A_1 (R)	A_1 (R)	A_1 (R,IR)	A_g (R)	A_g (R)	A_g (R)	A (R,IR)	A (R)	A (R)	A (R)	A_1 (R,IR)
	524	B_{1g} (R)	B_1 (R)	B_1 (R)	B_2 (R,IR)	B_1 (R)	B_g (R)	A_g (R)	B_{1g} (R)	B (R)	B (R,IR)	A (R)	B_1 (R,IR)	A_1 (R,IR)
270.0	291	**A_{2u} (IR)**	**A_2 (IR)**	B_2 (R,IR)	B_2 (R,IR)	A_1 (R,IR)	**A_u (IR)**	**B_{1u} (IR)**	**B_{1u} (IR)**	A (R,IR)	B (R,IR)	B_1 (R,IR)	B_1 (R,IR)	A_1 (R,IR)
226.6 [d] 216.9 [d]	218	B_{2g} (R)	B_2 (R)	B_2 (R,IR)	B_1 (R)	B_2 (R)	B_g (R)	B_{1g} (R)	A_g (R)	B (R)	B (R,IR)	B_1 (R,IR)	A (R)	A_2 (R)
n.o.	n.o.	B_{2u} (n.o.)	**B_2 (R)**	A_2 (n.o.)	**A_1 (R)**	**B_1 (R)**	B_u (n.o.)	B_{1u} (IR)	A_u (n.o.)	**B (R)**	**A (R)**	**B_1 (R,IR)**	**A (R)**	**A_1 (R,IR)**
161.1	161 [e]	**E_u (IR)**	E (R,IR)	E (R,IR)	E (R,IR)	E (R,IR)	**E_u (IR)**	**B_{2u} (IR) + B_{3u} (IR)**	**B_{2u} (IR) + B_{3u} (IR)**	E (R,IR)	E (R,IR)	**B_2 (R,IR) + B_3 (R,IR)**	**B_2 (R,IR) + B_3 (R,IR)**	**B_1 (R,IR) + B_2 (R,IR)**
	R_z	A_{2g} (n.o.)	A_2 (IR)	A_2 (n.o.)	A_2 (n.o.)	A_2 (n.o.)	A_g (R)	B_{1g} (R)	B_{1g} (R)	A (R,IR)	A (R)	B_1 (R,IR)	B_1 (R,IR)	A_2 (R,IR)
226.6 [d] 216.9 [d]	R_x, R_y	E_g (R)	E (R,IR)	E (R,IR)	E (R,IR)	E (R,IR)	E_g (R)	B_{2g} (R) + B_{3g} (R)	B_{2g} (R) + B_{3g} (R)	E (R,IR)	E (R,IR)	B_2 (R,IR) + B_3 (R,IR)	B_2 (R,IR) + B_3 (R,IR)	B_1 (R,IR) + B_2 (R,IR)

Xe^{18}O$_2$ [b]	D_{4h}	$C_{2v}(C_2, \sigma_d)$	$C_{2v}(C_2')$	$C_{2v}(C_2'')$	$C_{2h}(C_2)$	$C_{2h}(C_2')$	$C_{2h}(C_2'')$	$C_2(C_2)$	$C_2(C_2')$	$C_2(C_2'')$	$C_s(\sigma_h)$	$C_s(\sigma_v)$	$C_s(\sigma_d)$	C_i
625.8	E_u	**B_1 (R,IR) + B_2 (R,IR)**	**A_1 (R,IR) + B_1 (R,IR)**	**A_1 (R,IR) + B_1 (R,IR)**	**$2B_u$ (IR)**	**A_u (IR) + B_u (IR)**	**A_u (IR) + B_u (IR)**	**$2B$ (R,IR)**	**A (R,IR) + B (R,IR)**	**A (R,IR) + B (R,IR)**	**$2A'$ (R,IR)**	**A' (R,IR) + A'' (R,IR)**	**A' (R,IR) + A'' (R,IR)**	**$2A_u$ (IR)**
542.6	A_{1g}	A_1 (R,IR)	A_1 (R,IR)	A_1 (R,IR)	A_g (R)	A_g (R)	A_g (R)	A (R,IR)	A (R,IR)	A (R,IR)	A' (R,IR)	A' (R,IR)	A' (R,IR)	A_g (R)
	B_{1g}	A_2 (R)	A_1 (R,IR)	B_1 (R,IR)	A_g (R)	A_g (R)	B_g (R)	A (R,IR)	A (R,IR)	B (R,IR)	A' (R,IR)	A' (R,IR)	A'' (R,IR)	A_g (R)
270.0	A_{2u}	A_1 (R,IR)	B_2 (R,IR)	B_2 (R,IR)	**A_u (IR)**	**B_u (IR)**	**B_u (IR)**	A (R,IR)	B (R,IR)	B (R,IR)	A'' (R,IR)	A' (R,IR)	A' (R,IR)	**A_u (IR)**
226.6 [d] 216.9 [d]	B_{2g}	A_1 (R,IR)	B_1 (R,IR)	A_1 (R,IR)	A_g (R)	B_g (R)	A_g (R)	A (R,IR)	B (R,IR)	A (R,IR)	A' (R,IR)	A'' (R,IR)	A' (R,IR)	A_g (R)
n.o.	B_{2u}	**A_2 (R)**	**B_2 (R,IR)**	**A_2 (R)**	A_u (IR)	B_u (IR)	A_u (IR)	**A (R,IR)**	**B (R,IR)**	**A (R,IR)**	**A'' (R,IR)**	**A' (R,IR)**	**A'' (R,IR)**	A_u (IR)
161.1	E_u	**B_1 (R,IR) + B_2 (R,IR)**	**A_1 (R,IR) + B_1 (R,IR)**	**A_1 (R,IR) + B_1 (R,IR)**	**$2B_u$ (IR)**	**A_u (IR) + B_u (IR)**	**A_u (IR) + B_u (IR)**	**$2B$ (R,IR)**	**A (R,IR) + B (R,IR)**	**A (R,IR) + B (R,IR)**	**$2A'$ (R,IR)**	**A' (R,IR) + A'' (R,IR)**	**A' (R,IR) + A'' (R,IR)**	**$2A_u$ (IR)**
	A_{2g}	A_2 (R)	B_1 (R,IR)	B_1 (R,IR)	A_g (R)	B_g (R)	B_g (R)	A (R,IR)	B (R,IR)	B (R,IR)	A' (R,IR)	A'' (R,IR)	A'' (R,IR)	A_g (R)
226.6 [d] 216.9 [d]	E_g	B_1 (R,IR) + B_2 (R,IR)	A_2 (R) + B_2 (R,IR)	A_2 (R) + B_2 (R,IR)	$2B_g$ (R)	A_g (R) + B_g (R)	A_g (R) + B_g (R)	$2B$ (R,IR)	A (R,IR) + B (R,IR)	A (R,IR) + B (R,IR)	$2A''$ (R,IR)	A' (R,IR) + A'' (R,IR)	A' (R,IR) + A'' (R,IR)	$2A_g$ (R)

[a] The irreducible representations and activities in bold red correspond to modes having Raman activities that are incompatible with the observed Raman bands of XeO_2. The abbreviations denote Raman-active (R) and infrared-active (IR) bands and not observed (n.o.). The only local XeO_2 symmetry that is consistent with the observed Raman activities is $D_{2d}(C_2')$. [b] The vibrational frequencies of $Xe^{18}O_2$ are compared with XeF_4 to minimize the mass difference between F and O. The spectral assignments of $Xe^{18}O_2$ are for square-planar oxygen-bridged $Xe^{18}O_4$ moieties. [c] From ref 186. The translatory modes of XeF_4 belong to the A_{2u} (T_z) and E_u (T_x, T_y) representations but their counterparts do not contribute vibrational modes in the extended structure of XeO_2. [d] The two bands either arise from splitting of the B_{2g} mode normally observed for XeF_4, or from a rotational mode that is rendered Raman active upon symmetry lowering. [e] This mode was not directly observed, but was obtained from the $2\nu_7$ overtone at 322 cm^{-1}.

atoms trans to one another. These modes are normally associated with $\nu_1(A_{1g})$ and $\nu_4(B_{2g})$ in an isolated square-planar molecule but are rendered degenerate in an extended lattice (structure II) because the elongation of four Xe–O bonds results in the compression of four Xe–O bonds of the four next nearest neighbor XeO_4 groups. The $\nu_2(B_{1g})$ mode of a square-planar molecule appears as two bands at 227.9 and 239.1 cm^{-1}. These bands exhibit ^{18}O isotopic shifts of −11.0 and −12.5 cm^{-1}, respectively, which are assigned to $\delta(XeO_{2c} + XeO_{2c})$.[191] The extended lattice of XeO_2 also renders modes Raman-active that would otherwise be exclusively infrared active in an isolated centrosymmetric square-planar molecule. A case in point is the weak band at 283.9 cm^{-1}, which is assigned to the out-of-plane XeO_4 bend, $\nu_3(A_{2u})$, and displays a low-frequency shift (−13.9 cm^{-1}) upon ^{18}O-enrichment. Similarly, the otherwise Raman-inactive modes, $XeO_t - XeO_t$, and the in-plane bend, XeO_{2t}, corresponding to $\nu_6(E_u)$ and $\nu_7(E_u)$, respectively, are observed at 632.3 cm^{-1} and 168.9 cm^{-1} with ^{18}O isotopic shifts of −6.5 and −7.8 cm^{-1}, respectively. The out-of-plane coupled bending mode, $\delta(XeO_{2t})$o.o.p. − $\delta(XeO_{2t})$, corresponding to $\nu_5(B_{2u})$, which is formally both Raman and infrared inactive in isolated square-planar centrosymmetric molecules, is also not observed for XeO_2.

The Raman spectrum of the yellow-orange, incompletely polymerized product (Figure 4.2) is very similar to that of the fully polymerized yellow solid with the exception of a broadened 570 cm^{-1} band, which tails off to higher frequency (~680 cm^{-1}), and a weak band at 310 cm^{-1}. These features may be attributed to shorter oligomers or smaller network structures that have not fully condensed.

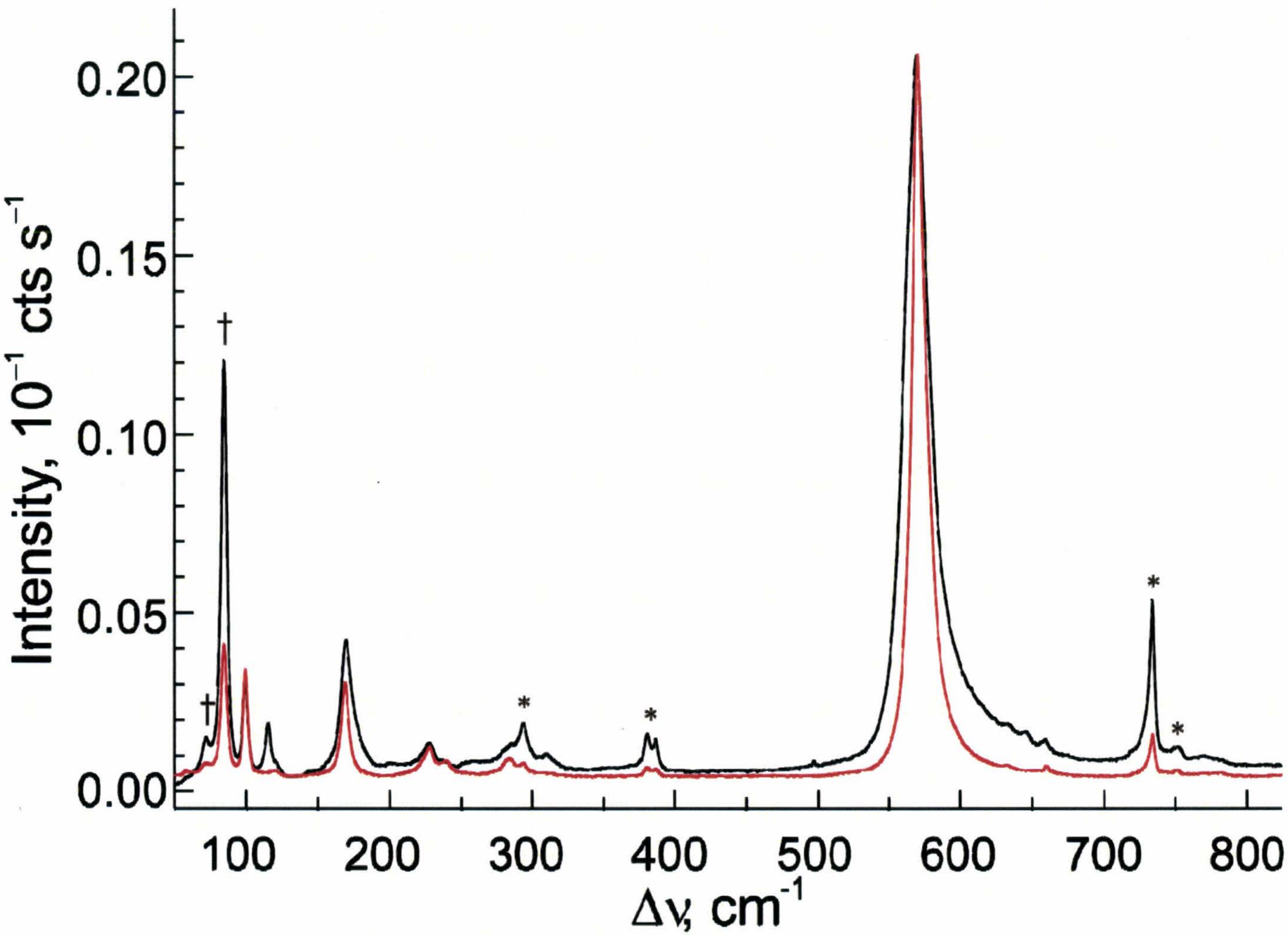

Figure 4.2. The natural abundance Raman spectra of yellow-orange incompletely polymerized product(s) (black trace) and yellow, macromolecular XeO_2 (red trace) recorded under solid water at –150 °C using 1064-nm excitation. Symbols denote FEP sample tube lines (*) and instrumental artifacts (†).

Prior work[178] reporting xenon doped SiO_2 has been re-examined in light of the present findings. The study assumed that xenon substitution for silicon in a SiO_2 lattice resulted in xenon occupancy at a tetrahedral site. For this reason, the local xenon geometry was compared with that of XeO_4,[193] assuming that the Xe–O bond lengths and vibrational frequencies of the gas-phase XeO_4 molecule are transferable.[178] Consequently, the latter assumption and ensuing comparisons are flawed. The valence shell of Xe(IV) in XeO_2 possesses two valence electron lone pairs. If Xe(IV) were to form bonds to four oxygen atoms in a silicate environment, they would be single bond domains and would adopt a local square-planar AX_4E_2 VSEPR[41] arrangement around Xe(IV) as in structure II. Xenon in tetrahedral XeO_4 is in the +8 oxidation state, forming four double bonds to the oxygen atoms.[193] The prior argument[178] ignores the formal oxidation state of xenon, formal Xe–O single bond orders and stereochemical activities of the two valence electron lone pairs on Xe(IV). Therefore, the bond lengths and Raman frequencies observed for gas-phase XeO_4 are not valid comparisons. The present arguments are supported by a recent report that provides several calculated models for xenon insertion into SiO_2 networks.[194] One such model positioned xenon at a tetrahedral site which, when energy optimized, gave a local square-planar geometry at xenon. Unfortunately, the steric effects of the free valence electron lone pairs on Xe(IV) and relevant VSEPR arguments were not considered and the optimized square-planar geometry was attributed to packing constraints and stabilization by the surrounding environment.[194]

Thermodynamic considerations in the prior reports of xenon doped SiO_2[178] attribute the formation of XeO_2 to *PV* work that resulted from an increase in unit cell size and to the high pressures attained in the experiment.[178] The PV work was estimated to be −700 kJ mol^{-1}, noting that it "favors the reaction that is otherwise inhibited at ambient conditions because of the high formation enthalpy predicted for XeO_2[189] compared with that of SiO_2". Although −700 kJ mol^{-1} is sufficient to overcome ΔH°_{f} $XeO_{2(g)}$ (487 kJ mol^{-1}),[189] an ambiguity arises when ΔH°_{f} $SiO_{2(quartz)}$ (−910.94 kJ mol^{-1})[195] and ΔH°_{sub} $Xe_{(s)}$ (−15.0(2) kJ mol^{-1})[196] are also considered in eq 4.9, resulting in a highly endothermic (713 kJ mol^{-1}) process when the volume reduction work is included.

$$SiO_{2(quartz)} + Xe_{(s)} \longrightarrow Si_{(s)} + XeO_{2(g)} \qquad \Delta H^{\circ} = 1413\ \text{kJ mol}^{-1} \qquad (4.9)$$

Equation 4.9 neglects the lattice enthalpy of XeO_2, which is unknown, but were it to exceed 713 kJ mol^{-1}, when coupled with the error in the estimated *PV* work, the process could be rendered spontaneous. The plausibility of reaction 4.9 is supported by a recent computational study relating to xenon insertion into SiO_2 networks.[194] This study concluded that xenon could be incorporated into the interstitial spaces of SiO_2 lattices under ambient conditions and that xenon could replace silicon at higher pressures in a two-step process. The initial step requires a substantial amount of energy and involves a redox process in which Si atoms are removed from the lattice and Si–O–O–Si peroxi-linkages are formed (eq 4.10). The xenon incorporation step (eq 4.11) has an energy barrier of 177 kJ mol^{-1}.[194]

$$(Si{-}O{-})_2{-}Si{-}({-}O{-}Si)_{2(quartz)} \longrightarrow 2\ Si{-}O{-}O{-}Si_{(s)} + Si_{(s)} \qquad (4.10)$$

$$2\ Si{-}O{-}O{-}Si_{(s)} + Xe_{(s)} \longrightarrow (Si{-}O{-})_2{-}Xe{-}({-}O{-}Si)_{2(s)} \qquad (4.11)$$

In view of the aforementioned computational results, which support xenon substitution into SiO_2 networks, the previous Raman spectrum of xenon doped SiO_2 obtained from a high-pressure and high-temperature study[178] was re-examined in light of the present findings. The spectrum is consistent with the presence of covalently bound xenon, but the vibrational bands were incorrectly assigned. A band at 588 cm^{-1} was assigned "to the main Raman band of SiO units, located at 596.4 cm^{-1} at room temperature in the gas phase".[178] The reference alluded to by the authors actually quotes SiO stretches ranging from 460.2 – 627.9 cm^{-1} for $(SiO)_n$ (n = 2–4) in a solid methane matrix at 25 K.[197] The 588 cm^{-1} band is in good agreement with the experimental frequency for bulk XeO_2 (570.3 cm^{-1}) obtained in the present study and more likely arises from modes whose descriptions approximate $\nu_s(XeO_4)$ and $\nu_{as}(XeO_{2t} - XeO_{2t})$. Bands at 814 and 356 cm^{-1} were also previously assigned to XeO_2,[178] but most likely arise from Si-O_{Xe} stretching and O-Si-O_{Xe} bending modes, respectively, where O_{Xe} denotes oxygen bound to xenon. These bands are in good agreement with the E and A_1 modes observed for solid SiO_2 at 795 and 356 cm^{-1}, respectively,[198] and are reassigned accordingly.

4.3. Conclusion

The present study has provided the synthesis and characterization of macroscopic amounts of XeO_2. Raman spectroscopic studies employing $^{16}O/^{18}O$ isotopic enrichment indicate that XeO_2 possesses an extended structure having a local square-planar XeO_4 geometry around Xe(IV). Xenon dioxide presently represents the only known covalent network structure for a noble-gas compound that exists under near-ambient conditions. The present Raman spectroscopic studies of XeO_2 also correct prior vibrational assignments of xenon-doped SiO_2 containing covalently bound xenon (2.2%) that had been substituted for silicon in a quartz matrix under high-temperature and high-pressure conditions.[178] Such xenon-doped SiO_2 lattices offer the possibility that covalently bound xenon occurs in natural silicates that have been cycled deep into Earth's crust. This could serve to deplete the amount of xenon relative to the lighter noble gases in the atmosphere, providing a plausible explanation for the Earth's missing xenon.

CHAPTER 5

$XeOF_3^-$, an Example of an AX_3YE_2 VSEPR Arrangement; Syntheses and Structural Characterizations of $[M][XeOF_3]$ ($M = Cs, N(CH_3)_4$)

5.1. Introduction

Although the xenon(IV) fluoride species, XeF_3^+,[48,51,52] XeF_4,[32,35,38] and XeF_5^- [53] have been well characterized spectroscopically and by single-crystal X-ray diffraction, the absence of a facile synthetic route to high-purity $XeOF_2$ had prevented extensive exploration of its fluoride ion donor–acceptor properties. The recent synthesis of pure $XeOF_2$[125] has provided an opportunity to extend the oxide fluoride chemistry of Xe(IV) and to study the fluoride ion acceptor properties of $XeOF_2$ with the view to synthesize and characterize salts of the $XeOF_3^-$ anion.

A prior publication has reported the synthesis of $[Cs][XeOF_3]$ and its characterization by low-temperature Raman spectroscopy.[67] The synthesis (eqs 5.1 and 5.2) utilized aHF as the solvent medium which was complicated by the fact that both F^-

$$CsF + m\text{HF} \xrightarrow[-78\ ^{\circ}\text{C}]{\text{HF}} [Cs][F(HF)_m] \qquad (5.1)$$

$$[Cs][F(HF)_m] + XeOF_2 \xrightarrow[0\ ^{\circ}\text{C}]{\text{dynamic vac.}} [Cs][XeOF_3] + m\text{HF} \qquad (5.2)$$

and $XeOF_2$[125] form HF solvates. Removal of HF under dynamic vacuum at −78 °C produced a mixture of $XeOF_2$ and $[Cs][F(HF)_n]$. Slow warming of the product mixture to room temperature under dynamic vacuum resulted in further removal of HF. The authors concluded that upon solvent removal, the reaction proceeded to the formation of

[Cs][$XeOF_3$], along with traces of [Cs][XeO_2F_3]; the latter was attributed to a disproportionation (eq 5.3).[67] The present work will show that a mixture of XeF_2, $XeOF_2$,

$$2[Cs][XeOF_3] \xrightarrow[0\ ^{\circ}C]{HF} [Cs][XeO_2F_3] + XeF_2 + CsF \tag{5.3}$$

[Cs][XeF_5], and [Cs][XeO_3F] was actually formed in the earlier reported work and that the $XeOF_3^-$ anion has eluded synthesis until the present work.

The $XeOF_3^-$ anion is of special interest because, to the best of the authors' knowledge, it represents the only example of an AX_3YE_2 VSEPR[41] arrangement in which the valence electron lone-pair domains and a double bond domain occupy positions where they are approximately 90° to one another (Structure I).

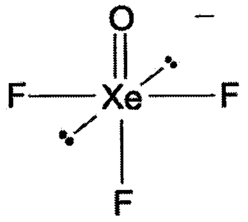

I

The present paper details the syntheses of the Cs^+ and $N(CH_3)_4^+$ salts of the $XeOF_3^-$ anion and their characterization by Raman spectroscopy. Quantum-chemical calculations and ^{18}O-enrichment have been employed to assign the Raman spectra of the $Xe^{16/18}OF_3^-$ anion and to aid in the assessment of its chemical bonding.

5.2. Results and Discussion

5.2.1. Syntheses of [M][$XeOF_3$] (M = $N(CH_4)$, Cs). 5.2.1.1. [M][$XeOF_3$] in CH_3CN Solvent. Reactions and the purities of all products were routinely monitored by recording the low-temperature Raman spectra (–150 °C) of the natural abundance and ^{18}O-enriched (98.6 atom %) $XeOF_3^-$ salts.

The $XeOF_3^-$ anion was obtained as the $N(CH_3)_4^+$ and Cs^+ salts by the low-temperature reaction of $XeOF_2$ with $[N(CH_3)_4][F]$ (CsF) in dry CH_3CN solvent according to eq 5.4, where M = $N(CH_3)_4$, Cs. Tetramethylammonium fluoride or CsF was added in

$$XeOF_2 + [M][F] \xrightarrow[-45\ ^{\circ}C]{CH_3CN} [M][XeOF_3] \quad (5.4)$$

ca. 3–5% excess to circumvent possible $XeOF_2$ contamination of the product. The $[N(CH_3)_4][XeOF_3]$ salt precipitated from solution as a very pale yellow, amorphous powder and was isolated by removal of the solvent under dynamic vacuum at –45 to –42 °C over a period of several hours. The synthesis of $[Cs][XeOF_3]$ was complicated by the low solubilities of CsF and $[Cs][XeOF_3]$ in CH_3CN solvent. Upon warming, $XeOF_2$ reacted in varying degrees with CsF, forming insoluble $[Cs][XeOF_3]$ in admixture with unreacted CsF. Unreacted $XeOF_2$, which imparted a yellow color to the supernatant, remained in solution and was removed by use of a cannula as previously described.[125] The residual solvent was removed under dynamic vacuum at –45 to –42 °C over a period of several hours, leaving behind a pale yellow powder. Reaction of [M][F] with $XeOF_2$ in 2:1 molar ratios yielded only $[M][XeOF_3]$ and did not result in the formation of $[M]_2[XeOF_4]$. Conversely, reaction of the fluoride salts with $XeOF_2$ in 1:2 molar ratios did not result in the formation of $F_2OXe{-}{-}{-}F{-}{-}{-}XeOF_2^-$ salts, yielding only $[M][XeOF_3]$ and unreacted $XeOF_2$.

5.2.1.2. Attempts to Replicate the Prior Synthesis of "$[Cs][XeOF_3]$" in aHF. A 1:1 molar ratio of CsF and $XeOF_2$ was prepared in aHF and dried under dynamic vacuum at

−78 °C. The product was shown by Raman spectroscopy to be $XeOF_2{\cdot}n HF$, but presumably also contained $[Cs][F(HF)_m]$. With further pumping, vigorous mixing, and slow warming to −10 °C to remove additional bound HF, the original pale yellow color of the sample intensified. The Raman spectrum of the resulting solid revealed a mixture of $XeOF_2$ and $[Cs][XeOF_3]$ (and presumably $[Cs][F(HF)_n]$, where $n \ll m$).

The previously reported synthesis of "$[Cs][XeOF_3]$", which was carried out at 0 °C,[67] closely resembles the present synthesis which was carried out at −10 °C. However, the Raman spectra of their respective products are significantly different. The Raman spectrum of the previously reported product mixture[67] has now been reassigned to XeF_2, $XeOF_2$, $[Cs][XeF_5]$, and $[Cs][XeO_3F]$ (Table 5.1). It is likely that none of the reactions leading to the latter products involve $[Cs][XeOF_3]$ as an intermediate because none of its vibrational bands were observed in the Raman spectra of the product mixtures based on the present Raman assignments for $[Cs][XeOF_3]$ (cf. Tables 5.1 and 5.2). The neutral molecules, $XeOF_2$ and XeF_2, likely form upon removal of HF from $XeOF_2{\cdot}n HF$ (eq 5.5),[125] followed by either xenon(IV) reduction to xenon(II) (eq 5.6)[125] or disproportionation (eq 5.7).[67,125] The previous report also noted that the reaction of XeF_4 and H_2O in HF solvent at −60 °C, which was used to synthesize $XeOF_2$, was incomplete and therefore contained unreacted XeF_4 and H_2O.[67] Xenon tetrafluoride, which has been shown to react with CsF to form $[Cs][XeF_5]$,[53] presumably reacts with $[Cs][F(HF)_n]$ according to eq 5.8.[199] Water and $[Cs][F(HF)_n]$ would form $[Cs][XeO_3F]$ by either hydrolysis of XeO_2F_2 (eq 5.9),[200] followed by fluoride ion addition[201] (eq 5.10), or by fluoride ion addition to XeO_2F_2[202] (eq 5.11), followed by hydrolysis (eq 5.12). Equations

Table 5.1. Reassigned Raman Spectra of Products Attributed to [Cs][$XeOF_3$] in Prior Work[a]

	assgnts[b]			
exptl	XeF_2	$XeOF_2$	[Cs][XeF_5]	[Cs][XeO_3F]
856(2)[c]				$\nu_{as}(Xe^{16}O^{18}O_{eq})$
837(2)[c]				$\nu_{as}(Xe^{18}O_{2eq})$
825(<1)[c]				$\nu_{s}(Xe^{16}O_{2eq})$
805(4)[c]				$\nu_{s}(Xe^{16}O^{18}O_{eq})$
793(3)[c]				$\nu_{s}(Xe^{18}O_{2eq})$
768(17)				$\nu(Xe^{16}O_{ax})$
755(3)[c]		$\nu(Xe^{16}O)$		
727(32)				$\nu(Xe^{18}O_{ax})$
716(5)[c]		$\nu(Xe^{18}O)$		
503(61)			$\nu_s(XeF_5)$ i.p.	
497(35)[c]	$\nu_s(XeF_2)$			
487(10)				
464(100)		$\nu_s(XeF_2)$		
434(4)[c]			$\nu_d(XeF_5)$ i.p.	
425(5)[c]				
381(5)			$\delta_s(XeF_5)$ i.p.	
370(6)				
292(1)		$\rho_{rock}(XeOF_2)$ i.p.		
270(5)				
260(8)				
219(1)				
167(6)				
145(11)[c]		$\delta(XeF_2)$ i.p.		
138(3)[c]				
124(19)[c]			lattice vibration	
118(3)[c]	lattice vibration			

[a] From ref 67. [b] The abbreviations denote symmetric (s), asymmetric (as), stretch (ν), bend (δ), rock (ρ_{rock}), and in-plane bend (i.p.). The in-plane mode descriptions are relative to the $XeOF_2$ and XeF_5 planes for $XeOF_2$ and XeF_5^-, respectively. The mode assignments were based on comparison with ref 203 (XeF_2), ref 125 ($XeOF_2$), ref 53 ([Cs][XeF_5]), and ref 201 (Cs][XeO_3F]). [c] Weak Raman bands that were present but were not reported in the prior work;[67] G. J. Schrobilgen, private communication.

Table 5.2. Experimental Raman Frequencies[a] and Intensities[b] for $XeOF_3^-$ in $Cs[XeOF_3]$ and $[N(CH_3)_4][XeOF_3]$

Cs^+ salt[c,d,e]			$N(CH_3)_4^+$ salt[c,d,f]			assgnts[h]
$Xe^{16}OF_3^-$	$Xe^{18}OF_3^-$	$\Delta\nu$	$Xe^{16}OF_3^-$	$Xe^{18}OF_3^-$[g]	$\Delta\nu$	(C_{2v}) symmetry
759.6(100)	721.4(100)	−38.2	730.1(100)	694.0(100)	−36.1	$\nu(XeO)$
757.2 sh	719.0 sh	−38.2				
748.9(20)	711.3(17)	−37.6				
512.8(6)	512.7(6)	−0.1	n.o.	n.o.		$\nu_{as}(XeF_{2a})$
509.7(4)	508.9(4)	−0.8				
498.9(5)	498.9(6)	0.0				
487.7(46)	487.6(45)	−0.1	471.3(12)	472.0(16)	0.7	$\nu_s(XeF_{2a}) + \nu(XeF_b)$
483.8(20)	483.7(22)	−0.1	457.3(31)	457.4(34)	−0.1	
474.5(26)	474.5(28)	0.0	447.6(63)	447.5(66)	−0.1	$\nu_s(XeF_{2a}) - \nu(XeF_b)$
470.2(65)	470.2(65)	0.0				
n.o.	n.o.		332.0(2)	332.4(1)	0.4	$\delta(XeOF_3)$ o.o.p.
301.6(8)	292.0(8)	−9.6	271.5(10)	261.9(11)	−9.6	$\rho_{rock}(OXeF_{2a})$ i.p.
283.2(7)	273.6(6)	−9.6	268.7(9)	259.4(9)	−9.3	
276.4(7)	263.2(6)	−13.2				fluorine bridge modes
250.9(2)	249.6(3)	−1.3				
246.6(3)	244.5(3)	−2.1				
241.4(1)	239.7 sh	−1.7				
223.4(2)	223.0(2)	−0.4				
201.2(3)	200.3(2)	−0.9	193.9(1)	193.1(1)	−0.8	$\delta(XeF_{2a})$ i.p.
186.8(4)	186.4(5)	−0.4	189.5(1)	189.0(1)	−0.5	
170.2(3)	166.7(2)	−3.5	156.5(2)	152.9(1)	−3.6	$[\delta(OXeF_b) - \delta(XeF_{2a})]$ o.o.p.
154.9(6)	147.5sh	−7.4				
144.9(8)	140.5(10)	−4.4	137.8(2)	137.7(3)	−0.1	$[\rho_{rock}(OXeF_{2a}) + \delta(F_bXeF_a)]$ i.p.
138.8 sh	134.9 sh	−3.9				
119.8(6)	119.1(7)	−0.7	64.0(<1)	63.8(<1)	−0.2	lattice modes
108.7(4)	108.7(5)	0.0				

[a] Frequencies are given in cm^{-1}. [b] Values in parentheses denote relative Raman intensities. [c] Raman spectra were recorded in FEP sample tubes at −150 °C using 1064-nm excitation. [d] The abbreviations denote shoulder (sh) and not observed (n.o.). [e] Weak bands at 454.7(4) and 763.1(sh) in the ^{16}O spectrum and at 454.5(7) and 724.8(sh) in the ^{18}O spectrum are attributed to a hydrolysis product(s). [f] The $N(CH_3)_4^+$ cation modes were observed at: $\nu_8(E)$, 377(2); $\nu_{19}(T_2)$, 460(2); $\nu_3(A_1)$, 761(13); $\nu_{18}(T_2)$, 951(10); $\nu_7(E)$, 1176(2), 1187(1); $\nu_{17}(T_2)$, 1287(1); $\nu_{16}(T_2)$, 1405(2), 1408(2); $\nu_2(A_1)$, $\nu_6(E)$, 1462(12), 1479(1), 1487(10); $\nu(CH_3)$ and combination bands, 2800(2), 2881sh, 2908(3), 2938(3), 2957(12), 2978sh, 2999sh, 3038(18) cm^{-1}. [g] Weak bands at 756.2(8), 749.4(5), 744.7(3), 721.3(5) 710.0(6), 702.1sh, 488.8(1), 481.9(3), and 478.2(6) in the ^{18}O spectrum are attributed to a hydrolysis product(s). The band at 472.0(16) also partially overlaps with a hydrolysis product band. [h] The abbreviations denote symmetric (s), asymmetric (as), stretch (ν), bend (δ), rock (ρ_{rock}), in-plane bend (i.p.), and out-of-plane bend (o.o.p.). The in-plane and out-of-plane mode descriptions are relative to the $XeOF_{2a}F_b$ plane, i.e., the anion lies in the *xz*-plane with the Xe–O bond colinear with the *z*-axis (see Figure 5.1).

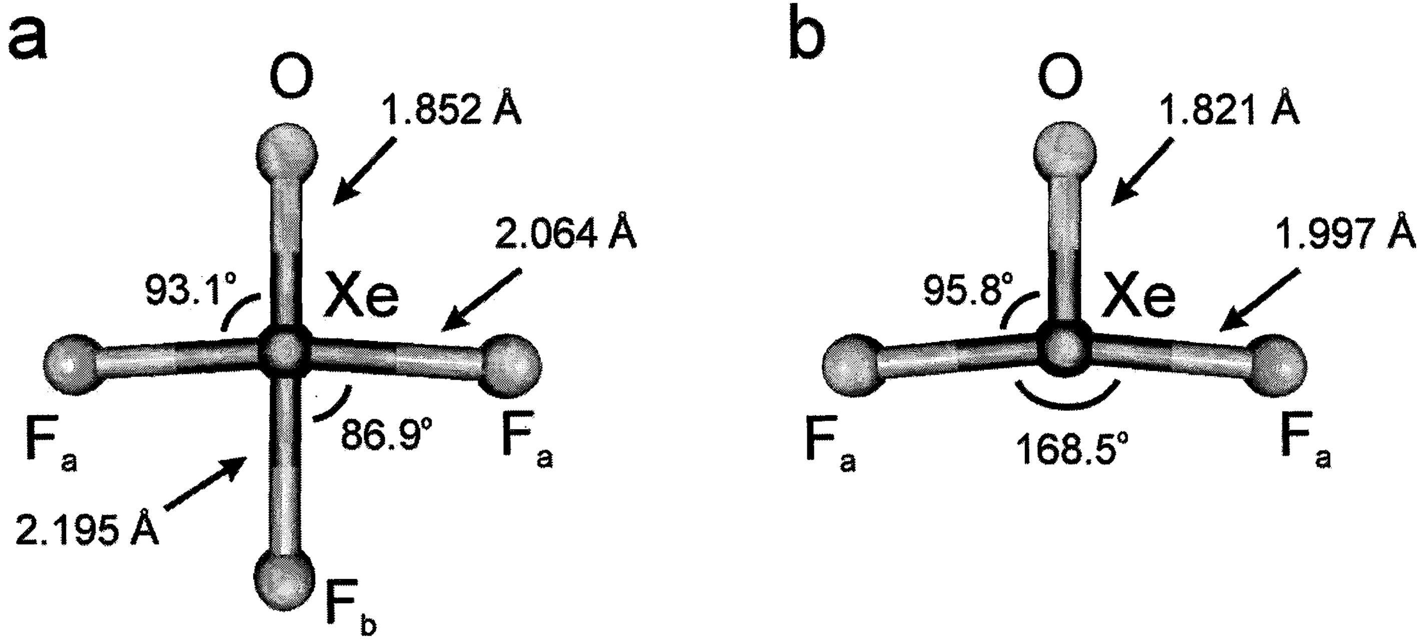

Figure 5.1. Calculated geometries [B3LYP/aug-cc-pVTZ(-PP)] for (a) $XeOF_3^-$ and (b) $XeOF_2$.

5.11 and 5.12 represent the most likely route to [Cs][XeO_3F] because [Cs][XeO_2F_3] was often observed in the Raman spectra of product mixtures but XeO_3 was not.[67] The hydrolysis of XeF_5^- in the presence of unreacted H_2O, which competes with Xe(VI) species in eqs 5.9 and 5.12, does not occur and is consistent with the higher oxophilicities of Xe(VI) species (see 5.2.3, Reactivities of $XeOF_3^-$ Salts).

$$XeOF_2{\cdot}n HF \longrightarrow XeOF_2 + nHF\uparrow \tag{5.5}$$

$$XeOF_2 \longrightarrow XeF_2 + \tfrac{1}{2}O_2 \tag{5.6}$$

$$XeOF_2 \longrightarrow \tfrac{1}{2}XeF_2 + \tfrac{1}{2}XeO_2F_2 \tag{5.7}$$

$$XeF_4 + [Cs][F(HF)_n] \longrightarrow [Cs][XeF_5] + nHF\uparrow \tag{5.8}$$

$$XeO_2F_2 + H_2O \longrightarrow XeO_3 + 2HF \tag{5.9}$$

$$XeO_3 + [Cs][F(HF)_n] \longrightarrow [Cs][XeO_3F] + nHF\uparrow \tag{5.10}$$

$$XeO_2F_2 + [Cs][F(HF)_n] \longrightarrow [Cs][XeO_2F_3] + nHF\uparrow \tag{5.11}$$

$$[Cs][XeO_2F_3] + H_2O \longrightarrow [Cs][XeO_3F] + 2HF \tag{5.12}$$

5.2.1.3. An Alternative Synthesis of [Cs][$XeOF_3$]. High-purity [Cs][$XeOF_3$] was obtained when HF solvent was removed from a stoichiometric mixture of CsF and $XeOF_2$ at −78 °C, followed by warming the reaction mixture to −45 °C under dynamic vacuum. Solid $XeOF_2$, which forms an insoluble HF solvate,[125] appeared to liquify and became intense yellow in color prior to formation of a dry yellow powder under dynamic vacuum. The Raman spectrum of this intermediate mixture showed only $XeOF_2$. It is presumed that [Cs][$F(HF)_m$] was also present but could not be observed in the Raman spectrum because the bands were too broad and weak. Extraction of residual HF with an aliquot of CH_3CN at −20 °C resulted in high-purity $[Cs][XeOF_3]$. The present method avoids decomposition arising from higher reaction temperatures and heterogeneous reaction conditions that result from the synthetic procedure outlined in the section above by using CH_3CN to partially or completely solubilize $XeOF_2$ and CsF.

5.2.2. Hydrolytic and Thermal Stabilities of $[M][XeOF_3]$ ($M = N(CH_4)$, Cs). Dry $[N(CH_3)_4][XeOF_3]$ is shock sensitive at low temperatures but does not exhibit shock sensitivity under CH_3CN upon standing at room temperature for 10 min. Dry $[N(CH_3)_4][XeOF_3]$ is kinetically stable at −78 °C for indefinite periods of time but begins to slowly decompose upon warming from 0 to 10 °C. The low-temperature (−150 °C) Raman spectra of samples briefly warmed to 25 °C and then quenched at −150 °C show the growth of the $\nu_s(XeF_2)$ band of XeF_2 at 498 cm^{-1},[203] and the $\nu(CH_3)$ bands of $[N(CH_3)_4][F]$ at 2957 and 3038 cm^{-1}.[204–206] The $[Cs][XeOF_3]$ salt is also stable at −78 °C for indefinite periods of time but slowly decomposes at room temperature to XeF_2, $XeO_2F_3^-$, O_2, and CsF. Although $[Cs][XeOF_3]$ appears to be less shock sensitive than the $N(CH_3)_4^+$ salt, detonations have occurred when attempting to transfer the finely-powdered salt in a drybox.

Two decomposition pathways have been inferred for $XeOF_3^-$ based on these observations. The major decomposition pathway is through reduction to Xe(II) (eq 5.13), and the minor decomposition pathway is through disproportionation (eq 5.14) to Xe(II) and Xe(VI) (see 5.2.5.3, Thermochemistry).

$$[M][XeOF_3] \longrightarrow XeF_2 + \tfrac{1}{2}O_2 + [M][F] \qquad (5.13)$$

$$[M][XeOF_3] \longrightarrow \tfrac{1}{2}XeF_2 + \tfrac{1}{2}[M][XeO_2F_3] + \tfrac{1}{2}[M][F] \qquad (5.14)$$

While $[Cs][XeOF_3]$ and $[N(CH_3)_4][XeOF_3]$ can be obtained as pure salts when exact stoichiometric ratios of XeF_4 and H_2O are used for the synthesis of $XeOF_2$, both salts hydrolyze when H_2O is used in excess. Characterization of the hydrolysis products by Raman spectroscopy showed several bands in the frequency range 720–785 cm^{-1}. The bands appearing between 720 and 765 cm^{-1} correspond to the $\nu(XeO)$ regions for $XeOF_2$,[125] $F_2OXeNCCH_3$,[125] $XeOF_2{\cdot}n HF$,[125] and $XeOF_3^-$ while the bands appearing between 745 and 785 cm^{-1} correspond to the $\nu_s(XeO_3)$ regions for XeO_3F^- [201] and XeO_3.[179] The findings indicate that the decomposition pathway resulting from hydrolysis involves disproportionation to Xe(VI)-containing species that likely occurs according to eqs 5.15 and 5.16. Although the exact nature of the decomposition product(s) could not be established, it is likely to be a compound(s) having the general formulation(s) $[Cs]_x[(XeO_3)_yF_x(XeOF_2)_z]$.

$$XeOF_3^- + H_2O \xrightarrow[-45\,^{\circ}C]{CH_3CN} [XeO_2F^-] + 2HF \qquad (5.15)$$

$$[XeO_2F^-] \xrightarrow[-45\,^{\circ}C]{CH_3CN} \tfrac{1}{2}XeO_3F^- + \tfrac{1}{2}Xe + \tfrac{1}{2}O_2 + \tfrac{1}{2}F^- \qquad (5.16)$$

5.2.3. Reactivities of $XeOF_3^-$ Salts.

The insolubilities and/or reactivities of the $N(CH_3)_4^+$ and Cs^+ salts in CH_3CN, SO_2, SO_2ClF, HF, $XeOF_4$, ONF, and O_2NF have prevented crystal growth and NMR characterization.

Attempts to dissolve $[N(CH_3)_4][XeOF_3]$ in SO_2 at −78 °C resulted in sample detonation, and it is proposed that $XeOF_3^-$ oxidizes SO_2 to SO_3 according to eq 5.17. An

$$[N(CH_3)_4][XeOF_3] + SO_2 \xrightarrow[-78\,^{\circ}C]{neat} XeF_2 + SO_3 + [N(CH_3)_4][F] \qquad (5.17)$$

attempt to dissolve $[Cs][XeOF_3]$ in $XeOF_4$ at ca. 20 °C resulted in oxygen/fluorine metathesis to give XeF_4, XeO_2F_2, and $[Cs][F(XeOF_4)_m]$[127] according to eq 5.18.

$$[Cs][XeOF_3] + (m+1)XeOF_4 \xrightarrow[20\ ^\circ C]{neat} XeF_4 + XeO_2F_2 + [Cs][F(XeOF_4)_m] \quad (5.18)$$

The syntheses of the NO^+ and NO_2^+ salts of $XeOF_3^-$ were attempted. Contact of ONF with $XeOF_2$ at –78 °C resulted in an explosion in which $XeOF_2$ likely oxidizes ONF to O_2NF (eq 5.19). The white residue that remained and coated the fractured FEP reaction vessel had an odor reminiscent of XeF_2. Addition of O_2NF to $XeOF_2$ at –78 °C resulted in an immediate color change from yellow to white upon contact with liquid O_2NF. The Raman spectrum of the product mixture showed modes corresponding to XeF_4, N_2O_5 (the spectrum corresponded to the ionic solid-state formulation $[NO_2][NO_3]$[207]) and XeF_5^- anion bands. The Raman spectrum (Table 5.3) indicates that $XeOF_2$ transfers oxygen to O_2NF to give XeF_4 and N_2O_5 (eq 5.20) and a subsequent reaction of O_2NF with XeF_4 gives the XeF_5^- anion (eq 5.21).

$$ONF + XeOF_2 \xrightarrow[-78\ ^\circ C]{neat} O_2NF + XeF_2 \quad (5.19)$$

$$2O_2NF + XeOF_2 \xrightarrow[-78\ ^\circ C]{neat} XeF_4 + N_2O_5 \quad (5.20)$$

$$XeF_4 + O_2NF \xrightarrow[-78\ ^\circ C]{neat} [NO_2][XeF_5] \quad (5.21)$$

5.2.4. Raman Spectroscopy. The low-temperature Raman spectra of $[N(CH_3)_4][Xe^{16/18}OF_3]$ and $[Cs][Xe^{16/18}OF_3]$ are shown in Figures 5.2 and 5.3, respectively. The observed and calculated frequencies and their assignments are listed in Tables 5.2, 5.4, and A2.1. In the absence of a crystal structure, the energy-minimized geometry of the $XeOF_3^-$ anion was calculated at several levels of theory (Tables 5.4 and A2.1) using the

Table 5.3. Raman Spectrum of the Products Formed in the Reaction of $XeOF_2$ with O_2NF

	assgnt [a]				
exptl	$[NO_2][NO_3]$ ($D_{\infty h}$, C_{2v})	XeF_4 (D_{4h})	$[NO_2][XeF_5]$ ($D_{\infty h}$, D_{5h})	$XeOF_2$ (C_{2v})	O_2NF (C_{2v})
1411(3)			$\nu_1(\Sigma^+_g)$, $\nu_s(NO_2^+)$		
1397(69)	$\nu_1(\Sigma^+_g)$, $\nu_s(NO_2^+)$				
1385(4)			$\nu_1(\Sigma^+_g)$, $\nu_s(NO_2^+)$		
1349(3)	$\nu_3(E')$, $\nu_{as}(NO_3^-)$				
1300br(5)					$\nu_1(A_1)$, $\nu_s(NO_2)$
1078(1)	$2\nu_2(\Pi_u)$, $\delta(NO_2^+)$				
1064(2)	$2\nu_2(\Pi_u)$, $\delta(NO_2^+)$				
1047(68)	$\nu_1(A_1')$, $\nu_s(NO_3^-)$				
750(4)				$\nu_1(A_1)$, $\nu(XeO)$	
721(7)	$\nu_4(E')$, $\delta(NO_3^-)_{i.p.}$				
554(15)		$\nu(A_{1g})$, $\nu_s(XeF_4)$			
548(6)			$2\nu_2(A_1')$, $\delta(XeF_5)$		
545(100)		$\nu(A_{1g})$, $\nu_s(XeF_4)$			
533(12)	$\nu_2(\Pi_u)$, $\delta(NO_2^+)$				
512(12)			$\nu_1(A_1')$, $\nu_s(XeF_5)$		
508(28)		$\nu(B_{1g})$, $\nu_{as}(XeF_{2t} - XeF_{2t})$			
504(83)		$\nu(B_{1g})$, $\nu_{as}(XeF_{2t} - XeF_{2t})$			
468(5)				$\nu_2(A_1)$, $\nu_s(XeF_2)$	
284(3)			$\nu_2(A_1')$, $\delta(XeF_5)$		
280(3)			$\nu_2(A_1')$, $\delta(XeF_5)$		
239(2)		$\nu(B_{1g})$, $\nu_{as}(XeF_{2t} - XeF_{2t})$			
215(2)		$\nu(B_{2u})$, $\delta(XeF_{2t})_{o.o.p.} - \delta(XeF_{2t})_{o.o.p.}$			
160(23)	lattice vibrations				
155sh	lattice vibrations				
105(35)	lattice vibrations				

[a] The abbreviations denote symmetric (s), asymmetric (as), stretch (ν), bend (δ), in-plane bend (i.p.), and out-of-plane bend (o.o.p.). The in-plane and out-of-plane mode descriptions are relative to the molecular planes for XeF_4 and NO_3^-. The mode assignments are based on comparison with ref 127 ($[NO_2][NO_3]$), refs 32,35,38 (XeF_4), ref 53 ($[NO_2][XeF_5]$), ref 125 ($XeOF_2$), and ref 116 (O_2NF).

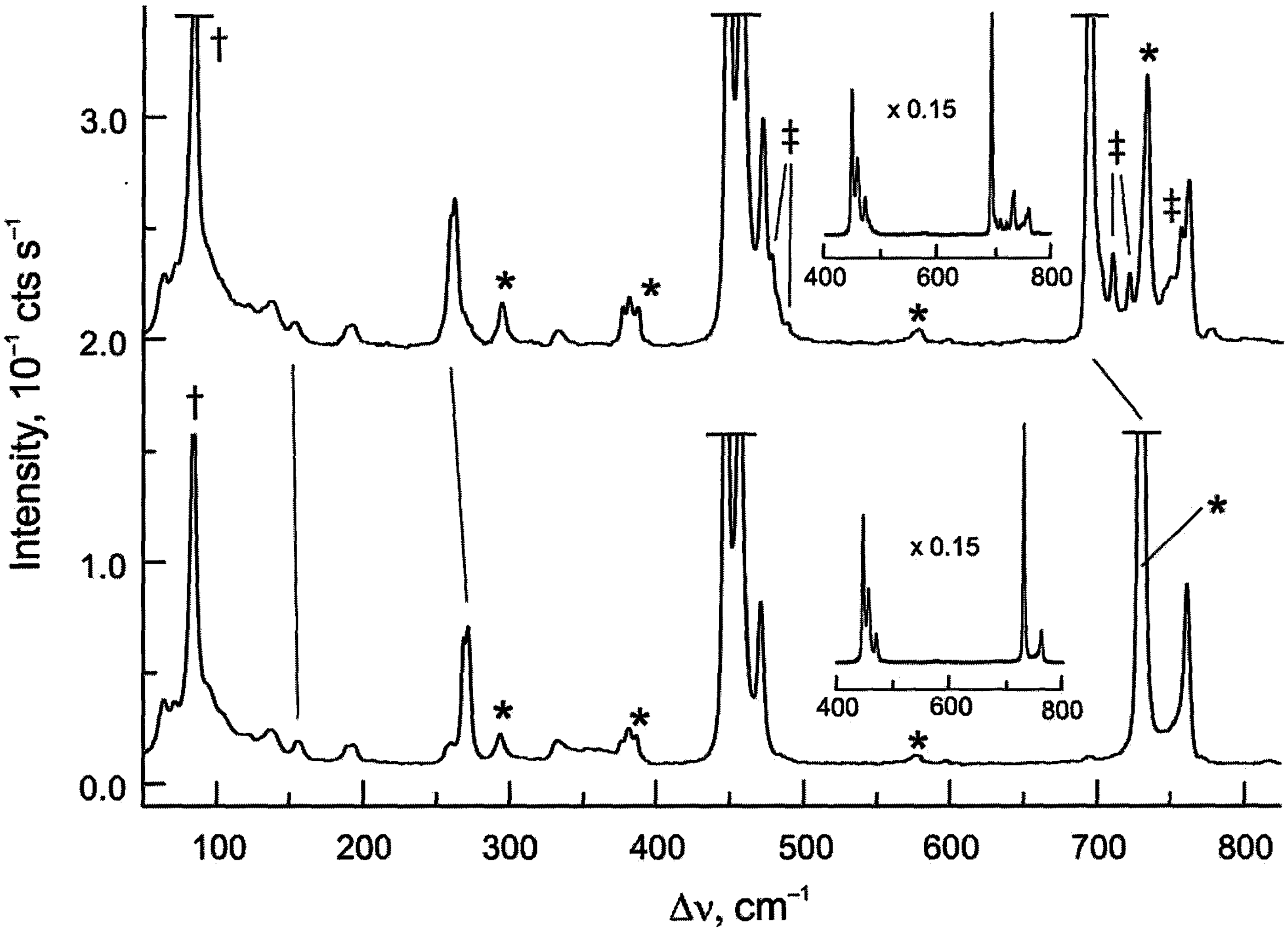

Figure 5.2. Raman spectra of natural abundance (lower trace) and 97.8% ^{18}O-enriched (upper trace) $[N(CH_3)_4][XeOF_3]$ recorded at –150 °C using 1064-nm excitation. Symbols denote FEP sample tube lines (*), instrumental artifact (†), and minor hydrolysis product(s) (‡).

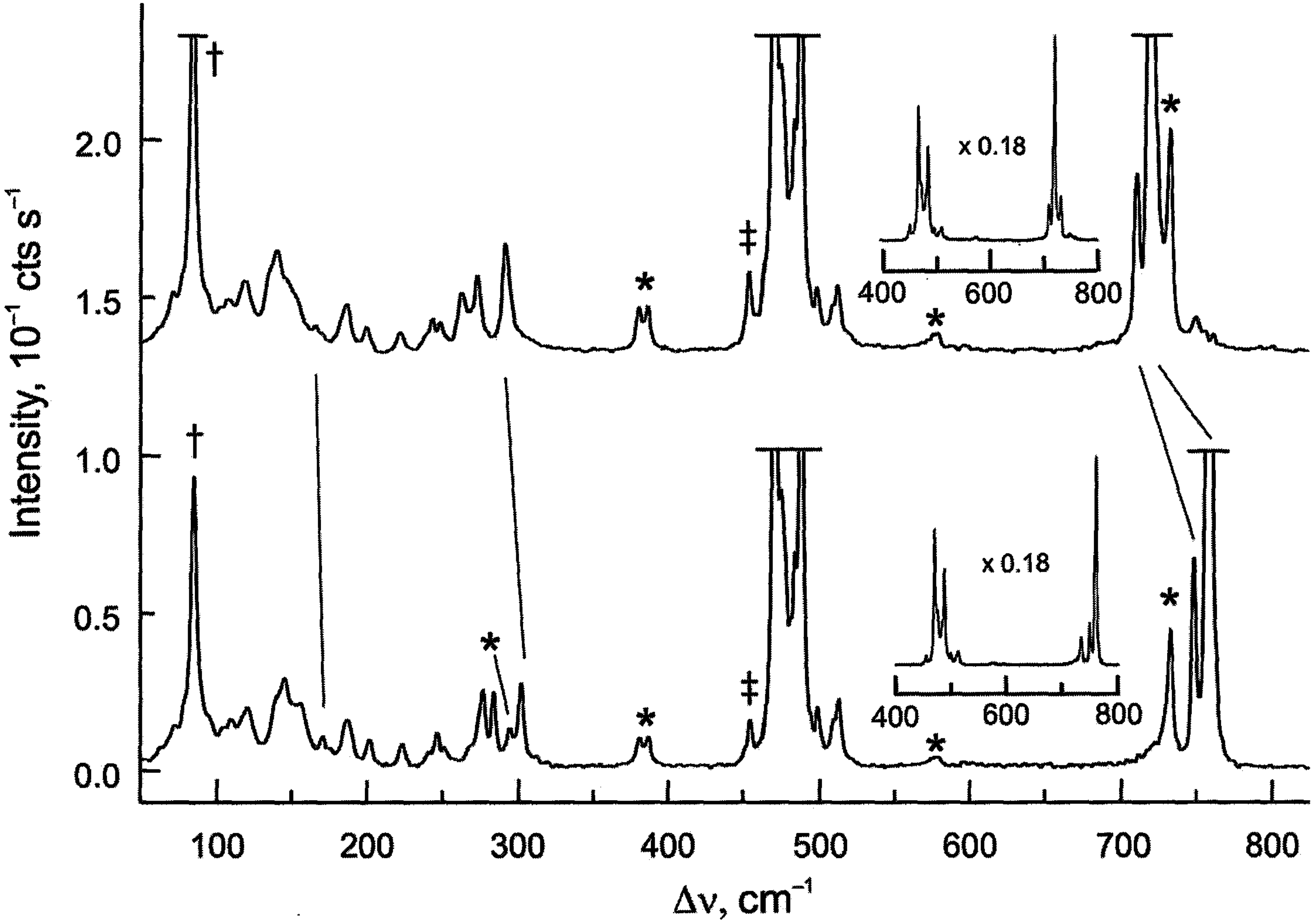

Figure 5.3. Raman spectra of natural abundance (lower trace) and 97.8% ^{18}O-enriched (upper trace) Cs[XeOF$_3$] recorded at –150 °C using 1064-nm excitation. Symbols denote FEP sample tube lines (*), instrumental artifact (†), and minor hydrolysis product(s) (‡).

aug-cc-pVDZ(-PP) and aug-cc-pVTZ(-PP) basis sets. The calculated vibrational frequencies, intensities, and $^{16/18}$O-isotopic shifts were used to assign the Raman spectra of $Xe^{16}OF_3^-$ and $Xe^{18}OF_3^-$ in their Cs^+ and $N(CH_3)_4^+$ salts. Regardless of the level of theory or basis set used, the frequency, intensity, and isotopic shift trends are similar and consistent. The frequency ranges cited in the ensuing discussion refer to isotopic shifts and are the values obtained for the entire range of theory levels, showing good agreement with experiment regardless of the level of theory used. The experimental and calculated vibrational frequencies for monomeric $XeOF_2$ and their assignments (Table A2.2) have been previously discussed[125] and were also used to aid in the vibrational assignments of $XeOF_3^-$. The $Xe^{16/18}OF_3^-$ anion possesses C_{2v} symmetry which results in nine fundamental vibrational modes that span the irreducible representations $4A_1 + 3B_1 + 2B_2$ (the xz-plane is the molecular plane and the Xe–O bond lies along the z-axis) which are both Raman and infrared active.

5.2.4.1. $[N(CH_3)_4][XeOF_3]$. The frequencies associated with the $N(CH_3)_4^+$ cation have been assigned based on comparisons with the previous literature.[204–206] The $XeOF_3^-$ anion of $[N(CH_3)_4][XeOF_3]$ is in overall good agreement with the calculated gas-phase anion. As predicted from the calculated frequencies and Raman intensities, the highest frequency and most intense $XeOF_3^-$ band occurs at 730.1 cm^{-1} and is assigned to ν(XeO). This mode displays a large low-frequency shift (−36.1 cm^{-1}) upon ^{18}O substitution that is in very good agreement with the calculated values (−33.5 to −42.8 cm^{-1}). The asymmetric $\nu_{as}(XeF_{2a})$ mode is expected to be weak to very weak in the Raman spectrum and was not observed. The bands at 457.3/471.3 and 447.6 cm^{-1} are of medium intensity

Table 5.4. Calculated Vibrational Frequencies^a and Infrared and Raman Intensities^b for the Xe$^{16/18}$OF$_3^-$ Anion^c

Xe^{16}OF$_3^-$							
MP2	SVWN5	BP86	PBE1PBE	B3LYP	B3PW91	MPW1PW91	assgnt ^{d}
867.9(25)[241]	735.8(48)[163]	690.1(50)[150]	771.2(59)[160]	729.6(62)[152]	752.9(58)[157]	767.8(59)[157]	ν(XeO)
493.6(<1)[283]	482.9(<1)[285]	439.6(<1)[265]	491.2(<0.1)[340]	467.3(<0.1)[319]	479.3(<0.1)[324]	489.8(<0.1)[339]	ν_{as}(XeF$_{2a}$)
460.7(27)[152]	447.6(29)[88]	405.5(34)[92]	460.5(34)[54]	432.7(37)[66]	445.8(35)[62]	458.7(34)[55]	ν_s(XeF$_{2a}$) + ν(XeF$_b$)
379.2(20)[34]	389.2(15)[59]	347.8(21)[42]	372.3(10)[131]	356.9(13)[106]	366.6(12)[113]	371.2(10)[129]	ν_s(XeF$_{2a}$) − ν(XeF$_b$)
286.8(<1)[54]	256.9(<1)[41]	242.7(<1)[39]	269.4(<1)[48]	256.3(<1)[47]	263.8(<1)[47]	268.8(<1)[48]	δ(XeOF$_3$) o.o.p.
250.6(4)[<1]	227.2(4)[1]	222.7(5)[<1]	259.9(3)[<1]	246.9(4)[<1]	253.1(4)[<1]	260.2(3)[1]	ρ_{rock}(OXeF$_{2a}$) i.p.
171.2(<1)[2]	166.5(<<1)[3]	163.8(<<1)[3]	183.6(<1)[1]	177.2(<1)[2]	180.5(<1)[1]	183.9(<1)[1]	δ(XeF$_{2a}$) i.p.
132.6(<1)[<0.1]	125.9(<1)[<0.1]	115.4(<1)[<0.1]	136.6(<1)[<1]	127.5(<1)[<1]	131.6(<1)[<1]	135.8(<1)[<1]	[δ(OXeF$_b$) − δ(XeF$_{2a}$)] o.o.p.
150.5(<1)[2]	125.1(<1)[2]	128.9(<1)[2]	115.6(1)[1]	119.8(1)[1]	120.0(1)[1]	115.9(<1)[<1]	[ρ_{rock}(OXeF$_{2a}$) + δ(F$_b$XeF$_a$)] i.p.

Xe^{18}OF$_3^-$							
MP2	SVWN5	BP86	PBE1PBE	B3LYP	B3PW91	MPW1PW91	assgnt ^{d}
825.1(22)[224]	700.1(42)[155]	656.6(43)[143]	733.4(53)[51]	694.0(54)[145]	716.1(51)[149]	729.9(52)[149]	ν(XeO)
494.8(<1)[284]	484.1(<1)[286]	440.7(<1)[266]	492.5(<0.1)[341]	468.5(<0.1)[319]	480.5(<0.1)[325]	490.9(<0.1)[339]	ν_{as}(XeF$_{2a}$)
461.0(27)[151]	447.5(29)[85)	405.3(35)[90]	460.6(10)[129]	432.8(38)[65]	445.9(36)[61]	458.7(35)[54]	ν_s(XeF$_{2a}$) + ν(XeF$_b$)
379.3(20)[33]	389.2(15)[58]	347.8(21)[42]	372.3(10)[129]	356.8(13)[104]	366.6(12)[111]	370.9(10)[127]	ν_s(XeF$_{2a}$) − ν(XeF$_b$)
283.0(<1)[52]	253.7(<1)[39]	239.6(<1)[38]	266.6(<1)[46]	253.4(<1)[46]	260.9(<1)[45]	266.0(<1)[46]	δ(XeOF$_3$) o.o.p.
242.6(4)[<1]	219.5(4)[1]	215.2(5)[<1]	250.8(3)[<1]	238.4(4)[<1]	244.3(4)[<1]	250.9(3)[<1]	ρ_{rock}(OXeF$_{2a}$) i.p.
171.2(<1)[2]	166.5(<0.1)[3]	163.8(<0.1)[3]	183.6(<1)[1]	177.2(<1)[2]	180.5(<1)[1]	183.9(<1)[1]	δ(XeF$_{2a}$) i.p.
131.1(<1)[0]	124.4(<1)[<0.1]	114.0(<1)[<0.1]	134.7(<1)[<1]	125.8(<1)[<1]	129.8(<1)[<1]	133.9(<1)[<1]	[δ(OXeF$_b$) − δ(XeF$_{2a}$)] o.o.p.
149.3(<1)[2]	124.4(<1)[2]	128.1(<1)[2]	115.0(1)[1]	119.2(1)[1]	119.4(<1)[1]	115.8(1)[1]	[ρ_{rock}(OXeF$_{2a}$) + δ(F$_b$XeF$_a$)] i.p.

[a] Frequencies are given in cm^{-1}. [b] Values in parentheses denote calculated Raman intensities (Å^4 u^{-1}). Values in square brackets denote calculated infrared intensities (km mol^{-1}). [c] The aug-cc-pVTZ(-PP) basis set was used. [d] The abbreviations denote symmetric (s), asymmetric (as), stretch (ν), bend (δ), rock (ρ_{rock}), in-plane bend (i.p.), and out-of-plane bend (o.o.p.). The in-plane and out-of-plane mode descriptions are relative to the XeOF$_{2a}$F$_b$ plane (see Figure 5.1 and footnote *h* of Table 5.2).

and are assigned to the in-plane stretching modes $\nu_s(XeF_{2a}) + \nu(XeF_b)$ and $\nu_s(XeF_{2a}) - \nu(XeF_b)$, respectively. Their frequencies are essentially unshifted upon ^{18}O-enrichment, which is expected for modes that do not involve oxygen atom displacements. The band at 332.0 cm^{-1} is assigned to the out-of-plane deformation mode, $\delta(XeOF_3)$, and appears as a weak band, in agreement with the calculated Raman intensity, and shows no ^{18}O dependence although the calculations predict a small isotopic shift (−2.8 to −3.8 cm^{-1}). The split band at 268.7, 271.5 cm^{-1} is sensitive to isotopic substitution and is assigned to the in-plane deformation mode, $\rho_{rock}(XeOF_{2a})$. The experimental ^{18}O isotopic shift for this mode, −9.3, −9.6 cm^{-1}, is in good agreement with the calculated values (−7.5 to −9.3 cm^{-1}). The weak bands at 189.5, 193.9 cm^{-1} are insensitive to ^{18}O substitution and are assigned to the in-plane XeF_2 bending mode. The band at 156.5 cm^{-1} is assigned to the out-of-plane $\delta(XeOF_b) - \delta(XeF_{2a})$ mode and shows a small isotopic shift (−3.6 cm^{-1}) in agreement with the calculated values (−1.4 to −1.9 cm^{-1}). The lowest frequency band at 137.8 cm^{-1} is also weak, displaying no isotopic shift, in accordance with the small calculated values (−0.1 to −1.2 cm^{-1}), and is assigned to the in-plane deformation mode, $\rho_{rock}(OXeF_{2a}) + \delta(F_bXeF_a)$.

The low-frequency shifts of the stretching modes relative to their counterparts in $XeOF_2$ and $F_2OXeNCCH_3$[125] are consistent with anion formation and increased Xe−O and Xe−F bond polarities in the anion. These low-frequency shifts are reproduced by the quantum-chemical calculations.

5.2.4.2. [Cs][XeOF$_3$]. The Raman spectrum of the Cs$^+$ salt is very similar to that of the N(CH$_3$)$_4^+$ salt, although the bands are shifted to higher frequencies, which likely results from significant cation–anion contacts. The bands that are the most affected are shifted by as much as 30 cm^{-1} and correspond to modes that involve oxygen atom displacements, i.e., ν(XeO) and ρ_{rock}(XeOF$_{2a}$), indicating that the Cs$^+$ cation likely coordinates most strongly to the oxygen atom. These findings are in agreement with the NBO analysis (see 5.2.5.2, Computational Results), which assigns most of the negative charge to the oxygen atom. Weak bands between 223 and 276 cm^{-1} in the Cs$^+$ salt are absent in the N(CH$_3$)$_4^+$ salt. These bands are in the appropriate region and are of appropriate intensity for stretching modes associated with fluorine-bridges,[127] suggesting an oligomeric or chain structure for [Cs][XeOF$_3$]. Such long contacts most likely result in coupling between XeOF$_3^-$ units which would not only account for the splittings of the vibrational bands but may also result in symmetry reduction and observation of the ν_{as}(XeF$_{2a}$) stretching mode at 498.9, 509.7, and 512.8 cm^{-1} which was not observed in the N(CH$_3$)$_4^+$ salt.

5.2.5. Computational Results. Because a crystal structure for a XeOF$_3^-$ salt is not available, a series of quantum-chemical calculations at different levels of theory with different basis sets were carried out (Tables 5.4, 5.5, A2.1 and A2.3). All calculations resulted in stationary points with all frequencies real. The calculations established that trends in the vibrational frequencies persisted at all levels of theory and for all basis sets used. The calculated frequencies and their trends were then compared with the observed trends, allowing reliable assignments of the experimental Raman frequencies to be made.

Table 5.5. Calculated Geometrical Parameters for the $XeOF_3^-$ Anion[a]

	MP2	SVWN5	BP86	PBE1PBE	B3LYP	B3PW91	MPW1PW91
				bond lengths (Å)			
$Xe\text{-}F_a$	2.060	2.064	2.106	2.032	2.064	2.048	2.034
$Xe\text{-}O$	1.821	1.859	1.881	1.830	1.852	1.840	1.831
$Xe\text{-}F_b$	2.129	2.143	2.188	2.173	2.195	2.178	2.175
				bond angles (deg)			
$O\text{-}Xe\text{-}F_a$	94.8	93.7	93.7	92.9	93.1	93.0	92.8
$F_a\text{-}Xe\text{-}F_b$	85.2	86.3	86.3	87.1	86.9	87.0	87.2
$F_a\text{-}Xe\text{-}F_a$	170.3	172.6	172.5	174.3	173.9	173.9	174.4

[a] The aug-cc-pVTZ(-PP) basis set was used.

The parent compound, $XeOF_2$,[125] was used as a benchmark for the calculations (Table A2.2). Values for the aug-cc-pVDZ(-PP) basis set are given in square brackets.

5.2.5.1. Geometries. The geometry of the $XeOF_3^-$ anion optimized at C_{2v} symmetry, yielding a planar structure that is in accord with that predicted by the VSEPR model of molecular geometry[41] (see 5.2.4, Raman Spectroscopy). As noted for $XeOF_2$,[125] the use of a larger basis set tends to give shorter bond lengths and smaller $O–Xe–F_a$ bond angles. With the exception of the BP86 method, where the bonds are significantly elongated, all bond lengths fall within relatively narrow ranges (Xe–O, 1.821−1.859 [1.854−1.890] Å; $Xe–F_a$, 2.032−2.064 [2.061−2.096] Å; $Xe–F_b$, 2.129−2.195 [2.131−2.205] Å). As predicted by the VSEPR rules,[41] the $Xe–F_a$ bonds are shorter than the $Xe–F_b$ bond. In general, all bond angles are also within a narrow range, with the exception of the MP2 value, which gives a larger $O–Xe–F_a$ angle than other levels of theory. The fluorine atoms, F_a, are bent away from the oxygen atom with an $O–Xe–F_a$ angle of 92.8−93.7

[93.1−94.2]° and an F$_a$–Xe–F$_a$ angle of 172.5−174.4 [171.7−173.9]°. When compared with $XeOF_2$, the net −1 charge of $XeOF_3^-$ results in longer Xe–F$_a$ and Xe–O bonds and a F$_a$–Xe–F$_a$ angle that is closer to linearity than in $XeOF_2$ (164.8–170.8°).

5.2.5.2. Natural Bond Orbital (NBO) Analyses. The NBO[163−166] analyses were carried out for all optimized gas-phase geometries of $XeOF_3^-$ and $XeOF_2$ for comparison and are summarized in Tables 5.6 and 5.7. The results, at all levels of theory, are similar and therefore only the MP2 values are referred to in the ensuing discussion.

The natural population analysis (NPA) charges of 2.11 and 2.13 for Xe in $XeOF_3^-$ and $XeOF_2$, respectively, show that the charge on xenon remains essentially unchanged upon anion formation and is approximately half of the formal charge that is given by a purely ionic model, indicating that the anion bonds are polar covalent. Upon formation of $XeOF_3^-$ from $XeOF_2$, the net negative charge of the anion is dispersed among the more electronegative atoms, yielding natural charges for O (−1.038), F$_a$ (−0.762 each), and F$_b$ (−0.654) that are higher than the corresponding values in $XeOF_2$. The charge on O is about half of its formal oxidation number, while the F charges are approximately two-thirds of their formal oxidation number, indicating that the bonds are more ionic in the anion than in neutral $XeOF_2$. Among the plausible valence bond Structures I–IX for $XeOF_3^-$, the calculated charges are best represented by Structure V, which is an average of Structures II–IV, with a somewhat larger contribution from Structure II. The Xe–O/Xe–F$_a$ and Xe–O/Xe–F$_b$ bond order ratios, 3.43 and 2.65 respectively, and

Table 5.6. NBO Valencies, Bond Orders, and Natural Population Analysis (NPA) Charges for the $XeOF_3^-$ Anion [a]

	MP2	SVWN5	BP86	PBE1PBE	B3LYP	B3PW91	MPW1PW91
				Charges [valencies]			
Xe	2.108 [1.509]	1.945 [1.561]	1.958 [1.549]	2.064 [1.527]	2.065 [1.509]	2.047 [1.519]	2.065 [1.523]
O	−1.038 [0.703]	−0.969 [0.672]	−0.974 [0.668]	−1.000 [0.673]	−1.001 [0.663]	−0.995 [0.670]	−1.000 [0.672]
F_a	−0.762 [0.213]	−0.721 [0.223]	−0.725 [0.219]	−0.768 [0.213]	−0.765 [0.206]	−0.761 [0.212]	−0.768 [0.213]
F_b	−0.654 [0.257]	−0.627 [0.290]	−0.629 [0.288]	−0.648 [0.283]	−0.650 [0.275]	−0.646 [0.282]	−0.649 [0.283]
				bond orders			
Xe-O	0.737	0.712	0.707	0.706	0.703	0.703	0.704
Xe-F_a	0.215	0.225	0.221	0.214	0.210	0.214	0.214
Xe-F_b	0.278	0.313	0.310	0.303	0.298	0.301	0.302

[a] The aug-cc-pVTZ(-PP) basis set was used.

Table 5.7. Calculated Geometrical Parameters, NBO Valencies, Bond Orders, and Natural Population Analysis (NPA) Charges for $XeOF_2$ [a]

	MP2	SVWN5	BP86	PBE1PBE	B3LYP	B3PW91	MPW1PW91
				bond lengths (Å)			
Xe-O	1.770	1.806	1.834	1.800	1.821	1.807	1.802
Xe-F_a	1.971	1.987	2.028	1.968	1.997	1.981	1.968
				bond angles (deg)			
O-Xe-F_a	95.9	96.7	97.6	94.9	95.8	95.5	94.6
F_a-Xe-F_a	168.2	166.7	164.8	170.1	168.5	169.1	170.8
				Charges [valencies]			
Xe	2.134 [1.480]	1.962 [1.580]	1.920 [1.485]	2.052 [1.561]	2.021 [1.498]	2.028 [1.539]	2.049 [1.555]
O	-0.893 [0.788]	-0.807 [0.800]	-0.775 [0.755]	-0.837 [0.763]	-0.813 [0.745]	-0.823 [0.760]	-0.834 [0.758]
F_a	-0.620 [0.292]	-0.578 [0.351]	-0.572 [0.328	-0.607 [0.350]	-0.604 [0.333]	-0.602 [0.345]	-0.607 [0.349]
				bond orders			
Xe-O	0.848	0.845	0.795	0.813	0.790	0.807	0.809
Xe-F_a	0.316	0.368	0.344	0.374	0.354	0.366	0.373

[a] The aug-cc-pVTZ(-PP) basis set was used.

Xe/O/F_a/F_b valencies (1.509/0.703/0.213/0.257) are in overall agreement with a composite of these resonance contributions.

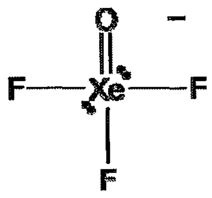

I

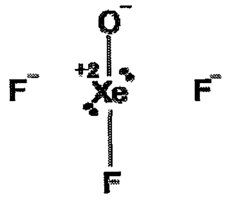

II

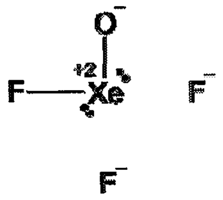

III

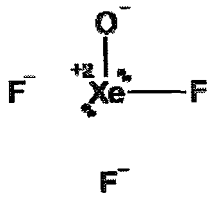

IV

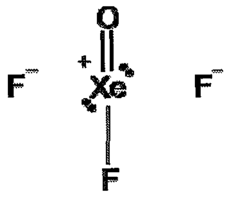

VI

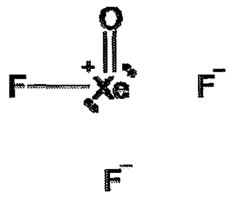

VII

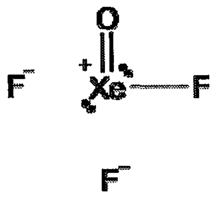

VIII

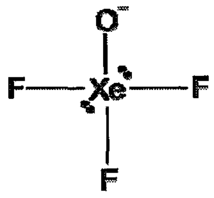

IX

Upon anion formation, donation of electron density by the fluoride ion into the xenon valence shell results in substantial decreases in the Xe–O and Xe–F bond orders and Xe valency and increases in the O and F valencies relative to those of $XeOF_2$. Thus, the Xe–O and Xe–F bonds are somewhat more ionic in $XeOF_3^-$ when compared with $XeOF_2$.

5.2.5.3. Thermochemistry. To account for the different decomposition routes for $[N(CH_3)_4][XeOF_3]$ and $[Cs][XeOF_3]$, quantum-chemical calculations and established semi-empirical methods[208–212] were used in conjunction with known thermodynamic quantities to estimate ΔH°, ΔS°, and ΔG° for eqs 5.13 and 5.14.

The standard enthalpies for the decomposition reactions were determined by analyzing their Born–Fajans–Haber cycles. The enthalpy changes for the gas-phase reduction (eq 5.22) and disproportionation (eq 5.23) reactions were calculated using the

$$XeOF_3{}^-{}_{(g)} \longrightarrow XeF_{2(g)} + \tfrac{1}{2}O_{2(g)} + F^-{}_{(g)} \tag{5.22}$$

$$\Delta H^\circ = +52.6\ \text{kJ mol}^{-1} \qquad \text{MP2/aug-cc-pVTZ(-PP)}$$

$$XeOF_3{}^-{}_{(g)} \longrightarrow \tfrac{1}{2}XeF_{2(g)} + \tfrac{1}{2}XeO_2F_3{}^-{}_{(g)} + \tfrac{1}{2}F^-{}_{(g)} \tag{5.23}$$

$$\Delta H^\circ = +56.3\ \text{kJ mol}^{-1} \qquad \text{MP2/aug-cc-pVTZ(-PP)}$$

MP2 method. The experimental value for the enthalpy of sublimation (ΔH_{sub}) for XeF_2 (55.71 kJ mol^{-1}) was used.[213] The lattice enthalpies of [M][F], [M][$XeOF_3$], and [M][XeO_2F_3] (Table 5.8) were estimated by use of the volume-based method of Bartlett et al.[208,209] as generalized by Jenkins et al.[210,211] in eq 5.24, where R is the gas constant

$$\Delta H^\circ{}_L = 2I\left(\frac{\alpha}{\sqrt[3]{V_m}} + \beta\right) + pRT \tag{5.24}$$

(8.314 J K^{-1}mol^{-1}), I is the ionicity of the salt and the constants, α, β, and p, depend on the nature of the salt. For the salts under investigation, which are singly charged and non-linear, the following values were used: $I = 1$, $\alpha = 117.3$ nm kJ mol^{-1}, $\beta = 51.9$ kJ mol^{-1}, and $p = 2$. In this formalism, $\Delta H^\circ{}_L$ is the lattice enthalpy and is defined as the energy required to break the crystal lattice, and therefore has a positive value. This approach is generally accurate to ~4% for salts with $\Delta H^\circ{}_L$ less than 5000 kJ mol^{-1},[211] and is

Table 5.8. Estimated Volumes, Lattice Enthalpies, and Entropies for $N(CH_3)_4^+$ and Cs^+ Salts of F^-, $XeOF_3^-$, and $XeO_2F_3^-$

Salt	V_m (nm^3)	ΔH°_L (kJ mol^{-1}) [a]	S° (J mol^{-1} K^{-1}) [b]
$[N(CH_3)_4][F]$	0.1460 [c]	554.4	213.5
$[N(CH_3)_4][XeOF_3]$	0.2168 [d]	499.3	309.9
	0.2192 [e]	497.9	313.1
$[N(CH_3)_4][XeO_2F_3]$ [e]	0.2302 [f]	491.6	328.0
$[Cs][F]$	0.0573 [c]	717.3	92.9
$[Cs][XeOF_3]$	0.1282 [d]	574.1	189.3
	0.1305 [e]	571.3	192.5
$[Cs][XeO_2F_3]$ [e]	0.1415 [f]	559.0	207.4

[a] The lattice enthalpies (ΔH°_L) were calculated as described in ref 210. [b] The standard entropies were calculated as described in ref 212. [c] The formula unit volumes, V_m, for $[N(CH_3)_4][F]$ and CsF, were obtained from their crystallographic unit cells at –163 °C (ref 111) and 25 °C (ref 214), respectively. [d] The values for $V_m[M][XeOF_3]$ were estimated by: $V_m(F_2OXeNCCH_3$; 0.1324 nm^3, ref 125) – $V_m(CH_3CN$; 0.0616 nm^3, ref 215) + $V_m([M][F])$. [e] The V_m values for $[M][XeOF_3]$ were estimated by: $V_m([M][F])$ + [$V_m(XeF_2$; 0.0622 nm^3, ref 216) + $V_m(XeO_2F_2$; 0.0842 nm^3, ref 148)]/2. [f] The V_m values for $[M][XeO_2F_3]$ were estimated by: $V_m([M][F])$ + $V_m(XeO_2F_2$; 0.0842 nm^3, ref 148).

particularly useful because the formula unit volume (V_m) of an unknown salt can be estimated with reasonable accuracy using several methods.[211,217] The net enthalpies of decomposition (eq 5.25 and 5.26) calculated for the reductions (ΔH°_{red}) and disproportionations (ΔH°_{dis}) of [M][$XeOF_3$] (M = $N(CH_3)_4$, Cs) are summarized in Table 5.9.

$$\Delta H^{\circ}_{red} = \Delta H^{\circ}_{L}([M][XeOF_3]) - \Delta H^{\circ}(\text{eq } 5.22) - \Delta H^{\circ}_{L}([M][F]) - \Delta H^{\circ}(\text{sub } XeF_2) \qquad (5.25)$$

$$\Delta H^{\circ}_{dis} = \Delta H^{\circ}_{L}([M][XeOF_3]) - \Delta H^{\circ}(\text{eq } 5.23) - \tfrac{1}{2}\Delta H^{\circ}_{L}([M][F]) - \tfrac{1}{2}\Delta H^{\circ}_{L}([M][XeO_2F_3] - \Delta H^{\circ}(\text{sub } XeF_2) \qquad (5.26)$$

A method for estimating the absolute standard entropy of a salt from its unit volume has been reported by Jenkins and Glasser (eq 5.27) where $k = 1360\ JK^{-1}mol^{-1}$

$$S^{\circ} = kV_m + c \qquad (5.27)$$

(nm^{-3} formula $unit^{-1}$) and $c = 15\ JK^{-1}mol^{-1}$.[212] Entropies for the [M][F], [M][$XeOF_3$], and [M][XeO_2F_3] salts under consideration are provided in Table 5.8. When coupled with the experimental standard entropies of $O_{2(g)}$ (206 J mol^{-1} K^{-1})[195] and $XeF_{2(s)}$ (115.09 J mol^{-1} K^{-1}),[213] this method allows ΔS° (eq 5.28, 5.29) and ΔG° (eq 5.30) to be calculated for the

$$\Delta S^{\circ}_{red} = \tfrac{1}{2}S^{\circ}(O_2) + S^{\circ}([M][F]) + S^{\circ}(XeF_2) - S^{\circ}([M][XeOF_3]) \qquad (5.28)$$

$$\Delta S^{\circ}_{dis} = \tfrac{1}{2}S^{\circ}([M][F]) + \tfrac{1}{2}S^{\circ}(XeF_2) + \tfrac{1}{2}S^{\circ}([M][XeO_2F_3]) - S^{\circ}([M][XeOF_3]) \quad (5.29)$$

$$\Delta G^{\circ} = \Delta H^{\circ} - T\Delta S^{\circ} \qquad (5.30)$$

reactions of interest. The ΔS° and ΔG° values obtained for these reactions are summarized in Table 5.9. Estimates of the unit volume of $XeOF_2$ using either the difference method ($V_m(F_2OXeNCCH_3) - V_m(CH_3CN) = 0.0708\ nm^3$) or an average of the

Table 5.9. Values of ΔH°, ΔS°, and ΔG° Calculated for the Decomposition Reactions of $[M][XeOF_3]$ ($X = N(CH_3)_4$, Cs)

	ΔH° (kJ mol^{-1})^{a}		ΔS° (J mol^{-1} K^{-1})^{a}		ΔG° (kJ mol^{-1})^{a}	
$[N(CH_3)_4][XeOF_3]_{(s)} \rightarrow XeF_{2(s)} + \frac{1}{2}O_{2(g)} + [N(CH_3)_4][F]_{(s)}$	–58.2	–59.6	121.3	118.1	–94.3	–94.7
$[N(CH_3)_4][XeOF_3]_{(s)} \rightarrow \frac{1}{2}XeF_{2(s)} + \frac{1}{2}[N(CH_3)_4][XeO_2F_3]_{(s)} + \frac{1}{2}[N(CH_3)_4][F]_{(s)}$	4.9	3.5	18.4	15.2	–0.6	–1.1
$[Cs][XeOF_3]_{(s)} \rightarrow XeF_{2(s)} + \frac{1}{2}O_{2(g)} + [Cs][F]_{(s)}$	–146.3	–145.1	121.3	118.1	–182.4	–184.3
$[Cs][XeOF_3]_{(s)} \rightarrow \frac{1}{2}XeF_{2(s)} + \frac{1}{2}[Cs][XeO_2F_3]_{(s)} + \frac{1}{2}[Cs][F]_{(s)}$	–35.6	–38.4	18.4	15.2	–41.1	–42.9

[a] The first column under the headings ΔH°, ΔS°, and ΔG° was obtained from $V_m([M][XeOF_3]) = V_m(F_2OXeNCCH_3) - V_m(CH_3CN) + V_m[M][F]$, whereas the second column was obtained from V_m $([M][XeOF_3]) = V_m[M][F] + [V_m(XeF_2) + V_m(XeO_2F_2)]/2$.

unit volumes of XeF_2 and XeO_2F_2 (0.0731 nm^3) only differ by 0.0023 nm^3 and lead to essentially the same ΔH^o and ΔG^o values.

Based on the aforementioned thermochemical calculations, both the gas-phase reduction and disproportionation pathways are endothermic, and the decompositions of the [M][$XeOF_3$] salts are largely driven by lattice enthalpies. This is illustrated by the greater ΔH^o and ΔG^o values for the Cs^+ salt relative to those of the $N(CH_3)_4^+$ salt which result from the smaller size of Cs^+ and greater lattice enthalpies of CsF and [Cs][XeO_2F_3].

The entropy term is also a major contributor in the reduction pathways because O_2 gas is evolved. The liberation of O_2 greatly increases the entropy of the reaction (119.7 J mol^{-1} K^{-1}) relative to the small entropy gain in the disproportionation pathways (16.8 J mol^{-1} K^{-1}). This results in the contribution of an additional −30.7 kJ mol^{-1} to the Gibbs free energies for the reduction pathways which, combined with the lattice enthalpies, renders the reduction pathways significantly more favorable than the disproportionation pathways for both salts.

Although the disproportionation of [Cs][$XeOF_3$] is less favorable than reduction, the former is spontaneous. In contrast, ΔH^o and ΔG^o of the corresponding disproportionation reaction for [$N(CH_3)_4$][$XeOF_3$] are close to zero. The larger size of the $N(CH_3)_4^+$ cation lowers the lattice enthalpies of [$N(CH_3)_4$][F] and [$N(CH_3)_4$][XeO_2F_3] such that they no longer overcome the gas-phase disproportionation enthalpy. The thermochemical calculations are in accordance with the observed decomposition products ([$N(CH_3)_4$][F] and XeF_2) for [$N(CH_3)_4$][$XeOF_3$], which can only decompose by the reduction pathway (eq 5.13). In contrast, [Cs][$XeOF_3$], which can decompose by either the reduction (eq 5.13) or disproportionation (eq 5.14) pathway, resulted in the formation of predominantly XeF_2 and a small amount of [Cs][XeO_2F_3].

5.3. Conclusion

The fluoride ion acceptor properties of $XeOF_2$ have been demonstrated by the high-yield syntheses of the endothermic salts, [M][$XeOF_3$] (M = $N(CH_3)_4$, Cs), in high purity. Both salts are kinetically stable at −78 °C but slowly decompose at 10–25 °C. Their decomposition pathways, inferred from their decomposition products, are supported by their thermochemical cycles. The latter show that the proposed disproportionation and reduction pathways are mainly driven by lattice energy contributions, with entropy playing a significant role in the pathways that lead to reduction of Xe(IV) to Xe(II) and O_2 evolution. The thermochemical cycles also reveal that disproportionation of Xe(IV) to Xe(II) and Xe(VI) is favored for [Cs][$XeOF_3$] but not for [$N(CH_3)_4$][$XeOF_3$], in accordance with experiment.

Comparison of the solid-state vibrational spectrum of [$N(CH_3)_4$][$XeOF_3$] with that of the calculated gas-phase $XeOF_3^-$ anion indicates little interaction between the anion and cation. The Raman spectra of the Cs^+ and $N(CH_3)_4^+$ salts of $XeOF_3^-$ also show that significant interactions occur between the Cs^+ cation and the oxygen atom of the $XeOF_3^-$ anion and that the anions interact with one another by means of fluorine bridges. The $XeOF_3^-$ anion is presently the only example of an AX_3YE_2 VSEPR arrangement known in which a double-bond domain subtends angles of ca. 90° with two valence electron lone pair domains. Comparisons of the experimental frequencies of $[Cs][XeOF_3]$ with those previously reported for $[Cs][XeOF_3]$[67] reveal that the product obtained in an earlier study was a mixture of XeF_2, $XeOF_2$, $[Cs][XeF_5]$, and $[Cs][XeO_3F]$. Thus, the present work represents the first bona fide synthesis and characterization of the $XeOF_3^-$ anion.

CHAPTER 6

$[H(OXeF_2)_n][AsF_6]$ and $[FXe^{II}(OXe^{IV}F_2)_n][AsF_6]$ ($n = 1, 2$): Examples of Xenon(IV) Hydroxy and Oxide Fluoride Cations; and the Crystal Structures of $[XeF_3 \cdot HF][Sb_2F_{11}]$ and $([XeF_3 \cdot HF][Sb_2F_{11}])_2 \cdot [H_5F_4][SbF_6]$

6.1. Introduction

While many compounds containing xenon in the +2 or +6 oxidation states are known, relatively few compounds exist where xenon is in the +4 oxidation state.[1,7] Among the factors that contribute to the relative scarcity of Xe(IV) compounds is the propensity for the oxides and oxide-fluorides to undergo reduction to Xe(II) and O_2 and redox disproportionation to Xe(II) and Xe(VI).[68,69,125,126] Examples of Xe(IV) cations are presently limited to $C_6F_5XeF_2^+$,[62] XeF_3^+,[45–52] and $F_xXe(OTeF_5)_{3-x}^+$ ($x = 0–2$).[61] Although di- and trixenon cations of Xe(II), ($Xe_2F_3^+$ [45,73] and $Xe_3OF_3^+$,[71])and Xe(VI) ($Xe_2F_{11}^+$ [10,218] and $F(O)_2Xe–F–Xe(O)_2F^+$ [219]) are known and XeF_2 form adducts with XeF_5^+ ($XeF_2 \cdot XeF_5^+$, $2XeF_2 \cdot XeF_5^+$ and $XeF_2 \cdot 2XeF_5^+$ [220]) attempts to synthesize polynuclear cations of Xe(IV) have, to date, proven unsuccessful. With the exception of the $Xe_3OF_3^+$ cation, all of the aforementioned dixenon cations contain fluorine-bridged xenon atoms, even when the option to form oxygen bridges is available, e.g., $F(O)_2Xe–F–Xe(O)_2F^+$.[219] Fluorine-bridge formation is also observed in the polynuclear xenon anion, $[Cs][(XeOF_4)_3F]$, in preference to oxygen-bridge formation.[221,222]

The only confirmed hydroxy derivative of xenon is perxenic acid, H_4XeO_6,[223] which has only been observed in solution, and several speculative reports of xenic acid (H_2XeO_4).[185,224–227] To date, no other hydroxy derivatives of xenon have been reported, and none have been characterized in the solid state. Similarly, HF adducts of main-group and transition-metal centers are known which have been the subject of a recent review,[82] e.g., $[La(HF)_2][AsF_6]_3$, $[Pb(HF)][AsF_6]_2$, $[Ca(HF)][AsF_6]_2$, $[Cd(HF)][AsF_6]_2$, $[Mg(HF)_2][SbF_6]_2$, $[Ca(HF)_2][SbF_6]_2$, $[Hg(HF)][SbF_6]_2$, $[OsO_3F(HF)_2][AsF_6]$, $[OsO_3F(HF)][SbF_6]$, $[Au(HF)_2][SbF_6]_2{\cdot}2HF$, and $Mg(HF)AuF_4AuF_6$, but none exist where HF is coordinated to a non-metal center. The reaction conditions that are used to synthesize HF adducts are also of interest because the adducts are often times formed in superacidic media.[82] The HF/SbF_5 superacid medium is of particular interest because acidium ion salts having the formulations $[H_2F][Sb_2F_{11}]$, $[H_3F_2][Sb_2F_{11}]$, $[H_2F][SbF_6]$, $[H_3F_2][SbF_6]$, $[H_4F_3][SbF_6]$, and $[H_7F_6][SbF_6]$, have been proposed,[228] however, only $[H_2F][Sb_2F_{11}]$,[229] $[H_3F_2][Sb_2F_{11}]$,[229] and $[H_7F_6][SbF_6]$[228] have been isolated and characterized by X-ray crystallography.

The syntheses and characterizations of several new Xe(IV) cations derived from HF/AsF_5 and HF/SbF_5 superacid media are described in the present paper, and provide the first examples of isolated hydroxy derivatives of xenon, the first Xe(IV)-containing mixed-oxidation state polynuclear compounds, and the first examples of HF coordinated to xenon. Quantum-chemical calculations and $^{1/2}H$- and $^{16/18}O$-enrichment have been employed to assign the Raman spectra of the aforementioned cations and to aid in the assessment of their chemical bonding.

6.2. Results and Discussion

6.2.1. Syntheses and Properties. The reactions and the purities of all products were routinely monitored by recording the low-temperature Raman spectra (−150 °C) of the natural abundance, ^{18}O-enriched (98.6 atom %), and ^{2}H-enriched (99.5 atom %) salts.

6.2.1.1. [HOXeF$_2$][AsF$_6$]. (i) Synthesis. The salt, [HOXeF$_2$][AsF$_6$], was obtained by the low-temperature reaction of XeOF$_2$·*n*HF with AsF$_5$ in anhydrous HF (aHF) according to eq 6.1. The reaction proceeds to a significant degree with only slight mixing but was

$$\mathrm{XeOF_2{\cdot}}n\mathrm{HF} + \mathrm{AsF_5} \xrightarrow[-78\,^{\circ}\mathrm{C}]{\mathrm{HF}} [\mathrm{HOXeF_2}][\mathrm{AsF_6}] + (n-1)\mathrm{HF} \qquad (6.1)$$

allowed to stand for 12 h at −78 °C to ensure complete reaction, yielding an insoluble white solid. The solvent and any residual AsF$_5$ were removed under dynamic vacuum at −78 °C, yielding [HOXeF$_2$][AsF$_6$] as a friable, white powder.

Prior to reaction with AsF$_5$, it was necessary to ensure that XeOF$_2$ was fully solvolyzed to the HF adduct and not merely suspended in HF, otherwise extensive decomposition to [XeF][AsF$_6$] was observed. Formation of XeOF$_2$·*n*HF was confirmed by Raman spectroscopy.[125] The XeF$^+$ cation likely resulted from the formation of the unstable intermediate, XeOF$^+$ (eq 6.2), which then decomposed by O$_2$ elimination to yield XeF$^+$(eq 6.3). This decomposition pathway also consistent with the large negative

$$\mathrm{XeOF_2} + \mathrm{AsF_5} \xrightarrow[-78\,^{\circ}\mathrm{C}]{\mathrm{HF}} ([\mathrm{XeOF}][\mathrm{AsF_6}]) \qquad (6.2)$$

$$([\mathrm{XeOF}][\mathrm{AsF_6}])_{(s)} \xrightarrow[-78\,^{\circ}\mathrm{C}]{\mathrm{HF}} [\mathrm{XeF}][\mathrm{AsF_6}]_{(s)} + \tfrac{1}{2}\mathrm{O_2}_{(g)} \qquad (6.3)$$

$\Delta G_{194.15}$ is for eq 6.3 (−313.0 kJ mol^{-1}) obtained from a Born-Fajans-Haber thermochemical cycle using available experimental thermodynamic parameters and values derived from volume-based thermodynamics (VBT). The calculated exothermicity is consistent with explosive behavior of the reaction of $XeOF_{2(s)}$ with $AsF_{5(l)}$.[67]

Solid $[HOXeF_2][AsF_6]$ is stable indefinitely at −78 °C in the absence of moisture but outgases rapidly upon warming to −35 °C. The resulting film, coating the reactor walls, was shown by Raman spectroscopy to be $[XeF][AsF_6]$. It is likely that the hydroxy salt decomposed according to eq 6.4 which has a $\Delta G_{194.15}$ of −288.6 kJ mol^{-1} (Table 6.1).

$$[HOXeF_2][AsF_6]_{(s)} \longrightarrow [XeF][AsF_6]_{(s)} + \tfrac{1}{2}O_{2\,(g)} + HF_{(l)} \qquad (6.4)$$

Attempts to dissolve $[HOXeF_2][AsF_6]$ were unsuccessful. Warming a suspension of $[HOXeF_2][AsF_6]$ to −40 °C in aHF showed no apparent solubility and gave a Raman spectrum at −150 °C that showed it had completely decomposed to $[XeF][AsF_6]$. A suspension of $[HOXeF_2][AsF_6]$ in AsF_5 that had been warmed to −40 °C showed the onset of decomposition to $[XeF][AsF_6]$, but no xenon-containing products were formed and no solubility was detected. Dissolution in a superacid media was also attempted in which $[HOXeF_2][AsF_6]$ was suspended in a 1:3 v/v of $HF:AsF_5$. On warming to −56 °C no solubility was discernable and the compound decomposed to $[XeF][AsF_6]$ upon warming to −50 °C.

(ii) Reactivity of $[HOXeF_2][AsF_6]$. The decomposition of $HOXeF_2^+$ to XeF^+ may be induced by the heat of reaction resulting from the formation of $HOXeF_2^+$ (eq 6.1). In an attempt to isolate a sample of $[HOXeF_2][AsF_6]$ that is free of $[XeF][AsF_6]$, a half equivalent of AsF_5 was added to a reactor containing $XeOF_2{\cdot}n$HF and allowed to react for 12 h at −78 °C. Instead of pale yellow $[HOXeF_2][AsF_6]$, the product was a bright yellow

Table 6.1. Values of Δ*H*, Δ*S*, and Δ*G* Calculated for the Decomposition Reactions of $[XeOF][AsF_6]$, $[HOXeF_2][AsF_6]$, $[HOXe(F)_2OXeF_2][AsF_6]$, $[FXeOXeF_2][AsF_6]$, and $[FXeOXe(F)_2OXeF_2][AsF_6]$

	Δ*H* (kJ mol^{-1})		Δ*S* (J mol^{-1} K^{-1})		Δ*G* (kJ mol^{-1})		
	298.15 K	194.15 K	298.15 K	194.15 K	298.15 K	194.15 K	eq
$[XeOF][AsF_6]_{(s)} \xrightarrow{} [XeF][AsF_6]_{(s)} + \frac{1}{2}O_{2\,(g)}$	−294.6	−294.8	93.7	93.7	−322.5	−313.0	3
$[HOXeF_2][AsF_6]_{(s)} \xrightarrow{} [XeF][AsF_6]_{(s)} + \frac{1}{2}O_{2\,(g)} + HF_{(l)}$	−148.3	−260.7	242.1	143.7	−220.5	−288.6	4
$3[HOXe(F)_2OXeF_2][AsF_6]_{(s)} + 3H_2O_{(l)} \xrightarrow{} 2[Xe_3OF_3][AsF_6]_{(s)} + 3O_{2\,(g)} + 6HF_{(l)} + [H_3O][AsF_6]_{(s)}$	−1845.5	−1326.8	1341.5	817.3	−2245.5	−1485.5	6
$[HOXe(F)_2OXeF_2][AsF_6]_{(s)} \xrightarrow{} [Xe_2F_3][AsF_6]_{(s)} + O_{2\,(g)} + HF_{(l)}$	−549.9	−421.1	362.7	264.3	−658.0	−472.4	7
$[FXeOXeF_2][AsF_6]_{(s)} \xrightarrow{} [Xe_2F_3][AsF_6]_{(s)} + \frac{1}{2}O_{2\,(g)}$	−202.6	−205.7	120.6	120.6	−238.6	−229.1	11
$[FXeOXe(F)_2OXeF_2][AsF_6]_{(s)} \xrightarrow{} [Xe_2F_3][AsF_6]_{(s)} + O_{2\,(g)} + XeF_{2\,(s)}$	−544.1	−385.1	242.4	242.4	−616.4	−432.2	12
$3[FXeOXeF_2][AsF_6]_{(s)} + 3H_2O_{(l)} \xrightarrow{} 2[Xe_3OF_3][AsF_6]_{(s)} + \frac{3}{2}O_{2\,(g)} + 3HF_{(l)} + [H_3O][AsF_6]_{(s)}$	−611.3	−670.4	615.3	386.2	−794.8	−745.4	13
$[FXeOXe(F)_2OXeF_2][AsF_6]_{(s)} + H_2O_{(l)} \xrightarrow{} [Xe_3OF_3][AsF_6]_{(s)} + O_{2\,(g)} + 2HF_{(l)}$	−630.4	−438.6	446.6	271.9	−763.2	−491.4	14

Values of Δ*H*, Δ*S*, and Δ*G* were calculated as decrobed in Appendix 3.

solid having a Raman spectrum that was consistent with the formation of the mixed oxidation state salt, $[FXe^{II}OXe^{IV}(F)_2][AsF_6]$ (vide infra).

6.2.1.2. $[HOXe(F)_2OXeF_2][AsF_6]$. When samples containing $XeOF_2{\cdot}n HF$ and HF were allowed to stand for ~3 weeks at −78 °C, traces of water apparently diffused through the FEP reactor walls. Reaction of half an equivalent of AsF_5 for 12 h resulted in a bright yellow solid that was consistent with the formation of $[HOXe(F)_2OXeF_2][AsF_6]$. Although this compound was also synthesized from a stoichiometric amount of $XeOF_2{\cdot}n HF$, H_2O, and AsF_5 in HF, a more controlled approach involved the low-temperature (−78 °C) reaction of half an equivalent of $[H_3O][AsF_6]$ with $XeOF_2{\cdot}n HF$ in aHF (eq 6.5). Both reactions are essentially the same because H_2O forms $[H_3O][AsF_6]$ in

$$2XeOF_2{\cdot}n HF + [H_3O][AsF_6] \xrightarrow[-78\ ^{\circ}C]{HF} [HOXe(F)_2OXeF_2][AsF_6] + H_2O_{(HF)} + 2n HF \qquad (6.5)$$

the presence of AsF_5 and HF, but the direct use of $[H_3O][AsF_6]$ allowed for a more precise titration to be carried out under similar reaction conditions. Raman spectra of the solid products were recorded under HF solvent. Reaction of a 4:1 molar ratio of $XeOF_2{\cdot}n HF$ with $[H_3O][AsF_6]$ revealed a mixture of $XeOF_2{\cdot}n HF$ and $[HOXe(F)_2OXeF_2][AsF_6]$ while 2:1 and 1:1 molar ratios of reactants revealed only $[HOXe(F)_2OXeF_2][AsF_6]$. In the latter reaction, it was presumed that unreacted $[H_3O][AsF_6]$ remained dissolved in the HF solvent and could not be observed in the Raman spectrum.

It is noteworthy that oxygen isotope scrambling was not observed when $Xe^{18}OF_2{\cdot}n$HF reacted with $[H_3{}^{16}O][AsF_6]$, producing only $[H^{18}OXe(F)_2{}^{18}OXeF_2][AsF_6]$. This indicates that the acidium ion is only involved in protonation and is not otherwise involved in the reaction pathway.

Solid $[HOXe(F)_2OXeF_2][AsF_6]$ was stable when isolated and stored under HF for several days at −78 °C. However, over the course of a month, samples that were maintained at −78 °C under HF formed deep red-orange colored crystals that were shown by Raman spectroscopy and unit cell determinations of several crystals to be $[Xe_3OF_3][AsF_6]$.[71] Gas evolution was also observed in the samples. It is presumed that the $HOXe(F)_2OXeF_2{}^+$ cation decomposes to a xenon(II) intermediate, XeF_2 and/or XeF^+, with the release of O_2, which is followed by its reaction with residual water (eq 6.6) resulting from the synthesis of $[HOXe(F)_2OXeF_2][AsF_6]$ (eq 6.5). The same decomposition products were observed when samples of $[HOXe(F)_2OXeF_2][AsF_6]$ were warmed to −50 °C in aHF. The thermochemical cycle for eq 6.6 indicates the proposed reaction is spontaneous, with a $\Delta G_{194.15}$ of −1485.5 kJ (Table 6.1).

$$3[HOXe(F)_2OXeF_2][AsF_6]_{(s)} + 3H_2O_{(l)} \xrightarrow[-78\,^\circ C]{HF} 2[Xe_3OF_3][AsF_6]_{(s)} + 3O_{2\,(g)} + 6HF_{(l)} + [H_3O][AsF_6]_{(s)} \qquad (6.6)$$

The reaction of an additional equivalent of AsF_5 with $[HOXe(F)_2OXeF_2][AsF_6]$ at −78 °C did not lead to $[HOXeF_2][AsF_6]$ as expected, but instead, catalyzed its decomposition to $[Xe_2F_3][AsF_6]$ (eq 6.7) ($\Delta G_{194.15}$ = −420.0 kJ mol^{-1}; Table 6.1). In addition, AsF_5 also reacted with HF and H_2O, the latter was produced in the synthesis of $[HOXe(F)_2OXeF_2][AsF_6]$, and formed $[H_3O][AsF_6]$ (eq 6.8).

$$[HOXe(F)_2OXeF_2][AsF_6]_{(s)} \xrightarrow[-78\ ^{\circ}C]{HF/AsF_5} [Xe_2F_3][AsF_6]_{(s)} + O_{2\,(g)} + HF_{(l)} \quad (6.7)$$

$$HF + H_2O + AsF_5 \xrightarrow[-78\ ^{\circ}C]{HF/AsF_5} [H_3O][AsF_6] \quad (6.8)$$

In an effort to solubilize the $HOXe(F)_2OXeF_2^+$ cation, an attempt was made to synthesize the SbF_6^- salt from $[H_3O][SbF_6]$ and $XeOF_2{\cdot}n HF$ by analogy with the synthesis of the AsF_6^- salt (eq 6.5). Instead, the SbF_6^- salt proved to be unstable, rapidly decomposing to $[Xe_3OF_3][SbF_6]$ within a matter of minutes when $[H_3O][SbF_6]$ and $XeOF_2{\cdot}n HF$ were mixed in HF at −78 °C. This result indicates that the AsF_6^- anion plays a major role in stabilizing the $HOXe(F)_2OXeF_2^+$ cation because of its greater fluorobasicity relative to that of SbF_6^-.[46]

6.2.1.3. $[FXe^{II}OXe^{IV}F_2][PnF_6]$ (Pn = As, Sb) and $[FXe^{II}OXe^{IV}(F)_2OXe^{IV}F_2][AsF_6]$.

The propensity of the Xe–O bond of $XeOF_2$ to protonate and the existence of several unidentified peaks in the Raman spectrum of $[HOXeF_2][AsF_6]$ led to attempts to synthesize an $XeOF_2$ adduct with XeF^+ containing a Xe–O–Xe bridge.

Both $[FXeOXeF_2][AsF_6]$ and $[FXeOXe(F)_2OXeF_2][AsF_6]$ were synthesized by the reaction of $[XeF][AsF_6]$ with stoichiometric amounts of fully solvated $XeOF_2{\cdot}n HF$ suspended in aHF at −78 °C (eq 6.9). Over the course of 5−10 min, the pale yellow solid

$$m XeOF_2{\cdot}n HF + [XeF][AsF_6] \xrightarrow[-78\ ^{\circ}C]{HF} [FXe(OXeF_2)_m][AsF_6] + mn HF \quad (m = 1, 2) \quad (6.9)$$

turned bright yellow;however, occasional agitation and reaction times of approximately one week (two weeks for $[FXeOXe(F)_2OXeF_2][AsF_6]$) were required for complete reaction. Oxygen-18 enriched samples that had been similarly prepared exhibited significant kinetic isotope effects, requiring as long as a month for complete reaction at −78 °C. The products were isolated by removal of HF under dynamic vacuum at −78 °C, leaving behind bright yellow powders. In both stoichiometric reactions, when $XeOF_2$ was merely suspended in aHF and not fully solvolyzed, a mixture of $XeOF_2{\cdot}n HF$, $[XeF][AsF_6]$, $[FXeOXeF_2][AsF_6]$, and $[FXeOXe(F)_2OXeF_2][AsF_6]$ resulted which required reaction times of approximately one month or more to go to completion. It is therefore important to completely solvolyze $XeOF_2$ in aHF to $XeOF_2{\cdot}n HF$ prior to reaction. The results also showed that $[FXeOXeF_2][AsF_6]$ and $[FXeOXe(F)_2OXeF_2][AsF_6]$ interconvert when additional $XeOF_2{\cdot}n HF$ or $[XeF][AsF_6]$ are present.

Several studies were carried out under the aforementioned conditions using 4:1, 2:1, 4:3, 1:1, and 1:2 molar ratios of $XeOF_2{\cdot}n HF$ and $[XeF][AsF_6]$ to determine if longer chain length cations could be formed. In the 4:1 reaction, the Raman spectrum showed only $[FXeOXe(F)_2OXeF_2][AsF_6]$ and unreacted $XeOF_2{\cdot}n HF$. The 2:1 ratio gave pure $[FXeOXe(F)_2OXeF_2][AsF_6]$ while the 4:3 ratio yielded a mixture of $[FXeOXe(F)_2OXeF_2][AsF_6]$ and $[FXeOXe(F)_2][AsF_6]$. Finally, the 1:1 and 1:2 ratios yielded $[FXeOXe(F)_2][AsF_6]$, with unreacted $[XeF][AsF_6]$ also being present when a 1:2 ratio was used. The results indicated that no cations other than $[FXeOXeF_2][AsF_6]$ and $[FXeOXe(F)_2OXeF_2][AsF_6]$ were formed and stable at −78 °C.

The $FXeOXeF_2^+$ cation can also be obtained by the reaction of $XeOF_2{\cdot}n HF$ with half an equivalent of AsF_5 in aHF solvent at −78 °C. It is presumed that the superacidic conditions catalyze O_2 elimination to give the mixed oxidation state cation according to eq 6.10.

$$2XeOF_2{\cdot}nHF + AsF_5 \xrightarrow[-78\ ^\circ C]{HF/AsF_5} [FXeOXeF_2][AsF_6] + \tfrac{1}{2}O_2 + 2nHF \quad (6.10)$$

Both $[FXeOXeF_2][AsF_6]$ and $[FXeOXe(F)_2OXeF_2][AsF_6]$ are stable under HF solvent and as dry powders for several weeks at −78 °C under anhydrous conditions but began to decompose to $[Xe_2F_3][AsF_6]$ upon warming to −40 °C (eqs 6.11 and 6.12). The

$$[FXeOXeF_2][AsF_6]_{(s)} \xrightarrow{-40\ ^\circ C} [Xe_2F_3][AsF_6]_{(s)} + \tfrac{1}{2}O_{2\,(g)} \quad (6.11)$$

$$[FXeOXe(F)_2OXeF_2][AsF_6]_{(s)} \xrightarrow{-40\ ^\circ C} [Xe_2F_3][AsF_6]_{(s)} + O_{2\,(g)} + XeF_{2\,(s)} \quad (6.12)$$

factors contributing to the negative $\Delta G_{194.15}$ values for both reactions (−229.1 kJ mol^{-1} and −432.2 kJ mol^{-1}; Table 6.1) are dominated by the higher lattice energy associated with the formation of $[Xe_2F_3][AsF_6]$ and the increase in entropy associated with O_2 formation. Sample storage for approximately one month at −78 °C resulted in water diffusion through the FEP walls of the reactor and hydrolysis of both samples to $[Xe_3OF_3][AsF_6]$ (eq 6.13 and 6.14) as evidenced by the formation of deep red-orange

$$3[FXeOXeF_2][AsF_6]_{(s)} + 3H_2O_{(l)} \longrightarrow$$
$$2[Xe_3OF_3][AsF_6]_{(s)} + \tfrac{3}{2}O_{2\,(g)} + 3HF_{(l)} + [H_3O][AsF_6]_{(s)} \quad (6.13)$$

$$[FXeOXe(F)_2OXeF_2][AsF_6]_{(s)} + H_2O_{(l)} \longrightarrow$$
$$[Xe_3OF_3][AsF_6]_{(s)} + O_{2\,(g)} + 2HF_{(l)} \quad (6.14)$$

crystals which were shown to be $[Xe_3OF_3][AsF_6]$ by Raman spectroscopy.[71] This decomposition pathway is also supported by thermochemical cycles which give negative $\Delta G_{194.15}$ values for both reactions (−745.4 kJ and −491.4 kJ mol^{-1}; Table 6.1). Further reaction of $[FXeOXeF_2][AsF_6]$ with one equivalent of AsF_5 yielded a mixture of

$[HOXeF_2][AsF_6]$ and $[XeF][AsF_6]$ (eq 6.15), showing that AsF_5 must be added in a single amount to prevent $[XeF][AsF_6]$ formation. Two-step additions also lead to formation of the hydroxy cation.

$$[FXeOXeF_2][AsF_6] + AsF_5 + HF \xrightarrow[-78\,^{\circ}C]{HF/AsF_5} [HOXeF_2][AsF_6] + [XeF][AsF_6] \quad (6.15)$$

In an attempt to solubilize the $FXeOXeF_2^+$ and $FXeOXe(F)_2OXeF_2^+$ cation salts, the syntheses of the SbF_6^- salts were attempted in reactions analogous to those given in eq 6.9, using $[XeF][SbF_6]$. The reactions proceeded more rapidly than in the cases of the arsenic analogues, requiring only 24 h to go to completion. However, only $[FXeOXeF_2][SbF_6]$ formed, which had a more intense yellow color than $[FXeOXeF_2][AsF_6]$. When the synthesis of the longer chain cation was attempted, a mixture of $[FXeOXeF_2][SbF_6]$ and $XeOF_2{\cdot}n HF$ resulted, which was observed by Raman spectroscopy, even after the sample had been warmed to −50 °C for 2 h. These results indicate the anion plays a significant role in stabilizing the cations. Unfortunately, $[FXeOXeF_2][SbF_6]$ also exhibited behavior that was similar to that of the arsenic analogue, and began to decompose to $[Xe_2F_3][SbF_6]$ when warmed to −40 °C with no discernable solubility in aHF.

In a further attempt to solubilize a salt of $FXeOXeF_2^+$, the formation of the CH_3CN adduct of this cation was attempted in a manner similar to that used for the formation of $FXe\text{-}NCCH_3^+$.[104] However, CH_3CN displaced $XeOF_2$ and the reaction resulted in the formation of the longer chain salt, $[FXeOXe(F)_2OXeF_2][AsF_6]$ (eq 6.16).

$$2[FXeOXeF_2][AsF_6] + CH_3CN \xrightarrow[-78\,^{\circ}C]{HF}$$

$$[FXeOXe(F)_2OXeF_2][AsF_6] + [FXe\text{-}NCCH_3][AsF_6] \quad (6.16)$$

6.2.1.4. $[XeF_3{\cdot}HF][Sb_2F_{11}]$. In an effort to obtain a soluble salt of the $HOXeF_2^+$ cation for crystal growth, the synthesis of an SbF_6^- salt was attempted. Because SbF_5 freezes at 7 °C,[230] it could not be added in a manner analogous to AsF_5 (eq 6.1). An aHF solution of SbF_5 (~17 mol %) was decanted into the reactor containing $XeOF_2{\cdot}n HF$ under aHF and was warmed to −78 °C and thoroughly mixed. The sample was then warmed to −50 °C until all the solid dissolved, and was followed by cooling to −78 °C. Over the course of 24 h, colorless crystals formed that were found to be a mixture of $([XeF_3{\cdot}HF][Sb_2F_{11}])_2{\cdot}[H_5F_4][SbF_6]$, $[XeF_3{\cdot}HF][Sb_2F_{11}]$, and $[XeF_3][SbF_6]$. Under highly superacidic conditions (~17 mol % SbF_5 in HF) the hydroxyl group of the cation is displaced, yielding XeF_3^+ and H_3O^+ (eqs 6.17, 6.18 or 6.19, 6.20), with the latter

$$XeOF_2{\cdot}n HF + SbF_5 \xrightarrow[-78\ ^{\circ}C]{HF/SbF_5} ([HOXeF_2][SbF_6]) + (n{-}1)HF \quad (6.17)$$

$$([HOXeF_2][SbF_6]) + (m{+}1)SbF_5 + 3HF \xrightarrow[-78\ ^{\circ}C]{HF/SbF_5}$$

$$[XeF_3{\cdot}HF][Sb_2F_{11}] + [H_3O][F(SbF_5)_m] \quad (m = 1, 2) \quad (6.18)$$

$$XeOF_2{\cdot}n HF + 3HF + m SbF_5 \xrightarrow[-78\ ^{\circ}C]{HF/SbF_5} XeF_4 + [H_3O][F(SbF_5)_m] + n HF \quad (6.19)$$

$$XeF_4 + HF + 2SbF_5 \xrightarrow[-78\ ^{\circ}C]{HF/SbF_5} [XeF_3{\cdot}HF][Sb_2F_{11}] \quad (6.20)$$

remaining in solution. The high acidity of this medium resulted in the formation of $Sb_2F_{11}^-$, which is not readily observed in unacidified HF,[231] and the formation of the previously unobserved acidium ion salt, $[H_5F_4][SbF_6]$.

6.2.2. X-ray Crystallography. A summary of the refinement results and other crystallographic information for $([XeF_3{\cdot}HF][Sb_2F_{11}])_2{\cdot}[H_5F_4][SbF_6]$, $[XeF_3{\cdot}HF][Sb_2F_{11}]$, and $[XeF_3][SbF_6]$ is given in Table 6.2. Important bond lengths, bond angles, and

Table 6.2. Summary of Crystal Data and Refinement Results for β-[XeF_3][SbF_6], ([XeF_3·HF][Sb_2F_{11}])$_2$·[H_5F_4][SbF_6], and [XeF_3·HF][Sb_2F_{11}]

	([XeF_3·HF][Sb_2F_{11}])$_2$ ·[H_5F_4][SbF_6]	[XeF_3·HF][Sb_2F_{11}]	β-[XeF_3][SbF_6]
space group	$P\bar{1}$ (No. 2)	$C2/c$ (No. 15)	$P2_1/c$ (No. 14)
a (Å)	7.5604(8)	13.4120(4)	5.2321(2)
b (Å)	8.4967(9)	8.4709(4)	15.6025(5)
c (Å)	13.017(1)	10.4543(4)	8.6225(3)
α (deg)	85.469(4)	90	90
β (deg)	78.082(3)	110.493(2)	102.825(1)
γ (deg)	66.350(3)	90	90
V (Å^3)	749.44(14)	1112.56(8)	686.33(4)
Z (molecules/unit cell)	2	4	4
mol. wt. (g mol^{-1})	977.60	660.81	424.05
ρ_{calc} (g cm^{-3})	4.332	3.945	4.104
T (°C)	–173	–173	–173
μ (mm^{-1})	7.87	8.04	8.99
λ (Å)	0.71073	0.71073	0.71073
$R_1{}^a$	0.0389	0.0251	0.0281
$wR_2{}^b$	0.1011	0.0582	0.0612

[a] $R_1 = \Sigma \| F_o | - | F_c \| / \Sigma | F_o |$ for $I > 2\sigma(I)$.

[b] wR_2 is defined as $\{\Sigma[w(F_o^2 - F_c^2)^2]/\Sigma w(F_o^2)^2\}^{1/2}$ for $I > 2\sigma(I)$.

contacts for ([XeF_3·HF][Sb_2F_{11}])$_2$·[H_5F_4][SbF_6], [XeF_3·HF][Sb_2F_{11}], and [XeF_3][SbF_6] are listed in Tables 6.3 and A3.2. The crystal structure of [XeF_3][SbF_6] has been reported previously[52] but the present low-temperature (−173 °C) crystal structure of [XeF_3][SbF_6] was obtained in admixture with the aforementioned salts and has been included in the Supporting Information because of its higher precision and to allow for a more suitable comparison with the structural parameters of the XeF_3·HF^+ cation in the present study.

6.2.2.1 The XeF_3·HF^+ Cation. The XeF_3·HF^+ cation can either be described as an HF adduct of the XeF_3^+ cation, or as a protonated XeF_4 molecule. Both are valid descriptions (see Computational Results), however, as a result of the similarity of the geometric parameters of XeF_3·HF^+ to those of XeF_3^+ in [XeF_3][SbF_6] (Figure 6.1) and [XeF_3][Sb_2F_{11}],[45,51] the adduct description is used in the ensuing discussion.

(i) ([XeF_3·HF][Sb_2F_{11}])$_2$·[H_5F_4][SbF_6]. Both [XeF_3·HF][Sb_2F_{11}] ion pairs in the unit cell of ([XeF_3·HF][Sb_2F_{11}])$_2$·[H_5F_4][SbF_6] are related by symmetry and pack in alternating planes of $Sb_2F_{11}^-$ anions with XeF_3^+·HF and $H_5F_4^+$ cations (Figure 6.2). The Xe–F$_e$ bond length (1.838(2) Å) is equal to that of the SbF_6^- salt (1.839(2) Å), but is significantly shorter than the Xe–F bonds in XeF_4 (1.953(2) Å).[32] Similarly, the Xe–F$_a$ bond lengths (1.880(2) and 1.890(2) Å) are comparable to those of the SbF_6^- salt (1.894(2) and 1.901(2) Å), and are also shorter than in XeF_4. In contrast to other salts of the XeF_3^+ cation, which make contacts to their corresponding anions,[45,51,52] the XeF_3^+ cations of ([XeF_3·HF] [Sb_2F_{11}])$_2$·[H_5F_4][SbF_6] each have a short (2.462(2) Å) secondary contact to a HF molecule that lies in the XeF_3^+ molecular plane. This contact is similar to the short secondary contact (2.485(1) Å) that occurs between the cation and anion in

Table 6.3. Experimental and Calculated Bond Lengths (Å) and Bond Angles (deg) for the $XeF_3^+\cdot HF$ Adduct.

	$XeF_3^+\cdot HF$				
	exptl		calcd[a]		
	$([XeF_3\cdot HF][Sb_2F_{11}])_2\cdot[H_5F_4][SbF_6]$	$[XeF_3\cdot HF][Sb_2F_{11}]$	B3LYP	PBE1PBE	MP2
Xe(1)-F(1)	1.880(2)	1.865(1)	1.916	1.894	1.892
Xe(1)-F(2)	1.838(2)	1.865(1)	1.870	1.847	1.839
Xe(1)-F(3)	1.890(2)	2.186(2)	1.916	1.894	1.892
Xe(1)---F(10)	2.462(2)	2.186(2)	2.556	2.537	2.550
F(10)-H			0.937	0.933	0.934
F(1)-Xe(1)-F(2)	81.4(1)	81.40(8)	84.7	84.1	83.7
F(1)-Xe(1)-F(3)	162.3(1)	161.12(6)	169.3	168.3	167.4
F(1)-Xe(1)---F(10)	78.8(1)	79.72(6)	95.3	95.8	96.3
F(2)-Xe(1)-F(3)	81.0(1)	79.72(6)	84.7	84.1	83.7
F(2)-Xe(1)---F(10)	160.2(1)	161.12(6)	176.7	176.8	177.1
F(3)-Xe(1)---F(10)	118.77(9)	119.15(9)	95.4	95.9	96.3
Xe(1)---F(10)-H			141.9	141.9	152.8

[a] The aug-cc-pVTZ(-PP) basis set was used.

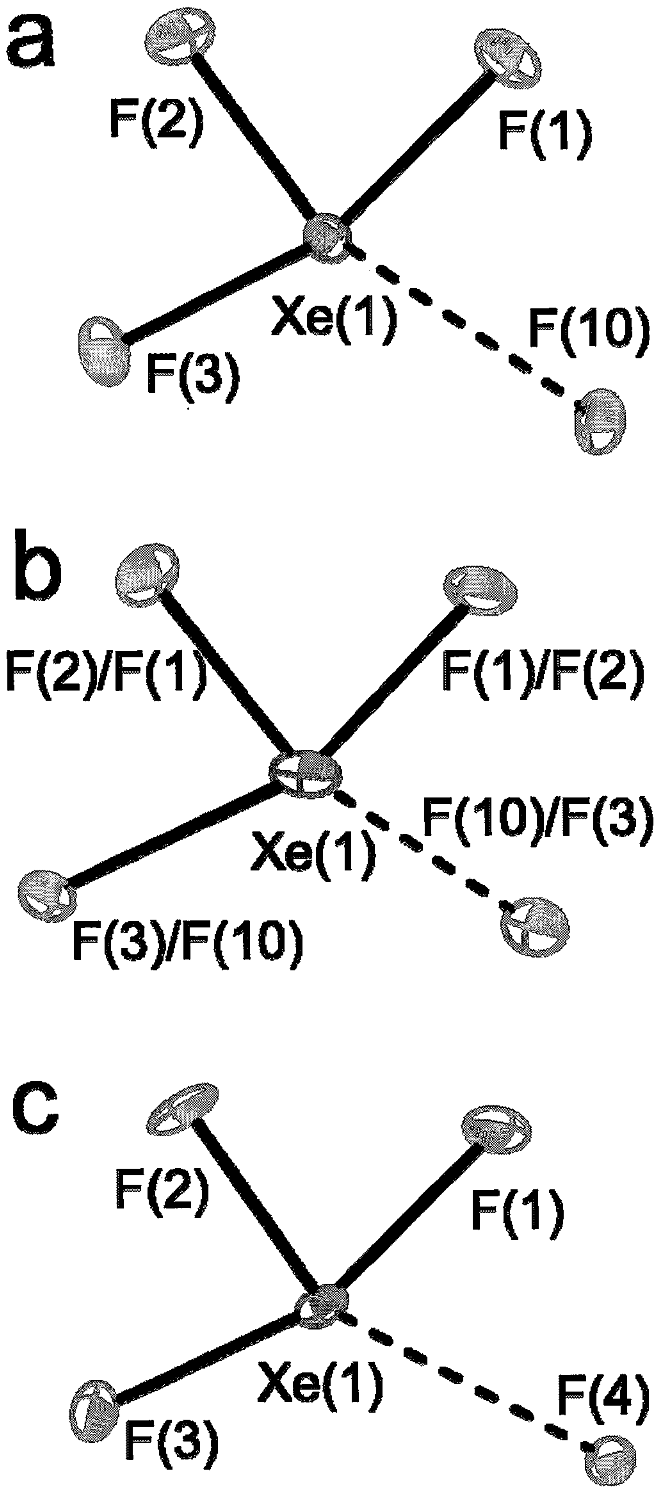

Figure 6.1. The XeF_3^+ cations in the X-ray crystal structures of (a) $([XeF_3{\cdot}HF][Sb_2F_{11}])_2{\cdot}[H_5F_4][SbF_6]$, (b) $[XeF_3{\cdot}HF][Sb_2F_{11}]$, and (c) $[XeF_3][SbF_6]$; thermal ellipsoids are shown at the 50% probability level.

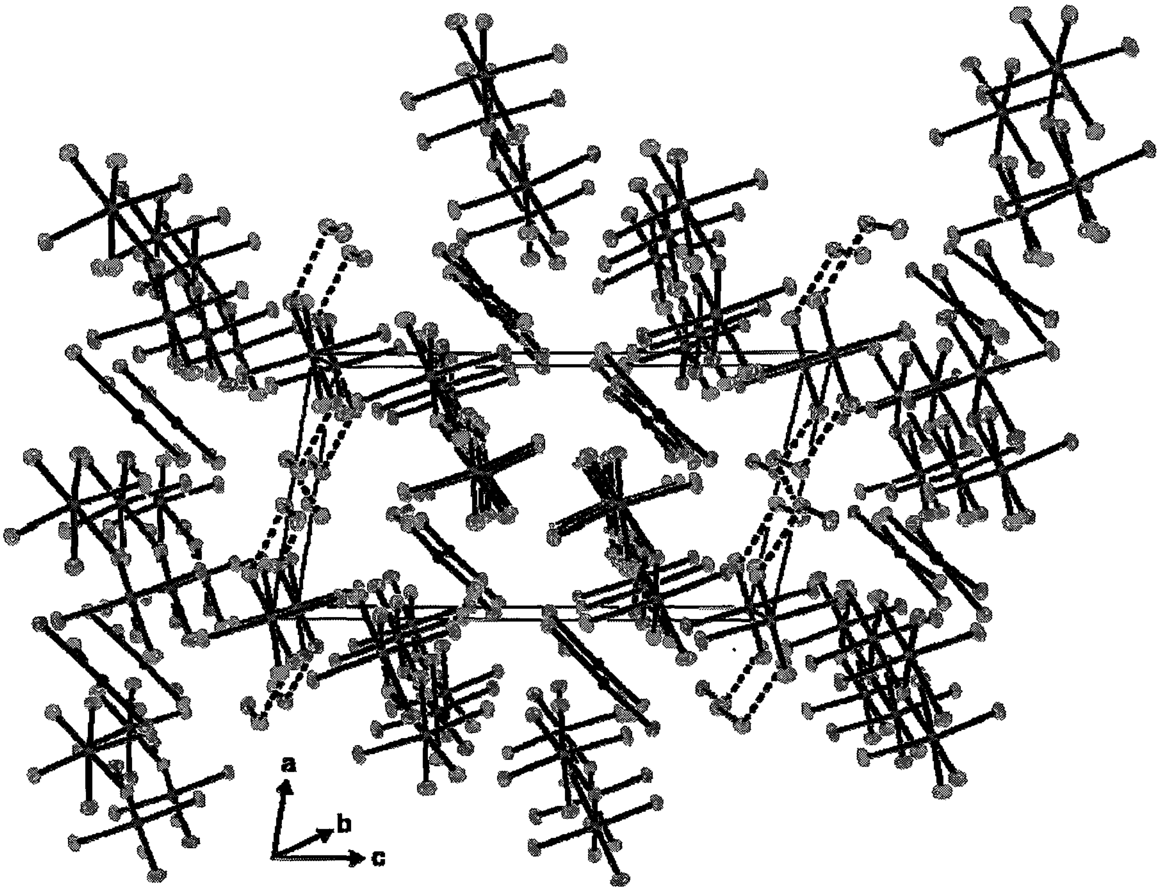

Figure 6.2. Crystal packing for ([$XeF_3 \cdot HF$][Sb_2F_{11}])$_2 \cdot$[H_5F_4][SbF_6] viewed along the *b*-axis; thermal ellipsoids are shown at the 50% probability level.

[XeF_3][SbF_6]. The F_e–Xe–F_a (81.4(1)°, 81.0(1)°), F_a–Xe–F_a (162.3(1)°), and F_a–Xe–F_{HF} (78.8(1)°, 118.77(9)°) bond angles of XeF_3·HF are also comparable to those in [XeF_3][SbF_6] [F_e–Xe–F_a, 79.72(8)°, 79.74(7)°; F_a–Xe–F_a, 159.45(8)°; F_a–Xe–F_{SbF6} 73.06(6)°, 127.47(6)°].

(ii) [XeF_3·HF][Sb_2F_{11}]. The [XeF_3·HF][Sb_2F_{11}] salt was also isolated in the absence of the acidium ion salt, [H_5F_4][SbF_6]. However, in the crystal structure of [XeF_3·HF][Sb_2F_{11}] (Figure 6.3), there is a two-fold positional disorder about the diagonal that bisects the F_1–Xe–F_2 angle where the equatorial fluorine atom (F_1) and one of the axial fluorine atoms (F_2) are indistinguishable from one another and the remaining axial fluorine atom (F_3) cannot be distinguished from the fluorine atom (F_{10}) of the coordinated HF molecule (Table 6.3 and Figure 6.1). The positionally averaged bond lengths are 1.865(1) and 2.186(1) Å, respectively, and are in good agreement with the averages of the corresponding bond lengths in ([XeF_3·HF][Sb_2F_{11}])$_2$·[H_5F_4][SbF_6], 1.859(3) and 2.176(3) Å, respectively.

The secondary coordination spheres are very similar in the crystal structures of [XeF_3·HF] [Sb_2F_{11}] and ([XeF_3·HF][Sb_2F_{11}])$_2$·[H_5F_4][SbF_6] (Figure 6.4) with the contacts ranging from 2.935(1) to 2.967(1) Å and 2.847(3) to 3.088(3) Å, respectively. There is an additional contact (3.088(3) Å) in the ordered structure, ([XeF_3·HF][Sb_2F_{11}])$_2$·[H_5F_4][SbF_6], that occurs between the XeF_3^+ cation and the $Sb_2F_{11}^-$ anion which presumably better anchors the cation to give an ordered structure.

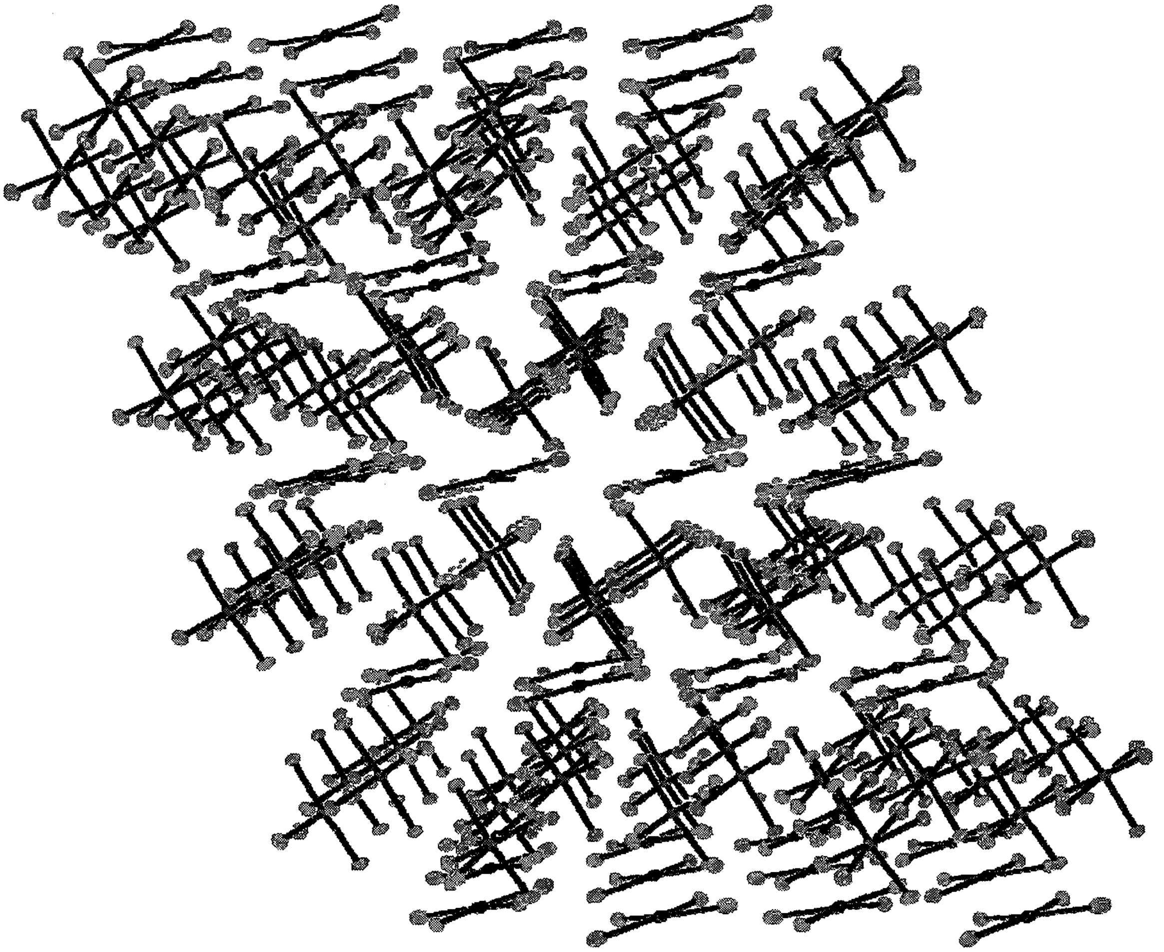

Figure 6.3. Crystal packing for $[XeF_3{\cdot}HF][Sb_2F_{11}]$ viewed along the *b*-axis; thermal ellipsoids are shown at the 50% probability level.

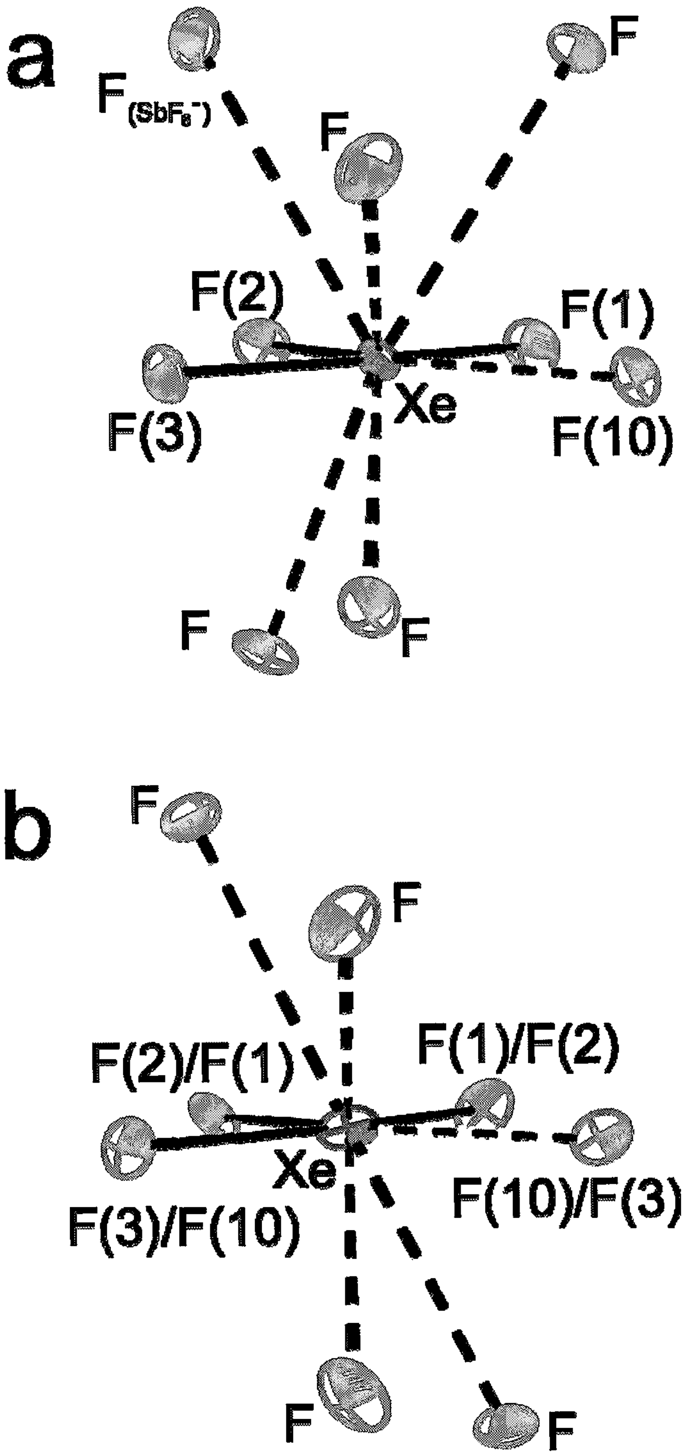

Figure 6.4. Secondary coordination sphere of the XeF_3^+·HF adduct-cation subunit in the X-ray crystal structures of (a) ($[XeF_3·HF][Sb_2F_{11}])_2·[H_5F_4][SbF_6]$ and (b) $[XeF_3·HF][Sb_2F_{11}]$; thermal ellipsoids are shown at the 50% probability level.

6.2.2.2. [H_5F_4][SbF_6]. The hydrogen atoms of the acidium ion in the crystal structure of ([$XeF_3{\cdot}HF$][Sb_2F_{11}])$_2$·[H_5F_4][SbF_6] could not be observed in the difference map, which is also the case for the $H_3F_2^+$ and H_2F^+ cations,[229] but not for $H_7F_6^+$, where the hydrogen atoms were observed.[228] The SbF_6^- anion and fluorine atoms of the $H_5F_4^+$ cation form a chain structure (Figure 6.5) that is consistent with the other acidium ion salts.[228,229] The F---F distances between the SbF_6^- anion and the closest fluorine atom of the cation decrease from 2.444(4) Å to 2.337(3) Å, between the next closest fluorine atoms, and finally to 2.293(5) Å between the two central fluorine atoms of the $H_5F_4^+$ cation. These distances are in excellent agreement with previously observed F---F interatomic distances in $H_7F_6^+$ (2.284(4)–2.450(2) Å),[228] $H_3F_2^+$ (2.30(1)–2.41(1) Å),[229] and H_2F^+ (2.64–2.78 Å).[229]

6.2.3. Raman Spectroscopy. The low-temperature Raman spectra of solid [$^{1/2}H^{16/18}OXeF_2$][AsF_6], [$H^{16/18}OXe(F)_2{}^{16/18}OXeF_2$][$AsF_6$], [$FXe^{16/18}OXeF_2$][$AsF_6$], and [$FXe^{16/18}OXe(F)_2{}^{16/18}OXeF_2$] [$AsF_6$], are identical to low-temperature spectra recorded under solid HF solvent, with the latter providing better signal to noise ratios. Consequently, the Raman spectra depicted in Figures 6.6–6.9 and the observed and calculated frequencies and their assignments listed in Tables 6.4–6.7 and A3.3–A3.7 are for spectra recorded under HF.

The spectral assignments for [$^{1/2}H^{16/18}OXeF_2$][AsF_6], [$H^{16/18}OXe(F)_2{}^{16/18}OXeF_2$] [$AsF_6$], [$FXe^{16/18}OXeF_2$][$AsF_6$], and [$FXe^{16/18}OXe(F)_2{}^{16/18}OXeF_2$][$AsF_6$] were made by comparison with the calculated frequencies and Raman intensities (Tables 6.4–6.7) of the

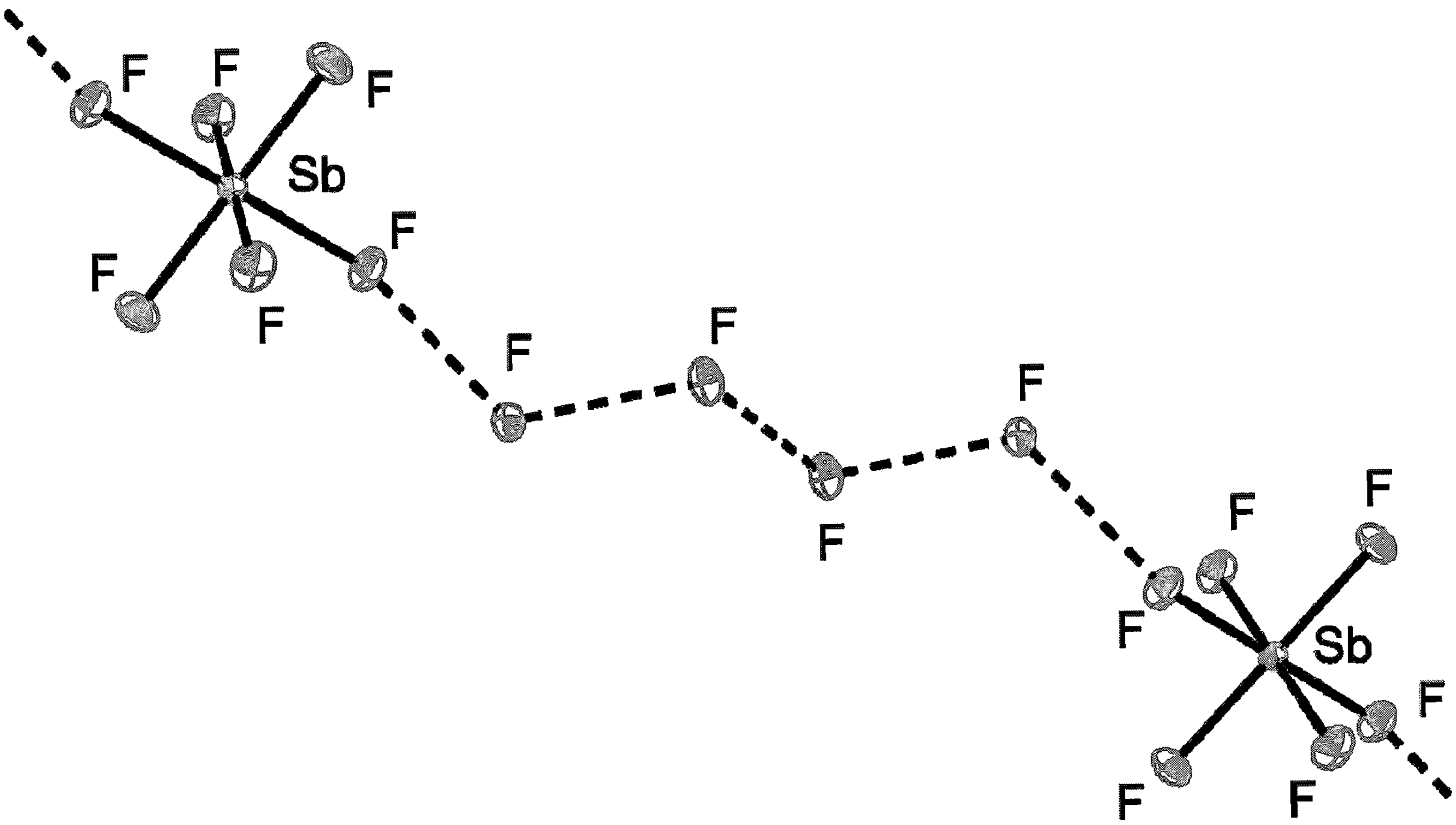

Figure 6.5. The $[H_5F_4][SbF_6]$ unit in the X-ray crystal structure of $([XeF_3{\cdot}HF][Sb_2F_{11}])_2{\cdot}[H_5F_4][SbF_6]$; thermal ellipsoids are shown at the 50% probability level.

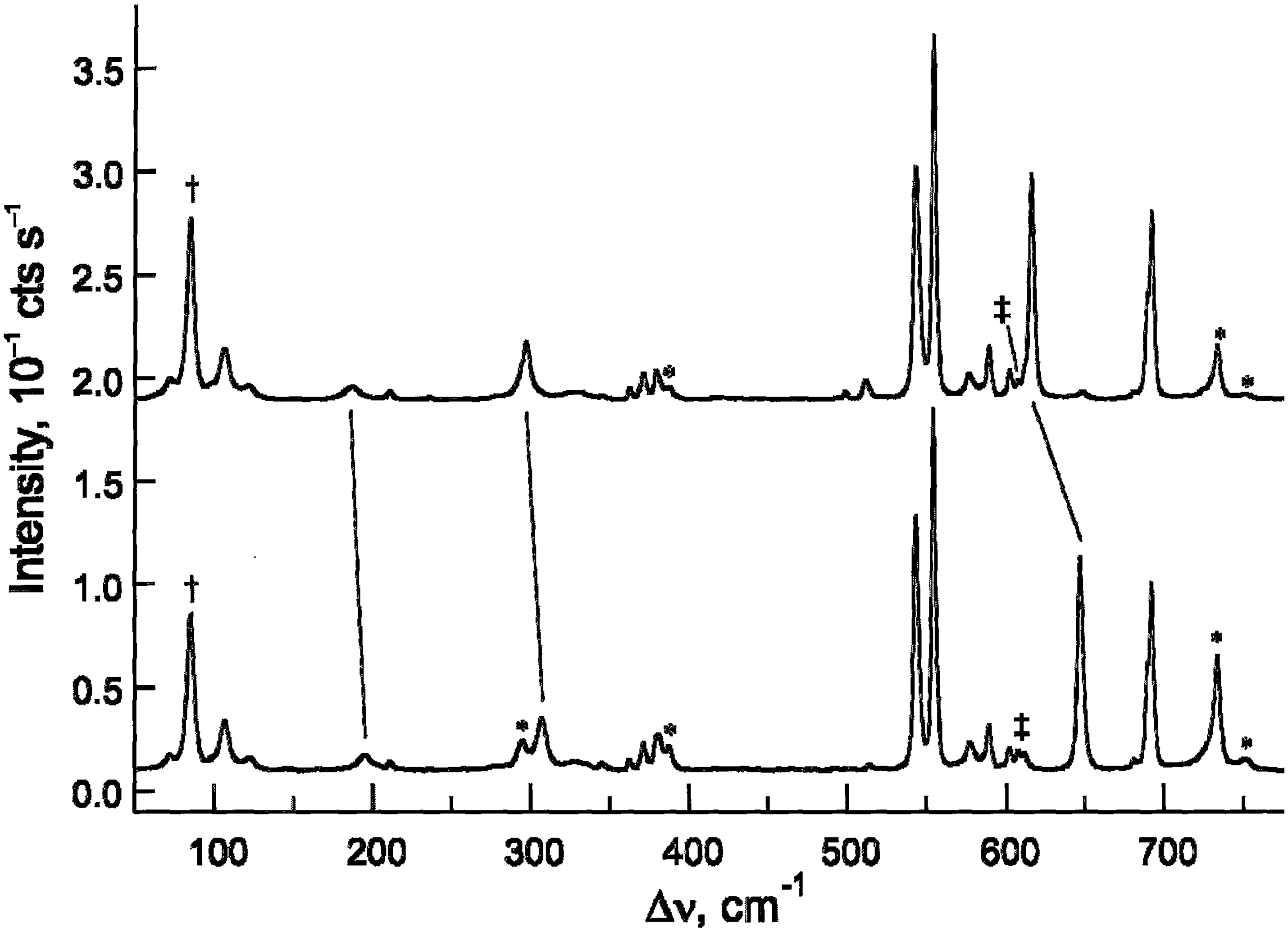

Figure 6.6. Raman spectra of natural abundance (lower trace) and 97.8% ^{18}O-enriched (upper trace) of $[HOXeF_2][AsF_6]$ recorded at −150 °C under HF solvent using 1064-nm excitation. Symbols denote FEP sample tube lines (*), instrumental artifact (†), and $[XeF][AsF_6]$ impurity (‡).

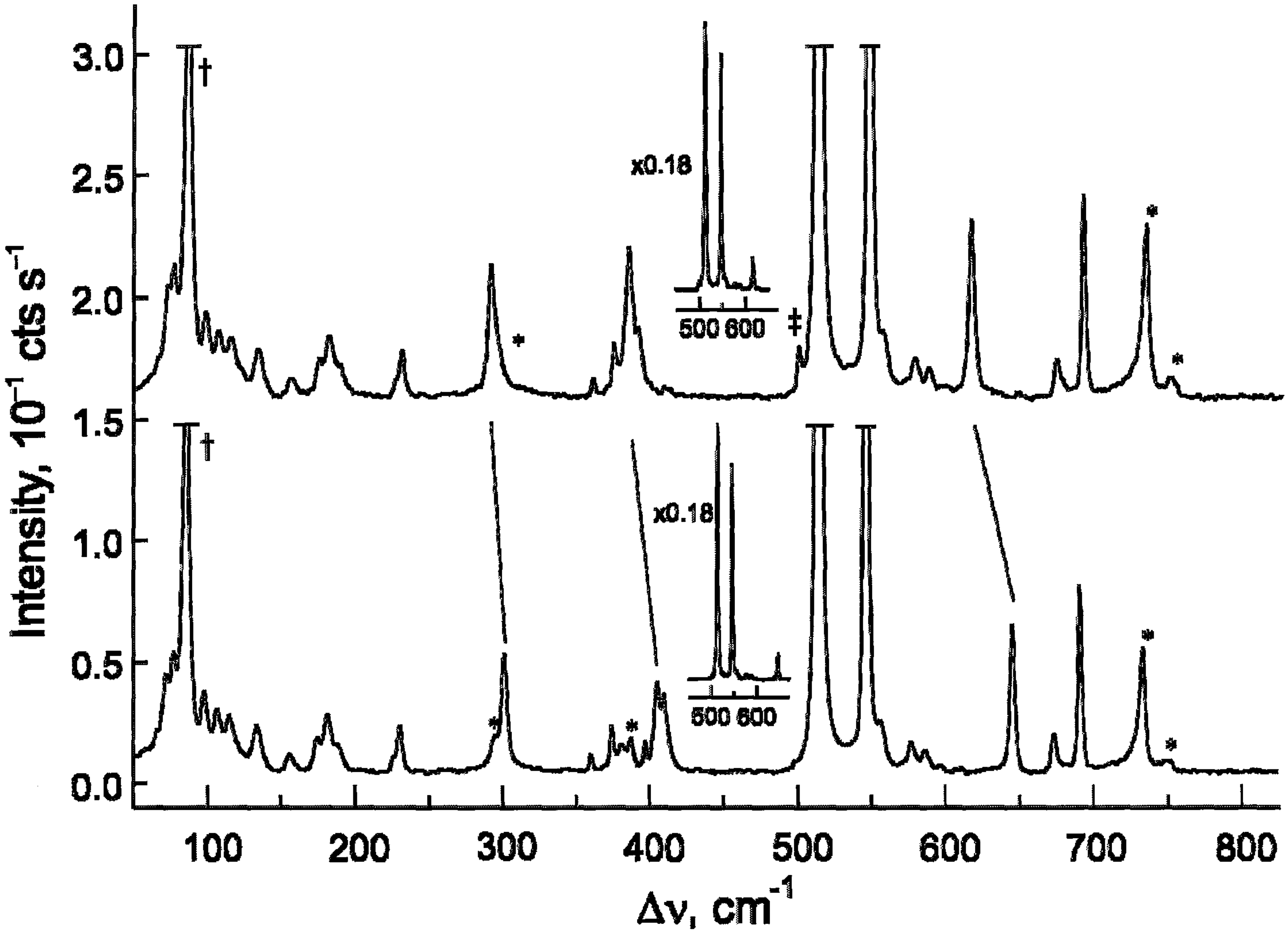

Figure 6.7. Raman spectra of natural abundance (lower trace) and 97.8% ^{18}O-enriched (upper trace) of $[FXeOXeF_2][AsF_6]$ recorded at −150 °C under HF solvent using 1064-nm excitation. Symbols denote FEP sample tube lines (*), instrumental artifact (†), and $[FXe^{18}OXe(F)_2{}^{18}OXe(F)_2][AsF_6]$ impurity (‡).

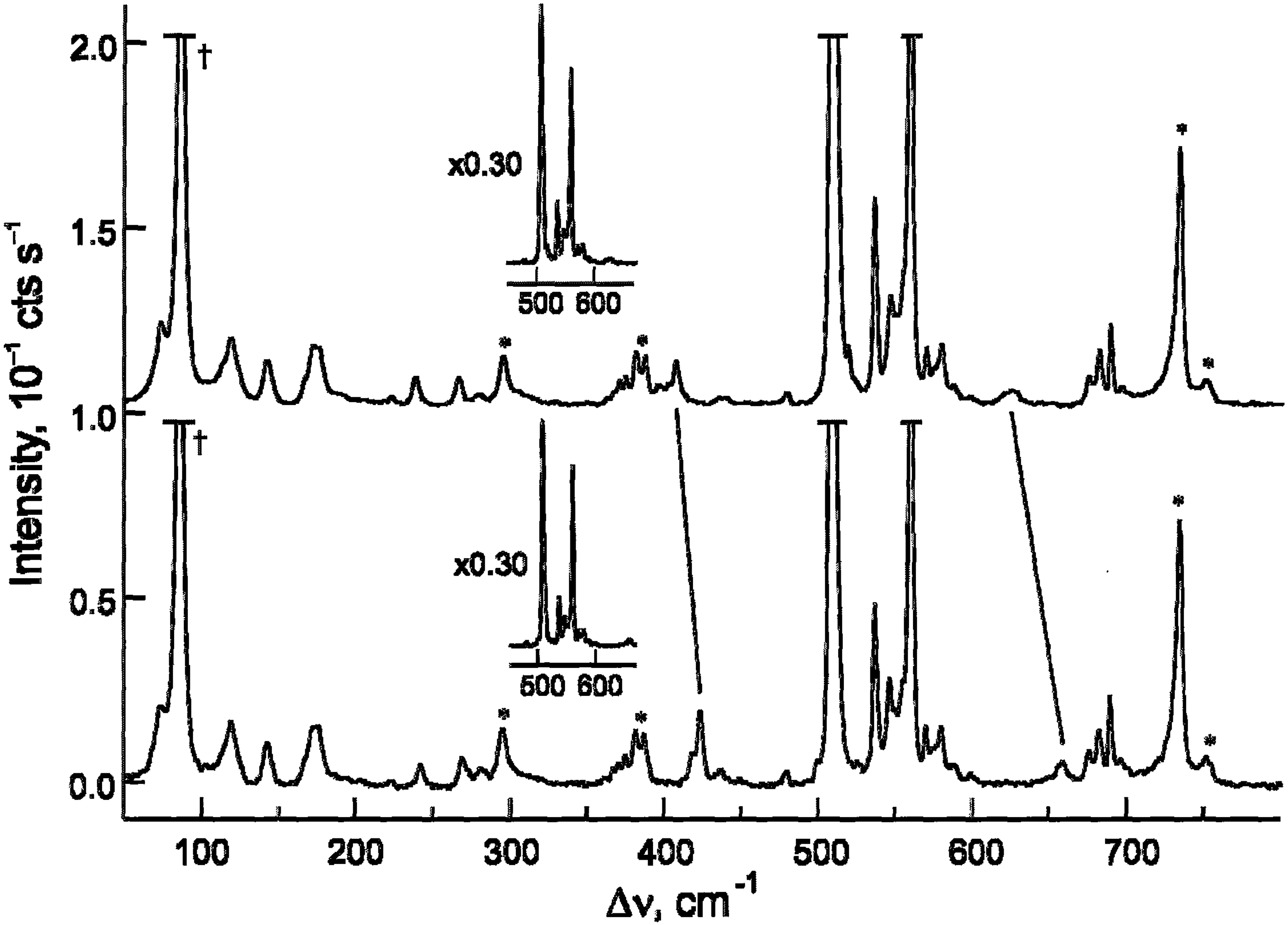

Figure 6.8. Raman spectra of natural abundance (lower trace) and 97.8% ^{18}O-enriched (upper trace) of $[HOXe(F)_2OXe(F)_2][AsF_6]$ recorded at −150 °C under HF solvent using 1064-nm excitation. Symbols denote FEP sample tube lines (*) and instrumental artifact (†).

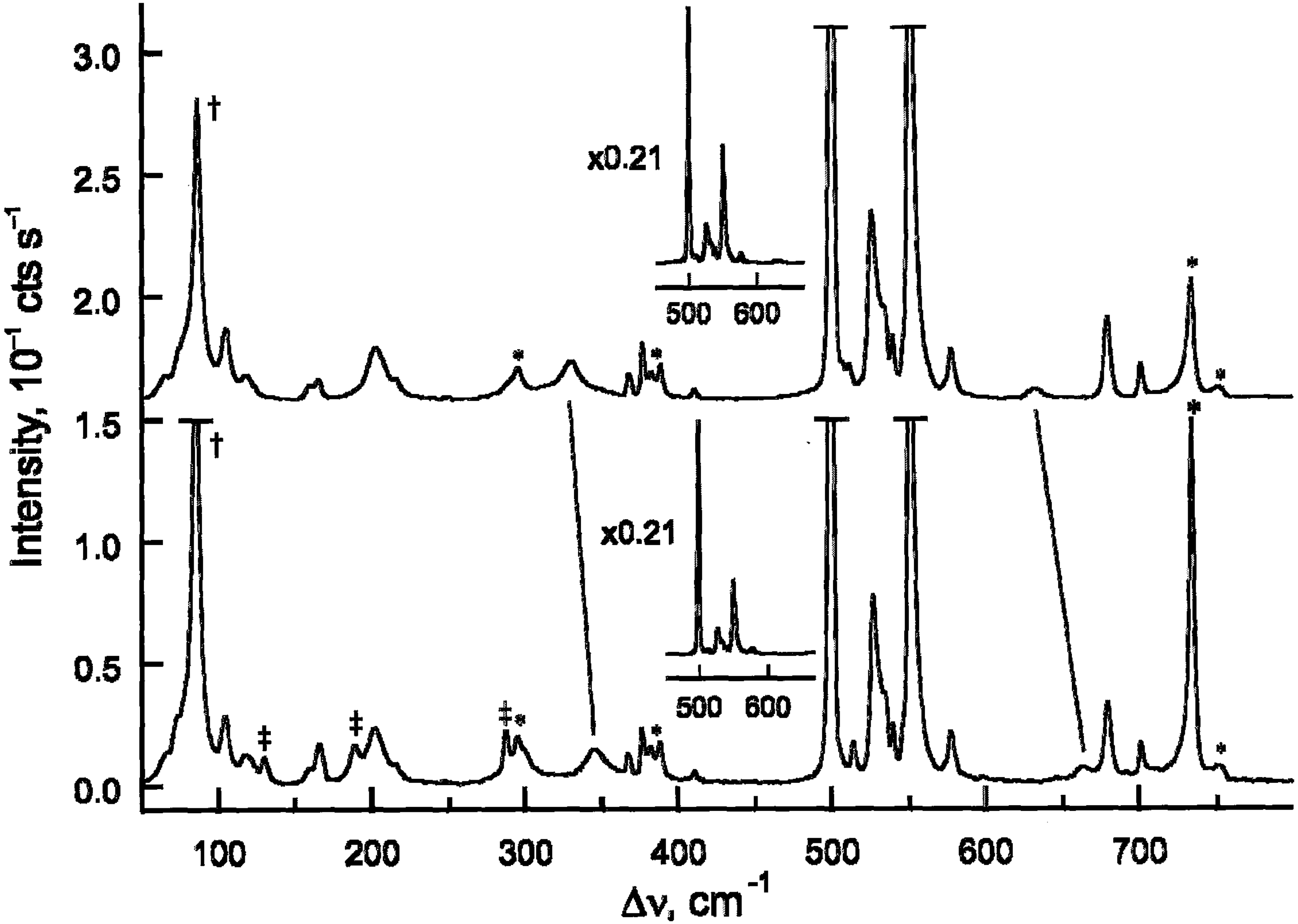

Figure 6.9. Raman spectra of natural abundance (lower trace) and 97.8% ^{18}O-enriched (upper trace) of $[FXeOXe(F)_2OXe(F)_2][AsF_6]$ recorded at −150 °C under HF solvent using 1064-nm excitation. Symbols denote FEP sample tube lines (*), instrumental artifact (†), and $XeOF_2{\cdot}n$HF(‡).

Table 6.4. Experimental Raman Frequencies[a] and Intensities[b] for $[^{1/2}H^{16/18}OXeF_2][AsF_6]$[c]

$^{1}H^{16}O$	$^{1}H^{18}O$	$^{16/18}\Delta\nu$	$^{2}H^{16}O$	$^{2}H^{18}O$	$^{16/18}\Delta\nu$	$^{1(16)/2(16)}\Delta\nu$	$^{1(18)/2(18)}\Delta\nu$	assgnt[d]
n.o.	n.o.	n.o.	n.o.	n.o.	n.o.	n.o.	n.o.	$\nu(O_1H)$
1264.6(2)	1261.2(2)	−3.4	927.6(1)	922.0(1)	−5.6	−337.0	−339.2	$\delta(Xe_1O_1H)$
692.0(52)	692.0(52)	0.0	692.0(66)	691.9(55)	0.1	0.0	−0.1	$\nu_1(A_{1g})\ (AsF_6^-)$
689.7(30)	689.6(29)	−0.1	689.2(32)	689.1(31)	−0.1	−0.5	−0.5	
646.7(59)	615.8(62)	−30.9	640.9(66)	611.0(68)[f]	−29.9	−5.8	−4.8	$\nu(Xe_1O_1)$
602.0(6)	601.9(8)	−0.1	600.5(7)	600.3(9)	−0.2	−1.5	−1.6	$\nu(Xe_1F_1) - \nu(Xe_1F_2)$
588.8(12)	588.4(14)	−0.4	588.1(16)	587.8(18)	−0.3	−0.7	−0.6	$\nu_2(E_g)\ (AsF_6^-)$
577.0(7)	576.3(7)	−0.7	567.8(7)	567.1(9)	−0.7	−9.2	−9.2	
554.7(100)	554.6(100)	−0.1	554.6(100)	554.5(100)	−0.1	−0.1	−0.1	$\nu(Xe_1F_1) + \nu(Xe_1F_2)$
543.6(71)	543.5(64)	−0.1	543.5(66)	543.1(62)	−0.4	−0.1	−0.4	
380.2(4)[e]	379.2(6)[e]	−1.0	379.2(4)	378.9(6)	−0.3	−1.0	−0.3	$\nu_5(T_{2g})\ (AsF_6^-)$
371.6(7)	371.0(7)	−0.6	371.1(7)	370.7(9)	−0.4	−0.5	−0.3	
362.3(3)	362.3(3)	0.0	362.4(3)	362.2(4)	−0.2	0.1	−0.1	
328.0(2),br	327.5(2),br	−0.5	260.8(3),br	259.2(3),br	−1.6	−67.2	−68.3	$\rho_w(Xe_1O_1H)$
307.0(14)	296.9(13)	−10.1	313.1(9)	301.9(9)	−11.2	6.1	5.0	$\delta(OXe_1F_1) - \delta(OXe_1F_2)$
235.6(1)	236.1(1)	0.5	235.5(1)	236.2(1)	0.7	0.1	0.1	$\delta(F_1Xe_1F_2)_{o.o.p.}$
210.4(2)	210.3(2)	−0.1	208.8(2)	208.4(3)	−0.4	−1.6	−1.9	$\delta(F_1Xe_1F_2)_{i.p.}$
194.6(4),br	186.4(4),br	−8.2	187.6(4),br	181.6(4),br	−6.0	−7.0	−4.8	$\rho_r(HO_1Xe_1F_1\ F_2)_{o.o.p.}$
122.3(3)	121.0(4)	−1.3	121.8(5)	120.3(7)	−1.5	−0.5	−0.7	
106.3(14)	106.1(14)	−0.2	106.2(15)	106.1(15)	−0.1	0.1	0.0	

[a] Frequencies are given in cm^{-1}. [b] Values in parentheses denote relative Raman intensities. [c] Raman spectra were recorded in FEP sample tubes at −150 °C using 1064-nm excitation. The abbreviations denote broad (br) and not observed (n.o.). Weak bands at 611.7(5) and 607.6(5) in the spectra (not listed) are assigned to $[XeF][AsF_6]$.[154] [d] The abbreviations denote stretch (ν), bend (δ), wag (ρ_w), rock (ρ_r), in-plane bend (i.p.), and out-of-plane bend (o.o.p.). The in-plane and out-of-plane mode descriptions are relative to the $XeOF_2$ plane (Figure 6.10). [e] The band intensity has been corrected for overlap with a FEP band. [f] The band intensity has been corrected for overlap with a $[XeF][AsF_6]$ band.

Table 6.5. Experimental Raman Frequencies[a] and Intensities[b] for [FXe$^{16/18}$OXeF$_2$][AsF$_6$][c]

^{16}O	^{18}O[d]	$^{16/18}\Delta\nu$	assgnt[e]
691.2(12)	691.3(13)	0.1	$\nu_1(A_{1g})$ (AsF_6^-)
673.7(2)	673.5(3)	–0.2	
645.4(10)	615.6(12)	–29.8	$\nu(Xe_1O_1) - \nu(Xe_2O_1)$
586.2(1)	587.1 sh	0.9	$\nu_2(E_g)$ (AsF_6^-)
577.1(2)	577.2(3)[f]	0.2	
556.0(3)	555 sh	–1.0	$\nu(Xe_2F_3)$
545.6(84)	545.6(89)	0.0	
513.5(100)	511.1(100)	–2.4	$\nu(Xe_1F_1) + \nu(Xe_1F_2)$
409.4(5)	390.3(5)	–19.1	$\nu(Xe_1O_1) + \nu(Xe_2O_1)$
405.1(6)	384.0(6)	–21.1	
397.0(2)			$\nu_5(T_{2g})$ (AsF_6^-)
373.9(3)	373.8 sh	–0.1	
360.1(1)	359.8(1)	–0.2	
300.6(8)	290.0(7)	–10.6	$\delta(OXe_1F_1) - \delta(OXe_1F_2)$
229.9(2)	229.6(3)	–0.3	$\delta(F_1Xe_1F_2)_{o.o.p.}$
225.6(1)	225.6(1)	0.0	
187.7(2)	187.6(2)	–0.1	$\delta(F_1Xe_1F_2)_{i.p.}$
181.3(4)	181.1(4)	–0.2	
174.7(2)	173.9(2)	–0.8	coupled deformation modes
155.7(1)	155.5(1)	–0.2	
132.9(3)	132.4(3)	–0.5	
119.8(2)	120.3(2)	0.5	
114.2(4)	114.3(4)	0.1	
106.2(4)	105.4(7)	–0.8	
97.2(5)	96.9(7)	–0.3	
76.0(8)	75.7(12)	–0.3	
71.3(7)	71.6(9)	0.3	

[a] Frequencies are given in cm^{-1}. [b] Values in parentheses denote relative Raman intensities. [c] Raman spectra were recorded in FEP sample tubes at −150 °C using 1064-nm excitation. The abbreviation denotes a shoulder (sh). [d] A weak band at 498.5(3) in the ^{18}O spectrum is attributed to [FXe^{18}OXe(F)$_2$^{18}OXeF$_2$][AsF$_6$]. [e] The abbreviations denote stretch (ν), bend (δ), in-plane bend (i.p.), and out-of-plane bend (o.o.p.). The in-plane and out-of-plane mode descriptions are relative to the XeOF$_2$ plane (Figure 6.10). [f] The band intensity has been corrected for overlap with the FEP band occurring at 578 cm^{-1}.

Table 6.6. Experimental Raman Frequencies[a] and Intensities[b] for $[H^{16/18}OXe(F)_2{}^{16/18}OXeF_2][AsF_6]$[c]

^{16}O[d]	^{18}O[d]	$^{16/18}\Delta\nu$	assgnt[e]
695.6(3)	695.7(2)	0.1	$\nu_1(A_{1g})$ (AsF_6^-)
688.6(11)	688.7(8)	0.1	
681.4(6)[f]	681.3(5)	–0.1	
675.4(4)	676.0 sh	0.6	
658.1(3), br	624.6(1), br	–33.5	$[\nu(Xe_3O_2) - \nu(Xe_1O_2)] + \nu(Xe_1O_1)$
586.8(2)	586.8(2)	0.0	$\nu_2(E_g)$ (AsF_6^-)
579.2(7)	579.2(7)	0.0	
573.6(5)	573.8(4)	–0.2	
569.1(7)	569.1(6)	0.0	
559.4(82)	558.9(62)	–0.5	$\nu(Xe_1F_1) + \nu(Xe_1F_2)$
549.7(9)	549.8(9)	0.1	
545.9(13)	546.1(11)	0.2	
536.1(22)	535.6(21)	–0.5	
510.5 sh	510.2 sh	–0.3	$\nu(Xe_3F_4) + \nu(Xe_3F_5)$
507.3(100)	506.8(100)	–0.5	
436.4(2)	438.1(1)	1.7	
422.9(9)	406.5(4)	–16.4	$\delta(O_2Xe_3F_4) - \delta(O_2Xe_3F_5)$
418.2(4)	395.2(2)	–23.0	
374.5(4)	373.9(3)	–0.6	$\nu_5(T_{2g})$ (AsF_6^-)
370.0(2)	370.4(3)	0.4	
366.6(2)	366.4(1)	–0.2	
281.4(2)	278.8(1)	–2.6	$\delta(O_1Xe_1F_1) - \delta(O_1Xe_1F_2)$
268.5(3)	265.3(2)	–3.2	
241.4(2)	237.5(3)	–3.9	
221.5(1)	221.9(1)	0.4	$\delta(F_4Xe_3F_5)_{i.p.} + \delta(F_1Xe_1F_2)_{o.o.p.}$
173.5(7), br	171.4(6), br	–2.1	$\delta(F_1Xe_1F_2)_{i.p.} + \delta(F_4Xe_3F_5)_{i.p.}$
142.2(5)	140.7(5)	–1.5	
118.2(8)	116.9(8)	–1.3	

[a] Frequencies are given in cm^{-1}. [b] Values in parentheses denote relative Raman intensities. [c] Raman spectra were recorded in FEP sample tubes at −150 °C using 1064-nm excitation. The abbreviations denote shoulder (sh) and broad (br). [d] Weak bands observed at 598.1(1), 554.4 sh, 479.7(2) in the ^{16}O spectrum and at 479.3(1) in the ^{18}O spectrum are assigned to $Xe_3OF_3^+$. [e] The abbreviations denote stretch (ν), bend (δ), in-plane bend (i.p.), and out-of-plane bend (o.o.p.). The in-plane and out-of-plane mode descriptions are relative to the local $XeOF_2$ plane (Figure 6.10). [f] The band intensity has been corrected for overlap with the AsF_6^- band of $[Xe_3OF_3][AsF_6]$ occurring at 681 cm^{-1}.[71]

Table 6.7. Experimental Raman Frequencies[a] and Intensities[b] for $[\mathrm{FXe^{16/18}OXe(F)_2{}^{16/18}OXeF_2}][\mathrm{AsF_6}]$[c]

^{16}O	^{18}O	$^{16/18}\Delta\nu$	assgnt[d]
700.8(3)	700.8(3)	0.0	$\nu_1(A_{1g})$ (AsF_6^-)
679.1(7)	679.1(15)	0.0	
662.4(1) br	632.1(1) br	–30.3	$[\nu(Xe_3O_2) - \nu(Xe_1O_2)] + [\nu(Xe_1O_1) - \nu(Xe_2O_1)]$
577.1(4)	576.9(7)	–0.2	$\nu_2(E_g)$ (AsF_6^-)
550.3(46)	550.2(45)	–0.1	$\nu(Xe_2F_3)$
539.4(5)	539.3(5)	–0.1	$[\nu(Xe_1F_1) + \nu(Xe_1F_2)] + [\nu(Xe_3F_4) + \nu(Xe_3F_5)]$
534.0 sh	533.5 sh	–0.5	
526.7(16)	525.5(15)	–1.2	
513.6(3)[e]	510.6(3)[e]	–3.0	$[\nu(Xe_1F_1) + \nu(Xe_1F_2)] - [\nu(Xe_3F_4) + \nu(Xe_3F_5)]$
498.6(100)	498.7(100)	0.1	
409.9(1)	409.9(1)	0.0	
375.5(5)	375.6(4)	0.1	$\nu_5(T_{2g})$ (AsF_6^-)
366.6(2)	366.7(2)	0.1	
344.7(3) br	329.7(3) br	–15.0	$\delta(O_2Xe_3F_4) - \delta(O_2Xe_3F_5)$
299.2 sh	287.8 sh	–11.4	$\delta(O_1Xe_1F_1) - \delta(O_1Xe_1F_2)$
214.7(2)	214.9(2)	0.2	$\delta(F_4Xe_3F_5)_{i.p.} + \delta(F_1Xe_1F_2)_{o.o.p.}$
201.7(2)	201.9(4)	0.2	$\delta(F_4Xe_3F_5)_{i.p.} + \delta(F_1Xe_1F_2)_{i.p.}$
165.8(1)[f]	164.2(2)	–1.6	$\delta(F_3Xe_2O_1)_{i.p.} + \delta(F_1Xe_1F_2)_{i.p.}$
159.0(1)	159.0(1)	0.0	$\delta(F_3Xe_2O_1)_{i.p.} - [\delta(F_1Xe_1F_2)_{i.p.}]_{small}$
117.5(2)	117.0(2)	–0.5	
104.0(6)	103.6(6)	–0.4	

[a] Frequencies are given in cm^{-1}. [b] Values in parentheses denote relative Raman intensities. [c] Raman spectra were recorded in FEP sample tubes at −150 °C using 1064-nm excitation. The abbreviations denote shoulder (sh) and broad (br). [d] The abbreviations denote stretch (ν), bend (δ), in-plane bend (i.p.), and out-of-plane bend (o.o.p.). The in-plane and out-of-plane mode descriptions are relative to the local $XeOF_2$ plane (Figure 6.10). [e] These bands may arise from $FXe^{16}OXeF_2^+$. [f] The band intensity has been corrected for overlap with the $Xe^{16}OF_2.n$HF band occurring at 166.0 cm^{-1}.[125]

energy-minimized geometries (Figure 6.10). Vibrational frequencies calculated at the PBE1PBE, B3LYP, and MP2 levels of theory (Tables A3.3–A3.7) reproduced the observed frequency trends across the series of compounds and therefore only the PBE1PBE values are referred to in the ensuing discussion. It should be noted that the calculated Raman intensities of the to Xe–O stretching bands are consistently overestimated for each system when compared with the experimental intensities, as observed for $Xe_3OF_3^+$.[71] In all cases, symmetry lowering splits the three Raman-active modes expected for octahedral AsF_6^-, namely $\nu_1(A_{1g})$, $\nu_2(E_g)$, and $\nu_5(T_{2g})$. The additional splittings, which include the A_{1g} band, can only be accounted for by vibrational coupling within the unit cell (factor-group splitting). The anion bands were assigned by comparison with other AsF_6^- salts in which there are significant interactions by means of fluorine bridging between the cations and the anions.[43,154,232]

6.2.3.1. [HOXeF$_2$][AsF$_6$]. The Raman spectra of $[^{1/2}H^{16/18}OXeF_2][AsF_6]$ exhibit two bands that are $^{1/2}$H-dependent, and four bands that are both $^{1/2}$H- and $^{16/18}$O-dependent, in good agreement with the calculated spectra where one band is predicted to be $^{1/2}$H-dependent, and five bands are both $^{1/2}$H- and $^{16/18}$O-dependent. The minor vibrational differences that arise between experimental and calculated frequencies of modes involving the hydrogen atom presumably arise because the calculated ion-pair models, $[^{1/2}H^{16/18}OXeF_2][AsF_6]$, are for isolated gas-phase ion pairs (see Computational Results), whereas it is also expected that there will be significant hydrogen bonding between nearest neighbor ion pairs in the solid state.

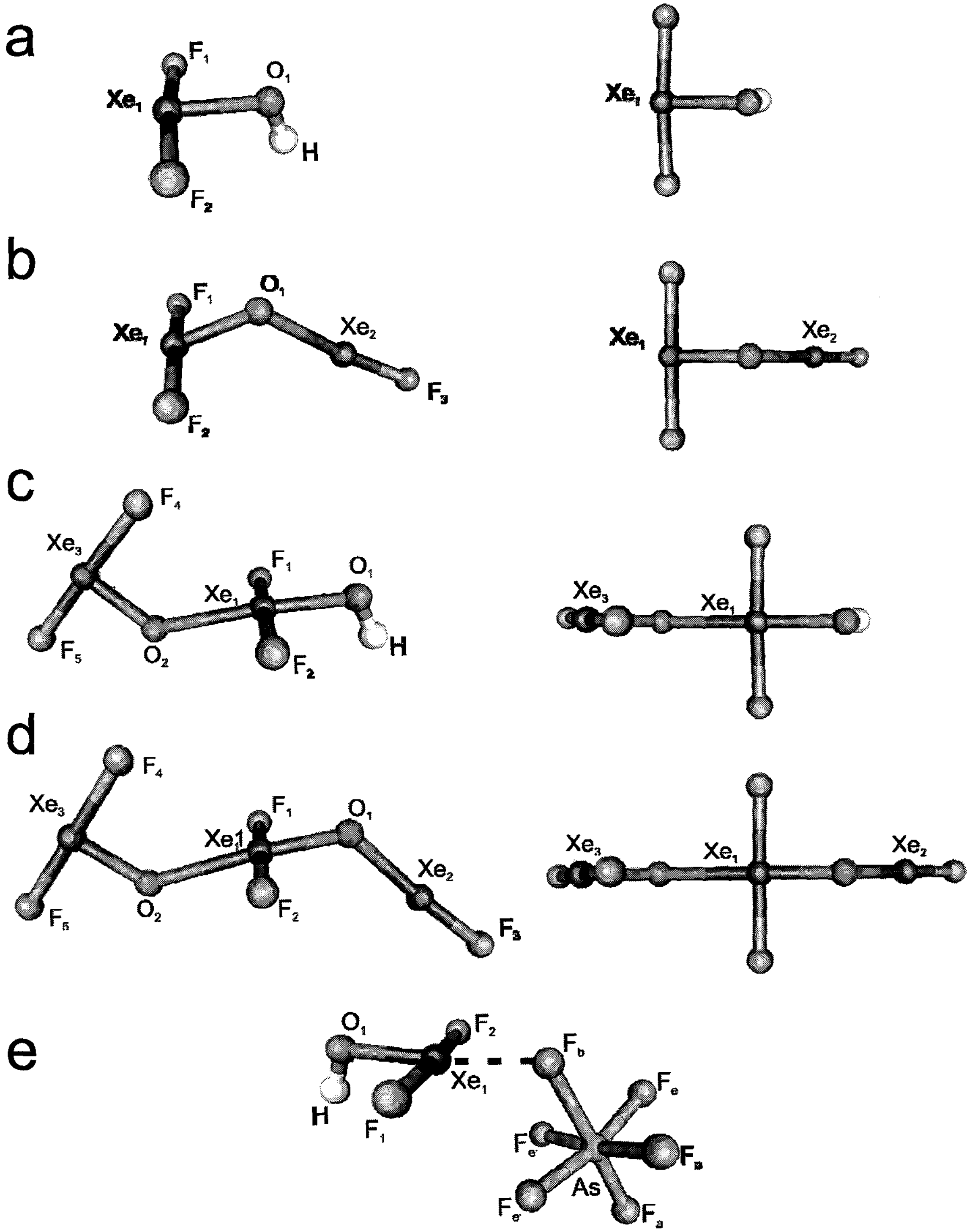

Figure 6.10. Calculated geometries [B3LYP/aug-cc-pVTZ(-PP)] for (a) $HOXeF_2^+$, (b) $FXeOXeF_2^+$, (c) $HOXe(F)_2OXeF_2^+$, (d) $FXeOXe(F)_2OXeF_2^+$, and (e) $[HOXeF_2][AsF_6]$.

The most intense bands in the spectra occur at 543.6 and 554.7 cm^{-1} and do not show isotopic shifts. These bands correspond to the factor-group split symmetric XeF_2 stretching mode, $\nu(Xe_1F_1) + \nu(Xe_1F_2)$, in excellent agreement with the calculated value of 562.8 cm^{-1}, and with the symmetric stretching mode of the axial Xe–F bonds in $[XeF_3][SbF_6]$ (573(88); 564(94), 576(94) cm^{-1}).[46] The out-of-phase $\nu(Xe_1F_1) - \nu(Xe_1F_2)$ mode is assigned to the weaker band at 602.0 cm^{-1} and is also well modelled by calculations (618.9 cm^{-1}). The most substantial $^{16/18}O$-isotopic shift (−30.9 cm^{-1}) occurs for the band at 646.7 cm^{-1}. This band also shows a $^{1/2}H$-isotopic shift (−5.8 cm^{-1}) and is assigned to $\nu(Xe_1O_1)$, which is postulated to show $^{1/2}H$- and $^{16/18}O$-isotopic shifts of −27.6 and −6.8 cm^{-1}, respectively. The in-plane bend, $\delta(OXe_1F_1) - \delta(OXe_1F_2)$, is also expected to show a $^{16/18}O$-isotopic shift (−10.3 cm^{-1}) and is assigned to the band at 307.0 which shows an isotopic shift of −10.1 cm^{-1}. The broad band at 194.6 cm^{-1} also shows $^{1/2}H$- and $^{16/18}O$-sensitivity and is assigned to $\rho_r(HOXe_1F_1F_2)_{o.o.p.}$, in agreement with the calculated values.

The highest frequency mode expected for the $HOXeF_2^+$ cation is $\nu(O_1H)$. It is predicted to occur at 3763.9 cm^{-1} and is expected to show significant $^{1/2}H$- and $^{16/18}O$-sensitivities (−1023 and −12.5 cm^{-1}, respectively). However, the Raman band corresponding to this mode could not be observed, which is likely the result of the low polarizability change associated with the O–H stretch, causing the band to be weak. The XeOH bending and wagging modes are observed as a weak band at 1264.2 cm^{-1} and a broad, weak band at 328.0 cm^{-1} which display ^{2}H-isotopic shifts of −337.0 and −67.2 cm^{-1}, respectively, with the bending mode also displaying a ^{18}O-isotopic shift of −3.4

cm^{-1}. While the isotopic shifts are well modeled by the calculations [^{2}H: −306.2, −61.5 cm^{-1}; ^{18}O: −3.3 cm^{-1}], the XeOH wagging mode is likely underestimated because the simplified model neglects hydrogen bonding involving neighboring ion pairs which would shift the mode to higher frequency.[233]

The in-plane and out-of-plane XeF_2 bending modes occur at 210.4 and 235.6 cm^{-1}, respectively, and display neither $^{1/2}$H- nor $^{16/18}$O-isotopic shifts, in agreement with the calculated ion pair frequencies.

6.2.3.2. [$F^{II}XeO^{IV}XeF_2$][PnF_6] (Pn = As, Sb). The Raman spectra of [$FXeOXeF_2$][AsF_6] and [$FXeOXeF_2$][SbF_6] are almost identical, with the exception of the anion modes. In general, the spectra of $FXe^{16/18}OXeF_2^+$ resemble those of $H^{16/18}OXeF_2^+$, although the latter frequencies are slightly higher, and they are in accord with the frequency trend that is modeled by the calculations.

The Xe^{II}–O and Xe^{IV}–O bonds of $FXeOXeF_2^+$ are not symmetric (see Calculated Geometries) and therefore the coupled $\nu(Xe_1O_1) - \nu(Xe_2O_2)$ and $\nu(Xe_1O_1) + \nu(Xe_2O_2)$ modes occur at significantly different frequencies. The former mode occurs at 645.4 cm^{-1} and displays a $^{16/18}$O-isotopic shift of −29.8 cm^{-1} which is in agreement with the calculated values and with ν(XeO) in $HOXeF_2^+$ (646.7, $^{16/18}\Delta\nu$: −30.9 cm^{-1}). The in-phase mode, $\nu(Xe_1O_1) + \nu(Xe_2O_1)$ is factor-group split and occurs at 405.1 and 409.4 cm^{-1} with $^{16/18}$O-isotopic shifts of −21.1 and −19.1 cm^{-1}, which are in good agreement with the calculated frequencies and isotopic shifts. The only other band that displayed a $^{16/18}$O-isotopic shift (−10.6 cm^{-1}) occurred at 300.6 cm^{-1} and is assigned to $\delta(OXe_1F_1)$ −

δ(OXe_1F_2) which also agrees well with the calculated frequency and isotopic shift, and with the corresponding band in [$HOXeF_2$][AsF_6] (307.0, $^{16/18}\Delta\nu$: −10.1 cm^{-1}).

The bands at 545.6 and 556.0 are assigned to the terminal ν(Xe_2F_3) stretch which occur to significantly lower frequency than ν(XeF) in [XeF][AsF_6] (608 and 610 cm^{-1})[154] and is indicative of significant bonding between O_1 and Xe_2, which renders Xe_2 less electropositive. The symmetric stretch, ν(Xe_1F_1) + ν(Xe_1F_2), of $FXeOXeF_2^+$ occurs at lower frequency (513.5 cm^{-1}) relative to $HOXeF_2^+$ (543.6, 554.7 cm^{-1}) but is higher than in $XeOF_2$ (467 cm^{-1}),[125] which is consistent with cation formation. The bands corresponding to the in-plane and out-of-plane F_1–Xe_1–F_2 bending modes are each factor-group split and are observed at 181.7 and 187.7 cm^{-1} and 225.6 and 229.9 cm^{-1}, respectively. Both modes are also in good agreement with the calculated values.

6.2.3.3. [$HOXe(F)_2OXeF_2$][AsF_6] and [$F^{II}XeO^{IV}Xe(F)_2O^{IV}XeF_2$][$AsF_6$]. The Raman spectra of [$HOXe(F)_2OXeF_2$][AsF_6] and [$F^{II}XeO^{IV}Xe(F)_2O^{IV}XeF_2$][$AsF_6$] are very similar to each other, as is the case for the $HOXeF_2^+$ and $FXeOXeF_2^+$ cations discussed above. In general, the vibrational frequencies of the longer chain cations occur at frequencies similar to the corresponding modes in the shorter chain cations. Only three bands display $^{16/18}O$-isotopic dependencies in [$FXeOXe(F)_2OXeF_2$][AsF_6] and belong to three distinct vibrational modes. The related three modes are observed in [$HOXe(F)_2OXeF_2$][AsF_6], however, the lower frequency bands, which correspond to bending modes, are factor-group split. The highest frequency, isotopically dependent modes occur at 658.1 and 662.4 cm^{-1} for the $HOXe(F)_2OXeF_2^+$ and $FXeOXe(F)_2OXeF_2^+$ cations, respectively, and are assigned to the coupled Xe–O stretches, [ν(Xe_3O_2) – ν(Xe_1O_2)] + ν(Xe_1O_1) and [ν(Xe_3O_2) – ν(Xe_1O_2)] + [ν(Xe_1O_1) – ν(Xe_2O_1)], respectively. The calculated Xe_1–O_1 and Xe_3–O_2 stretching frequencies occur at significantly different values ($HOXe(F)_2OXeF_2^+$: 626.2, 685.1 cm^{-1}; $FXeOXe(F)_2OXeF_2^+$: 671.4, 708.1 cm^{-1}). The gas-phase calculations of the cation, however,do not take into account ion-pairing of the cations with the AsF_6^- anions which would render Xe_3 significantly less electropositive and lower [ν(Xe_3O_2) – ν(Xe_1O_2)] to an extent where the stretches would be expected to couple more strongly. The remaining two bands that display $^{16/18}O$-isotopic dependencies are δ($O_2Xe_3F_4$) – δ($O_2Xe_3F_5$) and δ($O_1Xe_1F_1$) – δ($O_1Xe_1F_2$) with the former occuring at higher frequencies. The bands are factor-group split in [$HOXe(F)_2OXeF_2$][AsF_6], appearing at 418.2 and 422.9 cm^{-1} and at 241.4, 268.5, and 281.4 cm^{-1}, respectively, with the corresponding bands occuring at 344.7 and 299.2 cm^{-1}, respectively, in [$FXeOXe(F)_2OXeF_2$][AsF_6]. Both the greater frequency difference for these modes in the hydroxy salt relative to those of $FXeOXe(F)_2OXeF_2^+$ and the $^{16/18}O$-isotopic shift trends for δ($O_2Xe_3F_4$) – δ($O_2Xe_3F_5$) and δ($O_1Xe_1F_1$) – δ($O_1Xe_1F_2$) are reproduced by the calculations.

All the remaining bands are insensitive to $^{16/18}O$-isotopic enrichment. The bands at 536.1, 545.9, and 549.7 cm^{-1} in the spectrum of $HOXe(F)_2OXeF_2^+$ are assigned to the factor-group split ν(Xe_1F_1) + ν(Xe_1F_2) mode while those at 507.3 and 510.5 cm^{-1} are also factor-group split and are assigned to ν(Xe_3F_4) + ν(Xe_3F_5). The corresponding modes in $FXeOXe(F)_2OXeF_2^+$ are also factor-group split but are coupled in-phase and out-of-phase, appearing as bands at 526.7, 534.0 and 539.4 cm^{-1} and at 498.6 and 513.6 cm^{-1}, respectively, with the terminal $Xe_3–F_3$ stretch occuring at 550.3 cm^{-1}. The only other modes whose bands are observed for either cation are the in-plane F–Xe–F bends, which are coupled in both salts. The bands at 221.5 and 214.7 cm^{-1} are assigned to $\delta(F_4Xe_3F_5)_{ip}$ + $\delta(F_1Xe_1F_2)_{oop}$ and those appearing at 173.5 and 201.7 cm^{-1} and are assigned to $\delta(F_1Xe_1F_2)_{ip}$ + $\delta(F_4Xe_3F_5)_{ip}$ for the $HOXe(F)_2OXeF_2^+$ and $FXeOXe(F)_2OXeF_2^+$ cations, respectively.

It is interesting to note that $^{1/2}$H-isotopic substitution in $[HOXe(F)_2OXeF_2][AsF_6]$ did not show any isotopic dependencies in the Raman spectrum. It is likely that the hydrogen-dependent modes are too weak and broad to be observed by Raman spectroscopy.

6.2.4. Computational Results. The geometries of $^{1/2}H^{16/18}OXeF_2^+$, $[^{1/2}H^{16/18}OXeF_2][AsF_6]$, $H^{16/18}OXe(F)_2{}^{16/18}OXeF_2^+$, $FXe^{16/18}OXeF_2^+$, $FXe^{16/18}OXe(F)_2{}^{16/18}OXeF_2^+$, $XeF_3^+\cdot HF$, and $[XeF_3][AsF_6]$ were optimized starting from C_1 symmetries. All of the structures resulted in stationary points with all frequencies real. The PBE1PBE/aug-cc-pVTZ(-PP), B3LYP/aug-cc-pVTZ(-PP), and MP2/aug-cc-pVTZ(-PP) results all reproduce the vibrational frequency trends across the series of compounds reported in the present work (Figures 6.10 and 6.11 and Tables A3.2–A3.8; also see Experimental Section). In the case of $XeF_3^+\cdot HF$, two different starting geometries were optimized, one starting from an optimized XeF_4 geometry with a nearby (2.840 Å) H^+ ion, and the second starting from an optimized XeF_3^+ geometry with a nearby (2.941 Å) HF molecule. Both starting geometries optimized to the same final geometry suggesting

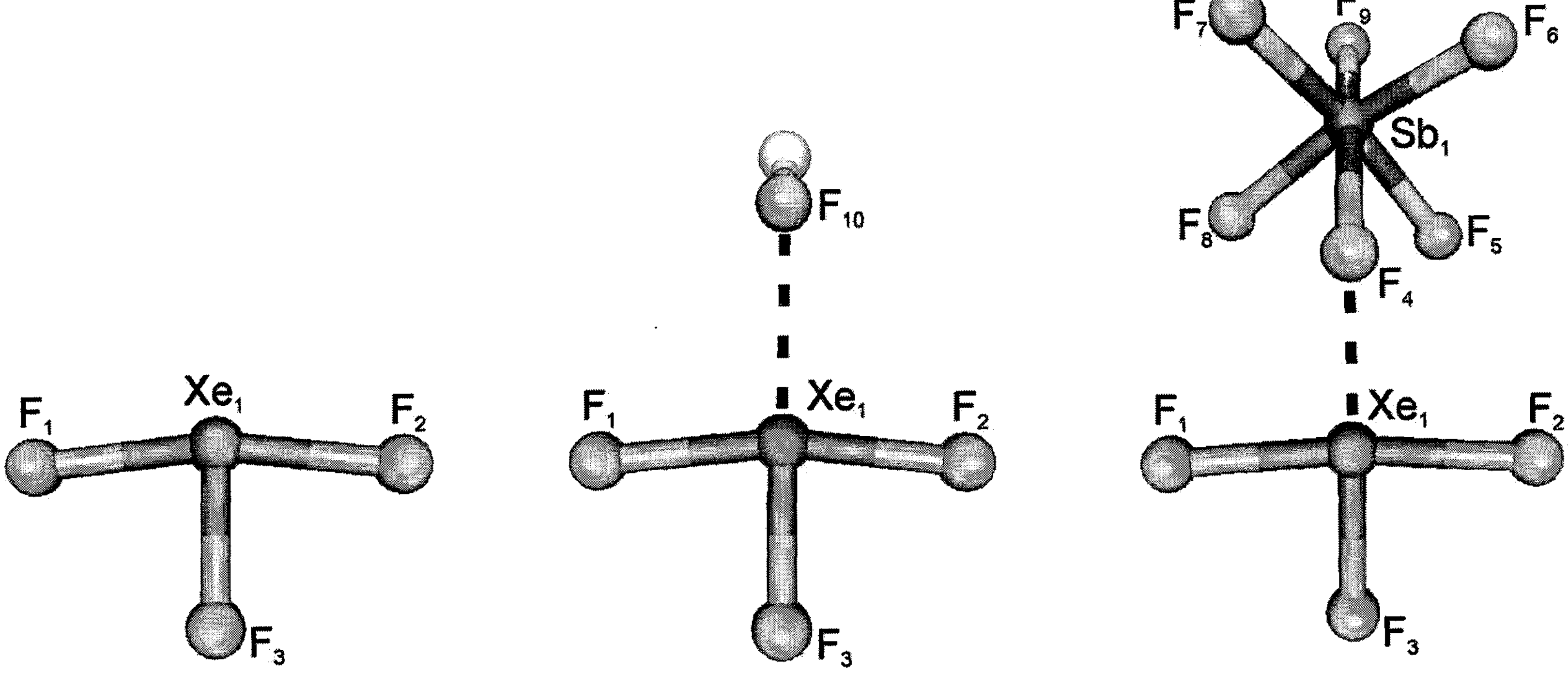

Figure 6.11. Calculated geometries [B3LYP/aug-cc-pVTZ(-PP)] for (a) XeF_3^+, (b) $XeF_3^+{\cdot}HF$, (c) $[XeF_3][AsF_6]$.

that XeF_3^+·HF can be described as either an HF adduct of XeF_3^+ or a protonated XeF_4 molecule.

6.2.4.1. Geometries. (i) $HOXeF_2^+$, [$HOXeF_2$][AsF_6], and $FXeOXeF_2^+$. The Xe_1–O_1 bond in $FXeOXeF_2^+$ (1.837–1.885 Å) is elongated relative to that of $XeOF_2$ (1.770–1.821 Å),[126] however, the bond is lengthened even more in $HOXeF_2^+$ (1.880–1.929 Å) and in the ion-pair, [$HOXeF_2$][AsF_6], (1.931–1.965 Å) which is consistent with the transfer of electron density from oxygen to the Lewis acid centers. The increased bond lengths result in greater single-bond character which is also manifested in the Raman spectra by lower Xe–O stretching frequencies relative to that of $XeOF_2$ (vide supra). The greater Xe_1–O_1 single bond characters also result in decreased O_1–Xe_1–F bond angles as a result of the reduced steric requirements of the Xe_1–O_1 single bond domains in the cations ($FXeOXeF_2^+$: 89.3–89.9°; $HOXeF_2^+$: 87.1–87.7°; [$HOXeF_2$][AsF_6]: 87.2–88.0°) relative to the Xe–O double bond domain in $XeOF_2$ (94.9–95.9°).[126] However, the O_1–Xe_1–F bond angles are still greater than the F_{ax}–Xe_1–F_{eq} bond angles in XeF_3^+ (83.3–84.2°) where the formal Xe–F bond order is one which indicates some Xe–O double bond character remains. In contrast with the Xe_1–O_1 bond lengths, the Xe_1–F bond lengths follow the reverse trend and are shorter in the cations ($FXeOXeF_2^+$: 1.921–1.946 Å; $HOXeF_2^+$: 1.903–1.927 Å; [$HOXeF_2$][AsF_6]: 1.938–1.963 Å) relative to $XeOF_2$ (1.968–1.997 Å)[126] but are longer than the related Xe–F_{ax} bonds of XeF_3^+ (1.883–1.906 Å). It is noteworthy that the Xe_2–O_1 bond (2.240–2.296 Å) in $FXeOXeF_2^+$ is significantly longer than the Xe_1–O_1 bond (1.837–1.885 Å) which can be attributed to the greater electronegativity of Xe(IV) relative to Xe(II). The Xe_1–O_1–Xe_2 bond angle

(123.8−129.7°) is also greater than the $Xe_1{-}O_1{-}H$ bond angle (108.1°), which is likely a consequence of the Xe−Xe (3.460−3.588 Å) steric interaction of the XeF group relative to that of hydrogen, as well as the greater electron lone pair − electron bond pair interaction present in the more covalent O−H bond relative to the more polar covalent Xe−F bond (see Table A3.9).

(ii) $HOXe(F)_2OXeF_2^+$ and $FXeOXe(F)_2OXeF_2^+$. Coordination of a second $XeOF_2$ molecule has very little impact on the geometries of these cations in the remainder of their chains. In both cations, the Xe, O_1, O_2, F_1, and F_2 atoms are coplanar. The $Xe_1{-}O_1$ and $Xe_1{-}F$ bonds in $HOXe(F)_2OXeF_2^+$ (1.914−1.945 Å and 1.929−1.958 Å, respectively) and $FXeOXe(F)_2OXeF_2^+$ (1.863−1.899 Å and 1.922−1.962 Å, respectively) are slightly elongated relative to those of the shorter chain cations whereas the related bond angles remain essentially unchanged. Upon coordination, the geometric parameters of the terminal $XeOF_2$ moieties follow the same trends as observed in $HOXeF_2^+$ and $FXeOXeF_2^+$, leading to $Xe_1{-}O_1$ bond elongation and the $Xe_1{-}F$ bond shortening, although to a lesser extent, and are almost unchanged relative to those of free $XeOF_2$.[126]

(iii) $XeF_3^+{\cdot}HF$ and $[XeF_3][SbF_6]$. Coordination of HF to XeF_3^+ has very little effect on the geometry of XeF_3^+. The $Xe{-}F_e$ (1.839−1.870 Å) and $Xe{-}F_a$ (1.892−1.916 Å) bond lengths of the adduct are the same as those in XeF_3^+ ($Xe{-}F_e$: 1.838−1.867 Å; $Xe{-}F_a$ 1.883−1.906 Å) but slightly shorter than in $[XeF_3][SbF_6]$ ($Xe{-}F_e$: 1.894−1.921 Å; $Xe{-}F_a$ 1.926−1.950 Å). The $F_e{-}Xe{-}F_a$ bond angles (XeF_3^+: 83.3−84.2°; $XeF_3^+{\cdot}HF$: 83.7−84.7°;

[XeF_3][SbF_6]: 86.0–86.8°). The poorest agreement between the calculated $XeF_3^+{\cdot}HF$ and [XeF_3][SbF_6] geometries and experimental geometries occurs for the contact angles and distances. In both models, the F_e–Xe---F bond angles are ~180° instead of the ~160° angle observed in their respective crystal structures. The Xe---F distances are overestimated and underestimated for $XeF_3^+{\cdot}HF$ and [XeF_3][SbF_6], respectively ($XeF_3^+{\cdot}HF$: 2.537–2.556 Å; [XeF_3][AsF_6]: 2.127–2.136 Å), relative to their crystal structures ($XeF_3^+{\cdot}HF$: 2.462(2); [XeF_3][AsF_6]: 2.485(1) Å). These discrepancies presumably result from the deformability of these angles which are strongly influenced by crystal packing.

6.3. Conclusion

The Lewis base properties of oxygen in $XeOF_2$ have been demonstrated by the high-yield syntheses of the noble-gas salts, [$^{1/2}H^{16/18}OXeF_2$][AsF_6], [$H^{16/18}OXe(F)_2{}^{16/18}OXeF_2$][$AsF_6$], [$FXe^{16/18}OXeF_2$][$AsF_6$], and [$FXe^{16/18}OXe(F)_2{}^{16/18}OXeF_2$][$AsF_6$], in high purity. The salts represent the first new Xe(IV) cations to have been synthesized in over 35 years, with the [$^{1/2}H^{16/18}OXeF_2$][AsF_6] and [$H^{16/18}OXe(F)_2{}^{16/18}OXeF_2$][$AsF_6$] salts also representing the only examples of xenon hydroxides to have been isolated and characterized in the solid state. All of the aforementioned salts are kinetically stable at −78 °C (with the exception of [$H^{16/18}OXe(F)_2{}^{16/18}OXeF_2$][$AsF_6$], which slowly decomposes at −78 °C) but slowly decompose upon warming to between −50 and −35 °C. Their decomposition pathways, inferred from their decomposition products, are supported by their thermochemical cycles. The latter show that the proposed reduction pathways of Xe(IV) to Xe(II) and O_2 are mainly driven by lattice energy contributions with entropy change associated with O_2 evolution also playing a significant role.

In an attempt to synthesize $[HOXeF_2][SbF_6]$, crystals of $[XeF_3{\cdot}HF][Sb_2F_{11}]$, $([XeF_3{\cdot}HF][Sb_2F_{11}])_2{\cdot}[H_5F_4][SbF_6]$, and $[XeF_3][SbF_6]$ were grown in admixture. The crystal structure of $([XeF_3{\cdot}HF][Sb_2F_{11}])_2{\cdot}[H_5F_4][SbF_6]$ contains the previously unknown acidium ion, $H_5F_4^+$. The secondary coordination spheres of xenon are very similar in the crystal structures of $[XeF_3{\cdot}HF]$ $[Sb_2F_{11}]$ and $([XeF_3{\cdot}HF][Sb_2F_{11}])_2{\cdot}[H_5F_4][SbF_6]$, however, the former cation displays a 2-fold positional disorder. An additional contact in $([XeF_3{\cdot}HF][Sb_2F_{11}])_2{\cdot}[H_5F_4][SbF_6]$, between xenon of the XeF_3^+ cation and a fluorine atom of the SbF_6^- anion in the acidium salt affects the crystal packing sufficiently to give an ordered structure. Quantum-chemical calculations indicate that the $XeF_3^+{\cdot}HF$ cation can be described as either a protonated XeF_4 molecule or a HF adduct of XeF_3^+. The experimental and calculated geometries of the XeF_3^+ cation in $[XeF_3{\cdot}HF][Sb_2F_{11}]$, $([XeF_3{\cdot}HF][Sb_2F_{11}])_2{\cdot}[H_5F_4][SbF_6]$, and $[XeF_3][SbF_6]XeF_3^+{\cdot}HF$ are very similar.

CHAPTER 7

A Rare Example of a Krypton Difluoride Coordination Compound; $[BrOF_2][AsF_6]\cdot 2KrF_2$

7.1. Introduction

The precursor to all known krypton compounds, KrF_2, has been structurally well characterized[12] and has been the subject of several theoretical studies.[99,168] The chemistry of krypton is restricted to the +2 oxidation state, presently consisting of several KrF^+ and $Kr_2F_3^+$ salts,[3,75,109,234–239] $Kr(OTeF_5)_2$,[103] a number of nitrile adducts of KrF^+, namely, $FKrN{\equiv}CR^+$ (R = H, CF_3, C_2F_5, n-C_3F_7),[104,105] preliminary evidence, but no structural characterization, for $KrF_2\cdot VF_5$[240] and $KrF_2\cdot MnF_4$,[241] and a series of KrF_2 Lewis acid–base adducts with group 6 d^0 transition metal centers, namely $MOF_4\cdot KrF_2$ (M = Cr,[106] Mo,[107] W[107]). The structural characterizations of the latter KrF_2 adducts were limited to solution ^{19}F NMR and solid-state Raman spectroscopy. In all three cases, the Raman and ^{19}F NMR spectra indicate that the adducts result from weak coordination of KrF_2 through a fluorine bridge to the metal atom. In the absence of X-ray crystal structures, an assessment of the degree of coordination, based on the relative bond lengths of terminal and bridge Kr–F bonds could not be made.

To date, there is no X-ray crystal structure in which KrF_2 serves as a ligand towards a metal atom, nor are there any examples in which KrF_2 coordinates to a main-group atom. Two criteria are required for KrF_2 coordination: (1) KrF_2 must interact with a Lewis acid center which is not sufficiently strong to “completely” abstract a fluoride ion from KrF_2 and (2) the Lewis acid must be resistant to oxidation by the powerful oxidative fluorinator, KrF_2. These criteria are met in the aforementioned low-temperature studies of the $MOF_4{\cdot}KrF_2$ adducts.[106,107] Earlier studies have shown that the $BrOF_2^+$ cation meets these criteria for the less strongly oxidizing XeF_2 ligand in $[BrOF_2][AsF_6]{\cdot}XeF_2$,[129] which has been characterized in solution by ^{19}F and ^{129}Xe NMR spectroscopy and in the solid state by Raman spectroscopy, offering promise for the synthesis of a KrF_2 analogue.

The present study extends the little studied coordination chemistry of krypton to the synthesis and characterization of the first main-group coordination compound of KrF_2, namely, $[BrOF_2][AsF_6]{\cdot}2KrF_2$. In addition to structural characterization by solid-state Raman spectroscopy and single-crystal X-ray diffraction, the nature of the adduct bonding is examined using quantum-chemical calculations in conjunction with electron localization function (ELF) calculations.

7.2. Results and Discussion

7.2.1. Synthesis and Properties of $[BrOF_2][AsF_6]{\cdot}2KrF_2$. Reaction progress and the purities of all products were routinely monitored by recording the low-temperature Raman spectra (–150 °C) of the solids.

The $[BrOF_2][AsF_6]{\cdot}XeF_2$ adduct was synthesized as previously described.[129] Rather than through the direct combination of $BrOF_3$ and AsF_5, the salt, $[BrOF_2][AsF_6]$, was synthesized in high purity by removal of XeF_2 from $[BrOF_2][AsF_6]{\cdot}XeF_2$ under dynamic vacuum at 0 °C (eq 7.1). This synthetic route to $[BrOF_2][AsF_6]$ circumvents

$$[BrOF_2][AsF_6]{\cdot}XeF_2 \xrightarrow[0\,^{\circ}C]{\text{dynamic vac.}} [BrOF_2][AsF_6] + XeF_2 \qquad (7.1)$$

difficulties associated with the synthesis and isolation of $BrOF_3$ from the reaction of $K[BrF_4O]$ and $[O_2][AsF_6]$ in HF[242,243] and the possibility of explosion during the hydrolysis of BrF_5 to form $BrOF_3$.[216]

Addition of KrF_2 to $[BrOF_2][AsF_6]$ (2:1 molar ratio) that had been precipitated and suspended in aHF at –78 °C resulted in a significant volume increase with respect to the original volume of suspended $[BrOF_2][AsF_6]$. The Raman spectra of the solid product under frozen HF solvent and of the product isolated by removal of HF at –78 °C were identical. Both spectra revealed that the bands corresponding to $BrOF_2^+$ were shifted to lower frequencies relative to those of $[BrOF_2][AsF_6]$ and that the KrF_2 stretching band, associated with uncomplexed KrF_2, was replaced by two pairs of Kr–F stretching bands (see 7.2.3., Raman Spectroscopy). The spectrum was consistent with the formation of $[BrOF_2][AsF_6]{\cdot}2KrF_2$, according to eq 7.2. The adduct is stable for at least five days at

$$[BrOF_2][AsF_6] + 2KrF_2 \xrightarrow[12\text{ h @ }-78\,^{\circ}C]{HF} [BrOF_2][AsF_6]{\cdot}2KrF_2 \qquad (7.2)$$

–78 °C as a solid and under aHF solvent. The adduct is also stable in aHF up to 25 °C for at least 1 h, with Raman spectroscopy showing no discernable decomposition when the adduct was isolated by removal of the solvent under dynamic vacuum at –78 °C.

Attempts to form the 1:1 adduct, $[BrOF_2][AsF_6]{\cdot}KrF_2$, by reaction of a 1:1 molar ratio of $[BrOF_2][AsF_6]$ and KrF_2 in aHF at –78 °C yielded only a mixture of $[BrOF_2][AsF_6]{\cdot}2KrF_2$ and $[BrOF_2][AsF_6]$ upon removal of the solvent under dynamic vacuum at –78 °C. Similar attempts to form a 3:1 adduct yielded only $[BrOF_2][AsF_6]{\cdot}2KrF_2$ and unreacted KrF_2.

7.2.2. X-ray Crystal Structure of $[BrOF_2][AsF_6]\cdot 2KrF_2$. A summary of the refinement results and other crystallographic information are given in Table 7.1. Important bond lengths, bond angles, and contacts are listed in Table 7.2.

The structure of $[BrOF_2][AsF_6]\cdot 2KrF_2$ consists of a $BrOF_2^+$ cation that interacts by means of short Br---F contacts with a single fluorine atom of the AsF_6^- anion and a fluorine atom from each of two KrF_2 ligands (Figure 7.1a). The $[BrOF_2][AsF_6]\cdot 2KrF_2$ structural units are relatively isolated, with the shortest intermolecular contacts (3.134 – 3.404 Å) occurring between the fluorine and krypton atoms of neighboring KrF_2 molecules, which are near or slightly under the sum of the fluorine and krypton van der Waals radii (3.49).[55]

The primary coordination sphere of Br(V) in $BrOF_2^+$ is trigonal pyramidal. The secondary coordination sphere comprises a fluorine atom of the AsF_6^- anion coordinated trans to the oxygen atom of $BrOF_2^+$, and the fluorine atoms of two KrF_2 molecules coordinated trans to the fluorine atoms of $BrOF_2^+$ so that the geometry of the F_2OBrF_3 moiety is pseudo-octahedral.

The Kr–F bond lengths of both coordinated KrF_2 molecules are distorted relative to those of free KrF_2 (1.894(5) Å),[99] with elongated bridge bonds (1.943(4), 1.933(4) Å) and terminal bonds that are shortened by nearly equal amounts (1.840(5), 1.847(4) Å). The differences between the terminal and bridging Kr–F bond lengths are significantly less than in KrF^+ and $Kr_2F_3^+$ salts: $[KrF][AsF_6]$ (Kr–F_b, 2.131(2) Å; Kr–F_t, 1.765(2) Å),[99] $[Kr_2F_3][AsF_6]\cdot[KrF][AsF_6]$ (Kr–F_b, 2.061(6), 2.049(6), 2.106(6) Å; Kr–F_t, 1.780(7), 1.803(6), 1.783(6) Å),[3] $[KrF][SbF_6]$ (Kr–F_b, 2.140(3) Å; Kr–F_t, 1.765(3) Å),[99]

Table 7.1. Summary of Crystal Data and Refinement Results for $[BrOF_2][AsF_6]\cdot 2KrF_2$

chem formula	$AsBrOF_{12}Kr_2$
space group	$P2_1/c$ (No. 14)
a (Å)	5.7166(6)
b (Å)	13.644(1)
c (Å)	15.105(2)
β (deg.)	111.446(4)
V (Å^3)	1096.6(2)
Z (molecules/unit cell)	4
mol. wt. (g mol^{-1})	2265.72
ρ_{calc} (g cm^{-3})	3.431
T (°C)	–173
μ (mm^{-1})	14.91
λ (Å)	0.71073
R_1[a]	0.0693
wR_2[b]	0.1715

[a] $R_1 = \Sigma \| F_o | - | F_c \| / \Sigma | F_o |$ for $I > 2\sigma(I)$. [b] wR_2 is defined as $\{\Sigma[w(F_o^2 - F_c^2)^2] / \Sigma w(F_o^2)^2\}^{1/2}$ for $I > 2\sigma(I)$.

Table 7.2. Experimental and Calculated (C_1) Geometrical Parameters for $[BrOF_2][AsF_6]\cdot 2KrF_2$

exptl^a			PBE1PBE^a	B3LYP^a
		Bond Lengths (Å)		
Br(1)–O(1)	1.564(5)	Br(1)–O(1)	1.556	1.569
Br(1)–F(1)	1.727(4)	Br(1)–F(1)	1.731	1.757
Br(1)–F(2)	1.723(4)	Br(1)–F(2)	1.730	1.757
Br(1)---F(3)	2.318(4)	Br(1)---F(3)	2.350	2.363
Br(1)---F(5)	2.356(4)	Br(1)---F(5)	2.302	2.338
Br(1)---F(7)	2.576(4)	Br(1)---F(7)	2.579	2.529
Kr(1)–F(3)	1.943(4)	Kr(1)–F(3)	1.951	1.984
Kr(1)–F(4)	1.840(5)	Kr(1)–F(4)	1.814	1.843
Kr(2)–F(5)	1.933(4)	Kr(2)–F(5)	1.957	1.984
Kr(2)–F(6)	1.847(4)	Kr(2)–F(6)	1.808	1.837
As(1)–F(7)	1.742(4)	As(1)–F(7)	1.789	1.813
As(1)–F(8)	1.711(4)	As(1)–F(8)	1.709	1.722
As(1)–F(9)	1.732(4)	As(1)–F(9)	1.743	1.752
As(1)–F(10)	1.732(4)	As(1)–F(10)	1.724	1.742
As(1)–F(11)	1.712(4)	As(1)–F(11)	1.705	1.720
As(1)–F(12)	1.709(4)	As(1)–F(12)	1.761	1.773
		Bond Angles (deg)		
F(1)–Br(1)–F(2)	89.3(2)	F(1)–Br(1)–F(2)	89.1	89.8
F(1)–Br(1)–O(1)	103.3(3)	F(1)–Br(1)–O(1)	102.0	102.0
F(1)–Br(1)---F(3)	85.1(2)	F(1)–Br(1)---F(3)	83.9	85.7
F(1)–Br(1)---F(5)	162.4(2)	F(1)–Br(1)---F(5)	166.9	166.5
F(1)–Br(1)---F(7)	80.5(2)	F(1)–Br(1)---F(7)	89.9	86.1
F(2)–Br(1)–O(1)	102.8(3)	F(2)–Br(1)–O(1)	100.0	100.1
F(2)–Br(1)---F(3)	166.7(2)	F(2)–Br(1)---F(3)	172.5	173.7
F(2)–Br(1)---F(5)	84.9(2)	F(2)–Br(1)---F(5)	82.4	83.4

Table 7.2. continued…

F(2)–Br(1)---F(7)	83.5(2)	F(2)–Br(1)---F(7)	72.1	74.1
O(1)–Br(1)---F(3)	90.2(2)	O(1)–Br(1)---F(3)	84.1	85.3
O(1)–Br(1)---F(5)	94.2(2)	O(1)–Br(1)---F(5)	89.3	90.7
O(1)–Br(1)---F(7)	172.6(2)	O(1)–Br(1)---F(7)	165.7	170.2
F(3)–Kr(1)–F(4)	179.9(2)	F(3)–Kr(1)–F(4)	177.2	176.9
F(3)---Br(1)---F(5)	96.9(2)	F(3)---Br(1)---F(5)	104.0	100.1
F(3)---Br(1)---F(7)	83.7(2)	F(3)---Br(1)---F(7)	105.3	101.1
F(5)–Kr(2)–F(6)	178.7(2)	F(5)–Kr(2)–F(6)	177.5	177.7
F(5)---Br(1)---F(7)	82.3(2)	F(5)---Br(1)---F(7)	78.0	80.8
Br(1)---F(3)–Kr(1)	132.1(2)	Br(1)---F(3)–Kr(1)	138.9	139.6
Br(1)---F(5)–Kr(2)	139.9(2)	Br(1)---F(5)–Kr(2)	129.4	129.4
Br(1)---F(7)–As(1)	131.1(2)	Br(1)---F(7)–As(1)	114.8	123.7
F(7)–As(1)–F(8)	179.4(2)	F(7)–As(1)–F(8)	175.8	176.6
F(7)–As(1)–F(9)	89.1(2)	F(7)–As(1)–F(9)	86.8	87.4
F(7)–As(1)–F(10)	88.8(2)	F(7)–As(1)–F(10)	88.6	87.9
F(7)–As(1)–F(11)	88.4(4)	F(7)–As(1)–F(11)	90.1	89.6
F(7)–As(1)–F(12)	89.5(2)	F(7)–As(1)–F(12)	85.6	85.6
F(8)–As(1)–F(9)	90.4(2)	F(8)–As(1)–F(9)	91.5	91.9
F(8)–As(1)–F(10)	91.6(2)	F(8)–As(1)–F(10)	92.9	92.6
F(8)–As(1)–F(11)	91.2(2)	F(8)–As(1)–F(11)	93.8	93.8
F(8)–As(1)–F(12)	90.8(2)	F(8)–As(1)–F(12)	90.5	91.0
F(9)–As(1)–F(10)	177.9(2)	F(9)–As(1)–F(10)	174.5	174.5
F(9)–As(1)–F(11)	90.4(2)	F(9)–As(1)–F(11)	91.1	91.2
F(9)–As(1)–F(12)	89.1(2)	F(9)–As(1)–F(12)	87.6	87.9
F(10)–As(1)–F(11)	90.1(2)	F(10)–As(1)–F(11)	91.9	91.6
F(10)–As(1)–F(12)	90.4(2)	F(10)–As(1)–F(12)	89.1	88.9
F(11)–As(1)–F(12)	177.8(2)	F(11)–As(1)–F(12)	175.5	175.1

---

[a] The aug-cc-pVTZ(-PP) basis set was used. The symmetry of the energy-minimized geometry is C_1. The labeling scheme corresponds to that used in Figures 7.1a and 7.1b.

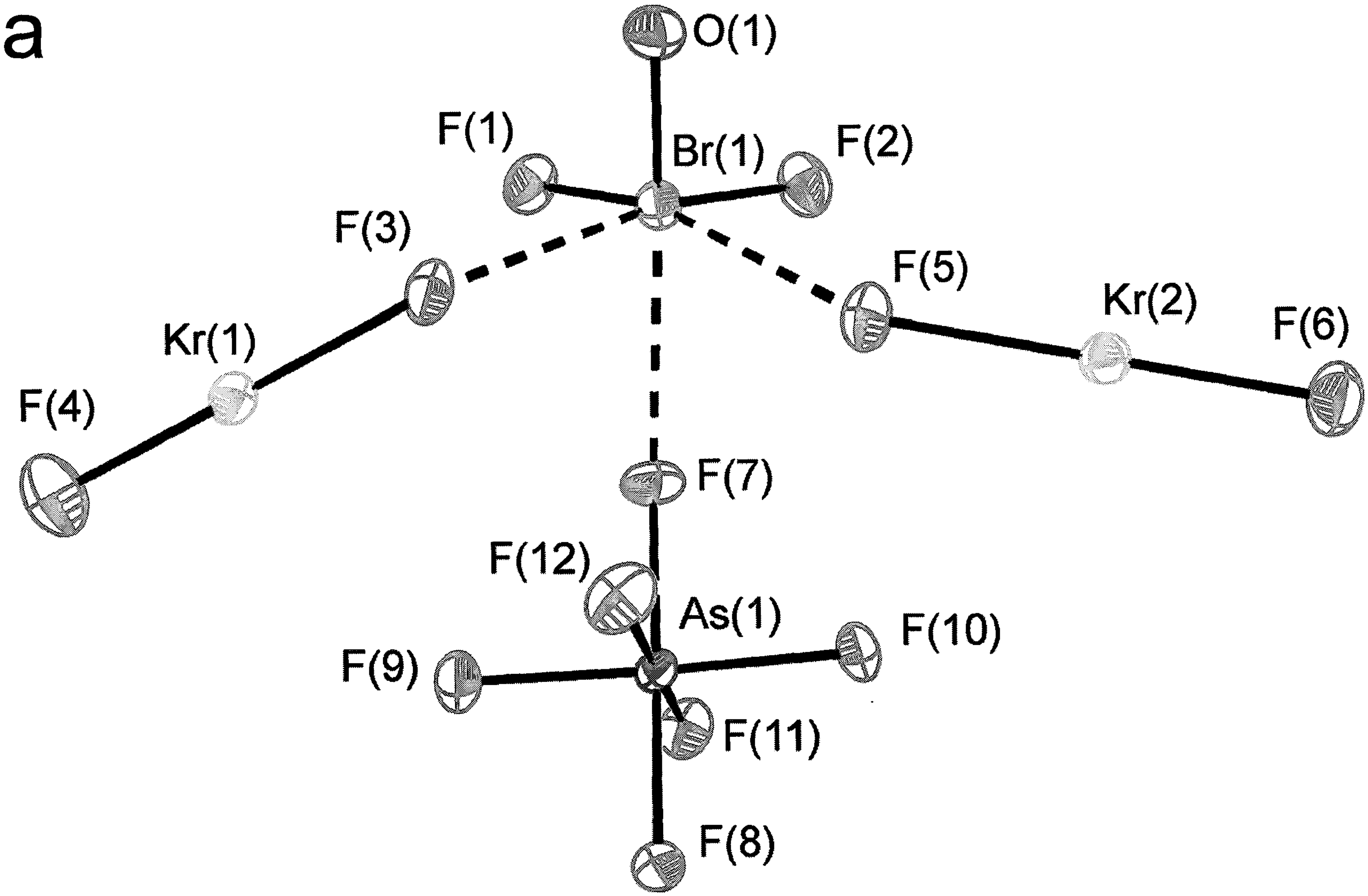
a
O(1)
F(1)
Br(1)
F(2)
F(3)
F(5)
Kr(2)
F(6)
Kr(1)
F(4)
F(7)
F(12)
As(1)
F(10)
F(9)
F(11)
F(8)

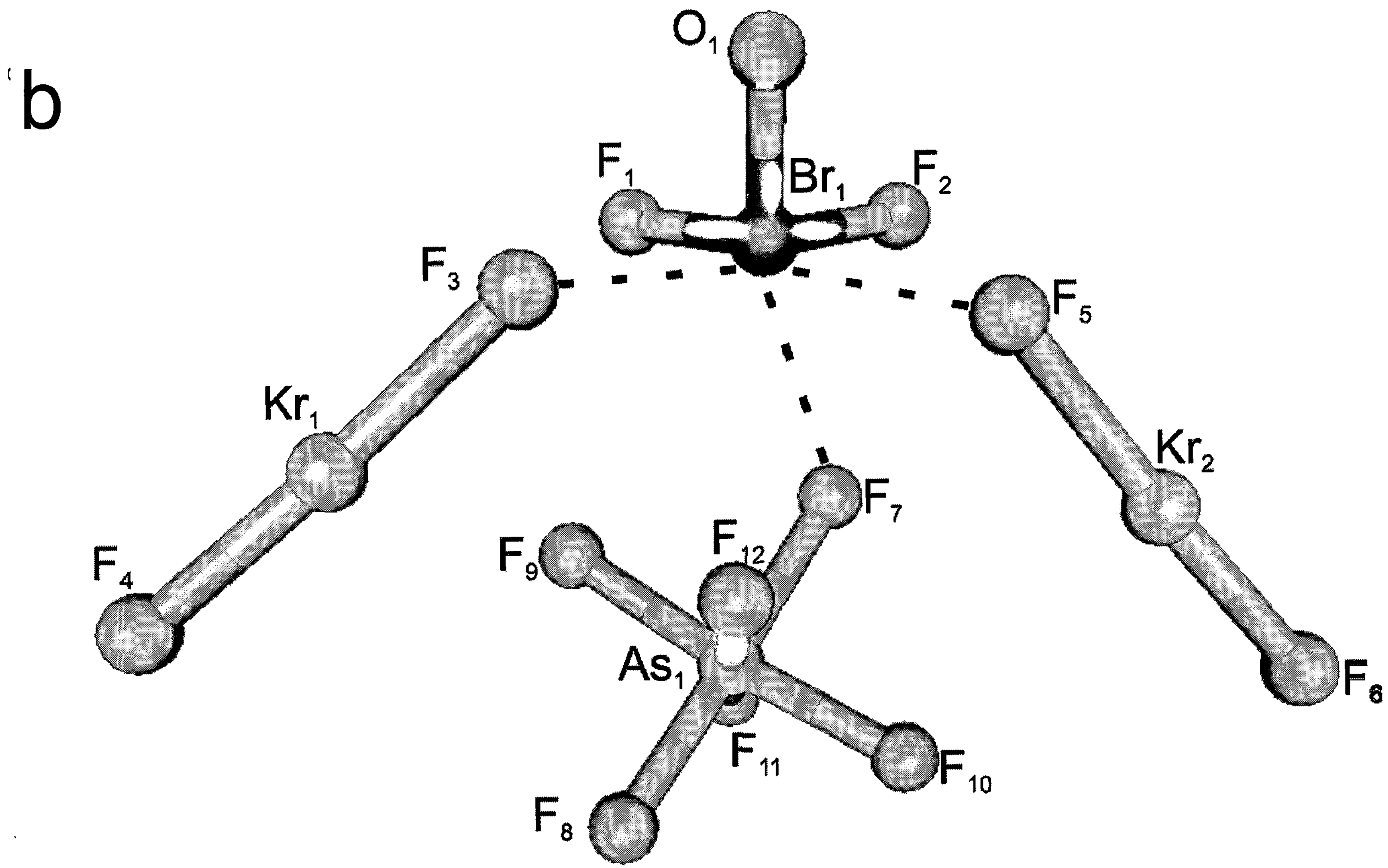

Figure 7.1. (a) The structural unit in the X-ray crystal structure of $[BrOF_2][AsF_6]\cdot 2KrF_2$; thermal ellipsoids are shown at the 50% probability level and (b) the calculated geometry (PBE1PBE/aug-cc-pVTZ(-PP)) of $[BrOF_2][AsF_6]\cdot 2KrF_2$ showing the pseudo-octahedral coordination around bromine(V).

$[KrF][BiF_6]$ (Kr–F_b, 2.090(6) Å; Kr–F_t, 1.774(6) Å),[99] $[Kr_2F_3]_2[SbF_6]_2{\cdot}KrF_2$ (Kr–F_b, 2.041(4), 2.065(4), 2.052(5), 2.056(4) Å; Kr–F_t, 1.805(5), 1.799(4), 1.797(5), 1.787(4) Å),[99] and $[Kr_2F_3][SbF_6]{\cdot}KrF_2$ (Kr–F_b, 2.027(5), 2.046(5) Å; Kr–F_t, 1.800(5), 1.790(5) Å).[99] This indicates that the Kr–F_b bonds in $[BrOF_2][AsF_6]{\cdot}2KrF_2$ have considerably more covalent character relative to those of KrF^+ and $Kr_2F_3^+$ salts and that the KrF_2 molecules behave as coordinating ligands rather than as fluoride ion donors.

The KrF_2 molecules coordinate to the cation by means of Br---F(3) and Br---F(5) contacts of 2.318(4) and 2.356(4) Å, respectively, which are relatively short and significantly less than the sum of the van der Waals radii of Br and F (3.32 Å). The fluorine bridges, Br(1)---F(3)–Kr(1) and Br(1)---F(5)–Kr(2), are bent as a consequence of the AX_2E_2 VSEPR[41] arrangement of bond pair and electron lone pair domains of the bridging fluorine atom, resulting in angles of 132.1(2)° and 139.9(2)°, respectively. The NBO analysis (PBE1PBE and B3LYP values are taken from Table 7.3; B3LYP values are in parentheses) assigns a bond order of 0.10 (0.08) for Br---F compared to 0.50 (0.39) for the Br–F bond of the $BrOF_2^+$ cation in the complex and 0.38 (0.37) for the terminal and 0.25 (0.24) for the bridge Kr–F bonds of the coordinated KrF_2 molecules. Because the lone pair-bond pair repulsions are less for these long and very ionic bridge bonds, the angles will be significantly more open than the ideal tetrahedral angle of an AX_2E_2 VSEPR arrangement. Similar reasoning applies to the Br(1)---F(7)–As(1) angle where the Br---F and As–F bond orders are 0.04 (0.04) and 0.47 (0.46), respectively. The Br---F_b–Kr angles appear to be little influenced by steric interactions, with $F_b{\cdots}F_b$ distances of 3.25–3.50 Å and $F_b{\cdots}F_{Br}$ distances of 2.77–2.93 Å compared to the van der Waals sum of

Table 7.3. NBO Valencies, Bond Orders, and Charges (NPA) for $BrOF_2^+$, $[BrOF_2][AsF_6]\cdot 2KrF_2$, and KrF_2

	$BrOF_2^+$		$[BrOF_2][AsF_6]\cdot 2KrF_2$		KrF_2	
Charges [Valencies]	PBE1PBE	B3LYP	PBE1PBE	B3LYP	PBE1PBE	B3LYP
Br(1)	2.326 [1.325]	2.298 [1.294]	2.411 [2.270]	2.381 [1.893]		
O(1)	-0.586 [0.594]	-0.563 [0.602]	−0.715 [0.953]	−0.695 [0.843]		
F(1)	-0.370 [0.271]	-0.368 [0.257]	−0.446 [0.457]	−0.445 [0.357]		
F(2)	-0.370 [0.271]	-0.368 [0.257]	−0.445 [0.455]	−0.446 [0.355]		
Kr(1)			1.081 [0.645]	1.065 [0.619]	1.032 [0.619]	1.013 [0.588]
F(3)			−0.579 [0.351]	−0.570 [0.326]	−0.516 [0.326]	−0.506 [0.309]
F(4)			−0.432 [0.394]	−0.420 [0.378]	−0.516 [0.326]	−0.506 [0.309]
Kr(2)			1.084 [0.667]	1.065 [0.635]	1.032 [0.619]	1.013 [0.588]
F(5)			−0.576 [0.372]	−0.566 [0.341]	−0.516 [0.326]	−0.506 [0.309]
F(6)			−0.422 [0.404]	−0.414 [0.380]	−0.516 [0.326]	−0.506 [0.309]
As(1)			2.638 [3.222]	2.640 [3.152]		
F(7)			−0.634 [0.464]	−0.636 [0.443]		
F(8)			−0.573 [0.502]	−0.571 [0.490]		
F(9)			−0.612 [0.466]	−0.606 [0.460]		
F(10)			−0.589 [0.490]	−0.593 [0.473]		
F(11)			−0.566 [0.506]	−0.565 [0.492]		
F(12)			−0.626 [0.467]	−0.623 [0.447]		
Bond Orders						
Br(1)-O(1)	0.670	0.674	1.023	0.905		
Br(1)-F(1)	0.328	0.310	0.493	0.389		
Br(1)-F(2)	0.328	0.310	0.497	0.391		
Br(1)---F(3)			0.092	0.075		
Br(1)---F(5)			0.103	0.081		
Br(1)---F(7)			0.042	0.041		
Kr(1)-F(3)			0.244	0.234	0.310	0.294
Kr(1)-F(4)			0.380	0.365	0.310	0.294
Kr(2)-F(5)			0.250	0.241	0.310	0.294
Kr(2)-F(6)			0.389	0.368	0.310	0.294
As(1)-F(7)			0.474	0.455		
As(1)-F(8)			0.574	0.564		
As(1)-F(9)			0.530	0.526		
As(1)-F(10)			0.555	0.539		
As(1)-F(11)			0.580	0.567		
As(1)-F(12)			0.508	0.502		

2.94 Å.[55] The only other short intramolecular contacts are Kr(1)---F(9) (3.22 Å) and Kr(2)---F(10) (3.40 Å), which are near the van der Waals sum for krypton and fluorine (3.49 Å). The KrF_2 ligands retain their linearity with F(3)–Kr(1)–F(4) and F(5)–Kr(2)–F(6) angles of 179.9(2)° and 178.7(2)°, respectively. One fluorine atom of the AsF_6^- anion forms a relatively short Br---F_b bridge bond (2.576(4) Å) with the $BrOF_2^+$ cation, giving rise to a distorted octahedral arrangement around arsenic in which the As–F_b bond (1.742(4) Å) is elongated relative to the As–F bond trans to it (1.711(4) Å) and with the equatorial bond lengths ranging from 1.709(4) to 1.732(4) Å.

The Br–O bond length (1.564(5) Å) is equal, within ±3σ, to that of $BrOF_4^-$ in $[NO][BrOF_4]$ (1.575(3) Å),[244] and the neutral parent molecule, $BrOF_3$, in $[NO_2][BrF_4]\cdot 2BrOF_3$ (1.569, 1.606 Å),[244] but is significantly shorter than in the neutral species $O_2Br–O–BrO_2$ (1.606 (12), 1.611(2), 1.613(2), 1.606(2) Å),[245] and $O_2BrOTeF_5$ (1.595(4), 1.608(3) Å),[246] and in the BrO_2^+ cation of $[BrO_2][SbF_6]$ (1.595(2) Å).[247] The Br–O bond length is also comparable to the Se–O bond length in isoelectronic $SeOF_2$ (1.576 Å), which was measured in the gas phase by microwave spectroscopy.[248] The Br–F bond lengths in $[BrOF_2][AsF_6]\cdot 2KrF_2$ (1.727(4), 1.723(4) Å) are equal, within ±3σ, to the axial Br–F bond lengths of the BrF_4^+ cation in $[BrF_4][Sb_2F_{11}]$ (Br–F_{ax}, 1.728(3), 1.729(3) Å (Br–F_{eq}, 1.664(3), 1.667(2) Å)),[249] the equatorial Br–F bond lengths in the neutral parent molecule, $BrOF_3$, in $[NO_2][BrF_4]\cdot 2BrOF_3$ (Br–F_{ax}, 1.820, 1.839, 1.822, 1.836 Å; Br–F_{eq}, 1.725, 1.692 Å),[244] and to the Se–F bond lengths of the isoelectronic $SeOF_2$ molecule (1.7295 Å).[248] They are, however, significantly shorter than the Br–F bonds in $[NO][BrOF_4]$ (1.846(2), 1.912(2) Å).[244]

The valence electron lone pair of bromine in $[BrOF_2][AsF_6]\cdot2KrF_2$ is expected to occupy a region opposite the three primary bond domains, giving a tetrahedral AX_2YE VSEPR[41] arrangement at Br(V). Thus, a stereochemically active valence electron lone pair is expected to occupy a region at the center of the triangular arrangement defined by the three long contacts that comprise the more open face of the pseudo-octahedron. The sum of the F(3)---Br(1)---F(5) (96.9(2)°), F(3)---Br(1)---F(7) (83.7(2)°), and F(5)---Br(1)---F(7) (82.3(2)°) angles is 262.9(6)°, whereas the face of the octahedron containing the primary contacts is significantly more open (F(1)–Br(1)–O(1), 103.3(3)°; F(1)–Br(1)–F(2), 89.3(2)°; F(2)–Br(1)–O(1), 102.8(3)°) with an angle sum of 295.4(8)°. The angle sums are attributable to the greater steric requirement of the Br–O double bond domain. The short secondary contact distances observed in $[BrOF_2][AsF_6]\cdot2KrF_2$ render the valence electron lone pair domain of bromine more compact and localized around the bromine atom relative to that of free $BrOF_2^+$. The steric crowding of the Br(V) valence electron lone pair represents an example of a "weakly active" electron lone pair[250] (see 7.2.4, Computational Results).

7.2.3. Raman Spectroscopy. The low-temperature Raman spectrum of $[BrOF_2][AsF_6]\cdot2KrF_2$ is shown in Figure 7.2. The observed and calculated frequencies and their detailed assignments are listed in Table 7.4. The spectral assignments for $[BrOF_2][AsF_6]\cdot2KrF_2$ were made by comparison with the calculated vibrational frequencies and Raman intensities (Table 7.4) of the energy-minimized geometry (Figure 7.1b), as well as those of KrF_2 (Table A4.1). In both the crystal structure and the

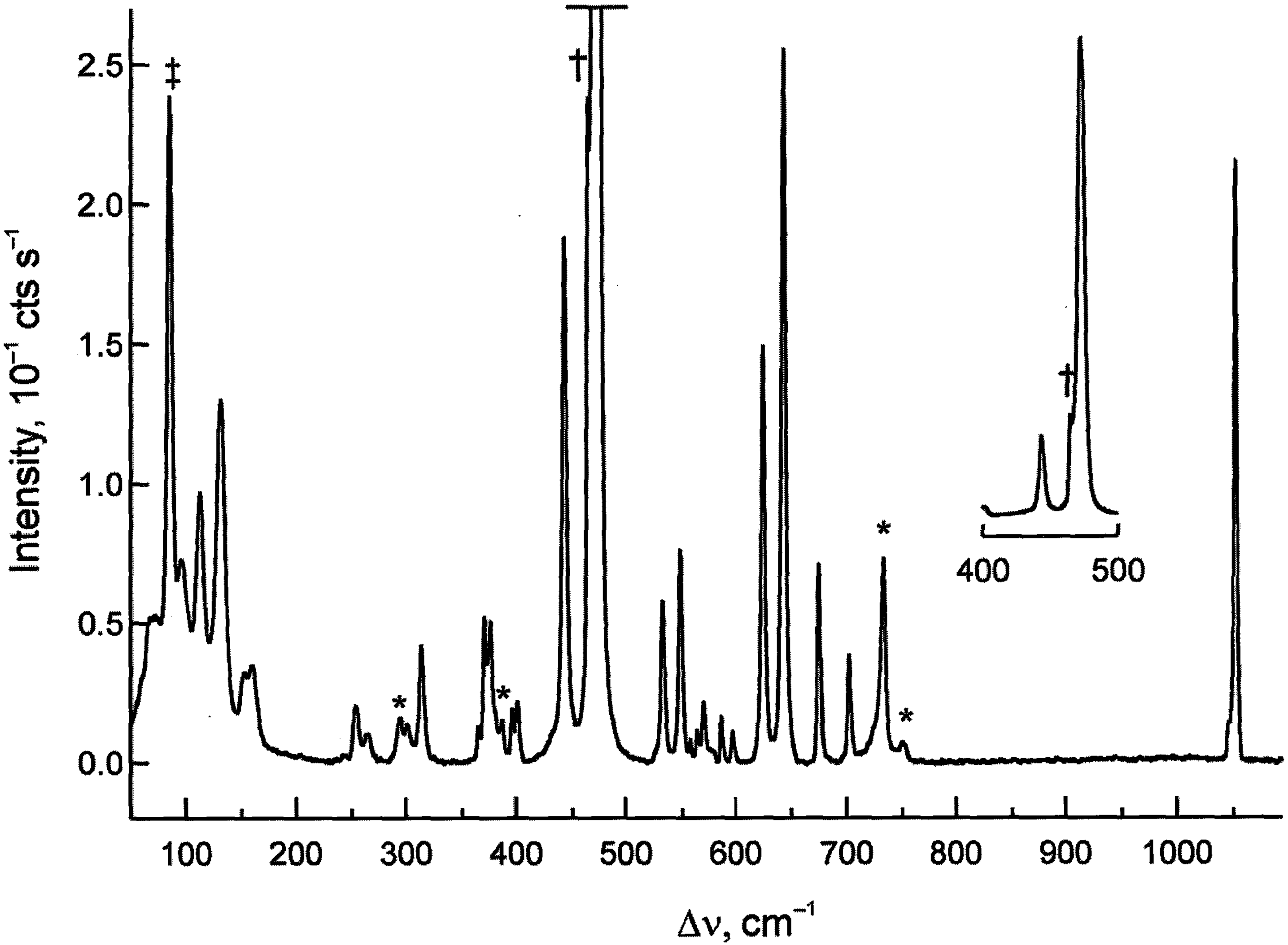

Figure 7.2. Raman spectrum of $[BrOF_2][AsF_6]\cdot 2KrF_2$ recorded at −150 °C using 1064-nm excitation. Symbols denote FEP sample tube lines (*), unreacted KrF_2 (†), and instrumental artifact (‡).

Table 7.4. Experimental and Calculated Vibrational Frequencies[a] for $[BrOF_2][AsF_6]\cdot 2KrF_2$

exptl[b]	PBE1PBE[c]	B3LYP[c]	assgnts (C_1)[d] $[BrOF_2][AsF_6]\cdot 2KrF_2$	AsF_6^- (O_h)
1053(19) 1047(1)	1071(68)[69]	1021(80)[69]	$\nu(BrO)$	
702(3)	745(6)[174]	718(6)[167]	$\nu(AsF_{11}) - \nu(AsF_{12})$	$\nu_3(T_{1u})$
	729(3)[165]	707(4)[157]	$\nu(AsF_8)$	
	724(<1)[232]	698(<1)[229]	$\nu(AsF_9) - \nu(AsF_{10})$	
675(6)	662(18)[71]	637(56)[45]	$\nu(AsF_7) + \nu(AsF_9) + \nu(AsF_{10}) + \nu(AsF_{12})$[e]	$\nu_1(A_{1g})$
644(22)	683(58)[85]	644(32)[45]	$\nu(BrF_1) + \nu(BrF_2)$[f]	
625(13)	652(26)[68]	612(31)[67]	$\nu(BrF_1) - \nu(BrF_2)$	
549(7)	610(28)[182]	577(20)[194]	$\nu(Kr_2F_6) + [\nu(Kr_1F_4) - \nu(BrF_1)]_{small}$	
533(5)	587(21)[295]	549(12)[295]	$\nu(Kr_1F_4) - [\nu(Kr_2F_6) + \nu(BrF_2)]_{small}$	
597(1) 587(1)	571(4)[6]	557(6)[70]	$[\nu(AsF_9) + \nu(AsF_{10})] - [\nu(AsF_{11}) + \nu(AsF_{12})]$	$\nu_2(E_g)$
565(1) 558(1)	536(5)[31]	504(20)[50]	$\nu(AsF_7) - \nu(AsF_{12})_{small}$	
472(100), br	489(76)[124]	473(87)[84]	$\nu(Kr_1F_3) + [\nu(Kr_2F_5) - \nu(AsF_7)]_{small}$	
443(17)	467(33)[270]	450(43)[231]	$\nu(Kr_2F_5) - \nu(Kr_1F_3)_{small}$	
401(2)	401(<1)[45]	391(<1)[49]	$\delta(F_9AsF_{12}) - \delta(F_{10}AsF_{11}) + \rho_w(F_7AsF_8)$	$\nu_4(T_{1u})$
	396(<1)[26]	385(<1)[32]	$\delta(F_8AsF_9) - \delta(F_7AsF_{10}) + \rho_w(F_{11}AsF_{12})$	
	394(<1)[39]	383(<1)[31]	$\delta(AsF_7F_9F_{11})_{oop} - \delta(AsF_8F_{10}F_{12})_{oop}$	
397(2)	386(4)[123]	368(4)[103]	$\delta(OBrF_1F_2)$	
366(1)	367(1)[<1]	359(1)[<1]	$\delta(F_9AsF_{12}) + \delta(F_{10}AsF_{11})$	$\nu_5(T_{2g})$
	362(1)[1]	352(1)[3]	$\delta(F_7AsF_{12}) + \delta(F_8AsF_{11})$	
	356(<1)[<1]	344(<1)[<1]	$\delta(F_7AsF_9) + \delta(F_8AsF_{10})$	
377(4) 371(5)	334(5)[84]	319(4)[69]	$\rho_w(OBrF_2) + \rho_t(F_1BrF_2)$	
314(4)	304(<1)[7]	283(<1)[9]	$\delta(F_1BrF_2)$	
301(1)	291(1)[44]	274(1)[34]	$\delta(F_5Kr_2F_6)_{oop}$	
266(1)	269(2)[67]	258(1)[53]	$\delta(F_3Kr_1F_4)_{ip}$	
254(2)	256(<1)[7]	243(<1)[8]	$\delta(F_5Kr_2F_6)_{ip}$	

Table 7.4. (continued…)

	246(<0.1)[5]	241(<0.1)[4]	$\rho_w(F_7AsF_8) - \rho_w(F_9AsF_{10}) + [\delta(F_3Kr_1F_4)_{oop}]_{small}$	
	244(1)[9]	234(1)[12]	$\delta(F_3Kr_1F_4)_{oop} + [\rho_w(F_7AsF_8) - \rho_w(F_9AsF_{10})]_{small}$	$\nu_6(T_{2u})$
	235(<1)[<1]	227(<0.1)[<1]	$\rho_w(F_{11}AsF_{12}) - \rho_w(F_7AsF_8) + \rho_w(F_9AsF_{10})$	
	230(<0.1)[<1]	221(<0.1)[<1]	$\rho_w(F_9AsF_{10}) - \rho_w(F_{11}AsF_{12}) + \rho_w(F_7AsF_8)$	
161(3)	174(2)[5]	166(4)[5]	$\rho_r(OBrF_2) + \rho_t(F_5Kr_2F_6)$	
153(1)	169(2)[22]	165(<1)[19]	$\rho_t(F_1BrF_2) + \rho_t(F_5Kr_2F_6)$	
	148(<1)[7]	146(1)[9]	$\rho_t(OBrF_1F_2) + \rho_t(F_5Kr_2F_6)_{small}$	
	127(<1)[7]	119(1)[6]	$\rho_r(OBrF_1F_2)$	
	109(4)[27]	106(3)[16]	$\rho_r(OBrF_1F_2) + \rho_t(F_3Kr_1F_4)$	
	101(2)[1]	100(3)[2]	$\rho_r(F_5Kr_2F_6) - \rho_r(F_3Kr_1F_4) + \rho_t(OBrF_1F_2)_{small}$	
	89(2)[<1]	86(<1)[<1]	deformation and torsional modes of $[BrOF_2][AsF_6]\cdot 2KrF_2$	
	80(1)[5]	82(2)[2]		
	72(<1)[<1]	64(<1)[<1]		
	62(<1)[1]	61(1)[<1]		
	51(<1)[1]	48(<1)[<1]		
	48(<1)[<1]	44(<1)[<1]		
	42(2)[<1]	40(3)[<1]		
	39(<1)[<1]	33(<1)[1]		
	30(<1)[<1]	19(1)[<1]		
	22(1)[<1]	11(<0.1)[<1]		
132(11)			lattice modes	
113(8)				
96(6)				

[a] Frequencies are given in cm^{-1}. [b] The Raman spectrum was recorded in an FEP sample tube at −150 °C using 1064-nm excitation. Values in parentheses denote relative Raman intensities. An additional band observed at 465(21) cm^{-1} was assigned to unreacted KrF_2. [c] The aug-cc-pVTZ(-PP) basis set was used. Values in parentheses denote Raman intensities (Å^4 amu^{-1}). Values in square brackets denote infrared intensities (km mol^{-1}). [d] Vibrational assignments were based on modes calculated at the PBE1PBE level of theory. The abbreviations denote stretch (ν), bend (δ), rock (ρ_r), twist (ρ_t), wag (ρ_w), in-plane bend (ip), and out-of-plane bend (oop). [e] This band is assigned to $\nu(BrF_1) + \nu(BrF_2)$ at the B3LYP level. [f] This band is assigned to $\nu(AsF_{13}) + \nu(AsF_{14}) + \nu(AsF_{10}) + \nu(AsF_9)$ at the B3LYP level

calculated geometry, the $[BrOF_2][AsF_6]\cdot2KrF_2$ structural unit possesses C_1 symmetry and the Raman spectrum has been assigned under that symmetry. Vibrational frequencies calculated at both the PBE1PBE and B3LYP (values in parentheses) levels of theory reproduced the observed frequency trends. The AsF_6^- anion, under ideal octahedral symmetry (O_h), has three Raman-active bands, $\nu_1(A_{1g})$, $\nu_2(E_g)$, and $\nu_5(T_{2g})$, two infrared-active bands, $\nu_3(T_{1u})$ and $\nu_4(T_{1u})$, and one inactive band, $\nu_6(T_{2u})$. In the present instance, the fluorine-bridged AsF_6^- anion is distorted, with local C_1 symmetry which gives rise to 15 Raman- and infrared-active bands. Only eight bands were observed in the Raman spectrum for AsF_6^- and their assignments were guided by comparison with other coordinated AsF_6^- anions having local C_1 or C_s symmetries.[71,154]

All 45 vibrational modes of $[BrOF_2][AsF_6]\cdot2KrF_2$ belong to A irreducible representations and are predicted to be Raman- and infrared-active. Additional bands appear in the Raman spectrum that cannot be accounted for by site symmetry lowering alone because correlation of the gas-phase adduct symmetry (C_1) to the crystal site symmetry (C_1) results in no additional band splitting (Table 7.5). The additional bands are associated with vibrational coupling within the crystallographic unit cell. Correlation of the site symmetry to the centrosymmetric unit cell symmetry (C_{2h} with $Z = 4$) results in equal apportioning of the $4(3N - 6)$ vibrational modes among A_g, A_u, B_g, and B_u symmetries. Thus, of the 180 coupled vibrational modes for $[BrOF_2][AsF_6]\cdot2KrF_2$ in its unit cell, 45 A_g and 45 B_g Raman-active and 45 A_u and 45 B_u infrared-active components are predicted. Of the predicted 90 Raman bands, only 25, including eight AsF_6^- bands,

Table 7.5. Factor-Group Analysis for $[BrOF_2][AsF_6]\cdot 2KrF_2$

free $[BrOF_2][AsF_6]\cdot 2KrF_2$ (C_1)		crystal site (C_1)	unit cell[a] (C_{2h})		
$4(\nu_1$-ν_{45}, 3R, 3T)	A	4A	A_g	ν_1-ν_{45}, 2R (−R), 3T	R
			B_g	ν_1-ν_{45}, 1R (−2R), 3T	
			A_u	ν_1-ν_{45}, 3R, 2T (−T)	IR
			B_u	ν_1-ν_{45}, 3R, T (−2R)	

[a] The crystallographic space group is $P2_1/c$ with $Z = 4$ structural units per unit cell.

were observed, implying vibrational coupling within the unit cell is, except in a few instances, too weak to be observed.

Upon coordination of KrF_2, the cation stretching frequencies shift to lower frequency relative to those of $[BrOF_2][AsF_6]$.[128] The highest frequency bands at 1047, 1053 cm^{-1} are assigned to the factor-group split Br–O stretching mode. The in-phase and out-of-phase BrF_2 stretching bands occur at 644 and 625 cm^{-1}, respectively, and show no factor-group splitting. The in-phase band occurs at higher frequency and is more intense, in agreement with the trends expected from the calculated values. The two bands are also slightly shifted to lower frequency compared to those observed for free $BrOF_2^+$.[128] The trends in the cation stretching frequencies can be accounted for by donation of electron density from the KrF_2 ligands to the bromine atom, rendering bromine less electropositive (see 7.2.4.2, Natural Bond Orbital Analyses) and shifting the modes to lower frequency. The cation bands at 314, 371/377, and 397 cm^{-1} are assigned to $BrOF_2^+$ deformation modes and are in good agreement with the calculated values.

The most intense modes in the spectrum of $[BrOF_2][AsF_6]{\cdot}2KrF_2$ are those of the KrF_2 ligand. Coordination of KrF_2 to $BrOF_2^+$ results in removal of the center of symmetry at krypton, which is manifested in the Raman spectrum by the appearance of bands to high and to low frequency of free KrF_2 (ν(KrF), 465 cm^{-1}),[100] with the higher frequency band assigned to the terminal $Kr{-}F_t$ stretch and the lower frequency and more intense band assigned to the bridging $Kr{-}F_b$ stretch. These trends have been observed in XeF_2 adducts with metal cations.[82,83] The vibrational displacements calculated at the PBE1PBE and B3LYP levels reveal that while there is no intraligand coupling for the $Kr{-}F_t$ and $Kr{-}F_b$ stretching modes, interligand coupling occurs giving rise to in-phase (KrF_t) + ν$(Kr'F_t)$ and out-of-phase (KrF_t) − ν$(Kr'F_t)$ modes at 549 and 533 cm^{-1}, respectively, where the KrF_t and $Kr'F_t$ displacement amplitudes are unequal in both coupled modes. These modes occur at similar frequencies, in accordance with their calculated frequencies, 610 (577) and 587 (549) cm^{-1}, respectively. The bands at 443 and 472 cm^{-1} are associated with analogous interligand coupling of the $Kr{-}F_b$ bridging stretching modes and are in good agreement with the calculated values, 467 (450) and 489 (473) cm^{-1}. In contrast to the coupled $Kr{-}F_t$ and $Kr'{-}F_t$ modes, the coupled $Kr{-}F_b$ and $Kr'{-}F_b$ displacement amplitudes are nearly equal. The $Kr{-}F_t$ stretching frequencies are comparable to ν(KrF_t) of $KrF_2{\cdot}CrOF_4$ (550 cm^{-1})[106] but are somewhat lower than those of $KrF_2{\cdot}MoOF_4$ (566, 579 cm^{-1}),[107] and $KrF_2{\cdot}WOF_4$ (571, 581 cm^{-1}).[107] The value is, however, much lower than that of ν(KrF) in β-[KrF][AsF$_6$] (615, 619 cm^{-1}),[99] [KrF][SbF$_6$] (615 cm^{-1}),[99] and [KrF][BiF$_6$] (604, 610 cm^{-1}),[99] indicating that the coordinated KrF$_2$ molecules in [BrOF$_2$][AsF$_6$]·2KrF$_2$ are adducted and do not behave as fluoride ion donors towards the Lewis acid, BrOF$_2^+$, as inferred from their relative crystallographic bond lengths (see X-ray Crystallography).

The Kr–F$_b$ bridging frequencies are in better agreement with those of KrF$_2$·WOF$_4$ (450, 469 cm^{-1})[107] than with those of KrF$_2$·CrOF$_4$ (486 cm^{-1})[106] or KrF$_2$·MoOF$_4$ (462, 479 cm^{-1}).[107] Comparison of the frequency differences between the Kr–F$_t$ and Kr–F$_b$ modes reveals an increase over the series: KrF$_2$·CrOF$_4$ (64 cm^{-1}),[106] KrF$_2$·MoOF$_4$ (102 cm^{-1}),[107] and KrF$_2$·WOF$_4$ (116 cm^{-1}),[107] following the anticipated Lewis acidity trend of the metal oxide tetrafluorides. This trend suggests that the strengths of the Br---F adduct bonds in [BrOF$_2$][AsF$_6$]·2KrF$_2$, with a frequency difference between the Kr–F$_t$ and Kr–F$_b$ modes of 84 cm^{-1}, are intermediate with respect to those of KrF$_2$·CrOF$_4$ and KrF$_2$·MoOF$_4$.

The present vibrational assignments of coordinated KrF$_2$ are in accordance with those reported for XeF$_2$ homoleptically coordinated to a variety of metal cations.[82,83] In these coordination complexes, the high-frequency Xe–F stretching bands are assigned to Xe–F$_t$ stretches and the low-frequency ones are assigned to Xe–F$_b$ stretches without invoking intramolecular coupling in the vibrational mode descriptions of coordinated XeF$_2$. The calculated vibrational displacements of coordinated KrF$_2$ in [BrOF$_2$][AsF$_6$]·2KrF$_2$ also do not show intramolecular coupling. Instead, the vibrational coupling of the Kr–F stretches is interligand in nature occurring between Kr–F$_b$

stretching modes that have near-equal displacement amplitudes, and between Kr–F$_t$ stretching modes which have unequal displacement amplitudes.

The double degeneracy of the KrF_2 bending mode of free KrF_2 (ν_2, Π_u) is removed when it is fluorine bridged to bromine, resulting in splitting into out-of-plane and in-plane F_t–Kr–F_b bending modes with respect to the plane containing the two KrF_2 molecules and the bromine atom. The vibrational bands are shifted to higher frequency relative to that of free KrF_2 (236 cm^{-1}),[93] and occur at slightly different frequencies because one KrF_2 ligand is somewhat more strongly bound than the other in the crystal structure and in the calculated gas-phase structure (see 7.2.2, X-ray Crystal Structure and 7.2.4.1, Computational Results). The δ(FKrF) modes are not coupled (Table 7.4), where $\delta(F_5KrF_6)_{ip}$ and $\delta(F_5KrF_6)_{oop}$ are observed at 254 and 301 cm^{-1}, respectively, and $\delta(F_3KrF_4)_{ip}$ is observed at 266 cm^{-1}. The $\delta(F_3KrF_4)_{oop}$ bend was not observed but is calculated at 244 (234) cm^{-1} and is expected to be weak. The calculated frequencies are also in excellent agreement with the experimental frequencies. These bands occur at much higher frequencies than those that are assigned for the MOF_4 adducts, i.e., 176 cm^{-1} ($KrF_2{\cdot}CrOF_4$),[106] 170 cm^{-1} ($KrF_2{\cdot}MoOF_4$),[107] and 172 cm^{-1} ($KrF_2{\cdot}WOF_4$),[107] suggesting that the latter may have been erroneously assigned in the earlier work and likely should be re-assigned to the bands reported at 256/283, 303/312, and 301/312, respectively.

7.2.4. Computational Results. The geometry of $[BrOF_2][AsF_6]{\cdot}2KrF_2$ was energy minimized starting from the crystallographic coordinates and resulted in stationary points with all frequencies real. The PBE1PBE/aug-cc-pVTZ(-PP) and B3LYP/aug-cc-pVTZ(-

PP) (B3LYP values are in parentheses) results are reported in Tables 7.2 and 7.43, and Figure 7.1b.

7.2.4.1. Geometries. The gas-phase geometry of $[BrOF_2][AsF_6]\cdot2KrF_2$ optimized at C_1 symmetry at both levels of theory and did not deviate significantly from that observed in the X-ray crystal structure (Figure 7.1a). The largest angle discrepancies occur for F(3)---Br(1)---F(7) and Br(1)---F(7)–As(1) which are over- and underestimated, respectively, with respect to the experimental values (Figure 7.1b).

The calculated Br–O bond length was 1.556 (1.569) Å and the Br–F bond lengths were 1.731 (1.757) Å and 1.730 (1.757) Å, in very good agreement with the experimental Br–O (1.564(5) Å) and Br–F (1.727(4), 1.723(4) Å) bond lengths. The calculated O–Br–F_1 (102.0 (102.0)°) and O–Br–F_2 (100.0 (100.1)°) angles are more open than the F–Br–F angle of (89.1 (89.8)°), and all three bond angles are in good agreement with the experimental values. The three contact distances, Br---$F_{3,5,7}$, 2.350 (2.363) Å, 2.302 (2.338) Å, and 2.579 (2.529) Å, respectively, reproduce the observed distances (2.318(4), 2.356(4), 2.576(4) Å), with the contact opposite the oxygen atom, Br---F_7, being the longest.

The KrF_2 ligand geometries are also well modeled by the calculations, i.e., the bridging krypton–fluorine bond lengths, Kr–$F_{3,5}$, 1.951 (1.984) Å and 1.957 (1.984) Å, respectively, are longer than the terminal krypton-fluorine bond lengths, Kr–$F_{4,6}$, 1.814 (1.843) Å and 1.808 (1.837) Å, respectively. The KrF_2 ligands are also predicted to be near linear (177.2 (176.9)°, 177.5 (177.7)°), as observed experimentally.

The bond lengths, bond angles, and their trends for the pseudo-octahedral fluorine-bridged AsF_6^- anion are also well reproduced but not as well as for the cation. The arsenic–fluorine bridge bond length, As–F_7, 1.789 (1.813) Å, is elongated relative to the other As–F bonds. The remaining calculated As–F bond lengths range from 1.705 (1.720) Å to 1.761 (1.773) Å.

7.2.4.2. Natural Bond Orbital (NBO) Analyses. The NBO[163–166] analyses were carried out for the PBE1PBE- and B3LYP-optimized gas-phase geometries of $[BrOF_2][AsF_6]\cdot2KrF_2$ and KrF_2 with the results given in Table 7.3. Both the PBE1PBE and B3LYP results are very similar; only the PBE1PBE results are referred to in the ensuing discussion.

The natural population analysis (NPA) charges given by the NBO analysis for Br (+2.41), O (−0.72), and F(−0.45) in the $BrOF_2^+$ cation of $[BrOF_2][AsF_6]\cdot2KrF_2$ total +0.79 and are approximately half of the formal charges that are given by a purely ionic model (+5, −2, and −1, respectively), indicating that the cation bonds are polar covalent. The natural charges are also consistent with a cation having a net charge of +1 where the charge difference, −0.21, is primarily transferred from the KrF_2 ligands and, to a lesser extent, from the AsF_6^- anion (−0.05), providing a total anion charge of −0.95. Of the plausible valence bond contributions that can be considered for the $BrOF_2^+$ cation (Structures I–IV), Structure IV best represents the calculated charges, the Br–O/Br–F bond order ratio (2.06), and Br/O/F/ valencies (2.27/0.95/0.46).

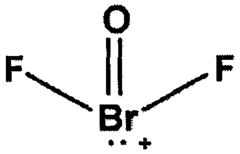

I

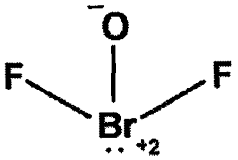

II

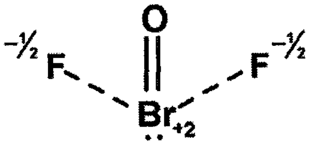

III

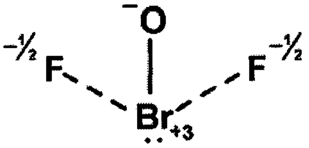

IV

Among the three plausible valence bond structures for KrF_2, V, VI, and VII, the calculated charges (Kr: 1.08, 1.08; F: −0.58, −0.43, −0.58, −0.42), bond orders (0.24, 0.38, 0.25, 0.39), and valencies (Kr: 0.64, 0.67; F: 0.35, 0.39, 0.37, 0.40) of the coordinated molecules are best represented by $^{-1/2}\mathrm{F}\text{--}\mathrm{Kr}^{+}\text{--}\mathrm{F}^{-1/2}$, the average of Structures VI and VII, which are customarily used to describe the bonding in KrF_2.[99] Upon adduct formation, the total of the fluorine atom charges of KrF_2 remains essentially unchanged, however, the charge distributions of the KrF_2 molecules are polarized towards the positive bromine atom, with ~0.07 e transferred from F_t to F_b. A minor contribution from Structure VI accounts for the charge drift and also accounts for the decreased Kr–F_b bond order, increased Kr–F_t bond order, and increased F_t valence. In addition, upon coordination, the krypton atoms become somewhat more positively charged and there is an overall charge transfer of 0.08 e from each KrF_2 ligand to the $[BrOF_2][AsF_6]$ ion pair.

F–Kr–F	$^{-}$F $^{+}$Kr–F	F–Kr^{+} F^{-}
V	**VI**	**VII**

The valence bond description of $BrOF_2^+\cdot 2KrF_2$, which takes Structures IV and VI/VII into account, is represented by Structures VIII and IX, where Structure VIII is the dominant contributor and best accounts for the bonding in the adduct. A minor contribution from Structure IX accounts for the small increase in positive charge on the krypton atoms, the low $Br{-}F_b$ bond orders (0.09, 0.10), and a small degree of charge transfer from the KrF_2 ligands.

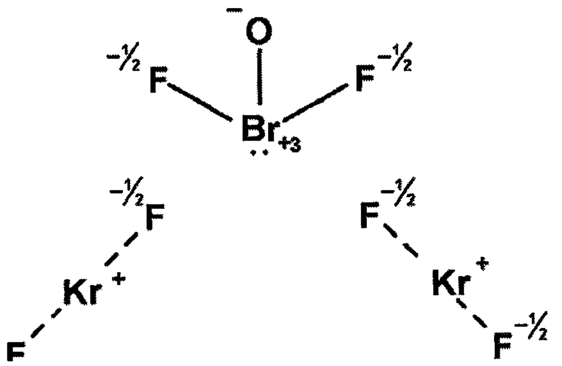

VIII

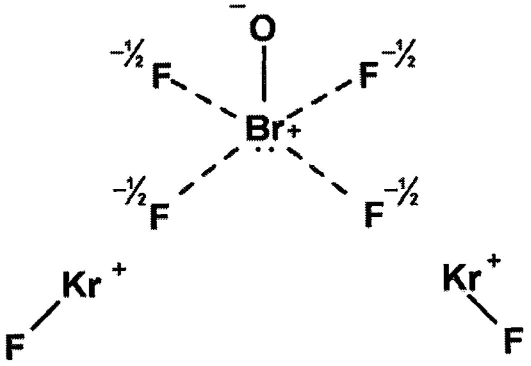

IX

7.2.4.3. QTAIM and ELF Analyses. The bonding was investigated by complementary use of the quantum theory of atoms in molecules (QTAIM)[251] and the topological analysis[252] of the Becke and Edgecombe electron localization function (ELF).[253] Both methods partition molecular space into adjacent nonoverlapping regions with the help of the gradient dynamical system theory, a technique very similar to that used in hydrology to determine drainage basins and drainage divides. An outline of QTAIM and ELF is provided in Appendix 4. For the ensuing discussion, the following abbreviations denote atomic populations, $\bar{N}(A)$; electron localization function, $\eta(\mathbf{r})$; core basins, C(A);

valence basins, V(A, B, ...); monosynaptic basins, V(A); disynaptic basins, V(A, B); and closed isosurfaces, $\eta(\mathbf{r}) = f$, where f is defined as the isosurface contour. The QTAIM and ELF analyses of KrF_2, $BrOF_2^+$, and AsF_6^- fragments are provided in Appendix 4.

Bonding in [$BrOF_2$][AsF_6]·2KrF_2. The NBO, AIM and ELF bonding analyses provide a consistent picture of the reorganization of electron density that result from formation of the KrF_2 complex, i.e., the net electron density transfer towards the $BrOF_2^+$ group and the polarization of the KrF_2 ligands. The very large electronegativity differences between $BrOF_2^+$ and KrF_2 (7.6 eV) and between $BrOF_2^+$ and AsF_6^- (14.2 eV) using Parr's definition of electronegativity,[254] accounts for the direction of the charge transfer, whereas the hardness values[254] of KrF_2 (6.5 V) and AsF_6^- (10.1 V) account for the magnitudes of the contributions. The NPA and QTAIM populations provide global charge transfer values that are in agreement within a few hundredths of an electron. About 0.1 e is transferred from each KrF_2 and 0.05 e from AsF_6^-. In the complex molecular graph, the bromine atom is linked to the two bridging fluorines, F_3 and F_5, of the KrF groups and to F_7 of AsF_6^-. The values of the Laplacian of the electron density at the bond critical points are positive and decrease with the Br–F internuclear distance, i.e., 0.166 (Br–F_5), 0.157 (Br–F_3) and 0.122 (Br–F_7). Moreover, there is a degenerate critical point between Br and F_9. The delocalization indexes between Br and the weakly bonded fluorine atoms show almost the same trends: δ(Br, F_3), 0.24; δ(Br, F_5), 0.22; δ(Br, F_7), 0.14; and δ(Br, F_9), 0.02. The localization domains of the complex at $\eta(\mathbf{r}) = 0.75$ are shown in Figure 7.3a whereas the hierarchy of the ELF basins is given in Scheme 7.1. Although the bromine coordination number has increased to 6, the V(Br) ("valence

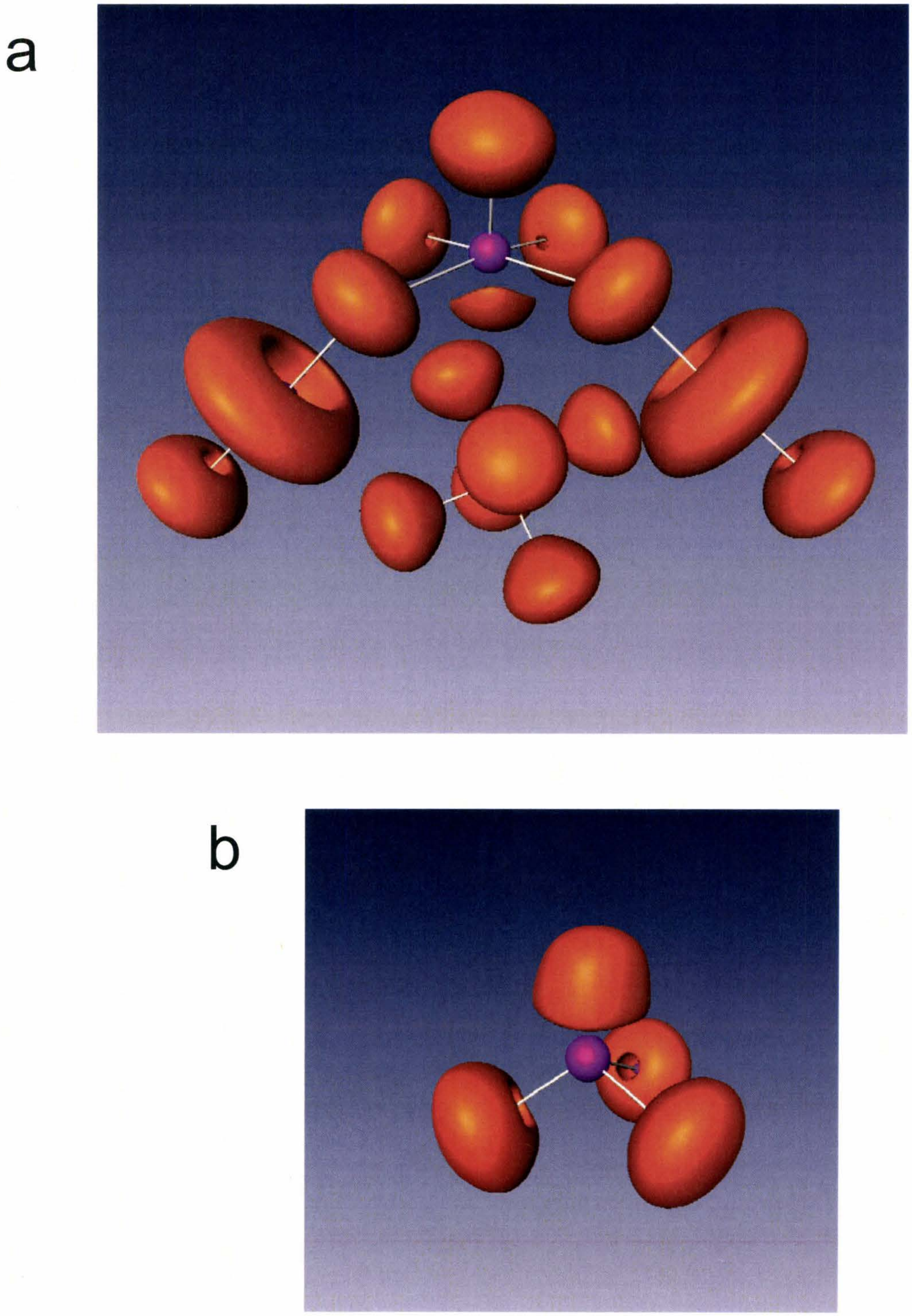

Figure 7.3. ELF localization domains for (a) $[BrOF_2][AsF_6]\cdot 2KrF_2$ compared with those of (b) $BrOF_2^+$. The isosurface value is $\eta(\mathbf{r}) = 0.75$. Color code: magenta = core, brick-red = monosynaptic basin.

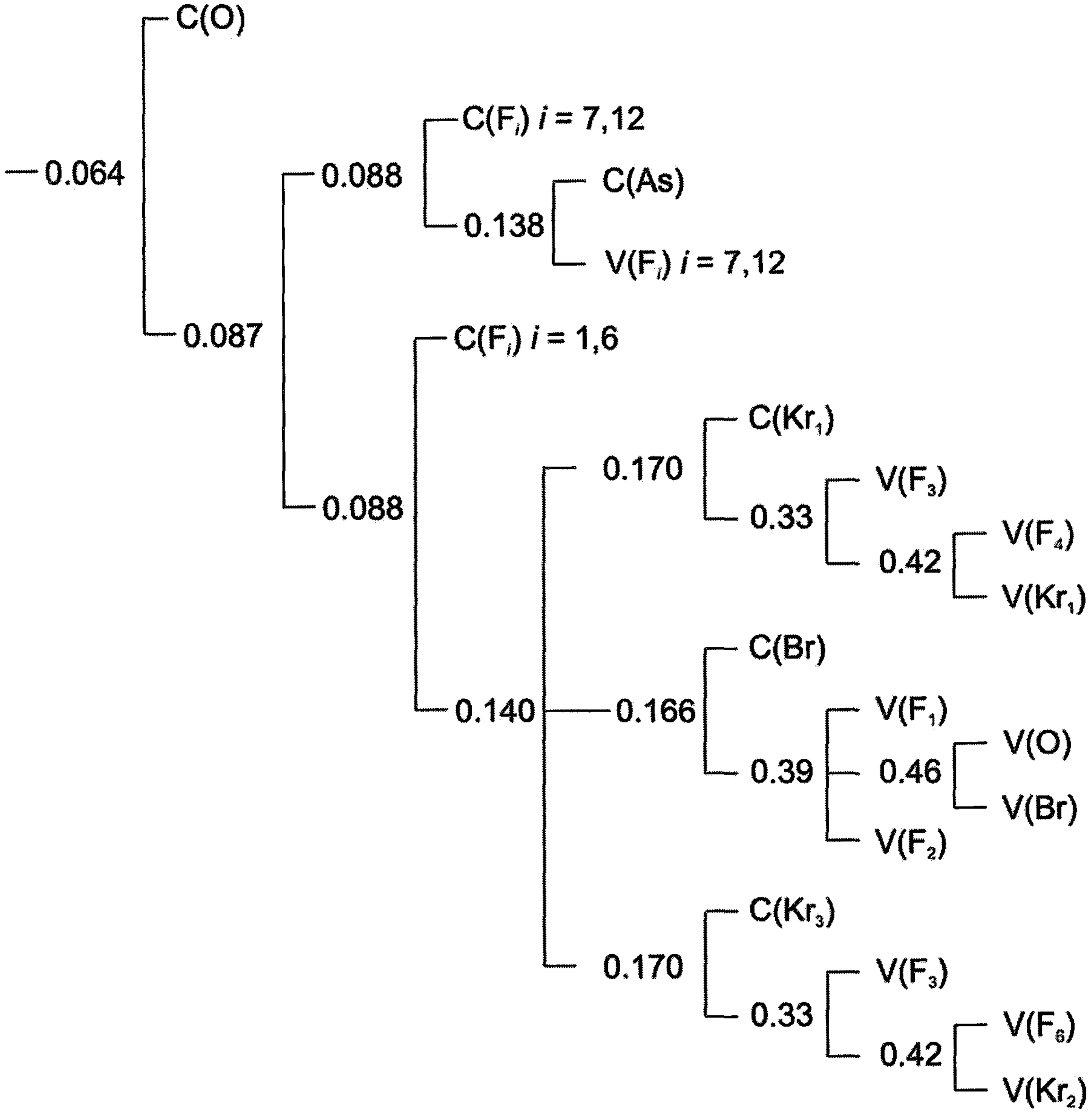

Scheme 7.1. Reduction of localization diagram for $[BrOF_2][AsF_6]\cdot 2KrF_2$ showing the ordering of localization nodes and the boundary isosurface value, $\eta(\mathbf{r})$, at which the reducible domains split. The labeling scheme corresponds to that used in Figures 7.3a.

electron lone pair on Br") basin population remains unchanged in the complex while its $\eta(\mathbf{r})$ = 0.75 localization domain appears to be contracted in the complex (Figure 7.3a) compared to the free $BrOF_2^+$ cation (Figure 7.3b). In fact, the V(Br) basin accommodates its shape and volume to the environment. In the complex it is confined within the cage formed by the F_1, F_2, F_3, F_5 and F_7 atoms, whereas there are no constraints in the free cation. In contrast to the classical AX_6E arrangement predicted by VSEPR rules,[41] the bond pair and electron lone pair arrangement around Br appears to be a hybrid of distorted octahedral, square pyramidal, and trigonal pyramidal geometries that are predicted for AX_6, AX_5E and AX_3E arrangements. The angles subtended at bromine have the following values: O–Br–F_1, 102.0°; O–Br–F_2, 100.1°; O–Br–F_3, 90.7°; O–Br–F_5, 85.3 °; O–Br–V(Br), 133.2°; and O–Br–F_7, 170.3°.

The deviations from the octahedral (or square pyramidal) value occur for those angles involving F_1 and F_2, which correspond to the shortest F–O internuclear distances (largest repulsions), and for F_7, which is close to the V(Br) basin. It is worth noting that the degenerate critical point mentioned above lies on a line linking F_9 to V(Br).

The interaction of the different groups also induces a redistribution of their electronic densities among their basins. The $BrOF_2^+$ cation attracts 0.25 e which is almost equally distributed among the V(F) and V(O) basins, whereas the V(Br) population remains unchanged. In the AsF_6^- anion, the V(As, F) basins vanish in the complex and merge into the corresponding V(F) basins. Within the KrF_2 ligands, there is a density flow from the terminal fluorine and the krypton atomic basins towards the bridging fluorine whose net population is increased by 0.08 e. Paradoxically, the populations of the V(F_4) and V(F_6) basins increase with respect to the uncomplexed KrF_2 molecule at the expense of V(Kr). This polarization increases the covalent character of the Kr–F_4 and Kr–F_6 interactions; the Kr atomic basin contributions to V(F_4) and V(F_6) are 0.63 and 0.93 e whereas the V(F_3) and V(F_5) basins only belong to the F_3 and F_5 atomic basins. This effect explains the contraction of the Kr–F_4 and Kr–F_6 internuclear distances with respect to uncomplexed KrF_2.

7.3. Conclusion

The Lewis acid properties of the $BrOF_2^+$ cation and its resistance to oxidation have provided the avenue to the synthesis of a KrF_2 coordination complex with a main-group atom. The synthesis and crystal structure of $[BrOF_2][AsF_6]\cdot 2KrF_2$ provide a rare example in which KrF_2 functions as a ligand and represents a significant extension of krypton chemistry, accounting for much of what is presently known about the coordination chemistry of KrF_2. The vibrational assignments of the KrF_2 ligands and their descriptions substantiate those of known homoleptic XeF_2 coordination complexes with metal cations. The present findings may be expected to facilitate the extension of KrF_2 coordination chemistry to the syntheses of KrF_2 complexes with other main-group and metal centers.

The NBO, AIM and ELF bonding analyses indicate that $[BrOF_2][AsF_6]\cdot 2KrF_2$ is organized around $BrOF_2^+$ and its stabilization is due to its Coulomb interaction with the AsF_6^- anion and to electron delocalization and charge transfers involving the KrF_2 ligands. This charge transfer increases the ionic character of the Br–O and Br–$F_{1,2}$ bonds.

The polarization of the KrF_2 ligands is a result of the electric field imposed by the $BrOF_2^+$ cation. Its main effect is to enhance the anionic character of each bridging fluorine atom, thereby giving rise to an electrostatic interaction with the positively charged bromine atom of the $[BrOF_2][AsF_6]$ ion pair. However, the stabilization energy is not large enough to enable significant local rearrangement of the ligands around the bromine atom and consequently the two KrF_2 ligands are adjacent to one another. The study has provided two structurally related examples that illustrate strong ($BrOF_2^+$) and weak ($[BrOF_2][AsF_6]\cdot 2KrF_2$) valence electron lone pair behavior.[250]

CHAPTER 8

XeF_2 Coordination to a Halogen Center; Raman Spectra ($n = 1, 2$) and X-ray Crystal Structures ($n = 2$) of $[BrOF_2][AsF_6]\cdot nXeF_2$ and $[XOF_2][AsF_6]$ (X = Cl, Br)

8.1. Introduction

Xenon difluoride behaves as a fluoride ion donor toward strong fluoride ion acceptors such as AsF_5, SbF_5, and BiF_5 forming XeF^+ and $Xe_2F_3^+$ salts.[19,44,74,76,255] Relatively few examples are known in which XeF_2 behaves as a coordinating ligand towards weaker Lewis acid centers. Coordination of a weak to moderate strength, oxidatively resistant Lewis acid to a fluorine atom of XeF_2 may also occur without "complete" fluoride ion transfer. A considerable number of metal cations satisfy these criteria, and their XeF_2 coordination complexes have been synthesized and structurally characterized, e.g., Li^+, Mg^{2+}, Ca^{2+}, Cu^{2+}, Zn^{2+}, Sr^{2+}, Ag^+, Cd^{2+}, Ba^{2+}, La^{3+}, Nd^{3+}, Pb^{2+}.[82,83] Xenon difluoride coordination complexes with the neutral metal oxide tetrafluorides, WOF_4 and $MoOF_4$, have also been synthesized and characterized in the solid-state by Raman spectroscopy and by solution ^{19}F and ^{129}Xe NMR spectroscopy.[107,256] A number of molecular addition compounds of XeF_2 are also known in which XeF_2 exhibits no tendency to coordinate. These are exemplified by $IF_5\cdot XeF_2$,[257] $XeF_4\cdot XeF_2$,[258] and $XeOF_4\cdot XeF_2$,[259] which show that the vibrational frequencies of XeF_2 and the Xe–F bond lengths are essentially unaffected relative to solid XeF_2.

Presently, the only examples known in which XeF_2 coordinates to a nonmetal center are $2XeF_2\cdot[XeF_5][AsF_6]$, $XeF_2\cdot[XeF_5][AsF_6]$, and $XeF_2\cdot2([XeF_5][AsF_6])$, where XeF_2 coordinates to the Xe(VI) atom of XeF_5^+,[220] and $[BrOF_2][AsF_6]\cdot XeF_2$, where XeF_2 coordinates to $BrOF_2^+$ through Br(V).[129] In both cases, XeF_2 coordinates end-on through fluorine to the electropositive atom of the cation. Although the XeF_5^+ adducts have been characterized by X-ray crystallography, $[BrOF_2][AsF_6]\cdot XeF_2$ has only been characterized by Raman spectroscopy and by solution ^{19}F and ^{129}Xe NMR spectroscopy. In a recent related study, $[BrOF_2][AsF_6]\cdot2KrF_2$[232] has been synthesized and structurally characterized, showing that the KrF_2 molecules are each coordinated to Br(V) through a single fluorine bridge. The study suggested that the synthesis of $[BrOF_2][AsF_6]\cdot2XeF_2$ should also be possible.

The present study describes the syntheses and structural characterizations of $[BrOF_2][AsF_6]$, $[ClOF_2][AsF_6]$, $[BrOF_2][AsF_6]\cdot XeF_2$, and $[BrOF_2][AsF_6]\cdot2XeF_2$. The extension of this chemistry to the $ClOF_2^+$ analogue is also considered, as well as its Lewis acid behavior toward the less fluoro-basic and more strongly oxidizing XeF_4 molecule.

8.2. Results and Discussion

8.2.1. Syntheses of $[BrOF_2][AsF_6]$, $[BrOF_2][AsF_6]\cdot XeF_2$, and $[BrOF_2][AsF_6]\cdot2XeF_2$. The progress of each reaction and the purities of all products were routinely monitored by recording the low-temperature Raman spectra of the solids at –150 °C.

Low-temperature solvolysis of $[XeOTeF_5][AsF_6]$ in liquid BrF_5 resulted in an XeF_2 adduct of $BrOF_2^+$ that also contained BrF_5 (eq 8.1). This compound was isolated as

$$[XeOTeF_5][AsF_6] + (n+1)BrF_5 \xrightarrow[20\ ^{\circ}C]{neat} [BrOF_2][AsF_6]\cdot XeF_2\cdot nBrF_5 + TeF_6 \qquad (8.1)$$

a very pale yellow powder upon removal of the bulk solvent under a dynamic vacuum at –52 to –50 °C. Continued pumping on the polycrystalline solid for several hours at –52 to –50 °C was shown by Raman spectroscopy (Table 8.1) to result in slow removal of BrF_5 from the crystal lattice, leaving behind $[BrOF_2][AsF_6]\cdot XeF_2$ as an amorphous white powder (eq 8.2). Further pumping at 0 °C for several hours resulted in slow removal of adducted XeF_2 (eq 8.3), forming $[BrOF_2][AsF_6]$ as a white powder.

$$[BrOF_2][AsF_6]\cdot nBrF_5\cdot XeF_2 \xrightarrow[-52\ to\ -50\ ^{\circ}C]{dynamic\ vac.} [BrOF_2][AsF_6]\cdot XeF_2 + nBrF_5 \qquad (8.2)$$

$$[BrOF_2][AsF_6]\cdot XeF_2 \xrightarrow[0\ ^{\circ}C]{dynamic\ vac.} [BrOF_2][AsF_6] + XeF_2 \qquad (8.3)$$

The Raman spectrum of the product was in agreement with the previously reported spectrum,[128] however, contrary to the earlier report, samples of $[BrOF_2][AsF_6]$ that were left at room temperature overnight showed no signs of decomposition to Br_2^+ either visually or by Raman spectroscopy, i.e., the Br–Br stretching mode at 360 cm^{-1} was absent.[260] Hydrogen fluoride solutions of $[BrOF_2][AsF_6]$ were also warmed to 50 °C for several minutes followed by slow cooling to 22 °C over 24 h, and showed no signs of decomposition.

Addition of aHF to $[BrOF_2][AsF_6]\cdot XeF_2$ and dissolution at –20 °C resulted in a clear, colorless solution. Upon cooling to –78 °C, a white precipitate formed. The Raman spectrum of the solid under HF and the Raman spectrum recorded after HF had been removed under dynamic vacuum at –78 °C were identical and revealed that a mixture of $[BrOF_2][AsF_6]\cdot 2XeF_2$ and $[BrOF_2][AsF_6]$ had formed according to eq 8.4. Under similar

Table 8.1. Raman Spectra[a] Acquired During the Removal of BrF_5 (–50 °C) from a BrF_5 Solution of $[BrOF_2][AsF_6]{\cdot}XeF_2$, and the Raman Spectra of Uncoordinated XeF_2,[b] BrF_5,[b] and $[BrOF_2][AsF_6]{\cdot}XeF_2$

		BrF$_5$-Solvate (approximate pumping time in hours)						
XeF_2 ^{b}	BrF_5 ^{b}	0.25 ^{c,d}	0.50 ^{d,e}	0.75 (pure BrF$_5$-solvate) ^{f}	1.0 ^{g}	4.0 ^{g}	9.0 ^{g}	13.0 $[BrOF_2][AsF_6]{\cdot}XeF_2$ ^{h}
			1065(3)		1063(1)	1063(10)	1067(2)	1062(3)
		1051(8)	1048(39)	1047(32)	1048(31)	1049(41)	1050(38)	1050(34)
						1043(23)	1043(22)	1043(22)
			751(4)	751(5)	750(3)	751(10)	749(3)	752(3)
					745(2)	744(11)	744(6)	744(7)
						739(10)		
						733(35)		
				718(2)		722(14)		
				708(2)	709(2)	707(9)	707(3)	706(3)
		697(20)			697(2)	697(9)	698(2)	698(2)
		687sh ^{i}	686(90) ^{i}	686(66) ^{i}	686(60) ^{i}	686(36) ^{i}	686(5) ^{i}	
	681(81)	681(100)	681(19)					
				678(4)	679(4)	674(14)	674(11)	674(11)
					674(5)			
							668(4)	669(4)
			660(3)					
				655(5)				651 sh
	646(1)							
		651br(4)	645(57)	644(51)	645(61)	646(96)	646(79)	646(75)
			630(22)	630(21)	633(29)	633(46)	633(41)	634(38)
					630 sh			
	628(2)	627(2)						
				625(9)	624 sh	621(11)		
						614(12)		
	601(7)	602(5)						
			598(3) ^{i}	598(2) ^{i}	598(2) ^{i}	599(9) ^{i}		
			589(4) ^{i}	589(4) ^{i}	588(4) ^{i}	589(9) ^{i}		586(2)
	581(26)	581(26)						
		570br(43) ^{i}	574(99) ^{i}	574(69) ^{i}	574(60) ^{i}	574(47) ^{i}	574(18) ^{i}	575(14)
			568(30) ^{i}					
					565(1)	566(12)	565(6)	565(7)
	561(100)	561(86)						
					560(10)	559(44)	559(44)	559(45)
			549(100)	549(100)	549(100)	548(80)	547(60)	546(51)
					543(45)	543(100)	543(100)	543(100)
	538(39)	538(82) ^{i}	538(78) ^{i}	538(50) ^{i}	538(48) ^{i}	539(40) ^{i}		
						533(17)		531(11)
	523(68)	523(72)						
496(100)								
	477(1)							

Table 8.1. (continued...)

		BrF$_5$-Solvate (approximate pumping time in hours)						
XeF$_2$ ^{b}	BrF$_5$ ^{b}	0.25 ^{c,d}	0.50 ^{d,e}	0.75 (Pure BrF$_5$-Solvate)^f	1.0 ^{g}	4.0 ^{g}	9.0 ^{g}	13.0 [BrOF$_2$][AsF$_6$]·XeF$_2$ ^{h}
			467(72) ^{j}	466(80) ^{j}	466(78) ^{j}	466(49) ^{j}	466(24) ^{j}	466(17)
								447(8) br
					422(1)	425(13)	428(7)	426(10) br
	421(12)	421(17)						
		417sh	418(9)	418(2)	417(2)			
			416(7)		412(3)	412(13)	412(8)	411(11)
	412(8)	412(7)						
			407(13)	407(16)	407(15)	407(15)		408 sh
			402(3)		403(4)	402(15)	402(9)	402(12)
		396(1)	395(2)	394(4)	394(5)	392(17)	391(12)	392(14)
					391(4)			
			387(4)	387(8)	387(5)	387(19)	387(12)	387(7)
						381(11)		
		373sh	372(22)	372(18)	372(20)	373(29)	373(19)	373(21)
			369(15)	368(13)	369(13)			
	371(4)	371(10)						
	364(20)	363(25)		364(59)	364(10)	364(22)	364(14)	364(17)
			362(13)	361(8)	361(12)			
					326(4)	325(11)	325(6)	325(10)
	317(11)	317(22)	318(19)	318(13)	318(12)	318(11)		
	311(13)	311(28)	311(17)	310(12)	310(11)	313(11)	314(2)	314(4)
		294(3)	294(6)	293(9)	293(6)	292(13)	293(7)	293(8)
			288(4)		286(4)			
	244(2)	245(5)	242(4)	243(1)	242(2)			244(3)
	237(3)	237(5)						
	234(3)	234(5)						
	232(2)							
			223(3)	223(2)	223(2)			
			162(2)	162(2)	160(3)			
					153(4)	153(11)	153(6)	152(11)
					140(3)	140(10)	139(4)	140(9)
	121(1)				122(8)	122(10)		
		117(7)	117(8)	117(5)			119(4)	
110(10)								
		95(14)		95(9)	96(11)	97(15)		98(11)

Table 8.1. (continued…)

[a] Frequencies are given in cm^{-1}. The Raman spectra were recorded in an FEP sample tube at −150 °C using 1064-nm excitation. Values in parentheses denote relative Raman intensities. The abbreviations denote a shoulder (sh) and broad (br). [b] The frequencies and intensities were obtained in this work for the pure solids. [c] A saturated frozen BrF_5 solution, produced by removal of excess BrF_5. [d] Free BrF_5 is more readily removed in the early stages of pumping with times varying from sample to sample. [e] The solid product contained clumps resulting from residual BrF_5 solvent. [f] A pure sample of the BrF_5-solvate of $[BrOF_2][AsF_6]\cdot XeF_2$ was obtained as a friable powder. [g] Removal of associated BrF_5 was slow and the samples were rarely homogenous, with the pumping time varying from sample to sample. [h] The spectrum corresponds to the spectrum in Figure 8.6 and Table 8.7. [i] These BrF_5 bands are most influenced by association with $[BrOF_2][AsF_6]\cdot XeF_2$ and are similar to the bands of solid BrF_5 but are shifted to higher frequencies. [j] This band is associated with $\nu(XeF_b)$ and is sensitive to BrF_5 solvation.

$$2[BrOF_2][AsF_6]\cdot XeF_2 \xrightarrow[-20\ ^{\circ}C]{HF} [BrOF_2][AsF_6]\cdot 2XeF_2 + [BrOF_2][AsF_6] \quad (8.4)$$

conditions, 1, 1.5, 2, and 3 equiv of XeF_2 were allowed to react with 1 equiv of $[BrOF_2][AsF_6]$ in HF solvent. Using 1 or 1.5 equiv of XeF_2, the Raman spectrum of the isolated product showed them to be mixtures of $[BrOF_2][AsF_6]$ and $[BrOF_2][AsF_6]\cdot 2XeF_2$; with 2 equiv of XeF_2, the only product was $[BrOF_2][AsF_6]\cdot 2XeF_2$, and with 3 equiv, a mixture of $[BrOF_2][AsF_6]\cdot 2XeF_2$ and XeF_2 was obtained. No other adduct stoichiometries were detected.

Both $[BrOF_2][AsF_6]\cdot XeF_2$ and $[BrOF_2][AsF_6]\cdot 2XeF_2$ are kinetically stable for indefinite periods of time under anhydrous conditions at –78 °C. Concentrated (ca. 0.6 M) and dilute (ca. 0.3 M) HF solutions of both salts that had been warmed to 20 °C and then rapidly cooled to –78 °C showed only a mixture of $[BrOF_2][AsF_6]$ and $[BrOF_2][AsF_6]\cdot 2XeF_2$, and $[BrOF_2][AsF_6]\cdot 2XeF_2$, respectively, when their Raman spectra were recorded under frozen HF. Upon slow cooling of both concentrated solutions from 20 to –78 °C over several hours, two colorless phases formed as a result of the complex salting out of solution. Soon thereafter the denser phases in both samples rapidly crystallized to give a mixture of $[BrOF_2][AsF_6]$ and $[BrOF_2][AsF_6]\cdot 2XeF_2$, as well as $[BrOF_2][AsF_6]\cdot 2XeF_2$, respectively. However, slow cooling of both dilute solutions from 20 to –78 °C over several hours resulted in predominantly the starting materials but also significant amounts of the fluoride ion abstraction products, $BrOF_3$ and $[Xe_2F_3][AsF_6]$ which formed according to equation 8.5. Both products were observed in the Raman spectrum and $[Xe_2F_3][AsF_6]$ was also confirmed by several single-crystal unit cell determinations (trigonal phase[73]). The calculated Gibbs free energy for the major gas-

$$BrOF_2{}^+{}_{(g)} + 2XeF_{2\,(g)} \rightleftharpoons Xe_2F_3{}^+{}_{(g)} + BrOF_{3(g)} \qquad (8.5)$$

$\Delta H^o_{rxn} = -44.3$ kJ mol^{-1} $\Delta G^o_{rxn} = +6.4$ kJ mol^{-1} MP2/(aug-)cc-pVTZ

$\Delta H^o_{rxn} = -33.5$ kJ mol^{-1} $\Delta G^o_{rxn} = +4.8$ kJ mol^{-1} B3LYP/(aug-)cc-pVTZ

phase decomposition pathway (eq 8.5) shows that the reaction is near equilibrium so that small changes in temperature, concentration or solution conditions could account for an equilibrium shift that favors the formation of $Xe_2F_3{}^+$ and $BrOF_3$ in solution. The large positive $\Delta H_{rxn}{}^o$ and $\Delta G_{rxn}{}^o$ values associated with internal fluoride ion abstraction starting from the associated adduct (eq 8.6) relative to starting from its dissociated components (eq 8.5) suggests that the adduct is already at equilibrium with its dissociation products in HF solutions.

$$BrOF_2{}^+{\cdot}2XeF_{2\,(g)} \rightleftharpoons Xe_2F_3{}^+{}_{(g)} + BrOF_{3(g)} \qquad (8.6)$$

$\Delta H^o_{rxn} = +158.0$ kJ mol^{-1} $\Delta G^o_{rxn} = +124.6$ kJ mol^{-1} B3LYP/(aug-)cc-pVTZ

8.2.2. ^{129}Xe and ^{19}F NMR Spectroscopy. The ^{129}Xe and ^{19}F NMR spectra of $[BrOF_2][AsF_6]{\cdot}XeF_2$ had been previously recorded in BrF_5 solvent at −59 °C at an external field strength of 2.349 T (^{19}F, 94.1 MHz; ^{129}Xe, 27.86 MHz).[129] The study indicated that XeF_2 exchange was sufficiently fast on the NMR time scale to collapse the ^{19}F–^{19}F couplings between the fluorine environments of coordinated XeF_2 ("XeF_2") and $BrOF_2{}^+$. In the present study, a sample of $[BrOF_2][AsF_6]{\cdot}XeF_2$ was dissolved in BrF_5 solvent, and the ^{129}Xe and ^{19}F NMR spectra were recorded at −60 °C at an external field strength of 11.744 T (^{19}F, 470.593 MHz; ^{129}Xe, 139.051 MHz) in an attempt to slow the chemical exchange rate sufficiently to observe the $^1J(^{19}F_t–^{129}Xe)$, $^1J(^{19}F_b–^{129}Xe)$,

$^2J(^{19}F_t–^{19}F_b)$, $^2J(^{19}F_b–^{19}F_{Br})$, and $^3J(^{19}F_{Br}–^{129}Xe)$ couplings among the fluorine and xenon environments of "XeF_2" and $BrOF_2^+$. The ^{129}Xe and ^{19}F NMR spectra were similar to those reported previously [δ(^{19}F, 163.9 ppm), $\Delta\nu_{½}$ = 27 Hz; δ(^{129}Xe, −1358 ppm), $\Delta\nu_{½}$ = 38 Hz; $^1J(^{19}F–^{129}Xe)$ = 5680 Hz][129] with the exception of broadened lines for "XeF_2" in the ^{19}F ($\Delta\nu_{½}$ = 1180 Hz [^{19}F]) and ^{129}Xe ($\Delta\nu_{½}$ = 230 Hz [^{129}Xe]) spectra, which indicated that "XeF_2" exchange was slowed, but not sufficiently to resolve any of the spin–spin couplings of the complex cation.

The ^{129}Xe and ^{19}F NMR spectra were also recorded for $[BrOF_2][AsF_6]\cdot2XeF_2$ dissolved in BrF_5 solvent (−60 °C). The spectra were similar to those of the 1:1 adduct with single ^{19}F (−174.2 ppm) and ^{129}Xe (−1489 ppm) resonances for "XeF_2" but were more shielded than those of $[BrOF_2][AsF_6]\cdot XeF_2$ [δ(^{129}Xe, −1368 ppm; δ(^{19}F, −165.8 ppm)] and less shielded than that of XeF_2 recorded in BrF_5 solvent [δ(^{129}Xe), −1708 ppm, −40 °C;[49] δ(^{19}F), −181.8 ppm, −20 °C[109]]. The ^{19}F resonance of "XeF_2" was also narrower in $[BrOF_2][AsF_6]\cdot2XeF_2$ ($\Delta\nu_{½}$ = 320 Hz [^{19}F]; $^1J(^{19}F–^{129}Xe)$ = 5660 Hz) when compared with that of $[BrOF_2][AsF_6]\cdot XeF_2$ ($\Delta\nu_{½}$ = 1180 Hz; $^1J(^{19}F–^{129}Xe)$ = 5678 Hz), indicating that "XeF_2" exchange was more rapid for $[BrOF_2][AsF_6]\cdot2XeF_2$. The ^{129}Xe resonances of "XeF_2" were slightly broader in $[BrOF_2][AsF_6]\cdot2XeF_2$ ($\Delta\nu_{½}$ = 310 Hz) when compared with that of $[BrOF_2][AsF_6]\cdot XeF_2$ ($\Delta\nu_{½}$ = 230 Hz). Exchange between coordinated "XeF_2" and free XeF_2 is expected to result in more pronounced broadening in the ^{129}Xe NMR spectrum than in the ^{19}F spectrum because of the greater frequency differences between complexed and free XeF_2 [δ(^{129}Xe, "XeF_2") – δ(^{129}Xe, XeF_2) ≈ 9400

Hz versus $\delta(^{19}F, “XeF_2”) - \delta(^{19}F, XeF_2) \approx 1500$ Hz].[49,109] However, the significant line narrowing that occurs in the ^{19}F NMR spectrum of “XeF_2” results from collapse of the $^{2}J(^{19}F_b-^{19}F_{Br})$ coupling, whereas collapse of the smaller $^{3}J(^{129}Xe-^{19}F_{Br})$ coupling in the ^{129}Xe NMR spectrum would not be expected to have a significant effect on the ^{129}Xe line width.

8.2.3. Attempted Syntheses of $[ClOF_2][AsF_6]\cdot2XeF_2$, and XeF_4 Coordination Complexes of $[ClOF_2][AsF_6]$ and $[BrOF_2][AsF_6]$. An attempt to synthesize a XeF_4 adduct of $[BrOF_2][AsF_6]$ proved unsuccessful when an equimolar mixture of XeF_4 and $[BrOF_2][AsF_6]$ was dissolved at 50 °C in HF and cooled to 22 °C. A white precipitate formed which was shown by Raman spectroscopy to be a mixture of the starting materials. This is not unexpected because the fluoride ion donor strength of XeF_4 is much less than that of XeF_2.[261]

Attempts were made to synthesize XeF_2 and XeF_4 adducts of $[ClOF_2][AsF_6]$ in the hope that the chlorine analogue, by virtue of the greater electronegativity of chlorine, would prove to be a stronger Lewis acid. Mixtures of $XeF_2/[ClOF_2][AsF_6]$ and $XeF_4/[ClOF_2][AsF_6]$ dissolved in HF at −50 and 50 °C, respectively, were cooled to −78 °C, whereupon white solids precipitated. Raman spectra of both products were recorded under HF solvent and after the solvent had been removed under a dynamic vacuum at −78 °C. In both cases, the solids proved to be mixtures of the starting materials. In the case of the $XeF_2/[ClOF_2][AsF_6]$ system, warming of the HF solution to room temperature resulted in fluoride ion abstraction from XeF_2 by $ClOF_2^+$ to form $Xe_2F_3^+$ and $ClOF_3$ (eq

8.7). Evidence for fluoride ion abstraction is based on Raman spectroscopy of the frozen

$$[ClOF_2][AsF_6] + 2XeF_2 \xrightarrow[25\ ^{\circ}C]{HF} ClOF_3 + [Xe_2F_3][AsF_6] \qquad (8.7)$$

samples under HF and the unit cell dimensions of several of $[Xe_2F_3][AsF_6]$ crystals (trigonal phase).[73] Raman spectroscopy confirmed the presence of $[Xe_2F_3][AsF_6]$ but $ClOF_3$ presumably remained in the frozen HF solvent phase and was too dilute to be observed in the Raman spectrum.

8.2.4. X-ray Crystallography. Summaries of the refinement results and other crystallographic information for $[BrOF_2][AsF_6]{\cdot}2XeF_2$, $[BrOF_2][AsF_6]$, and $[ClOF_2][AsF_6]$ are provided in Table 8.2. Important bond lengths, bond angles, and contacts for $[BrOF_2][AsF_6]{\cdot}2XeF_2$ and $[ClOF_2][AsF_6]$ are listed in Tables 8.3 and 8.4.

8.2.4.1. $[BrOF_2][AsF_6]{\cdot}2XeF_2$. The compound, $[BrOF_2][AsF_6]{\cdot}2XeF_2$, is isomorphous with $[BrOF_2][AsF_6]{\cdot}2KrF_2$[232] and belongs to the $P2_1/c$ space group with a unit cell volume that is 87.7(3) Å^3 larger than that of the krypton analogue at the same temperature (−173 °C). The structure consists of well-separated $[BrOF_2][AsF_6]{\cdot}2XeF_2$ units. The primary coordination sphere of the $BrOF_2^+$ cation is trigonal pyramidal, as observed in the KrF_2 analogue. A fluorine ligand of the AsF_6^- anion is coordinated trans to the oxygen atom, while the fluorine electron pair donor atoms of two XeF_2 molecules are coordinated trans to the fluorine atoms of $BrOF_2^+$ so that the coordination sphere around bromine is pseudo-octahedral (Figures 8.1 and 8.2) as observed in the KrF_2 analogue.[232]

The geometrical parameters of $BrOF_2^+$ in $[BrOF_2][AsF_6]{\cdot}2XeF_2$ and $[BrOF_2][AsF_6]{\cdot}2KrF_2$ are equal to within ±3σ. Although the Br–O bond length (1.549(5)

Table 8.2. Summary of Crystal Data and Refinement Results for $[BrOF_2][AsF_6]$, $[ClOF_2][AsF_6]$, and $[BrOF_2][AsF_6]\cdot 2XeF_2$

	$[BrOF_2][AsF_6]$	$[ClOF_2][AsF_6]$	$[BrOF_2][AsF_6]\cdot 2XeF_2$
space group	$P2/_13$ (No. 198)	$Pna2/_1$ (No. 33)	$P2_1/c$ (No. 14)
a (Å)	8.6144(3)	14.686(2)	5.9282(3)
b (Å)	8.6144(3)	5.2072(6)	13.9789(8)
c (Å)	8.6144(3)	8.1070(9)	15.3983(9)
β (deg.)	90	90	111.859(2)
V (Å^3)	639.3(1)	620.0(2)	1184.3(1)
Z (molecules/unit cell)	4	4	4
mol. wt. (g mol^{-1})	1291.32	1113.48	2645.72
ρ_{calc} (g cm^{-3})	3.354	2.982	3.710
T (°C)	−173	−173	−173
μ (mm^{-1})	11.68	6.03	12.01
λ (Å)	0.71073	0.71073	0.71073
R_1[a]	0.0198	0.0304	0.0450
wR_2[b]	0.0370	0.0634	0.0932

[a] $R_1 = \Sigma\|F_o| - |F_c\|/\Sigma|F_o|$ for $I > 2\sigma(I)$. [b] wR_2 is defined as $\{\Sigma[w(F_o^2 - F_c^2)^2]/\Sigma w(F_o^2)^2\}^{1/2}$ for $I > 2\sigma(I)$.

Table 8.3. Complete List of Experimental and Calculated Geometrical Parameters for $[BrOF_2][AsF_6]\cdot 2XeF_2$

exptl[a]			PBE1PBE[a]	B3LYP[a]
		Bond Lengths (Å)		
Br(1)–O(1)	1.549(5)	Br(1)–O(1)	1.556	1.569
Br(1)–F(1)	1.736(4)	Br(1)–F(1)	1.733	1.758
Br(1)–F(2)	1.733(4)	Br(1)–F(2)	1.734	1.760
Br(1)---F(3)	2.306(4)	Br(1)---F(3)	2.303	2.323
Br(1)---F(5)	2.292(4)	Br(1)---F(5)	2.296	2.325
Br(1)---F(7)	2.610(4)	Br(1)---F(7)	2.579	2.561
Xe(1)–F(3)	2.052(4)	Xe(1)–F(3)	2.074	2.101
Xe(1)–F(4)	1.960(4)	Xe(1)–F(4)	1.948	1.971
Xe(2)–F(5)	2.053(4)	Xe(2)–F(5)	2.081	2.106
Xe(2)–F(6)	1.956(5)	Xe(2)–F(6)	1.945	1.968
As(1)–F(7)	1.746(4)	As(1)–F(7)	1.789	1.812
As(1)–F(8)	1.719(4)	As(1)–F(8)	1.710	1.723
As(1)–F(9)	1.720(4)	As(1)–F(9)	1.744	1.756
As(1)–F(10)	1.728(4)	As(1)–F(10)	1.725	1.740
As(1)–F(11)	1.719(4)	As(1)–F(11)	1.706	1.720
As(1)–F(12)	1.720(4)	As(1)–F(12)	1.758	1.771
		Bond Angles (deg)		
F(1)–Br(1)–F(2)	89.6(2)	F(1)–Br(1)–F(2)	89.0	89.4
F(1)–Br(1)–O(1)	102.8(3)	F(1)–Br(1)–O(1)	101.8	101.8
F(1)–Br(1)---F(3)	84.8(2)	F(1)–Br(1)---F(3)	84.3	85.1
F(1)–Br(1)---F(5)	165.8(2)	F(1)–Br(1)---F(5)	166.5	166.1
F(1)–Br(1)---F(7)	84.9(2)	F(1)–Br(1)---F(7)	88.8	88.7
F(2)–Br(1)–O(1)	102.6(3)	F(2)–Br(1)–O(1)	100.0	100.2
F(2)–Br(1)---F(3)	163.2(2)	F(2)–Br(1)---F(3)	171.8	171.5
F(2)–Br(1)---F(5)	84.9(2)	F(2)–Br(1)---F(5)	82.4	83.2
F(2)–Br(1)---F(7)	81.0(2)	F(2)–Br(1)---F(7)	73.0	74.9
O(1)–Br(1)---F(3)	94.1(2)	O(1)–Br(1)---F(3)	86.1	87.3
O(1)–Br(1)---F(5)	91.2(2)	O(1)–Br(1)---F(5)	90.0	91.1
O(1)–Br(1)---F(7)	171.4(2)	O(1)–Br(1)---F(7)	167.3	168.5
F(3)–Xe(1)–F(4)	178.4(2)	F(3)–Xe(1)–F(4)	174.8	174.4
F(3)---Br(1)---F(5)	96.7(2)	F(3)---Br(1)---F(5)	103.2	100.8
F(3)---Br(1)---F(7)	82.7(2)	F(3)---Br(1)---F(7)	102.1	98.5
F(5)–Xe(2)–F(6)	179.8(2)	F(5)–Xe(2)–F(6)	175.9	176.3
F(5)---Br(1)---F(7)	81.3(2)	F(5)---Br(1)---F(7)	78.7	78.1
Br(1)---F(3)–Xe(1)	142.4(2)	Br(1)---F(3)–Xe(1)	149.5	151.0
Br(1)---F(5)–Xe(2)	134.1(2)	Br(1)---F(5)–Xe(2)	130.4	130.6
Br(1)---F(7)–As(1)	135.5(2)	Br(1)---F(7)–As(1)	116.6	123.3

Table 8.3. (continued…)

F(7)–As(1)–F(8)	179.4(2)	F(7)–As(1)–F(8)	176.1	176.6
F(7)–As(1)–F(9)	89.2(2)	F(7)–As(1)–F(9)	86.9	87.3
F(7)–As(1)–F(10)	88.8(2)	F(7)–As(1)–F(10)	88.7	88.2
F(7)–As(1)–F(11)	88.4(4)	F(7)–As(1)–F(11)	89.9	89.6
F(7)–As(1)–F(12)	90.0(2)	F(7)–As(1)–F(12)	85.8	85.8
F(8)–As(1)–F(9)	91.2(2)	F(8)–As(1)–F(9)	91.4	91.6
F(8)–As(1)–F(10)	90.7(2)	F(8)–As(1)–F(10)	92.8	92.8
F(8)–As(1)–F(11)	91.2(2)	F(8)–As(1)–F(11)	93.6	93.7
F(8)–As(1)–F(12)	90.3(2)	F(8)–As(1)–F(12)	90.7	90.9
F(9)–As(1)–F(10)	178.0(2)	F(9)–As(1)–F(10)	174.9	174.8
F(9)–As(1)–F(11)	90.3(2)	F(9)–As(1)–F(11)	90.9	91.0
F(9)–As(1)–F(12)	90.0(2)	F(9)–As(1)–F(12)	87.8	87.9
F(10)–As(1)–F(11)	90.2(2)	F(10)–As(1)–F(11)	91.7	91.6
F(10)–As(1)–F(12)	89.4(2)	F(10)–As(1)–F(12)	89.2	89.2
F(11)–As(1)–F(12)	178.5(2)	F(11)–As(1)–F(12)	175.5	175.3

[a] The aug-cc-pVTZ(-PP) basis set was used. The energy-minimized geometry was C_1. The atom labeling scheme corresponds to that used in Figures 8.1 and 8.2.

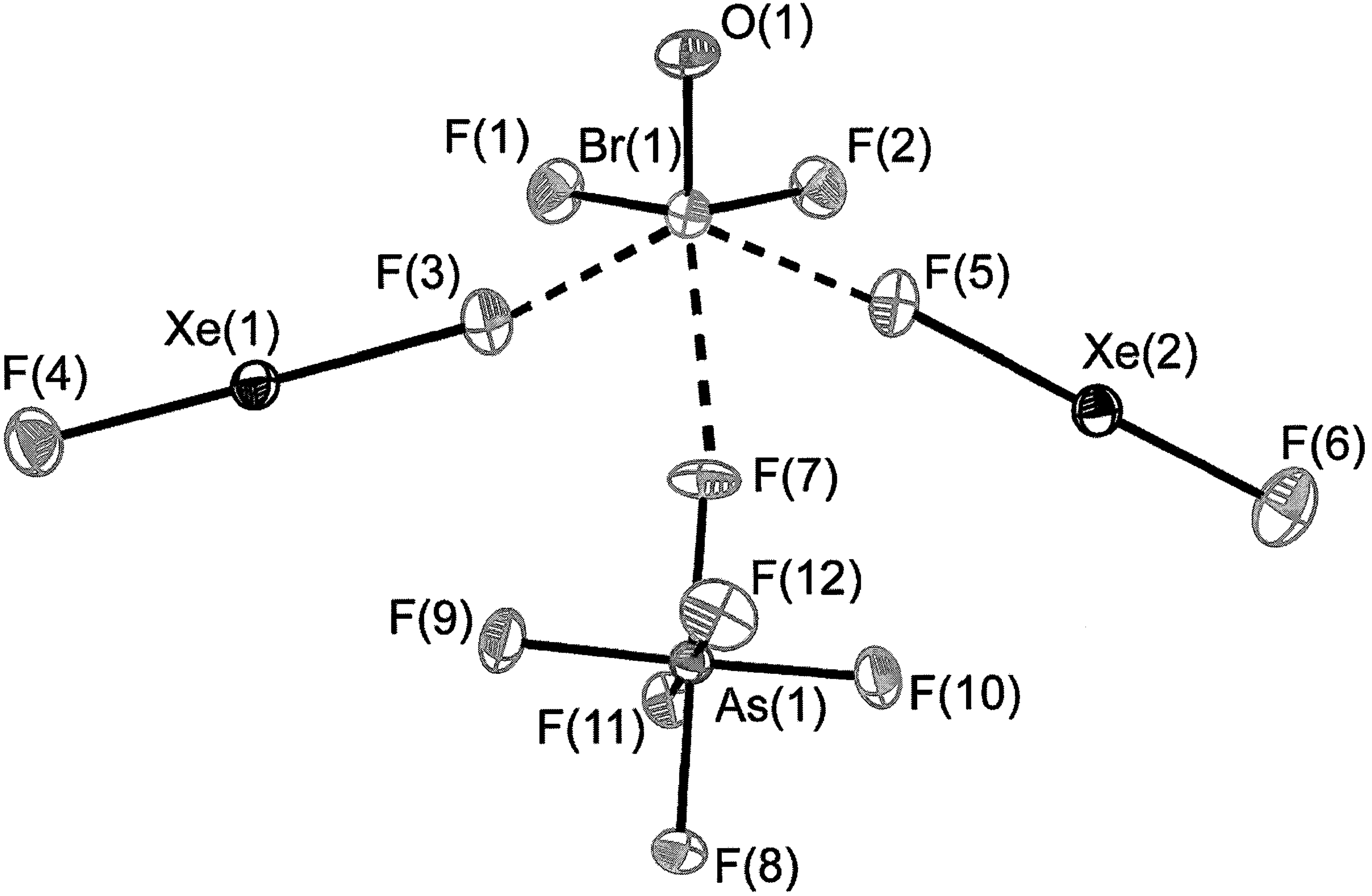

Figure 8.1. The structural unit in the X-ray crystal structure of $[BrOF_2][AsF_6]{\cdot}2XeF_2$; thermal ellipsoids are shown at the 50% probability level.

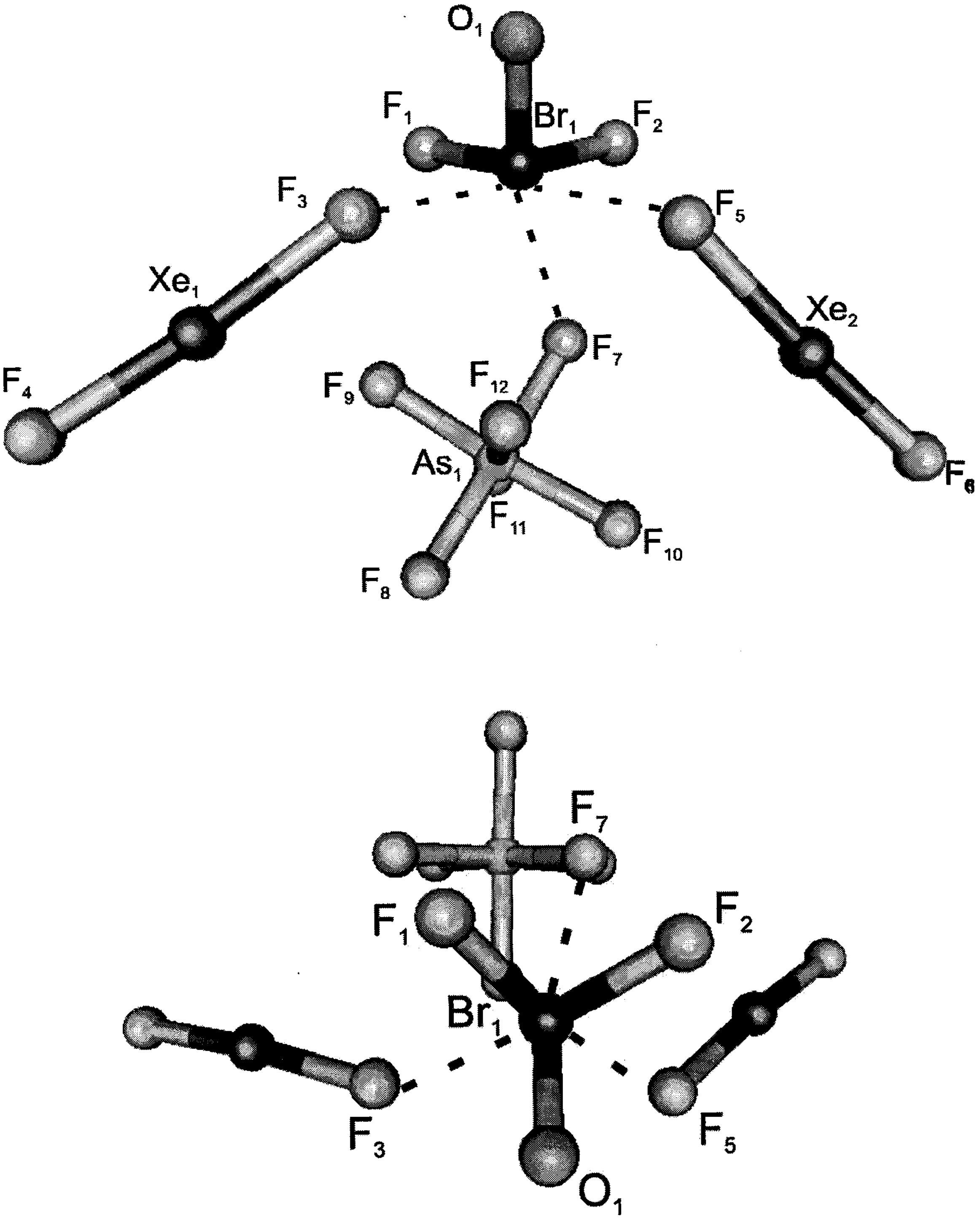

Figure 8.2. The calculated geometry (PBE1PBE/aug-cc-pVTZ(-PP)) of $[BrOF_2][AsF_6]\cdot 2XeF_2$ showing the pseudo-octahedral coordination around bromine(V).

Table 8.4. Complete List of Geometrical Parameters for [ClOF$_2$][AsF$_6$] (Exptl) and [ClOF$_2$][AsF$_6$]$_3^{2-}$ (Calcd)

exptl^a			PBE1PBE^b	B3LYP^b		PBE1PBE^b	B3LYP^b		PBE1PBE^b	B3LYP^b
Bond Lengths (Å)										
Cl(1)–O(1)	1.455(2)	Cl–O$_1$	1.409	1.421						
Cl(1)–F(1)	1.522(2)	Cl–F$_1$	1.627	1.660						
Cl(1)–F(2)	1.543(2)	Cl–F$_2$	1.627	1.659						
Cl(1)---F(3)	2.476(2)	Cl---F$_{3A}$	2.304	2.317						
Cl(1)---F(4A)	2.523(2)				Cl---F$_{3A'}$	2.305	2.317			
Cl(1)---F(5B)	2.598(2)							Cl---F$_{3B}$	2.484	2.490
As(1)–F(3)	1.740(2)	As$_A$–F$_{3A}$	1.798	1.811	As$_A$–F$_{3A'}$	1.797	1.811	As$_B$–F$_{3B}$	1.772	1.782
As(1)–F(4)	1.731(2)	As$_A$–F$_{4A}$	1.732	1.740	As$_A$–F$_{4A'}$	1.732	1.740	As$_B$–F$_{4B}$	1.737	1.745
As(1)–F(5)	1.747(2)	As$_A$–F$_{5A}$	1.733	1.740	As$_A$–F$_{5A'}$	1.734	1.742	As$_B$–F$_{5B}$	1.737	1.745
As(1)–F(6)	1.715(2)	As$_A$–F$_{6A}$	1.736	1.744	As$_A$–F$_{6A'}$	1.736	1.744	As$_B$–F$_{6B}$	1.743	1.752
As(1)–F(7)	1.710(2)	As$_A$–F$_{7A}$	1.742	1.750	As$_A$–F$_{7A'}$	1.742	1.750	As$_B$–F$_{7B}$	1.744	1.752
As(1)–F(8)	1.709(2)	As$_A$–F$_{8A}$	1.731	1.739	As$_A$–F$_{8A'}$	1.730	1.738	As$_B$–F$_{8B}$	1.736	1.744
Bond Angles (deg)										
F(1)–Cl(1)–F(2)	98.7(1)	F$_1$–Cl–F$_2$	90.6	90.3						
F(1)–Cl(1)–O(1)	105.5(1)	F$_1$–Cl–O$_1$	104.7	104.5						
F(1)–Cl(1)---F(3)	163.3(1)	F$_1$–Cl---F$_{3A}$	163.9	163.7						
F(1)–Cl(1)---F(4A)	91.5(1)				F$_1$–Cl---F$_{3A'}$	83.0	83.6			
F(1)–Cl(1)---F(5B)	84.1(1)							F$_1$–Cl---F$_{3B}$	76.6	77.3
F(2)–Cl(1)–O(1)	104.2(1)	F$_2$–Cl–O$_1$	104.7	104.5						
F(2)–Cl(1)---F(3)	84.7(1)	F$_2$–Cl---F$_{3A}$	82.4	83.1						
F(2)–Cl(1)---F(4A)	157.7(1)				F$_2$–Cl---F$_{3A'}$	164.6	164.3			
F(2)–Cl(1)---F(5B)	80.29(9)							F$_2$–Cl---F$_{3B}$	77.5	78.1
O(1)–Cl(1)---F(3)	89.3(1)	O$_1$–Cl---F$_{3A}$	91.1	91.6						
O(1)–Cl(1)---F(4A)	92.1(1)				O$_1$–Cl---F$_{3A'}$	90.6	91.1			
O(1)–Cl(1)---F(5B)	168.5(1)							O$_1$–Cl---F$_{3B}$	177.4	176.7
F(3)---Cl(1)---F(4A)	80.20(7)	F$_{3A}$---Cl---F$_{3A'}$	100.0	98.9						
F(3)---Cl(1)---F(5B)	80.41(7)							F$_{3A}$---Cl---F$_{3B}$	87.7	86.7
F(4A)---Cl(1)---F(5B)	81.10(7)				F$_{3A'}$---Cl---F$_{3B}$	87.4	86.7			

Table 8.4. (continued...)

Cl(1)---F(3)–As(1)	141.2(1)	Cl---F$_{3A}$–As$_{A}$	131.2	132.1						
Cl(1)---F(4A)–As(1A)	145.0(1)				Cl---F$_{3A}$–As$_{A'}$	128.9	130.4			
Cl(1)---F(5B)–As(1B)	137.7(1)							Cl---F$_{3B}$–As$_{B}$	135.0	137.4
F(3)–As(1)–F(4)	88.5(1)	F$_{3A}$–As$_{A}$–F$_{4A}$	88.6	88.5	F$_{3A}$–As$_{A}$–F$_{4A'}$	88.7	88.6	F$_{3B}$–As$_{B}$–F$_{4B}$	89.4	89.4
F(3)–As(1)–F(5)	88.06(9)	F$_{3A}$–As$_{A}$–F$_{5A}$	88.7	88.6	F$_{3A}$–As$_{A}$–F$_{5A'}$	88.4	88.4	F$_{3B}$–As$_{B}$–F$_{5B}$	89.3	89.3
F(3)–As(1)–F(6)	177.0(1)	F$_{3A}$–As$_{A}$–F$_{6A}$	179.6	179.6	F$_{3A}$–As$_{A}$–F$_{6A'}$	179.4	179.5	F$_{3B}$–As$_{B}$–F$_{6B}$	179.7	179.8
F(3)–As(1)–F(7)	90.7(1)	F$_{3A}$–As$_{A}$–F$_{7A}$	88.2	88.1	F$_{3A}$–As$_{A}$–F$_{7A'}$	88.1	88.1	F$_{3B}$–As$_{B}$–F$_{7B}$	89.1	89.1
F(3)–As(1)–F(8)	90.4(1)	F$_{3A}$–As$_{A}$–F$_{8A}$	88.9	88.9	F$_{3A}$–As$_{A}$–F$_{8A'}$	89.0	89.0	F$_{3B}$–As$_{B}$–F$_{8B}$	89.4	89.4
F(4)–As(1)–F(5)	88.5(1)	F$_{4A}$–As$_{A}$–F$_{5A}$	90.2	90.3	F$_{4A}$–As$_{A}$–F$_{5A'}$	90.3	90.3	F$_{4B}$–As$_{B}$–F$_{5B}$	90.4	90.3
F(4)–As(1)–F(6)	90.1(1)	F$_{4A}$–As$_{A}$–F$_{6A}$	91.8	91.9	F$_{4A}$–As$_{A}$–F$_{6A'}$	91.8	91.8	F$_{4B}$–As$_{B}$–F$_{6B}$	90.9	90.9
F(4)–As(1)–F(7)	178.2(1)	F$_{4A}$–As$_{A}$–F$_{7A}$	176.7	176.6	F$_{4A}$–As$_{A}$–F$_{7A'}$	176.8	176.6	F$_{4B}$–As$_{B}$–F$_{7B}$	178.5	178.5
F(4)–As(1)–F(8)	90.7(1)	F$_{4A}$–As$_{A}$–F$_{8A}$	90.4	90.4	F$_{4A}$–As$_{A}$–F$_{8A'}$	90.3	90.3	F$_{4B}$–As$_{B}$–F$_{8B}$	90.2	90.2
F(5)–As(1)–F(6)	89.4(1)	F$_{5A}$–As$_{A}$–F$_{6A}$	91.2	91.2	F$_{5A}$–As$_{A}$–F$_{6A'}$	91.3	91.3	F$_{5B}$–As$_{B}$–F$_{6B}$	90.7	90.6
F(5)–As(1)–F(7)	90.0(1)	F$_{5A}$–As$_{A}$–F$_{7A}$	89.6	89.6	F$_{5A}$–As$_{A}$–F$_{7A'}$	89.4	89.4	F$_{5B}$–As$_{B}$–F$_{7B}$	89.5	89.6
F(5)–As(1)–F(8)	178.3(1)	F$_{5A}$–As$_{A}$–F$_{8A}$	177.4	177.4	F$_{5A}$–As$_{A}$–F$_{8A'}$	177.3	177.3	F$_{5B}$–As$_{B}$–F$_{8B}$	178.6	178.7
F(6)–As(1)–F(7)	90.8(1)	F$_{6A}$–As$_{A}$–F$_{7A}$	91.4	91.5	F$_{6A}$–As$_{A}$–F$_{7A'}$	91.5	91.5	F$_{6B}$–As$_{B}$–F$_{7B}$	90.7	90.7
F(6)–As(1)–F(8)	92.2(1)	F$_{6A}$–As$_{A}$–F$_{8A}$	91.3	91.3	F$_{6A}$–As$_{A}$–F$_{8A'}$	91.3	91.3	F$_{6B}$–As$_{B}$–F$_{8B}$	90.6	90.6
F(7)–As(1)–F(8)	90.8(1)	F$_{7A}$–As$_{A}$–F$_{8A}$	89.6	89.6	F$_{7A}$–As$_{A}$–F$_{8A'}$	89.9	89.8	F$_{7B}$–As$_{B}$–F$_{8B}$	89.9	89.9

[a] The atom labeling scheme corresponds to that used in Figure 8.3. [b] The Stutt Huzpolar 2 basis set was used. The energy-minimized geometry was C_1. The atom labeling scheme corresponds to that used in Figure 8.4.

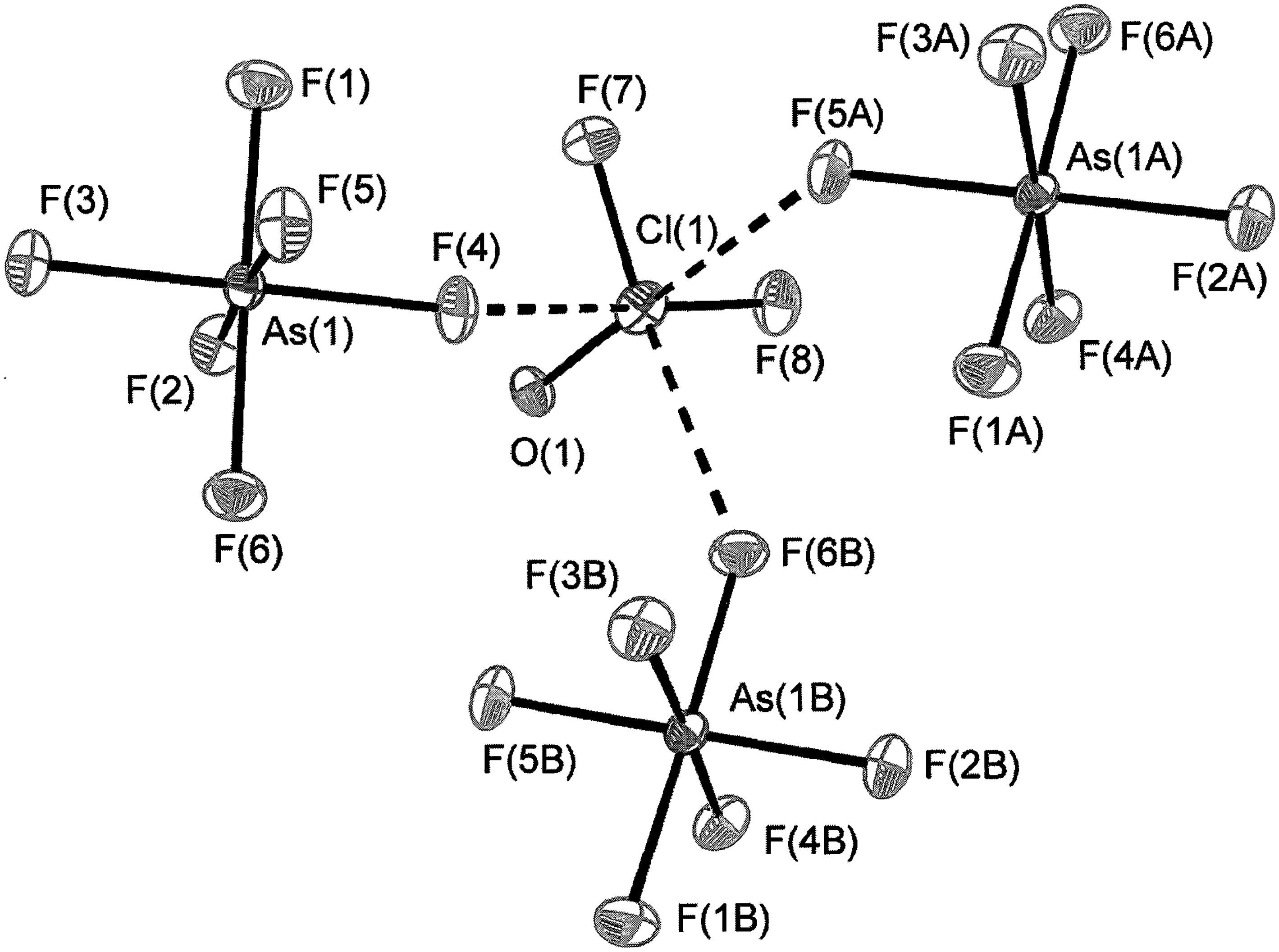

Figure 8.3. The X-ray crystal structure of [$ClOF_2$][AsF_6] showing the pseudo-octahedral coordination around chlorine(V); thermal ellipsoids are shown at the 50% probability level.

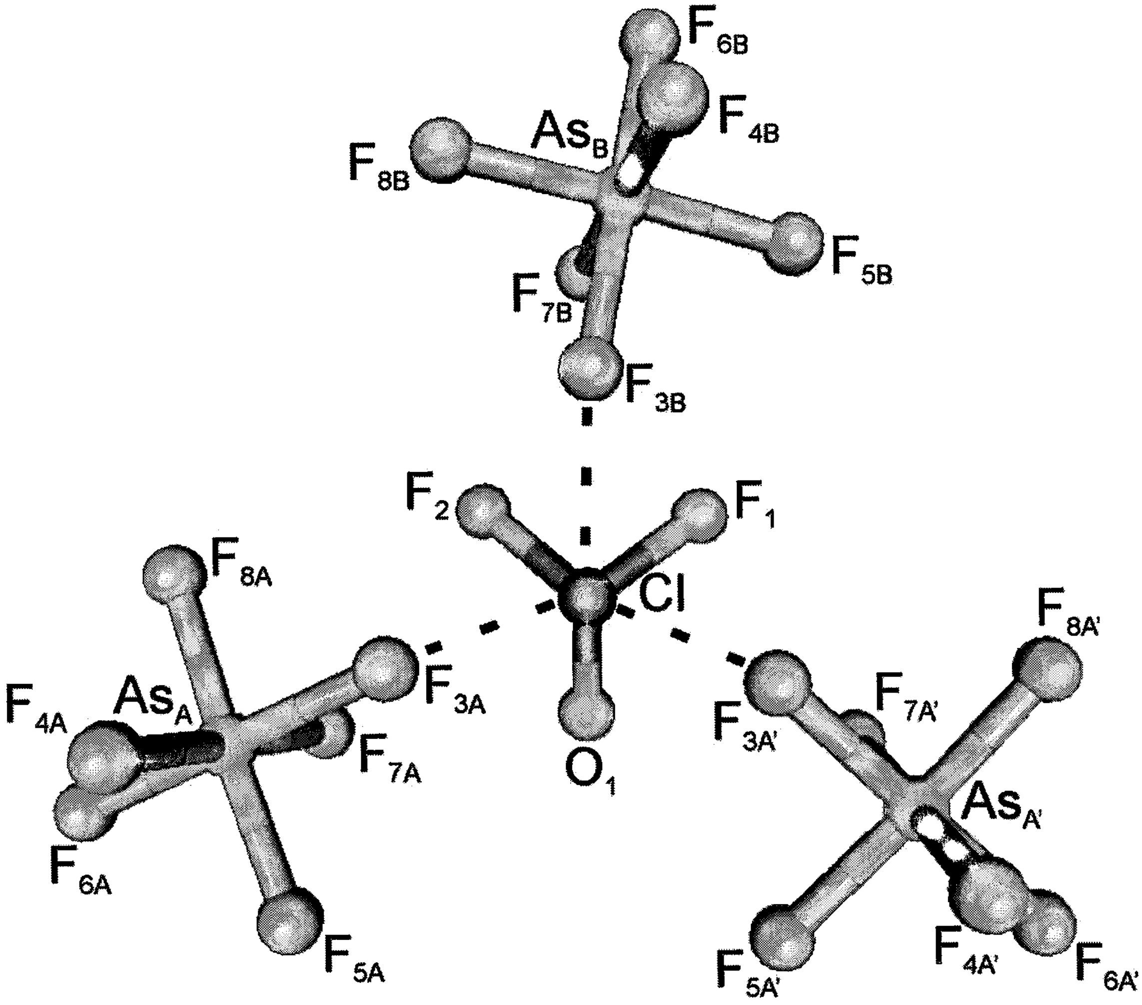

Figure 8.4. The calculated geometry (PBE1PBE/Stutt Huzpolar.2) of $[ClOF_2][AsF_6]_3^{2-}$ (C_1) showing the pseudo-octahedral coordination around chlorine(V).

Å) is very similar to that of the KrF_2 analogue (1.564(5) Å),[232] it is significantly shorter than those of other Br(V) compounds, including the $BrOF_4^-$ anion in $[NO][BrOF_4]$ (1.575(3) Å),[244] $O_2Br{-}O{-}BrO_2$ (1.606 (12), 1.611(2), 1.613(2), 1.606(2) Å)[245] $O_2BrOTeF_5$ (1.595(4), 1.608(3) Å),[246] the parent molecule, $BrOF_3$, in $[NO_2][BrF_4]{\cdot}BrOF_3$ (1.569, 1.606 Å),[244] and the related cation, BrO_2^+, in $[BrO_2][SbF_6]$ (1.595(2) Å).[247] The Br–O bond length is also shorter than the Se–O bond length of isoelectronic $SeOF_2$ (1.576 Å).[248] The Br–F bond lengths in $[BrOF_2][AsF_6]{\cdot}2XeF_2$ (1.734(4), 1.736(4) Å) are intermediate with respect to the axial and equatorial Br–F bond lengths in the neutral parent molecule, $BrOF_3$ ($Br{-}F_{ax}$ = 1.820, 1.839, 1.822, 1.836 Å; $Br{-}F_{eq}$ = 1.725, 1.692 Å),[244] shorter than in the $BrOF_4^-$ anion (1.846(2), 1.912(2) Å),[244] and are essentially equal to those of the KrF_2 analogue, $[BrOF_2][AsF_6]{\cdot}2KrF_2$ (1.727(4), 1.723(4) Å)[232] and the axial Br–F bond lengths of BrF_4^+ in $[BrF_4][Sb_2F_{11}]$ ($Br{-}F_{ax}$ = 1.728(3), 1.729(3) Å; $Br{-}F_{eq}$ = 1.664(3), 1.667(2) Å),[249] and the Se–F bond lengths in $SeOF_2$ (1.7255 Å).[248]

The fluorine bridge distances, Br---F, between the $BrOF_2^+$ cation and the coordinated XeF_2 molecules (Br---F(3), 2.306(4) and Br---F(5), 2.292(4) Å) and between the $BrOF_2^+$ cation and the AsF_6^- anion (Br---F(7), 2.610(4) Å) are significantly less than the sum of the van der Waals radii of Br and F (3.32 Å).[55]

Coordination of XeF_2 to the $BrOF_2^+$ cation results in asymmetric Xe–F bond lengths, with the $Xe{-}F_b$ (2.052(4), 2.053(4) Å) and $Xe{-}F_t$ (1.960(4), 1.956(5) Å) bonds elongated and shortened, respectively, relative to those of solid XeF_2 at −173 °C (1.999(4) Å).[216] Such asymmetries have been previously observed for the KrF_2 analogue[232] and for XeF_2 terminally coordinated to metal centers.[82,83] The present $Xe{-}F_b$

and Xe–F$_t$ bond lengths are comparable to those in [Ca(XeF$_2$)$_5$][PF$_6$]$_2$,[262] [Cd(XeF$_2$)$_5$][PF$_6$]$_2$,[262] [Cd(XeF$_2$)][BF$_4$]$_2$,[263] [Mg(XeF$_2$)$_4$][AsF$_6$]$_2$,[264] [Mg(XeF$_2$)$_2$][AsF$_6$]$_2$,[264] and [Ca$_2$(XeF$_2$)$_9$][AsF$_6$]$_4$[265] where the Xe–F$_b$ bonds range from 2.026(7) to 2.087(8) Å and the Xe–F$_t$ bonds range from 1.913(5) to 1.966(6) Å. The AsF$_6^-$ anion in the present structure is a distorted octahedron in which the As–F$_b$ bridge bond is elongated relative to the other As–F bonds.

The XeF$_2$ ligands coordinate to bromine with Br(1)---F(3)–Xe(1) and Br(1)---F(5)–Xe(2) angles of 142.4(2)° and 134.1(2)°, respectively, which are bent as a result of steric repulsion between the two valence electron lone pairs of each bridging fluorine atom and their respective bridge bond pair domains. Both XeF$_2$ ligands are near-linear with F(3)–Xe(1)–F(4) and F(5)–Xe(2)–F(6) angles equal to 178.4(2)° and 179.8(2)°, respectively, consistent with other XeF$_2$ adducts.[82,83,262–265]

8.2.4.2. [BrOF$_2$][AsF$_6$]. The unit cell of [BrOF$_2$][AsF$_6$] contains four structural units and is in agreement with the previously reported cell parameters obtained from an earlier powder diffraction study.[128] The cubic space group, *P*2/$_1$3, results in a three-fold positional disorder around the bromine atom in which the oxygen and fluorine atoms of the trigonal pyramidal BrOF$_2^+$ cation are indistinguishable. The observed Br–O/F bond length (1.647(1) Å) is slightly shorter than the weighted average of the Br–O and Br–F bond lengths in [BrOF$_2$][AsF$_6$]·2XeF$_2$ (1.673(4) Å) (vide supra), and is consistent with the greater electronegativity of the bromine atom in [BrOF$_2$][AsF$_6$] relative to that in [BrOF$_2$][AsF$_6$]·2XeF$_2$. Using a weighted apportioning of the calculated Br–O to Br–F bond length ratio (0.891) obtained from the calculated structures of $[BrOF_2][AsF_6]_3^{2-}$ (see 8.2.6.1, Computational Results), Br–O and Br–F bond lengths of 1.523 and 1.709 Å, respectively, may be assigned.

The bromine atom also makes three longer contacts with one fluorine atom of three different AsF_6^- anions, resulting in pseudo-octahedral coordination around the bromine atom. These contacts (2.506(1) Å) are significantly less than the sum of the van der Waals radii for Br and F (3.32 Å).[55]

8.2.4.3. $[ClOF_2][AsF_6]$. The unit cell contains four $[ClOF_2][AsF_6]$ structural units and differs from that deduced previously from an X-ray powder diffraction study which reported six structural units per unit cell.[123] The present study represents the first single-crystal X-ray structure determination of the $ClOF_2^+$ cation and, unlike the bromine analogue, the $ClOF_2^+$ cation is ordered.

The structure of $[ClOF_2][AsF_6]$ consists of a $ClOF_2^+$ cation which interacts by means of three non-equivalent short contacts with fluorine atoms from of three AsF_6^- anions within the unit cell (Figure 8.3), providing the chlorine atom with a pseudo-octahedral coordination sphere similar to that of bromine in $[BrOF_2][AsF_6]$ and $[BrOF_2][AsF_6]\cdot 2XeF_2$ (vide supra). Three fluorine atoms of each AsF_6^- anion coordinate to three different $ClOF_2^+$ cations, generating a two-dimensional zig-zag pattern of alternating $ClOF_2^+$ and AsF_6^- ions (Figure 8.5), which is manifested in the crystal morphology, with the salt having a propensity to crystallize in very thin plates.

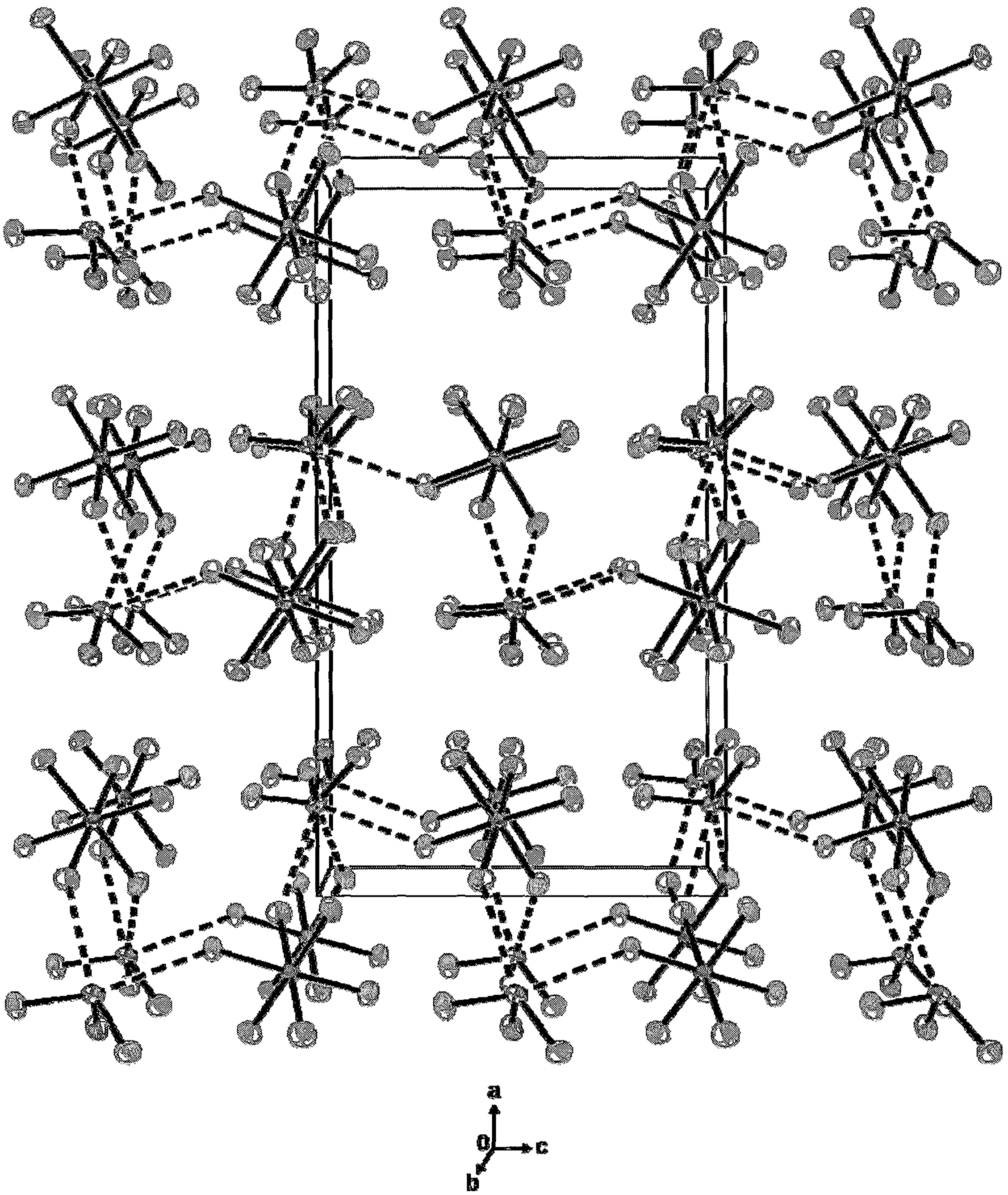

Figure 8.5. The crystal packing of [$ClOF_2$][AsF_6] (along the *b*-axis); thermal ellipsoids are shown at the 50% probability level.

The Cl–O bond length (1.455(2) Å) is significantly longer than those of other Cl(V) species, including the ClO_2^+ cation in $[ClO_2][SbF_6]$ (1.385(5) Å),[247] $[ClO_2][RuF_6]$ (1.379(9) Å),[266] $[ClO_2][BF_4]$ (1.405(1), 1.408(1);[267] 1.397(2), 1.390(2)[268] Å), $[ClO_2][ClO_4]$ (1.406(2), 1.410(2) Å),[269] and $ClOF_3$ (1.405(3) Å; gas-phase electron diffraction),[270] and the estimated Cl–O bond length of $ClOF_2^+$ (1.41 Å) used to calculate its force constants.[124] Comparisons could not be made with the solid-state structure of $ClOF_3$ because the oxygen atom and the equatorial fluorine atom are positionally disordered. The Cl–O bond of $ClOF_2^+$ is also longer than the S–O bond in isoelectronic SOF_2 (1.412(1) Å)[271] but shorter than the Cl–O bond in the ClO_3^- anion of $[Na][ClO_3]$(1.502(3) Å).[272] This is in accord with the average lower formal Cl–O bond order of the ClO_3^- anion (5/3) compared to formal Cl–O and S–O bond orders of 2 for $ClOF_2^+$ and SOF_2. When compared with the calculated structure (see 8.2.6.1, Computational Results), the experimental fluorine contact distance (Cl---F(5B)) opposite the oxygen atom is significantly shorter than the other Cl---F contact distances and is likely a result of crystal packing. This would account for lengthening of the Cl–O bond trans to it.

The Cl–F bond lengths (1.522(2), 1.543(2) Å) of $[ClOF_2][AsF_6]$ are comparable to the equatorial bond lengths of ClF_4^+ in $[ClF_4][SbF_6]$ (1.530(2) Å),[273] but are significantly shorter than the axial bonds of ClF_4^+ in $[ClF_4][SbF_6]$ (1.618(2) Å),[273] the axial and equatorial Cl–F bonds in gas-phase $ClOF_3$ (Cl–F_{ax} = 1.713(3) Å; Cl–F_{eq} = 1.603(4) Å),[270] and the S–F bonds in SOF_2 (1.585(1) Å),[271] as well as the estimated Cl–F bond length used to calculate the force constants of $ClOF_2^+$ (1.62 Å).[124]

The chlorine atom of $ClOF_2^+$ makes three additional long contacts with three neighboring AsF_6^- anions (Cl(1)---F(3) = 2.476(2) Å, Cl(1)---F(4A) = 2.523(2) Å, Cl(1)---F(5B) = 2.598(2) Å) that are substantially less than the sum of the van der Waals radii for Cl and F (3.22 Å).[55] As a result, the AsF_6^- anions display distorted octahedral arrangements in which the three As–F bridge bonds are elongated and the bonds trans to the As–F bridge bonds are shortened.

8.2.5. Raman Spectroscopy. The low-temperature Raman spectra of solid $[BrOF_2][AsF_6]$, $[ClOF_2][AsF_6]$, $[BrOF_2][AsF_6]\cdot XeF_2$, and $[BrOF_2][AsF_6]\cdot 2XeF_2$, are shown in Figures 8.6–8.9. The observed and calculated frequencies and their assignments are listed in Tables 8.5–8.8. The Raman spectra of $[BrOF_2][AsF_6]$ and $[ClOF_2][AsF_6]$ were assigned using the calculated $[BrOF_2][AsF_6]_3^{2-}$ and $[ClOF_2][AsF_6]_3^{2-}$ anions as models in which the cation coordinates by means of fluorine bridges to three different AsF_6^- anions, providing good approximations of the cation environments observed in their respective crystal structures (see 8.2.6.1, Computational Results). The current work also shows that the previously reported Raman spectrum of $[BrOF_2][AsF_6]\cdot XeF_2$[129] contained small amounts of residual BrF_5 which was incorrectly assigned to $[BrOF_2][AsF_6]\cdot XeF_2$ (Table 8.1).

The spectral assignments for $[BrOF_2][AsF_6]$, $[ClOF_2][AsF_6]$, $[BrOF_2][AsF_6]\cdot XeF_2$, and $[BrOF_2][AsF_6]\cdot 2XeF_2$ were made by comparison with the calculated frequencies and Raman intensities (Tables 8.5–8.8) of the energy-minimized geometries (Figures 8.2, 8.4, 8.10, and 8.11) and for $[BrOF_2][AsF_6]\cdot 2XeF_2$ by

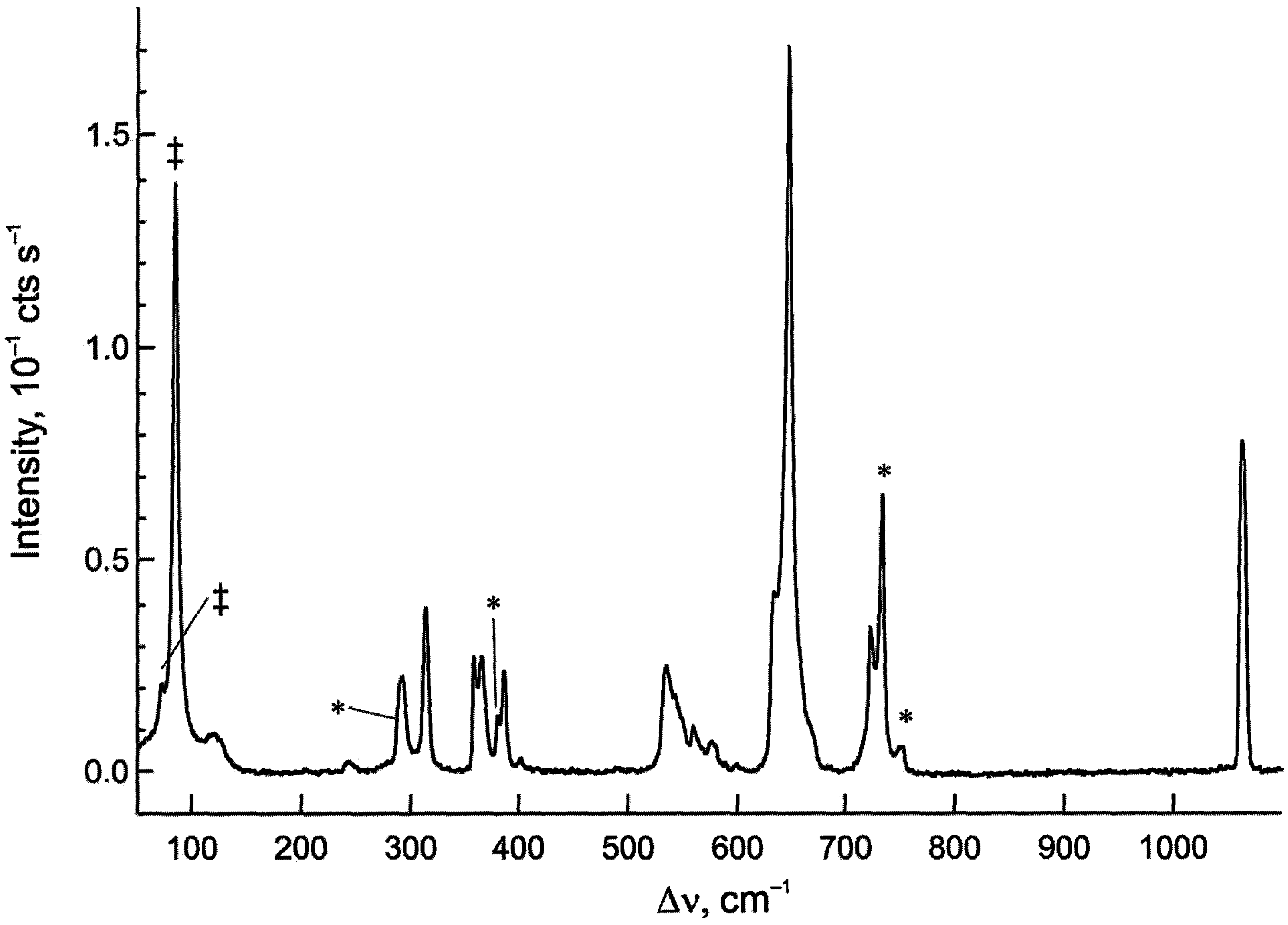

Table 8.6. Raman spectrum of $[BrOF_2][AsF_6]$ recorded at −150 °C using 1064-nm excitation. Symbols denote FEP sample tube lines (*) and instrumental artifact (‡).

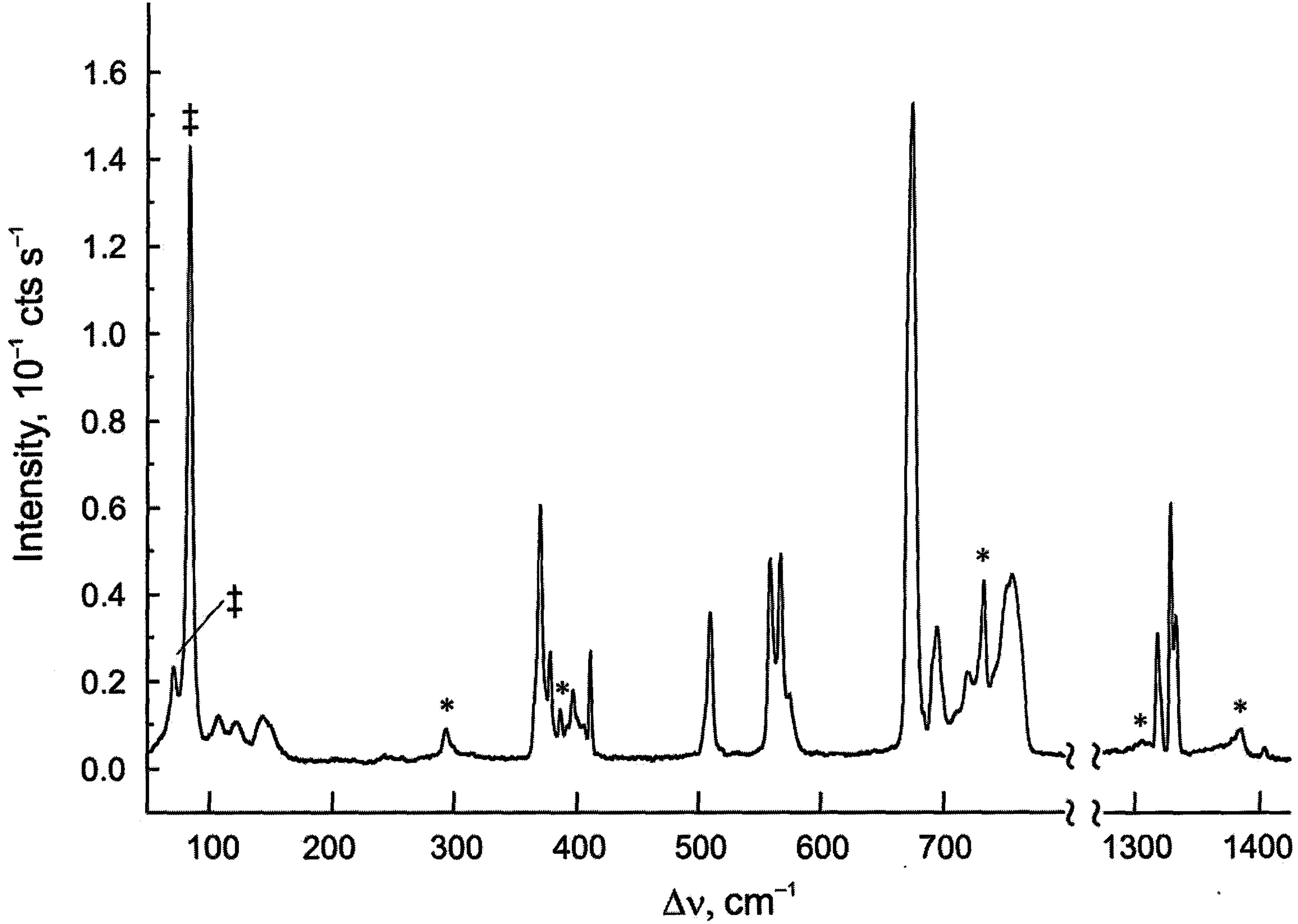

Table 8.7. Raman spectrum of $[ClOF_2][AsF_6]$ recorded at −150 °C using 1064-nm excitation. Symbols denote FEP sample tube lines (*) and instrumental artifact (‡).

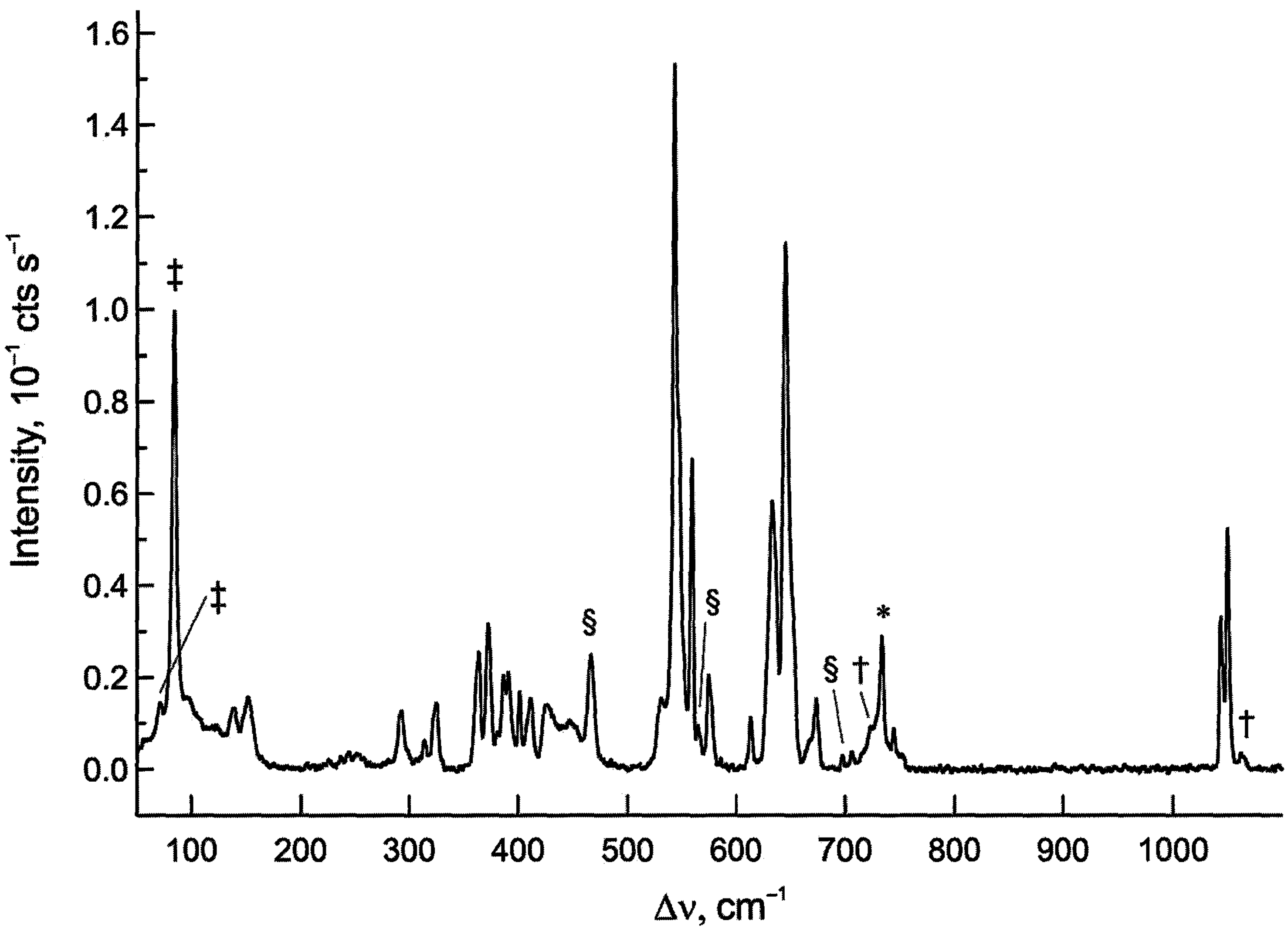

Table 8.8. Raman spectrum of $[BrOF_2][AsF_6]\cdot XeF_2$ recorded at −150 °C using 1064-nm excitation. Symbols denote FEP sample tube lines (*), $[BrOF_2][AsF_6]$ (†) and instrumental artifact (‡).

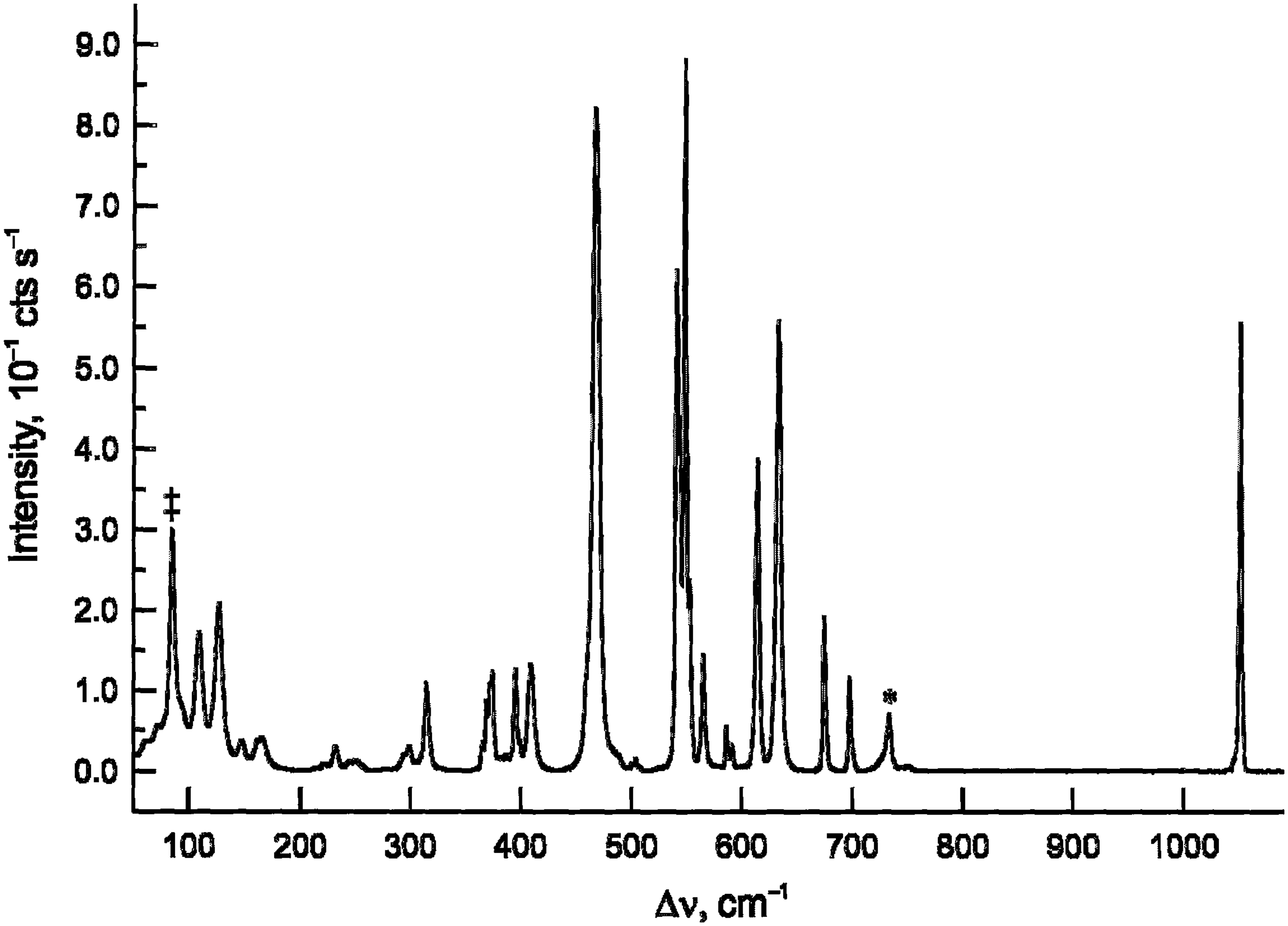

Table 8.9. Raman spectrum of $[BrOF_2][AsF_6]\cdot 2XeF_2$ recorded at −150 °C using 1064-nm excitation. Symbols denote FEP sample tube lines (*) and instrumental artifact (‡).

Table 8.5. Complete List of Vibrational Frequencies[a] for $[\mathrm{BrOF_2}][\mathrm{AsF_6}]$ (Exptl) and $[\mathrm{BrOF_2}][\mathrm{AsF_6}]_3^{2-}$ (Calcd)

exptl[b]			calcd[c]		assgnts
Raman[d,e]	infrared[d]	Raman[e,f]	PBE1PBE	B3LYP	$[\mathrm{BrOF_2}][\mathrm{AsF_6}]_3^{2-}$ (C_1)[g]
1059(50)	1055 m	1064(45)	1048(40)[78]	997(46)[72]	$\nu(\mathrm{BrO})$
			729(1)[260]	708(1)[259]	$[\nu(\mathrm{As_AF_{5A}}) - \nu(\mathrm{As_AF_{8A}})] + [\nu(\mathrm{As_{A'}F_{5A'}}) - \nu(\mathrm{As_{A'}F_{8A'}})]$
			725(<1)[249]	705(<1)[227]	$[\nu(\mathrm{As_AF_{5A}}) - \nu(\mathrm{As_AF_{8A}})] + [\nu(\mathrm{As_{A'}F_{8A'}}) - \nu(\mathrm{As_{A'}F_{5A'}})] + [\nu(\mathrm{As_BF_{5B}}) - \nu(\mathrm{As_BF_{8B}})]$
			722(1)[489]	701(2)[475]	$[\nu(\mathrm{As_AF_{4A}}) - \nu(\mathrm{As_AF_{7A}})] + [\nu(\mathrm{As_{A'}F_{4A'}}) - \nu(\mathrm{As_{A'}F_{7A'}})] + [\nu(\mathrm{As_BF_{4B}}) - \nu(\mathrm{As_BF_{7B}})]_{\mathrm{sm}}$
			718(1)[4]	697(1)[4]	$[\nu(\mathrm{As_AF_{4A}}) - \nu(\mathrm{As_AF_{7A}})] + [\nu(\mathrm{As_{A'}F_{7A'}}) - \nu(\mathrm{As_{A'}F_{4A'}})]$
			714(<0.1)[90]	693(<0.1)[91]	$[\nu(\mathrm{As_BF_{5B}}) - \nu(\mathrm{As_BF_{8B}})]$
			709(1)[97]	688(1)[98]	$[\nu(\mathrm{As_BF_{4B}}) - \nu(\mathrm{As_BF_{7B}})]$
720(17)	730 sh	723(20)	687(26)[8]	665(25)[9]	$[\nu(\mathrm{As_AF_{6A}}) + \nu(\mathrm{As_{A'}F_{6A'}}) + \nu(\mathrm{As_BF_{6B}})] + [\nu(\mathrm{BrF_1}) + \nu(\mathrm{BrF_2})]$
688(1)			676(2)[171]	656(2)[179]	$[\nu(\mathrm{As_AF_{6A}}) - \nu(\mathrm{As_{A'}F_{6A'}})]$
			670(<1)[253]	649(<1)[245]	$\nu(\mathrm{As_BF_{6B}})$
			650(1)[91]	631(1)[108]	$[\nu(\mathrm{As_AF_{3A}}) + \nu(\mathrm{As_AF_{4A}}) + \nu(\mathrm{As_AF_{5A}}) + \nu(\mathrm{As_AF_{7A}}) + \nu(\mathrm{As_AF_{8A}}) - \nu(\mathrm{As_AF_{6A}})] - [\nu(\mathrm{As_{A'}F_{3A'}}) + \nu(\mathrm{As_{A'}F_{4A'}}) + \nu(\mathrm{As_{A'}F_{5A'}}) + \nu(\mathrm{As_{A'}F_{7A'}}) + \nu(\mathrm{As_{A'}F_{8A'}}) - \nu(\mathrm{As_{A'}F_{6A'}})]$
	660 w	667 sh	657(7)[35]	635(39)[<1][h]	$[\nu(\mathrm{BrF_1}) + \nu(\mathrm{BrF_2})] - [\nu(\mathrm{As_AF_{3A}}) + \nu(\mathrm{As_AF_{4A}}) + \nu(\mathrm{As_AF_{5A}}) + \nu(\mathrm{As_AF_{6A}}) + \nu(\mathrm{As_AF_{7A}}) + \nu(\mathrm{As_AF_{8A}})] + [\nu(\mathrm{As_{A'}F_{3A'}}) + \nu(\mathrm{As_{A'}F_{4A'}}) + \nu(\mathrm{As_{A'}F_{5A'}}) + \nu(\mathrm{As_{A'}F_{6A'}}) + \nu(\mathrm{As_{A'}F_{7A'}}) + \nu(\mathrm{As_{A'}F_{8A'}})] + [\nu(\mathrm{As_BF_{3B}}) + \nu(\mathrm{As_BF_{4B}}) + \nu(\mathrm{As_BF_{5B}}) + \nu(\mathrm{As_BF_{6B}}) + \nu(\mathrm{As_BF_{7B}}) + \nu(\mathrm{As_BF_{8B}})]_{\mathrm{small}}$
649(100)		647(100)	649(36)[176]	617(63)[81][i]	$[\nu(\mathrm{BrF_1}) + \nu(\mathrm{BrF_2})] + [\nu(\mathrm{As_AF_{8A}}) + \nu(\mathrm{As_AF_{5A}}) + \nu(\mathrm{As_AF_{3A}}) + \nu(\mathrm{As_AF_{4A}}) + \nu(\mathrm{As_AF_{7A}}) - \nu(\mathrm{As_AF_{6A}})] + [\nu(\mathrm{As_{A'}F_{8A'}}) + \nu(\mathrm{As_{A'}F_{5A'}}) + \nu(\mathrm{As_{A'}F_{3A'}}) + \nu(\mathrm{As_{A'}F_{4A'}}) + \nu(\mathrm{As_{A'}F_{7A'}}) - \nu(\mathrm{As_{A'}F_{6A'}})] - [\nu(\mathrm{As_{A'}F_{8A'}}) + \nu(\mathrm{As_{A'}F_{5A'}}) + \nu(\mathrm{As_{A'}F_{3A'}}) - \nu(\mathrm{As_{A'}F_{6A'}})]$
			648(46)[9]	629(3)[135][j]	$[\nu(\mathrm{As_BF_{8B}}) + \nu(\mathrm{As_BF_{5B}}) + \nu(\mathrm{As_BF_{3B}}) + \nu(\mathrm{As_BF_{4B}}) + \nu(\mathrm{As_BF_{7B}}) - \nu(\mathrm{As_BF_{6B}})] + [\nu(\mathrm{BrF_1}) + \nu(\mathrm{BrF_2})]$
634 sh	630 sh	634(25)	627(16)[191]	590(20)[159]	$[\nu(\mathrm{BrF_1}) - \nu(\mathrm{BrF_2})]$
558 sh		560(6)	592(5)[<0.1]	576(5)[<0.1]	$[\nu(\mathrm{As_AF_{8A}}) + \nu(\mathrm{As_AF_{5A}})] - [\nu(\mathrm{As_AF_{4A}}) + \nu(\mathrm{As_AF_{7A}})] + [\nu(\mathrm{As_{A'}F_{8A'}}) + \nu(\mathrm{As_{A'}F_{5A'}})] - [\nu(\mathrm{As_AF_{4A'}}) + \nu(\mathrm{As_AF_{7A'}})]$
			591(2)[<1]	574(3)[3]	$[\nu(\mathrm{As_AF_{8A}}) + \nu(\mathrm{As_AF_{5A}})] - [\nu(\mathrm{As_AF_{4A}}) + \nu(\mathrm{As_AF_{7A}})] - [\nu(\mathrm{As_{A'}F_{8A'}}) + \nu(\mathrm{As_{A'}F_{5A'}})] + [\nu(\mathrm{As_{A'}F_{4A'}}) + \nu(\mathrm{As_{A'}F_{7A'}})]$
			583(3)[<1]	566(3)[<1]	$[\nu(\mathrm{As_BF_{8B}}) + \nu(\mathrm{As_BF_{5B}})] - [\nu(\mathrm{As_BF_{4B}}) + \nu(\mathrm{As_BF_{7B}})]$
		549 sh	538(18)[25]	520(22)[29]	$[\nu(\mathrm{As_BF_{3B}}) - \nu(\mathrm{BrF_{3B}})] + \nu(\mathrm{As_BF_{6B}})$
		543(10)	494(16)[146]	472(18)[150]	$[\nu(\mathrm{As_AF_{3A}}) + \nu(\mathrm{As_{A'}F_{3A'}}) - \nu(\mathrm{As_BF_{3B}})] - [\nu(\mathrm{BrF_{3A}}) + \nu(\mathrm{BrF_{3A'}}) - \nu(\mathrm{BrF_{3B}})]$
531(12)	535 m	535(14)	474(11)[224]	453(12)[218]	$[\nu(\mathrm{As_AF_{3A}}) - \nu(\mathrm{As_{A'}F_{3A'}})] + [\nu(\mathrm{BrF_{3A'}}) - \nu(\mathrm{BrF_{3A}})]$
398(1)	405 sh	403(2)	401(2)[122]	393(3)[106]	$[\delta(\mathrm{F_{4A}As_AF_{3A}}) - \delta(\mathrm{F_{7A}As_AF_{6A}}) + \rho_w(\mathrm{F_{8A}As_AF_{5A}})] + [\delta(\mathrm{F_{4A'}As_{A'}F_{3A'}}) - \delta(\mathrm{F_{7A'}As_{A'}F_{6A'}}) + \rho_w(\mathrm{F_{8A'}As_{A'}F_{5A'}})] + [\delta(\mathrm{F_{4B}As_BF_{3B}}) - \delta(\mathrm{F_{7B}As_BF_{6B}}) + \rho_w(\mathrm{F_{8B}As_BF_{5B}})]_{\mathrm{small}} + \delta(\mathrm{BrOF_1F_2})_{\mathrm{small}}$

Table 8.5. (continued…)

			391(<1)[7]	384(2)[10]	$[\delta(F_{4A}As_AF_{3A}) - \delta(F_{7A}As_AF_{6A}) + \rho_w(F_{8A}As_AF_{5A})] - [\delta(F_{4A'}As_{A'}F_{3A'}) - \delta(F_{7A'}As_{A'}F_{6A'}) + \rho_w(F_{8A'}As_{A'}F_{5A'})]$
			388(<1)[32]	383(<1)[38]	$\delta(F_{4B}As_BF_{3B}) - \delta(F_{7B}As_BF_{6B}) + \rho_w(F_{8B}As_BF_{5B})$
			386(<1)[48]	382(<1)[57]	$[\delta(F_{4B}As_BF_{6B}) - \delta(F_{7B}As_BF_{3B}) + \rho_w(F_{8B}As_BF_{5B})]$
			382(<0.1)[80]	378(<0.1)[79]	$\delta(As_BF_{4B}F_{7B}F_{3B}F_{6B})_{o.o.p.}$
			380(<1)[42]	375(<1)[60]	$\delta(As_AF_{4A}F_{7A}F_{3A}F_{6A})_{o.o.p.} + \delta(As_{A'}F_{4A'}F_{7A'}F_{3A'}F_{6A'})_{o.o.p.}$
			378(<1)[138]	374(1)[125]	$\delta(As_BF_{4B}F_{7B}F_{8B}F_{5B})_{o.o.p.} - \delta(As_AF_{4A}F_{7A}F_{8A}F_{5A})_{o.o.p.} - \delta(As_{A'}F_{4A'}F_{7A'}F_{8A'}F_{5A'})_{o.o.p.}$
387(6)	385 ms	387(6)*	377(1)[143]	371(2)[158]	$[\delta(As_AF_{4A}F_{6A}F_{8A}) - \delta(As_AF_{3A}F_{5A}F_{7A})] - [\delta(As_{A'}F_{4A'}F_{6A'}F_{8A'}) - \delta(As_{A'}F_{3A'}F_{5A'}F_{7A'})] + \delta(OBrF_1)_{small}$
			377(<0.1)[1]	373(<0.1)[13]	$\delta(As_AF_{4A}F_{7A}F_{3A}F_{6A})_{o.o.p.} - \delta(As_{A'}F_{4A'}F_{7A'}F_{3A'}F_{6A'})_{o.o.p.}$
360(18)	355 sh	366(16)	359(3)[12]	346(3)[16]	$\delta(BrOF_1F_2)$
			356(1)[<1]	351(2)[<1]	$[\delta(F_{4A}As_AF_{8A}) + \delta(F_{7A}As_AF_{5A})] + [\delta(F_{4A'}As_{A'}F_{8A'}) + \delta(F_{7A'}As_{A'}F_{5A'})]$
			356(<1)[<0.1]	351(<1)[<0.1]	$[\delta(F_{4A}As_AF_{8A}) + \delta(F_{7A}As_AF_{5A})] - [\delta(F_{4A'}As_{A'}F_{8A'}) + \delta(F_{7A'}As_{A'}F_{5A'})]$
			351(1)[<1]	347(1)[<1]	$[\delta(F_{4B}As_BF_{8B}) + \delta(F_{7B}As_BF_{5B})]$
		359(16)	347(<1)[7]	342(<1)[4]	$[\delta(F_{4A}As_AF_{6A}) + \delta(F_{7A}As_AF_{3A})] + [\delta(F_{4A'}As_{A'}F_{6A'}) + \delta(F_{7A'}As_{A'}F_{3A'})] - [\delta(F_{4B}As_BF_{6B}) + \delta(F_{7B}As_BF_{3B})]$
			347(1)[4]	341(1)[8]	$[\delta(F_{4A}As_AF_{3A}) + \delta(F_{7A}As_AF_{6A})] - [\delta(F_{4A'}As_{A'}F_{3A'}) + \delta(F_{7A'}As_{A'}F_{6A'})] + \delta(OBrF_1)_{small}$
			344(3)[11]	339(3)[11]	$[\delta(F_{4B}As_BF_{6B}) + \delta(F_{7B}As_BF_{3B})]$
			339(1)[<0.1]	335(2)[<1]	$[\delta(F_{8B}As_BF_{6B}) + \delta(F_{5B}As_BF_{3B})]$
			333(1)[<1]	329(2)[<1]	$[\delta(F_{5A}As_AF_{3A}) + \delta(F_{8A}As_AF_{6A})] + [\delta(F_{5A'}As_{A'}F_{3A'}) + \delta(F_{8A'}As_{A'}F_{6A'})]$
			332(<1)[<0.1]	328(<1)[<0.1]	$[\delta(F_{8A}As_AF_{3A}) + \delta(F_{5A}As_AF_{6A})] - [\delta(F_{8A'}As_{A'}F_{3A'}) + \delta(F_{5A'}As_{A'}F_{6A'})]$
311(18)		314(23)	312(3)[90]	302(3)[79]	$\delta(OBrF_1)$
289(6)		292(6)*	283(<1)[24]	270(1)[21]	$\delta(F_1BrF_2)$
239(1)		244(1)	245(<0.1)[2]	241(<1)[2]	$[\rho_w(F_{8A}As_AF_{5A}) - \rho_w(F_{3A}As_AF_{6A})] + [\rho_w(F_{8A'}As_{A'}F_{5A'}) - \rho_w(F_{3A'}As_{A'}F_{6A'})]$
			238(<0.1)[31]	234(<0.1)[30]	$[\rho_w(F_{8A}As_AF_{5A}) - \rho_w(F_{3A}As_AF_{6A})] - [\rho_w(F_{8A'}As_{A'}F_{5A'}) - \rho_w(F_{3A'}As_{A'}F_{6A'})]$
			234(<0.1)[5]	231(<0.1)[5]	$\rho_w(F_{8B}As_BF_{5B}) - \rho_w(F_{3B}As_BF_{6B})$
			229(<0.1)[<0.1]	225(<0.1)[<0.1]	$\rho_w(F_{4B}As_BF_{7B}) - \rho_w(F_{3B}As_BF_{6B})$
			229(<1)[2]	225(<1)[2]	$[\rho_w(F_{4A}As_AF_{7A}) - \rho_w(F_{3A}As_AF_{6A})] + [\rho_w(F_{4A'}As_{A'}F_{7A'}) - \rho_w(F_{3A'}As_{A'}F_{6A'})]$
			228(<0.1)[<1]	225(<0.1)[<1]	$[\rho_w(F_{4A}As_AF_{7A}) - \rho_w(F_{3A}As_AF_{6A})] - [\rho_w(F_{4A'}As_{A'}F_{7A'}) - \rho_w(F_{3A'}As_{A'}F_{6A'})]$
			216(<0.1)[<1]	212(<0.1)[<0.1]	$\rho_w(F_{4B}As_BF_{7B}) - \rho_w(F_{8B}As_BF_{5B})$
			210(<0.1)[<0.1]	206(<0.1)[<0.1]	$[\rho_w(F_{4A}As_AF_{7A}) - \rho_w(F_{8A}As_AF_{5A})] + [\rho_w(F_{4A'}As_{A'}F_{7A'}) - \rho_w(F_{8A'}As_{A'}F_{5A'})]$
			210(<0.1)[<1]	206(<0.1)[<1]	$[\rho_w(F_{4A}As_AF_{7A}) - \rho_w(F_{8A}As_AF_{5A})] - [\rho_w(F_{4A'}As_{A'}F_{7A'}) - \rho_w(F_{8A'}As_{A'}F_{5A'})]$
119(4)		121(5)	162(<1)[33]	156(<1)[32]	$\rho_r(BrF_1F_2)$
			153(<1)[33]	149(<1)[18]	$\rho_r(BrOF_1F_2)$
			127(<1)[3]	120(<1)[5]	$\rho_t(BrOF_1F_2)$

Table 8.5. (continued…)

	125(<1)[6]	124(<1)[6]	coupled deformation modes
96(10)	94(<1)[25]	91(<1)[24]	
	91(<1)[15]	89(<1)[15]	
	52(<0.1)[4]	50(<1)[4]	
	51(<1)[<1]	48(<1)[<1]	
	48(<1)[2]	45(<1)[2]	
	39(<1)[<1]	38(<1)[<0.1]	
	37(<1)[<0.1]	37(<1)[<0.1]	
	27(<0.1)[<0.1]	26(<0.1)[<0.1]	
	26(<1)[1]	25(<1)[<1]	
	18(<0.1)[<0.1]	16(<0.1)[<0.1]	
	17(<0.1)[<0.1]	15(<0.1)[<0.1]	
	11(<0.1)[<0.1]	12(<0.1)[<0.1]	
	10(<0.1)[<0.1]	12(<0.1)[<0.1]	
	7(<0.1)[<0.1]	7(<0.1)[<0.1]	
81(10)			lattice mode

---

[a] Frequencies are given in cm^{-1}. [b] The abbreviations denote shoulder (sh). [c] The Stutt Huzpolar 2 basis set was used. Values in parentheses denote Raman intensities (Å^4 u^{-1}). Values in square brackets denote infrared intensities (km mol^{-1}). [d] From ref 128. [e] Values in parentheses denote relative Raman intensities. [f] The Raman spectrum was recorded in a FEP sample tube at −150 °C using 1064-nm excitation. An asterisk, *, indicates overlap with a FEP sample tube band; the relative Raman intensity does not include the FEP contribution. [g] Vibrational assignments were based on the modes at the PBE1PBE level. The abbreviations denote stretch (ν), bend (δ), rock (ρ_r), wag (ρ_w), twist (ρ_t), and out-of-plane bend (o.o.p.). [h] $[\nu(\mathrm{As_AF_{8A}}) + \nu(\mathrm{As_AF_{5A}}) + \nu(\mathrm{As_AF_{3A}}) + \nu(\mathrm{As_AF_{6A}}) + \nu(\mathrm{As_AF_{4A}}) + \nu(\mathrm{As_AF_{7A}})] + [\nu(\mathrm{As_{A'}F_{8A'}}) + \nu(\mathrm{As_{A'}F_{5A'}}) + \nu(\mathrm{As_{A'}F_{3A'}}) + \nu(\mathrm{As_{A'}F_{6A'}}) + \nu(\mathrm{As_{A'}F_{4A'}}) + \nu(\mathrm{As_{A'}F_{7A'}})] + [\nu(\mathrm{As_BF_{8B}}) + \nu(\mathrm{As_BF_{5B}}) + \nu(\mathrm{As_BF_{3B}}) + \nu(\mathrm{As_BF_{6B}})]_{\mathrm{small}} + [\nu(\mathrm{BrF_1}) + \nu(\mathrm{BrF_2})]_{\mathrm{small}}$. [i] $[\nu(\mathrm{BrF_1}) + \nu(\mathrm{BrF_2})]$. [j] $[\nu(\mathrm{As_{A'}F_{8A'}}) + \nu(\mathrm{As_{A'}F_{5A'}}) + \nu(\mathrm{As_{A'}F_{3A'}}) + \nu(\mathrm{As_{A'}F_{4A'}}) + \nu(\mathrm{As_{A'}F_{7A'}}) - \nu(\mathrm{As_{A'}F_{6A'}})]$.

Table 8.6. Complete List of Vibrational Frequencies[a] for $[ClOF_2][AsF_6]$ (Exptl) and $[ClOF_2][AsF_6]_3^{2-}$ (Calcd)

exptl[b]			calcd[c]		assgnts
Raman[d]	ir[d]	exptl[e,f]	PBE1PBE	B3LYP	$[ClOF_2][AsF_6]_3^{2-}$ (C_1)[g]
1333(2) 1320(1)	1331 ms 1319 mw	1333(21) 1329(39) 1321(10)	1303(41)[136]	1228(51)[126]	$\nu(ClO)$
757(3)	750 br	757(26) br 752 (24) br	749(76)[299]	708(39)[386][h]	$[\nu(ClF_1) + \nu(ClF_2)]$
		720(8)	729(14)[309]	702(3)[305][i]	$[\nu(ClF_1) - \nu(ClF_2)] + [\nu(As_AF_{5A}) - \nu(As_AF_{8A})] - [\nu(As_{A'}F_{5A'}) - \nu(As_{A'}F_{8A'})] + [\nu(As_BF_{5B}) - \nu(As_BF_{8B})]$
		710(1)	721(2)[239]	698(13)[375][j]	$[\nu(As_AF_{5A}) - \nu(As_AF_{8A})] + [\nu(As_{A'}F_{5A'}) - \nu(As_{A'}F_{8A'})]$
			716(6)[107]	691(17)[22]	$[\nu(As_AF_{5A}) - \nu(As_AF_{8A})] - [\nu(As_{A'}F_{5A'}) - \nu(As_{A'}F_{8A'})] + [\nu(As_{A'}F_{7A'}) - \nu(As_{A'}F_{4A'})] + [\nu(ClF_1) - \nu(ClF_2)]_{small}$
			713(8)[297]	690(27)[95]	$[\nu(As_AF_{4A}) - \nu(As_AF_{7A})] + [\nu(As_{A'}F_{7A'}) - \nu(As_{A'}F_{4A'})]$
			709(<1)[96]	689(<1)[90]	$[\nu(As_{A'}F_{7A'}) - \nu(As_{A'}F_{4A'})] + [\nu(As_BF_{8B}) - \nu(As_BF_{5B})]$
696(1)	695 vs	695(16) 692 sh	703(4)[40]	668(11)[12][k]	$[\nu(As_AF_{4A}) - \nu(As_AF_{7A})] + [\nu(As_BF_{7B}) - \nu(As_BF_{4B})] + [\nu(As_BF_{5B}) - \nu(As_BF_{8B})] + [\nu(ClF_1) - \nu(ClF_2)]_{small}$
			700(4)[33]	680(15)[51][l]	$[\nu(As_{A'}F_{4A'}) - \nu(As_{A'}F_{7A'})] + [\nu(As_BF_{7B}) - \nu(As_BF_{4B})] + [\nu(As_BF_{8B}) - \nu(As_BF_{5B})] + [\nu(ClF_1) - \nu(ClF_2)]_{small}$
			677(<1)[30]	653(4)[28]	$[\nu(As_AF_{6A}) + \nu(As_{A'}F_{6A'}) + \nu(As_BF_{6B})] + [\nu(ClF_1) + \nu(ClF_2)]_{small}$
		685(3)	670(2)[353]	648(3)[326]	$[\nu(As_AF_{6A}) + \nu(As_{A'}F_{6A'}) - \nu(As_BF_{6B})]$
			667(6)[336]	641(17)[300][m]	$[\nu(As_AF_{6A}) - \nu(As_{A'}F_{6A'})] + [\nu(ClF_1) - \nu(ClF_2)]_{small}$
674(10)	675 sh	675(100)	651(70)[4]	631(80)[5]	$[\nu(As_AF_{3A}) + \nu(As_AF_{4A}) + \nu(As_AF_{5A}) + \nu(As_AF_{7A}) + \nu(As_AF_{8A})] + [\nu(As_{A'}F_{3A'}) + \nu(As_{A'}F_{4A'}) + \nu(As_{A'}F_{5A'}) + \nu(As_{A'}F_{7A'}) + \nu(As_{A'}F_{8A'})] + [\nu(As_BF_{3B}) + \nu(As_BF_{4B}) + \nu(As_BF_{5B}) + \nu(As_BF_{7B}) + \nu(As_BF_{8B})]$
			648(2)[87]	629(3)[113]	$[\nu(As_AF_{3A}) + \nu(As_AF_{4A}) + \nu(As_AF_{5A}) + \nu(As_AF_{7A}) + \nu(As_AF_{8A})] + [\nu(As_{A'}F_{3A'}) + \nu(As_{A'}F_{4A'}) + \nu(As_{A'}F_{5A'}) + \nu(As_{A'}F_{7A'}) + \nu(As_{A'}F_{8A'})] - [\nu(As_BF_{3B}) + \nu(As_BF_{4B}) + \nu(As_BF_{5B}) + \nu(As_BF_{7B}) + \nu(As_BF_{8B})]$
			648(2)[136]	628(4)[189]	$[\nu(As_AF_{3A}) + \nu(As_AF_{4A}) + \nu(As_AF_{5A}) + \nu(As_AF_{7A}) + \nu(As_AF_{8A})] - [\nu(As_{A'}F_{3A'}) + \nu(As_{A'}F_{4A'}) + \nu(As_{A'}F_{5A'}) + \nu(As_{A'}F_{7A'}) + \nu(As_{A'}F_{8A'})]$
		576(9)	586(4)[<1]	571(4)[1]	$[\nu(As_AF_{4A}) + \nu(As_AF_{7A})] - [\nu(As_AF_{5A}) + \nu(As_AF_{8A})] + [\nu(As_{A'}F_{4A'}) + \nu(As_{A'}F_{7A'})] - [\nu(As_{A'}F_{5A'}) + \nu(As_{A'}F_{8A'})]$
			585(3)[<1]	569(3)[1]	$[\nu(As_AF_{4A}) + \nu(As_AF_{7A})] - [\nu(As_AF_{5A}) + \nu(As_AF_{8A})] - [\nu(As_{A'}F_{4A'}) + \nu(As_{A'}F_{7A'})] + [\nu(As_{A'}F_{5A'}) + \nu(As_{A'}F_{8A'})]$
			578(3)[<1]	562(3)[<1]	$[\nu(As_BF_{5B}) + \nu(As_BF_{8B})] - [\nu(As_BF_{4B}) + \nu(As_BF_{7B})]$
563(3)	561 ms	568(31) 559(30)	552(14)[2]	533(19)[6]	$[\nu(As_BF_{3B}) + \nu(As_BF_{6B})] - [\nu(As_BF_{4B}) + \nu(As_BF_{7B})] - [\nu(As_BF_{5B}) + \nu(As_BF_{8B})]$
			525(17)[95]	501(24)[112]	$[\nu(As_AF_{3A}) + \nu(As_{A'}F_{3A'}) - \nu(As_BF_{3B})] - [\nu(ClF_{3A}) + \nu(ClF_{3A'}) - \nu(ClF_{3B})] + \delta(ClOF_1F_2)_{small}$
			507(14)[166]	484(18)[185]	$[\nu(As_AF_{3A}) - \nu(As_{A'}F_{3A'})] + [\nu(ClF_{3A'}) - \nu(ClF_{3A})]$
511(2)	509 ms	510(22)	476(4)[36]	452(2)[43]	$\delta(ClOF_1F_2) + [\nu(As_AF_{3A}) + \nu(As_{A'}F_{3A'})] - [\nu(ClF_{3A}) + \nu(ClF_{3A'})]_{small}$

Table 8.6. (continued…)

406(2)	407 sh	411(16)	406(2)[8]	391(2)[40]	$\delta(OClF_1)$
			400(2)[120]	393(4)[90]	$[\delta(F_{4A}As_AF_{8A}) - \delta(F_{5A}As_AF_{7A}) + \rho_w(F_{3A}As_AF_{6A})] + [\delta(F_{4A'}As_{A'}F_{8A'}) - \delta(F_{5A'}As_{A'}F_{7A'}) + \rho_w(F_{3A'}As_{A'}F_{6A'})]$
		406(5) 400 sh	392(<1)[3]	386(2)[16]	$[\delta(F_{6A}As_AF_{7A}) - \delta(F_{3A}As_AF_{4A}) + \rho_w(F_{5A}As_AF_{8A})] + [\delta(F_{6A'}As_{A'}F_{7A'}) - \delta(F_{3A'}As_{A'}F_{6A'}) + \rho_w(F_{5A'}As_{A'}F_{8A'})]$
			390(<0.1)[10]	385(<1)[12]	$[\delta(F_{6B}As_BF_{7B}) - \delta(F_{3B}As_BF_{4B}) + \rho_w(F_{5B}As_BF_{8B})]$
		396(10) 392(5)	388(<0.1)[4]	383(<1)[7]	$\delta(As_BF_{4B}F_{7B}F_{8B}F_{5B})_{\text{o.o.p.}} + \delta(As_AF_{4A}F_{7A}F_{8A}F_{5A})_{\text{o.o.p.}} + \delta(As_{A'}F_{4A'}F_{7A'}F_{8A'}F_{5A'})_{\text{o.o.p.}}$
			385(1)[74]	377(2)[39]	$\delta(F_1ClF_2) + \delta(As_BF_{4B}F_{7B}F_{8B}F_{5B})_{\text{o.o.p.}} - \delta(As_AF_{4A}F_{7A}F_{8A}F_{5A})_{\text{o.o.p.}} - \delta(As_{A'}F_{4A'}F_{7A'}F_{8A'}F_{5A'})_{\text{o.o.p.}}$
			383(<0.1)[76]	379(<0.1)[76]	$\delta(As_BF_{4B}F_{7B}F_{3B}F_{6B})_{\text{o.o.p.}}$
			381(<1)[87]	377(<1)[147]	$\delta(As_AF_{4A}F_{7A}F_{3A}F_{6A})_{\text{o.o.p.}} + \delta(As_{A'}F_{4A'}F_{7A'}F_{3A'}F_{6A'})_{\text{o.o.p.}}$
			378(<0.1)[6]	374(<0.1)[6]	$\delta(As_AF_{4A}F_{7A}F_{3A}F_{6A})_{\text{o.o.p.}} - \delta(As_{A'}F_{4A'}F_{7A'}F_{3A'}F_{6A'})_{\text{o.o.p.}}$
	388 s		370(<1)[141]	363(<1)[113]	$[\delta(As_AF_{4A}F_{6A}F_{8A}) - \delta(As_AF_{3A}F_{5A}F_{7A})] + [\delta(As_{A'}F_{3A'}F_{5A'}F_{7A'}) - \delta(As_{A'}F_{4A'}F_{6A'}F_{8A'})] + \delta(OClF_1)_{\text{small}}$
			362(<1)[40]	329(1)[33]	$\delta(F_1ClF_2) + [\delta(As_BF_{4B}F_{6B}F_{8B}) - \delta(As_BF_{3B}F_{5B}F_{7B})]_{\text{small}}$
378(1)	378 sh	378(16)	353(1)[9]	349(1)[8]	$[\delta(F_{4A'}As_{A'}F_{8A'}) + \delta(F_{5A'}As_{A'}F_{7A'})]$
			352(1)[<1]	348(1)[<1]	$[\delta(F_{4A}As_AF_{8A}) + \delta(F_{5A}As_AF_{7A})]$
			352(1)[6]	347(1)[8]	$[\delta(F_{4A}As_AF_{5A}) + \delta(F_{8A}As_AF_{7A})] + [\delta(F_{4A'}As_{A'}F_{5A'}) + \delta(F_{8A'}As_{A'}F_{7A'})]$
			349(1)[<1]	345(1)[<1]	$[\delta(F_{4B}As_BF_{5B}) + \delta(F_{8B}As_BF_{7B})]$
371(4)		370(39)	344(3)[26]	349(1)[<1]	$[\delta(F_{6B}As_BF_{8B}) + \delta(F_{3B}As_BF_{5B})] + \delta(F_1ClF_2)_{\text{small}}$
			342(3)[18]	337(2)[2]	$[\delta(F_{6B}As_BF_{8B}) + \delta(F_{3B}As_BF_{5B})]$
			340(2)[47]	332(3)[38]	$[\delta(F_{4A}As_AF_{6A}) + \delta(F_{3A}As_AF_{7A})] + [\delta(F_{4B}As_BF_{6B}) + \delta(F_{3B}As_BF_{7B})] + \delta(OClF_2)_{\text{small}}$
			338(<1)[2]	333(<1)[26]	$[\delta(F_{3A}As_AF_{8A}) + \delta(F_{5A}As_AF_{6A})]$
			337(1)[7]	335(3)[23]	$[\delta(F_{3A'}As_{A'}F_{8A'}) + \delta(F_{5A'}As_{A'}F_{6A'}) + \rho_t(F_{4A'}As_{A'}F_{7A'})]$
			247(<0.1)[2]	244(<0.1)[2]	$[\rho_w(F_{3A}As_AF_{6A}) - \rho_w(F_{5A}As_AF_{8A})] + [\rho_w(F_{3A'}As_{A'}F_{6A'}) - \rho_w(F_{5A'}As_{A'}F_{8A'})]$
			239(<1)[12]	235(<1)[16]	$[\rho_w(F_{3A}As_AF_{6A}) - \rho_w(F_{5A}As_AF_{8A})] + [\rho_w(F_{3A'}As_{A'}F_{6A'}) - \rho_w(F_{4A'}As_{A'}F_{7A'})] + [\rho_w(F_{5B}As_BF_{8B}) - \rho_w(F_{3B}As_BF_{6B})]$
			238(<0.1)[5]	234(<0.1)[4]	$[\rho_w(F_{4B}As_BF_{7B}) - \rho_w(F_{3B}As_BF_{6B}) + \rho_w(F_{5B}As_BF_{8B})]$
			233(<1)[3]	229(<1)[2]	$[\rho_w(F_{3A}As_AF_{6A}) - \rho_w(F_{4A}As_AF_{7A})]$
			230(<1)[2]	226(<1)[1]	$[\rho_w(F_{3A'}As_{A'}F_{6A'}) - \rho_w(F_{4A'}As_{A'}F_{7A'}) - \rho_w(F_{5A'}As_{A'}F_{8A'})]$
			229(<0.1)[1]	225(<0.1)[1]	$[\rho_w(F_{3B}As_BF_{6B}) - \rho_w(F_{4B}As_BF_{7B})]$
			219(<0.1)[<1]	216(<1)[<1]	$[\rho_w(F_{4B}As_BF_{7B}) - \rho_w(F_{5B}As_BF_{8B})]$
			216(<0.1)[<1]	212(<0.1)[<1]	$[\rho_w(F_{4A}As_AF_{7A}) - \rho_w(F_{5A}As_AF_{8A})]$
			214(<0.1)[<1]	211(<0.1)[<1]	$[\rho_w(F_{4A'}As_{A'}F_{7A'}) - \rho_w(F_{5A'}As_{A'}F_{8A'})]$
			181(<1)[32]	175(<1)[32]	$\rho_r(ClF_1F_2)$

Table 8.6. (continued…)

	175(<1)[14]	171(<1)[15]	$\rho_r(ClOF_1F_2)$
	154(<1)[2]	144(<1)[3]	$\rho_t(ClOF_1F_2)$
	135(<1)[6]	134(<1)[6]	coupled deformation modes
	106(<1)[34]	102(<1)[31]	
	104(<1)[19]	100(<1)[19]	
	70(<0.1)[<1]	66(<0.1)[1]	
	64(<0.1)<1]	59(<0.1)[1]	
	56(<0.1)[<1]	52(<1)[<1]	
	44(<0.1)-<1]	40(<1)[<1]	
	41(<0.1)[<1]	38(<0.1)[<1]	
	34(<0.1)[<0.1]	31(<0.1)[<0.1]	
	27(<0.1)[<1]	25(<1)[<1]	
	21(<0.1)[<0.1]	19(<0.1)[<0.1]	
	19(<0.1)[<0.1]	16(<0.1)[<0.1]	
	16(<0.1)[<0.1]	12(<0.1)[<0.1]	
	13(<0.1)[<0.1]	9(<0.1)[<0.1]	
	8(<0.1)[<0.1]	8(<0.1)[<0.1]	
150(3)			lattice modes
143(5)			
122(4)			
108(5)			

---

[a] Frequencies are given in cm^{-1}. [b] The abbreviations denote shoulder (sh) and broad (br). [c] The Stutt Huzpolar 2 basis set was used. Values in parentheses denote Raman intensities (Å^4 u^{-1}). Values in square brackets denote infrared intensities (km mol^{-1}). [d] From ref 124. [e] Values in parentheses denote relative Raman intensities. [f] The Raman spectrum was recorded in an FEP sample tube at −150 °C using 1064-nm excitation. Several weak bands were are also observed at 1065(2), 1045(4), 1039(1) and are assigned to combination bands. [g] Vibrational assignments were based on the modes at the PBE1PBE level. The abbreviations denote stretch (ν), bend (δ), rock (ρ_r), twist (ρ_t), wag (ρ_w), and out-of-plane bend (o.o.p.). [h] $[\nu(ClF_1) + \nu(ClF_2)] + [\nu(As_AF_{8A}) - \nu(As_AF_{5A})] + [\nu(As_{A'}F_{8A'}) - \nu(As_{A'}F_{5A'})]$. [i] $[\nu(As_AF_{5A}) - \nu(As_AF_{8A})] - [\nu(As_{A'}F_{5A'}) - \nu(As_{A'}F_{8A'})] + [\nu(As_BF_{5B}) - \nu(As_BF_{8B})] + [\nu(ClF_1) - \nu(ClF_2)]_{small}$. [j] $[\nu(As_AF_{5A}) - \nu(As_AF_{8A})] + [\nu(As_{A'}F_{5A'}) - \nu(As_{A'}F_{8A'})] + [\nu(ClF_1) + \nu(ClF_2)]_{small}$. [k] $[\nu(ClF_1) - \nu(ClF_2)] + [\nu(As_AF_{6A}) - \nu(As_{A'}F_{6A'})] - [\nu(As_BF_{5B}) - \nu(As_BF_{8B})]$. [l] $[\nu(As_BF_{4B}) - \nu(As_BF_{7B})] + [\nu(As_AF_{6A}) + \nu(As_{A'}F_{6A'})]_{small} + [\nu(ClF_1) + \nu(ClF_2)]_{small}$. [m] $[\nu(ClF_1) - \nu(ClF_2)] + [\nu(As_AF_{6A}) - \nu(As_{A'}F_{6A'})]$.

Table 8.7. Complete List of Experimental and Calculated Vibrational Frequencies[a] for $[BrOF_2][AsF_6]\cdot XeF_2$

exptl[b]	calcd[c]		assgnts	AsF_6^-
	PBE1PBE	B3LYP	$[BrOF_2][AsF_6]\cdot XeF_2$ (C_1)[d]	
1050(25) [e] 1043(22)	1090(40)[57]	1020(44)[55]	$\nu(BrO)$	
752(3)	753(2)[197]	731(1)[192]	$\nu(AsF_5) - \nu(AsF_8)$	$\nu_3(T_{1u})$
744(7)	749(5)[137]	727(3)[135]	$\nu(AsF_7) - \nu(AsF_{10})$	
706(3)	745(8)[120]	724(12)[128]	$\nu(AsF_9)$	
651 sh 646(63) [f]	670(39)[94]	644(9)[73]	$\nu(BrF_1) + \nu(BrF_2)$	
674(9) [e] 669(4)	662(31)[76]	640(82)[79]	$\nu(AsF_5) + \nu(AsF_7) + \nu(AsF_{10}) + [\nu(BrF_1) + \nu(BrF_2)]_{small}$	$\nu_1(A_{1g})$
634(27) [e,f]	632(20)[163]	603(24)[160]	$\nu(BrF_1) - \nu(BrF_2)$	
559(45) 543(100) 531(11)	589(31)[159]	584(29)[181]	$\nu(XeF_9)$	
575(14)	573(3)[22]	564(3)[22]	$[\nu(AsF_5) + \nu(AsF_8)] - [\nu(AsF_7) + \nu(AsF_{10})]$	$\nu_2(E_g)$
447(8) br 426(10) br	463(36)[343]	472(58)[349]	$\nu(XeF_3) + [\nu(AsF_6) - \nu(Br{-}{-}{-}F_6)]_{small}$	
	437(2)[18]	423(3)[22]	$\nu(AsF_6) + \nu(Br{-}{-}{-}F_6)$	
	419(2)[61]	407(2)[35]	$[\nu(AsF_6) - \nu(Br{-}{-}{-}F_6)] + \delta(F_6AsF_8) - \delta(F_5AsF_9) + \rho_w(F_7AsF_{10})$	
411(11)	389(1)[52]	378(<1)[53]	$\delta(OBrF_1F_2) + \delta(F_5AsF_{10}) - \delta(F_7AsF_8) + \rho_w(F_6AsF_9)$	$\nu_4(T_{1u})$
	385(2)[22]	374(2)[13]	$\delta(F_5AsF_7) - \delta(F_8AsF_{10}) + \rho_w(F_6AsF_9)$	
402(12)	375(2)[25]	365(1)[5]	$\delta(F_5AsF_7) + \delta(F_8AsF_{10}) + [\delta(OBrF_1F_2)]_{small}$	
392(14)	370(1)[60]	357(2)[38]	$\delta(OBrF_1F_2) + \delta(AsF_7F_8F_9)$	
387(7) [g]	354(1)[102]	340(1)[135]	$\delta(F_5AsF_6) - \delta(F_5AsF_9) + \delta(OBrF_1)$	$\nu_5(T_{2g})$
	343(<1)[3]	333(<1)[7]	$\delta(F_6AsF_7) + \delta(F_9AsF_{10})$	
373(19) [e] 364(17)	313(5)[76]	301(4)[96]	$\rho_w(OBrF_2) + \rho_t(F_1BrF_2) + [\nu(AsF_6) - \nu(Br{-}{-}{-}F_6)]_{small}$	
325(10)	294(<1)[11]	276(<1)[10]	$\delta(F_1BrF_2)$	

Table 8.7. (continued…)

	259(<1)[39]	251(<1)[50]	$\rho_w(F_7AsF_{10}) - \rho_w(F_6AsF_9) + \delta(F_8AsF_9)$	
293(8)[g]	244(<1)[21]	233(<1)[4]	$\rho_w(F_5AsF_8) - \rho_w(F_6AsF_9) + \delta(F_3XeF_4)_{i.p.}$	
	234(<1)[19]	231(<1)[8]	$\rho_w(F_5AsF_8) - \rho_w(F_6AsF_9) - \delta(F_3XeF_4)_{i.p.}$	
	221(<0.1)[1]	226(<0.1)[13]	$\rho_w(F_5AsF_8) - \rho_w(F_7AsF_{10})$	$\nu_6(T_{2u})$
244(3)	207(<1)[9]	213(<0.1)[2]	$\delta(F_3XeF_4)_{o.o.p.}$	
	159(<1)[9]	154(<1)[10]	$\rho_r(F_1BrF_2) + \rho_w(OBrF_2) + \rho_r(F_7AsF_8)$	
152(11)	151(<1)[3]	148(<1)[4]	$\rho_r(OBrF_2) + \rho_r(F_8AsF_9)_{small}$	
140(9)	139(1)[13]	133(1)[12]	$\rho_w(OBrF_1) + \rho_r(AsF_7F_8F_{10}) + \rho_r(F_3XeF_4)$	
	103(2)[3]	106(<1)[<1]	$\rho_t(F_3XeF_4) + \rho_r(OBrF_1F_2)$	
	79(1)[2]	82(3)[4]	$\rho_r(OBrF_1F_2) + \rho_r(F_3XeF_4)$	
	72(<1)[<1]	73(<1)[1]	deformation modes $[BrOF_2][AsF_6]\cdot XeF_2$	
	63(<1)[2]	66(<1)[2]		
	47(<1)[<1]	63(<1)[<1]		
	35(<1)[<1]	44(<0.1)[<1]		
	27(1)[<1]	40(<1)[<1]		
	14(<1)[<1]	25(<1)[<1]		
124(7)			lattice modes	
98(11)				

[a] Frequencies are given in cm^{-1}. [b] The Raman spectrum was recorded in an FEP sample tube at −150 °C using 1064-nm excitation. Values in parentheses denote relative Raman intensities. The abbreviations denote shoulder (sh) and broad (br). Several weak bands were observed and assigned to the $[BrOF_2][AsF_6]$ ion pair [1062(3), 723(2), 314(4) cm^{-1}] and to the $[BrOF_2][AsF_6]\cdot 2XeF_2$ adduct [698(2), 674(2), 614(7), 586(2), 565(7), 547(sh), 466(17), 408(sh), 314(4) cm^{-1}]; the relative intensities have been corrected for the overlap. [c] The aug-cc-pVTZ(-pp) basis set was used. Values in parentheses denote Raman intensities ($Å^4$ u^{-1}) and values in square brackets denote infrared intensities (km mol^{-1}). [d] Vibrational assignments were based on the modes at the PBE1PBE level.The abbreviations denote stretch (ν), bend (δ), rock (ρ_r), twist (ρ_t), wag (ρ_w), in-plane bend (i.p.), and out-of-plane bend (o.o.p.). [e] The band overlaps with a $[BrOF_2][AsF_6]\cdot 2XeF_2$ band; the relative intensity was corrected for overlap. [f] The band overlaps with a $[BrOF_2][AsF_6]$ band; the relative intensity was corrected for overlap. [g] The band overlaps with a FEP sample tube line; the relative intensity was corrected for overlap.

Table 8.8. Complete List of Experimental and Calculated Vibrational Frequencies[a] for $[BrOF_2][AsF_6]\cdot 2XeF_2$

exptl[b]	calcd[c]		assgnts	
	PBE1PBE	B3LYP	$[BrOF_2][AsF_6]\cdot 2XeF_2$ (C_1)[d]	AsF_6^-
1051(62) 1045(1)	1071(67)[71]	1022(77)[69]	$\nu(BrO)$	
701 sh 697(13)	744(6)[172]	717(6)[167]	$\nu(AsF_{11}) - \nu(AsF_{12})$	$\nu_3(T_{1u})$
	727(3)[163]	703(4)[158]	$\nu(AsF_8)$	
	721(<1)[232]	696(<1)[223]	$\nu(AsF_9) - \nu(AsF_{10})$	
675(21)	662(21)[68]	636(67)[52]	$\nu(AsF_7) + \nu(AsF_9) + \nu(AsF_{10}) + \nu(AsF_{12})$ [e]	$\nu_1(A_{1g})$
634(63)	678(62)[87]	642(36)[97]	$\nu(BrF_1) + \nu(BrF_2)$ [f]	
614(43)	646(29)[84]	609(41)[61]	$\nu(BrF_1) - \nu(BrF_2)$	
552(26) 548(100)	604(46)[81]	584(41)[94]	$\nu(Xe_1F_4) + \nu(Xe_2F_6)$	
543(49) 540(69)	600(25)[236]	578(22)[256]	$\nu(Xe_1F_4) - \nu(Xe_2F_6)$	
591(2) 586(5)	573(2)[5]	556(2)[3]	$[\nu(AsF_9) + \nu(AsF_{10})] - [\nu(AsF_{11}) + \nu(AsF_{12})]$	$\nu_2(E_g)$
565(15) 561 sh	535(7)[95]	511(23)[210]	$\nu(AsF_7) + [\nu(Xe_1F_3) - \nu(AsF_{12})]_{small}$	
467(93), br 460 sh	503(47)[218]	485(38)[156]	$\nu(Xe_1F_3) + [\nu(Xe_2F_5) - \nu(AsF_7)]_{small}$	
409(15), br	463(18)[364]	434(20)[325]	$\nu(Xe_2F_5) - \nu(Xe_1F_3)_{small}$	
400(4)	400(<1)[53]	390(<1)[42]	$\delta(F_9AsF_{12}) - \delta(F_{10}AsF_{11}) + \rho_w(F_7AsF_8)$	$\nu_4(T_{1u})$
	395(<1)[27]	385(<1)[42]	$\delta(F_8AsF_9) - \delta(F_7AsF_{10}) + \rho_w(F_{11}AsF_{12})$	
	394(<1)[34]	383(<1)[25]	$\delta(AsF_7F_9F_{11}) - \delta(AsF_8F_{10}F_{12})$	
395(15)	386(3)[119]	368(3)[99]	$\delta(OBrF_1F_2)$	
372 sh 366(3)	366(1)[<1]	357(1)[<0.1]	$\delta(F_9AsF_{12}) + \delta(F_{10}AsF_{11})$	$\nu_5(T_{2g})$
	361(1)[<1]	352(2)[2]	$\delta(F_7AsF_{12}) + \delta(F_8AsF_{11})$	
	356(<1)[<1]	345(<1)[<1]	$\delta(F_7AsF_9) + \delta(F_8AsF_{10})$	
375(13) 369(10)	338(4)[90]	322(4)[79]	$\rho_w(OBrF_2) + \rho_t(F_1BrF_2)$	
315(12)	305(<1)[6]	286(<1)[6]	$\delta(F_1BrF_2)$	

Table 8.8. (continued…)

299(3)	270(<1)[67]	258(<1)[59]	$\delta(F_5Xe_2F_6)_{o.o.p.}$	
	248(<0.1)[8]	242(<1)[8]	$[\rho_w(F_9AsF_{10}) - \rho_w(F_7AsF_8)] - \delta(F_3Xe_1F_4)_{i.p.}$	
	240(<1)[15]	234(<1)[13]	$[\rho_w(F_9AsF_{10}) - \rho_w(F_7AsF_8)] + \delta(F_3Xe_1F_4)_{i.p.}$	
250(1)	238(<1)[<1]	228(<1)[1]	$\delta(F_5Xe_2F_6)_{i.p.}$	
	235(<1)[2]	226(<1)[9]	$\rho_w(F_{11}AsF_{12}) - \rho_w(F_7AsF_8) + \rho_w(F_9AsF_{10})$	$\nu_6(T_{2u})$
	229(<0.1)[<1]	222(<0.1)[<1]	$\rho_w(F_9AsF_{10}) - \rho_w(F_{11}AsF_{12}) + \rho_w(F_7AsF_8)$	
232(3)	216(<1)[18]	198(<1)[10]	$\delta(F_3Xe_1F_4)_{o.o.p.}$	
222(1)	181(1)[6]	175(2)[7]	$\rho_t(OBrF_1F_2) + [\rho_t(F_5Xe_2F_6) + \rho_t(F_3Xe_1F_4)]_{small}$	
166(4)	159(1)[18]	154(2)[19]	$\rho_t(F_5Xe_2F_6) + \rho_t(OBrF_1F_2)_{small}$	
161(3)	155(1)[4]	149(1)[2]	$\rho_t(OBrF_1) + \rho_t(F_5Xe_2F_6)$	
147(3)	129(1)[5]	130(2)[6]	$\rho_r(OBrF_1F_2) + \rho_r(F_3Xe_1F_4)$	
	116(2)[4]	108(<1)[4]	$\rho_r(OBrF_1F_2) - \rho_r(F_3Xe_1F_4)$	
	104(2)[16]	95(<1)[8]	$\rho_r(F_3Xe_1F_4) + \rho_t(OBrF_1F_2)_{small}$	
	101(<1)[4]	93(1)[4]	$\rho_r(F_5Xe_2F_6) + \rho_t(OBrF_1F_2)_{small}$	
	81(<1)[2]	73(1)[<1]	deformation modes $[BrOF_2][AsF_6]\cdot 2XeF_2$	
	68(<1)[<1]	63(1)[<1]		
	61(<1)[<1]	58(<1)[<1]		
	54(<1)[<1]	46(<1)[<1]		
	46(<1)[<1]	42(<1)[1]		
	43(<1)[1]	38(<1)[<1]		
	39(<1)[<1]	33(<0.1)[<1]		
	29(<1)[<1]	24(<1)[1]		
	21(<1)[<1]	10(1)[<1]		
127(22)			lattice modes	
109(18)				
91(9)				
61(2)				

---

[a] Frequencies are given in cm^{-1}. [b] The Raman spectrum was recorded in an FEP sample tube at −150 °C using 1064-nm excitation. Values in parentheses denote relative Raman intensities. The abbreviations denote a shoulder (sh) and broad (br). [c] The aug-cc-pVTZ(-pp) basis set was used. Values in parentheses denote Raman intensities ($Å^4$ u^{-1}). Values in square brackets denote infrared intensities (km mol^{-1}). [d] Vibrational assignments were based on the modes at the PBE1PBE level. The abbreviations denote stretch (ν), bend (δ), rock (ρ_r), twist (ρ_t), wag (ρ_w), in-plane bend (i.p.), and out-of-plane bend (o.o.p.). [e] $\nu(BrF_1) + \nu(BrF_2)$ also contributes at B3LYP level. [f] $\nu(AsF_{13}) + \nu(AsF_{14}) + \nu(AsF_{10}) + \nu(AsF_9)$ also contributes at B3LYP level.

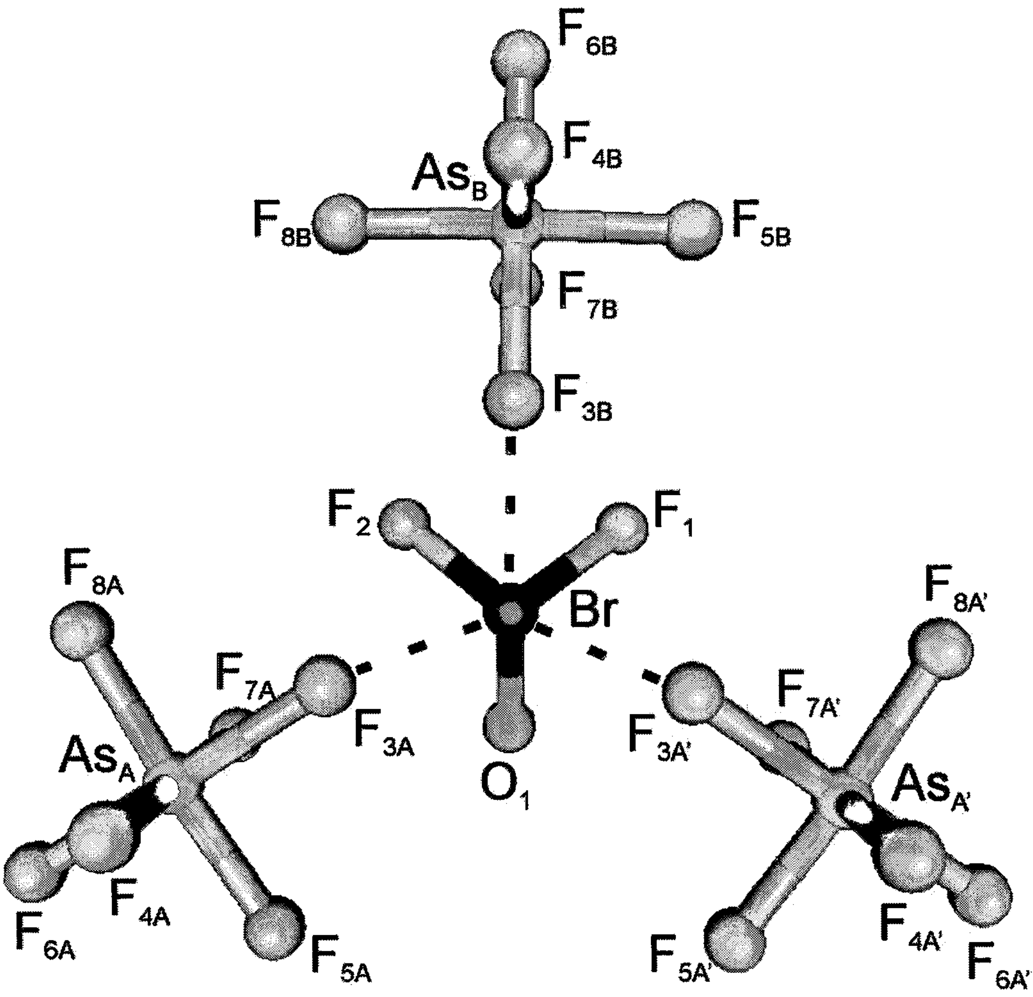

Figure 8.10. The calculated geometry (PBE1PBE/Stutt Huzpolar 2) of $[BrOF_2][AsF_6]_3^{2-}$ (C_1) showing the pseudo-octahedral coordination around bromine(V).

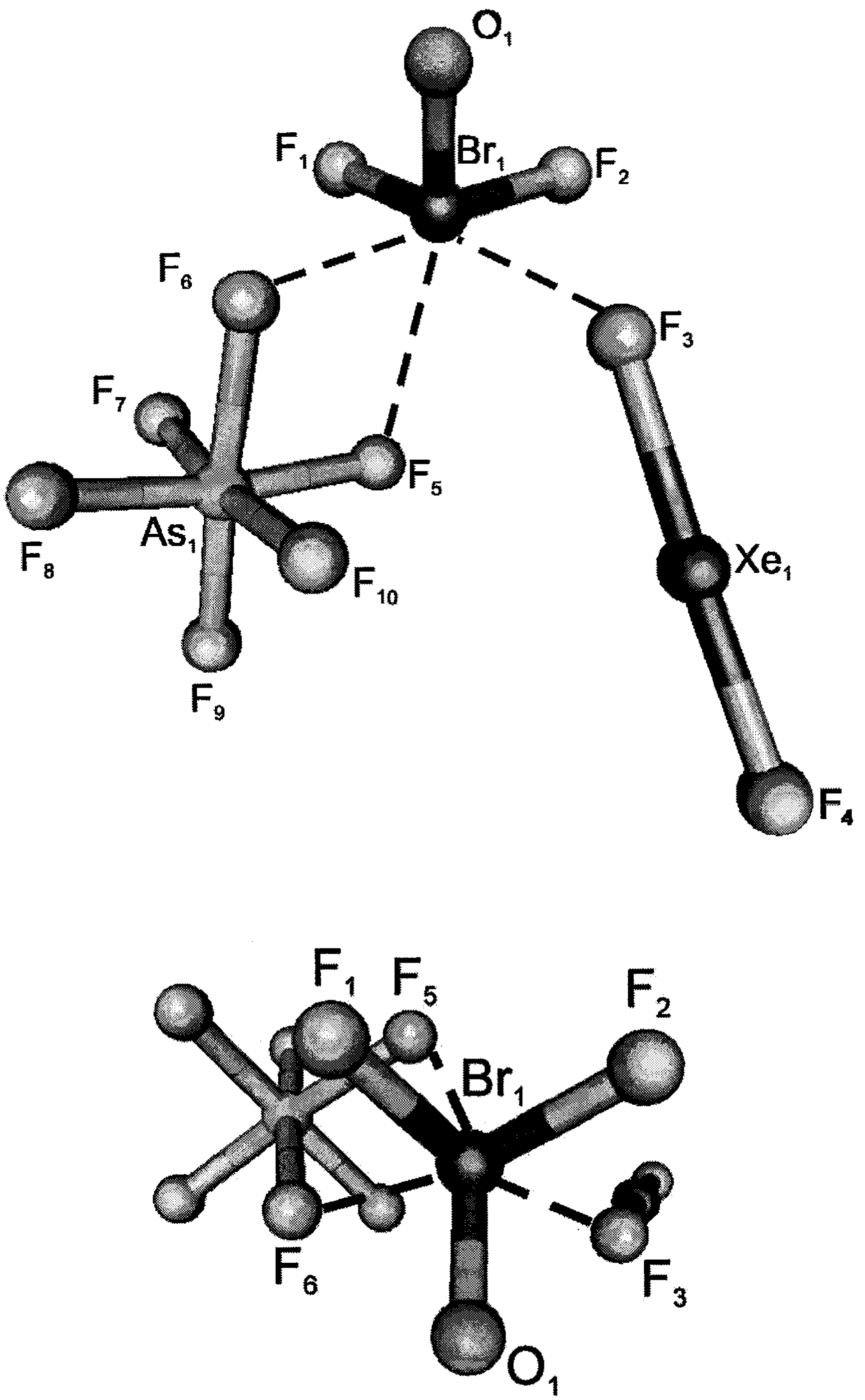

Figure 8.11. The calculated geometry (PBE1PBE/aug-cc-pVTZ(-PP)) of $[BrOF_2][AsF_6]\cdot XeF_2$ (C_1) showing the pseudo-octahedral coordination around bromine(V).

comparison with $[BrOF_2][AsF_6]\cdot 2KrF_2$.[232] Vibrational frequencies calculated at the PBE1PBE and B3LYP (values in parentheses) levels of theory well reproduced the observed frequencies across the series of compounds. In each case, the AsF_6^- anion is distorted from its ideal octahedral geometry. The AsF_6^- anion, under O_h symmetry, has three Raman-active bands, $\nu_1(A_{1g})$, $\nu_2(E_g)$, and $\nu_5(T_{2g})$, two infrared-active bands, $\nu_3(T_{1u})$ and $\nu_4(T_{1u})$, and one inactive band, $\nu_6(T_{2u})$. In the present examples, the fluorine-bridged AsF_6^- anions are distorted, each with local C_1 symmetry, which results in a maximum of 15 Raman- and infrared-active bands. The bands that were observed in the Raman spectrum of AsF_6^- were assigned by comparison with other coordinated AsF_6^- anions having local C_1 or C_s symmetries.[71,154]

8.2.5.1. $[BrOF_2][AsF_6]$. Although $[BrOF_2][AsF_6]$ has been previously characterized by Raman spectroscopy at room temperature,[128] the spectrum has been re-examined at low temperature to properly assess the effects of adduct formation on the $BrOF_2^+$ modes in $[BrOF_2][AsF_6]\cdot XeF_2$ and $[BrOF_2][AsF_6]\cdot 2XeF_2$. The experimental spectrum is in overall good agreement with the previously reported spectrum.

The cubic space group in which the crystal structure was solved implies the anion and cation of $[BrOF_2][AsF_6]$ are situated on special positions with C_3 symmetry, thus imposing a 3-fold disorder on the cation. Consequently, the Raman spectrum was assigned based on the calculated C_1 geometry. Under C_1 symmetry, all vibrational modes (27 A) of the $[BrOF_2][AsF_6]$ ion pair are predicted to be Raman- and infrared-active. Minor discrepancies are expected to arise between experimental and calculated modes involving the anion because the calculated model, $[BrOF_2][AsF_6]_3^{2-}$, is for a single cation coordinated to three anions (see 8.2.6.1, Computational Results), whereas the crystal structure shows that each AsF_6^- anion is also coordinated to three other $BrOF_2^+$ cations.

In general, the cation bands are more intense than the anion bands, and little coupling occurs among their corresponding modes. The only significant exception is the in-phase Br–F stretching mode, $\nu(BrF_1) + \nu(BrF_2)$, which couples to As–F stretches of the anion (Table 8.5) and results in several bands appearing at 647, 667, and 723 cm^{-1}. In contrast, the out-of-phase $\nu(BrF_1) - \nu(BrF_2)$ stretching band appearing at 634 cm^{-1} shows no coupling with the anion and is significantly less intense than the in-phase band, in agreement with the calculated intensities. The highest frequency band in the spectrum occurs at 1064 cm^{-1} and is assigned to $\nu(BrO)$, in agreement with the calculated value, 1048 (997) cm^{-1}. The Br---F_3 and As–F_3 stretches are coupled to one another and are assigned to the bands at 535, 543, and 549 cm^{-1}. The $OBrF_1F_2$ bending mode, $\delta(OBrF_1F_2)$, occurs at 366 cm^{-1} and the remaining cation bending modes, $\delta(OBrF_1)$ and $\delta(F_1BrF_2)$, occur at 314 cm^{-1} and 292 cm^{-1}, respectively.

8.2.5.2. [ClOF$_2$][AsF$_6$]. The title compound has been previously characterized by Raman spectroscopy at room temperature.[124] However, a better-resolved, low-temperature spectrum is reported in the present work. The crystal structure of $[ClOF_2][AsF_6]$ has also made possible a more detailed analysis of the Raman spectrum which has been reassigned based on a factor-group analysis.

All vibrational modes (27 A) of the $[ClOF_2][AsF_6]$ ion pair (C_1) are predicted to be Raman- and infrared-active. Although only 24 Raman bands were observed, several high-frequency stretching bands were split into two or three bands that cannot be accounted for by site symmetry lowering alone because correlation of the gas-phase ion-pair symmetry (C_1) to the crystal site symmetry (C_1) results in no additional band splittings. The additional bands therefore arise from vibrational coupling within the crystallographic unit cell. Correlation of the site symmetry to the centrosymmetric unit cell symmetry (C_{2v} with $Z = 4$) results in equal apportioning of the 4(3N − 6) vibrational modes among A_1, A_2, B_1, and B_2 components (Table 8.9). The 27 vibrational bands split into A_1, A_2, B_1, and B_2 components, resulting in 108 coupled vibrational modes for $[ClOF_2][AsF_6]$ in its unit cell. The A_1, B_1, and B_2 components are Raman- and infrared-active, and the A_2 components are Raman-active. The appearance of only 24 Raman-active bands, instead of the predicted 108, implies that vibrational coupling within the crystallographic unit cell is, for the most part, weak and cannot be resolved except for the highest frequency cation stretching modes.

Table 8.9. Factor-Group Analysis for $[ClOF_2][AsF_6]$

gas-phase $[ClOF_2][AsF_6]$ (C_1)		crystal site (C_1)	unit cell (C_{2v})		
4(ν_1-ν_{27}, 3R, 3T)	A	A	A_1	ν_1-ν_{27}, 3R, 2T (−T)	R, IR
			A_2	ν_1-ν_{27}, 2R (−R), 2T (−T)	R
			B_1	ν_1-ν_{27}, 2R (−R), 2T (−T)	R, IR
			B_2	ν_1-ν_{27}, 2R (−R), 3T)	R, IR

[a] The crystallographic space group is $Pna2/_1$ with $Z = 4$ structural units per unit cell.

When compared with the analogous bands in $[BrOF_2][AsF_6]$, the $ClOF_2^+$ bands are generally less intense than the AsF_6^- bands, in accordance with the lower polarizability of the Cl atom. Although the mode descriptions for $[ClOF_2][AsF_6]$ are very similar to those of the bromine analogue, there are small differences, including a general tendency for greater vibrational coupling between the cation and the anion modes in $[ClOF_2][AsF_6]$. The highest frequency bands at 1321, 1329, and 1333 cm^{-1} represent three of the four bands predicted for the factor-group split $\nu(ClO)$ mode which occur at higher frequencies than $\nu(BrO)$, in accordance with the greater electronegativity of chlorine and greater covalencies of the Cl–O and Cl–F bonds as well as lower mass of chlorine. The coupling trends between the As–F and Br–F stretching modes of $[BrOF_2][AsF_6]$ are reversed in $[ClOF_2][AsF_6]$. The bands at 752 and 757 cm^{-1} are assigned to the in-phase $\nu(ClF_1) + \nu(ClF_2)$ mode and show no coupling to the anion modes, whereas the out-of-phase $\nu(ClF_1) - \nu(ClF_2)$ mode displays extensive coupling to As–F stretching modes with contributions observed at 685, 692, 695, 710, and 720 cm^{-1} with the major $\nu(ClF_1) - \nu(ClF_2)$ contribution assigned to the band at 720 cm^{-1}. The bands at 559 and 568 cm^{-1} arise from fluorine bridge stretches and are assigned to the different $\nu(AsF_3) - \nu(Cl{-}{-}{-}F_3)$ combinations of the three anions. The deformation modes of the cation are generally underestimated by the calculations and show significant coupling to the anion deformation modes. The mode having $\delta(OClF_1F_2)$ as its main contribution is coupled to the AsF_6^- deformation modes and is assigned to the band at 510 cm^{-1}, which appears at much higher frequency than the analogous band in $[BrOF_2][AsF_6]$. However, the latter mode, $\delta(OBrF_1F_2)$, is not coupled to any of the AsF_6^-

deformation modes. The δ($OClF_1$) and δ(F_1ClF_2) bending modes also appear at higher frequency than in [$BrOF_2$][AsF_6] and contribute to the bands at 411 and 296, 392 cm^{-1}, respectively.

8.2.5.3. [$BrOF_2$][AsF_6]·XeF_2 and [$BrOF_2$][AsF_6]·2XeF_2. The current work has shown that the previously reported Raman spectrum[129] of [$BrOF_2$][AsF_6]·XeF_2 contained residual BrF_5 solvent (Table 8.1). A sample of pure [$BrOF_2$][AsF_6]·XeF_2 was synthesized, and the spectrum was re-assigned. The Raman spectrum of the related [$BrOF_2$][AsF_6]·2XeF_2 adduct has also been assigned.

Several modes in the [$BrOF_2$][AsF_6]·2XeF_2 spectrum are split into two components. The splittings cannot be accounted for by site symmetry lowering because correlation of the gas-phase adduct symmetry (C_1) to the crystal site symmetry (C_1) results in no additional band splittings. The splittings must therefore result from vibrational coupling within the crystallographic unit cell (C_{2v} with Z = 4). Based on a factor-group analysis (Table 8.10), each Raman- and infrared-active band is predicted to be split into an A_g and a B_g component in the Raman spectrum and into an A_u and a B_u component in the infrared spectrum.

The most intense bands in the spectra of [$BrOF_2$][AsF_6]·XeF_2 and [$BrOF_2$][AsF_6]·2XeF_2 are associated with the XeF_2 ligand modes although they are not as intense as the KrF_2 ligand bands in [$BrOF_2$][AsF_6]·2KrF_2.[232] The interaction between the XeF_2 molecule and the $BrOF_2^+$ cation observed in the crystal structure renders the Xe–F bonds inequivalent for each XeF_2 molecule, giving rise to two bond types, Xe–F_b and

Table 8.10. Factor-Group Analysis for $[BrOF_2][AsF_6]\cdot 2XeF_2$

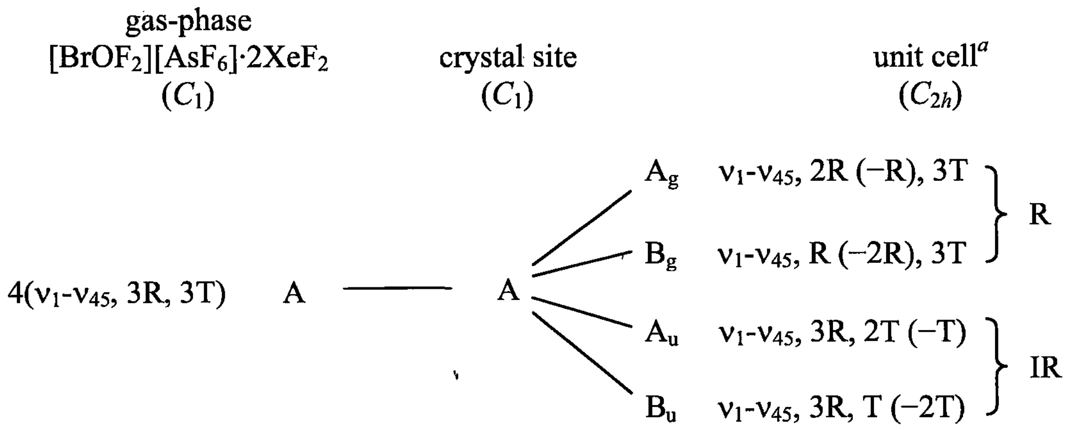

[a] The crystallographic space group is *P2₁/c* with $Z = 4$ structural units per unit cell.

Xe–F$_t$. The higher frequency bands of $[BrOF_2][AsF_6]\cdot XeF_2$ at 531, 543, and 559 cm^{-1} are assigned to the factor-group split terminal Xe–F$_t$ stretch. Like the KrF_2 analogue, the occurrence of two Xe–F$_t$ bonds in the $[BrOF_2][AsF_6]\cdot 2XeF_2$ adduct gives rise to factor-group split in-phase (548 and 552 cm^{-1}) and out-of-phase (540 and 543 cm^{-1}) bands, which are in good agreement with their respective calculated values, 604 (584) and 600 (578) cm^{-1}. The split band at 426, 447 cm^{-1} in the 1:1 adduct primarily corresponds to the bridging fluorine stretch $\nu(XeF_b)$, with a small contribution from $\nu(AsF_6) - \nu(Br\text{---}F_6)$. A factor-group split band at 460, 467 cm^{-1} and a band at 409 cm^{-1} are observed for the 2:1 adduct and are assigned to $\nu(XeF_b)$. However, unlike the $\nu(XeF_t)$ modes, the $\nu(XeF_b)$ modes are only weakly coupled with each other. This contrasts with the KrF_2 adduct,[232] where the Kr–F_b stretches are more strongly coupled than the Kr–F_t stretches. The present assignments for the XeF_2 modes are in agreement with those reported for XeF_2 homoleptically coordinated to metal cations,[82,83] where the higher frequency bands range from 544 to 584 cm^{-1} and are assigned to Xe–F_t stretching modes and the lower frequency bands range from 411 to 479 cm^{-1} and are assigned to Xe–F_b stretching modes. The doubly degenerate Π_u bend of free XeF_2, δ(FXeF), which is infrared-active but Raman inactive, splits into two components upon coordination, $\delta(F_tXeF_b)_{o.o.p.}$ and $\delta(F_tXeF_b)_{i.p.}$, where the bends are with respect to the plane containing the two XeF_2 molecules and the bromine atom and are both Raman- and infrared-active. Both components are shifted to higher frequency relative to Π_u in the infrared spectrum of XeF_2 (213 cm^{-1}).[203] In the 1:1 adduct, the $\delta(F_tXeF_b)_{o.o.p.}$ mode is observed at 244 cm^{-1} and the $\delta(F_tXeF_b)_{i.p.}$ mode at 293 cm^{-1}. Similarly, in $[BrOF_2][AsF_6]\cdot 2XeF_2$, the two out-of-plane bending modes are observed at 232 and 299 cm^{-1}, and an in-plane bend is observed as a weak band at 250 cm^{-1}. The second in-plane bend is predicted by calculations to be even weaker than the aforementioned modes and was not observed.

The observed and calculated frequencies for the anion and cation of $[BrOF_2][AsF_6]\cdot 2XeF_2$ are similar to those observed and calculated for the KrF_2 analogue.[232] All three adducts, $[BrOF_2][AsF_6]\cdot 2KrF_2$,[232] $[BrOF_2][AsF_6]\cdot 2XeF_2$, and $[BrOF_2][AsF_6]\cdot XeF_2$, demonstrate that, upon adduct formation, the stretching frequencies of $BrOF_2^+$ shift to lower values. When a single XeF_2 molecule coordinates to $BrOF_2^+$, ν(BrO) is lowered with respect to ν(BrO) of $[BrOF_2][AsF_6]$ (1064 cm^{-1}) and splits into two bands at 1043 and 1050 cm^{-1}. The addition of a second XeF_2 molecule does not result in significant frequency lowering, with the factor-group split Br–O stretching band occurring at 1045 and 1051 $\mathrm{cm^{-1}}$. The opposite trend is observed for the Br–F stretching frequencies upon XeF_2 coordination. Coordination of XeF_2 in $[BrOF_2][AsF_6]{\cdot}XeF_2$ has little effect on $\nu(BrF_1) - \nu(BrF_2)$ and $\nu(BrF_1) + \nu(BrF_2)$, which are essentially unshifted at 634 and 646/651 $\mathrm{cm^{-1}}$, respectively, relative to the Br–F stretching frequencies of $[BrOF_2][AsF_6]$ at 634 and 647 $\mathrm{cm^{-1}}$. Coordination of a second XeF_2 molecule, however, results in low-frequency shifts of the out-of-phase and in-phase Br–F stretches to 614 and 634 $\mathrm{cm^{-1}}$, respectively. The two modes are shifted to somewhat lower frequency when compared with the observed (625; 644 $\mathrm{cm^{-1}}$) and calculated [652(612); 683(644) $\mathrm{cm^{-1}}$] frequencies of $[BrOF_2][AsF_6]{\cdot}2KrF_2$.[232] The trends in the cation stretching frequencies on going from KrF_2 to XeF_2 can be accounted for by considering the bromine coordination sphere. In both structures, the AsF_6^- anion is coordinated trans to the oxygen atom; hence their $\nu(BrO)$ stretching frequencies are similar. Because the NgF_2 ligands are coordinated trans to fluorine, the Br–F stretching modes are expected to experience a greater effect upon substitution. Because krypton is more electronegative, KrF_2 is a somewhat weaker fluoride ion donor than XeF_2 (eq 8.8 and 8.9) because krypton is more electronegative,

$$XeF_{2\,(g)} \longrightarrow XeF^+_{(g)} + F^-_{(g)} \qquad (8.8)$$

$\Delta H^{\circ}_{rxn} = 921.5, 922.3\ \mathrm{kJ\ mol^{-1}}$ $\Delta G^{\circ}_{rxn} = 885.0, 888.9\ \mathrm{kJ\ mol^{-1}}$ MP2, B3LYP aug-cc-pVTZ(-PP)

$$KrF_{2\,(g)} \longrightarrow KrF^+_{(g)} + F^-_{(g)} \qquad (8.9)$$

$\Delta H^{\circ}_{rxn} = 951.8, 953.6\ \mathrm{kJ\ mol^{-1}}$ $\Delta G^{\circ}_{rxn} = 917.4\ 919{,}4\ \mathrm{kJ\ mol^{-1}}$ MP2, B3LYP aug-cc-pVTZ(-PP) which is manifested by the shorter Br---F_b contacts in the crystal structure of $[BrOF_2][AsF_6]\cdot 2XeF_2$ (see 8.2.4.1, X-ray Crystallography) relative to those of $[BrOF_2][AsF_6]\cdot 2KrF_2$.[232] More electron density is expected to transfer to bromine in the XeF_2 adduct, shifting the Br–F stretching modes to lower frequency (vide supra). The cation deformation modes in $[BrOF_2][AsF_6]\cdot XeF_2$ and $[BrOF_2][AsF_6]\cdot 2XeF_2$ show little change upon XeF_2 coordination relative to those of $[BrOF_2][AsF_6]$. The $\delta(F_1BrF_2)$ bending mode occurs at 325 cm^{-1} for the 1:1 adduct and at 315 cm^{-1} for the 2:1 adduct. Similarly, the $\delta(OBrF_1F_2)$ bending mode is observed at 395 cm^{-1} in $[BrOF_2][AsF_6]\cdot 2XeF_2$ and is coupled to AsF_6^- bending modes in $[BrOF_2][AsF_6]\cdot XeF_2$, which appear at 392, 411 cm^{-1}. When compared with the KrF_2 adduct, the cation deformation frequencies of $[BrOF_2][AsF_6]\cdot 2XeF_2$ are essentially the same as those of $[BrOF_2][AsF_6]\cdot 2KrF_2$ and are in good agreement with the calculated values.

8.2.6. Computational Results. The energy-minimized geometries of the ion pairs $[BrOF_2][AsF_6]_3^{2-}$ and $[ClOF_2][AsF_6]_3^{2-}$, and the adduct $[BrOF_2][AsF_6]\cdot 2XeF_2$, were optimized at the PBE1PBE and B3LYP levels starting from their crystallographic coordinates and C_1 symmetry. The 1:1 adduct, $[BrOF_2][AsF_6]\cdot XeF_2$, although lacking a crystal structure, was optimized starting from the crystallographic coordinates of $[BrOF_2][AsF_6]\cdot 2XeF_2$, with one molecule of XeF_2 removed. All four structures resulted in stationary points with all frequencies real. The PBE1PBE and B3LYP (B3LYP values are given in parentheses) results are summarized in Tables 8.3–8.8, 8.11, 8.12, and A5.1–A5.4 and Figures 8.2, 8.4, 8.10, 8.11.

Table 8.11. NBO Valencies, Bond Orders, and Charges (NPA) for $[ClOF_2][AsF_6]_3^{2-}$ and $[BrOF_2][AsF_6]_3^{2-}$

X = Cl, Br	$[ClOF_2][AsF_6]_3^{2-}$				$[BrOF_2][AsF_6]_3^{2-}$				AsF_6^-			
	PBE1PBE		B3LYP		PBE1PBE		B3LYP		PBE1PBE		B3LYP	
							Charges [Valencies]					
X	2.145	[2.257]	2.091	[2.184]	2.410	[2.164]	2.364	[2.115]				
O_1	−0.581	[1.125]	−0.559	[1.102]	−0.740	[0.979]	−0.719	[0.962]				
F_1	−0.359	[0.447]	−0.353	[0.418]	−0.448	[0.413]	−0.440	[0.397]				
F_2	−0.360	[0.446]	−0.353	[0.419]	−0.448	[0.413]	−0.440	[0.397]				
As_A	2.925	[2.834]	2.929	[2.814]	2.925	[2.832]	2.929	[2.812]	2.925	[2.868]	2.930	[3.163]
F_{3A}	−0.648	[0.385]	−0.643	[0.376]	−0.642	[0.414]	−0.641	[0.405]	−0.654	[0.416]	−0.655	[0.411]
F_{4A}	−0.638	[0.437]	−0.638	[0.432]	−0.636	[0.437]	−0.635	[0.432]	−0.654	[0.416]	−0.655	[0.411]
F_{5A}	−0.639	[0.436]	−0.638	[0.430]	−0.635	[0.438]	−0.635	[0.431]	−0.654	[0.416]	−0.655	[0.411]
F_{6A}	−0.649	[0.435]	−0.649	[0.430]	−0.647	[0.437]	−0.648	[0.431]	−0.654	[0.416]	−0.655	[0.411]
F_{7A}	−0.650	[0.428]	−0.650	[0.421]	−0.640	[0.435]	−0.642	[0.429]	−0.654	[0.416]	−0.655	[0.411]
F_{8A}	−0.637	[0.434]	−0.636	[0.428]	−0.633	[0.437]	−0.633	[0.431]	−0.654	[0.416]	−0.655	[0.411]
$As_{A'}$	2.924	[2.837]	2.929	[2.816]	2.925	[2.832]	2.929	[2.812]				
$F_{3A'}$	−0.646	[0.385]	−0.642	[0.376]	−0.642	[0.414]	−0.641	[0.405]				
$F_{4A'}$	−0.638	[0.437]	−0.638	[0.432]	−0.636	[0.437]	−0.635	[0.432]				
$F_{5A'}$	−0.640	[0.433]	−0.640	[0.428]	−0.635	[0.438]	−0.635	[0.431]				
$F_{6A'}$	−0.648	[0.435]	−0.649	[0.430]	−0.647	[0.437]	−0.648	[0.432]				
$F_{7A'}$	−0.649	[0.426]	−0.649	[0.420]	−0.641	[0.435]	−0.641	[0.429]				
$F_{8A'}$	−0.636	[0.436]	−0.636	[0.430]	−0.633	[0.437]	−0.632	[0.431]				
As_B	2.928	[2.834]	2.933	[2.814]	2.929	[2.834]	2.933	[2.819]				
F_{3B}	−0.666	[0.389]	−0.666	[0.381]	−0.665	[0.405]	−0.666	[0.398]				
F_{4B}	−0.645	[0.431]	−0.646	[0.425]	−0.644	[0.429]	−0.644	[0.424]				
F_{5B}	−0.644	[0.428]	−0.645	[0.422]	−0.641	[0.430]	−0.641	[0.424]				
F_{6B}	−0.654	[0.427]	−0.655	[0.421]	−0.652	[0.428]	−0.654	[0.422]				
F_{7B}	−0.652	[0.421]	−0.652	[0.414]	−0.646	[0.421]	−0.647	[0.416]				
F_{8B}	−0.644	[0.430]	−0.644	[0.423]	−0.641	[0.430]	−0.641	[0.424]				

Table 8.11. (continued…)

	Bond Orders					
X-O	1.188	1.164	1.012	0.997		
$X\text{-}F_1$	0.483	0.455	0.452	0.436		
$X\text{-}F_2$	0.482	0.455	0.452	0.436		
$X\text{---}F_{3A}$	0.053	0.054	0.102	0.101		
$X\text{---}F_{3A'}$	0.053	0.055	0.102	0.101		
$X\text{---}F_{3B}$	0.023	0.024	0.056	0.056		
$As_A\text{-}F_{3A}$	0.395	0.389	0.373	0.368	0.478	0.475
$As_A\text{-}F_{4A}$	0.492	0.489	0.493	0.491	0.478	0.475
$As_A\text{-}F_{5A}$	0.491	0.489	0.494	0.491	0.478	0.475
$As_A\text{-}F_{6A}$	0.488	0.485	0.490	0.487	0.478	0.475
$As_A\text{-}F_{7A}$	0.478	0.475	0.488	0.484	0.478	0.475
$As_A\text{-}F_{8A}$	0.492	0.490	0.496	0.493	0.478	0.475
$As_{A'}\text{-}F_{3A'}$	0.396	0.390	0.373	0.368		
$As_{A'}\text{-}F_{4A'}$	0.492	0.490	0.493	0.491		
$As_{A'}\text{-}F_{5A'}$	0.489	0.487	0.494	0.491		
$As_{A'}\text{-}F_{6A'}$	0.488	0.485	0.490	0.487		
$As_{A'}\text{-}F_{7A'}$	0.479	0.476	0.488	0.484		
$As_{A'}\text{-}F_{8A'}$	0.494	0.491	0.496	0.493		
$As_B\text{-}F_{3B}$	0.422	0.418	0.410	0.406		
$As_B\text{-}F_{4B}$	0.487	0.484	0.488	0.485		
$As_B\text{-}F_{5B}$	0.486	0.483	0.489	0.486		
$As_B\text{-}F_{6B}$	0.482	0.478	0.483	0.480		
$As_B\text{-}F_{7B}$	0.476	0.474	0.484	0.480		
$As_B\text{-}F_{8B}$	0.488	0.484	0.489	0.486		

Table 8.12. NBO Valencies, Bond Orders, and Charges (NPA) for for $[BrOF_2][AsF_6]\cdot2XeF_2$, $[BrOF_2][AsF_6]\cdot2KrF_2$

	$[BrOF_2][AsF_6]\cdot2XeF_2$				$[BrOF_2][AsF_6]\cdot2KrF_2$[a]				XeF_2			
	PBE1PBE		B3LYP		PBE1PBE		B3LYP		PBE1PBE		B3LYP	
	Charges [Valencies]											
Br(1)	2.415	[2.257]	2.385	[1.886]	2.411	[2.270]	2.381	[1.893]				
O(1)	−0.720	[0.950]	−0.699	[0.845]	−0.715	[0.953]	−0.695	[0.843]				
F(1)	−0.448	[0.451]	−0.448	[0.350]	−0.446	[0.457]	−0.445	[0.357]				
F(2)	−0.451	[0.445]	−0.453	[0.345]	−0.445	[0.455]	−0.446	[0.355]				
Ng(1)	1.275	[0.606]	1.267	[0.582]	1.081	[0.645]	1.065	[0.619]	1.219	[0.586]	1.208	[0.562]
F(3)	−0.649	[0.350]	−0.644	[0.320]	−0.579	[0.351]	−0.570	[0.326]	−0.610	[0.309]	−0.604	[0.296]
F(4)	−0.548	[0.373]	−0.540	[0.361]	−0.432	[0.394]	−0.420	[0.378]	−0.610	[0.309]	−0.604	[0.296]
Ng(2)	1.273	[0.617]	1.263	[0.600]	1.084	[0.667]	1.065	[0.635]	1.219	[0.586]	1.208	[0.562]
F(5)	−0.641	[0.355]	−0.635	[0.329]	−0.576	[0.372]	−0.566	[0.341]	−0.610	[0.309]	−0.604	[0.296]
F(6)	−0.542	[0.374]	−0.536	[0.363]	−0.422	[0.404]	−0.414	[0.380]	−0.610	[0.309]	−0.604	[0.296]
As(1)	2.639	[3.225]	2.640	[3.154]	2.638	[3.222]	2.640	[3.152]				
F(7)	−0.635	[0.438]	−0.639	[0.415]	−0.634	[0.464]	−0.636	[0.443]				
F(8)	−0.575	[0.498]	−0.573	[0.488]	−0.573	[0.502]	−0.571	[0.490]				
F(9)	−0.614	[0.466]	−0.609	[0.458]	−0.612	[0.466]	−0.606	[0.460]				
F(10)	−0.590	[0.486]	−0.591	[0.472]	−0.589	[0.490]	−0.593	[0.473]				
F(11)	−0.566	[0.504]	−0.566	[0.492]	−0.566	[0.506]	−0.565	[0.492]				
F(12)	−0.623	[0.456]	−0.621	[0.443]	−0.626	[0.467]	−0.623	[0.447]				

Table 8.12. (continued…)

				Bond Orders		
Br(1)-O(1)	1.019	0.911	1.023	0.905		
Br(1)-F(1)	0.492	0.388	0.493	0.389		
Br(1)-F(2)	0.490	0.386	0.497	0.391		
Br(1)---F(3)	0.099	0.080	0.092	0.075		
Br(1)---F(5)	0.105	0.083	0.103	0.081		
Br(1)---F(7)	0.035	0.031	0.042	0.041		
Xe(1)-F(3)	0.238	0.226	0.244	0.234	0.293	0.281
Xe(1)-F(4)	0.359	0.348	0.380	0.365	0.293	0.281
Xe(2)-F(5)	0.236	0.231	0.250	0.241	0.293	0.281
Xe(2)-F(6)	0.360	0.350	0.389	0.368	0.293	0.281
As(1)-F(7)	0.476	0.458	0.474	0.455		
As(1)-F(8)	0.573	0.562	0.574	0.564		
As(1)-F(9)	0.530	0.523	0.530	0.526		
As(1)-F(10)	0.554	0.541	0.555	0.539		
As(1)-F(11)	0.579	0.567	0.580	0.567		
As(1)-F(12)	0.516	0.507	0.508	0.502		

8.2.6.1. Geometries. (i) $[BrOF_2][AsF_6]_3^{2-}$ and $[ClOF_2][AsF_6]_3^{2-}$. The crystal structures of $[BrOF_2][AsF_6]$ and $[ClOF_2][AsF_6]$ show that both cations coordinate to a fluorine atom from each of three different AsF_6^- anions (section, 8.2.4). Models were calculated reflecting the observed structures, i.e., one cation interacting with a single fluorine atom from each of three different AsF_6^- anions. Although a simplification, these models provide close approximations of the cation environments in their respective crystal structures and a means to study the effects of ion-pairing. There are, however, some disparities between the experimental and calculated Raman frequencies and intensities and their detailed mode descriptions. These primarily occur for the anion modes because they are only singly coordinated in the models, whereas they are coordinated to three cations in their crystal lattices.

For $[BrOF_2][AsF_6]_3^{2-}$, the calculated Br–O bond length is 1.568 (1.580) Å and the Br–F bond lengths are 1.755 (1.779) Å. The weighted average bond length, 1.693 Å, is slightly greater than the experimental bond length in the disordered $BrOF_2^+$ cation (1.647(1) Å (see 8.2.4.2, X-ray Crystallography). The fluorine atoms are bent away from the oxygen atom in $[BrOF_2][AsF_6]_3^{2-}$, with O–Br–F_1 and O–Br–F_2 angles of 101.1 (101.0) ° and 101.1 (100.9) °, respectively, and an F_1–Br–F_2 angle of 89.2 (89.3)° giving an average angle of 97.1 (97.1)°. The average angle is slightly less than the F/O–Br–O/F angle in the disordered crystal structure of $[BrOF_2][AsF_6]$ (99.89(6)°). The three contact distances are 2.306 (2.328), 2.306 (2.327), and 2.481 (2.503) Å with the contact trans to the oxygen atom being the longest, in agreement with the experimental results. All contacts are significantly less than the sum of the bromine and fluorine van der Waals radii (3.32).[55]

The VSEPR[41] model of molecular geometry predicts that substitution of bromine by chlorine should result in a more localized valence electron lone pair domain on chlorine, resulting in smaller O–Cl–F and F–Cl–F angles. Instead, small increases in the O–Cl–F_1, O–Cl–F_2 and F–Cl–F angles to 104.7 (104.5)°, 104.7 (104.5)°, and 90.6 (90.3)° are observed relative to those of the bromine analogue which are likely a consequence of the shorter Cl–O bond length [1.409 (1.421) Å] and Cl–F bond lengths [1.627 (1.660) and 1.627 (1.659) Å]. These differences can be accounted for by the ligand close packing model.[274] As expected, the three Cl---F_b contacts, 2.304 (2.317), 2.305 (2.317), and 2.484 (2.490) Å, in $[ClOF_2][AsF_6]$ are also shorter than in the bromine analogue, and are significantly less than the sum of the chlorine and fluorine van der Waals radii (3.22).[55] As is the case for the calculated geometry of the bromine analogue and in the crystal structure of $[ClOF_2][AsF_6]$, the longest X---F contact is trans to the oxygen atom.

In both $[BrOF_2][AsF_6]$ and $[ClOF_2][AsF_6]$, the AsF_6^- anion is distorted from its ideal octahedral geometry with the As–F_b bond lengths ranging from 1.785 (1.795) to 1.822 (1.834) Å in the $BrOF_2^+$ salt and from 1.772 (1.782) to 1.798 (1.811) Å in the $ClOF_2^+$ salt. Consequently, the As–F_t bond lengths are shorter, ranging from 1.728 (1.736) to 1.741 (1.750) Å in the $[BrOF_2][AsF_6]$ and from 1.730 (1.738) to 1.744 (1.752) Å in $[ClOF_2][AsF_6]$.

(ii) $[BrOF_2][AsF_6]{\cdot}XeF_2$. Although an experimental structure is unavailable for $[BrOF_2][AsF_6]{\cdot}XeF_2$, the Br(V) atom is expected to complete a pseudo-octahedral coordination sphere by making contacts with two different AsF_6^- anions in the crystal lattice. A simplified ion-pair model involving a single anion was calculated starting from the crystallographic coordinates of $[BrOF_2][AsF_6]{\cdot}2XeF_2$ with one XeF_2 molecule removed. The energy-minimized geometry optimized to C_1 symmetry. The bromine center displays pseudo-octahedral geometry when the contacts to the bridging fluorine atom of XeF_2 and the two fluorine atoms of the AsF_6^- anion are taken into account. When compared with $[BrOF_2][AsF_6]$, the cation is relatively unaffected by the introduction of one molecule of XeF_2 into the coordination sphere of Br(V), resulting in a Br–O bond length of 1.554 (1.567) Å and Br–F bond lengths of 1.730 (1.753) and 1.752 (1.777) Å. There is also little change in the O–Br–F_1 (102.8 (102.5)°), O–Br–F_2 (100.5 (100.5)°), and F_1–Br–F_2 (89.0 (89.4)°) angles upon coordination. The three contact distances to the cation are, however, significantly affected by XeF_2 coordination. The longest contact to F_5 of the AsF_6^- anion remains trans to the oxygen atom in $[BrOF_2][AsF_6]{\cdot}XeF_2$, but is lengthened (2.708 (2.729) Å) relative to $[BrOF_2][AsF_6]_3^{2-}$ (2.481 (2.503) Å). The Br---F contact with XeF_2, which is trans to a fluorine atom, is 2.369 (2.397) Å and is slightly longer than in the 2:1 adduct (2.303 (2.323); 2.296 (2.325) Å). The shortest contact to bromine (2.162 (2.178) Å) is with F_6 of the AsF_6^- anion, which is trans to the other fluorine atom of $BrOF_2^+$ and shorter than in $[BrOF_2][AsF_6]_3^{2-}$ (2.306 (2.327)Å).

The coordinated XeF_2 ligand is distorted relative to free XeF_2 (1.986 (2.010) Å) with the Xe–F_b bond elongated (2.068 (2.083) Å) and the Xe–F_t bond length shortened

(1.948 (1.976) Å) by equal amounts. As observed for the AsF_6^- anion in $[BrOF_2][AsF_6]$, the As–F_b bonds of the anion are elongated relative to the As–F_t bonds.

(iii) $[BrOF_2][AsF_6]\cdot2XeF_2$. The geometry of $[BrOF_2][AsF_6]\cdot2XeF_2$ optimized to C_1 symmetry, providing a good approximation of the structural unit in the X-ray crystal structure. The calculations predict very little effect on the cation when XeF_2 is substituted for KrF_2.[232] The Br–O bond length remains unchanged (1.556 (1.569) Å) and the Br–F bond lengths are only slightly lengthened (1.733 (1.758) and 1.734 (1.760) Å) relative to $[BrOF_2][AsF_6]\cdot2KrF_2$.[232] This behavior is also observed experimentally where both the Br–O (1.549(5) Å) and Br–F (1.736(4), 1.733(4) Å) bond lengths are equal to within $\pm3\sigma$ for the XeF_2 and KrF_2 adducts.[232] Similarly, the O–Br–F_1 (101.8 (101.8)°), O–Br–F_2 (100.0 (100.2)°), and F–Br–F (89.0 (89.4)°) angles in the calculated $[BrOF_2][AsF_6]\cdot2XeF_2$ structure are essentially unaffected by XeF_2 coordination, which is also observed in the crystal structures. In addition, the longest contact to F_7 of AsF_6^- (2.579 (2.561) Å), which is trans to the oxygen atom, is predicted to be unchanged. However, the two other contact distances to F_3 [2.303 (2.323) Å] and to F_5 [2.296 (2.325) Å] of the XeF_2 ligands are predicted to be shorter than in the KrF_2 adduct.[232] Shortening of these contacts upon coordination of XeF_2 is also observed in the crystal structures and is attributed to the greater fluoride ion donor strength of XeF_2 (see 8.2.5.3. Raman Spectroscopy).

The XeF_2 ligands are also well modeled by the calculations. The calculated Xe–F_t bond lengths (1.948 (1.971), 1.945 (1.968) Å) are shorter than the Xe–F_b bond lengths (2.074 (2.101) Å, 2.081 (2.106) Å), in agreement with experimental values (1.960(4), 1.956(5), and 2.052(4), 2.053(4) Å, respectively). The calculated F–Xe–F angles are slightly bent (174.8 (174.4) and 175.9 (176.3)°), as observed in the crystal structure (178.4(2), 179.8(2)°).

The bond lengths and bond angles are also well reproduced for the AsF_6^- anion and are almost identical to those predicted for the AsF_6^- anion in $[BrOF_2][AsF_6]{\cdot}2KrF_2$[232] where the AsF_6^- environment is very similar. The ideal octahedral anion symmetry is distorted by fluorine bridging to the cation. The calculated As–F_b bridge bond length is 1.789 (1.812) Å, which is elongated relative to the remaining As–F bonds (1.706 (1.720) – 1.758 (1.771) Å), as observed in the crystal structure.

8.2.6.2. Natural Bond Orbital (NBO) Analyses.

The NBO[163–166] analyses were carried out for the PBE1PBE- and B3LYP-optimized gas-phase geometries of $[ClOF_2][AsF_6]_3^{2-}$, $[BrOF_2][AsF_6]_3^{2-}$, $[BrOF_2][AsF_6]{\cdot}2XeF_2$, AsF_6^-, and XeF_2 with the results given in Tables 8.10, 8.11, and A5.4. The PBE1PBE and B3LYP results are similar across the series of compounds with the exception of the AsF_6^- anion, where the PBE1PBE valencies and bond orders are lower than the B3LYP values; only the B3LYP results are referred to in the ensuing discussion.

(i) $[ClOF_2][AsF_6]_3^{2-}$ and $[BrOF_2][AsF_6]_3^{2-}$. The positive charge is localized on the central halogen atoms of the $ClOF_2^+$ and $BrOF_2^+$ cations of $[ClOF_2][AsF_6]_3^{2-}$ and $[BrOF_2][AsF_6]_3^{2-}$ and is approximately half the halogen charge in the fully ionic model. The bromine charge (2.36) is higher than that of chlorine (2.09), which is in accordance with the lower electronegativity of bromine. The higher bromine charge is also accompanied by an increase in negative charge of the ligands that is primarily dispersed onto the oxygen atom, with the charge increased by −0.16, and onto the fluorine atoms, with the charges increased by −0.09 for each fluorine atom. The aforementioned charge differences are reflected in the greater X–O and X–F valencies and bond orders and are consistent with the greater covalent characters of the Cl–O and Cl–F bonds. Of the possible valence bond descriptions for XOF_2^+ (structures I–IV), the charges, valencies, and bond orders are best described for $ClOF_2^+$ by structure IV, with an almost equal contribution from structure I, and a minor contribution from structure III. In contrast, the NBO parameters of $BrOF_2^+$ are best represented by a much greater contribution from structures I and III.

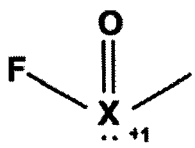

I

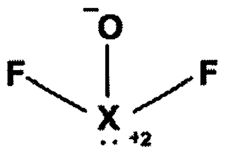

II

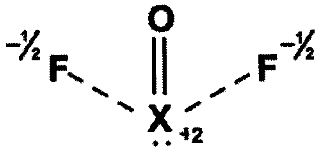

III

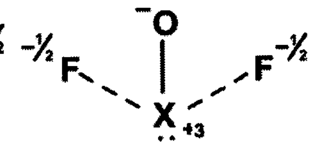

IV

The net positive charges for the $ClOF_2^+$ (0.83) and $BrOF_2^+$ (0.76) cations are indicative of similar charge transfers of ca. 0.17 and 0.24*e*, respectively, from the anions to the cation in their ion pairs. Anion-cation charge transfers in $[ClOF_2][AsF_6]_3^{2-}$ and in $[BrOF_2][AsF_6]_3^{2-}$ are also consistent with the Cl---F (0.054, 0.55, 0.024) and Br---F (0.101, 0.101, 0.056) bridge bond orders and polarization of the negative charge on the anion towards the halogen atom.

(ii) $[BrOF_2][AsF_6]\cdot 2XeF_2$. The XeF_2 ligands are polarized towards bromine with ca. 0.08*e* transferred from each XeF_2 molecule. The Br---F bond orders of the bridging fluorines are 0.08, indicating that the Br---F interaction is weakly covalent. The polarization trend, magnitude of charge transfer, and the bond orders are very similar to those observed for $[BrOF_2][AsF_6]\cdot 2KrF_2$.[232] In fact, coordination of either XeF_2 or KrF_2 has no significant effect on the net charge of the cation (0.78 *e*, $[BrOF_2][AsF_6]\cdot 2XeF_2$; 0.80 *e*, $[BrOF_2][AsF_6]\cdot 2KrF_2$[232]).

Instead of the cation experiencing the effects of the negative charge transfer from the XeF_2 and KrF_2 ligands, the charge is delocalized over the AsF_6^- anion, giving it a net charge of −0.96 for the XeF_2 adduct and −0.95 for the KrF_2 adduct, close to the net charge of the free AsF_6^- anion. In both adducts, the anion is weakly coordinated, as demonstrated by the low $Br{-}F_b$ bond orders of the XeF_2 and KrF_2 adducts (0.03 and 0.04, respectively). Overall, there is little effect on the anion when xenon is replaced by krypton. Thus, the dominant valence bond structures for $[BrOF_2][AsF_6]\cdot 2XeF_2$ are very similar to those of $[BrOF_2][AsF_6]\cdot 2KrF_2$[232] with the major contribution from Structure V and a smaller contribution from Structure VI.

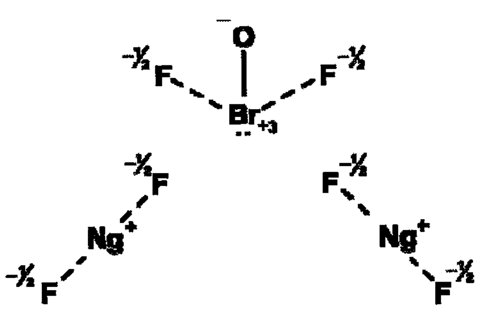

V

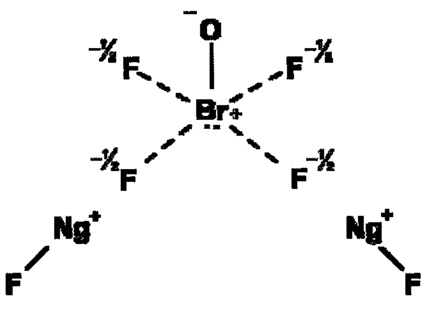

VI

8.2.6.3. QTAIM and ELF Analyses. The bonding was investigated by complementary use of the Quantum Theory of Atoms in Molecules (QTAIM)[251] and the topological analysis[252] of the Becke and Edgecombe Electron Localization Function (ELF).[253] For the ensuing discussion, the following abbreviations denote atomic populations, $\bar{N}(\mathrm{A})$; electron localization function, $\eta(\mathbf{r})$; core basins, C(A); valence basins, V(A, B, ...); monosynaptic basins, V(A); disynaptic basins, V(A, B); and closed isosurfaces, $\eta(\mathbf{r}) = f$, where f is defined as the isosurface contour. The QTAIM and ELF analyses of the XeF_2 and $[BrOF_2][AsF_6]_3^{2-}$ fragments are provided in Appendix 5.

Bonding in $[BrOF_2][AsF_6]{\cdot}XeF_2$. The QTAIM populations provide a charge transfer picture in which ca. 0.11 *e* is transferred from each XeF_2 and 0.05 *e* from AsF_6^- to $BrOF_2^+$. These transfers are almost equal to those calculated previously for the krypton analogue.[232]

In the molecular graph of the complex, the bromine center is linked to the two bridging fluorine atoms, F_3 and F_5, of the XeF_2 groups and to F_7, which belongs to the AsF_6^- unit. The values of the Laplacian of the electron density at the bond critical points are positive and decrease with the Br–F internuclear distances, i.e., 0.158 (BrF_3), 0.147 (BrF_5), 0.077 (BrF_7) and 0.015 (BrF_9). The delocalization indexes between bromine and the weakly bonded fluorine atoms show almost the same trends: $\delta(Br,F_3) = 0.26$, $\delta(Br,F_5) = 0.24$, $\delta(Br,F_7) = 0.12$, $\delta(Br,F_9) = 0.02$. The $\eta(r) = 0.75$ localization domains of the complex are shown in Figure 8.12 whereas the hierarchy of the ELF basins is given in Scheme 8.1. Although the coordination of bromine has increased to six, the V(Br) ("valence electron lone pair on Br") basin remains in the complex while its $\eta(\mathbf{r}) = 0.75$ localization domain follows a trend in which it contracts across the series $BrOF_2^+$ [232] >

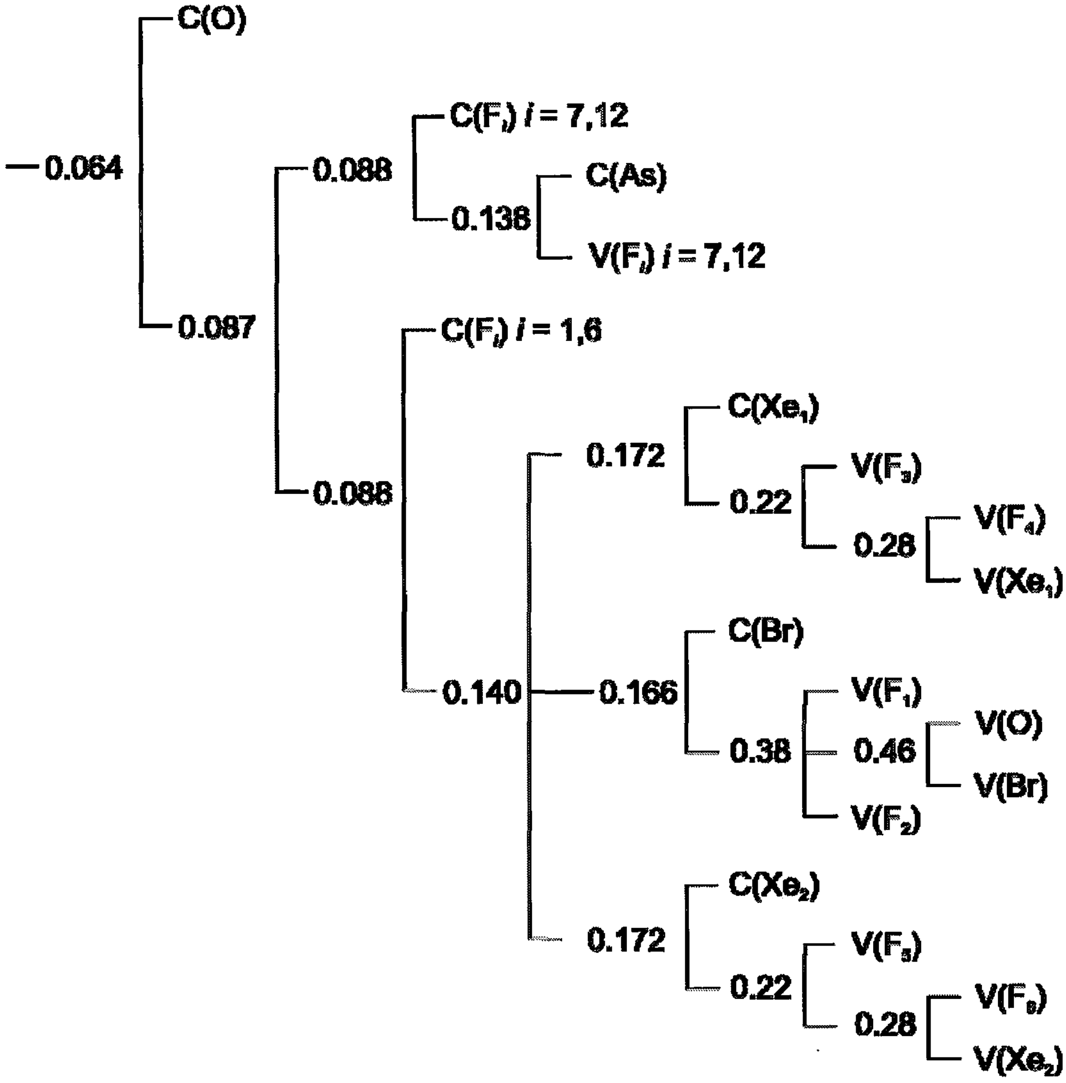

Scheme 8.1. Reduction of localization diagram for $[BrOF_2][AsF_6]\cdot 2XeF_2$ showing the ordering of localization nodes and the boundary isosurface value, $\eta(\mathbf{r})$, at which the reducible domains split. The labeling scheme corresponds to that used in Figures 8.1 and 8.2.

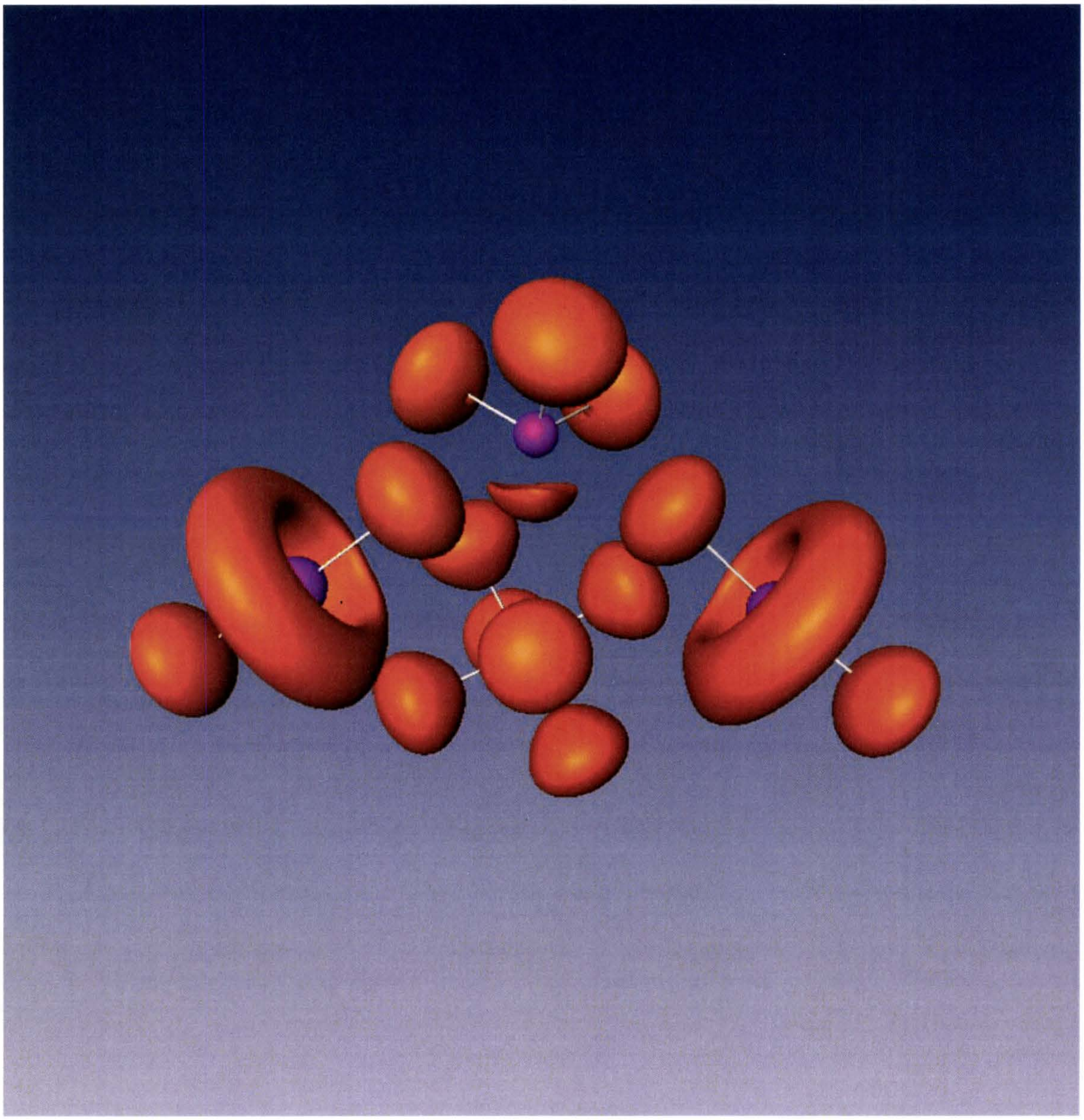

Figure 8.12. ELF localization domains for $[BrOF_2][AsF_6]\cdot 2XeF_2$. The isosurface value is $\eta(\mathbf{r}) = 0.75$. Color code: magenta = core, brick-red = monosynaptic basin.

$[BrOF_2][AsF_6]_3^{2-}$ (Figure A5.2) > $[BrOF_2][AsF_6]\cdot 2XeF_2$ (Figure 8.12) ≈ $[BrOF_2][AsF_6]\cdot 2KrF_2$[232] to accommodate their respective environments.

Although the bonding between the different components is very similar in the $[BrOF_2][AsF_6]\cdot 2XeF_2$ and $[BrOF_2][AsF_6]\cdot 2KrF_2$ complexes, there is a significant difference in the perturbation of the XeF_2 units relative to the KrF_2 units upon complexation. In $[BrOF_2][AsF_6]\cdot 2XeF_2$, the populations of the fluorine valence basins are almost equal and the covariance matrix elements of these populations with $\bar{N}$ [V(Xe)] have a rather small difference. In the complex, the Xe–F bonds involved in the fluorine bridges are more ionic than the Xe–F terminal bonds, in agreement with the respective lengthening and shortening of the corresponding internuclear distances relative to those of the uncomplexed species. In contrast, in the KrF_2 complex there is a large contribution of the noble-gas atomic basin to the valence basin of the nonbridging fluorine atom, which correlates with the large increase of the absolute value of the covariance matrix element. The different behaviors of the two noble-gas atoms is likely due to the greater ionic character of the bonding in XeF_2.

8.3. Conclusion

The current study has demonstrated the propensity of the XOF_2^+ (X = Cl, Br) cations to attain pseudo-octahedral coordination spheres. The crystal structures of $[BrOF_2][AsF_6]$ and $[ClOF_2][AsF_6]$ have three fluorine-bridge contacts between the halogen atom of the cation and three nearest-neighbour AsF_6^- anions. In contrast, the $BrOF_2^+$ cation of $[BrOF_2][AsF_6]\cdot 2XeF_2$ forms only one fluorine bridge contact to the

AsF_6^- anion and single fluorine bridges with each XeF_2 ligand. These structural features are reproduced in the calculated structures. Moreover, in the presence of HF at 78 °C, $[BrOF_2][AsF_6]\cdot XeF_2$ recombines to form $[BrOF_2][AsF_6]$ and $[BrOF_2][AsF_6]\cdot 2XeF_2$, thus attaining a coordination number of six at Br(V).

The X-ray crystal structure, vibrational spectrum, as well as the calculated structures and frequencies for $[BrOF_2][AsF_6]\cdot 2XeF_2$ are similar to those of the krypton analogue; however, notable differences occur. The contact distances between bromine and XeF_2 are shorter when compared with those of the KrF_2 analogue, consistent with greater ionic character of the Xe–F bonds in XeF_2. The $\nu(Xe{-}F_t)$ modes of the XeF_2 strongly couple to one another, and the bridging modes only weakly couple to one another, whereas the opposite behavior is observed for $[BrOF_2][AsF_6]\cdot 2KrF_2$. The XeF_2 adduct undergoes internal fluoride ion abstraction at room temperature in HF solution forming $BrOF_3$ and $[Xe_2F_3][AsF_6]$. This contrasts with the KrF_2 adduct, which is stable in HF solution for at least 1 h at 20 °C. The latter behavior is again consistent with the greater ionic character of the Ng–F bonds in XeF_2 when compared with those of KrF_2.

The ELF and QTAIM results indicate that the localization domain associated with the valence electron lone pair of bromine decreases across the series $BrOF_2^+$ > $[BrOF_2][AsF_6]_3^{2-}$ > $[BrOF_2][AsF_6]\cdot 2XeF_2$ ≈ $[BrOF_2][AsF_6]\cdot 2KrF_2$. The calculations also show that the covalencies of the $Kr{-}F_t$ bonds are significantly greater than those of the $Xe{-}F_t$ bond. In both adducts the $Ng{-}F_t$ bonds are more covalent than their $Ng{-}F_b$ bonds.

CHAPTER 9

$Xe_3OF_3^+$, a Precursor to a Noble-Gas Nitrate and the First Neutral Oxide Fluoride of Xe(II); Syntheses and Structural Characterizations of $FXeONO_2$ and $O(XeF)_2$

9.1. Introduction

The greatest variety of polyatomic ligand groups bonded to xenon occurs for xenon in the +2 oxidation state, and those bonded through oxygen are the most prevalent. Neutral mono- and disubstituted oxygen-bonded derivatives having the formulations FXeL and/or XeL_2 have been reported where L = $OC(O)CF_3$,[275] $OP(O)F_2$,[276] OSO_2CF_3,[277] OSO_2F,[278,279] $OClO_3$,[279] $OSeF_5$,[280] $OTeF_5$,[118,119] and $OIOF_4$.[281] With the exception of $OP(O)F_2$[276] and $OIOF_4$,[281] their syntheses have been accomplished by reaction of the parent acid, HL, with XeF_2 according to eq 9.1 (n = 1, 2), leading to HF formation, a significant thermodynamic driving force in these reactions. Alternative syntheses of the $OSeF_5$[282] and $OTeF_5$[38,58] derivatives also exist which do not involve HF displacement.

$$XeF_2 + nHL \longrightarrow F_{2-n}XeL_n + nHF \qquad (9.1)$$

Two prior studies have reported the formation of xenon(II) nitrates by HF displacement. The earlier study investigated the reactions of XeF_2 with anhydrous HNO_3 containing 20% NO_2 by weight at 20 °C.[80] Red-brown solids were obtained that rapidly decomposed at 23 °C, forming an intense, transient blue color. It is likely that the blue color arose from N_2O_3.[283] The formulations, $FXeONO_2$ and $Xe(ONO_2)_2$, were suggested, but no structural characterizations were provided. When these reactions were carried out at −20 °C, the red-brown solids were not obtained. In a subsequent study, $FXeONO_2$ was reported to have been generated by the reaction of XeF_2 with HNO_3 in CH_2Cl_2 at −30 °C, which was, in turn, reacted in situ with various alkenes to give 1,2-disubstituted fluoro-nitrato alkanes (1 = F, 2 = ONO_2).[81] No structural evidence was provided for the proposed intermediate, $FXeONO_2$, by way of in situ solution charaterization, nor was isolation attempted.

The absence of a well-characterized xenon(II) nitrate is surprising because the nitrate anion meets the general criteria that are normally associated with a ligand that is suitable for stabilization of Xe in its +2 oxidation state: (1) the least electronegative atom of the ligand (nitrogen) is in its highest oxidation state, (2) NO_3^- is the conjugate base of a strong monoprotic acid, and correspondingly, (3) the electronegativity of the $-ONO_2$ ligand group is high. Empirical correlations based on the ^1H chemical shift difference between the α- and β-^1H resonances of CH_3CH_2X derivatives have been previously used to assign group electronegativities[284] based on the halogen electronegativities of Huggins.[285] This approach has been employed here using Pauling electronegativities[57] to give a group electronegativity for ONO_2 of 3.95,[284] which is close to those of fluorine (3.98)[57] and $OTeF_5$ (3.87).[56]

Recent work has shown that XeF_2 and $[H_3O][AsF_6]$ react in anhydrous HF to form the only known oxide fluoride cation of Xe(II), $[FXeOXeFXeF][AsF_6]$.[71] This chemistry was extended to the syntheses of $FXeONO_2$ and $O(XeF)_2$ by the reaction of $FXeOXeFXeF^+$ with O_2NF and ONF, respectively.[72,286] However, several aspects of the latter study were left unfinished and/or required reinterpretations which are described in the present Chapter. Portions of the study that were previously completed, and therefore not included in this Chapter, may be found in references 72 and 286.

9.2. Results and Discussion

9.2.1. Synthesis and Decomposition of $FXeONO_2$. Deep red-orange to magenta $[FXeOXeFXeF][AsF_6]$[71] was allowed to react as a suspension with liquid NO_2F at −50 °C. A suspension of white solid formed over a 5 h period. Removal of excess NO_2F under vacuum at −110 °C yielded a white, powder comprised of a mixture of $FXeONO_2$, XeF_2, and $[NO_2][AsF_6]$. The reaction also proceeded to completion at −78 °C but required reaction times of 2−3 weeks. The latter method proved useful in establishing a proposed reaction pathway (Scheme 9.1). The solid changed in color from deep magenta to yellow-orange after 24 to 48 h, and finally to white. The yellow-orange color and resulting Raman spectrum of the intermediate reaction mixture showed the presence of a transient xenon oxide fluoride that is $O(XeF)_2$. The reaction pathway was also supported by an ^{18}O-enrichment and Raman spectroscopic study which showed that only $FXe^{16}ON(^{16}O^{18}O)$ was formed when $[FXe^{18}OXeFXeF][AsF_6]$ was used as the starting material. Failure to observe $FXe^{18}ONO_2$ indicated that no oxygen isotope scrambling had occurred among the bridging ^{16}O and terminal ^{18}O atoms (see 9.2.7.1, Raman Spectroscopy). Subsequent attempts to synthesize the $FXeON(O)F^+$ and $FXeFNO_2^+$ intermediates by the reactions of $[XeF][AsF_6]$ and NO_2F as a neat mixture or in HF solvent, and by the reaction of XeF_2 and $[NO_2][AsF_6]$ in HF solvent proved unsuccessful

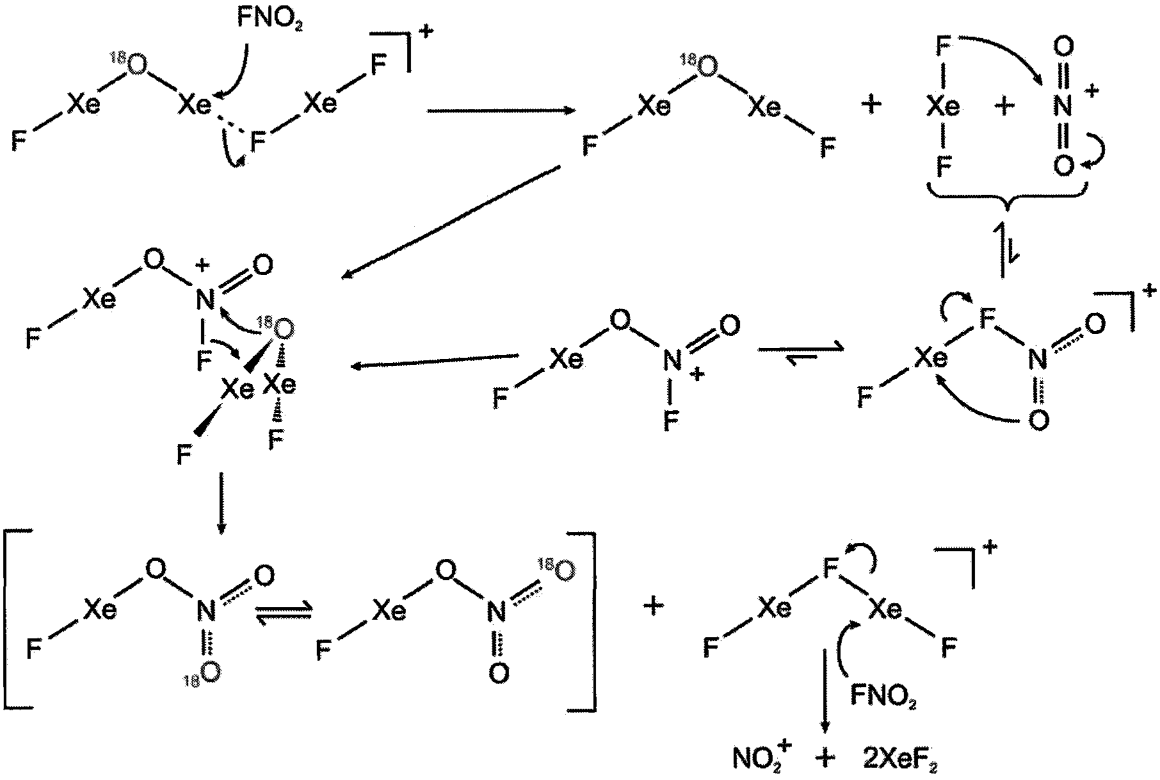

Scheme 9.1. Proposed pathway for the reaction of $FXe^{18}OXeFXeF^+$ with NO_2F

with only varying amounts of $[XeF][AsF_6]$, NO_2F, XeF_2, and $[NO_2][AsF_6]$ present. Therefore, a more likely reaction pathway (Scheme 9.2) has been proposed that is analogous to the decomposition pathway observed for $O(XeF)_2$ (see Scheme 9.4). A weak Raman band was observed at 1362 cm $^{-1}$ in the ^{18}O-enriched spectrum of the $FXe^{16}ON(^{16}O^{18}O)/[NO_2][AsF_6]$ product mixture. The band is attributed to the mixed $^{18}ON^{16}O^+$ cation which results from a minor exchange pathway (Scheme 9.3; 9.2.7.1 Raman Spectroscopy).

The polar-covalent compounds, $FXeONO_2$ and XeF_2, were separated from $[NO_2][AsF_6]$ and the decomposition products, N_2O_4 and N_2O_5, by rapidly extracting $FXeONO_2/XeF_2$ into SO_2ClF at −30 °C, followed by decanting the supernatant from solid

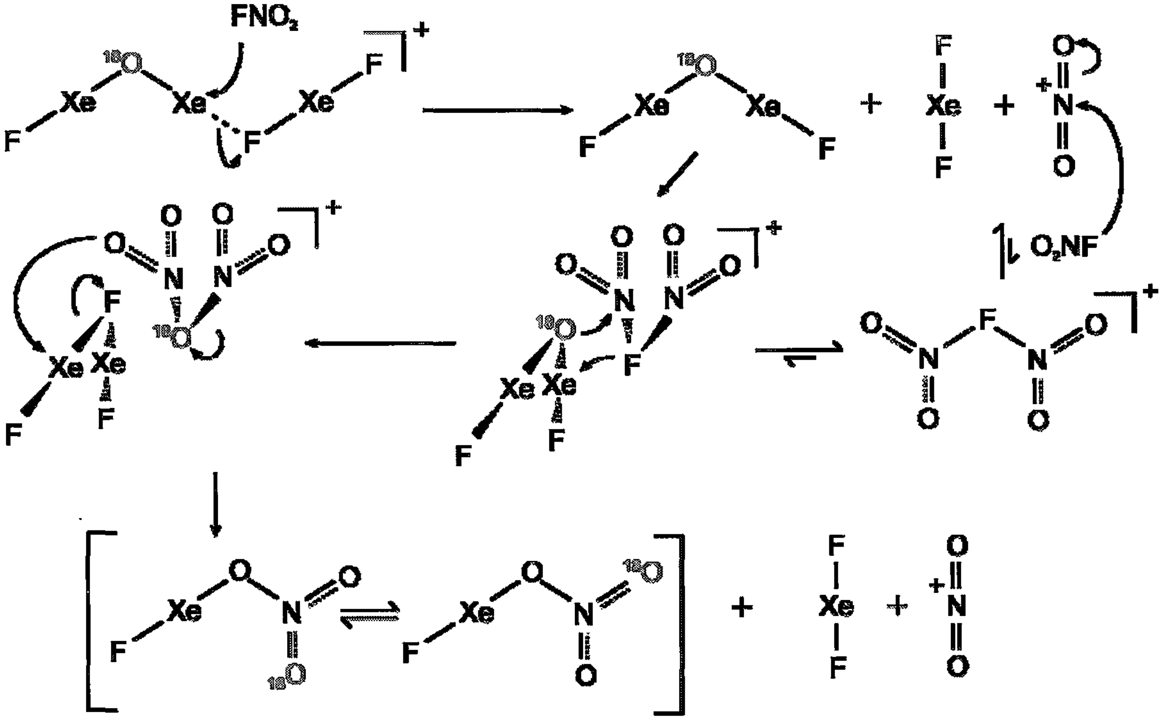

Scheme 9.2. New proposed pathway for the reaction of $FXe^{18}OXeFXeF^+$ with NO_2F

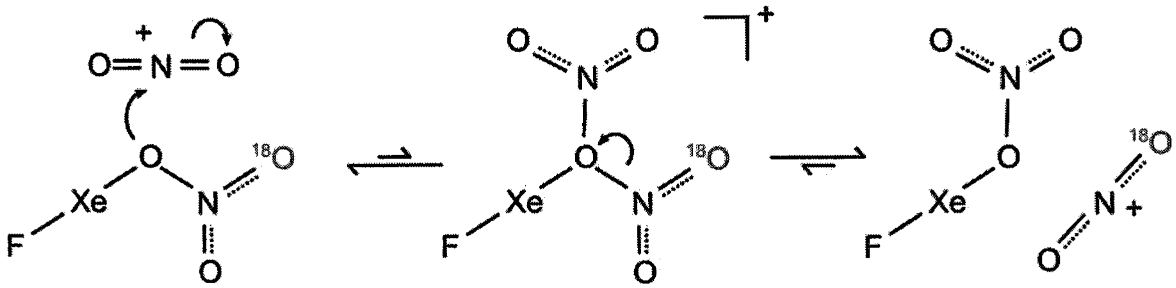

Scheme 9.3. Proposed pathway for the formation of the $^{18}ON^{16}O^+$ cation

$[NO_2][AsF_6]$, N_2O_4, and N_2O_5. A mixture of $FXeONO_2$ and XeF_2 was then precipitated from the supernatant at −78 °C (see Experimental Section). Prolonged extraction and mixing resulted in dissolution of significant amounts of $[NO_2][AsF_6]$ and its co-extraction with XeF_2 and $FXeONO_2$ (see 2.9.1. Experimental Section).

The ^{19}F NMR spectrum of a SO_2ClF solution containing extracted $FXeONO_2$ and XeF_2 was monitored at 0 °C and showed that $FXeONO_2$ was 50% decomposed after 6.5 h when the decomposition was quenched at −40 °C. The only fluorine-containing decomposition product observed was XeF_2 (−177.6 ppm, $^1J(^{19}F–^{129}Xe)$ = 5611Hz). Low-temperature Raman spectra of $FXeONO_2$ in admixture with XeF_2 and $[NO_2][AsF_6]$ (Figure 9.1) revealed that some N_2O_5 either remained unreacted following Scheme 9.2, or $FXeONO_2$ had partially decomposed to N_2O_5 and XeF_2 (presumably masked by excess already present) at −50 °C after 5 h. In contrast, $FXeONO_2$ had partially decomposed to N_2O_4 and $XeF_2{\cdot}N_2O_4$ at −78 °C after 7 days. The former decomposition pathway, leading to N_2O_5, likely proceeds through the unstable intermediate, O_2NOONO_2 (eq 9.2), which is known to rapidly decompose at −78 °C according to eq 9.3,[287,288] and by analogy with the decomposition of $FXeOSO_2F$ to XeF_2, FO_2SOOSO_2F, and Xe.[279] The latter

$$2FXeONO_2 \longrightarrow XeF_2 + [O_2NOONO_2] + Xe \tag{9.2}$$

$$[O_2NOONO_2] \longrightarrow N_2O_5 + \tfrac{1}{2}O_2 \tag{9.3}$$

decomposition pathway, leading to N_2O_4 and $XeF_2{\cdot}N_2O_4$, may occur through the unstable *N*-nitrito or O-nitrito intermediates, $FXeNO_2$ (eq 9.4) and FXeONO (eq 9.5) which would likely decompose according to eqs 9.6–9.8 and eqs 9.9 and 9.10, respectively.

$$FXeONO_2 \longrightarrow [FXeNO_2] + \tfrac{1}{2}O_2 \tag{9.4}$$

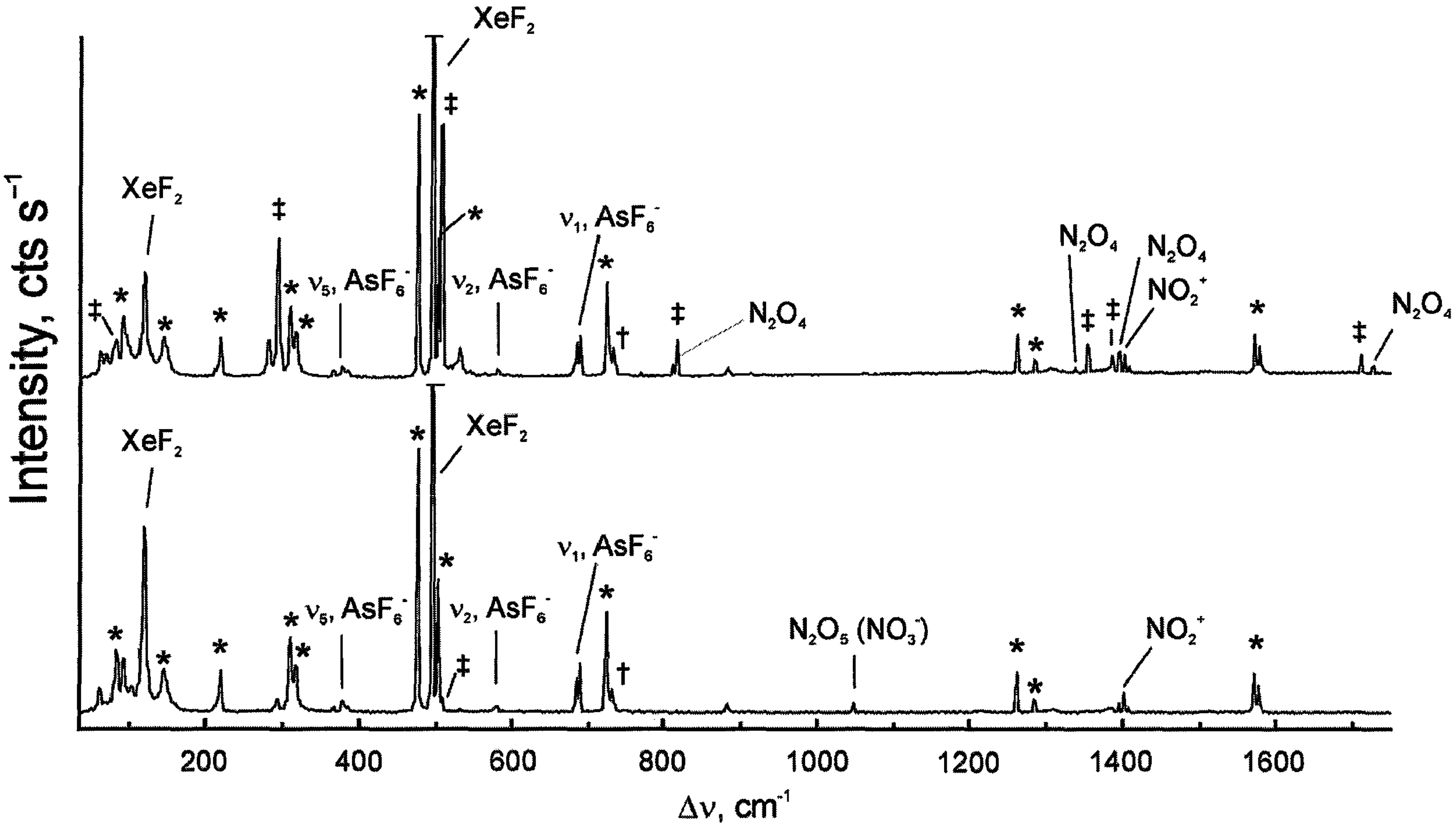

Figure 9.1. Raman spectra of $FXeONO_2$ recorded at –160 °C using 1064-nm excitation. Lower trace: recorded after 5 h at –50 °C. Upper trace: recorded after five days –78 °C. The symbols denote $FXeONO_2$ (*), FEP sample tube (†), and $XeF_2 \cdot N_2O_4$ (‡).

$$FXeONO_2 \longrightarrow [FXeONO] + \tfrac{1}{2}O_2 \quad (9.5)$$

$$2[FXeNO_2] \longrightarrow XeF_2 + Xe + N_2O_4 \quad (9.6)$$

$$XeF_2 + N_2O_4 \longrightarrow XeF_2{\cdot}N_2O_4 \quad (9.7)$$

$$[FXeNO_2] \longrightarrow Xe + NO_2F \quad (9.8)$$

$$2[FXeONO] \longrightarrow XeF_2 + Xe + N_2O_4 \quad (9.9)$$

$$[FXeONO] \longrightarrow Xe + NO_2F \quad (9.10)$$

The gas-phase thermochemical calculations at the MP2 level (Table 9.1) support the proposed decomposition pathways. The decomposition pathway for $FXeONO_2$ that leads to XeF_2, N_2O_5 (via N_2O_6), and Xe (eq 9.2 and 9.3) was found to be spontaneous under standard conditions ($\Delta G^o = -75.7$ kJ mol^{-1}) and at –78 °C ($\Delta G_{195.15} = -71.0$ kJ mol^{-1}) for the decomposition of 1 mol of $FXeONO_2$ to XeF_2 , N_2O_6, and Xe. A further –22.5 kJ mol^{-1} ($\Delta G_{195.15} = -17.9$ kJ mol^{-1}) is released when 0.5 mol of N_2O_6 decomposes to N_2O_5 and O_2, giving a net $\Delta G^o = -98.1$ kJ mol^{-1} ($\Delta G_{195.15} = -88.9$ kJ mol^{-1}) for the decomposition of 1 mol of $FXeONO_2$. The remaining proposed pathways, which involve the non-spontaneous generation of $FXeNO_2$ (eq 9.4, $\Delta G^o = 26.5$ kJ mol^{-1}, $\Delta G_{195.15} = 35.7$ kJ mol^{-1}) or FXeONO (eq 9.5, $\Delta G^o = 37.9$ kJ mol^{-1}, $\Delta G_{195.15} = 46.5$ kJ mol^{-1}) as intermediates, are more than compensated for by the spontaneous decompositions to XeF_2, Xe, and N_2O_4 ($FXeNO_2$ [one-half eq 9.6], $\Delta G^o = -139.2$ kJ mol^{-1}, $\Delta G_{195.15} = -136.3$ kJ mol^{-1}; FXeONO [one-half eq 9.9], $\Delta G^o = -150.6$ kJ mol^{-1}, $\Delta G_{195.15} = -147.1$ kJ mol^{-1}) or to NO_2F and Xe ($FXeNO_2$ [eq 9.8], ΔG^o, –217.6 kJ mol^{-1}; $\Delta G_{195.15}$, –207.4 kJ mol^{-1}; FXeONO [eq 9.10], ΔG^o, –229.0 kJ mol^{-1}; $\Delta G_{195.15}$, –218.2 kJ mol^{-1}).

Table 9.1. Gas-phase ΔH^{o}, ΔG^{o}, $\Delta H_{195.15}$, and $\Delta G_{195.15}$ for the Synthesis and Decomposition Reactions of $FXeONO_2$, $Xe(ONO_2)_2$, $XeONO_2^+$, and N_2O_6 (MP2/aug-cc-pVTZ and aug-cc-pVTZ(-PP))

	ΔH^{o}	$\Delta H_{195.15}$	ΔG^{o}	$\Delta G_{195.15}$	eq (9.)
$2FXeONO_2 \longrightarrow XeF_2 + N_2O_6 + Xe$	–123.7	–124.5	–151.4	–141.9	2
$N_2O_6 \longrightarrow N_2O_5 + ½O_2$	–18.4	–18.4	–45.0	–35.9	3
$2FXeONO_2 \longrightarrow XeF_2 + N_2O_5 + Xe + ½O_2$	–142.1	–142.8	–196.4	–177.8	2 + 3
$FXeONO_2 \longrightarrow FXeNO_2 + ½O_2$	53.3	52.6	26.5	35.7	4
$FXeONO_2 \longrightarrow FXeONO + ½O_2$	63.2	62.4	37.9	46.5	5
$2FXeNO_2 \longrightarrow XeF_2 + Xe + N_2O_4$	–261.5	–261.0	–278.5	–272.6	6
$FXeNO_2 \longrightarrow NO_2F + Xe$	–188.4	–187.6	–217.6	–207.4	8
$2FXeONO \longrightarrow XeF_2 + Xe + N_2O_4$	–281.2	–280.5	–301.2	–294.2	9
$FXeONO \longrightarrow NO_2F + Xe$	–198.3	–197.4	–229.0	–218.2	10
$Xe(ONO_2)_2 \longrightarrow Xe + N_2O_6$	–122.2	–122.5	–151.4	–141.4	13
$Xe(ONO_2)_2 \longrightarrow Xe + N_2O_5 + ½O_2$	–140.6	–140.9	–196.4	–177.2	4 + 13
$XeF_2 + HNO_3 \longrightarrow FXeONO_2 + HF$	–17.9	–21.3	–17.6	–20.2	11
$FXeONO_2 + HNO_3 \longrightarrow Xe(ONO_2)_2 + HF$	–19.3	–23.3	–17.5	–20.8	12
$FXeONO_2 + AsF_5 \longrightarrow XeONO_2^+ + AsF_6^-$	359.0	358.7	365.0	362.9	19
$XeONO_2^+ \longrightarrow Xe + ½O_2 + NO_2^+$	–142.7	–143.0	–189.5	–173.4	21
$XeF_2 + AsF_5 \longrightarrow XeF^+ + AsF_6^-$	493.2	493.4	499.9	497.7	
$FXeONO_2 + AsF_5 \longrightarrow XeF^+ + AsF_5ONO_2^-$	522.0	521.8	527.4	525.5	25

9.2.2. Reactions of XeF_2 with HNO_3. Attempts were made to prepare $FXeONO_2$ and $Xe(ONO_2)_2$ by reaction of XeF_2 with HNO_3. Xenon difluoride was allowed to react with 2 equiv of 100% HNO_3 in SO_2ClF solution. NMR spectroscopy at –30 °C in SO_2ClF solution revealed XeF_2 (–1684 ppm, $^1J(^{19}F–^{129}Xe)$ = 5630 Hz) and Xe gas (–5374 ppm) in the ^{129}Xe spectrum, and only XeF_2 (–183.4 ppm, $^1J(^{19}F–^{129}Xe)$ = 5633 Hz) and HF (–180.2 ppm, $\Delta\nu_{½}$ = 550 Hz) in the ^{19}F spectrum. Although the gas-phase syntheses (Table 9.1) for $FXeONO_2$ (eq 9.11, $\Delta G^o = -17.6$ kJ mol^{-1}, $\Delta G_{195.15} = -20.2$ kJ mol^{-1}) and $Xe(ONO_2)_2$ (eq 9.12, $\Delta G^o = -17.5$ kJ mol^{-1}, $\Delta G_{195.15} = -20.8$ kJ mol^{-1}) are near equilibrium, their rapid decompositions ($FXeONO_2$, eqs 9.2 and 9.3 or eqs 9.4–9.10; $Xe(ONO_2)_2$, eq 9.13 followed by eq 9.3) may preclude their observation by NMR

$$XeF_2 + HNO_3 \longrightarrow FXeONO_2 + HF \tag{9.11}$$

$$FXeONO_2 + HNO_3 \longrightarrow Xe(ONO_2)_2 + HF \tag{9.12}$$

$$Xe(ONO_2)_2 \longrightarrow O_2NOONO_2 + Xe \tag{9.13}$$

spectroscopy. Although $FXeONO_2$ and/or $Xe(ONO_2)_2$ could account for the decomposition products observed by NMR spectroscopy, in either case, the degree of reaction must have been small because neither decomposition product, N_2O_4 or N_2O_5, was observed in the Raman spectrum. Rather, $XeF_2{\cdot}HNO_3$ crystallized between –40 to –60 °C from SO_2ClF solution and was characterized in the solid state by Raman spectroscopy and by single-crystal X-ray diffraction.[72,286] These findings indicate that if $Xe(ONO_2)_2$ forms, it is inherently unstable toward decomposition. The gas-phase thermochemical calculations (Table 9.1) show a large negative Gibbs free energy for the spontaneous decomposition of $Xe(ONO_2)_2$ to Xe and the unstable intermediate, N_2O_6 (eq 9.13, $\Delta G^\circ = -151.4$ kJ mol^{-1}, $\Delta G_{195.15} = -141.4$ kJ mol^{-1}).

9.2.3. Reactions of XeF_2 and [XeF][AsF_6] with N_2O_5. Attempts to react XeF_2 or [XeF][AsF_6] with N_2O_5 in SO_2ClF to give $FXeONO_2$ and/or $Xe(ONO_2)_2$ were monitored by Raman spectroscopy. A 1.5:1 mixture of XeF_2 and N_2O_5 that was warmed stepwise from −40 to 10 °C showed essentially no reaction, with only a small amount of N_2O_5 decomposition to N_2O_4 and subsequent formation of $XeF_2{\cdot}N_2O_4$.[72,286] However, at −78 °C, equimolar amounts of [XeF][AsF_6] and N_2O_5 formed a transient orange, clumpy mixture which was consistent with [Xe_3OF_3][AsF_6] formation (eq 9.14). Gradual warming of the reaction mixture above −30 °C to dissolve N_2O_5 resulted in a white product. Low-temperature Raman spectroscopy showed a mixture of XeF_2, [NO_2][AsF_6], and unreacted N_2O_5 and the absence of $FXeONO_2$. The [Xe_3OF_3][AsF_6] salt, which is known to be unstable above −30 °C[71] likely decomposed (eq 9.15) to form XeF_2, O_2, Xe, and [XeF][AsF_6]. The latter would then re-enter the cycle (eqs 9.14 and 9.15) until completely consumed.

$$3[XeF][AsF_6] + N_2O_5 \longrightarrow [FXeOXeFXeF][AsF_6] + 2[NO_2][AsF_6] \quad (9.14)$$

$$[FXeOXeFXeF][AsF_6] \longrightarrow XeF_2 + \tfrac{1}{2}O_2 + Xe + [XeF][AsF_6] \quad (9.15)$$

9.2.4. Reaction of XeF_2 with N_2O_4. Dissolution of XeF_2 in liquid N_2O_4 at 0–30 °C resulted in NO_2F formation (eq 9.16; $\delta(^{19}F)$, 397.8 ppm at 30 °C). A small, steady-state concentration of $FXeONO_2$ was also observed which apparently arose as a result of the self-ionization of N_2O_4 (eq 9.17) and the reaction of XeF_2 with NO_3^- (eq 9.18). The self-ionization of N_2O_4 has been inferred by electrical conductivity

$$N_2O_4 + XeF_2 \longrightarrow 2NO_2F + Xe \tag{9.16}$$

$$N_2O_4 \rightleftharpoons NO^+ + NO_3^- \tag{9.17}$$

$$XeF_2 + NO^+ + NO_3^- \longrightarrow FXeONO_2 + NOF \tag{9.18}$$

measurements ($2.36 \times 10^{-13}\ \Omega^{-1}\ cm^{-1}$ at 17 °C)[289] and by measurement of the self-ionization constant of N_2O_4 in sulfolane at 30 °C ($K_{N_2O_4} = 7.1 \times 10^{-8}$ mol L^{-1}).[290] The small steady-state concentration of the NO_3^- anion (eq 9.17) and the instability of $FXeONO_2$ (eqs 9.2–9.10) at room temperature (vide supra), account for the low product concentrations.

Dissolution of XeF_2 in liquid N_2O_4 at 35 °C also resulted in the formation of $XeF_2{\cdot}N_2O_4$, which was observed by Raman spectroscopy of the frozen mixture at –160 °C (see 9.2.7.1, Raman Spectroscopy). The molecular addition compound, $XeF_2{\cdot}N_2O_4$, crystallized from a solution of XeF_2 in N_2O_4 at –3 °C and was characterized by single-crystal X-ray diffraction.[72,286]

9.2.5. Reaction of $FXeONO_2$ with AsF_5. In an attempt to form a salt of the $XeONO_2^+$ cation, a mixture of $FXeONO_2$ and XeF_2 was allowed to react with excess liquid AsF_5 at –78 °C. The reaction was monitored by low-temperature Raman spectroscopy over a period of 24 h and showed that AsF_5 reacted with XeF_2 to yield $[XeF][AsF_6]$, but $FXeONO_2$ did not react. Warming the reaction mixture to –50 °C for 12 h with periodic quenching and monitoring of the spectrum by Raman spectroscopy at –160 °C showed

$[XeF][AsF_6]$ and $[NO_2][AsF_6]$ were the only products. The findings are consistent with the formation of an unstable $XeONO_2^+$ salt (eq 9.19) that rapidly decomposed according to eq 9.20.

$$FXeONO_{2\,(s)} + AsF_{5\,(l)} \longrightarrow [XeONO_2][AsF_6]_{(s)} \qquad (9.19)$$

$$[XeONO_2][AsF_6]_{(s)} \longrightarrow [NO_2][AsF_6]_{(s)} + Xe_{(g)} + \tfrac{1}{2}\,O_{2\,(g)} \qquad (9.20)$$

Thermochemical calculations for the gas-phase reactions (Table 9.1) show there is a considerable barrier to fluoride ion abstraction from $FXeONO_2$ by AsF_5 to form $XeONO_2^+$ and AsF_6^- (eq 9.19 in the gas phase, $\Delta H^\circ = 359.0$ kJ mol^{-1}, $\Delta G^\circ = 365.0$ kJ mol^{-1}; $\Delta H_{195.15} = 358.7$ kJ mol^{-1}, $\Delta G_{195.15} = 362.9$ kJ mol^{-1}), but this barrier is considerably less than that for the gas-phase abstraction of fluoride ion from XeF_2 by AsF_5 ($\Delta H^\circ = 493.2$ kJ mol^{-1}, $\Delta G^\circ = 499.9$ kJ mol^{-1}; $\Delta H_{195.15} = 493.4$ kJ mol^{-1}, $\Delta G_{195.15} = 497.7$ kJ mol^{-1}). Volume-based thermochemical (VBT) calculations have been used to arrive at the thermodynamic properties of these systems in the solid state (see Solid-State Thermochemistry in Appendix 6), and show that the fluoride ion abstraction is essentially mitigated by the lattice enthalpy of $[XeONO_2][AsF_6]$. Once formed, the gas-phase $XeONO_2^+$ cation has a large negative Gibbs free energy that accompanies its spontaneous decomposition to Xe, O_2, and NO_2^+ (eq 9.21, $\Delta H^\circ = -142.7$ kJ mol^{-1}, $\Delta G^\circ = -189.5$ kJ mol^{-1}; $\Delta H_{195.15} = -143.0$ kJ mol^{-1}, $\Delta G_{195.15} = -173.4$ kJ mol^{-1}).

$$XeONO_2{}^+_{(g)} \longrightarrow Xe_{(g)} + \tfrac{1}{2}O_{2\,(g)} + NO_2{}^+_{(g)} \qquad (9.21)$$

The thermochemical parameters were also determined for eq 9.20 by application of VBT (see Solid State Thermochemistry in Appendix 6). The appropriate thermochemical cycle (eq 9.22) using the gas-phase standard enthalpy, $\Delta H^\circ(9.21)$) (Table

9.1), and Gibbs free energy, $\Delta G^{\circ}(9.21)$, according to eqs 9.23 and 9.24 show that the solid-state decomposition of $[XeONO_2][AsF_6]$ (eq 9.20) is significantly more exothermic than the gas-phase decomposition of the $XeONO_2^+$ cation (eq 9.21).

$$\Delta H^{\circ}(9.20) = \Delta H^{\circ}(9.21) - \Delta H^{\circ}_{L}([NO_2][AsF_6]) + \Delta H^{\circ}_{L}([XeONO_2][AsF_6])$$
$$= -188 \text{ kJ mol}^{-1} \qquad (9.22)$$

$$\Delta S^{\circ}(9.20) = S^{\circ}([NO_2][AsF_6]_{(s)}) + S^{\circ}(Xe_{(g)}) + \tfrac{1}{2}S^{\circ}(O_{2(g)}) - S^{\circ}([XeONO_2][AsF_6]_{(s)})$$
$$= 207 \text{ J mol}^{-1} \text{ K}^{-1} \qquad (9.23)$$

$$\Delta G^{\circ}(9.20) = \Delta H^{\circ}(9.20) - T\Delta S^{\circ}(9.20) = -250 \text{ kJ mol}^{-1} \qquad (9.24)$$

The gas-phase reaction (eq 9.25) has also been considered and is shown to be considerably more endothermic ($\Delta H^{\circ} = 522.0$ kJ mol^{-1}, $\Delta G^{\circ} = 527.4$ kJ mol^{-1}; $\Delta H_{195.15} = 521.8$ kJ mol^{-1}, $\Delta G_{195.15} = 525.5$ kJ mol^{-1}) than the gas-phase counterpart of eq 9.19, and therefore it has not been considered as a likely alternative reaction pathway.

$$FXeONO_2 + AsF_5 \longrightarrow XeF^+ + AsF_5ONO_2^- \qquad (9.25)$$

9.2.6. Synthesis and Reactivity of O(XeF)₂. The crystal structures of both $Xe_3OF_3^+$ salts have been obtained in which the cation is comprised of a FXeOXe---FXeF zig-zag chain. The long contact (2.510(8) Å, As; 2.508(7) Å, Sb)[71] between xenon and the bridging fluorine atom suggests that XeF_2 may be readily displaced from $Xe_3OF_3^+$ by a suitable oxidatively resistant base according to eq 9.26, where M = K or NO.

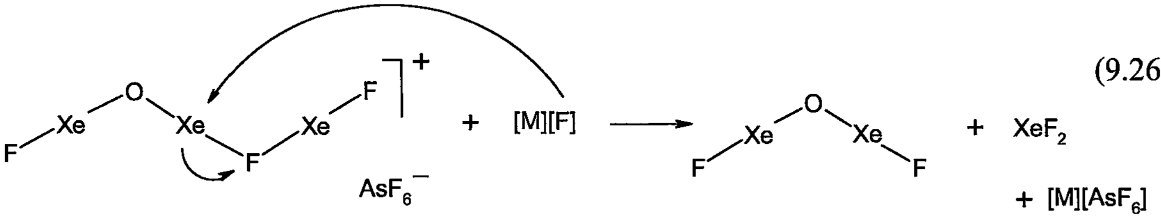

(9.26)

Reaction of the magenta-colored solid $[Xe_3OF_3][AsF_6]$ with liquid NOF at −78 °C afforded a pale blue-colored solid/liquid mixture, which yielded a pale yellow solid upon removal of excess NOF under dynamic vacuum at −78 °C (eq 9.27). The blue color

$$[Xe_3OF_3][AsF_6] + NOF \longrightarrow O(XeF)_2 + XeF_2 + [NO][AsF_6] \qquad (9.27)$$

presumably resulted from traces of N_2O_3,[283] that arose as a result of an excess of NOF, according to Scheme 9.4. The dry product mixture was found to be stable indefinitely at temperatures at or below −30 °C.

In addition, because an excess of NOF was used to react with $[Xe_3OF_3][AsF_6]$, products from the reaction of $[Xe_3OF_3][AsF_6]$ with the NO_2F impurity (ca. 3%) in the NOF sample could be observed in solution by ^{17}O, ^{19}F, and ^{129}Xe NMR spectroscopy ($FXeONO_2$), and in the solid state by low-temperature Raman spectroscopy ($XeF_2{\cdot}N_2O_4$).

Syntheses that employed ^{18}O-enriched (98.6%) $[Xe_3{}^{18}OF_3][AsF_6]$ confirmed the results derived from the natural abundance reaction, but further demonstrated that peaks assignable to the $N^{18}O^+$ cation were observed by Raman spectroscopy (see 9.2.7.2, Raman Spectroscopy). The $N^{18}O^+$ cation likely results from a minor exchange pathway in the solid state (Scheme 9.5) or in ONF solution (Scheme 9.6). Oxygen isotope scrambling was also observed in CH_3CN solution by NMR spectroscopy.

9.2.7. Raman Spectroscopy. The low-temperature, solid-state Raman spectra of $FXeONO_2$ and $O(XeF)_2$ are depicted in Figures 9.2 and 9.3, respectively. The experimental and calculated frequencies and their assignments are listed in Tables 9.2–9.4 and Tables A6.1 and A6.2. The spectra were calculated using the aug-cc-pVTZ(-PP) basis set at the B3LYP, PBE1PBE, and MP2 levels of theory and the experimental trends

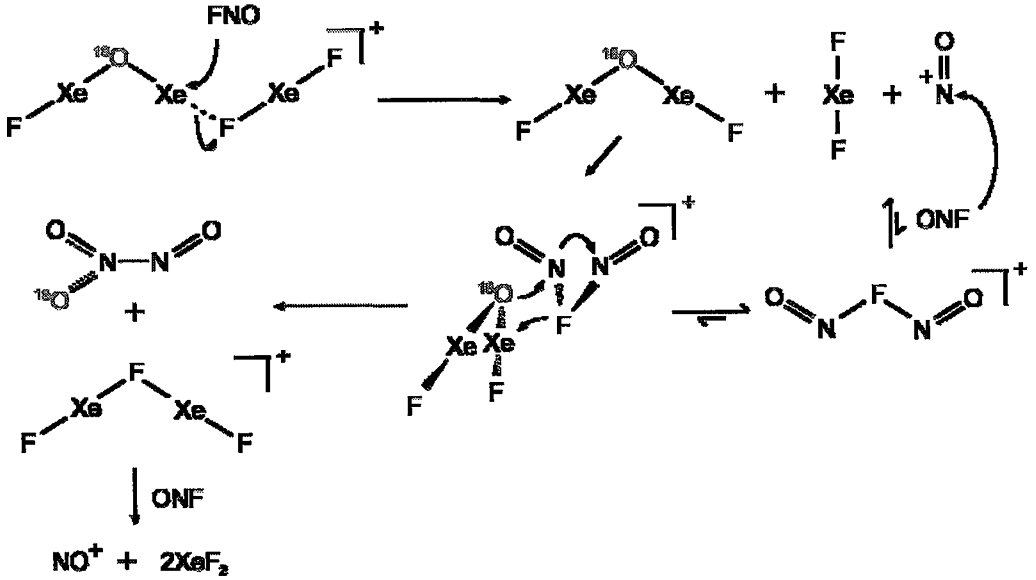

Scheme 9.4. Proposed pathway for the reaction of $FXe^{18}OXeFXeF^+$ with excess ONF.

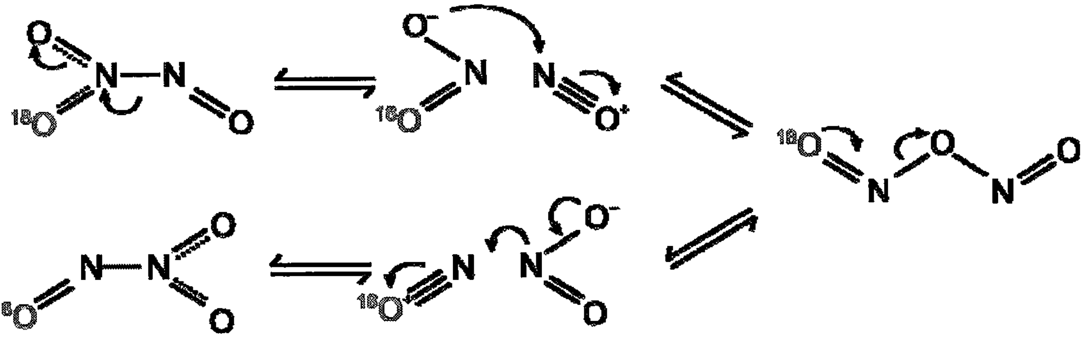

Scheme 9.5. Proposed pathway for the solid-state formation of the $^{18}ON^+$ cation.

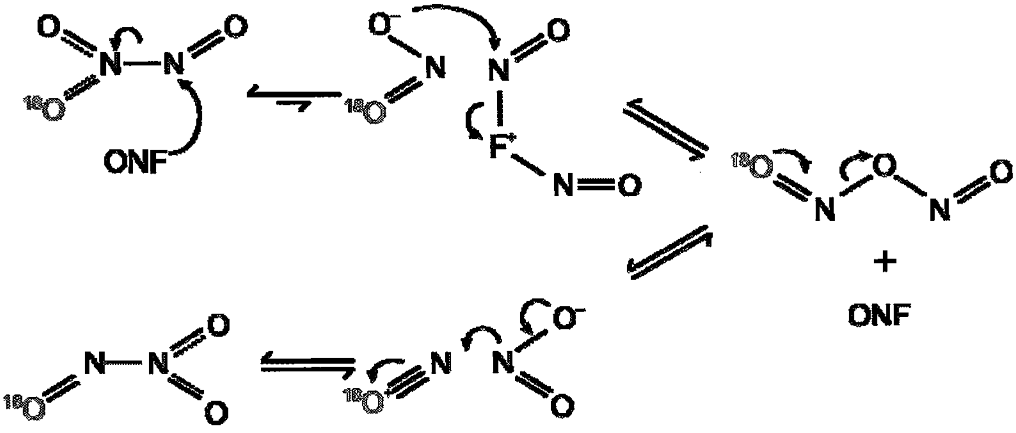

Scheme 9.6. Proposed pathway for the formation of the $^{18}ON^+$ cation in ONF solvent.

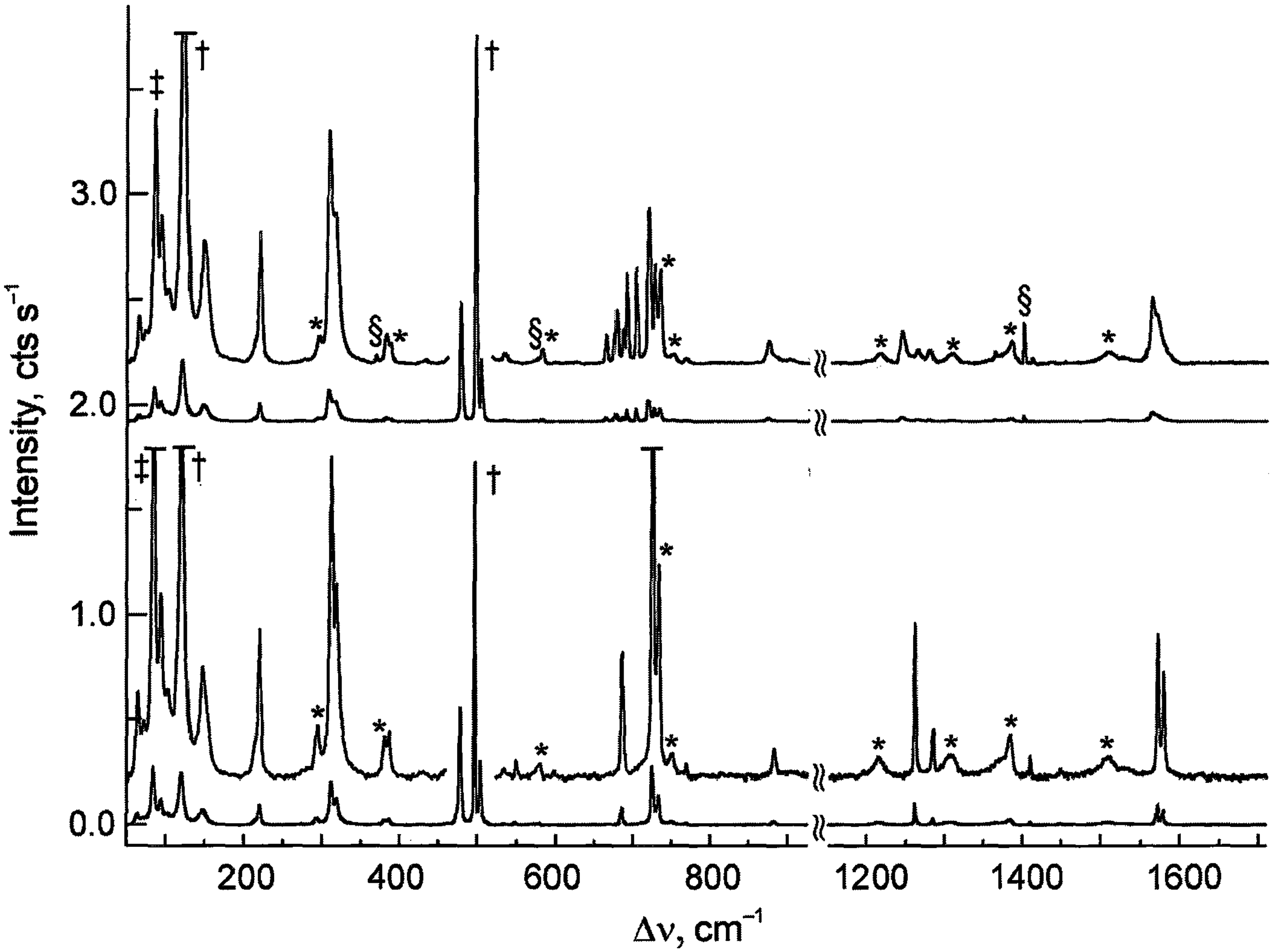

Figure 9.2. Raman spectrum of $FXeONO_2$ recorded at –160 °C using 1064–nm excitation for natural abundance (lower trace) and 98.6% ^{18}O-enriched (upper trace). Symbols denote XeF_2 (†), FEP (*), laser artifact (‡) and $[NO_2][AsF_6]$ (§).

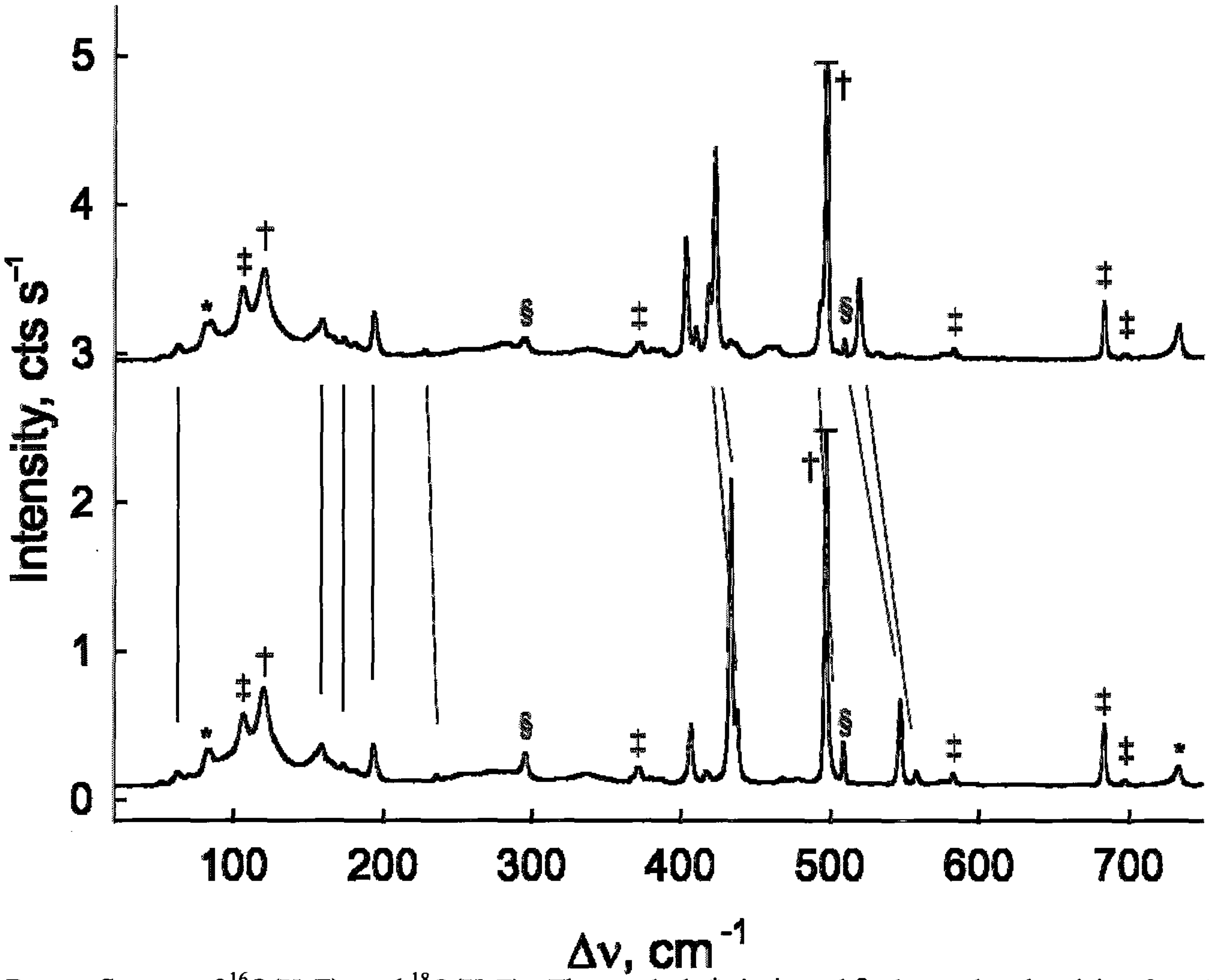

Figure 9.3. Raman Spectra of $^{16}O(XeF)_2$ and $^{18}O(XeF)_2$. The symbols *, †, ‡, and §, denote bands arising from FEP, XeF_2, $[NO][AsF_6]$, and $XeF_2 \cdot N_2O_4$, respectively. Lines denote Raman shifts between natural abundance and ^{18}O-enriched $O(XeF)_2$.

Table 9.2. Experimental Raman Frequencies and Intensities for $FXe^{16}O^{14}N^{16}O_2$, $FXe^{16}O^{14}N(^{16}O^{18}O)$, and $FXe^{16}O^{15}N^{16}O_2$

frequencies, cm^{-1}					
$FXe^{16}O^{14}N^{16}O_2$	$FXe^{16}O^{14}N(^{16}O^{18}O)$		$FXe^{16}O^{15}N^{16}O_2$		
exptl[a,b]	exptl[a,c]	$\Delta\nu^{16/18}$ [d]	exptl[a]	$\Delta\nu^{14/15}$ [e]	assgnt (C_s)[f]
1578.8(12) 1571.7(16)	1567.4br(6) 1561.8br(7)	−11.4 −9.9	1543.2(1) 1536.6(2)	−35.6 −35.1	$\nu_1(A')$, ν(NO − NO)
1285.5(5) 1262.1(17)	1278.7br(2) 1263.2br(2) 1244.6sh 1242.5br(4)	−16.6	1246.7(8)	−15.4	$\nu_2(A')$, ν(NO + NO)
882.9(3)	873.4br(2)	−9.5			$\nu_3(A')$, $\nu(O_{Xe}–N) + \delta(NO_2)$
769.4(2)	766.1(1)	−3.3			$\nu_{10}(A'')$, $\rho_w(NO_3)$
725.5(49)	725.2(11) 718.4(18) 717.1(17) 701.6(11)	−9.9 (av)	723.2(8)	−2.3	$\nu_4(A')$, $\delta(O_{Xe}–N–O) + \rho_r(NO_2)$
685.4(15)	684.3(4) 676.6(6) 674.1(3) 663.1(3)	−10.9 (av)	690.3(100)[g] 683.5(61)	1.5	$\nu_5(A')$, $\nu(O_{Xe}–N) − \delta(NO_2)$
503.8(54) 478.1(100)	503.5(54) 477.0(100)	−0.3 −1.1	503.6(14) 478.4(73)	−0.2 0.3	$\nu_6(A')$, ν(Xe–F)
318.9(23) 312.7(37)	315.0(17) 307.2(26)	−3.9 −5.5	317.9(4) 310.9(14)	−1.0 −1.8	$\nu_7(A')$, $\nu(Xe–O) + \rho_r(NO_3)$
220.6(15)	218.6(15)	−2.0	220.3(10)	−0.3	$\nu_{11}(A'')$, $\rho_w(F–Xe–O)$
146.9(14)	145.4(11)	−1.5	146.4(8)	−0.5	$\nu_8(A')$, $\delta(F–Xe–O) + \rho_r(NO_3)$
102.2(11) 93.6(16)	101.1(8) 91.7(17)	−1.1 −1.9			$\nu_9(A')$, $\delta(F–Xe–O) − \rho_r(NO_3)$
64.3(11)	62.8(5)	−1.5			$\nu_{12}(A'')$, ρ_t about Xe–O bond

[a] Relative Raman intensities are given in parentheses. Abbreviations denote shoulder (sh), and broad (br). [b] Two modes were also observed at 1448.3(<1) and 1410.3(2) cm^{-1} and were tentatively assigned as combination modes. [c] Three modes were also observed at 1436.1(<1), 1410.7(1) and 1362.4(1) cm^{-1} and were tentatively assigned as combination modes. [d] $\Delta\nu^{16/18} = \nu(^{18}O) - \nu(^{16}O)$. [e] $\Delta\nu^{14/15} = \nu(^{15}N) - \nu(^{14}N)$. [f] Abbreviations denote stretch (ν), bend (δ), twist (ρ_t), wag (ρ_w),

Table 9.3. Calculated[a] Vibrational Frequencies, Raman and Infrared Intensities for $FXe^{16}O^{14}N^{16}O_2$, $FXe^{18}O^{14}N^{16}O_2$, $FXe^{16}O^{14}N^{18}O_A{}^{16}O_S$, $FXe^{16}O^{14}N^{16}O_A{}^{18}O_S$, $FXe^{18}O^{14}N^{18}O_A{}^{16}O_S$, $FXe^{18}O^{14}N^{16}O_A{}^{18}O_S$ and $FXe^{16}O^{15}N^{16}O_2$[b]

$FXe^{16}ON^{16}O_2$	$FXe^{18}ON^{16}O_2$	$\Delta^{16/18}$[c]	$FXe^{16}ON^{18}O_A{}^{16}O_S$	$\Delta^{16/18A}$[d]	$FXe^{16}ON^{16}O_A{}^{18}O_S$	$\Delta^{16/18S}$[e]	$FXe^{18}ON^{18}O_A{}^{16}O_S$	$\Delta^{16/18\text{-}18A}$[f]	$FXe^{18}ON^{16}O_A{}^{18}O_S$	$\Delta^{16/18\text{-}18S}$[g]	$FXeO^{15}NO_2$	$\Delta^{14/15}$[h]	assgnt
1657.5(63)[329]	1657.3(63)[329]	–0.2	1640.4(58)[314]	–17.1	1647.4(65)[330]	–10.1	1640.1(58)[314]	–17.4	1647.1(65)[330]	–10.4	1619.5(61)[317]	–38.0	$\nu_1(A')$
1300.9(13)[373]	1300.6(14)[379]	–0.3	1279.7(14)[388]	–21.2	1273.8(10)[381]	–27.1	1279.5(14)[394]	–21.4	1273.5(11)[386]	–27.4	1286.1(14)[331]	–14.8	$\nu_2(A')$
880.0(3)[330]	874.1(3)[302]	–5.9	869.3(3)[319]	–10.7	868.3(3)[319]	–11.7	862.6(3)[290]	–17.4	861.7(3)[290]	–18.3	867.1(3)[333]	–12.9	$\nu_3(A')$
782.3(<0.1)[10]	780.3(<0.1)[10]	–2.0	778.3(<0.1)[10]	–4.0	778.3(<0.1)[10]	–4.0	776.3(<0.1)[10]	–6.0	776.3(<0.1)[10]	–6.0	761.9(<1)[10]	–20.4	$\nu_{10}(A'')$
719.3(16)[16]	695.5(12)[13]	–23.8	713.0(15)[15]	–6.3	712.2(18)[22]	–7.1	688.9(11)[11]	–30.4	687.9(14)[18]	–31.4	718.0(16)[18]	–1.3	$\nu_4(A')$
666.9(21)[68]	642.0(20)[70]	–24.9	659.7(23)[66]	–7.2	659.8(19)[56]	–7.1	635.2(21)[69]	–31.7	635.6(18)[59]	–31.3	666.9(21)[69]	–0.0	$\nu_5(A')$
510.2(54)[255]	510.7(54)[259]	0.5	510.8(55)[254]	0.6	510.9(54)[256]	0.7	510.6(55)[256]	0.4	510.7(54)[258]	0.5	510.9(54)[257]	0.7	$\nu_6(A')$
316.8(28)[31]	311.6(28)[30]	–5.2	310.4(26)[30]	–6.4	315.4(28)[31]	–1.4	305.2(26)[29]	–11.6	309.9(28)[31]	–6.9	316.2(27)[30]	–0.6	$\nu_7(A')$
203.1(<1)[9]	198.7(<1)[9]	–4.4	203.3(<1)[9]	0.2	203.5(<1)[9]	0.4	198.5(<1)[9]	–4.6	198.7(<1)[9]	–4.4	203.5(<1)[9]	0.4	$\nu_{11}(A'')$
198.0(8)[6]	197.7(8)[6]	–0.3	198.3(8)[6]	0.3	195.2(7)[6]	–2.8	197.3(8)[6]	–0.7	194.3(7)[6]	–3.7	198.0(8)[6]	0.0	$\nu_8(A')$
116.1(3)[4]	116.0(3)[4]	–0.1	115.6(3)[4]	–0.5	114.7(3)[4]	–1.4	115.3(3)[4]	–0.8	114.4(3)[4]	–1.7	116.1(3)[4]	0.0	$\nu_9(A')$
73.9(<1)[2]	73.3(<1)[1]	–0.6	72.1(<0.1)[1]	–1.8	73.5(<1)[2]	–0.4	71.4(<1)[1]	–2.5	72.8(<1)[1]	–1.1	74.0(<1)[2]	0.1	$\nu_{12}(A'')$

[a] B3LYP/aug-cc-pVTZ(-PP). Values in parentheses denote Raman intensities ($Å^4\ u^{-1}$). Values in square brackets denote infrared intensities ($km\ mol^{-1}$). [b] A denotes ^{18}O anti and S denotes ^{18}O syn with respect to the O–Xe–F group. [c] $\Delta\nu^{16/18} = \nu(FXe^{18}ON^{16}O_2) - \nu(FXe^{16}ON^{16}O_2)$. [d] $\Delta\nu^{16/18a} = \nu(FXe^{16}ON^{18}O_A{}^{16}O_S) - \nu(FXe^{16}ON^{16}O_2)$. [e] $\Delta\nu^{16/18s} = \nu(FXe^{16}ON^{16}O_A{}^{18}O_S) - \nu(FXe^{16}ON^{16}O_2)$. [f] $\Delta\nu^{16/18\text{-}18a} = \nu(FXe^{18}ON^{18}O_A{}^{16}O_S) - \nu(FXe^{16}ON^{16}O_2)$. [g] $\Delta\nu^{16/18\text{-}18s} = \nu(FXe^{18}ON^{16}O_A{}^{18}O_S) - \nu(FXe^{16}ON^{16}O_2)$. [h] $\Delta\nu^{14/15} = \nu(FXeO^{15}NO_2) - \nu(FXe^{16}ON^{16}O_2)$.

Table 9.4. Experimental and Calculated[a] Frequencies for $O(XeF)_2$

frequencies, cm^{-1}						
exptl[b]			calcd[a,b]			
$^{16}O^{c,d}$	$^{17}O^{c,d}$	$^{18}O^{c}$	^{16}O	^{17}O	^{18}O	assignts (C_{2v})[e]
558.5(4) 547.5(28)	532.3 sh	531.9(1) 519.2(36)	563.8(10)[318]	548.7(9)[317]	534.4(8)[315]	$\nu_7(B_2)$, $\nu_{as}(XeO)_2$
498.0 sh 496.8[f]	n.o.	496.8[f] 493.2(3)	511.7(50)[68]	511.2(55)[66]	510.1(60)[64]	$\nu_1(A_1)$, $\nu_s(XeO)_2 - \nu_s(XeF)_2$
437.7(7) 433.1(100)	427.4(100)	422.5(100) 418.3(14)	431.4(81)[5]	421.5(73)[7]	412.1(67)[8]	$\nu_2(A_1)$, $\nu_s(XeO)_2 + \nu_s(XeF)_2$
416.7(5) 406.6(20)		409.5(15) 403.2(58)	469.6(21)[402]	470.0(22)[391]	470.0(22)[380]	$\nu_8(B_2)$, $\nu_{as}(XeF)_2$
235.6(1)	228.9(5)	227.4(2)	218.1(<0.1)[25]	214.7(<0.1)[25]	211.5(<0.1)[24]	$\nu_6(B_1)$, $\delta(FXeO)$ o.o.p.
193.1(10)	193.0(72)	193.1(18)	171.4(7)[5]	172.6(7)[5]	172.6(8)[5]	$\nu_3(A_1)$, $\delta(FXeO + \delta(FXeO)$
173.7(2)	173.7(36)	173.7(3)	151.3(2)[0]	152.0(2)[0]	151.9(2)[0]	$\nu_5(A_2)$, $\rho_t(FXeO)$
159.3(6)	159.3(64)	159.3(11)	147.3(<1)[1]	148.0(<1)[1]	147.9(<1)[1]	$\nu_9(B_2)$, $\delta(FXeO - \delta(FXeO)$
62.4(2)	62.2(18)	62.4(4)	60.1(9)[3]	60.2(9)[3]	60.1(8)[3]	$\nu_4(A_1)$, $\delta(XeOXe)$

[a] B3LYP/aug-cc-pVTZ(-PP). [b] Values in parentheses denote Raman intensities (Å^4 u^{-1}). Values in square brackets denote infrared intensities (km mol^{-1}). [b] A denotes ^{18}O anti and S denotes ^{18}O syn with respect to the O–Xe–F group. [c] The abbreviations (sh) and n.o. denotes a shoulder and not observed, respectively. [d] The abbreviations denote stretch (ν), bend (δ), twist (ρ_t), and out-of-plane (o.o.p.). Bond elongations and angle openings are denoted by plus (+) signs and bond contractions and angle closings are denoted by minus (−) signs.

were reproduced at all levels. Calculated values referred to in the ensuing discussion are those obtained at the B3LYP method.

The spectral assignments for $FXe^{16}O^{14}N^{16}O_2$, $FXe^{16}O^{14}N(^{16}O^{18}O)$, and $FXe^{16}O^{15}N^{16}O_2$ were made by comparison with the calculated frequencies and Raman intensities for all possible $^{16/18}O$-isotopomers (Table 9.3).

9.2.7.1. $FXeONO_2$. The $FXeONO_2$ molecule (C_s symmetry) possesses 12 fundamental vibrational modes that span the irreducible representations 9A′ + 3A″, which are Raman and infrared active. The four $FXeONO_2$ molecules in the crystallographic unit cell have C_1 site symmetry. A factor-group analysis for $FXe^{16}ON^{16}O_2$ (Table 9.5) predicts that each gas-phase Raman- and infrared-active mode of $FXeONO_2$ is split, as a result of vibrational mode coupling within the centrosymmetric unit cell (C_{2h} unit cell symmetry), into a maximum of two Raman-active (A_g and B_g) and two infrared-active (A_u and B_u)

Table 9.5. Factor-Group Analysis for $FXeONO_2$

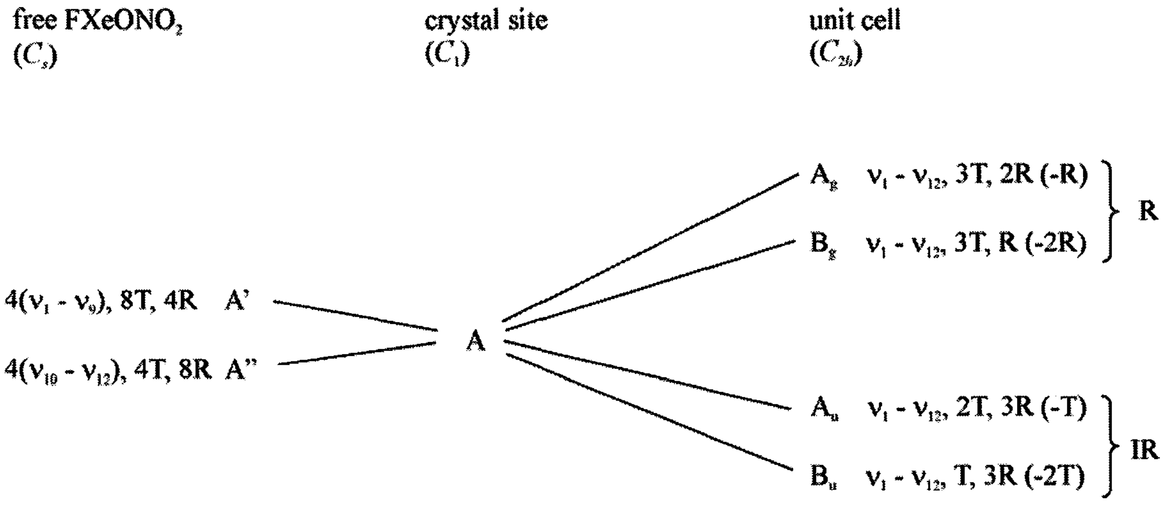

components. Accordingly, two components were resolved for every stretching mode of the natural abundance molecule except for ν(O_{Xe}–N) + δ(NO_2).

Vibrational frequencies calculated at all levels of theory (Tables 9.3 and A6.1) reproduced experimental frequency and $^{16/18}O$ isotopic shift trends for $FXe^{16}O^{14}N^{16}O_2$, $FXe^{16}O^{14}N(^{16}O^{18}O)$, and $FXe^{16}O^{15}N^{16}O_2$ given in Table 9.2. The calculations clearly show that the experimental ^{18}O-enriched spectrum is not that of $FXe^{18}ON^{16}O_2$ because, in this case, near-zero isotopic shifts are predicted for $\nu_1(A')$, ν(NO – NO) and $\nu_2(A')$, ν(NO + NO) at 1576 and 1274 cm^{-1}, respectively. The $FXe^{18}ON(^{16}O_A{}^{18}O_S)$ and $FXe^{18}ON(^{16}O_S{}^{18}O_A)$ conformers (A denotes ^{18}O anti and S denotes ^{18}O syn with respect to the O–Xe–F group) are also eliminated because, in contrast with the observed average $^{16/18}O$ isotopic shifts of −9.9 and −10.9 cm^{-1}, respectively, a significantly larger isotopic shift (−31 cm^{-1}) is predicted for both $\nu_4(A')$ and $\nu_5(A')$. The experimental ^{18}O-enriched spectrum has therefore been assigned to an equimolar mixture of $FXe^{16}ON(^{16}O_A{}^{18}O_S)$ and $FXe^{16}ON(^{16}O_S{}^{18}O_A)$ conformers and establishes that scrambling of ^{18}O among the bridge site and terminal sites does not occur.

The Raman spectra of $FXe^{16}ON(^{16}O_A{}^{18}O_S)$ and $FXe^{16}ON(^{16}O_S{}^{18}O_A)$ exhibit levels of complexity that are not reproduced by the calculated spectra. The calculations show that the only modes where the *syn*- and *anti*-conformers might be differentiated are ν_1 and ν_2, with calculated splittings of 7 and 6 cm^{-1}, respectively. However, these splittings are not resolved in the experimental spectra but are manifested on the factor-group split ν_1 and ν_2 bands as significant line broadenings (Figure 9.2). The attribution of these broadenings to equal populations of the $FXe^{16}ON(^{16}O_A{}^{18}O_S)$ and $FXe^{16}ON(^{16}O_S{}^{18}O_A)$

conformers is supported by the spectrum of $FXe^{16}ON^{16}O_2$ (Figure 9.2), which displays narrow factor-group split bands for ν_1 and ν_2. Moreover, ^{18}O isotopic enrichment does not result in similar line broadenings on bands other than the symmetric and asymmetric NO_2 stretching bands.

In the case of $FXe^{16}ON(^{16}O^{18}O)$, additional line splittings are observed for ν_1, ν_2, ν_4–ν_7, and ν_9, which are attributed to lowering of the "vibrational unit cell symmetry" of $FXe^{16}ON^{16}O_2$ from C_{2h} symmetry to lower noncentrosymmetric unit cell symmetries. Symmetry lowering in the unit cell results from the combinations and permutations of $FXe^{16}ON(^{16}O_A{}^{18}O_S)$ and $FXe^{16}ON(^{16}O_S{}^{18}O_A)$ isomers that occur among the four vibrationally coupled molecules of the crystallographic unit cell, giving rise to 16 unit cells having the following symmetries (relative weights are given in parentheses): C_{2h} (2), C_i (2), C_s (2), C_2 (2), and C_1 (8). With the exception of the C_{2h} and C_i symmetric cells, the remaining 12 unit cell symmetries are not centrosymmetric with respect to the *syn-/anti-*conformations of ^{16}O and ^{18}O in their NO_2 groups. As a consequence, the counterparts of the formally Raman-inactive and infrared-active A_u and B_u components in the factor-group analysis of $FXe^{16}ON^{16}O_2$ are both infrared and Raman active under C_s (A″), C_2 (B), and C_1 (A) unit cell symmetries (Table 9.6), potentially doubling the number of factor-group split lines that can be observed when compared with the spectrum of $FXe^{16}ON^{16}O_2$. Although the additional factor-group components that correspond to A_u and B_u under C_{2h} symmetry are not resolved for ν_1, ν_6, ν_7, and ν_9, they are resolved for ν_2, ν_4, and ν_5, which exhibit the predicted four-line splittings consistent with noncentrosymmetric unit cell symmetries. The vibrational modes of the remaining two

Table 9.6. Factor-Group Analyses for $FXe^{16}ON^{16}O_2$ and $FXe^{16}ON^{16}O^{18}O$

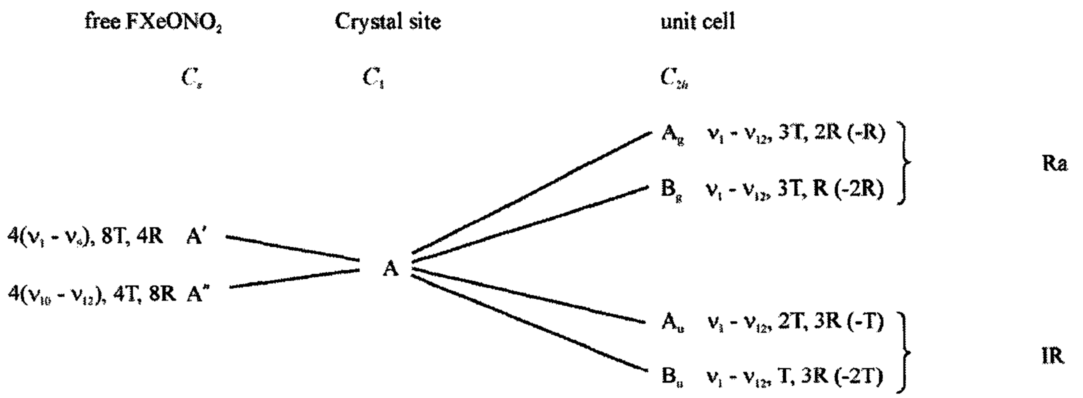

^{a}Z = 4; $P2_1/c$.

Factor-group analyses for the symmetry-reduced unit cells resulting from ^{18}O-substitution on the -NO_2 group of $FXeONO_2$ to give unit cells (Z = 4) comprised of mixtures of $FXe^{16}ON^{16}O_A{}^{18}O_S$ and $FXe^{16}ON^{16}O_S{}^{18}O_A$, where A denotes anti and S denotes syn about the N-O bridge bond and with respect to the O-Xe-F group.

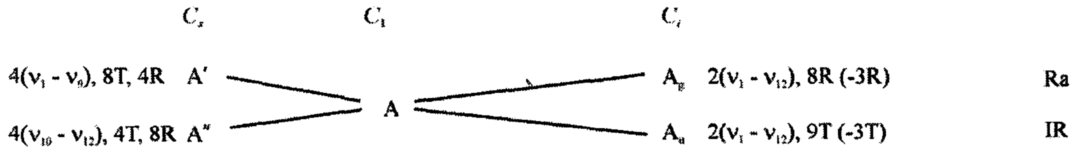

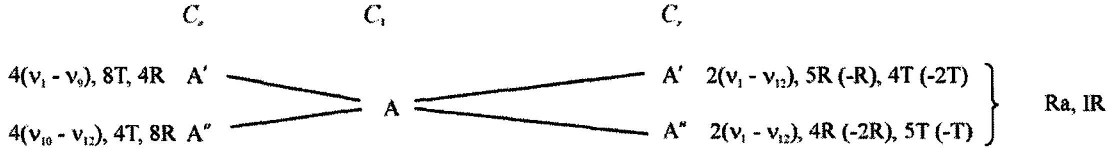

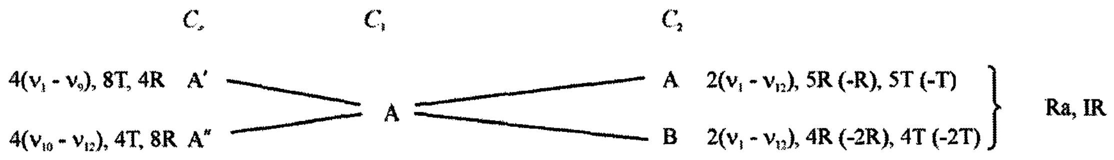

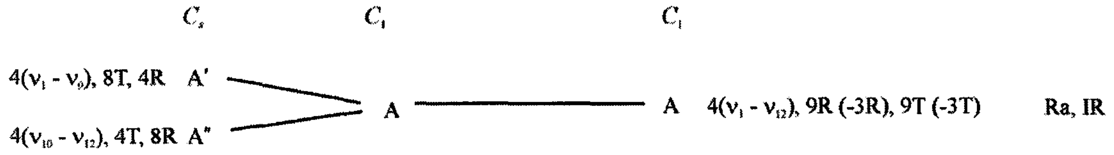

centrosymmetric unit cells having C_i symmetry belong to A_g and A_u representations (Table 9.6). Factor-group analyses of the C_i symmetric cells predict that each vibrational band of free $FXeONO_2$ will be split into two Raman-active A_g and two infrared-active A_u components. As in the case of $FXe^{16}ON^{16}O_2$, the two remaining centrosymmetric unit cells possessing C_{2h} symmetry will give rise to two Raman-active (A_g and B_g) and two infrared-active (A_u and B_u) components (Table 9.6).

These observations establish that ^{18}O is exclusively terminally bonded to nitrogen and is not scrambled among the terminal and bridge oxygen sites of $FXeONO_2$ when the latter molecule is synthesized by the low-temperature reaction of $FXe^{18}OXe{-}{-}{-}FXeF^+$ with NO_2F, in accordance with the reaction mechanism proposed in Scheme 9.2. A weak band at 1362 cm^{-1} (Table 9.2 and Figure 9.2) also appears in the ^{18}O-enriched spectrum of $FXe^{16}ON(^{16}O^{18}O)$ and the products that result from Scheme 9.2. The band is assigned to the in-phase $^{18}ON^{16}O$ stretch of the mixed cation in $[^{18}ON^{16}O][AsF_6]$ which arises according to Scheme 9.3. The band is shifted 34 cm^{-1} to low frequency of $\nu_s(NO_2)$ in $[N^{16}O_2][AsF_6]$ and is in good agreement with the calculated ^{18}O isotopic shift of -42 cm^{-1} for $^{18}ON^{16}O^+$ (Table A6.3). Both the out-of-phase $^{18}ON^{16}O$ stretch and $\delta(^{18}ON^{16}O)$ are predicted to be weak, with $\delta(^{18}ON^{16}O)$ displaying a small isotopic shift (-6 cm^{-1}), but neither was observed.

The highest frequency modes of natural abundance $FXeONO_2$ occur at 1571.7, 1578.8 cm^{-1} and 1262.1, 1285.5 cm^{-1} and are assigned to the factor-group split $\nu(NO - NO)$ and $\nu(NO + NO)$ stretches, respectively. These bands exhibit the greatest sensitivity to ^{18}O and ^{15}N substitution, displaying substantial isotopic shifts upon ^{18}O or ^{15}N

enrichment (^{18}O, −9.9, −11.4 and −16.6 cm^{-1}, respectively; ^{15}N: −35.1, −35.6 and −15.4 cm^{-1}, respectively), which are in good agreement with the calculated isotopic shifts (^{18}O, −13.6, and −24.2 cm^{-1}; ^{15}N: −38.0 and −14.8 cm^{-1}, respectively). The bands assigned to $\nu(O_{Xe}–N) + \delta(NO_2)$ (882.9 cm^{-1}), $\delta(O_{Xe}–N–O) + \rho_r(NO_2)$ (725.5 cm^{-1}), and $\nu(O_{Xe}–N) - \delta(NO_2)$ (685.4 cm^{-1}) also exhibit significant sensitivities upon ^{18}O substitution (−9.5, −9.9 and −10.9 cm^{-1}, respectively), in good agreement with the calculated shifts (−11.2, −6.7 and −7.1 cm^{-1}, respectively). The band assigned to $\rho_w(NO_3)$ (769.4 cm^{-1}) shifts only −3.3 cm^{-1} to lower frequency, in good agreement with the calculated value of −4.4 cm^{-1}. The ν(Xe–F) stretching band is also factor-group split (478.1, 503.8 cm^{-1}) and is readily assigned because it is the most intense feature in the spectrum and because the bands are insensitive to both ^{15}N and ^{18}O substitution.

The bands assigned to $\nu(Xe–O) + \rho_w(NO_3)$ (312.7, 318.9 cm^{-1}) exhibit a significant ^{16}O/^{18}O isotopic shift (−5.5, −3.9 cm^{-1}), with a much smaller ^{14}N/^{15}N isotopic shift (−1.8, −1.0 cm^{-1}), in agreement with the calculated shifts (^{18}O, −3.9 cm^{-1}; ^{15}N, −0.6 cm^{-1}). The modes occurring below 221 cm^{-1} were readily assigned with the aid of the calculated vibrational frequencies and showed no or very small isotopic dependencies, as expected for low-frequency bending and rocking modes.

9.2.7.2. $O(XeF)_2$. The $O(XeF)_2$ molecule (C_{2v}) possesses nine fundamental vibrational modes belonging to the irreducible representations 4 A_1 + A_2 + 3 B_1 + B_2, all of which are Raman active and all but the A_2 mode are infrared active. The stretching modes are each split two bands, presumably as a result of vibrational coupling within the unit cell

(Figure 9.3 and Table 9.4). The highest frequency modes at 547.4 and 558.5 cm^{-1} are assigned to the $\nu_{as}(XeO)_2$ stretch, which display a substantial low-frequency shift (−28.3, −26.6 cm^{-1}) upon substitution of ^{18}O, in good agreement with the calculated $^{16/18}O$ isotope shift (−29.4 cm^{-1}). The $\nu_s(XeO)_2$ mode is coupled to $\nu_s(XeF)_2$ with the out-of-phase component, $\nu_s(XeO)_2 - \nu_s(XeF)_2$, predicted at higher frequency with a negligible calculated $^{16/18}O$ isotopic shift (−1.4 cm^{-1}), and the in-phase component, $\nu_s(XeO)_2 + \nu_s(XeF)_2$, predicted to be the most intense mode in the spectrum, at lower frequency, and with a substantial calculated $^{16/18}O$ isotopic shift (−19.3 cm^{-1}). In the experimental spectrum, the shoulder at 498 cm^{-1} and a band that overlaps with $\nu_s(XeF_2)$ of XeF_2 at 496.8 cm^{-1} are assigned to the out-of-phase mode which displays a small $^{16/18}O$ isotopic shift of ~4 cm^{-1} while the bands at 433.1 and 437.7 cm^{-1} are assigned to the totally symmetric in-phase with $^{16/18}O$ isotope shifts of −15.2 and −14.8 cm^{-1}, respectively, in agreement with the calculations. The $\nu_{as}(XeF)_2$ mode is not significantly coupled and appears at 406.6 and 416.7 cm^{-1}, displaying small $^{16/18}O$ isotopic shifts of −3.4 and −7.2 cm^{-1}, respectively, in agreement with the calculated shift (0.4 cm^{-1}), as expected for a mode in which the oxygen atom is not expected to have a large displacement. However, the frequency of $\nu_{as}(XeF)_2$ is substantially overestimated in the calculations. The remaining modes have been assigned as bending and twisting modes, and only the bend at 235.6 cm^{-1} displays a significant isotopic shift of −8.2 cm^{-1}, compared to the expected shift of −6.6 cm^{-1}.

The ^{18}O-enrichment experiments have also provided valuable information about the reaction pathway of $[Xe_3OF_3][AsF_6]$ with NOF, as enriched $N^{18}O^+$ was observed in the Raman spectra. The ν(NO) stretch for $N^{18}O^+$ occurs at 2196.8 cm^{-1} and displays an isotopic shifts of 56.7 cm^{-1} relative to $N^{16}O^+$ (calculated shifts, 63.8 cm^{-1}).

9.3. Conclusions

The synthesis and structural characterization of $FXeONO_2$ confirms the ability of the nitrate ligand to stabilize the +2 oxidation state of xenon. The present synthesis of $FXeONO_2$ from $[FXeOXeFXeF][AsF_6]$ and NO_2F is the only synthetic route presently known that yields isolable amounts of $FXeONO_2$ and provides an interesting synthetic application of the $Xe_3OF_3^+$ cation, the only known oxide fluoride cation of xenon(II). Raman and NMR spectroscopic studies, as well as an X-ray crystallographic study, show that $FXeONO_2$ is strongly covalently bound to xenon, which is corroborated by gas-phase quantum-chemical calculations. The mechanism leading to the formation of $FXeONO_2$ has also been explored using ^{18}O-labeled $[FXe^{18}OXeFXeF][AsF_6]$. The exclusive occurrence of $FXe^{16}ON(^{16}O^{18}O)$ as the labeled product is consistent with the formation of $^{18}O(XeF)_2$ as a reaction intermediate. The absence of $^{16/18}O$ isotopic scrambling among the oxygen sites of $FXeONO_2$ was confirmed by factor-group analyses of the 16 isotopomeric crystallographic unit cells that result from *syn-/anti*-isomerization, $FXe^{16}ON(^{16}O_A{}^{18}O_S)/FXe^{16}ON(^{16}O_S{}^{18}O_A)$, among the four $FXeONO_2$ molecules of the unit cell. A second pathway for oxygen exchange between $FXe^{16}ON(^{16}O^{18}O)$ and $N^{16}O_2^+$ led to the formation of a minor amount of $^{16}ON^{18}O^+$.

The calculated Δ*H* and Δ*G* values at 298.15 and 195.15 K show that the gas-phase decompositions of $FXeONO_2$ and $Xe(ONO_2)_2$ are spontaneous for all reaction channels considered and are consistent with the experimental decomposition products. Although the gas-phase thermochemical parameters for the reaction of $FXeONO_2$ and AsF_5 to form $XeONO_2^+$ and AsF_6^- is very endothermic and nonspontaneous, the low-temperature experimental reaction of $FXeONO_2$ with liquid AsF_5 is spontaneous, forming $[NO_2][AsF_6]$, Xe, and O_2. The sought-after $[XeONO_2][AsF_6]$ salt was not observed as an intermediate by low-temperature Raman spectroscopy. The findings are consistent with volume-based thermodynamic calculations which indicate that, while the reaction of $FXeONO_2$ and AsF_5 to form $[XeONO_2][AsF_6]$ is spontaneous under standard conditions, the salt is unstable with respect to the observed decomposition products.

The missing neutral oxide fluoride of xenon(II), $O(XeF)_2$, has also been synthesized, showing marked stability at temperatures at or below –30 °C. The ^{17}O- and ^{18}O-enrichment studies have also provided useful mechanistic data, allowing for an explanation for the redistribution of enriched oxygen among NO^+. The compound has been characterized in the solid state by Raman spectroscopy, and shows the expected isotopic shifts upon ^{18}O-substitution. The Raman characterization and mechanistic data from $O(XeF)_2$ has also assisted in establishing the formation mechanism of $FXeONO_2$.

CHAPTER 10

Conclusions and Directions for Future Work

10.1. Conclusions

The missing Xe(IV) oxide, XeO_2, has been synthesized at 0 °C by hydrolysis of XeF_4 in water and 2.00 M $H_2SO_{4(aq)}$ and characterized by low-temperature Raman spectroscopy. The Raman spectra of XeO_2 amend prior vibrational assignments of xenon doped SiO_2 and are in accordance with prior speculation that xenon depletion from the Earth's atmosphere could occur by xenon insertion at high temperatures and high pressures into SiO_2 in the Earth's crust.

A reliable synthetic route to bulk amounts of the precursor oxide fluoride, $XeOF_2$, and a thorough characterization of the compound was lacking in the literature but has now been obtained with $XeOF_2$, $F_2OXeN{\equiv}CCH_3$, and $XeOF_2{\cdot}n HF$ having been characterized in the solid state by Raman spectroscopy. Xenon oxide difluoride has now been characterized in CH_3CN solution by ^{19}F, ^{17}O, and ^{129}Xe NMR spectroscopy. The low-temperature X-ray crystal structure of $F_2OXeN{\equiv}CCH_3$ represents a rare example of a Xe(IV)–N bond.

The development of a reliable synthetic protocol for $XeOF_2$ has extended Xe(IV) oxide fluoride chemistry by the study of the Lewis donor and acceptor properties of $XeOF_2$. Reaction of $XeOF_2$ with fluoride ion sources such as CsF or the so-called "naked fluoride ion source," $[N(CH_3)_4][F]$, have yielded the corresponding anion, $XeOF_3^-$. The calculated anion geometry is based on a square planar AX_3YE_2 VSEPR arrangement with the longest Xe–F bond trans to the oxygen atom. The electron-pair donor abilities of $XeOF_2$ towards Lewis acids such as $[XeF][AsF_6]$ and in superacidic media such as HF/AsF_5 and HF/SbF_5 were also examined and resulted in $[H(OXeF_2)_n][AsF_6]$, $[FXe^{II}(OXe^{IV}F_2)_n][AsF_6]$ (n = 1, 2), $([XeF_3{\cdot}HF][Sb_2F_{11}])_2{\cdot}[H_5F_4][SbF_6]$, $[XeF_3{\cdot}HF][Sb_2F_{11}]$, and $[XeF_3][SbF_6]$ salts. The $[H(OXeF_2)_n][AsF_6]$ and $[FXe^{II}(OXe^{IV}F_2)_n][AsF_6]$ have been synthesized and structurally characterized in the solid state by low-temperature Raman spectroscopy and quantum-chemical calculations while $[XeF_3{\cdot}HF][Sb_2F_{11}]$, $([XeF_3{\cdot}HF][Sb_2F_{11}])_2{\cdot}[H_5F_4][SbF_6]$, and $[XeF_3][SbF_6]$ were characterized by single-crystal X-ray diffraction. Vibrational frequency assignments for all of the aforementioned compounds were aided by ^{18}O enrichment, and where appropriate by ^{2}H enrichment.

In related noble-gas adduct chemistry, the syntheses of XeF_2 and KrF_2 adducts with the $BrOF_2^+$ cation have been completed and have been characterized by single-crystal X-ray diffraction and Raman spectroscopy with the latter providing the first KrF_2 adduct to a non-metal main-group center. In addition, ELF and QTAIM studies of these systems have shed light on the stereochemical activity of the valence electron lone pair of Br(V) and how it is affected by coordination (steric crowding). This study has convincingly demonstrated that the Kr–F bond is significantly more covalent than the Xe–F bond and that XeF_2 is a better fluoride ion donor than KrF_2.

A more indepth study of the formation and characterization of the only example of a xenon nitrate, $FXeONO_2$ has been carried out. The syntheses of $FXeON^{16}O_2$ and $FXeON(^{18}OO)$ has shed light on the mechanism leading to the formation of $FXeONO_2$. Raman spectroscopy indicated the absence of $^{16/18}O$ isotopic scrambling among the oxygen sites of $FXeONO_2$ which was confirmed by factor-group analyses of the 16 isotopomeric crystallographic unit cells that result from *syn-/anti*-isomerization, $FXe^{16}ON(^{16}O_A{}^{18}O_S)/FXe^{16}ON(^{16}O_S{}^{18}O_A)$, among the four $FXeONO_2$ molecules of the unit cell. The intermediate oxide fluoride, $O(XeF)_2$, was observed in the synthesis of $FXeONO_2$ and a reinterpretation of its solid-state ^{16}O- and ^{18}O-enriched Raman spectra was carried out.

10.2. Future Work

10.2.1. $OTeF_5$ Derivatives of Xe(IV)

The teflate group ($-OTeF_5$) is known to have a chemistry similar to that of the fluorine ligand in main-group chemistry.[291] The $OTeF_5$ derivative of $XeOF_2$, $O{=}Xe(OTeF_5)_2$, as well as the mixed species, $O{=}XeF(OTeF_5)$, have been previously prepared according to eq 10.1 and 10.2 while attempting to form the $OTeF_5$ derivative of

$$Xe(OTeF_5)_4 + TMA^+F^- \xrightarrow[-40\ ^\circ C]{CH_3CN} O{=}XeF(OTeF_5) + F_5TeOTeF_5 + TMA^+OTeF_5^- \quad (10.1)$$

$$2\ O{=}XeF(OTeF_5) \rightleftharpoons O{=}Xe(OTeF_5)_2 + O{=}XeF_2 \quad (10.2)$$

XeF_5^-.[292] Multi-NMR studies were carried out on these systems in CH_3CN solvent, however, the species have never been isolated in the solid state and fully structurally characterized. It would be interesting to obtain crystalline $O{=}Xe(OTeF_5)_2$ and $O{=}XeF(OTeF_5)$ from these CH_3CN solutions and to compare their X-ray structures with those of $F_2OXeNCCH_3$[125] and $O_2Xe(OTeF_5)_2$.[60]

The $OTeF_5$ analogue of $[XeF][SbF_6]$, has been prepared according to eq 10.3.[291] The $Xe(OTeF_5)_3^+$ cation is the Xe(IV) analogue of XeF_3^+ but has only been characterized in

$$2Xe(OTeF_5)_2 + Sb(OTeF_5)_3 \xrightarrow[-20\ ^{\circ}C]{SO_2ClF} [XeOTeF_5][Sb(OTeF_5)_6] + Xe \qquad (10.3)$$

SbF_5 solutions of $Xe(OTeF_5)_4$ in complex mixtures of the $F_xXe(OTeF_5)_{3-x}^+$ cations.[61] The $Xe(OTeF_5)_3^+$ cation is expected to be a stronger oxidant than $XeOTeF_5^+$ but less strongly oxidizing than XeF_3^+. The potential syntheses could be carried out in SO_2ClF solvent according to eqs 10.4–10.7. Owing to the thermal instability of $Sb(OTeF_5)_5$, the

$$3XeF_2 + 2B(OTeF_5)_3 \rightarrow 3Xe(OTeF_5)_2 + 2BF_3 \qquad (10.4)$$

$$3XeF_4 + 4B(OTeF_5)_3 \rightarrow 3Xe(OTeF_5)_4 + 4BF_3 \qquad (10.5)$$

$$Xe(OTeF_5)_2 + Sb(OTeF_5)_3 \rightarrow Sb(OTeF_5)_5 + Xe \qquad (10.6)$$

$$Xe(OTeF_5)_4 + Sb(OTeF_5)_5 \rightarrow Xe(OTeF_5)_3{}^+Sb(OTeF_5)_6{}^- \qquad (10.7)$$

aforementioned reactions must be carried out at low temperature (–78 °C). An alternative synthetic approach involves the low-temperature reaction of $FXe(OTeF_5)_3$ with $Sb(OTeF_5)_5$ in SO_2ClF according to eq 10.8. The latter salt is expected to form a fluorine-bridged ion

$$FXe(OTeF_5)_3 + Sb(OTeF_5)_5 \rightarrow Xe(OTeF_5)_3{}^+FSb(OTeF_5)_5{}^- \qquad (10.8)$$

pair, $(OTeF_5)_3Xe^+$---F–$Sb(OTeF_5)_5^-$, which is expected to be labile in solution but should be easier to crystallize and be more stable than $Xe(OTeF_5)_3{}^+Sb(OTeF_5)_6{}^-$.

10.2.2. XeF_2, XeF_4, and KrF_2 Adducts to Transition Metal Centers

As outlined in Section 7.1, a series of KrF_2 Lewis acid–base adducts with group 6 d^0 transition metal centers, namely $MOF_4{\cdot}KrF_2$ (M = Cr,[106] Mo,[107] W[107]) have been synthesized, with XeF_2 adducts of Mo and W as well.[107] The structural characterizations of the adducts were limited to solution ^{19}F NMR and solid-state Raman spectroscopy. In all cases, the Raman and ^{19}F NMR spectra indicate that the adducts result from weak coordination of NgF_2 (Ng = Xe, Kr) through a fluorine bridge to the metal atom. In the absence of X-ray crystal structures, an assessment of the degree of coordination, based on the relative bond lengths of terminal and bridge Ng–F bonds could not be made. The successful growth of $[BrOF_2][AsF_6]\cdot 2NgF_2$ crystals from HF solvent suggests the possibility of isolating crystals of $XOF_4\cdot nNgF_2$ (X = Cr, Mo, W; n = 1, 2) (eq 10.9). It is

$$XOF_4 + nNgF_2 \xrightarrow{HF} XOF_4\cdot nNgF_2 \tag{10.9}$$

also possible that this chemistry may be extended to the syntheses of XeF_4 adducts with XOF_4 (eq 10.10), which would represent the only known XeF_4 adducts other than $[Mg(XeF_2)(XeF_4)][AsF_6]_2$.[42]

$$XOF_4 + XeF_4 \xrightarrow{HF} XOF_4\cdot XeF_4 \tag{10.10}$$

A large class of compounds in which KrF_2 is coordinated to metal cation centers may be prepared (eq 10.11) using synthetic routes that are analogous to those that have been used to synthesize the XeF_2 adducts.[82,83]

$$[M^{n+}][PnF_6^-]_n + mKrF_2 \xrightarrow{HF} [M(KrF_2)_p{}^{n+}][PnF_6^-]_n + (m-p)KrF_2 \tag{10.11}$$

10.2.3. Syntheses of Oxofluoro-Anions and Neutral Oxofluorides of Xe(VIII)

It was shown in Section 5.2.3 that O_2NF undergoes metathesis with $XeOF_2$ to form N_2O_5 and $[NO_2][XeF_5]$. It has been shown that solutions of XeO_4 can be prepared in the oxidatively resistant solvents SO_2ClF[193] and anhydrous HF and that these solutions only slowly decompose at −30 °C. The use of O_2NF as a potential oxide acceptor may provide opportunities to study the reactions of XeO_4 with O_2NF (eqs 10.12 and 10.13), and could lead to simplified procedures for the preparation of the known, but ill-characterized Xe(VIII) oxofluorides, XeO_3F_2 and XeO_2F_4.

$$XeO_4 + 2O_2NF \longrightarrow XeO_3F_2 + N_2O_5 \qquad (10.12)$$

$$XeO_4 + 4O_2NF \longrightarrow XeO_2F_4 + 2N_2O_5 \qquad (10.13)$$

A possible approach to preparing a Xe(VIII) oxofluoro-anion involves the fluorination of perxenate salts (e.g. Na_4XeO_6)[180,181] according to eq. 10.14. The $XeO_3F_3^-$

$$XeO_6^{4-} + 3O_2NF \longrightarrow XeO_3F_3^- + 3NO_3^- \qquad (10.14)$$

anion is expected to have a meridional geometry based on VSEPR[41] theory, but may also adopt a facial geometry.

References

(1) Schrobilgen, G. J., Moran, M. D. "Noble Gas Compounds" in *Kirk-Othmer Encyclopedia of Chemical Technology*, 5th Ed., John Wiley & Sons, Inc., Hoboken, NJ, **2006**, Chapter 17, pp 323–343.

(2) Schrobilgen, G. J. "Noble Gas Chemistry" in *Encyclopedia of Physical Science and Technology*, 3rd ed., M.F. Hawthorne, Ed.; Academic Press: San Diego, 2002, Vol. 10, pp. 449–461.

(3) Selig, H.; Holloway, J. H. In *Topics in Current Chemistry*; Bosche, F. L., Ed.; Springer-Verlag: Berlin, 1984; Vol. 124, pp 33–90.

(4) Holloway, J. H. *J. Fluorine Chem.* **1986**, *33*, 149–158.

(5) Holloway, J. H.; Hope, E. G. *Adv. Inorg. Chem.* **1998**, *46*, 51–100.

(6) Schrobilgen, G. J. In *Synthetic Fluorine Chemistry*; Olah, G. A., Prakash, G. K. S., Chambers, R. D., Eds.; John Wiley & Sons, Inc.: New York, 1999, pp 31–42.

(7) Gerken, M.; Schrobilgen, G. J. *Coord. Chem. Rev.* **2000**, *197*, 335–395.

(8) Brel, V. K.; Pirkuliev, N. S.; Zefirov, N. S. *Russ. Chem. Rev. (Engl. Transl.)* **2001**, *70*, 231–264.

(9) Schrobilgen, G. J. "Lewis Acid Properties of Noble Gas Cations", In *Synthetic Fluorine Chemistry*, R.D. Chambers, G.A. Olah and G.K.S. Prakash, eds., New York: Wiley and Sons, 1992, Chapter 1, pp. 1–30.

(10) Žemva, B. *Croat. Chem. Acta* **1988**, *61*, 163–187.

(11) Žemva, B. "The Chapter Noble Gases: Inorganic Chemistry" in *Encyclopedia of Inorganic Chemistry*, John Wiley & Sons, Inc., New York, 1994, Vol. 5, pp 2660–2680.

(12) Lehmann, J. F.; Mercier, H. P. A.; Schrobilgen, G. J. *Coord. Chem. Rev.* **2002**, *233-234*, 1–39 and references therein.

(13) Laszlo, P.; Schrobilgen, G. J. *Angew. Chem. Int. Ed. Engl.* **1988**, *27*, 479–489.

(14) Ball, P., "Not So Noble", In *Elegant Solutions: Ten Beautiful Experiments in Chemistry*, The Royal Society of Chemistry, Cambridge, UK, 2005, Chapter 7, pp. 139–150.

(15) Moissan, H. *Compt. Rend.* **1895**, *120* , 966–968.

(16) von Antropoff, A.; Frauenhof, H.; Krüger, K. H. *Naturwissenschaften* **1933**, *21*, 315.

(17) Yost, D. M.; Kaye, A. L. *J. Am. Chem. Soc.* **1933**, *55*, 3890–3892.

(18) Bartlett, N. *Proc. Chem. Soc.,* **1962,** 218.

(19) Sladky, F. O.; Bulliner, P. A.; Bartlett, N. *J. Chem. Soc. A* **1969**, 2179–2188.

(20) Graham, L.; Graudejus, O.; Jha, N. K.; Bartlett, N. *Coord. Chem. Rev.* **2000**, *197*, 321–334.

(21) (a) Hoppe, R.; Dähne, W.; Mattauch, H.; Rödder, K. *Angew. Chem.* **1962**, *74*, 903; *Angew. Chem. Int. Ed. Engl.* **1962**, *1*, 599. (b) Hoppe, R.; Mattauch, H.; Rödder, K.; Dähne, W. *Z. Anorg. Allg. Chem.* **1963**, *324*, 214–224.

(22) Claassen, H. H.; Selig, H.; Malm, J. G. J. *Am. Chem. Soc.* **1962**, *84*, 3593.

(23) Fields, P. R.; Stein, L.; Ziran, M. H. *J. Am. Chem. Soc.* **1962**, *84*, 4164–4165.

(24) Stein, L. *J. Am. Chem. Soc.* **1969**, *91*, 5396–5397.

(25) Stein, L. *Science* **1972**, *175*, 1463–1465.

(26) Khriachtchev, L.; Petterson, M.; Runeberg, N.; Lundell, J.; Räsänen, M. *Nature* **2000**, *406*, 874–876.

(27) Runeberg, N.; Petterson, M.; Khriachtchev, L.; Lundell, J.; Räsänen, M. *J. Chem. Phys.* **2001**, *114*, 836–841.

(28) Berkowitz, J.; Chupka, W. A.; *Chem. Phys. Lett.* **1970**, *7*, 447–450.

(29) Khriachtchev, L.; Domanskaya, A.; Lundell, J.; Akimov, A.; Räsänen, M.; Misochko, E. *J. Phys. Chem. A* **2010**, *114*, 4181–4187.

(30) Khriachtchev, L.; Lignell, A.; Tanskanen, H.; Lundell, J.; Kiljunen, H.; Räsänen, M. *J. Phys. Chem. A* **2006**, *110*, 11876.

(31) Chernick, C. L.; Malm, J. G. *Inorg. Synth.* **1966**, *8*, 254–258.

(32) Levy, H. A.; Burns, J. H.; Agron, P. A. *Science*, **1963**, *139*, 1208–1209.

(33) Templeton, D. H.; Zalkin, A.; Forrester, J. D.; Williamson, S. M. *J. Am. Chem. Soc.* **1963**, *85*, 817.

(34) Ibers, J. A.; Hamilton, W. C. *Science*, **1963**, *139*, 106–107.

(35) Claasen, H. H.; Chernick, C.L.; Malm, J. G. *J. Am. Chem. Soc.* **1963**, *85*, 1927–1928.

(36) Yeranos, W. *Mol. Phys.* **1965**, *9*, 449–454.

(37) Bartlett, N.; Jha, N. K. In *Noble-Gas Compounds*, Hymann, H. H., ed.; University of Chicago Press, Chicago, 1963; pp. 23–30.

(38) Schumacher, G. A.; Schrobilgen, G. J. *Inorg. Chem.* **1984**, *23*, 2923–2929.

(39) Brown, T. H.; Whipple, E. B.; Verdier, P.H. *Science*, **1963**, *140*, 178.

(40) Rutenberg, A. C. *Science*, **1963**, *140*, 993–994.

(41) Gillespie, R. J.; Hargittai, I. In *The VSEPR Model of Molecular Geometry*; Allyn and Bacon: Boston, MA. 1991.

(42) Tavčar, G. Žemva, B. *Angew. Chem. Int. Ed.* **2009**, *48*, 1432–1434.

(43) Brock, D. S.; Casalis de Pury, J. J.; Mercier, H. P. A.; Schrobilgen, G. J.; Silvi, B. *Inorg. Chem.* **2010**, *49*, 6673–6689.

(44) Zalkin, A.; Ward, D. L.; Biagioni, R. N.; Templeton, D. H.; Bartlett, N. *Inorg. Chem.* **1978**, *17*, 1318–1322.

(45) Elliott, H. A.; Lehmann, J. F.; Mercier, H. P. A.; Jenkins, D. B.; Schrobilgen, G. J. *Inorg. Chem.* **2010**, *49*, 8504–8523.

(46) Gillespie, R. J.; Landa, B.; Schrobilgen, G. J. *Inorg. Chem.* **1976**, *15*, 1256–1263.

(47) Gillespie R. J.; Schrobilgen, G. J. *Inorg. Chem.* **1974**, *13*, 2370–2374.

(48) Gillespie, R. J.; Landa, B.; Schrobilgen, G. J. *J. Chem. Soc. D* **1971**, 1543–1544.

(49) Schrobilgen, G. J.; Holloway, J. H.; Granger, P.; Brevard, C. *Inorg. Chem.* **1978**, *17*, 980.

(50) McKee, D. E.; Adams, C. J.; Bartlett, N. *Inorg. Chem.* **1973**, *12*, 1722–1725.

(51) McKee, D. E.; Zalkin, A.; Bartlett, N. *Inorg. Chem.* **1973**, *12*, 1713–1717.

(52) Boldrini, P.; Gillespie, R. J.; Ireland, P. R.; Schrobilgen, G. J. *Inorg. Chem.* **1974**, *13*, 1690–1694.

(53) Christe, K. O.; Curtis, E. C.; Dixon, D. A.; Mercier, H. P. A.; Sanders, J. C. P.; Schrobilgen, G. J. *J. Am. Chem. Soc.* **1991**, *113*, 3351–3361.

(54) Adams, W. J.; Thompson, H. B.; Bartell, L. S. *J. Chem. Phys.* **1970**, *53*, 4040–4046.

(55) Bondi, A. *J. Phys. Chem.* **1964**, *68*, 441–451.

(56) Birchall, T.; Myers, R. D.; de Waard, H.; Schrobilgen, G. J. *Inorg. Chem.* **1982**, *21*, 1068–1073.

(57) Allred, A. L. *J. Inorg. Nucl. Chem.* **1961**, *17*, 215–221.

(58) Jacob, E.; Lentz, D.; Seppelt, K.; Simon, A. *Z. Anorg. Allg. Chem.* **1981**, *472*, 7–25.

(59) Lentz, D.; Seppelt, K. *Angew. Chem., Int. Ed. Engl.* **1978**, *17*, 356–361.

(60) Turowsky, L.; Seppelt, K. *Z. Anorg. Allg. Chem.* **1992**, *609*, 153–156.

(61) Syvret, R. G.; Mitchell, K. M.; Sanders, J. C. P.; Schrobilgen, G. J. *Inorg. Chem.* **1992**, *31*, 3381–3385.

(62) Frohn, H. –J.; LeBlond, N; Lutar, K.; Žemva, B. *Angew. Chem., Int. Ed. Engl.* **2000**, *39*, 391–393.

(63) Koppe, K. Ph. D. Thesis, Universität Duisburg-Essen, Duisburg, Germany, 2005.

(64) Syvret, R. G.; Schrobilgen, G. J., *J. Chem. Soc., Chem. Commun.* **1985**, 1529–1530.

(65) Ogden, J. S.; Turner, J. J., *Chem. Comm.* **1966**, *19*, 693–694.

(66) Jacob, E.; Opferkuch, R. *Angew. Chem. Int. Ed. Engl.* **1976**, *15*, 158–159.

(67) Gillespie, R. J.; Schrobilgen, G. J. *J. Chem. Soc., Chem. Commun.* **1977**, 595–597.

(68) Williamson, S. M.; Koch, C. W. *Science* **1963**, *139*, 1046–1047.

(69) Appelman, E. H.; Malm, J. G. *J. Am. Chem. Soc.* **1964**, *86*, 2141–2148.

(70) Yamanishi, M.; Hirao, K.; Yamashita, K. *J. Chem. Phys.* **1998**, *108*, 1514–1521.

(71) Gerken, M.; Moran, M. D.; Mercier, H. P. A.; Pointner, B. E.; Schrobilgen, G. J.; Hoge, B.; Christe, K. O.; Boatz, J. A. *J. Am. Chem. Soc.* **2009**, *131*, 13474–13489.

(72) Moran, M. D. Ph. D. Thesis, McMaster University, Hamilton, ON, Canada, 2007.

(73) Fir, B. A.; Gerken, M.; Pointner, B. E.; Mercier, H. P. A.; Dixon, D. A.; Schrobilgen, G. J. *J. Fluorine Chem.* **2000**, *105*, 159–167.

(74) Gillespie, R. J.; Landa, B. *Inorg. Chem.* **1973**, *12*, 1383–1389.

(75) Gillespie, R. J.; Martin, D.; Schrobilgen, G. J. *J. Chem. Soc., Dalton Trans.* **1980**, 1898–1903.

(76) Frlec, B.; Holloway, J. H. *J. Chem. Soc., Dalton Trans.* **1975**, 535–540.

(77) Gillespie, R. J.; Netzer, A.; Schrobilgen, G. J. *Inorg. Chem.* **1974**, *13*, 1455–1459.

(78) Dixon, D. A.; Arduengo III, A. J.; Farnham, W.B. *Inorg. Chem.* **1989**, *28*, 4589–4593.

(79) Sladky, F. O.; Bullinger, P. A.; Bartlett, N.; DeBoer, B. G.; Zalkin, A. *Chem. Commun.* **1968**, 1048–1049.

(80) Eisenberg, M.; DesMarteau, D. D. *Inorg. Nucl. Chem. Lett.* **1970**, *6*, 29–34.

(81) Zefirov, N. S.; Gakh, A. A.; Zhdankin, V. V.; Stang, P. J. *J. Org. Chem.* **1991**, *56*, 1416–1418.

(82) Tramšek, M.; Žemva, B. *J. Fluorine Chem.* **2006**, *127*, 1275–1284 and references therein.

(83) Tavčar, G.; Tramšek, M.; Bunič, T.; Benkič, P.; Žemva, B. *J. Fluorine Chem.* **2004**, *125*, 1579–1584.

(84) Žemva, B. 234th ACS National Meeting, Boston, MA, USA, 2007.

(85) Grosse, A.V.; Kirshenbaum, A.D.; Streng, A.G.; Streng, L.V. *Science* **1963,** *139*, 1047–1048.

(86) Schreiner, F.; Malm, J.G.; Hindman, J.C. *J. Am. Chem. Soc.* **1965**, *87*, 25–28.

(87) Gunn, S. R. *J. Am. Chem. Soc.* **1966**, *88*, 5924.

(88) Gunn, S. R. *J. Phys. Chem.* **1967**, *71*, 2934–2937.

(89) MacKenzie, D. R. *Science* **1963**, *141*, 1171.

(90) MacKenzie, D. R.; Fajer, J. *Inorg. Chem.* **1966**, *5*, 699–700.

(91) Prusakov, V. N.; Sokolov, V. B. *At. Energ.* **1971**, *31*, 259–268; *Sov. At. Energ.* **1971**, *31*, 990–999.

(92) Sessa, P. A.; McGee Jr, H. A. *J. Phys. Chem.* **1969**, *73*, 2078–2080.

(93) Turner, J. J.; Pimentel, G. C. *Science* **1963**, *140*, 974–975.

(94) Streng, L. V.; Streng, A. G. *Inorg. Chem.* **1966**, *5*, 328–329.

(95) (a) Slivnik, J.; Šmalc, A.; Lutar, K.; Žemva, B.; Frlec, B. *J. Fluorine Chem.* **1975**, *5*, 273–274. (b) Šmalc, A. Yugoslavian patent no. 37501 P 159/75, Jan. 23, 1975.

(96) Šmalc, A.; Lutar, K.; Žemva, B. *Inorg. Synth.* **1992**, *29*, 11–15.

(97) Kinkead, S. A.; FitzPatrick, J. R.; Foropoulos, Jr, J.; Kissane, R. J.; Purson, J. D. *ACS Symp. Ser.* **1994**, *555*, 40–55.

(98) Bezmel'nitsyn, V. N.; Legasov, V. A.; Chaivanov, B.B. *Dokl. Akad. Nauk. SSSR* **1977**, *235*, 96–98; *Dokl. Chem.* **1977**, *235*, 365–367.

(99) Lehmann, J. F.; Dixon, D. A.; Schrobilgen, G. J. *Inorg. Chem.* **2001**, *40*, 3002–3017.

(100) Al-Mukhtar, M.; Holloway, J. H.; Hope, E. G.; Schrobilgen, G. J. *J. Chem. Soc., Dalton Trans.* **1991,** 2831–2834.

(101) Burbank, R. D.; Falconer, W. E.; Sunder, W. A. *Science* **1972,** *178*, 1285–1286.

(102) Harshberger, W.; Bohn, R. K.; Bauer, S. H. *J. Am. Chem. Soc.* **1967**, *89*, 6466–6469.

(103) Sanders, J. C. P.; Schrobilgen, G. J. *J. Chem. Soc., Chem. Commun.* **1989**, 20, 1576–1578.

(104) Schrobilgen, G. J. *J. Chem. Soc., Chem. Commun.* **1988**, 1506–1508.

(105) Schrobilgen, G. J. *J. Chem. Soc., Chem. Commun.* **1988**, 863–865.

(106) Christe, K. O.; Wilson, W. W.; Bougon, R. A. *Inorg. Chem.* **1986**, *25*, 2163–2169.

(107) Holloway, J. H.; Schrobilgen, G. J. *Inorg. Chem.* **1981**, *20*, 3363–3368.

(108) Leblond, N. Ph. D. Thesis, McMaster University, Hamilton, ON, Canada, 1998.

(109) Gillespie, R. J.; Schrobilgen, G. J. *Inorg. Chem.* **1976**, *15*, 22–31.

(110) Winfield, J. M. *J. Fluorine Chem.* **1984**, *25*, 91–98.

(111) Christe, K. O.; Wilson, W. W.; Wilson, R. D.; Bau, R.; Feng, J. *J. Am. Chem. Soc.* **1990**, *112*, 7619–7625.

(112) Mercier, H. P. A.; Sanders, J. C. P.; Schrobilgen, G. J.; Tsai, S. S. *Inorg. Chem.* **1993**, *32*, 386–393.

(113) Emara, A. A. A.; Lehmann, J. F.; Schrobilgen, G. J. *J. Fluorine Chem.* **2005**, *126*, 1373–1376.

(114) Christe, K. O.; Schack, C. J.; Wilson, R. D. *Inorg. Chem.* **1975**, *14*, 2224–2230.

(115) Gerken, M. Ph. D. Thesis, McMaster University, Hamilton, ON, Canada, 2000.

(116) Faloon, A. V.; Kenna, W. B. *J. Am. Chem. Soc.* **1951**, *73*, 2937–2938.

(117) Ruff, O.; Menzel, W.; Neumann, W. *Z. Anorg. Allg. Chem.* **1932,** *208*, 293–303.

(118) Sladky, F. O. *Monatsh. Chem.* **1970**, *101*, 1571–1577.

(119) Sladky, F. O. *Monatsh. Chem.* **1970**, *101*, 1559–1570.

(120) Shack, C. J.; Wilson, R. D. *Inorg. Synth.* **1986**, *24*, 1–3.

(121) Schmeisser, M.; Eckermann, W.; Gundlach, K. P. Naumann, D. *Z. Naturforsch.* **1980**, *35b*, 1143–1145.

(122) Pilipovich, D.; Lindahl, C. B.; Schack, C. J.; Wilson, R. D.; Christe, K. O. *Inorg. Chem.* **1972**, *11*, 2189–2192.

(123) Christe, K. O.; Schack, C. J.; Pilipovich, D. *Inorg. Chem.* **1972**, *11*, 2205–2208.

(124) Christe, K. O.; Curtis, E. C.; Schack, C. J. *Inorg. Chem.* **1972**, *11*, 2212–2215.

(125) Brock, D. S.; Bilir, V.; Mercier, H. P. A.; Schrobilgen, G. J. *J. Am. Chem. Soc.* **2007**, *129*, 3598–3611.

(126) Brock, D. S.; Mercier, H. P. A.; Schrobilgen, G. J. *J. Am. Chem. Soc.* **2010**, *132*, 10935–10943.

(127) There is precedent for polynuclear anions of the type $F(XeOF_4)_m^-$ with the synthesis and structural characterization of the $(XeOF_4)_3F^-$ anion as its Cs^+ salt: Holloway, J. H.; Kaučič, V.; Martin-Rovet, D.; Russell, D. R.; Schrobilgen, G. J.; Selig, H. *Inorg. Chem.* **1985**, *24*, 678–683.

(128) Bougon, R.; Huy, T. B.; Charpin, P.; Gillespie, R. J.; Spekkens, P. H. *J. Chem. Soc., Dalton Trans.* **1979**, *1*, 6–12.

(129) Keller, N.; Schrobilgen, G. J. *Inorg. Chem.* **1981**, *20*, 2118–2129.

(130) Gerken, M.; Dixon, D. A.; Schrobilgen, G. J. *Inorg. Chem.* **2000**, *39*, 4244–4255.

(131) *SMART*, release 5.611, and *SAINT*, release 6.02; Siemens Energy and Automotive Analytical Instrumentation, Inc.: Madison, WI, 1999.

(132) Sheldrick, G. M. *SADABS* (Siemens Area Detector Absorption Corrections), version 2.10; Siemens Analytical X-ray Instruments, Inc.: Madison, WI, 2004.

(133) *APEX2*, release 2.0-2; Bruker AXS Inc.: Madison, WI, 1995.

(134) Sheldrick, G. M. *SHELXTL*, release 5.1; Siemens Analytical X-ray Instruments, Inc.: Madison, WI, 1998.

(135) Sheldrick, G. M. *SHELXTL*, release 6.14; Siemens Analytical X-ray Instruments, Inc.: Madison, WI, 2000-2003.

(136) Spek, A. L. *J. Appl. Crystallogr.* **2003**, *36*, 7−13.

(137) Gaussian 03, Revision **D.01**, Frisch, M. J.; Trucks, G. W.; Schlegel, H. B.; Scuseria, G. E.; Robb, M. A.; Cheeseman, J. R.; Montgomery, Jr., J. A.; Vreven, T.; Kudin, K. N.; Burant, J. C.; Millam, J. M.; Iyengar, S. S.; Tomasi, J.; Barone, V.; Mennucci, B.; Cossi, M.; Scalmani, G.; Rega, N.; Petersson, G. A.; Nakatsuji, H.; Hada, M.; Ehara, M.; Toyota, K.; Fukuda, R.; Hasegawa, J.; Ishida, M.; Nakajima, T.; Honda, Y.; Kitao, O.; Nakai, H.; Klene, M.; Li, X.; Knox, J. E.; Hratchian, H. P.; Cross, J. B.; Bakken, V.; Adamo, C.; Jaramillo, J.; Gomperts, R.; Stratmann, R. E.; Yazyev, O.; Austin, A. J.; Cammi, R.; Pomelli, C.; Ochterski, J. W.; Ayala, P. Y.; Morokuma, K.; Voth, G. A.; Salvador, P.; Dannenberg, J. J.; Zakrzewski, V. G.; Dapprich, S.; Daniels, A. D.; Strain, M. C.; Farkas, O.; Malick, D. K.; Rabuck, A. D.; Raghavachari, K.; Foresman, J. B.; Ortiz, J. V.; Cui, Q.; Baboul, A. G.; Clifford, S.; Cioslowski, J.; Stefanov, B. B.; Liu, G.; Liashenko, A.; Piskorz, P.; Komaromi, I.; Martin, R. L.; Fox, D. J.; Keith, T.; Al-Laham, M. A.; Peng, C. Y.; Nanayakkara, A.; Challacombe, M.; Gill, P. M. W.; Johnson, B.; Chen, W.; Wong, M. W.; Gonzalez, C.; and Pople, J. A.; Gaussian, Inc., Wallingford CT, 2004.

(138) Gaussian 09, Revision A.02, Frisch, M. J.; Trucks, G. W.; Schlegel, H. B.; Scuseria, G. E.; Robb, M. A.; Cheeseman, J. R.; Scalmani, G.; Barone, V.; Mennucci, B.; Petersson, G. A.; Nakatsuji, H.; Caricato, M.; Li, X.; Hratchian, H. P.; Izmaylov, A. F.; Bloino, J.; Zheng, G.; Sonnenberg, J. L.; Hada, M.; Ehara, M.; Toyota, K.; Fukuda, R.; Hasegawa, J.; Ishida, M.; Nakajima, T.; Honda, Y.; Kitao, O.; Nakai, H.; Vreven, T.; Montgomery, Jr., J. A.; Peralta, J. E.; Ogliaro, F.; Bearpark, M.; Heyd, J. J.; Brothers, E.; Kudin, K. N.; Staroverov, V. N.; Kobayashi, R.; Normand, J.; Raghavachari, K.; Rendell, A.; Burant, J. C.; Iyengar, S. S.; Tomasi, J.; Cossi, M.; Rega, N.; Millam, N. J.; Klene, M.; Knox, J. E.; Cross, J. B.; Bakken, V.; Adamo, C.; Jaramillo, J.; Gomperts, R.; Stratmann, R. E.; Yazyev, O.; Austin, A. J.; Cammi, R.; Pomelli, C.; Ochterski, J. W.; Martin, R. L.; Morokuma, K.; Zakrzewski, V. G.; Voth, G. A.; Salvador, P.; Dannenberg, J. J.; Dapprich, S.; Daniels, A. D.; Farkas, Ö.; Foresman, J. B.; Ortiz, J. V.; Cioslowski, J.; Fox, D. J. Gaussian, Inc., Wallingford CT, 2009.

(139) Basis sets and pseudo-potentials were obtained from the Extensible Computational Chemistry Environment Basis set Database, version 2/25/04, as developed and distributed by the Molecular Science Computing Facility, Environmental and Molecular Science Laboratory, which is part of the Pacific Northwest Laboratory, P.O. Box 999, Richland, WA 99352.

(140) Feller, D. *J. Comp. Chem.* **1996**, *17*, 1571−1586.

(141) Schuchardt, K. L.; Didier, B. T.; Elsethagen, T.; Sun. L.; Gurumoorthi, V.; Chase, J.; Li, J.; Windus, T. L. *J. Chem. Inf. Model.* **2007**, 47.

(142) *GaussView*, release 3.0; Gaussian Inc.: Pittsburgh, PA, 2003.

(143) Whalen, J. M.; Schrobilgen, G. J. *Helium-Group Gases, Compounds*, 4 ed.; John Wiley & Sons, Inc.: New York, 1994; Vol. 13; pp 38−53.

(144) Fujiwara, F. Y.; Martin, J. S. *J. Am. Chem. Soc.* **1974**, *96*, 7625−7631. This reference established that HF is molecular in CH_3CN solvent; $\delta(^{19}F) = -181.1$ ppm and $^{1}J(^{19}F-^{1}H) = 476$ Hz at −40 °C. In the present work, $^{1}J(^{19}F-^{1}H)$ was collapsed to a broad line which is presumably the result of exchange with residual H_3O^+ (vide infra).

(145) Bucher, G.; Scaiano, J. C. *J. Phys. Chem.* **1994**, *98*, 12471−12473.

(146) Pasinszki, T.; Westwood, N. P. C. *J. Phys. Chem. A* **2001**, *105*, 1244−1253.

(147) Pointner, B. E.; Suontamo, R. J.; Schrobilgen, G. J. *Inorg. Chem.* **2006**, *45*, 1517−1534.

(148) Peterson, S. W.; Willett, R. D.; Huston, J. L. *J. Chem. Phys.* **1973**, *59*, 453−459.

(149) Schrobilgen, G. J.; LeBlond, N.; Dixon, D. A. *Inorg. Chem.* **2000**, *39*, 2473−2487.

(150) Gunderson, G.; Hedberg, K.; Huston, J. L. *J. Chem. Phys.* **1970**, *52*, 812−815.

(151) Faggiani, R.; Kennepohl, D. K.; Lock, C. J. L.; Schrobilgen, G. J. *Inorg. Chem.* **1986**, *25*, 563−571.

(152) Fir, B. A.; Whalen, J. M.; Mercier, H. P. A.; Dixon, D. A.; Schrobilgen, G. J. *Inorg. Chem.* **2006**, *45*, 1978−1996.

(153) Sawyer, J. F.; Schrobilgen, G. J.; Sutherland, S. J. *Inorg. Chem.* **1982**, *21*, 4064−4072.

(154) Smith, G. L.; Mercier, H. P. A.; Schrobilgen G. J. *Inorg. Chem.* **2007**, *46*, 1369−1378.

(155) Frohn, H.-J.; Jakobs, S.; Henkel, G. *Angew. Chem., Int. Ed. Engl.* **1989**, *28*, 1506−1507.

(156) Gillespie, R. J. In *Noble Gas Compounds*; Hyman, H. H., Ed.; The University of Chicago Press: Chicago, 1963; pp. 333−339.

(157) Von Ahsen, B.; Bley, B.; Proemmel, S.; Wartchow, R.; Willner, H.; Aubke, F. *Z. Anorg. Allg. Chem.* **1998**, *624*, 1225–1234.

(158) Swanson, B.; Shriver, D. F. *Inorg. Chem.* **1970**, *9*, 1406–1416.

(159) Swanson, B.; Shriver, D. F. *Inorg. Chem.* **1971**, *10*, 1354–1365.

(160) Mason, M. G.; Von Holle, W. G.; Robinson, D. W. *J. Chem. Phys.* **1971**, *54*, 3491–3499.

(161) Kittelberger, J. S.; Hornig, D. F. *J. Chem. Phys.* **1967**, *46*, 3099–3108.

(162) Tubino, R.; Zerbi, G. *J. Chem. Phys.* **1969**, *51*, 4509–4514.

(163) Reed, A. E.; Weinstock, R. B.; Weinhold, F. *J. Chem. Phys.* **1985**, *83*, 735–746.

(164) Reed, A. E.; Curtiss, L. A.; Weinhold, F. *Chem. Rev.* **1998**, *88*, 899–926.

(165) Glendening, E. D.; Reed, A. E.; Carpenter, J. E.; Weinhold, F. *NBO Version 3.1*; Gaussian Inc.: Pittsburgh, PA, 1990.

(166) Glendening, E. D.; Badenhoop, J. K.; Reed, A. E.; Carpenter, J. E.; Bohmann, C. M.; Morales, C. M.; Weinhold, F. *NBO Version 5.0*; Theoretical Chemistry Institute, University of Wisconsin: Madison, WI, 2001.

(167) Christe, K. O. In *XXIVth International Congress of Pure and Applied Chemistry*; Butterworth: London, 1974; Vol. 4, p 115.

(168) MacDougall, P. J.; Schrobilgen, G. J.; Bader, R. F. W. *Inorg. Chem.* **1989**, *28*, 763–769.

(169) Anders, E.; Owen, T. *Science* **1977**, *198*, 453–465.

(170) Ozima, M.; Podosek, F. A. *J. Geophys. Res.* **1999**, *104*, 25493–25499.

(171) Kunz, J.; Staudacher, T.; Allegre, C. J. *Science* **1998**, *280*, 877–880.

(172) Caldwell, W. A.; Nguyen, J. H.; Pfrommer, B. G.; Mauri, F.; Louie, S. G.; Jeanloz R. *Science* **1997**, *277*, 930–933.

(173) Nishio-Hamane, D.; Yagi, T.; Sata, N.; Fujita, T.; Okada, T. *Geophys. Res. Lett.* **2010**, *37*, L04302.

(174) Wacker, J. F.; Anders, E. *Geochim. Cosmochim. Acta* **1984**, *48*, 2373–2380.

(175) Sill, G. T.; Wilkening, L. L. *Icarus* **1978**, *33*, 13–22.

(176) Matsuda, J.-I.; Matsubara, K. *Geophys. Res. Lett.* **1989**, *16*, 81–84.

(177) Pepin, R. O. *Icarus* **1991**, *92*, 2–79.

(178) Sanloup, C.; Schmidt, B. C.; Chamorro Perez, E. M.; Jambon, A.; Gregoryanz, E.; Mohamed Mezouar, M. *Science* **2005**, *310*, 1174–1177.

(179) Smith, D. F. *J. Am. Chem. Soc.* **1963**, *85*, 816–817.

(180) Selig, H.; Claassen, H. H.; Chernick, C. L.; Malm, J. G.; Huston, J. L. *Science* **1964**, *143*, 1322–1323.

(181) Huston, J. L.; Studier, M. H.; Sloth, E. N. *Science*, **1964**, *143*, 1161–1162.

(182) Gunn, S. R. *J. Am. Chem. Soc.* **1965**, *87*, 2290–2291.

(183) Bartlett, N.; Rao, P. R. *Science*, **1963**, *139*, 506.

(184) Williamson, S. M.; Koch, C. W. In *Noble Gas Compounds*; Hyman, H. H. Ed.; University of Chicago Press: Chicago, IL, 1963; pp 149–151.

(185) Claassen, H. H.; Knapp, G. *J. Am. Chem. Soc.* **1964**, *86*, 2341–2342.

(186) Tsao, P.; Cobb, C. C.; Claassen, H. H. *J. Chem. Phys.* **1971**, *54*, 5247–5253.

(187) It is possible for a Xe–F stretch to couple with a Xe–O stretch and therefore show an isotopic dependence. However, this possibility was discounted because the corresponding out-of-phase mode was not observed. The latter would produce a second, intense, stretching band at a significantly different frequency in the Xe–F/Xe–O stretching region.

(188) The bands for the symmetric Xe–O–Xe stretch of $[Xe_3OF_3][AsF_6]$, which couple with the terminal Xe–F stretching modes, occur at 419, 430, and 480 cm^{-1}. Because they correspond to a Xe(II) cation, they are among the highest Xe–O stretching frequencies expected for a Xe(II)–O bonded species. Gerken, M.; Moran, M. D.; Mercier, H. P. A.; Pointner, B. E.; Schrobilgen, G. J.; Hoge, B.; Christe, K. O.; Boatz, J. A. *J. Am. Chem. Soc.* **2009**, *131*, 13474–13489.

(189) Pyykkö, P.; Tamm, T. *J. Phys. Chem. A* **2000**, *104*, 3826–3828.

(190) Nakamoto, K. In *Infrared and Raman Spectra of Inorganic and Coordination Compounds, Part A*, 6th ed.; John Wiley & Sons, Inc.: Hoboken, NJ 200; pp 278–279 and references therein.

(191) Nakamoto, K. In *Infrared and Raman Spectra of Inorganic and Coordination Compounds, Part A*, 6th ed.; John Wiley & Sons, Inc.: Hoboken, NJ 200; pp 129–134.

(192) Alternatively, one of the two bands at 227.9 and 239.1 cm^{-1} may result from the extended lattice. Rotational modes that are otherwise unobserved for free XeF_4 may be observed in a XeO_2 network structure. A site-symmetry analysis (see Table 4.2) indicates that a doubly degenerate E-mode originating from a rotational mode is rendered Raman active upon symmetry lowering from D_{4h} to D_{2d} in an extended structure and could account for the presence of one of the aforementioned bands.

(193) Gerken, M.; Schrobilgen, G. J. *Inorg. Chem.* **2002**, *41*, 198–204.

(194) Probert, M. I. J. *J. Phys.: Condens. Matter* **2010**, *22*, 025501.

(195) Chase, M. W. Jr. *NIST JANAF Thermochemical Tables*; American Institute of Physics: New York, 1998.

(196) Schwalbe, L. A.; Crawford, R. K.; Chen, H. H.; Aziz, R. A. *J. Chem. Phys.* **1977**, *66*, 4493–4502.

(197) Friesen, M.; Junker, M.; Zumbusch, A.; Schnöckel, H. *J. Chem. Phys.* **1999**, *111*, 7881–7887.

(198) Ranieri, V.; Bourgogne, D.; Darracq, S.; Cambon, M.; Haines, J.; Cambon, O.; Leparc, R.; Levelut, C.; Largeteau, A.; Demazeau, G. *Phys. Rev. B* **2009**, *79*, 224304.

(199) To confirm this assumption, an intimate mixture of XeF_4 and $[Cs][F(HF)_n]$ was created by dissolving an equimolar mixture of XeF_4 and CsF in aHF. The solution was quenched at −196 °C, and HF was removed under dynamic vacuum at −78 °C. Warming this $XeF_4/[Cs][F(HF)_n]$ mixture to 0 °C under dynamic vacuum yielded a small amount of $[Cs][XeF_5]$ in admixture with XeF_4, which was verified by Raman spectroscopy at −150 °C.

(200) Huston, J. L. *J. Phys. Chem.* **1967**, *71*, 3339–3341.

(201) LaBonville, P.; Ferraro, J. R.; Spittler, T. M. *J. Chem. Phys.* **1971**, *55*, 631–640.

(202) Christe, K. O.; Wilson, W. W. *Inorg. Chem.* **1988**, *27*, 3763–3768.

(203) Agron, P. A.; Begun, G. M.; Levy, H. A.; Mason, A. A.; Jones, C. G.; Smith, D. F. *Science*, **1963**, *139*, 842–844.

(204) Berg, R. W. *Spectrochim Acta* **1978**, *34A*, 655–659.

(205) Kabisch, G.; Klose, M. *J. Raman Spectrosc.* **1978**, *7*, 311–315.

(206) Kabisch, G. *J. Raman Spectrosc.* **1980**, *9*, 279–285.

(207) Wilson, W. W. Christe, K. O. *Inorg. Chem.* **1987**, *26*, 1631–1633.

(208) Bartlett, N.; Yeh, S.; Kourtakis, K.; Mallouk, T. *J. Fluorine Chem.* **1984**, *26*, 97–116.

(209) Shen,C.; Hagiwara, R.; Mallouk, T.; Bartlett, N. In *Inorganic Fluorine Chemistry, Toward the 21st Century*; Thrasher, J. S., Strauss, S. H., Eds.; ACS Symposium Series 555; American Chemical Society: Washington, DC, 1994; Chapter 2, pp 26–39.

(210) Jenkins, H. D. B.; Tudela, D; Glasser, L. *Inorg. Chem.* **2002**, *41*, 2364–2367.

(211) Jenkins, H. D. B.; Roobottom, H. K.; Passmore, J.; Glasser, L. *Inorg. Chem.* **1999**, *38*, 3609–3620.

(212) Jenkins, H. D. B.; Glasser, L. *Inorg. Chem.* **2003**, *42*, 8702–8708.

(213) Osborne, D. W.; Flotow, H. E.; Malm, J. G. *J. Chem. Phys.* **1972**, *57*, 4670–4675.

(214) Cortona, P. *Phys. Rev. B: Condens. Matter* **1992**, *46*, 2008–2014.

(215) Torrie, B. H.; Powell, B. M. *Mol. Phys.* **1992**, *75*, 613–622.

(216) Lehmann, J. F. Ph. D. Thesis, McMaster University, Hamilton, ON, 2004.

(217) Jenkins, H. D. B.; Glasser, L.; Klapötke, T. M.; Crawford, M.-J.; Bhasin, K. K.; Lee, J.; Schrobilgen, G. J.; Sunderlin, L. S.; Liebman, J. F. *Inorg. Chem.* **2004**, *43*, 6238–6248.

(218) Bartlett, N.; Zalkin, A.; Leary, K. *Inorg. Chem.* **1974**, *13*, 775–779.

(219) Christe, K. O.; Wilson, W. W. *Inorg. Chem.* **1988**, *27*, 2714–2718.

(220) Žemva, B.; Jesih, A.; Templeton, D. H.; Zalkin, A.; Cheetham, A. K.; Bartlett, N. *J. Am. Chem. Soc.* **1987**, *109*, 7420–7427.

(221) Schrobilgen, G. J.; Martin-Rovet, D.; Charpin, P.; Lance, M. *J. Chem. Soc., Chem. Commun.* **1980**, *19*, 894–897.

(222) Holloway, J. H.; Kaucic, V.; Martin-Rovet, D.; Russell, D. R.; Schrobilgen, G. J.; Selig, H. *Inorg. Chem.* **1985**, *24*, 678–683.

(223) Kläning, U. K.; Appelman, E. H. *Inorg. Chem.* **1988**, *27*, 3160–3162.

(224) Jaselskis, B. *Science* **1964**, *146*, 263–264.

(225) Holloway, J. H. *Talanta* **1967**, *14*, 871–873.

(226) Margraff, R.; Adloff, J. P. *J. Chromatog.* **1967**, *26*, 555–556.

(227) Reuben, J.; Samuel, D.; Selig, H.; Shamir, J. *Proc. Chem. Soc.* **1963**, 270.

(228) Mootz, D.; Bartmann, K.; *Z. Naturforsch., B: Chem. Sci.* **1991**, *46*, 1659–1663.

(229) Mootz, D.; Bartmann, K.; *Angew. Chem. Int. Ed.* **1988**, *27*, 391–392.

(230) *CRC Handbook of Chemistry and Physics,* 81st ed. Lide, D.R., Ed.; CRC Press: Boca Raton, FL, 2000; Chapter 2, 177.

(231) Dean, P. A.W.; Gillespie, R. J.; Hulme, R.; Humphreys, D. A. *J. Chem. Soc. A*, **1971**, 341–346.

(232) Brock, D. S.; Casalis de Pury, J. J.; Mercier, H. P. A.; Schrobilgen, G. J.; Silvi, B. *J. Am. Chem. Soc.* **2010**, *132*, 3533–3542.

(233) Sundaraganesan, N.; Anand, B.; Meganathan, C.; Dominic Joshua, B.; Saleem, H. *Spectrochim. Acta, Part A* **2008**, *69*, 198–204.

(234) Selig, H.; Peacock, R. D. *J. Am. Chem. Soc.* **1964**, *86*, 3895.

(235) Frlec, B.; Holloway, J. H. *J. Chem. Soc., Chem. Commun.* **1973**, 370–371.

(236) Frlec, B.; Holloway, J. H. *J. Chem. Soc., Chem. Commun.* **1974**, 89–90.

(237) Gillespie, R. J.; Schrobilgen, G. J. *J. Chem. Soc., Chem. Commun.* **1974**, 90–92.

(238) Holloway, J. H.; Schrobilgen, G. J. *J. Chem. Soc., Chem. Commun.* **1975**, 623–624.

(239) Frlec, B.; Holloway, J. H. *Inorg. Chem.* **1976**, *15*, 1263–1270.

(240) Žemva, B.; Slivnik, J.; Šmalc, A. *J. Fluorine Chem.* **1975**, *6*, 191–193.

(241) Lutar, K.; Jesih, A.; Žemva, B. *Polyhedron* **1988**, *7*, 1217–1219.

(242) Bougon, R.; Huy, T. B. *Compt. Rend.* **1976**, *C283* , 461–463.

(243) Gillespie, R. J.; Spekkens, P. *J. Chem. Soc., Dalton Trans.* **1977**, 1539–1546.

(244) Ellern, A.; Boatz, J. A.; Christe, K. O.; Drews, T.; Seppelt, K. *Z. Anorg. Allg. Chem.* **2002**, *628*, 1991–1999.

(245) Leopold, D.; Seppelt, K. *Angew. Chem., Int. Ed. Engl.* **1994**, *33*, 975–976; *Angew. Chem.* **1994**, *106*, 1043–1044.

(246) Hwang, I.-C.; Kuschel, R.; Seppelt, K. *Z. Anorg. Allg. Chem.* **1997**, *623*, 379–383.

(247) Lehmann, J. F.; Riedel, S.; Schrobilgen, G. J. *Inorg. Chem.* **2008**, *47*, 8343–8356.

(248) Bowater, I. C.; Brown, R. D.; Burden, F. R. *J. Mol. Spectrosc.* **1968**, *28*, 461–470.

(249) Vij, A.; Tham, F. S.; Vij, V.; Wilson, W. W.; Christe, K. O. *Inorg. Chem.* **2002**, *41*, 6397–6403.

(250) Pilmé, J.; Robinson, E. A.; Gillespie, R. J. *Inorg. Chem.* **2006**, *45*, 6198–6204.

(251) Bader, R. F. W. *Atoms in Molecules: A Quantum Theory*, Oxford University Press: Oxford, 1990.

(252) Silvi, B.; Savin, A. *Nature* **1994**, *371*, 683–686.

(253) Becke, A. D.; Edgecombe, K. E. *J. Chem. Phys.* **1990**, *92*, 5397–5403.

(254) Parr, R. G.; Yang, W. *Density-Functional Theory of Atoms and Molecules*, Oxford University Press: Oxford, 1989; pp 90–98.

(255) Martin, D.; Gillespie, R. J.; Schrobilgen, G. J. *J. Chem. Soc., Dalton Trans.* **1980**, 1898–1903.

(256) Holloway, J. H.; Schrobilgen, G. J. *Inorg. Chem.* **1980**, *19*, 2632–2640.

(257) Jones, G. R.; Burbank, R. D.; Bartlett, N. *Inorg. Chem.* **1970**, *9*, 2264–2268.

(258) Burns, J. H.; Ellison, R.D.; Levy, H.A. *Acta Crystallogr.* **1965**, *18*, 11–16.

(259) Bartlett, N.; Wechsberg, M. *Z. Anorg. Allg. Chem.* **1971**, *385*, 5–17.

(260) Gillespie, R. J.; Morton, M. J. *Chem. Commun.* **1968**, *24*, 1565–1567.

(261) $XeF_{2(g)} \longrightarrow XeF^{+}_{(g)} + F^{-}_{(g)}$: $\Delta H_{rxn}{}^{o} = +921.4$ kJ mol^{-1}; $\Delta G_{rxn}{}^{o} = +885.0$ kJ mol^{-1} MP2/(aug-)cc-pVTZ(-PP).
$XeF_{4(g)} \longrightarrow XeF_{3}{}^{+}_{(g)} + F^{-}_{(g)}$: $\Delta H_{rxn}{}^{o} = +951.0$ kJ mol^{-1}; $\Delta G_{rxn}{}^{o} = +920.0$ kJ mol^{-1} MP2/(aug-)cc-pVTZ(-PP).

(262) Bunič, T.; Tavčar, G.; Tramšek, M.; Žemva, B. *Inorg. Chem.* **2006**, *45*, 1038–1042.

(263) Tavčar, G.; Žemva, B. *Inorg. Chem.* **2005**, *44*, 1525–1529.

(264) Tramšek, M.; Benkič, T.; Žemva, B. *Inorg. Chem.* **2004**, *43*, 699–703.

(265) Tramšek, M.; Benkič, T.; Žemva, B. *Angew. Chem. Int. Ed.* **2004**, *43*, 3456–3458.

(266) Bougon, R.; Cicha, W. V.; Lance, M.; Meublat, L.; Nierlich, M.; Vigner, J. *Inorg. Chem.* **1991**, *30*, 102–109.

(267) Antipin, M. Y.; Ellern, A. M.; Sukhoverkhov, V. F.; Struchkov, Y. T.; Buslaev, Y. A. *Dokl. Akad. Nauk SSSR* **1987**, *293*, 1152–1155; *Dokl. Akad. SSSR, Engl.* **1987**, *293*, 354.

(268) Mallouk, T. E.; Rosenthal, G. L.; Müller, G.; Brusasco, R.; Bartlett, N. *Inorg. Chem.* **1984**, *23*, 3167–3173.

(269) Tobias, K. M.; Jansen, M. *Z. Anorg. Allg. Chem.* **1987**, *550*, 16–26.

(270) Oberhammer, H.; Christe, K. O. *Inorg. Chem.* **1982**, *21*, 273–275.

(271) Ferguson, R. C. *J. Am. Chem. Soc.* **1954**, *76*, 850–853.

(272) Burke-Laing, M. E.; Trueblood, K. N. *Acta Crystallogr., Sect. B* **1977**, *33*, 2698–2699.

(273) Christe, K. O.; Zhang, X.; Sheehy, J. A.; Bau, R. *J. Am. Chem. Soc.* **2001**, *123*, 6338–6348.

(274) Gillespie, R. J.; Robinson, E. A.; Pilmé, J. *Chem. Eur. J.* **2010**, *16,* 3663–3675.

(275) Musher, J. I. *J. Am. Chem. Soc.* **1968**, *90*, 7371–7372.

(276) Eisenberg, M.; DesMarteau, D. D. *Inorg. Chem.* **1972**, *11*, 1901–1904.

(277) Naumann, D.; Tyrra, W.; Gnann, R.; Pfolk, D. *J. Chem. Soc., Chem. Commun.* **1994**, 2651–2653.

(278) Bartlett, N.; Wechsberg, M.; Jones, G. R.; Burbank, R. D. *Inorg. Chem.* **1972**, *11*, 1124–1127.

(279) Wechsberg, M.; Bulliner, P. A.; Sladky, F. O.; Mews, R.; Bartlett, N. *Inorg. Chem.* **1972**, *11*, 3063–3070.

(280) Seppelt, K.; Nothe, D. *Inorg. Chem.* **1973**, *12*, 2727–2730.

(281) Syvret, R. G.; Schrobilgen, G. J. *Inorg. Chem.* **1989**, *28*, 1564–1573.

(282) Seppelt, K.; Lentz, D. *Inorg. Synth.* **1986**, *24*, 27–31.

(283) Beattie, I. R. *Prog. Inorg. Chem.* **1963**, *5*, 1–26.

(284) Dailey, B. P.; Shoolery, J. N. *J. Am. Chem. Soc.* **1955**, *77*, 3977–3981.

(285) Huggins, M. L. *J. Am. Chem. Soc.* **1953**, *75*, 4123–4126.

(286) Moran, M. D.; Brock, D. S.; Mercier, H. P. A.; Schrobilgen, G. J. *J. Am. Chem. Soc.* **2010**, *132*, 13823–13839.

(287) Khadzhi-Ogly, M. R.; Yagodovskaya, T. V.; Nekrasov, L. I. *Zh. Fiz. Khim.* **1981**, *55*, 3124–3127.

(288) Khadzhi-Ogly, M. R.; Yagodovskaya, T. V.; Nekrasov, L. I. *Zh. Fiz. Khim.* **1982**, *56*, 1807–1809.

(289) Bradley, R. S. *Trans. Faraday Soc.* **1956**, *52*, 1255–1259.

(290) Wartel, M.; Boughriet, A.; Fischer, J. C. *Anal. Chem. Acta* **1979**, *110*, 211–217.

(291) Mercier, H. P. A.; Moran, M. D.; Schrobilgen, G. J.;Steinberg, C.; Suontamo, R. J. *J. Am. Chem. Soc.* **2004**, *126*, 5533–5548, and references therein.

(292) G.J. Schrobilgen, Final Technical Report No. PL-TR-93-3007, Aug. 1993, Contract F04611-91-K-0004, Phillips Laboratory, Propulsion Directorate, USAF Systems Command, Edwards Air Force Base, CA, vol. 1, part IV, pp. 1–11.

(293) Whalley, E. *Trans. Faraday Soc.* **1957**, *53*, 1578–1585.

(294) *CRC Handbook of Chemistry and Physics,* 81st ed. Lide, D.R., Ed.; CRC Press: Boca Raton, FL, 2000; Chapter 4, 42.

(295) Christe, K. O.; Charpin, P.; Soulie, E.; Bougon, R.; Fawcett, J.; Russell, D. R. *Inorg. Chem.*, **1984**, *23*, 3756–3766.

(296) Johnson, M. W.; Sándor, E.; Arzi, E. *Acta Crystallogr. Sect. B* **1975**, *B31*, 1998–2003.

(297) The entropy of solid H_2O was calculated from the $\Delta H_{\mathrm{fusion}}(H_2O)$ and melting point of water obtained from *CRC Handbook of Chemistry and Physics,* 81st ed. Lide, D.R., Ed.; CRC Press: Boca Raton, FL, 2000; Chapter 1, 10., and from the entropy of liquid water obtained from ref 195.

(298) Runtz, G. R.; Bader, R. F. W.; Messer, R. R. *Can. J. Chem.* **1977**, *55*, 3040–3045.

(299) Bader, R. F. W. *J. Phys. Chem. A* **1998**, *102*, 7314–7323.

(300) Fradera, X.; Austen, M. A.; Bader, R. F. W. *J. Phys. Chem. A* **1998**, *103*, 304–314.

(301) Savin, A.; Becke, A. D.; Flad, J.; Nesper, R.; Preuss, H.; von Schnering, H. G. *Angew. Chem. Int. Ed. Engl.* **1991**, *30*, 409–412.

(302) Silvi, B. *J. Phys. Chem. A* **2003**, *107*, 3081–3085.

(303) Kohout, M.; Pernal, K.; Wagner, F. R.; Grin, Y. *Theor. Chem. Acc.* **2004**, *112*, 453–459.

(304) Silvi, B. *J. Mol. Struct.* **2002**, *614*, 3–10.

(305) Silvi, B. *Phys. Chem. Chem. Phys.* **2004**, *6*, 256–260.

(306) Bader, R. F. W.; Stephens, M. E. *Chem. Phys. Lett.* **1974**, *26*, 445–449.

(307) Cances, E.; Keriven, R.; Lodier, F.; Savin, A. *Theor. Chem. Acc.* **2004**, *111*, 373–380.

(308) Savin, A.; Silvi, B.; Colonna, F. *Can. J. Chem.* **1996**, *74*, 1088–1096.

(309) Calatayud, M.; Andrés, J.; Beltrán, A.; Silvi, B. *Theor. Chem. Acc.* **2001**, *105*, 299–308.

(310) Raub, S.; Jansen, G. *Theor. Chem. Acc.* **2001**, *106*, 223–232.

(311) Shaik, S.; Maitre, P.; Sini, G.; Hiberty, P. C. *J. Am. Chem. Soc.* **1992**, *114*, 7861–7866.

(312) Shaik, S.; Danovich, D.; Silvi, B.; Lauvergnat, D.; Hiberty, P. *Chem. Eur. J.* **2005**, *21*, 6358–6371.

(313) Shaik, S.; Danovich, D.; Wu, W.; Hiberty, P. *Nature Chemistry* **2009**, *1*, 443–449.

(314) Sanderson, R. T. *Polar Covalence*. Academic Press: New York, NY, 1983.

(315) Preut, H.; Bernstein, D.; Minkwitz, R. *Acta Crystallogr., Sect. C* **1991**, *C47*, 176–177.

(316) Churney, K. L.; Nuttall, R. L., *N.B.S. Tables of Chemical Thermodynamic Properties*. Selected Values for Inorganic, C1, and C2 Organic Substances in SI uits. *J. Phys. Chem. Ref. Data,* Vol. *11*, Supplement No. 2, **1982,** 1–392.

(317) (a) O'Hare, P. A. G. *J. Chem. Thermodyn.* **1993**, *25*, 391–402. (b) Nagarajan, G. *Bull. Soc. Chim. Belg.* **1962**, *71*, 324–328.

(318) Latimer, W. M. "*Oxidation Potentials*", 2nd Ed., Prentice Hall: Englewood Cliffs, New Jersey, **1961,** Appendix III, p. 359.

(319) Latimer, W. M. *J. Am. Chem. Soc.* **1921,** *43*, 818–826.

(320) Burgess, J.; Peacock, R. D.; Sherry, R. J. *J. Fluorine Chem.* **1982,** *20,* 541–554.

APPENDIX 1

Table A1.1. Experimental and Calculated (C_{3v}) Vibrational Frequencies for $CH_3C\equiv N$

expt[b,c]	calc		assgnts
	SVWN[d,e]	MP2[d,f]	(C_{3v}) symmetry
2999.0(54)	3062(65)[<1]	3193.6(55)[<1]	ν_5(E), ν_{as}(CH$_3$)
2937.9(97)	2981(186)[<1]	3100.1(159)[2]	ν_1(A$_1$), ν_s(CH$_3$)
2911.7(1) 2885.7(2) 2849.8(1)			2ν_6
2736.3(6)			2ν_3
2295.1(2)			$\nu_3 + \nu_4$
2248.4(100)	2332(71)[14]	2218.0(38)[~0]	ν_2(A$_1$), ν(C≡N)
1457.3(11) 1454.3(7) 1425.2(3) 1420.8(4)	1391(8)[14]	1495.8(7)[10]	ν_6(E), CH$_3$ def. as
1375.6(15) 1370.8(3)	1335(9)[10]	1417.8(4)[2]	ν_3(A$_1$), CH$_3$ def. s
1042.3(1)	999(<<1)[5]	1065.8(<<1)[2]	ν_7(E), ρ_r(CH$_3$)
921.5(20)	959(4)[<1]	934.7(5)[1]	ν_4(A$_1$), ν(C-C)
399.9(3) 395.0(12) 392.0(9) 386.8(5)	377(2)[<<1]	361.0(2)[<1]	ν_8(E), δ(CCN)
116.4(18) 107.6(13) 102.3(15) 95.5(32)			lattice modes

[a] Frequencies are given in cm^{-1}. [b] Present work. [c] The Raman spectrum of CH$_3$CN was recorded in a 5-mm glass tube at −150 °C using 1064-nm excitation. Values in parentheses denote Raman intensities. [d] SDB-cc-pVTZ. Values in parentheses denote Raman intensities (Å^4 amu^{-1}). Values in square brackets denote infrared intensities (km mol^{-1}). [e] Calculated bond lengths (Å): N–C, 1.155; C–C, 1.433. [f] Calculated bond lengths (Å): N–C, 1.169; C–C, 1.457.

Table A1.2. Experimental Vibrational Frequencies[a] for $CH_3CN \cdot m HF$

expt[b,c]	assgnts [d]
3016.9(40)	$\nu_{as}(CH_3)$
2950.2(80)	$\nu_s(CH_3)$
2724.8(3)	overtone (2 x 1367.5)
2313.2(48)	combination mode (1367.5 + 935.9)
2286.0(100)	$\nu(C{\equiv}N)$
1449.6(14) 1414.3(31)	CH_3 def. as
1367.5(68)	CH_3 def. s
935.9(40)	$\nu(C\text{-}C)$
392.4(57)	$\delta(CCN)$
131.3(22) 113.2(17) 70.8(14) 59.9(17)	lattice modes

[a] Frequencies are given in cm^{-1}. [b] Present work. The sample was prepared from a 2:1 molar ratio of HF and CH_3CN. [c] The Raman spectrum of $CH_3CN \cdot m HF$ was recorded in a ¼ -in FEP tube at −150 °C using 1064-nm excitation. Values in parentheses denote Raman intensities. [d] Because the structure of $CH_3CN \cdot m HF$ is unknown, the vibrational mode descriptions are based on those of CH_3CN and do not take into account possible coupling with associated HF. The modes corresponding to associated HF were not observed.

Table A1.3. Calculated Vibrational Frequencies[a] and Geometries for $Xe^{16/18}OF_2{\cdot}HF$ (O---H Coordinated)

calc[b]				assgnts	
SVWN[c]		MP2[d]		(C_1) symmetry	
$Xe^{16}OF_2{\cdot}HF$	$Xe^{18}OF_2{\cdot}HF$	$Xe^{16}OF_2{\cdot}HF$	$Xe^{18}OF_2{\cdot}HF$		
3268.8(92)[644]	3260.8(92)[650]	3826.4(51)[468]	3831.0(51)[468]	ν_1	ν(HF) + minor ν(O---H-F)
962.6(5)[367]	968.5(5)[366]	738.1(6)[318]	733.7(6)[326]	ν_2	δ(O---H-F)
762.6(16)[26]	724.4(14)[25]	897.1(8)[49]	852.7(9)[39]	ν_3	ν(XeO)
747.3(<1)[101]	750.0(<1)[100]	623.8(1)[270]	620.8(1)[289]	ν_4	HF o.o.p. wag
584.3(<1)[179]	585.9(<1)[180]	584.3(<1)[67]	584.0(<1)[49]	ν_5	$\nu_{as}(XeF_2)$ + minor HF o.o.p. wag
518.6(25)[8]	518.6(25)[8]	521.3(36)[10]	521.3(36)[10]	ν_6	$\nu_s(XeF_2)$
347.6(2)[46]	336.6(1)[41]	286.9(4)[1]	276.1(4)[<1]	ν_7	$\delta(F_HXeO)$
248.8(4)[1]	239.5(4)[1]	245.8(1)[62]	239.4(1)[59]	ν_8	$\rho_{rock}(XeOF_2)$ i.p. + minor HF o.o.p. wag
204.2(<<1)[21]	204.8(<<1)[21]	214.0(<1)[6]	213.5(<1)[4]	ν_9	$\delta(XeF_2)$ o.o.p.
162.9(<1)[20]	162.7(<1)[20]	182.8(<1)[29]	182.7(<1)[29]	ν_{10}	$\delta(XeF_2)$ i.p.
119.7(<1)[9]	118.9(<1)[9]	85.6(<1)[11]	84.4(<1)[11]	ν_{11}	$\rho_{rock}(XeOF_2)$ o.o.p. + ν(HF---Xe)
43.9(2)[<1]	44.3(2)[1]	41.1(<1)[<<1]	40.6(1)[<1]	ν_{12}	XeF_2 torsion about XeO bond

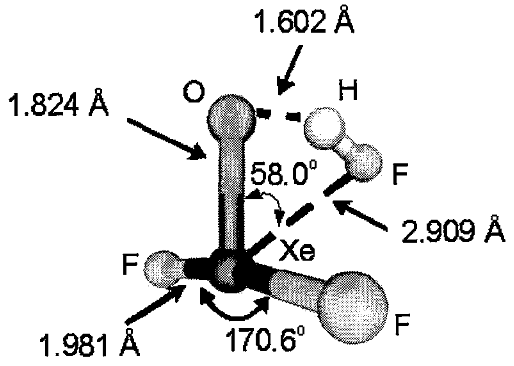

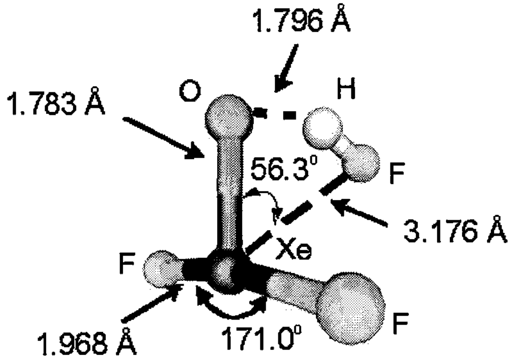

[a] Frequencies are given in cm^{-1}. [b] Values in parentheses denote Raman intensities ($Å^4$ amu^{-1}). Values in square brackets denote infrared intensities (km mol^{-1}). [c] SVWN/SDB-cc-pVTZ. [d] MP2/SDB-cc-pVTZ.

Table A1.4. Calculated Vibrational Frequencies[a] for $Xe^{16/18}OF_2{\cdot}DF$ (O---D Coordinated)

calc[b]					assgnts
SVWN[c]		MP2[d]			(C_1) symmetry
$Xe^{16}OF_2{\cdot}DF$	$Xe^{18}OF_2{\cdot}DF$	$Xe^{16}OF_2{\cdot}DF$	$Xe^{18}OF_2{\cdot}DF$		
2368.4(48)[338]	2368.3(48)[338]	2776.0(27)[243]	2780.2(27)[243]	ν_1	ν(DF) + minor ν(O---D-F)
763.2(15)[36]	724.6(14)[37]	897.6(9)[62]	851.7(9)[56]	ν_3	ν(XeO)
694.2(3)[160]	693.6(3)[159]	540.0(11)[88]	537.0(14)[78]	ν_2	δ(O---D-F)
591.9(<<1)[243]	591.6(<<1)[242]	598.1(<1)[264]	598.0(<1)[263]	ν_5	$\nu_{as}(XeF_2)$ + minor DF o.o.p. wag
537.1(<<1)[5]	536.0(<<1)[6]	443.3(<1)[33]	438.3(<1)[34]	ν_4	DF o.o.p. wag
518.4(25)[9]	518.3(25)[10]	516.7(27)[56]	515.2(25)[70]	ν_6	$\nu_s(XeF_2)$
342.1(2)[51]	330.5(2)[45]	240.6(1)[67]	235.0(1)[62]	ν_7	$\delta(F_DXeO)$
246.7(4)[<1]	237.8(4)[<<1]	283.8(4)[<1]	273.5(4)[<1]	ν_8	$\rho_{rock}(XeOF_2)$ + minor DF o.o.p. wag
204.7(~0)[20]	204.7(~0)[20]	213.5(<1)[4]	212.1(<1)[2]	ν_9	$\delta(XeF_2)$ o.o.p.
163.0(<1)[21]	162.7(<1)[20]	182.8(<1)[31]	182.5(<1)[31]	ν_{10}	$\delta(XeF_2)$ i.p.
119.4(<<1)[8]	118.6(<1)[8]	85.5(<1)[10]	84.1(<1)[11]	ν_{11}	$\rho_{rock}(XeOF_2)$ o.o.p. + ν(DF---Xe)
44.3(2)[<<1]	44.2(2)[<1]	41.0(1)[<1]	40.4(1)[<1]	ν_{12}	XeF_2 torsion about XeO bond

[a] Frequencies are given in cm^{-1}. [b] Values in parentheses denote Raman intensities ($Å^4$ amu^{-1}). Values in square brackets denote infrared intensities (km mol^{-1}). [c] SVWN/SDB-cc-pVTZ. [d] MP2/SDB-cc-pVTZ.

Table A1.5. Calculated Vibrational Frequencies[a] and Geometries for $F_2{}^{16/18}OXe \cdot HF$ (F---H Coordinated)

calc[b]				assgnts
SVWN[c]		MP2[d]		(C_1) symmetry
$Xe^{16}OF_2 \cdot HF$	$Xe^{18}OF_2 \cdot HF$	$Xe^{16}OF_2 \cdot HF$	$Xe^{18}OF_2 \cdot HF$	
3121.8(68)[414]	3124.7(68)[413]	3894.1(27)[246]	3894.1(27)[246]	ν(HF)
1007.8(9)[404]	1006.6(9)[404]	664.6(5)[258]	664.8(5)[257]	δ(F---H-F)
802.1(30)[36]	762.6(27)[35]	954.7(11)[57]	907.5(10)[51]	ν(XeO)
781.8(1)[101]	780.5(1)[101]	575.5(1)[133]	575.5(8)[132]	HF o.o.p. wag
549.2(6)[178]	550.1(6)[180]	550.5(8)[330]	551.5(8)[334]	$\nu_{as}(XeF_2)$
477.7(18)[12]	477.6(18)[11]	477.9(32)[52]	478.0(32)[52]	$\nu_s(XeF_2)$
306.0(6)[76]	305.6(6)[77]	279.2(2)[93]	278.0(1)[90]	δ(HF---XeF) + minor ρ_{rock}(HF---XeO)
228.9(3)[10]	220.4(2)[10]	240.8(5)[7]	233.0(4)[10]	$\rho_{rock}(XeOF_2)$ + minor δ(HF---XeO)
189.7(<<1)[14]	189.6(<<1)[14]	209.7(<<1)[14]	210.0(<<1)[14	$\delta(XeF_2)$ o.o.p.
185.6(<<1)[13]	185.3(<<1)[12]	145.9(<1)[6]	145.6(<<1)[6]	minor $\delta(XeF_2)$ i.p. + ν(HF---Xe)
102.5(<1)[2]	102.0(<1)[2]	81.4(<1)[8]	81.2(<1)[8]	$\delta(XeF_2)$ i.p. - minor ν(HF---Xe)
87.1(<1)[3]	84.9(<1)[3]	58.8(1)[5]	57.1(1)[4]	δ(HF---XeF) o.o.p. - δ(FXeO) o.o.p.

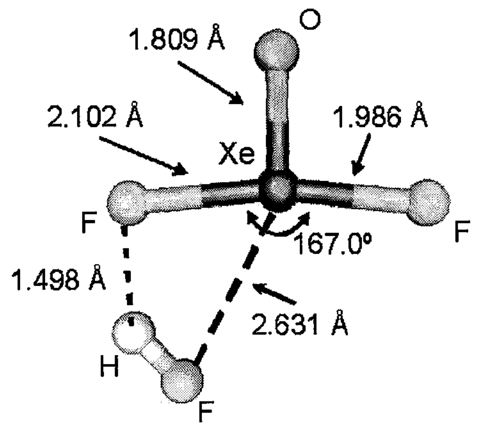

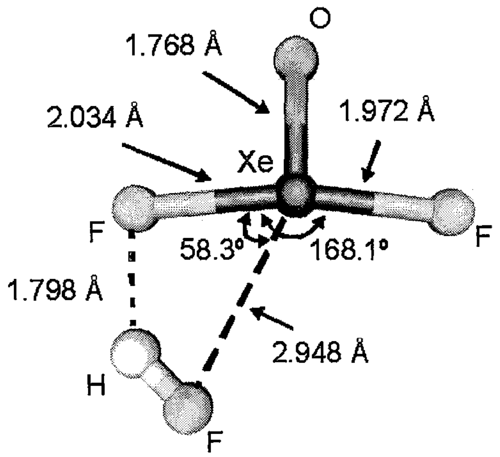

[a] Frequencies are given in cm^{-1}. [b] Values in parentheses denote Raman intensities ($Å^4$ amu^{-1}). Values in square brackets denote infrared intensities (km mol^{-1}). [c] SVWN/SDB-cc-pVTZ. [d] MP2/SDB-cc-pVTZ.

Table A1.6. Calculated Vibrational Frequencies[a] for $F_2{}^{16/18}OXe\cdot DF$ (F---D Coordinated)

calc[b]				assgnts
SVWN[c]		MP2[d]		(C_1) symmetry
$Xe^{16}OF_2\cdot DF$	$Xe^{18}OF_2\cdot DF$	$Xe^{16}OF_2\cdot DF$	$Xe^{18}OF_2\cdot DF$	
2268.7(36)[217]	2268.7(36)[217]	2824.0(14)[129]	2824.0(14)[129]	ν(DF)
803.2(31)[31]	762.7(28)[25]	955.6(11)[64]	907.2(10)[58]	ν(XeO)
724.6(3)[3]	724.5(3)[194]	464.0(4)[254]	463.9(4)[255]	δ(F---D-F)
564.4(<1)[57]	564.4(<1)[57]	417.1(<1)[76]	417.1(<1)[76]	DF o.o.p. wag
549.0(6)[188]	548.9(6)[188]	573.0(3)[159]	572.9(3)[158]	$\nu_{as}(XeF_2)$
476.2(19)[10]	476.1(19)[10]	482.7(35)[6]	482.7(35)[6]	$\nu_s(XeF_2)$
302.8(6)[78]	302.5(6)[78]	272.9(2)[101]	271.6(2)[98]	δ(DF---XeF) + minor ρ_{rock}(DF---XeO)
228.9(3)[11]	220.5(2)[10]	240.1(5)[7]	240.0(4)[10]	$\rho_{rock}(XeOF_2)$ + minor δ(DF---XeO)
189.4(<<1)[11]	188.5(<<1)[13]	208.9(<<1)[13]	208.5(<<1)[12]	$\delta(XeF_2)$ o.o.p.
183.7(<<1)[2]	183.1(<<1)[11]	144.1(<<1)[5]	143.4(<<1)[5]	minor $\delta(XeF_2)$ i.p. + ν(DF---Xe)
102.3(<1)[2]	101.9(<1)[2]	81.2(<1)[8]	81.0(<1)[8]	$\delta(XeF_2)$ i.p. - minor ν(DF---Xe)
87.0(<1)[3]	84.8(<1)[3]	58.8(1)[5]	57.0(1)[4]	δ(DF---XeF) o.o.p. - δ(FXeO) o.o.p.

[a] Frequencies are given in cm^{-1}. [b] Values in parentheses denote Raman intensities ($Å^4$ amu^{-1}). Values in square brackets denote infrared intensities (km mol^{-1}). [c] SVWN/SDB-cc-pVTZ. [d] MP2/SDB-cc-pVTZ.

Table A1.7. Calculated Vibrational Frequencies[a] and Geometries for $F_2{}^{16/18}OXe \cdot 2HF$

calc[b]				assgnts
SVWN[c]		MP2[d]		(C_1) symmetry
$Xe^{16}OF_2 \cdot 2HF$	$Xe^{18}OF_2 \cdot 2HF$	$Xe^{16}OF_2 \cdot 2HF$	$Xe^{18}OF_2 \cdot 2HF$	
3348.9(123)[564]	3348.9(123)[564]	3988.6(42)[297]	3988.6(42)[297]	ν_s(HF)
3331.2(19)[51]	3331.(19)[51]	3983.4(7)[92]	3983.4(7)[92]	ν_{as}(HF)
914.3(19)[524]	914.3(19)[524]	570.4(12)[351]	570.3(12)[352]	δ(F3---H-F5) + δ(F4---H-F7)
870.9(<<1)[228]	871.1(<<1)[227]	595.5(1)[26]	596.5(1)[25]	δ(F3---H-F5) − δ(F4---H-F7)
801.9(41)[41]	762.3(38)[33]	960.0(12)[56]	912.6(11)[50]	ν(XeO)
705.0(<<1)[208]	705.0(<<1)[208]	498.1(<1)[243]	498.1(<1)[243]	H-F5---Xe---F7-H o.o.p. wag
697.2(2)[~0]	697.2(2)[~0]	491.6(2)[38]	491.6(2)[38]	H-F5---Xe---F7-H o.o.p. twist
500.3(<<1)[196]	501.0(<<1)[198]	469.2(1)[548]	469.5(1)[549]	$\nu_{as}(XeF_2)$
459.3(23)[1]	459.3(23)[1]	467.6(38)[22]	467.6(38)[22]	$\nu_s(XeF_2)$
326.5(10)[63]	326.5(10)[63]	231.1(2)[89]	231.1(2)[89]	δ(H-F5---XeF3) + δ(H-F7---XeF4)
325.1(3)[74]	323.6(3)[77]	286.0(5)[13]	276.8(5)[16]	$\rho_{rock}(XeOF_2)$
223.7(<<1)[25]	215.2(<<1)[21]	153.9(<1)[35]	152.8(<1)[34]	$\rho_{rock}(XeOF_{2H})$
175.0(<<1)[8]	174.6(<<1)[7]	207.6(<<1)[39]	207.3(<<1)[36]	$\delta(XeF_2)$ o.o.p.
165.0(<<1)[19]	165.1(<<1)[19]	127.8(<1)[6]	127.9(<1)[6]	ν_s(HF---Xe) + minor $\delta(XeF_2)$ i.p.
138.7(<<1)[9]	138.8(<<1)[9]	83.2(1)[4]	82.1(1)[14]	ν_{as}(HF---Xe)
126.8(<<1)[<<1]	126.9(<<1)[<<1]	63.5(1)[4]	63.5(<1)[4]	$\delta(XeF_{2H})$ i.p.
86.2(1)[3]	83.7(1)[3]	-26.8(1)[16]	-26.1(<1)[15]	δ(HF---XeF) o.o.p. - δ(HF---XeO) o.o.p.
20.6(<<1)[0]	20.6(<<1)[0]	28.2(<1)[<<1]	28.2(<1)[<<1]	XeF_2 & XeF_{2H} torsions about XeO bond

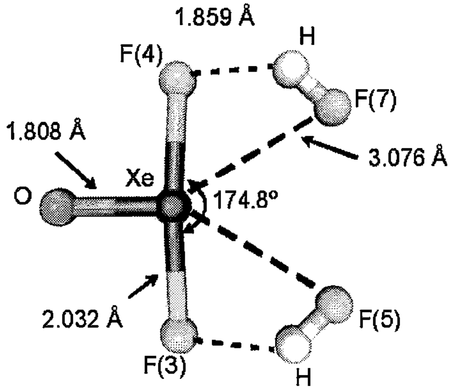

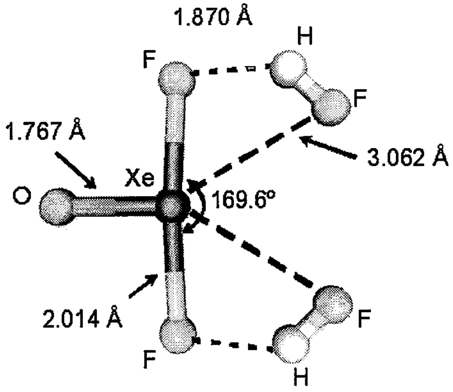

---

[a] Frequencies are given in cm^{-1}. [b] Values in parentheses denote Raman intensities ($Å^4$ amu^{-1}). Values in square brackets denote infrared intensities (km mol^{-1}). [c] SVWN/SDB-cc-pVTZ. [d] MP2/SDB-cc-pVTZ.

Table A1.8. Calculated Vibrational Frequencies[a] for $F_2{}^{16/18}OXe{\cdot}2DF$

calc[b]		assgnts
SVWN[c]		(C_1) symmetry
$Xe^{16}OF_2{\cdot}2DF$	$Xe^{18}OF_2{\cdot}2DF$	
2431.2(65)[294]	2431.2(65)[294]	ν_s(DF)
2418.1(9)[28]	2418.1(9)[28]	ν_{as}(DF)
803.0(38)[35]	762.4(34)[32]	ν(XeO)
656.0(9)[263]	655.8(9)[264]	δ(F3---D-F5) + δ(F4---D-F7)
635.3(<<1)[57]	635.3(<<1)[57]	δ(F3---D-F5) – δ(F4---D-F7)
510.5(<<1)[116]	510.5(<<1)[116]	D-F5---Xe---F7-D o.o.p. wag
502.6(<1)[<<1]	502.6(1)[<<1]	D-F5---Xe---F7-D o.o.p. twist
497.7(<1)[214]	497.6(<1)[214]	$\nu_{as}(XeF_2)$
457.4(24)[3]	457.4(24)[3]	$\nu_s(XeF_2)$
323.7(10)[69]	323.6(10)[68]	δ(D-F5---XeF3) + δ(D-F7---XeF4)
319.5(3)[75]	317.5(3)[79]	$\rho_{rock}(XeOF_2)$
221.5(<1)[29]	213.0(<1)[24]	$\rho_{rock}(XeOF_{2D})$
173.6(<1)[7]	172.5(<1)[6]	$\delta(XeF_2)$ o.o.p.
164.2(<1)[18]	164.0(<1)[18]	ν_s(DF---Xe) + minor $\delta(XeF_2)$ i.p.
138.3(<<1)[8]	138.3(<<1)[8]	ν_{as}(DF---Xe)
125.1(<1)[<<1]	125.0(<1)[<<1]	$\delta(XeF_{2D})$ i.p.
86.3(1)[3]	83.7(1)[3]	δ(DF---XeF) o.o.p. - δ(DF---XeO) o.o.p.
20.5(<1)[<<1]	20.5(<1)[<<1]	XeF_2 & XeF_{2D} torsions about XeO bond

[a] Frequencies are given in cm^{-1}. [b] Values in parentheses denote Raman intensities ($Å^4$ amu^{-1}). Values in square brackets denote infrared intensities (km mol^{-1}). [c] SVWN/SDB-cc-pVTZ.

Table A1.9. Calculated Vibrational Frequencies[a] for $(F_2{}^{16/18}OXe)_2$ Dimer

calc[b]		assgnts
SVWN[c]		(C_1) symmetry
$(Xe^{16}OF_2)_2$	$(Xe^{18}OF_2)_2$	
790.9(82)[59]	752.0(73)[55]	ν(Xe5O6)
756.8(48)[72]	719.4(48)[66]	ν(Xe1O2)
586.0(2)[198]	587.5(1)[199]	ν(Xe1F3 – Xe1F4)
540.9(8)[177]	542.0(8)[179]	ν(Xe5F7 – Xe5F8)
516.4(32)[23]	516.3(31)[23]	ν(Xe1F3 + Xe1F4)
457.3(21)[31]	457.3(22)[30]	ν(Xe5F8 + Xe5F7)
260.3(3)[6]	250.2(3)[6]	$\rho_{rock}(Xe1OF_2)$
238.2(14)[21]	228.9(14)[15]	$\rho_{rock}(Xe5OF_2)$ - ν(Xe1O2 + Xe5O2)
230.0(<1)[25]	224.3(1)[34]	$\rho_{rock}(Xe5OF_2)$ + ν(Xe1O2 + Xe5O2)
202.8(<1)[15]	202.4(<1)[14]	$\delta(Xe5F_2)$ o.o.p.
200.5(3)[24]	198.0(4)[19]	$\delta(Xe5F_2)$ i.p. + $\delta(Xe1F_2)$ o.o.p.
191.4(1)[3]	189.6(1)[3]	$\delta(Xe1F_2)$ o.o.p. + minor $\delta(Xe5F_2)$ i.p.
169.3(<1)[17]	169.3(<1)[18]	$\delta(Xe1F_2)$ i.p.
94.6(<1)[<1]	94.1(<1)[<1]	coupled deformations
89.2(1)[2]	86.4(1)[1]	
63.4(<1)[1]	63.2(<1)[2]	
35.8(1)[<1]	35.6(2)[<1]	
22.4(2)[<<1]	22.2(3)[<<1]	

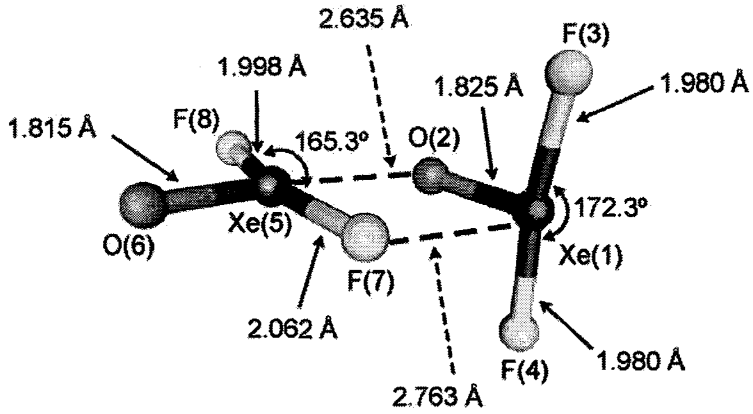

[a] Frequencies are given in cm^{-1}. [b] Values in parentheses denote Raman intensities ($Å^4$ amu^{-1}). Values in square brackets denote infrared intensities (km mol^{-1}). [c] SVWN/SDB-cc-pVTZ.

Table A1.10. Calculated Vibrational Frequencies[a] and Geometries for $(Xe^{16/18}OF_2)_3$

calc[b]		assgnts
SVWN[c]		(C_1) symmetry
$(Xe^{16}OF_2)_3$	$(Xe^{18}OF_2)_3$	
787.3(103)[66]	748.6(94)[62]	ν(Xe9O12)
753.9(9)[28]	716.5(8)[26]	ν(Xe1O4 – Xe5O4) + ν(Xe9O8 – Xe5O8)
734.4(345)[259]	698.4(307)[238]	ν(Xe1O4 – Xe5O4) – ν(Xe9O8 – Xe5O8)
592.1(1)[190]	593.7(1)[191]	ν(Xe1F2 – Xe1F3)
553.3(10)[178]	554.5(10)[179]	ν(Xe5F6 – Xe5F7)
537.3(9)[188]	538.4(9)[190]	ν(Xe9F10 – Xe9F11)
521.9(22)[30]	521.9(22)[31]	ν(Xe1F2 + Xe1F3)
471.2(82)[39]	471.2(84)[37]	ν(Xe5F6 + Xe5F7)
458.0(12)[15]	457.9(12)[14]	ν(Xe9F10 + Xe9F11)
272.5(13)[27]	261.2(11)[25]	ν(Xe9O8 + Xe5O8) + ρ_{rock}(Xe1OF$_2$)
253.3(17)[12]	243.0(13)[11]	ρ_{rock}(Xe1OF$_2$)
248.6(17)[15]	239.3(16)[9]	ν(Xe1O4 + Xe5O4) + ρ_{rock}(Xe5OF$_2$)
239.5(<1)[33]	231.1(<1)[39]	ν(Xe1O4 + Xe5O4) + ν(Xe9O8 + Xe5O8)
228.2(3)[8]	221.7(4)[12]	ρ_{rock}(Xe9OF$_2$)
209.6(6)[23]	209.1(6)[21]	δ(Xe9F$_2$) o.o.p.
202.7(1)[6]	202.3(1)[5]	δ(Xe5F$_2$) i.p. + δ(Xe1F$_2$) o.o.p. + δ(Xe9F$_2$) o.o.p.
197.8(5)[16]	195.8(6)[13]	δ(Xe1F$_2$) o.o.p. + δ(Xe9F$_2$) o.o.p.
193.6(5)[24]	191.7(4)[22]	δ(Xe9F$_2$) i.p. + δ(Xe5F$_2$) o.o.p.
186.2(2)[16]	184.9(3)[14]	δ(Xe5F$_2$) o.o.p.
168.9(1)[20]	168.8(1)[20]	Coupled deformation modes
111.0(<1)[<1]	110.0(<1)[<1]	
95.2(<1)[<1]	93.4(<1)[<1]	
85.0(1)[1]	84.0(1)[1]	
67.2(1)[<1]	66.9(1)[<1]	
60.5(<1)[2]	60.3(1)[2]	
48.4(2)[<1]	48.1(2)[<1]	
37.6(3)[<1]	37.3(3)[<1]	
25.6(1)[<<1]	25.6(1)[<<1]	
19.5(2)[<<1]	19.5(2)[<<1]	
10.4(1)[<1]	10.4(1)[<1]	

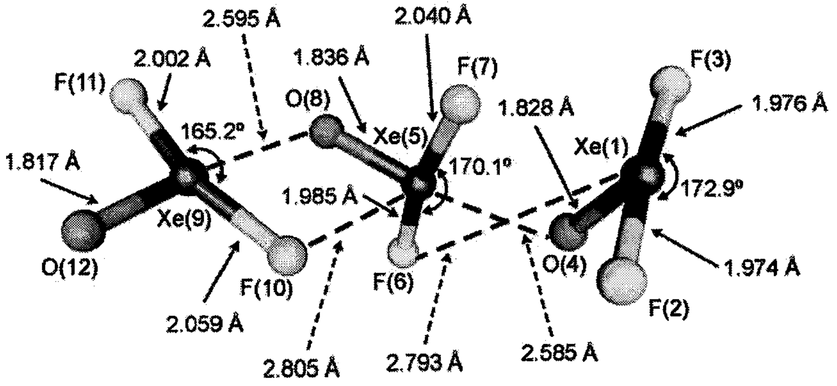

[a] Frequencies are given in cm^{-1}. [b] Values in parentheses denote Raman intensities (Å^4 amu^{-1}). Values in square brackets denote infrared intensities (km mol^{-1}). [c] SVWN/SDB-cc-pVTZ.

Table A1.11. Comparison of Calculated Vibrational Frequencies and Geometries for $XeOF_2$ Using Different Levels of Theory and Basis Sets

Frequencies (cm^{-1})												
exptl	B3LYP				SVWN				MP2			CCSD(T)
	321G	ccpVTZ	SDDAll	DZVP	ccpVTZ	ccpVQZ	SDDAll	DZVP	ccpVTZ	ccpVQZ	SDDAll	ccpVTZ
750.0(60)	727(3)	734(13)	713(12)	653(11)	795(22)	809(23)	788(23)	753(22)	939(60)	947(60)	928(64)	747
n.o.	658(34)	556(240)	558(261)	559(210)	572(213)	578(223)	573(234)	572(188)	582(252)	587(267)	582(9)	581
468.0(100)	563(3)	494(6)	496(7)	480(6)	505(7)	514(8)	506(9)	489(8)	509(7)	525(8)	507(9)	517
297.8(11)	271(6)	258(3)	253(3)	230(4)	244(3)	249(3)	240(3)	224(5)	283(3)	285(3)	279(4)	267
256.1(1) 251.6, sh	235(18)	209(23)	209(23)	211(24)	200(21)	204(19)	199(21)	193(22)	218(25)	219(22)	216(25)	217
175.5(1) 153.3(6)	218(15)	175(17)	177(18)	173(20)	155(14)	161(13)	153(14)	155(16)	176(19)	180(18)	173(20)	188
Geometrical Parameters												
Xe-O Å	1.885	1.817	1.828	1.881	1.809	1.795	1.818	1.851	1.770	1.763	1.782	1.811
Xe-F Å	1.978	1.999	1.999	2.050	1.996	1.975	1.998	2.039	1.980	1.963	1.990	1.974
F-Xe-F °	171.9	169.4	169.9	180.0	167.1	167.4	167.2	167.4	168.2	168.7	167.8	170.7
O-Xe-F °	94.0	95.3	95.1	94.7	96.4	96.3	96.4	96.3	95.9	95.7	96.1	94.6

Table A1.12. Calculated Vibrational Frequencies[a] and Geometries for XeF_4 (D_{4h})

frequencies			
exptl[b]	SVWN[c]	MP2[c]	assgnts[d]
586	590(225)	603(245)	$\nu(E_u)$, $\nu_{as}(XeF_t\text{-}XeF_t)$
543	547(<<1)	545(0)	$\nu(A_{1g})$, $\nu_s(XeF_4)$
502	514(<<1)	513(0)	$\nu(B_{1g})$, $\nu_{as}(XeF_{2t}\text{-}XeF_{2t})$
291	272(31)	295(39)	$\nu(A_{2u})$, $\delta(XeF_4)$ o.o.p., umbrella mode
235	196(0)	217(0)	$\nu(B_{2g})$, $\delta(XeF_{2c}+XeF_{2c})$
(221)	150(0)	166(0)	$\nu(B_{2u})$, $\delta(XeF_{2t})$ o.o.p. – $\delta(XeF_{2t})$ o.o.p.
123	140(0)	160(3)	$\nu(E_u)$, $\delta(XeF_{2t})$ i.p.
Bond Lengths (Å)			
Xe-F	1.971	1.960	

---

[a] Frequencies are given in cm^{-1}. [b] From *Mol. Phys.* **1965**, *9*, 449-454. [c] Values in parentheses denote infrared intensities (km mol^{-1}). [c] (SDB-)cc-pVTZ. [d] The abbreviations denote trans (t), cis (c), symmetric (s), asymmetric (as), stretch (ν), bend (δ), in-plane bend (i.p.), and out-of-plane bend (o.o.p.). The in-plane and out-of-plane mode descriptions are relative to the XeF_4 plane.

Table A2.1. Calculated Vibrational Frequencies [a] and Infrared and Raman Intensities [b] for the $Xe^{16/18}OF_3^-$ Anion [c]

				$Xe^{16}OF_3^-$			
MP2	SVWN5	BP86	PBE1PBE	B3LYP	B3PW91	MPW1PW91	assgnt [d]
880.0(37)[328]	716.2(47)[158]	670.6(47)[144]	746.3(60)[152]	706.1(62)[146]	730.2(58)[151]	742.9(60)[150]	$\nu(XeO)$
477.7(1)[297]	479.0(<1)[270]	434.0(<1)[250]	492.9(<0.1)[323]	465.7(<1)[302]	478.9(<1)[307]	491.5(<0.1)[321]	$\nu_{as}(XeF_{2a})$
457.7(29)[205]	443.5(29)[105]	401.9(34)[103]	454.1(38)[65]	425.4(40)[80]	439.1(38)[75]	452.4(38)[65]	$\nu_s(XeF_{2a}) + \nu(XeF_b)$
352.3(37)[14]	388.2(21)[33]	343.9(28)[22]	377.5(13)[113]	358.1(18)[84]	370.1(16)[92]	375.9(13)[111]	$\nu_s(XeF_{2a}) - \nu(XeF_b)$
277.3(<1)[53]	248.0(<1)[41]	234.2(<1)[40]	260.4(<1)[49]	247.7(<1)[48]	255.0(<1)[46]	260.0(<1)[49]	$\delta(XeOF_3)$ o.o.p.
230.8(5)[<1]	214.6(5)[4]	211.2(6)[1]	245.9(4)[1]	235.0(5)[1]	240.0(4)[1]	246.4(4)[1]	$\rho_{rock}(OXeF_{2a})$ i.p.
158.9(1)[2]	161.1(<0.1)[4]	158.5(<0.1)[3]	178.8(<1)[2]	173.2(<1)[2]	176.1(<1)[2]	179.5(<1)[2]	$\delta(XeF_{2a})$ i.p.
127.4(<1)[<1]	122.0(<1)[<<1]	111.7(<1)[<0.1]	133.1(<1)[<1]	124.3(<1)[<0.1]	128.1(<1)[<0.1]	132.4(<1)[<1]	$[\delta(OXeF_b) - \delta(XeF_{2a})]$ o.o.p.
163.6(<1)[3]	130.6(<1)[2]	132.9(<1)[2]	122.0(1)[1]	126.2(1)[1]	126.5(1)[1]	123.2(1)[1]	$[\rho_{rock}(OXeF_{2a}) + \delta(F_bXeF_a)]$ i.p.

				$Xe^{18}OF_3^-$			
MP2	SVWN5	BP86	PBE1PBE	B3LYP	B3PW91	MPW1PW91	assgnt [c]
836.4(33)[302]	681.7(40)[152]	638.3(41)[139]	709.9(53)[146]	671.8(54)[140]	694.7(51)[144]	706.7(52)[144]	$\nu(XeO)$
479.0(1)[297]	480.2(<1)[271]	435.2(<1)[250]	494.2(<<1)[324]	466.9(<1)[303]	480.2(<1)[308]	492.8(<0.1)[321]	$\nu_{as}(XeF_{2a})$
458.2(29)[204]	443.2(30)[101]	401.6(35)[100]	454.2(38)[64]	425.4(41)[78}	439.1(39)[74]	452.5(38)[64]	$\nu_s(XeF_{2a}) + \nu(XeF_b)$
352.4(37)[14]	388.1(21)[32]	343.8(28)[21]	377.3(13)[111]	357.9(18)[82]	369.9(16)[90]	375.7(13)[109]	$\nu_s(XeF_{2a}) - \nu(XeF_b)$
273.2(<1)[51]	244.7(<1)[39]	231.1(<1)[38]	257.5(<1)[47]	244.8(<1)[47]	252.0(<1)[46]	257.0(<1)[47]	$\delta(XeOF_3)$ o.o.p.
224.0(5)[<1]	207.3(5)[1]	204.0(5)[1]	237.2(4)[1]	226.8(4)[1]	231.7(4)[1]	237.8(4)[1]	$\rho_{rock}(OXeF_{2a})$ i.p.
158.8(1)[2]	161.1(<0.1)[3]	158.5(<<1)[3]	178.9(<1)[2]	173.2(<1)[2]	176.2(<1)[2]	179.5(<1)[2]	$\delta(XeF_{2a})$ i.p.
126.3(<1)[<1]	120.7(<1)[<0.1]	110.5(<1)[<0.1]	131.3(<1)[<1]	122.7(<1)[<0.1]	126.4(<1)[<0.1]	130.6(<1)[<1]	$[\delta(OXeF_b) - \delta(XeF_{2a})]$ o.o.p.
161.8(<1)[2]	129.8(<1)[2]	132.1(<1)[2]	121.5(1)[1]	125.5(1)[1]	125.8(1)[1]	122.6(1)[1]	$[\rho_{rock}(OXeF_{2a}) + \delta(F_bXeF_a)]$ i.p.

[a] Frequencies are given in cm^{-1}. [b] Values in parentheses denote calculated Raman intensities ($Å^4\ u^{-1}$). Values in square brackets denote calculated infrared intensities ($km\ mol^{-1}$). [c] The aug-cc-pVDZ(-PP) basis set was used. [d] The abbreviations denote symmetric (s), asymmetric (as), stretch (ν), bend (δ), rock (ρ_{rock}), in-plane bend (i.p.), and out-of-plane bend (o.o.p.). The in-plane and out-of-plane mode descriptions are relative to the $XeOF_{2a}F_b$ plane (see Figure 5.3 and footnote *h* of Table 5.1).

Table A2.2. Experimental and Calculated Vibrational Frequencies[a] and Infrared and Raman Intensities for $Xe^{16/18}OF_2$

exptl[a]	calcd[b]							assgnt[c]
	$Xe^{16}OF_2$							
	MP2	SVWN5	BP86	PBE1PBE	B3LYP	B3PW91	MPW1PW91	
749.9(83)	953.2(12)[66]	798.1(19)[24]	746.0(20)[21]	784.5(18)[18]	740.5(19)[15]	772.4(18)[18]	776.6(18)[16]	$\nu(XeO)$
[525.2(2)]	582.4(<1)[279]	572.0(<1)[231]	534.2(1)[217]	583.5(<1)[275]	557.3(<1)[260]	571.2(<1)[264]	582.2(<1)[274]	$\nu_{as}(XeF_2)$
467.8(100)	517.3(45)[9]	505.6(32)[9]	465.8(36)[10]	528.6(35)[7]	498.3(38)[8]	513.0(36)[8]	527.1(35)[7]	$\nu_s(XeF_2)$
298.1(13)	279.0(4)[3]	241.6(4)[3]	230.2(4)[3]	269.9(4)[4]	252.0(4)[3]	261.7(4)[3]	269.1(4)[3]	$\rho_{rock}(XeOF_2)$ i.p.
256.2(2) 251.4(1)	219.3(<0.1)[23]	202.9(<0.1)[19]	195.3(<0.1)[20]	215.6(<0.1)[21]	207.3(<0.1)[22]	211.5(<0.1)[21]	228.3(<0.1)[21]	$\delta(XeF_2)$ o.o.p.
175.7(1) 154.0(6)	174.4(<1)[19]	155.6(<1)[13]	145.2(<1)[13]	186.4(<1)[17]	172.7(<1)[17]	178.6(<1)[16]	190.5(<1)[17]	$\delta(XeF_2)$ i.p.
	$Xe^{18}OF_2$							
712.8(84)	905.9(11)[61]	758.7(17)[23]	709.1(18)[20]	745.6(16)[17]	703.7(17)[15]	734.0(16)[17]	776.7(18)[16]	$\nu(XeO)$
[525.0(2)]	583.9(<1)[280]	573.5(<1)[232]	535.6(1)[218]	585.0(<1)[276]	558.8(21)[261]	572.6(<1)[265]	582.2(<1)[274]	$\nu_{as}(XeF_2)$
467.8(100)	517.3(45)[9]	505.6(32)[9]	465.8(36)[10]	528.6(35)[8]	498.3(38)[8]	513.1(36)[8]	527.1(35)[7]	$\nu_s(XeF_2)$
289.0(14)	268.3(3)[3]	232.4(4)[3]	221.5(4)[2]	259.6(4)[3]	242.4(4)[3]	251.7(4)[3]	269.1(4)[3]	$\rho_{rock}(XeOF_2)$ i.p.
256.2(2) 251.8(1)	219.7(<0.1)[23]	203.2(<0.1)[19]	195.5(<0.1)[19]	216.1(<0.1)[21]	207.7(<0.1)[22]	211.9(<0.1)[21]	228.3(<0.1)[21]	$\delta(XeF_2)$ o.o.p.
175.7(1) 154.0(6)	174.5(<1)[19]	155.6(<1)[13]	145.3(<1)[13]	186.6(<1)[17]	172.8(<1)[17]	178.7(<1)[16]	190.5(<1)[17]	$\delta(XeF_2)$ i.p.

[a] Values in parentheses denote relative Raman intensities and are from ref 125. The value in square brackets is the corresponding mode observed in $F_2OXeNCCH_3$. [b] The aug-cc-pVTZ(-PP) basis set was used. Values in parentheses denote Raman intensities ($Å^4$ u^{-1}). Values in square brackets denote infrared intensities (km mol^{-1}). [c] The abbreviations denote symmetric (s), asymmetric (as), stretch (ν), bend (δ), rock (ρ_{rock}), in-plane bend (i.p.), and out-of-plane bend (o.o.p.). The in-plane and out-of-plane mode descriptions are relative to the $XeOF_2$ plane (Figure 5.1).

Table A2.3. Calculated Geometrical Parameters for the XeOF$_3^-$ Anion [a]

	MP2	SVWN5	BP86	PBE1PBE	B3LYP	B3PW91	MPW1PW91
			bond lengths (Å)				
Xe-F$_a$	2.096	2.086	2.139	2.061	2.094	2.078	2.063
Xe-O	1.854	1.890	1.918	1.866	1.889	1.876	1.867
Xe-F$_b$	2.131	2.148	2.198	2.183	2.205	2.188	2.185
			bond angles (deg)				
O-Xe-F$_a$	96.0	94.2	93.9	93.1	93.2	93.3	93.1
F$_a$-Xe-F$_b$	84.0	85.8	86.1	86.9	86.8	86.7	86.9
F$_a$-Xe-F$_a$	168.0	171.7	172.3	173.8	173.5	173.5	173.9

[a] The aug-cc-pVDZ(-PP) basis set was used.

APPENDIX 3

The standard enthalpies for the solid-state decomposition of $[XeOF][AsF_6]$ (eq A3.1), $[HOXeF_2][AsF_6]$ (eq A3.2), $[HOXe(F)_2OXeF_2][AsF_6]$ (eq A3.3), $[FXeOXeF_2][AsF_6]$ (eq A3.4), and $[FXeOXe(F)_2OXeF_2][AsF_6]$ (eq A3.5), as well as the hydrolyses of $[HOXe(F)_2OXeF_2][AsF_6]$ (eq A3.6), $[FXeOXeF_2][AsF_6]$ (eq A3.7), and $[FXeOXe(F)_2OXeF_2][AsF_6]$ (eq A3.8), were evaluated from the corresponding gas-phase

$$[XeOF][AsF_6]_{(s)} \longrightarrow [XeF][AsF_6]_{(s)} + \tfrac{1}{2}O_{2\,(g)} \qquad (A3.1)$$

$$[HOXeF_2][AsF_6]_{(s)} \longrightarrow [XeF][AsF_6]_{(s)} + \tfrac{1}{2}O_{2\,(g)} + HF_{(l)} \qquad (A3.2)$$

$$[HOXe(F)_2OXeF_2][AsF_6]_{(s)} \longrightarrow [Xe_2F_3][AsF_6]_{(s)} + O_{2\,(g)} + HF_{(l)} \qquad (A3.3)$$

$$[FXeOXeF_2][AsF_6]_{(s)} \longrightarrow [Xe_2F_3][AsF_6]_{(s)} + \tfrac{1}{2}O_{2\,(g)} \qquad (A3.4)$$

$$[FXeOXe(F)_2OXeF_2][AsF_6]_{(s)} \longrightarrow [Xe_2F_3][AsF_6]_{(s)} + O_{2(g)} + XeF_{2(s)} \qquad (A3.5)$$

$$3[HOXe(F)_2OXeF_2][AsF_6]_{(s)} + 3H_2O_{(l)} \longrightarrow$$
$$2[Xe_3OF_3][AsF_6]_{(s)} + 3O_{2\,(g)} + 6HF_{(l)} + [H_3O][AsF_6]_{(s)} \qquad (A3.6)$$

$$3[FXeOXeF_2][AsF_6]_{(s)} + 3H_2O_{(l)} \longrightarrow$$
$$2[Xe_3OF_3][AsF_6]_{(s)} + \tfrac{3}{2}O_{2\,(g)} + 3HF_{(l)} + [H_3O][AsF_6]_{(s)} \qquad (A3.7)$$

$$[FXeOXe(F)_2OXeF_2][AsF_6]_{(s)} + H_2O_{(l)} \longrightarrow$$
$$[Xe_3OF_3][AsF_6]_{(s)} + O_{2\,(g)} + 2HF_{(l)} \qquad (A3.8)$$

decompositions, lattice enthalpies of $[XeOF][AsF_6]$, $[HOXeF_2][AsF_6]$, $[HOXe(F)_2OXeF_2][AsF_6]$, $[FXeOXeF_2][AsF_6]$, $[FXeOXe(F)_2OXeF_2][AsF_6]$, $[XeF][AsF_6]$, $[Xe_2F_3][AsF_6]$, $[Xe_3OF_3][AsF_6]$, and $[H_3O][AsF_6]$ (Table A3.1), ΔH°(sub XeF_2) = 55.71 kJ mol^{-1},[213] ΔH°(sub H_2O) = 56.0 kJ mol^{-1},[293] ΔH°(vap H_2O) = 44.01 kJ mol^{-1},[294] and ΔH°(vap HF) = 28.68 kJ mol^{-1}.[195] The lattice enthalpies were estimated by use of the volume-based method of Bartlett et al.[208,209] as generalized by Jenkins et al.[210,211] in eq A3.9, where R is the gas constant (8.314 J mol^{-1} K^{-1}), I is the ionicity of the

$$\Delta H^\circ_L = 2I\left(\frac{\alpha}{\sqrt[3]{V_m}} + \beta\right) + pRT \qquad (A3.9)$$

salt and the constants, α, β, and p, depend on the nature of the salt. For the salts under investigation, which are singly charged and the following values were used: $I = 1$, α = 117.3 nm kJ mol^{-1}, β = 51.9 kJ mol^{-1}, and $p = 2$. In this formalism, ΔH°_L is the lattice enthalpy and is defined as the energy required to break the crystal lattice, and therefore has a positive value. This approach is generally accurate to ~4% for salts with ΔH°_L less than 5000 kJ mol^{-1},[211] and is particularly useful because the formula unit volume (V_m) of an unknown salt can be estimated with reasonable accuracy using several methods.[211] The values of $V_m([H_3O][AsF_6])$ = 0.1287 nm^3, $V_m([Xe_3OF_3][AsF_6])$ = 0.2634 nm^3, $V_m([XeF][AsF_6])$ = 0.1490 nm^3, and $V_m([Xe_2F_3][AsF_6])$ = 0.2327 nm^3 were determined directly from the X-ray crystal structures of $[H_3O][AsF_6]$,[295] $[XeF][AsF_6]$,[45] and $[Xe_2F_3][AsF_6]$,[45] respectively. The value for $V_m([XeOF][AsF_6])$ = 0.1558 nm^3 was determined from eq A3.10. Where $V_m(XeOF_2)$ = 0.0708,[126] $V_-(F^-)$ = 0.025(10),[211] and $V_-(AsF_6^-)$[211] = 0.110(7) nm^3. The value for $V_m[HOXeF_2][AsF_6])$ = 0.1745 nm^3 was determined from eq A3.11, where $V_m(HF)$ = 0.0187.[296] The values for

$V_m([HOXe(F)_2OXeF_2][AsF_6]) = 0.2453$ nm^3, $V_m([FXeOXeF_2][AsF_6]) = 0.2198$ nm^3, and $V_m([FXeOXe(F)_2OXeF_2][AsF_6]) = 0.2906$ nm^3, were determined from eq A3.12–14, respectively. Application of eq A3.9 yields ΔH^{o}_{L} for the salts which are listed in Table

$$V_m([XeOF][AsF_6]) = V_m(XeOF_2) - V_{-}(F^-) + V_{-}(AsF_6^-) = 0.1558\ \text{nm}^3 \quad (A3.10)$$

$$V_m([HOXeF_2][AsF_6]) = V_m(XeOF_2) + V_m(HF) - V_{-}(F^-) + V_{-}(AsF_6^-) = 0.1745\ \text{nm}^3 \quad (A3.11)$$

$$V_m([HOXe(F)_2OXeF_2][AsF_6]) = 2V_m(XeOF_2) + V_m(HF) - V_{-}(F^-) + V_{-}(AsF_6^-) = 0.2453\ \text{nm}^3 \quad (A3.12)$$

$$V_m([FXeOXeF_2][AsF_6]) = V_m(XeOF_2) + V_m([XeF][AsF_6]) = 0.2198\ \text{nm}^3 \quad (A3.13)$$

$$V_m([FXeOXe(F)_2OXeF_2][AsF_6]) = 2V_m(XeOF_2) + V_m([XeF][AsF_6]) = 0.2906\ \text{nm}^3 \quad (A3.14)$$

A3.1.The enthalpies, $\Delta H_{298.15}$ and $\Delta H_{195.15}$, for eqs A3.1—8 are listed in Table 6.1 and have been calculated by eqs A3.15–30.

$$\Delta H_{298.15}(A3.1) = \Delta H^{o}_{L}([XeOF][AsF_6]) - \Delta H^{o}_{L}([XeF][AsF_6]) + \Delta H_{(g)(298.15)}(A3.1) \quad (A3.15)$$
$$= 544.7 - 551.3 + (-288.0) = -294.6\ \text{kJ mol}^{-1}$$

$$\Delta H_{195.15}(A3.1) = \Delta H^{o}_{L}([XeOF][AsF_6]) - \Delta H^{o}_{L}([XeF][AsF_6]) + \Delta H_{(g)(195.15)}(A3.1) \quad (A3.16)$$
$$= 543.0 - 549.6 + (-288.2) = -294.8\ \text{kJ mol}^{-1}$$

$$\Delta H_{298.15}(A3.2) = \Delta H^{o}_{L}([HOXeF_2][AsF_6]) - \Delta H^{o}_{L}([XeF][AsF_6]) + \Delta H_{(g)(298.15)}(A3.2) \quad (A3.17)$$
$$= 528.6 - 551.3 + (-125.5) = -148.3\ \text{kJ mol}^{-1}$$

$$\Delta H_{195.15}(A3.2) = \Delta H^{o}_{L}([HOXeF_2][AsF_6]) - \Delta H^{o}_{L}([XeF][AsF_6]) + \Delta H_{(g)(298.15)}(A3.2) - \Delta H^{o}(\text{vap HF}) \quad (A3.18)$$
$$= 526.9 - 549.6 + (-209.3) - 28.68 = -260.7\ \text{kJ mol}^{-1}$$

$$\Delta H_{298.15}(A3.3) = \Delta H^{o}_{L}([HOXe(F)_2OXeF_2][AsF_6]) - \Delta H^{o}_{L}([Xe_2F_3][AsF_6]) + \Delta H_{(g)(298.15)}(A3.3) \quad (A3.19)$$
$$= 483.5 - 490.2 + (-543.2) = -549.9\ \text{kJ mol}^{-1}$$

$$\Delta H_{195.15}(A3.3) = \Delta H^{o}_{L}([HOXe(F)_2OXeF_2][AsF_6]) - \Delta H^{o}_{L}([Xe_2F_3][AsF_6]) + \Delta H_{(g)(195.15)}(A3.3) - \Delta H^{o}(\text{vap HF}) \quad (A3.20)$$
$$= 481.8 - 488.5 + (-385.7) - 28.68 = -421.1\ \text{kJ mol}^{-1}$$

$$\Delta H_{298.15}(A3.4) = \Delta H^{o}_{L}([FXeOXeF_2][AsF_6]) - \Delta H^{o}_{L}([Xe_2F_3][AsF_6]) + \Delta H_{(g)(298.15)}(A3.4) \quad (A3.21)$$
$$= 497.5 - 490.2 + (-209.9) = -202.6\ \text{kJ mol}^{-1}$$

$$\Delta H_{195.15}(A3.4) = \Delta H^{o}_{L}([FXeOXeF_2][AsF_6]) - \Delta H^{o}_{L}([Xe_2F_3][AsF_6]) + \Delta H_{(g)(195.15)}(A3.4) \quad (A3.22)$$
$$= 495.8 - 488.5 + (-213.0) = -205.7\ \text{kJ mol}^{-1}$$

$$\Delta H_{298.15}(A3.5) = \Delta H^{o}_{L}([FXeOXe(F)_2OXeF_2][AsF_6]) - \Delta H^{o}_{L}([Xe_2F_3][AsF_6]) + \Delta H_{(g)(298.15)}(A3.5) - \Delta H^{o}(\text{sub } XeF_2) \quad (A3.23)$$
$$= 462.9 - 490.2 + (-572.5) + 55.71 = -544.1\ \text{kJ mol}^{-1}$$

$$\Delta H_{195.15}(A3.5) = \Delta H^{o}_{L}([FXeOXe(F)_2OXeF_2][AsF_6]) - \Delta H^{o}_{L}([Xe_2F_3][AsF_6]) +$$

$\Delta H_{(g)(195.15)}(\mathrm{A3.5}) - \Delta H^{\circ}(\mathrm{sub\ XeF_2})$ (A3.24)
$= 461.2 - 488.5 + (-413.7) + 55.71 = -385.1\ \mathrm{kJ\ mol^{-1}}$

$\Delta H_{298.15}(\mathrm{A3.6}) = 3\Delta H^{\circ}_{L}([\mathrm{HOXe(F)_2OXeF_2}][\mathrm{AsF_6}]) - 2\Delta H^{\circ}_{L}([\mathrm{Xe_3OF_3}][\mathrm{AsF_6}]) +$
$\Delta H_{(g)(298.15)}(\mathrm{A3.6}) + 3\Delta H^{\circ}(\mathrm{vap\ H_2O}) -$
$\Delta H^{\circ}_{L}([\mathrm{H_3O}][\mathrm{AsF_6}])$ (A3.25)
$= 3(483.5) - 2(474.7) + (-1908.6) + 3(44.01) - 573.4$
$= -1845.5\ \mathrm{kJ\ mol^{-1}}$

$\Delta H_{195.15}(\mathrm{A3.6}) = 3\Delta H^{\circ}_{L}([\mathrm{HOXe(F)_2OXeF_2}][\mathrm{AsF_6}]) - 2\Delta H^{\circ}_{L}([\mathrm{Xe_3OF_3}][\mathrm{AsF_6}]) +$
$\Delta H_{(g)(298.15)}(\mathrm{A3.6}) + 3\Delta H^{\circ}(\mathrm{sub\ H_2O}) -$
$\Delta H^{\circ}_{L}([\mathrm{H_3O}][\mathrm{AsF_6}]) - 6\Delta H^{\circ}(\mathrm{vap\ HF})$ (A3.26)
$= 3(481.8) - 2(473.0) + (-1250.4) + 3(56.0) - 571.7 - 6(28.68)$
$= -1326.8\ \mathrm{kJ\ mol^{-1}}$

$\Delta H_{298.15}(\mathrm{A3.7}) = 3\Delta H^{\circ}_{L}([\mathrm{FXeOXeF_2}][\mathrm{AsF_6}]) - 2\Delta H^{\circ}_{L}([\mathrm{Xe_3OF_3}][\mathrm{AsF_6}]) +$
$\Delta H_{(g)(298.15)}(\mathrm{A3.7}) + 3\Delta H^{\circ}(\mathrm{vap\ H_2O}) -$
$\Delta H^{\circ}_{L}([\mathrm{H_3O}][\mathrm{AsF_6}])$ (A3.27)
$= 3(497.5) - 2(474.7) + (-713.0) + 3(44.01) - 573.4$
$= -611.3\ \mathrm{kJ\ mol^{-1}}$

$\Delta H_{195.15}(\mathrm{A3.7}) = 3\Delta H^{\circ}_{L}([\mathrm{FXeOXeF_2}][\mathrm{AsF_6}]) - 2\Delta H^{\circ}_{L}([\mathrm{Xe_3OF_3}][\mathrm{AsF_6}]) +$
$\Delta H_{(g)(195.15)}(\mathrm{A3.7}) + 3\Delta H^{\circ}(\mathrm{sub\ H_2O}) -$
$\Delta H^{\circ}_{L}([\mathrm{H_3O}][\mathrm{AsF_6}]) - 3\Delta H^{\circ}(\mathrm{vap\ HF})$ (A3.28)
$= 3(495.8) - 2(473.0) + (-722.1) + 3(56.0) - 571.7 - 3(28.68)$
$= -670.4\ \mathrm{kJ\ mol^{-1}}$

$\Delta H_{298.15}(\mathrm{A3.8}) = \Delta H^{\circ}_{L}([\mathrm{FXeOXe(F)_2OXeF_2}][\mathrm{AsF_6}]) - \Delta H^{\circ}_{L}([\mathrm{Xe_3OF_3}][\mathrm{AsF_6}]) +$
$\Delta H_{(g)(298.15)}(\mathrm{A3.8}) + \Delta H^{\circ}(\mathrm{vap\ H_2O})$ (A3.29)
$= 462.9 - 474.7 + (-662.4) + 44.01 = -630.4\ \mathrm{kJ\ mol^{-1}}$

$\Delta H_{195.15}(\mathrm{A3.8}) = \Delta H^{\circ}_{L}([\mathrm{FXeOXe(F)_2OXeF_2}][\mathrm{AsF_6}]) - \Delta H^{\circ}_{L}([\mathrm{Xe_3OF_3}][\mathrm{AsF_6}]) +$
$\Delta H_{(g)(195.15)}(\mathrm{A3.8}) + \Delta H^{\circ}(\mathrm{sub\ H_2O}) - 2\Delta H^{\circ}(\mathrm{vap\ HF})$(A3.30)
$= 461.2 - 473.0 + (-425.5) + 56.0 - 2(28.68) = -438.6\ \mathrm{kJ\ mol^{-1}}$

A method for estimating the absolute standard entropy of a salt from its unit volume has been reported by Jenkins and Glasser (eq A3.31) where $k = 1360\ \mathrm{J\ mol^{-1}\ K^{-1}}$ ($\mathrm{nm^{-3}}$ formula unit^{-1}) and $c = 15\ \mathrm{J\ mol^{-1}\ K^{-1}}$.[212] The standard entropies of the salts under

$$S^{\circ} = kV_{\mathrm{m}} + c \qquad \text{(A3.31)}$$

consideration are listed in Table A3.1. When coupled with the experimental standard entropies of $\mathrm{O_{2(g)}}$ (206 $\mathrm{J\ mol^{-1}\ K^{-1}}$),[195] $\mathrm{XeF_{2(g)}}$ (115.09 $\mathrm{J\ mol^{-1}\ K^{-1}}$),[213] $\mathrm{HF_{(g)}}$ (173.779 $\mathrm{J\ mol^{-1}\ K^{-1}}$),[195] $\mathrm{HF_{(l)}}$ (75.40 $\mathrm{J\ mol^{-1}\ K^{-1}}$),[195] $\mathrm{H_2O_{(l)}}$ (69.91 $\mathrm{J\ mol^{-1}\ K^{-1}}$),[195] and $\mathrm{H_2O_{(s)}}$ (47.91 $\mathrm{J\ mol^{-1}\ K^{-1}}$),[297] this method allows ΔS° and ΔG° to be calculated from eqs A3.32 and A3.33, respectively, with the values listed in Table 6.1.

$$\Delta S^{\circ} = S^{\circ}(\mathrm{products}) - S^{\circ}([\mathrm{XeONO_2}][\mathrm{AsF_6}]_{(s)}) \qquad \text{(A3.32)}$$

$$\Delta G^{\circ} = \Delta H^{\circ} - \mathrm{T}\Delta S^{\circ} \qquad \text{(A3.33)}$$

Table A3.1. Estimated Volumes, Lattice Enthalpies, and Entropies for $[XeOF][AsF_6]$, $[HOXeF_2][AsF_6]$, $[HOXe(F)_2OXeF_2][AsF_6]$, $[FXeOXeF_2][AsF_6]$, $[FXeOXe(F)_2OXeF_2][AsF_6]$, $[XeF][AsF_6]$, $[Xe_2F_3][AsF_6]$, $[Xe_3OF_3][AsF_6]$, and $[H_3O][AsF_6]$

Salt	V_m (nm^3)	ΔH_L° (kJ mol^{-1})		S° (J mol^{-1} K^{-1})
		298.15 K	195.15 K	
$[XeOF][AsF_6]$	0.1558	544.7	543.0	226.9
$[HOXeF_2][AsF_6]$	0.1745	528.6	526.9	252.3
$[HOXe(F)_2OXeF_2][AsF_6]$	0.2453	483.5	481.8	348.6
$[FXeOXeF_2][AsF_6]$	0.2198	497.5	495.8	313.9
$[FXeOXe(F)_2OXeF_2][AsF_6]$	0.2906	462.9	461.2	410.2
$[XeF][AsF_6]$	0.149	551.3	549.6	217.6
$[Xe_2F_3][AsF_6]$	0.2327	490.2	488.5	331.5
$[Xe_3OF_3][AsF_6]$	0.2634	474.7	473.0	373.2
$[H_3O][AsF_6]$	0.1287	573.4	571.7	190.0

Table A3.2. Calculated Bond Lengths (Å) and Bond Angles (deg) for the XeF_3^+ (C_{2v}) Cation and $XeF_3^+\cdot HF$ Adduct and a Complete List of Experimental and Calculated Geometrical Parameters for $([XeF_3\cdot HF][Sb_2F_{11}])_2\cdot[H_5F_4][SbF_6]$, $[XeF_3\cdot HF][Sb_2F_{11}]$, and the $[XeF_3][SbF_6]$ Ion Pair

	XeF_3^+		
	calcd[a]		
	B3LYP	PBE1PBE	MP2
Xe(1)-F(1)	1.906	1.884	1.883
Xe(1)-F(2)	1.867	1.845	1.838
Xe(1)-F(3)	1.906	1.884	1.883
F(1)-Xe(1)-F(2)	84.2	83.7	83.3
F(1)-Xe(1)-F(3)	168.4	167.3	166.6
F(2)-Xe(1)-F(3)	84.2	83.7	83.3

	$XeF_3^+\cdot HF$				
	exptl		calcd[a]		
	$([XeF_3\cdot HF][Sb_2F_{11}])_2\cdot[H_5F_4][SbF_6]$	$[XeF_3\cdot HF][Sb_2F_{11}]$	B3LYP	PBE1PBE	MP2
Xe(1)-F(1)	1.880(2)	1.865(1)	1.916	1.894	1.892
Xe(1)-F(2)	1.838(2)	1.865(1)	1.870	1.847	1.839
Xe(1)-F(3)	1.890(2)	2.186(2)	1.916	1.894	1.892
Xe(1)---F(10)	2.462(2)	2.186(2)	2.556	2.537	2.550
F(10)-H			0.937	0.933	0.934
F(1)-Xe(1)-F(2)	81.4(1)	81.40(8)	84.7	84.1	83.7
F(1)-Xe(1)-F(3)	162.3(1)	161.12(6)	169.3	168.3	167.4
F(1)-Xe(1)---F(10)	78.8(1)	79.72(6)	95.3	95.8	96.3
F(2)-Xe(1)-F(3)	81.0(1)	79.72(6)	84.7	84.1	83.7
F(2)-Xe(1)---F(10)	160.2(1)	161.12(6)	176.7	176.8	177.1
F(3)-Xe(1)---F(10)	118.77(9)	119.15(9)	95.4	95.9	96.3
Xe(1)---F(10)-H			141.9	141.9	152.8

Table A3.2. Continued...

	[XeF$_3$][SbF$_6$]			
	exptl	calcd[a]		
	β-[XeF$_3$][SbF$_6$]	B3LYP	PBE1PBE	MP2
Xe(1)-F(1)	1.894(2)	1.950	1.926	1.929
Xe(1)-F(2)	1.839(2)	1.921	1.894	1.895
Xe(1)-F(3)	1.901(2)	1.949	1.926	1.929
Xe(1)---F(4)	2.485(1)	2.136	2.131	2.127
Sb(1)-F(4)	1.917(1)	2.200	2.156	2.122
Sb(1)-F(5)	1.872(2)	1.906	1.890	1.888
Sb(1)-F(6)	1.855(2)	1.883	1.868	1.864
Sb(1)-F(7)	1.896(2)	1.883	1.868	1.864
Sb(1)-F(8)	1.861(1)	1.899	1.890	1.888
Sb(1)-F(9)	1.872(2)	1.875	1.861	1.857
F(1)-Xe(1)-F(2)	79.72(8)	86.8	86.0	86.3
F(1)-Xe(1)-F(3)	159.45(8)	173.3	171.7	172.4
F(1)-Xe(1)---F(4)	73.06(6)	93.1	94.0	93.6
F(2)-Xe(1)-F(3)	79.74(7)	86.2	86.0	86.4
F(2)-Xe(1)---F(4)	152.74(7)	178.1	177.9	177.7
F(3)-Xe(1)---F(4)	127.47(6)	93.3	94.0	93.6
F(4)-Sb(1)-F(5)	87.73(7)	79.7	80.1	80.0
F(4)-Sb(1)-F(6)	89.81(7)	84.5	85.0	85.3
F(4)-Sb(1)-F(7)	89.91(6)	84.6	85.0	85.3
F(4)-Sb(1)-F(8)	87.39(7)	80.7	80.1	80.0
F(4)-Sb(1)-F(9)	178.20(7)	176.3	175.9	175.4
F(5)-Sb(1)-F(6)	92.12(8)	89.3	89.7	89.8
F(5)-Sb(1)-F(7)	177.28(7)	164.3	165.0	165.1
F(5)-Sb(1)-F(8)	91.06(7)	86.4	86.1	85.8
F(5)-Sb(1)-F(9)	90.98(7)	97.3	96.9	96.7
F(6)-Sb(1)-F(7)	87.95(7)	90.4	90.7	90.9
F(6)-Sb(1)-F(8)	175.67(8)	165.1	165.0	165.1
F(6)-Sb(1)-F(9)	90.97(7)	97.7	97.9	97.9
F(7)-Sb(1)-F(8)	88.74(7)	89.8	89.7	89.8
F(7)-Sb(1)-F(9)	91.74(7)	98.4	97.9	97.9
F(8)-Sb(1)-F(9)	91.93(7)	97.0	96.9	96.7
Xe(1)---F(4)-Sb(1)	138.95(7)	122.2	119.3	116.8

[a] The aug-cc-pVTZ(-PP) basis set was used.

Table A3.3. Calculated Vibrational Frequencies [a] and Infrared and Raman Intensities [b] for the $HOXeF_2^+$ Cation [c]

				PBE1PBE				
$^{1}H^{16}O$	$^{1}H^{18}O$	$^{16/18}\Delta\nu$	$^{2}H^{16}O$	$^{2}H^{18}O$	$^{16/18}\Delta\nu$	$^{1(16)/2(16)}\Delta\nu$	$^{1(18)/2(18)}\Delta\nu$	assgnt[d]
3636.8(52)[300]	3624.6(52)[299]	−12.2	2649.1(25)[156]	2632.2(25)[155]	−16.9	−987.7	−992.4	$\nu(O_1H)$
1222.9(3)[69]	1219.2(3)[69]	−3.7	892.2(<1)[35]	886.0(<1)[35]	−6.2	−330.7	−333.2	$\delta(Xe_1O_1H)$
674.2(<0.1)[207]	675.9(<0.1)[209]	1.7	675.2(<0.1)[199]	675.1(<0.1)[199]	−0.1	1.0	−0.8	$\nu(Xe_1F_1) - \nu(Xe_1F_2)$
637.5(23)[2]	611.9(35)[<1]	−25.6	631.0(25)[1]	594.5(13)[3]	−36.5	−6.5	−3.8	$\nu(Xe_1O_1)$
603.6(29)[2]	598.3(15)[4]	−5.3	603.0(27)[2]	609.8(38)[<0.1]	6.8	−0.6	−2.1	$\nu(Xe_1F_1) + \nu(Xe_1F_2)$
298.0(3)[<1]	287.9(3)[<1]	−10.1	296.3(3)[4]	285.6(3)[3]	−10.7	−1.7	−2.3	$\delta(O_1Xe_1F_1) + \delta(O_1Xe_1F_2)$
215.0(<0.1)[14]	215.4(<0.1)[14]	0.4	215.5(<0.1)[14]	215.4(<0.1)[14]	−0.1	0.5	0.0	$\delta(F_1Xe_1F_2)_{o.o.p.}$
208.6(<1)[18]	208.8(<1)[18]	0.2	208.9(,1)[19]	208.6(,1)[18]	−0.3	0.3	−0.2	$\delta(F_1Xe_1F_2)_{i.p.}$
203.6(<1)[84]	202.8(<1)[84]	−0.8	147.4(<1)[41]	147.0(<1)[42]	−0.4	−56.2	−55.8	$\rho_w(Xe_1O_1H)$

				B3LYP				
$^{1}H^{16}O$	$^{1}H^{18}O$	$^{16/18}\Delta\nu$	$^{2}H^{16}O$	$^{2}H^{18}O$	$^{16/18}\Delta\nu$	$^{1(16)/2(16)}\Delta\nu$	$^{1(18)/2(18)}\Delta\nu$	assgnt[d]
3585.2(55)[291]	3573.2(56)[290]	−12.0	2611.6(26)[151]	2594.9(27)[150]	−16.7	−973.6	−978.3	$\nu(O_1H)$
1208.4(3)[69]	1204.6(3)[69]	−3.8	882.0(<1)[35]	875.8(<1)[34]	−6.2	−326.4	−328.8	$\delta(Xe_1O_1H)$
646.2(<0.1)[194]	647.8(<0.1)[196]	1.6	647.2(<0.1)[187]	647.2(<0.1)[187]	0.0	1.0	−0.6	$\nu(Xe_1F_1) - \nu(Xe_1F_2)$
590.8(28)[1]	576.2(41)[<1]	−32.0	585.1(32)[<1]	553.3(14)[2]	−31.8	−5.7	−5.5	$\nu(Xe_1O_1)$
572.8(28)[2]	558.8(13)[3]	3.4	571.5(23)[2]	575.9(40)[<1]	4.4	−1.3	−0.3	$\nu(Xe_1F_1) + \nu(Xe_1F_2)$
278.5(4)[<0.1]	269.4(4)[<0.1]	−9.1	275.7(4)[3]	265.9(3)[2]	−9.8	−2.8	−3.5	$\delta(O_1Xe_1F_1) + \delta(O_1Xe_1F_2)$
207.9(<0.1)[14]	208.4(<0.1)[14]	0.5	208.4(<0.1)[14]	208.4(<0.1)[14]	0.0	0.5	0.0	$\delta(F_1Xe_1F_2)_{o.o.p}$
193.7(<1)[18]	193.9(<1)[18]	0.2	193.9(<1)[18]	193.7(<1)[18]	−0.2	0.2	−0.2	$\delta(F_1Xe_1F_2)_{i.p.}$
185.7(<1)[84]	184.7(<1)[83]	−1.0	135.2(<1)[41]	134.7(<1)[42]	−0.5	−50.5	−50.0	$\rho_w(Xe_1O_1H)$

Table A3.3. Continued...

MP2								
$^{1}H^{16}O$	$^{1}H^{18}O$	$^{16/18}\Delta\nu$	$^{2}H^{16}O$	$^{2}H^{18}O$	$^{16/18}\Delta\nu$	$^{1(16)/2(16)}\Delta\nu$	$^{1(18)/2(18)}\Delta\nu$	assgnt[d]
3585(49)[290]	3573.8(49)[289]	–12.0	2614.0(23)[153]	2597.3(24)[151]	–16.7	–971.8	–981.5	$\nu(O_1H)$
1210.8(3)[74]	1207.2(3)[73]	–3.6	884.0(<1)[43]	877.1(<1)[41]	–6.9	–326.8	–330.1	$\delta(Xe_1O_1H)$
674.6(<0.1)[199]	676.3(<0.1)[200]	1.7	675.3(<0.1)[191]	675.3(<0.1)[191]	0.0	0.7	–1.0	$\nu(Xe_1F_1) - \nu(Xe_1F_2)$
697.1(13)[12]	663.7(13)[12]	–33.4	688.7(14)[7]	657.3(14)[8]	–31.4	–8.4	–6.4	$\nu(Xe_1O_1)$
596.5(34)[1]	595.9(33)[2]	–0.6	596.0(34)[1]	595.3(33)[1]	–0.4	–0.5	–0.6	$\nu(Xe_1F_1) + \nu(Xe_1F_2)$
309.9(3)[<1]	299.3(3)[<1]	–10.6	307.6(3)[4]	296.5(3)[3]	–11.1	–2.3	–2.8	$\delta(O_1Xe_1F_1) + \delta(O_1Xe_1F_2)$
215.9(<0.1)[14]	216.3(<0.1)[15]	0.4	216.4(<0.1)[15]	216.4(<0.1)[15]	0.0	0.5	0.1	$\delta(F_1Xe_1F_2)_{o.o.p.}$
210.0(<1)[19]	210.3(<1)[19]	0.3	210.2(<1)[19]	210.0(<1)[19]	–0.2	0.2	–0.3	$\delta(F_1Xe_1F_2)_{i.p.}$
188.0(<1)[84]	187.2(<1)[184]	–0.8	130.4(<1)[42]	130.0(<1)[42]	–0.4	–57.6	–57.2	$\rho_w(Xe_1O_1H)$

[a] Frequencies are given in cm^{-1}. [b] Values in parentheses denote calculated Raman intensities ($Å^4\ \mu^{-1}$). Values in square brackets denote calculated infrared intensities ($km\ mol^{-1}$). [c] The aug-cc-pVTZ(-PP) basis set was used. [d] The abbreviations denote stretch (ν), bend (δ), wag (ρ_w), in-plane bend (i.p.), and out-of-plane bend (o.o.p.). The in-plane and out-of-plane mode descriptions are relative to the $XeOF_2$ plane (Figure 6.10).

Table A3.4. Calculated Vibrational Frequencies [a] and Infrared and Raman Intensities [b] for the $[HOXeF_2][AsF_6]$ Ion Pair [c]

PBE1PBE								
$^{1}H^{16}O$	$^{1}H^{18}O$	$^{16/18}\Delta\nu$	$^{2}H^{16}O$	$^{2}H^{18}O$	$^{16/18}\Delta\nu$	$^{1(16)/2(16)}\Delta\nu$	$^{1(18)/2(18)}\Delta\nu$	assgnt [d]
3763.9(80)[207]	3751.4(81)[204]	–12.5	2740.9(37)[117]	2723.6(37)[114]	–17.3	–1023.0	–1027.8	$\nu(O_1H)$
1149.6(3)[53]	1145.7(3)[50]	–3.9	843.4(1)[40]	836.6(<1)[35]	–6.8	–306.2	–309.1	$\delta(Xe_1O_1H)$
760.1(3)[156]	760.4(4)[156]	0.0	760.0(3)[159]	760.0(3)[159]	0.0	–0.1	–0.1	$\nu(AsF_{2e}) - \nu(AsF_{2e'})$
757.6(1)[167]	757.7(1)[168]	0.1	757.6(1)[167]	757.6(1)[167]	0.0	0.0	–0.1	$[\nu(AsF_e) - \nu(AsF_{e'})] + [\nu(AsF_{e'}) - \nu(AsF_e)]$
754.1(8)[135]	754.0(7)[136]	–0.1	754.1(7)[137]	754.0(7)[138]	–0.1	0.0	0.0	$\nu(AsF_a)$
678.5(15)[38]	678.5(15)[38]	0.0	678.5(15)[38]	678.5(15)[38]	0.0	0.0	0.0	$\nu(AsF_{2e}) + \nu(AsF_{2e'})$
621.5(74)[88]	593.9(69)[77]	–27.6	614.7(73)[77]	589.0(69)[64]	–25.7	–6.8	–4.9	$\nu(Xe_1O_1)$
618.9(1)[214]	620.3(1)[218]	1.4	619.7(1)[208]	620.0(1)[208]	–0.3	0.8	–0.3	$\nu(Xe_1F_1) - \nu(Xe_1F_2)$
597.3(1)[21]	597.5(1)[18]	0.2	597.5(1)[18]	597.4(1)[18]	–0.1	0.2	–0.1	$[\nu(AsF_e) + \nu(AsF_{e'})] - [\nu(AsF_e) + \nu(AsF_{e'})]$
562.8(28)[10]	561.2(25)[21]	–1.6	562.5(28)[11]	560.1(24)[24]	–2.4	–0.3	–0.1	$\nu(Xe_1F_1) + \nu(Xe_1F_2)$
430.5(7)[91]	430.2(7)[88]	–0.3	430.5(7)[91]	430.1(7)[88]	–0.4	0.0	–0.1	$\nu(Xe_1{-}{-}{-}F_b) - \nu(As{-}F_b)$
404.6(<1)[19]	404.5(<1)[19]	–0.1	404.3(<1)[20]	404.2(<1)[20]	–0.1	–0.3	–0.3	$[\nu(Xe_1{-}{-}{-}F_b) + \nu(As{-}F_b)] + \delta_{umb}(AsF_{2e}F_{2e'})$
384.8(2)[1]	384.8(2)[1]	0.0	384.8(2)[1]	384.8(2)[1]	0.0	0.0	0.0	$\delta(F_eAsF_e) + \delta(F_{e'}AsF_{e'})$
381.9(<1)[38]	381.9(<1)[38]	0.0	381.9(<1)[38]	381.9(<1)[38]	0.0	0.0	0.0	$\delta(F_eAsF_{e'}) - \delta(F_eAsF_{e'}) + \rho_w(F_bAsF_a)$
369.9(<1)[11]	369.8(<1)[11]	–0.1	369.8(<1)[11]	369.7(<1)[11]	–0.1	–0.1	–0.1	$\delta(AsF_bF_{2e'}) - \delta(AsF_aF_{2e})$
324.1(<1)[<1]	324.1(<1)[<1]	0.0	324.1(<1)[<1]	324.1(<1)[<1]	0.0	0.0	0.0	$\rho_w(F_eAsF_{e'}) - \rho_w(F_eAsF_{e'}) + \rho_t(F_bAsF_a)$
305.2(1)[239]	305.1(1)[241]	–0.1	304.7(1)[240]	304.6(1)[241]	–0.1	–0.5	0.5	$\delta(O_1Xe_1F_b) - \delta(AsF_bF_{2e'})$
278.5(2)[10]	268.2(1)[9]	–10.3	278.1(2)[6]	267.8(2)[6]	–10.3	–0.4	–0.4	$\delta(O_1Xe_1F_1) + \delta(O_1Xe_1F_2)$
276.6(1)[104]	276.7(1)[103]	0.1	276.8(1)[105]	276.7(1)[105]	–0.1	0.2	0.0	$\delta(F_bAsF_a) + \rho_w(F_eAsF_e)$
229.6(<1)[29]	230.0(<1)[29]	0.4	229.8(<1)[28]	229.6(<1)[28]	–0.2	0.2	–0.4	$\delta(F_1XeF_2)_{oop}$
229.1(<1)[4]	229.0(<1)[4]	–0.1	228.8(<1)[<1]	228.7(<1)[<1]	–0.1	–0.3	–0.3	$\rho_w(F_bAsF_a) + \rho_w(Xe_1O_1H)$
223.2(2)[56]	223.2(2)[56]	0.0	161.7(1)[31]	161.6(1)[33]	–0.1	–61.5	–61.6	$\rho_w(Xe_1O_1H)$
197.2(1)[3]	197.2(1)[3]	0.0	197.2(1)[3]	196.8(1)[3]	–0.4	0.0	–0.4	$\delta(F_1Xe_1F_2)_{ip}$
196.5(<0.1)[<0.1]	196.5(<0.1)[<0.1]	0.0	196.6(<0.1)[<0.1]	196.6(<0.1)[<1]	0.0	0.1	0.1	$\rho_w(F_eAsF_{e'}) - \rho_w(F_eAsF_{e'})$
135.7(<1)[3]	135.7(<1)[3]	0.0	135.5 (<1)[4]	135.2(<1)[5]	–0.3	–0.2	–0.5	$\rho_r(AsF_aF_{2e}F_{2e'}) - \rho_r(HO_1Xe_1F_1F_2)_{i.p.}$
117.7(2)[13]	114.4(1)[11]	–3.3	114.7 (1)[11]	111.6(1)[10]	–3.1	–3.0	–2.8	$\rho_r(HO_1Xe_1F_1F_2)_{o.o.p.}$
71.4(<1)[<0.1]	71.2(<1)[<0.1]	–0.2	71.2 (<1)[0.1]	70.9(<1)[<0.1]	–0.3	–0.2	–0.3	$\rho_r(HO_1Xe_1F_1F_2)_{i.p.}$
60.0(<1)[<1]	59.6(<1)[<1]	–0.4	59.6(<1)[<1]	59.1(<1)[<1]	–0.4	–0.4	–0.5	$\delta(AsF_bXe_1)$
47.1(<1)[<0.1]	47.1(<1)[<0.1]	0.0	47.1(<1)[<0.1]	47.1(<1)[<0.1]	0.0	0.0	0.0	$\rho_t(F_eAsF_e) - \rho_t(F_{e'}AsF_{e'}) + \rho_r(HO_1Xe_1F_1F_2)_{o.o.p.}$
25.1(<1)[<1]	25.0(<1)[<1]	–0.1	24.9(<1)[<1]	24.8(<1)[<1]	–0.1	–0.2	–0.2	$\rho_t(AsF_{2e}F_{2e'}) - \rho_r(HO_1Xe_1F_1F_2)_{o.o.p.}$

Table A3.4. Continued...

				B3LYP				
$^{1}H^{16}O$	$^{1}H^{18}O$	$^{16/18}\Delta\nu$	$^{2}H^{16}O$	$^{2}H^{18}O$	$^{16/18}\Delta\nu$	$^{1(16)/2(16)}\Delta\nu$	$^{1(18)/2(18)}\Delta\nu$	assgnt^{d}
3708.1(90)[197]	3695.8(91)[194]	–12.3	2700.4(41)[112]	2683.3(42)[109]	–17.1	–1007.7	–1012.5	$\nu(O_1H)$
1132(3)[50]	1128.2(4)[47]	–3.9	830.5(<1)[38]	823(9)<1[]34	–6.6	–301.6	–304.3	$\delta(Xe_1O_1H)$
735.6(3)[143]	735.6(3)[143]	0.0	735.5(2)[144]	735.5(3)[143]	0.0	–0.1	–0.1	$\nu(AsF_{2e}) - \nu(AsF_{2e'})$
732.9(1)[161]	732.9(1)[161]	0.0	732.9(1)[160]	732.9(1)[160]	0.0	0.0	0.0	$[\nu(AsF_e) - \nu(AsF_{e'})] + [\nu(AsF_{e'}) - \nu(AsF_e)]$
731.6(9)[145]	731.6(9)[147]	0.0	731.6(9)[148]	731.5(9)[148]	–0.1	0.0	–0.1	$\nu(AsF_a)$
656.3(19)[30]	656.3(19)[29]	0.0	656.3(19)[30]	656.3(19)[29]	0.0	0.0	0.0	$\nu(AsF_{2e}) + \nu(AsF_{2e'})$
599.7(78)[89]	554.8(73)[73]	–24.9	573.5(77)[79]	550.4(73)[59]	–23.1	–6.2	–4.4	$\nu(Xe_1O_1)$
594.9(1)[163]	595.9(1)[173]	1.0	595.5(1)[163]	595.4(1)[163]	–0.1	0.6	–0.5	$\nu(Xe_1F_1) - \nu(Xe_1F_2)$
580.3(1)[60]	580.8(1)[51]	0.5	580.6(1)[52]	580.6(1)[52]	0.0	0.3	–0.2	$[\nu(AsF_e) + \nu(AsF_{e'})] - [\nu(AsF_e) + \nu(AsF_{e'})]$
532.2(30)[14]	530.5(25)[31]	–1.7	532.0(29)[16]	529.5(24)[38]	–2.5	–0.2	–1.0	$\nu(Xe_1F_1) + \nu(Xe_1F_2)$
419.7(12)[78]	419.2(13)[74]	–0.5	419.7(12)[78]	418.9(13)[73]	–0.8	0.0	–0.3	$\nu(Xe_1{---}F_b) - \nu(As{-}F_b)$
388.1(<1)[33]	388.1(<1)[33]	0.0	388.0(<1)[33]	387.9(<1)[33]	–0.1	–0.1	–0.2	$[\nu(Xe_1{---}F_b) + \nu(As{-}F_b)] + \delta_{umb}(AsF_{2e}F_{2e'})$
376.3(2)[4]	376.2(2)[4]	–0.1	376.2(2)[4]	376.2(2)[4]	0.0	–0.1	0.0	$\delta(F_eAsF_e) + \delta(F_{e'}AsF_{e'})$
372.8(<1)[36]	372.8(<1)[36]	0.0	372.8(<1)[36]	372.8(<1)[36]	0.0	0.0	–0.0	$\delta(F_eAsF_{e'}) - \delta(F_eAsF_{e'}) + \rho_w(F_bAsF_a)$
357.9(1)[6]	357.8(1)[6]	–0.1	357.8(1)[6]	357.6(1)[6]	–0.2	–0.1	–0.2	$\delta(AsF_bF_{2e'}) - \delta(AsF_aF_{2e})$
309.5(<1)[<0.1]	309.5(<1)[<0.1]	0.0	309.5(<1)[<1]	309.5(<1)[<0.1]	0.0	0.0	0.0	$\rho_w(F_eAsF_{e'}) - \rho_w(F_eAsF_{e'}) + \rho_t(F_bAsF_a)$
281.3(1)[122]	281.2(1)[124]	–0.1	280.7(1)[116]	280.5(1)[114]	–0.2	–0.6	–0.7	$\delta(O_1Xe_1F_b) - \delta(AsF_bF_{2e'})$
259.4(1)[15]	250.2(1)[16]	–9.2	258.2(2)[6]	248.8(2)[5]	–9.4	–1.2	–0.4	$\delta(O_1Xe_1F_1) + \delta(O_1Xe_1F_2)$
270.2(1)[190]	270.4(2)[190]	0.2	270.3(1)[197]	270.1(1)[201]	–0.2	0.1	–0.3	$\delta(F_bAsF_a) + \rho_w(F_eAsF_e)$
215.7(<1)[56]	216.0(<1)[56]	0.3	215.9(<1)[55]	215.7(<1)[54]	–0.2	0.2	–0.3	$\delta(F_1XeF_2)_{oop}$
218.6(<1)[4]	218.5(<0.1)[4]	–0.1	219.5(<1)[<1]	219.3(<1)[<1]	–0.2	0.9	0.8	$\rho_w(F_bAsF_a) + \rho_w(Xe_1O_1H)$
226.2(3)[50]	226.2(3)[48]	0.0	163.6(1)[30]	163.5(1)[30]	–0.1	–62.6	–62.7	$\rho_w(Xe_1O_1H)$
184.6(<1)[3]	184.6(1)[3]	0.0	184.6(<1)[3]	184.2(1)[3]	–0.4	0.0	–0.4	$\delta(F_1Xe_1F_2)_{ip}$
183.9(<0.1)[<0. 1]	183.9(<0.1)[<0.1]	0.0	184.0(<0.1)[<1]	184.0(<0.1)[<1]	0.0	0.1	0.1	$\rho_w(F_eAsF_{e'}) - \rho_w(F_eAsF_{e'})$
130.3(<1) [1]	130.2 (<1)[2]	–0.1	130.3(<1)[2]	130.1(<1)[2]	–0.2	0.0	–0.1	$\rho_r(AsF_aF_{2e}F_{2e'}) - \rho_r(HO_1Xe_1F_1F_2)_{i.p.}$
114.6(2)[14]	111.3(2)[13]	–3.3	111.6(2)[13]	108.6(2)[12]	–3.0	–3.0	–2.7	$\rho_r(HO_1Xe_1F_1F_2)_{o.o.p.}$
73.3(<1)[<1]	73.0(2)[13]	–0.3	72.9(<1)[<1]	72.5(2)[12]	–0.4	–0.4	–0.5	$\rho_r(HO_1Xe_1F_1F_2)_{i.p.}$
53.0(<1)[<1]	52.6(<1)[<1]	–0.4	52.6(<1)[<1]	52.1(<1)[<1]	–0.4	–0.4	–0.5	$\delta(AsF_bXe_1)$
46.8(<1)[<0.1]	46.8(<1)[<0.1]	0.0	46.8(<1)[<0.1]	46.7(<1)[<1]	0.1	0.0	–0.1	$\rho_t(F_eAsF_e) - \rho_t(F_{e'}AsF_{e'}) + \rho_r(HO_1Xe_1F_1F_2)_{o.o.p.}$
13.9(<1)[<1]	13.9(<1)[<1]	0.0	13.8(<1)[<1]	13.8(<1)[<1]	0.0	–0.1	–0.1	$\rho_t(AsF_{2e}F_{2e'}) - \rho_r(HO_1Xe_1F_1F_2)_{o.o.p.}$

Table A3.4. Continued...

MP2								
$^{1}H^{16}O$	$^{1}H^{18}O$	$^{16/18}\Delta\nu$	$^{2}H^{16}O$	$^{2}H^{18}O$	$^{16/18}\Delta\nu$	$^{1(16)/2(16)}\Delta\nu$	$^{1(18)/2(18)}\Delta\nu$	assgnt[d]
3694.3()[198]	3682.1()[194]	–12.2	2690.1()[113]	2673.1()[110]	–17.0	–1004.2	–1009.0	$\nu(O_1H)$
1137.1()[56]	1133.4()[53]	–3.7	833.6()[40]	827.0()[33]	–6.6	–303.5	–306.4	$\delta(Xe_1O_1H)$
778.8()[150]	778.8()[150]	0.0	778.7()[154]	778.7()[153]	0.0	–0.1	0.0	$\nu(AsF_{2e}) - \nu(AsF_{2e'})$
775.6()[161]	775.6()[162]	0.0	775.6()[161]	775.6()[161]	0.0	0.0	0.0	$[\nu(AsF_e) - \nu(AsF_{e'})] + [\nu(AsF_{e'}) - \nu(AsF_e)]$
773.5()[141]	773.4()[142]	–0.1	773.4()[146]	773.4()[146]	0.0	–0.1	0.0	$\nu(AsF_a)$
693.5()[37]	693.5()[37]	0.0	693.5()[38]	693.5()[38]	0.0	0.0	0.0	$\nu(AsF_{2e}) + \nu(AsF_{2e'})$
626.4()[98]	597.5()[87]	–28.9	620.1()[86]	592.7()[77]	–27.4	–6.3	–4.8	$\nu(Xe_1O_1)$
624.8()[138]	625.6()[148]	0.8	625.3()[140]	625.3()[139]	0.0	0.5	–0.3	$\nu(Xe_1F_1) - \nu(Xe_1F_2)$
607.4()[88]	608.1()[79]	0.7	607.9()[78]	607.9()[79]	0.0	0.5	–0.2	$[\nu(AsF_e) + \nu(AsF_{e'})] - [\nu(AsF_e) + \nu(AsF_{e'})]$
552.0()[14]	551.2()[20]	–0.8	551.9()[14]	550.9()[21]	–1.0	–0.1	–0.3	$\nu(Xe_1F_1) + \nu(Xe_1F_2)$
448.7()[118]	448.8()[115]	0.1	448.8()[118]	448.6()[115]	–0.2	0.1	–0.2	$\nu(Xe_1{-}{-}{-}F_b) - \nu(As{-}F_b)$
415.1()[10]	415.0()[10]	–0.1	414.7()[11]	414.6()[11]	–0.1	–0.4	–0.4	$[\nu(Xe_1{-}{-}{-}F_b) + \nu(As{-}F_b)] + \delta_{umb}(AsF_{2e}F_{2e'})$
386.2()[41]	386.2()[41]	0.0	386.2()[40]	386.2()[40]	0.0	0.0	0.0	$\delta(F_eAsF_e) + \delta(F_{e'}AsF_{e'})$
394.6()[3]	394.6()[3]	0.0	394.6()[3]	394.5()[3]	–0.1	0.0	–0.1	$\delta(F_eAsF_{e'}) - \delta(F_eAsF_{e'}) + \rho_w(F_bAsF_a)$
377.3()[21]	377.3()[21]	0.0	377.3()[21]	377.2()[21]	–0.1	0.0	–0.1	$\delta(AsF_bF_{2e'}) - \delta(AsF_aF_{2e})$
335.6()[<1]	335.6()[<1]	0.0	335.6()[<1]	335.6()[<1]	0.0	0.0	0.0	$\rho_w(F_eAsF_{e'}) - \rho_w(F_eAsF_{e'}) + \rho_t(F_bAsF_a)$
310.3()[198]	310.1()[201]	–0.2	309.8()[198]	309.6()[198]	–0.2	–0.5	–0.5	$\delta(O_1Xe_1F_b) - \delta(AsF_bF_{2e'})$
272.5()[12]	262.6()[12]	–9.9	271.8()[5]	261.9()[5]	–9.9	–0.7	–0.7	$\delta(O_1Xe_1F_1) + \delta(O_1Xe_1F_2)$
279.2()[155]	279.4()[154]	0.2	279.4()[157]	279.3()[158]	–0.1	0.2	–0.1	$\delta(F_bAsF_a) + \rho_w(F_eAsF_e)$
230.8()[40]	231.1()[40]	0.3	230.9()[39]	230.7()[38]	–0.2	0.1	–0.4	$\delta(F_1XeF_2)_{oop}$
234.6()[9]	234.5()[8]	–0.1	235.7()[<1]	235.5()[<1]	–0.2	1.1	1.0	$\rho_w(F_bAsF_a) + \rho_w(Xe_1O_1H)$
239.5()[48]	239.5()[48]	0.0	172.8()[31]	172.6()[31]	–0.2	–66.7	–66.9	$\rho_w(Xe_1O_1H)$
192.8()[2]	192.8()[2]	0.0	192.9()[2]	192.4()[2]	–0.5	0.1	–0.5	$\delta(F_1Xe_1F_2)_{ip}$
204.5()[<0.1]	204.5()[<0.1]	0.0	204.7()[<1]	204.7()[<1]	0.0	0.2	0.2	$\rho_w(F_eAsF_{e'}) - \rho_w(F_eAsF_{e'})$
138.0()[2]	137.1()[3]	–0.9	137.3()[3]	136.5()[4]	–0.8	–0.7	–0.6	$\rho_r(AsF_aF_{2e}F_{2e'}) - \rho_r(HO_1Xe_1F_1F_2)_{i.p.}$
116.8()[21]	114.3()[19]	–2.5	114.5()[19]	112.1()[18]	–2.4	–2.3	–2.2	$\rho_r(HO_1Xe_1F_1F_2)_{o.o.p.}$
84.2()[<0.1]	83.9()[<0.1]	–0.3	84.0()[<0.1]	83.6()[<0.1]	–0.4	–0.2	–0.3	$\rho_r(HO_1Xe_1F_1F_2)_{i.p.}$
72.9()[<1]	72.2()[<1]	–0.7	72.3()[<1]	71.5()[<1]	–0.8	–0.6	–0.7	$\delta(AsF_bXe_1)$
59.4()[<0.1]	59.4()[<0.1]	0.0	59.4()[<0.1]	59.3()[<0.1]	–0.1	0.0	–0.1	$\rho_t(F_eAsF_e) - \rho_t(F_{e'}AsF_{e'}) + \rho_r(HO_1Xe_1F_1F_2)_{o.o.p.}$
35.5()[<1]	35.3()[<1]	–0.2	35.2()[<1]	35.0()[<1]	–0.2	–0.3	–0.3	$\rho_t(AsF_{2e}F_{2e'}) - \rho_r(HO_1Xe_1F_1F_2)_{o.o.p.}$

[a] Frequencies are given in cm^{-1}. [b] Values in parentheses denote calculated Raman intensities ($Å^4\ \mu^{-1}$). Values in square brackets denote calculated infrared intensities ($km\ mol^{-1}$). [c] The aug-cc-pVTZ(-PP) basis set was used. [d] The abbreviations denote stretch (ν), bend (δ), wag (ρ_w), in-plane bend (i.p.), and out-of-plane bend (o.o.p.). The in-plane and out-of-plane mode descriptions are relative to the local $XeOF_2$ plane (Figure 6.10).

Table A3.5. Calculated Vibrational Frequencies [a] and Infrared and Raman Intensities [b] for the $FXeOXeF_2^+$ Cation [c]

PBE1PBE			B3LYP			MP2			assgnt [d]
^{16}O	^{18}O	$^{16/18}\Delta\nu$	^{16}O	^{18}O	$^{16/18}\Delta\nu$	^{16}O	^{18}O	$^{16/18}\Delta\nu$	
679.1(10)[57]	647.8(6)[20]	–31.3	627.8(8)[34]	601.8(13)[3]	–26.0	780.2(12)[204]	741.6(9)[172]	–38.6	$\nu(Xe_1O_1) - \nu(Xe_2O_1)$
648.3(1)[203]	650.0(1)[204)	1.7	620.7(2)[193]	622.3(2)[194]	1.6	645.8(1)[196]	647.5(1)[197]	1.7	$\nu(Xe_1F_1) - \nu(Xe_1F_2)$
616.4(110)[150]	615.3(114)[168]	–1.1	583.5(127)[149]	579.9(121)[158]	–3.6	598.7(110)[134]	599.2(111)[138]	0.5	$\nu(Xe_2F_3)$
580.2(28)[46]	579.3(28)[56]	–0.9	549.0(30)[50]	547.8(30)[65]	–1.2	567.9(36)[50]	567.5(36)[54]	–0.4	$\nu(Xe_1F_1) + \nu(Xe_1F_2)$
342.5(4)[45]	326.0(4)[42]	–16.5	325.9(5)[38]	310.3(4)[35]	–15.9	371.5(10)[63]	353.6(9)[58]	–17.9	$\nu(Xe_1O_1) + \nu(Xe_2O_1)$
298.2(2)[7]	286.5(2)[7]	–11.7	277.0(2)[6]	266.2(2)[6]	–10.8	314.3(2)[8]	301.9(2)[7]	–12.4	$\delta(OXe_1F_1) -$ $\delta(OXe_1F_2)$
216.2(<0.1)[12]	216.8(<0.1)[12]	0.6	208.8(<0.1)[11]	209.3(<0.1)[11]	0.5	218.0(<0.1)[12]	218.6(<0.1)[12]	0.6	$\delta(F_1Xe_1F_2)_{o.o.p.}$
212.2(<1)[13]	212.6(<1)[13]	0.4	198.6(<1)[12]	199.0(<1)[11]	0.4	212.3(<1)[13]	212.6(<1)[12]	0.3	$\delta(F_1Xe_1F_2)_{i.p.}$
146.4(<1)[3]	148.9(1)[14]	2.5	139.6(1)[13]	140.1(1)[14]	0.5	155.5(<1)[18]	156.1(<1)[19]	1.2	$\rho_w(O_1Xe_2F_3)$
148.4(1)[14]	146.8(<1)[3]	–1.6	138.7(<1)[3]	139.1(<1)[3]	0.4	152.1(<1)[3]	152.5(<1)[3]	0.4	$\delta(O_1Xe_2F_3) +$ $\delta(F_1Xe_2F_2)_{i.p.\ small}$
67.0(4)[1]	67.0(4)[1]	0.0	66.6(5)[1]	66.7(5)[1]	0.1	65.6(2)[1]	65.7(2)[1]	0.1	$\delta(Xe_1O_1Xe_2)$
12.4(3)[<0.1]	12.2(3)[<0.1]	–0.2	14.9(3)[<0.1]	14.7(3)[<0.1]	–0.2	15.8(3)[<0.1]	15.7(3)[<0.1]	–0.1	$\rho_t(F_1Xe_2F_2) +$ $\rho_t(O_1Xe_2F_3)$

[a] Frequencies are given in cm^{-1}. [b] Values in parentheses denote calculated Raman intensities ($Å^4\ \mu^{-1}$). Values in square brackets denote calculated infrared intensities (km mol^{-1}). [c] The aug-cc-pVTZ(-PP) basis set was used. [d] The abbreviations denote stretch (ν), bend (δ), wag (ρ_w), twist (ρ_t), in-plane bend (i.p.), and out-of-plane bend (o.o.p.). The in-plane and out-of-plane mode descriptions are relative to the local $XeOF_2$ plane (Figure 6.10).

Table A3.6. Calculated Vibrational Frequencies [a] and Infrared and Raman Intensities [b] for the $HOXe(F)_2OXeF_2^+$ Cation [c]

PBE1PBE			B3LYP			MP2			assgnt [d]
^{16}O -	^{18}O	$^{16/18}\Delta\nu$	^{16}O	^{18}O	$^{16/18}\Delta\nu$	^{16}O	^{18}O	$^{16/18}\Delta\nu$	
3704.6(98)[364]	3692.3(99)[360]	–12.3	3646.6(107)[359]	3633.6(109)[355]	–12.0	0□	0□	–	$\nu(OH)$
1170.3(12)[58]	1166.4(13)[56]	–3.9	1159.8(16)[58]	115.3(17)[55]	–4.5	0□	0□	–	$\delta(Xe_1O_1H)$
685.1(55)[94]	651.9(48)[87]	–33.2	634.6(51)[86]	603.9(50)[60]	–30.7	0□	0□	–	$\nu(Xe_3O_2) - \nu(Xe_1O_2)$
639.9(12)[202]	641.3(16)[192]	1.4	613.1(15)[187]	614.7(12)[198]	1.6	0□	0□	–	$\nu(Xe_3F_4) - \nu(Xe_3F_5)$
633.9(1)[235]	635.5(1)[236]	1.6	608.7(1)[220]	610.2(1)[221]	1.5	0□	0□	–	$\nu(Xe_1F_1) - \nu(Xe_1F_2)$
626.2(201)[112]	597.5(184)[108]	–28.7	579.8(228)[103]	554.6(200)[82]	–25.2	0□	0□	–	$\nu(Xe_1O_1)$
572.9(35)[2]	572.0(29)[1]	–0.9	543.2(35)[2]	541.4(28)[4]	–1.8	0□	0□	–	$\nu(Xe_1F_1) + \nu(Xe_1F_2)$
560.7(15)[27]	559.4(18)[35]	–1.3	531.3(19)[32]	529.0(32)[51]	–2.3	0□	0□	–	$\nu(Xe_3F_4) + \nu(Xe_3F_5)$
373.0(6)[33]	355.9(6)[30]	–17.1	357.3(5)[27]	340.6(5)[24]	–16.7	0□	0□	–	$\delta(O_2Xe_3F_4) - \delta(O_2Xe_3F_5)$
272.0(2)[4]	262.1(2)[2]	–9.9	254.0(2)[7]	244.7(3)[1]	–9.3	0□	0□	–	$\delta(O_1Xe_1F_1) - \delta(O_1Xe_1F_2)$
244.9(2)[77]	244.7(2)[79]	–0.2	243.8(3)[73]	242.9(1)[79]	–0.9	0□	0□	–	$\rho_w(Xe_1O_1H)$
233.3(<1)[4]	233.7(<1)[4]	0.4	223.7(<1)[5]	224.0(<1)[5]	0.3	0□	0□	–	$\delta(F_1Xe_1F_2)_{o.o.p.}$
221.1(<1)[13]	221.5(<1)[13]	0.4	209.1(1)[11]	209.2(1)[11]	0.1	0□	0□	–	$\delta(F_4Xe_3F_5)_{i.p.}$ + $\delta(F_1Xe_1F_2)_{o.o.p.}$
216.7(<0.1)[12]	217.2(<0.1)[12]	0.5	210.4(<0.1)[12]	211.0(<0.1)[12]	0.6	0□	0□	–	$\delta(F_4Xe_3F_5)_{o.o.p.}$
199.3(1)[41]	199.4(1)[40]	0.1	188.6(2)[39]	188.6(2)[39]	0.0	0□	0□	–	$\delta(F_1Xe_1F_2)_{i.p.}$ + $\delta(F_4Xe_3F_5)_{i.p.}$
115.7(<1)[3]	113.6(<1)[4]	–2.1	110.8(<1)[3]	109.0(<1)[4]	–1.8	0□	0□	–	
108.8(1)[5]	105.0(1)[8]	–3.8	105.1(<1)[3]	101.1(<1)[4]	–4.0	0□	0□	–	
103.5(<1)[10]	101.2(<1)[6]	–2.3	100.3(1)[11]	98.5(<1)[8]	–1.8	0□	0□	–	
58.3(2)[<1]	57.5(2)[<1]	–0.8	54.6(2)[<1]	5309(2)[<1]	–0.7	0□	0□	–	
17.9(1)[2]	17.7(1)[2]	–0.2	13.5(<1)[2]	13.5(<1)[2]	0.0	0□	0□	–	$\rho_r(Xe_1O_1F_1F_2O_2)$
16.5(2)[<0.1]	16.2(2)[<0.1]	–0.3	23.6(3)[<1]	23.7(3)[<1]	0.1	0□	0□	–	

[a] Frequencies are given in cm^{-1}. [b] Values in parentheses denote calculated Raman intensities (Å^4 μ^{-1}). Values in square brackets denote calculated infrared intensities (km mol^{-1}). [c] The aug-cc-pVTZ(-PP) basis set was used. [d] The abbreviations denote stretch (ν), bend (δ), wag (ρ_w), rock (ρ_r), in-plane bend (i.p.), and out-of-plane bend (o.o.p.). The in-plane and out-of-plane mode descriptions are relative to the local $XeOF_2$ plane (Figure 6.10).

Table A3.7. Calculated Vibrational Frequencies [a] and Infrared and Raman Intensities [b] for the $FXeOXe(F)_2OXeF_2^+$ Cation [c]

PBE1PBE			B3LYP			MP2			assgnt [d]
^{16}O	^{18}O	$^{16/18}\Delta\nu$	^{16}O	^{18}O	$^{16/18}\Delta\nu$	^{16}O	^{18}O	$^{16/18}\Delta\nu$	
708.1(86)[31]	673.2(78)[30]	–34.9	658.9(101)[35]	626.6(89)[35]	–32.3	835.8()[146]	794.4()[134]	–41.4	$\nu(Xe_3O_2) - \nu(Xe_1O_2)$
671.4(240)[304]	640.3(164)[178]	–31.1	622.1(245)[239]	595.4(119)[98]	–26.7	736.1()[529]	700.4()[442]	–35.7	$\nu(Xe_1O_1) - \nu(Xe_2O_1)$
631.4(19)[211]	632.9(15)[220]	1.5	603.6(24)[198]	605.1(25)[198]	1.5	632.1()[207]	633.7()[208]	1.6	$\nu(Xe_3F_4) - \nu(Xe_3F_5)$
620.6(<1)[210]	622.2(<1)[211]	1.6	594.9(<0.1)[199]	596.5(<1)[199]	1.6	609.7()[216]	611.3()[217]	1.6	$\nu(Xe_1F_1) - \nu(Xe_1F_2)$
594.8(248)[306]	593.7(296)[364]	–1.1	564.4(330)[320]	561.8(415)[394]	–2.6	578.1()[265]	578.0()[282]	–0.1	$\nu(Xe_2F_3)$
560.2(28)[60]	559.5(30)[78]	–0.7	530.0(32)[76]	529.1(39)[104]	–0.9	553.8()[32]	553.3()[41]	–0.5	$[\nu(Xe_1F_1) + \nu(Xe_1F_2)] + [\nu(Xe_3F_4) + \nu(Xe_3F_5)]$
555.0(17)[13]	554.5(18)[15]	–0.5	525.3(21)[8]	524.8(23)[10]	–0.5	535.9()[45]	535.5()[48]	–0.4	$[\nu(Xe_1F_1) + \nu(Xe_1F_2)] - [\nu(Xe_3F_4) + \nu(Xe_3F_5)]$
395.5(13)[31]	376.6(12)[29]	–18.9	375.0(13)[25]	357.1(11)[24]	–17.9	424.2()[59]	403.6()[54]	–20.6	$[\nu(Xe_3O_2) + \nu(Xe_1O_2)] - [\nu(Xe_1O_1) + \nu(Xe_2O_1)]$
343.0(15)[60]	327.5(13)[53]	–15.5	326.1(15)[51]	311.2(13)[45]	–14.9	362.6()[80]	346.4()[71]	–16.2	$\delta(O_2Xe_3F_4) - \delta(O_2Xe_3F_5)$
294.2(1)[6]	282.5(1)[5]	–11.7	274.9(1)[5]	264.0(1)[5]	–10.9	285.1()[4]	274.0()[4]	–11.1	$\delta(O_1Xe_1F_1) - \delta(O_1Xe_1F_2)$
230.6(1)[2]	231.4(2)[2]	0.8	219.6(1)[2]	220.4(2)[2]	0.8	230.9()[4]	231.5()[4]	0.6	$\delta(F_4Xe_3F_5)_{i.p.} + \delta(F_1Xe_1F_2)_{o.o.p.}$
218.6(<1)[7]	218.9(<1)[7]	0.3	207.9(<1)[7]	208.2(<1)[7]	0.3	233.5()[24]	232.3()[15]	–1.2	$\delta(F_4Xe_3F_5)_{i.p.} - \delta(F_1Xe_1F_2)_{o.o.p.}$
217.5(<0.1)[14]	218.0(<0.1)[14]	0.5	209.8(<0.1)[15]	210.3(<0.1)[15]	0.5	225.0()[14]	224.2()[19]	–0.8	$\delta(F_4Xe_3F_5)_{o.o.p.}$
208.8(<1)[45]	209.1(<1)[44]	0.3	196.6(,1)[43]	196.9(<1)[42]	0.3	206.3()[10]	204.8()[18]	–1.5	$\delta(F_4Xe_3F_5)_{i.p.} + \delta(F_1Xe_1F_2)_{i.p.}$
154.6(3)[11]	155.1(3)[11]	0.5	145.7(4)[11]	146.2(4)[11]	0.5	195.8()[34]	192.2()[24]	–3.6	$\delta(F_3Xe_2O_1)_{i.p.} + \delta(F_1Xe_1F_2)_{i.p.}$
151.9(1)[5]	152.4(1)[5]	0.5	144.3(<1)[4]	144.6(<1)[4]	0.3	159.3()[32]	159.3()[35]	0.0	$\delta(F_3Xe_2O_1)_{i.p.} - [\delta(F_1Xe_1F_2)_{i.p.}]_{small}$
99.2(3)[12]	97.8(5)[16]	–1.4	93.8(6)[13]	92.6(3)[5]	–1.2	153.8()[7]	154.3()[6]	0.5	$\delta(F_2Xe_1O_2) + \rho_t(F_5Xe_3O_2)$
95.4(3)[7]	92.4(2)[3]	–3.0	97.3(<1)[3]	94.2(4)[11]	–3.1	90.8()[5]	91.0()[5]	0.2	$\delta(F_1Xe_1O_2) + \rho_t(F_5Xe_3O_2)$
87.4(3)[3]	87.3(2)[3]	–0.1	83.9(3)[4]	83.9(3)[4]	0.0	68.9()[1]	69.0()[2]	0.1	$\delta(Xe_3O_2Xe_1) - \delta(Xe_1O_1Xe_2)$
48.2(2)[2]	48.3(2)[2]	0.1	45.7(2)[2]	45.7(2)[2]	0.0	59.6()[2]	59.3()[2]	–0.3	$\delta(Xe_3O_2Xe_1) + \delta(Xe_1O_1Xe_2)$
23.1(2)[<0.1]	23.2(2)[<0.1]	0.1	21.7(2)[<0.1]	21.7(2)[<0.1]	0.0	47.0()[<1]	46.9()[<1]	–0.1	coupled deformation modes
21.6(2)[<0.1]	21.6(2)[<0.1]	0.0	22.6(3)[<1]	22.5(3)[<1]	–0.1	38.0()[1]	37.6()[1]	–0.4	
12.8(2)[<1]	12.6(2)[<1]	–0.2	18.9(2)[<1]	18.4(2)[<1]	–0.5	17.9()[<1]	17.9()[<1]	0.0	
8.3(<1)[<1]	8.3(<1)[<1]	0.0	9.3(<1)[<1]	9.1(<1)[<1]	–0.2	10.7()[<0.1]	10.7()[<0.1]	0.0	

[a] Frequencies are given in cm^{-1}. [b] Values in parentheses denote calculated Raman intensities ($Å^4\ \mu^{-1}$). Values in square brackets denote calculated infrared intensities (km mol^{-1}). [c] The aug-cc-pVTZ(-PP) basis set was used. [d] The abbreviations denote stretch (ν), bend (δ), in-plane bend (i.p.), and out-of-plane bend (o.o.p.). The in-plane and out-of-plane mode descriptions are relative to the local $XeOF_2$ plane (Figure 6.10).

Table A3.8. Calculated Bond Lengths (Å) and Bond Angles (deg) for the $HOXeF_2^+$, $[HOXeF_2][AsF_6]$, $FXeOXeF_2^+$, $HOXe(F)_2OXeF_2^+$ and $FXeOXe(F)_2OXeF_2^+$ Cations [a]

	$HOXeF_2^+$		
	MP2	PBE1PBE	B3LYP
Xe$_1$-F$_1$	1.903	1.905	1.927
Xe$_1$-O$_1$	1.880	1.900	1.929
Xe$_1$-H	2.377	2.393	2.421
O$_1$-H	0.985	0.980	0.983
F$_1$-Xe$_1$-F$_2$	174.0	174.3	175.2
O$_1$-Xe$_1$-F$_1$	87.1	87.2	87.7
Xe$_1$-O$_1$-H	108.1	108.1	108.1
	$[HOXeF_2][AsF_6]$		
Xe$_1$–F$_1$	1.942	1.938	1.963
Xe$_1$–O$_1$	1.931	1.934	1.965
O$_1$–H	0.975	0.970	0.973
Xe$_1$---F$_b$	2.183	2.202	2.199
As–F$_b$	1.963	1.978	2.037
As–F$_a$	1.682	1.689	1.700
As–F$_e$	1.694	1.700	1.714
As–F$_{e'}$	1.725	1.729	1.740
F$_1$–Xe$_1$–F$_2$	175.8	174.3	175.4
O$_1$–Xe$_1$–F$_1$	88.0	87.2	87.7
H$_1$–O$_1$–Xe$_1$	106.8	107.7	107.7
O$_1$–Xe$_1$---F$_b$	176.1	175.8	176.0
F$_1$–Xe$_1$---F$_b$	91.9	92.8	92.2
Xe$_1$---F$_b$–As	115.0	117.4	119.8
F$_b$–As–F$_a$	177.1	177.5	177.8
F$_b$–As–F$_e$	85.4	85.3	84.7
F$_b$–As–F$_{e'}$	82.8	83.1	82.8
F$_a$–As–F$_e$	96.6	96.4	96.8
F$_a$–As–F$_{e'}$	95.1	95.1	95.6
F$_e$–As–F$_e$	91.2	91.0	90.7
F$_e$–As–F$_{e'}$	89.7	89.7 168.3	89.6 167.5
F$_{e'}$–As–F$_{e'}$	86.9	87.2	87.3
	$FXeOXeF_2^+$		
Xe$_1$-F$_1$	1.922	1.921	1.946
Xe$_1$-F$_2$	1.923	1.921	1.946
Xe$_1$-O$_1$	1.837	1.859	1.885
Xe$_2$-O$_1$	2.240	2.260	2.296
Xe$_2$-F$_3$	1.920	1.916	1.940
F$_1$-Xe$_1$-F$_2$	177.6	177.8	178.3
O$_1$-Xe$_1$-F$_1$	89.3	89.3	89.9
O$_1$-Xe$_1$-F$_2$	89.3	89.3	89.9
Xe$_1$-O$_1$-Xe$_2$	123.8	125.7	126.7
O$_1$-Xe$_2$-F$_3$	175.9	175.1	174.4

Table A.3.8. Continued...

	MP2	PBE1PBE	B3LYP
HOXe(F)$_2$OXeF$_2^+$			
Xe$_1$-F$_1$	1.931	1.930	1.953
Xe$_1$-F$_2$	1.958	1.929	1.952
Xe$_1$-O$_1$	1.914	1.915	1.945
O$_1$-H	0.980	0.975	0.978
Xe$_1$-O$_2$	2.318	2.392	2.417
Xe$_3$-O$_2$	1.828	1.851	1.877
Xe$_3$-F$_4$	1.938	1.949	1.972
Xe$_3$-F$_5$	1.917	1.913	1.936
F$_1$-Xe$_1$-F$_2$	176.1	176.7	177.4
O$_1$-Xe$_1$-F$_1$	92.4	88.4	88.7
O$_1$-Xe$_1$-F$_2$	91.4	88.5	88.9
Xe$_1$-O$_1$-H	108.6	108.8	108.6
O$_1$-Xe$_1$-O$_2$	173.6	175.4	175.2
Xe$_1$-O$_2$-Xe$_3$	120.5	128.3	128.5
O$_2$-Xe$_3$-F$_4$	88.5	88.5	88.9
O$_2$-Xe$_3$-F$_5$	89.2	89.1	89.4
F$_4$-Xe$_3$-F$_5$	177.3	177.7	178.3
FXeOXeF$_2$OXeF$_2^+$			
Xe$_1$-F$_1$	1.941	1.937	1.962
Xe$_1$-F$_2$	1.922	1.938	1.962
Xe$_1$-O$_1$	1.863	1.874	1.899
Xe$_2$-O$_1$	2.190	2.206	2.241
Xe$_2$-F$_3$	1.939	1.932	1.957
Xe$_1$-O$_2$	2.410	2.491	2.520
Xe$_3$-O$_2$	1.813	1.838	1.862
Xe$_3$-F$_4$	1.949	1.953	1.978
Xe$_3$-F$_5$	1.922	1.920	1.944
F$_1$-Xe$_1$-F$_2$	177.0	178.1	178.6
O$_1$-Xe$_1$-F$_1$	91.6	89.3	89.8
O$_1$-Xe$_1$-F$_2$	90.8	89.3	89.8
O$_1$-Xe$_1$-O$_2$	169.6	175.6	175.5
Xe$_1$-O$_1$-Xe$_2$	121.3	124.3	125.3
O$_1$-Xe$_2$-F$_3$	176.7	176.1	175.5
Xe$_1$-O$_2$-Xe$_3$	120.8	128.4	128.7
O$_2$-Xe$_3$-F$_4$	89.2	89.3	89.7
O$_2$-Xe$_3$-F$_5$	90.7	90.3	90.8
F$_4$-Xe$_3$-F$_5$	179.0	179.6	179.5

[a] The aug-cc-pVTZ(-PP) basis set was used.

Table A3.9. NBO Valencies, Bond Orders, and Charges (NPA) for $HOXeF_2^+$ and $FXeOXeF_2^{+\,a}$

	Charges [Valencies]			
	$HOXeF_2^+$		$FXeOXeF_2^+$	
Xe(1)	2.175	[1.456]	2.141	[1.529]
O(1)	−0.690	[1.167]	−0.836	[0.919]
F(1)	−0.509	[0.406]	−0.542	[0.383]
F(2)	−0.509	[0.406]	−0.542	[0.383]
H	1.268	[0.608]		
Xe(2)			1.240	[0.571]
F(3)			−0.460	[0.356]
	Bond Orders			
Xe(1)-O(1)	0.603		0.725	
Xe(1)-F(1)	0.426		0.404	
Xe(1)-F(2)	0.426		0.404	
O(1)-H	0.613			
O(1)-Xe(2)			0.228	
Xe(2)-F(3)			0.345	

[a] B3LYP/aug-cc-pVTZ(-PP)

APPENDIX 4

Table A4.1. Experimental and Calculated Frequencies[a] for KrF_2

exptl	PBE1PBE[b]	B3LYP[b]	assgnts[c]
580[d]	613(<1)[287]	584(<0.1)[260]	$\nu_3(\Sigma_u^-)$ $\nu_{as}(KrF_2)$
465.5[e] 469.5, 468.6[f]	526(51)[<1]	493(52)[<0.1]	$\nu_1(\Sigma_g^+)$ $\nu_s(KrF_2)$
236[d]	249(<0.1)[14]	234(<0.1)[13]	$\nu_2(\Pi_u)$ $\delta(KrF_2)$

[a] Frequencies are given in cm^{-1}. [b] The aug-cc-pVTZ(-PP) basis set was used. Values in parentheses denote Raman intensities ($Å^4$ amu^{-1}). Values in square brackets denote infrared intensities (km mol^{-1}). [c] The abbreviations denote symmetric (s), asymmetric (as), stretch (ν) and bend (δ). [d] Infrared values obtained from matrix-isolated KrF_2 in ref 93. [e] Raman frequencies for the α-phase of KrF_2 are from ref 100. [f] Raman frequencies for the β-phase of KrF_2 are from ref 100.

Outline of QTAIM and ELF. The QTAIM analysis provides a partition into atomic basins over which it is possible to integrate densities of properties in order to obtain atomic properties such as atomic populations, $\bar{N}(\mathrm{A})$. In the QTAIM framework, bonded atoms are linked by a bond path[298,299] which is defined as the union of the trajectories joining the bond critical point (bcp), a saddle point maximum in two directions located on the border surface of two atomic basins, to the two nuclei. The value of the Laplacian of the density at the bond critical point, as well as those of other functions, is used to further characterize the interaction: a negative value of $\nabla^2\rho(\mathrm{r}_{bcp})$ corresponds to a shared-electron (covalent) interaction whereas a positive value indicates an unshared-electron bonding mode. Moreover, insights into the delocalization in terms of delocalization indices[300] can be obtained by a covariance analysis of the atomic populations.

The electron localization function, denoted $\eta(\mathbf{r})$, was originally conceived as a local measure of the Fermi hole curvature around a reference point within the Hartree-Fock approximation.[253] A further interpretation, in terms of a local excess of kinetic energy due to the Pauli principle, was proposed by Savin et al.,[301] which legitimatized the calculation of the function with Kohn-Sham orbitals. More recently, it was shown that the ELF kernel can be rigorously derived by considering the same number of spin pairs contained in a sample around the reference point.[302,303] A cosmetic Lorentz transform that confines the ELF is the [0,1] interval; where 1 corresponds to regions dominated by an opposite spin pair or by a single electron, whereas low values are found at the boundaries between such regions. The basins of ELF attractors are closely related to Gillespie's electronic domains and recover the ideas of Lewis. There are two types of basins: core basins, denoted by C(A), encompassing the nucleus of atom A and valence basins, denoted by V(A, B, ...). The valence shell of an atom, say A, in a molecule is therefore the union of valence basins having a boundary with C(A). A valence basin may belong to several atomic valence shells. The synaptic order[304] is defined as the number of such valence shells which a valence basin participates in. There are therefore monosynaptic basins, V(A), corresponding to the lone pair, disynaptic basins V(A, B) corresponding to two center bonds, and higher polysynaptic basins for polycentric bonds. The basin populations and the associated covariance matrix are calculated by integration of the one electron and pair densities over the volumes of the basins, enabling a phenomenological interpretation of the population analysis in terms of the superposition of mesomeric structures.[305] The weights of these structures are estimated from the populations, the covariance matrices, and for the probabilities of finding N electrons in a given basin.[306,307] The concept of localization domain[252] has been introduced for graphical purposes and to also define a hierarchy of the localization basins which can be related to chemical properties. A localization domain is a volume limited by one or more closed isosurfaces denoted by $\eta(\mathbf{r}) = f$, where f is defined as the isosurface contour. A localization domain surrounds at least one attractor- in this case it is called irreducible. If the delocalization domain contains more than one attractor, it is termed reducible. Except for atoms and linear molecules, the irreducible domains are always filled volumes whereas the reducible domains can be either filled volumes, hollow volumes, or tori. Upon increasing the value of $\eta(\mathbf{r})$, which defines the boundary isosurface, a reducible domain splits into several domains, each containing less attractors than the parent one. The reduction of localization occurs at the turning points which are critical points of index 1 located on the separatrix of two basins involved in the parent domain. Ordering these turning points (localization nodes) by increasing $\eta(\mathbf{r})$ enables one to build tree-diagrams reflecting the hierarchies of the basins.[308,309]

The QTAIM approach provides a phenomenological representation of the molecular electron density, and therefore of the bonding, close to the superposition of promolecular atomic densities, whereas ELF intends to recover the VSEPR and Lewis pictures. An interesting combination of QTAIM and ELF has been proposed by Raub and Jansen[310] who considered the contributions of the atomic basins to the ELF valence basin populations. As a general rule, the number of contributing atomic basins is equal to the synaptic order. Indeed, the QTAIM and ELF analysis are almost equivalent in unshared-electron systems.

(i) Nature of the Bonding in KrF_2. In order to understand the nature of the Kr–F interaction in KrF_2, the KrF molecule was first considered. The ground state of KrF is a $^2\Sigma$ doublet, with an optimized internuclear distance of 2.437 and 2.410 Å using the PBE1PBE and B3LYP hybrid functionals. The calculated binding energy is rather weak; 10 kJ mol^{-1} with PBE1PBE and 16 kJ mol^{-1} with B3LYP. The AIM analysis provided the following information: (1) the atomic populations indicate a significant charge transfer of 0.15 e towards the fluorine atom, this value coincides with the NBA net positive charges of the KrF_2 ligands (0.19 and 0.09) (Table S3), (2) the spin density is mostly in the F basin (85%), (3) the delocalization index, $\delta = 0.42$, is typical of a weak interaction; β-spin electrons contribute three times more than the α-spin electrons to this index, (4) the density value at the bond critical point is small, $\rho(r_{bcp}) = 0.036$ e bohr^{-3}, and its Laplacian is positive ($\nabla^2\rho(r_{bcp}) = 0.157$ e bohr^{-5}).

The bonding is therefore characterized by a charge transfer and a small delocalization of the single electron over the two atoms. The QTAIM population analysis suggests a picture of the bonding represented by the following superposition of two promolecular densities:

Kr F↑ 85%

Kr^+↑ F 15%

The ELF reduction of the localization diagram of KrF (Scheme 4.1) shows that the Kr and F atoms can be considered as two independent interacting chemical systems because the separation of V(F) from V(Kr) occurs at almost the same value as the fluorine core-valence bifurcation. The population analysis is consistent with this picture and confirms the conclusions drawn from the QTAIM results: there is no disynaptic basin and the values of the basin populations, integrated spin densities, and covariance matrix elements are in complete agreement with those of QTAIM.

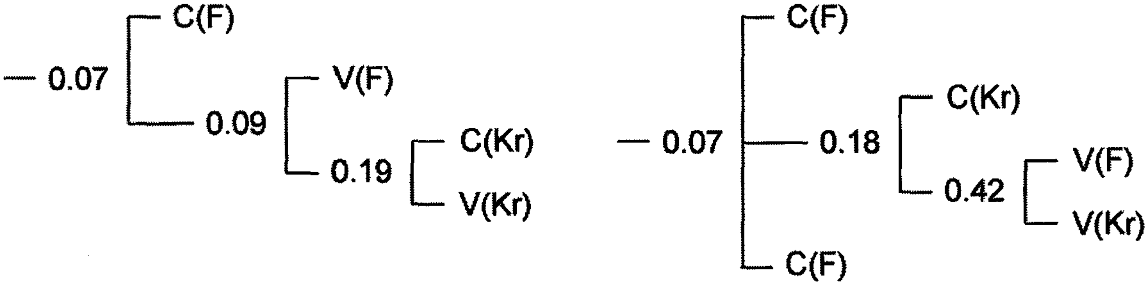

Scheme A4.1. Reduction of the localization diagrams for KrF (left) and KrF_2 (right) showing the ordering of localization nodes and the boundary isosurface value, $\eta(\mathbf{r})$, at which the reducible domains split.

The ground state of KrF_2 is a singlet $^1\Sigma_g$; the Kr–F internuclear distances are significantly shorter than in KrF, 1.860 and 1.890 Å, at the PBE1PBE and B3LYP levels, respectively, and the binding energy per fluorine is much larger; 58 (PBE1PBE) and 63 mol^{-1} (B3LYP). The atomic populations of Kr and F indicate a net density transfer of 0.48 e from Kr to each F, in good agreement with the NBO analysis which yields 0.52 e. The Kr–F and F–F delocalization indexes are 0.86 and 0.22, respectively. Finally, the Laplacian of the density at the KrF bond critical point is positive ($\nabla^2\rho(r_{bcp}) = 0.23$ e $bohr^{-5}$). The ELF reduction of localization diagram of KrF_2, Scheme 1, which is at variance with KrF, shows that the separation of the molecular valence shell into its atomic components occurs at a larger ELF value than the Kr core-valence separation. Therefore, KrF_2 can be considered as a single chemical entity rather than as a cluster of interacting atoms. Figure S4.1 displays the ELF localization domains for KrF_2 at $\eta(\mathbf{r})$ = 0.75, showing the absence of any disynaptic (bond) between Kr and F. The ELF population analysis, reported in Table S4.2, together with the QTAIM results suggests an interpretation of the bonding in terms of a large delocalization of the electron density between the Kr and F valence shells and of an electron density transfer towards the fluorine atom. This type of bonding looks very similar to the charge-shift bonds introduced by Shaik et al.,[311–313] but there are some important differences. If the Kr–F bond was a standard charge-shift bond, it should have almost the same properties in KrF and KrF_2. Comparison of the two molecules shows a cooperative effect that enhances the bond strength in KrF_2. The main difference between the ground states of these molecules is that KrF is a doublet and KrF_2 a singlet, therefore the addition of a second fluorine atom removes the spin density that is mostly localized on the first fluorine. Because there is no direct interaction between the two fluorine atoms, there is mediation on the part of the Kr atom which plays a role very similar to that of the non-magnetic anion in superexchange coupling. Weighted promolecular mesomeric forms can be proposed from the probabilities of finding n electrons in a given basin (Scheme 4.2).

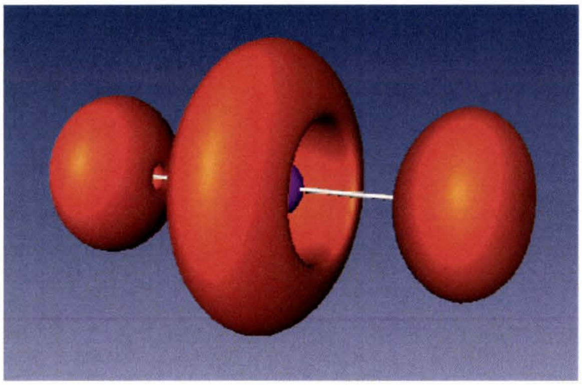

Figure A4.1. ELF localization domains of KrF_2. The isosurface value is $\eta(\mathbf{r}) = 0.75$. Color code: magenta = core, brick-red = monosynaptic basin.

The spacial symmetry and the diamagnetism of KrF_2 explain the multiplicity of each kind of structure. This multiplicity and the large increase in weighting of the ionic structures with respect to KrF contribute to the stabilization of the molecule.

Table A4.2. ELF Basin Population and Covariance Matrix Elements of KrF_2

	aug-cc-pVTZ		DGDZVP
	B3LYP	PBE1PBE	PBE1PB
$\bar{N}$ [C(F)]	2.11	2.16	2.13
$\bar{N}$ [C(Kr)] [a]	17.88	17.89	27.72
$\bar{N}$ [V(F)]	7.31	7.30	7.30
$\bar{N}$ [V(Kr)]	7.25	7.17	7.41
⟨*cov*[V(Kr),V(F)]⟩	−0.41	−0.42	−0.40
⟨*cov*[V(F),V(F')]⟩	−0.9	−0.8	−0.08

[a] The use of pseudo-potential calculations and the all electron calculation account for the differences in the Kr basin populations.

F↓	Kr	F↑	26%
F↑	Kr	F↓	
F↑	Kr^{+}↓	F^{-}	47%
F↓	Kr^{+}↑	F^{-}	
F^{-}	Kr^{+}↓	F↑	
F^{-}	Kr^{+}↑	F↓	
F^{-}	Kr^{2+}	F^{-}	27%

Scheme A4.2. Weighted promolecular mesomeric forms of KrF_2 and their probabilities.

(ii) Nature of the Bonding in $BrOF_2^+$. The $BrOF_2^+$ cation has a trigonal pyramidal geometry according to the VSEPR rules. Because all atoms have lone pairs, the lone-pair bond weakening effect (LPBWE)[314] is expected to be important. The QTAIM electronic populations localize a large positive charge (+2.25) on bromine and partial negative charges on the oxygen (−0.52) and fluorine (−0.36) atoms. These values are in good agreement with the NPA charges +2.30, −0.57, and −0.36 for Br, O and F, respectively. The delocalization indexes (δ) indicate delocalization between the Br and O basins (δ= 1.84) that is twice that of Br and F (δ= 0.98) as well as rather important interactions between non-bonded atoms such as between O and F (δ= 0.24), and between the two fluorines ($\delta = 0.12$). The values of the Laplacian of the electron density are both positive at the Br–O and Br–F bond critical points (0.39 and 0.29, respectively). Therefore, the bonding can be described as belonging to the unshared-electron type.

Figure 7.3 displays the localization domains of $BrOF_2^+$ which either belong to core or to monosynaptic valence basins at $\eta(\mathbf{r}) = 0.75$. The reduction of localization diagram (Scheme A4.3) indicates, however, that there is only one valence shell because the core valence separations occur at ELF values lower than the division of the valence density. While the atomic valence shells of O and F can be easily identified, each of them being the union of two monosynaptic basins, only V(Br) can be unambiguously assigned to the Br valence shell. In the ELF population analysis presented in Table A4.3, the two V(O) basins as well as the V(F) basins of each fluorine have merged into single basins. The population of the V(Br) basin, 3.11 e, is larger than expected for a single lone pair, and is a consequence of the LPBWE which tends to increase the lone pair population at the expense of bonding. The covariance matrix elements between V(Br) and the other valence basins are very large although these basins belong, in principle, to different atomic valence shells. The large contributions of the Br atomic basin to V(O) and to V(F), however, suggest participation of these basins in the Br valence shell. In particular, $\bar{N}$ [V(O)|Br] = 1.5 e, is consistent with a dative picture of the Br–O bond.

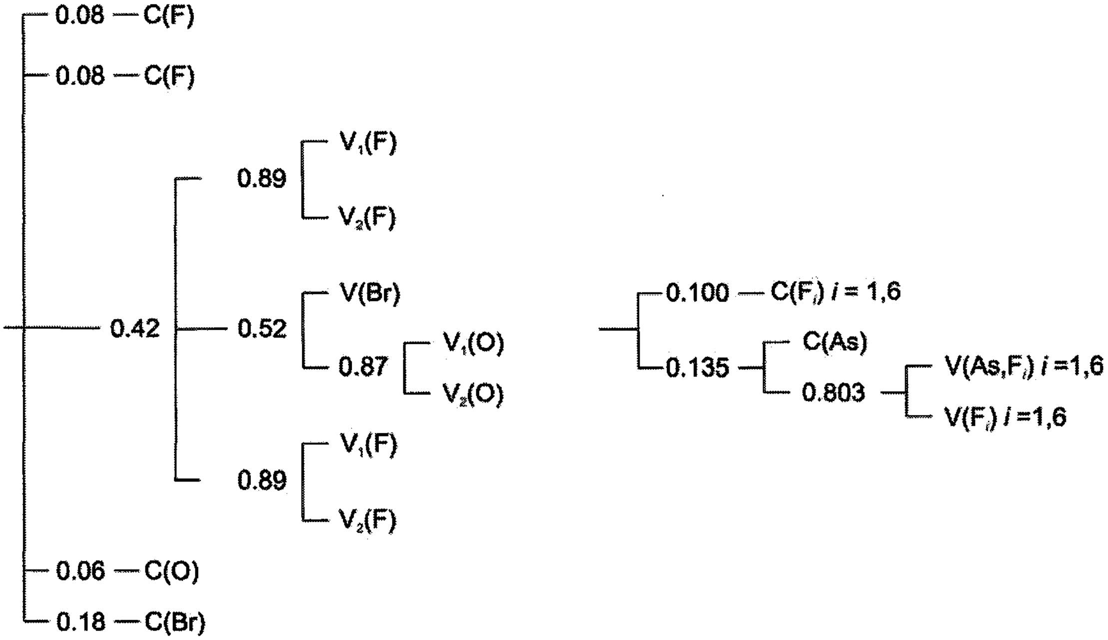

Scheme A4.3. Reduction of localization diagrams for $BrOF_2^+$ (left) and AsF_6^- (right) showing the ordering of localization nodes and the boundary isosurface values, $\eta(\mathbf{r})$, at which the reducible domains split.

(iii) Nature of the Bonding in AsF_6^-. Both QTAIM and ELF describe the bonding in the AsF_6^- anion as arising from both ionic and covalent resonance structures. Charge-shift bonding is not possible in this system because there is no lone pair on the As atom. From the QTAIM point of view, the large positive value of the Laplacian of the charge density at the As–F bond critical point, 0.613, is indicative of a dominant unshared-electron interaction whereas the fluorine net charge, −0.67 e, indicates that the weights of the contributing mesomeric structures involving covalent As–F are rather large. The ELF analysis confirms this picture because there are six V(As,F) disynaptic basins displayed in Figure A4.2. Although the population of this basin is very low, 0.16 e, the total contribution of the atomic As basin to the V(F) basins amounts to 1.26 e. Accordingly, the dominant resonance structures should be: $AsF^{4+}(F^-)_5$ (~31%), $AsF_2^{3+}(F^-)_4$ (~34%), and $AsF_3^{2+}(F^-)_3$ (~25%).

Table A4.3. ELF Basin Population, $\bar{N}[\Omega]$, Covariance Matrix Elements, $\langle cov(\bar{N}[\Omega], \bar{N}[\Omega'])\rangle$, and Bromine Atomic Basin Contribution, $(\bar{N}[\Omega|Br])$, of $BrOF_2^+$

Ω	$\bar{N}[\Omega]$	$\langle cov(\bar{N}[\Omega], \bar{N}[\Omega'])\rangle$				$\bar{N}[\Omega\|Br]$
		V(F)	V(O)	V(Br)	V(F')	
V(F)	7.45	1.07	−0.09	−0.26	−0.08	0.25
V(O)	7.91	−0.09	1.68	−0.45	−0.09	1.5
V(Br)	3.11	−0.26	−0.45	1.64	−0.26	3.11

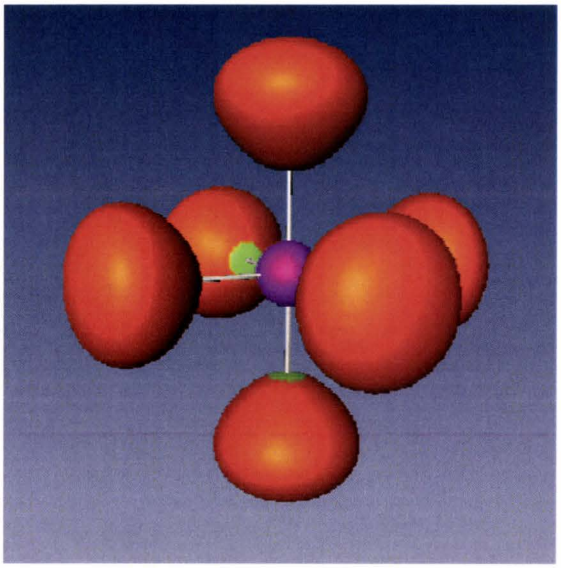

Figure A4.2. ELF localization domains for AsF_6^-. The isosurface value is $\eta(\mathbf{r}) = 0.75$. Color code: magenta = core, brick-red = monosynaptic basin, green = disynaptic basin.

APPENDIX 5

Table A5.1. Experimental and Calculated Vibrational Frequencies[a] for XeF_2

exptl[b]	PBE1PBE[f]	B3LYP[f]	assgnts[g]
555[c]	572(<0.1)[261]	550(<0.1)[246]	$\nu_3(\Sigma_u^+)$ $\nu_{as}(XeF_2)$
515,[d] 497[e]	535(44)[<0.1]	510(47)[<0.1]	$\nu_1(\Sigma_g^+)$ $\nu_s(XeF_2)$
213[c]	214(<0.1)[15]	205(<0.1)[15]	$\nu_2(\Pi_u)$ $\delta(XeF_2)$

[a] Frequencies are given in cm^{-1}. [b] From ref 203. [c] Values determined for gas-phase XeF_2 by infrared spectroscopy and are reported as intense. [d] Value obtained from a weak $\nu_1 + \nu_3$ combination band for gas-phase XeF_2 by infrared spectroscopy. [e] Value obtained from solid XeF_2 by Raman spectroscopy. [f] The aug-cc-pVTZ(-pp) basis set was used. Values in parentheses denote Raman intensities ($Å^4$ u^{-1}). Values in square brackets denote infrared intensities (km mol^{-1}). [g] The abbreviations denote symmetric (s), asymmetric (as), stretch (ν) and bend (δ).

Table A5.2. Calculated[a] Geometrical Parameters for $[BrOF_2][AsF_6]_3^{2-}$

	PBE1[b]	B3LYP		PBE1[b]	B3LYP		PBE1[b]	B3LYP
			Bond Lengths (Å)					
Br–O$_1$	1.568	1.580						
Br–F$_1$	1.755	1.779						
Br–F$_2$	1.755	1.779						
Br---F$_{3A}$	2.306	2.328						
			Br---F$_{3A'}$	2.306	2.327			
						Br---F$_{3B}$	2.481	2.503
As$_A$–F$_{3A}$	1.822	1.834	As$_{A'}$–F$_{3A'}$	1.822	1.834	As$_B$–F$_{3B}$	1.785	1.795
As$_A$–F$_{4A}$	1.731	1.739	As$_{A'}$–F$_{4A'}$	1.731	1.739	As$_B$–F$_{4B}$	1.736	1.744
As$_A$–F$_{5A}$	1.730	1.738	As$_{A'}$–F$_{5A'}$	1.730	1.738	As$_B$–F$_{5B}$	1.734	1.743
As$_A$–F$_{6A}$	1.733	1.741	As$_{A'}$–F$_{6A'}$	1.733	1.741	As$_B$–F$_{6B}$	1.741	1.750
As$_A$–F$_{7A}$	1.734	1.743	As$_{A'}$–F$_{7A'}$	1.734	1.743	As$_B$–F$_{7B}$	1.739	1.748
As$_A$–F$_{8A}$	1.728	1.736	As$_{A'}$–F$_{8A'}$	1.728	1.736	As$_B$–F$_{8B}$	1.734	1.743
			Bond Angles (deg)					
F$_1$–Br–F$_2$	89.2	89.3						
F$_1$–Br–O$_1$	101.1	101.0						
F$_1$–Br---F$_{3A}$	165.6	165.8						
			F$_1$–Br---F$_{3A'}$	83.9	84.6			
						F$_1$–Br---F$_{3B}$	78.6	79.1
F$_2$–Br–O$_1$	101.1	100.9						
F$_2$–Br---F$_{3A}$	83.9	84.7						
			F$_2$–Br---F$_{3A'}$	165.6	165.8			
						F$_2$–Br---F$_{3B}$	78.7	79.1
O$_1$–Br---F$_{3A}$	92.6	92.8						
			O$_1$–Br---F$_{3A'}$	92.6	92.8			
						O$_1$–Br---F$_{3B}$	179.6	179.9

Table A5.2. Continued.

F_{3A}---Br---$F_{3A'}$	99.9	98.3						
						F_{3A}---Br---F_{3B}	87.6	87.2
			$F_{3A'}$---Br---F_{3B}	87.6	87.2			
Br---F_{3A}–As_A	135.3	136.9						
			Br---$F_{3A'}$–$As_{A'}$	135.3	137.0			
						Br---F_{3B}–As_B	141.6	143.6
F_{3A}–As_A–F_{4A}	87.8	87.8	$F_{3A'}$–$As_{A'}$–$F_{4A'}$	87.8	87.8	F_{3B}–As_B–F_{4B}	88.8	88.9
F_{3A}–As_A–F_{5A}	88.1	88.1	$F_{3A'}$–$As_{A'}$–$F_{5A'}$	88.1	88.1	F_{3B}–As_B–F_{5B}	89.0	89.0
F_{3A}–As_A–F_{6A}	179.8	179.8	$F_{3A'}$–$As_{A'}$–$F_{6A'}$	179.8	179.8	F_{3B}–As_B–F_{6B}	179.8	179.9
F_{3A}–As_A–F_{7A}	88.1	88.0	$F_{3A'}$–$As_{A'}$–$F_{7A'}$	88.1	88.0	F_{3B}–As_B–F_{7B}	89.0	89.0
F_{3A}–As_A–F_{8A}	88.3	88.3	$F_{3A'}$–$As_{A'}$–$F_{8A'}$	88.3	88.3	F_{3B}–As_B–F_{8B}	89.0	89.0
F_{4A}–As_A–F_{5A}	90.1	90.1	$F_{4A'}$–$As_{A'}$–$F_{5A'}$	90.1	90.1	F_{4B}–As_B–F_{5B}	90.1	90.1
F_{4A}–As_A–F_{6A}	92.1	92.2	$F_{4A'}$–$As_{A'}$–$F_{6A'}$	92.1	92.2	F_{4B}–As_B–F_{6B}	91.0	91.1
F_{4A}–As_A–F_{7A}	175.8	175.8	$F_{4A'}$–$As_{A'}$–$F_{7A'}$	175.8	175.8	F_{4B}–As_B–F_{7B}	177.8	177.8
F_{4A}–As_A–F_{8A}	90.0	90.1	$F_{4A'}$–$As_{A'}$–$F_{8A'}$	90.0	90.1	F_{4B}–As_B–F_{8B}	90.1	90.1
F_{5A}–As_A–F_{6A}	91.8	91.7	$F_{5A'}$–$As_{A'}$–$F_{6A'}$	91.8	91.7	F_{5B}–As_B–F_{6B}	91.0	91.0
F_{5A}–As_A–F_{7A}	89.8	89.7	$F_{5A'}$–$As_{A'}$–$F_{7A'}$	89.8	89.7	F_{5B}–As_B–F_{7B}	89.8	89.8
F_{5A}–As_A–F_{8A}	176.4	176.4	$F_{5A'}$–$As_{A'}$–$F_{8A'}$	176.4	176.4	F_{5B}–As_B–F_{8B}	178.0	178.1
F_{6A}–As_A–F_{7A}	92.1	92.1	$F_{6A'}$–$As_{A'}$–$F_{7A'}$	92.1	92.1	F_{6B}–As_B–F_{7B}	91.1	91.1
F_{6A}–As_A–F_{8A}	91.8	91.8	$F_{6A'}$–$As_{A'}$–$F_{8A'}$	91.8	91.8	F_{6B}–As_B–F_{8B}	91.0	91.0
F_{7A}–As_A–F_{8A}	89.8	89.8	$F_{7A'}$–$As_{A'}$–$F_{8A'}$	89.8	89.8	F_{7B}–As_B–F_{8B}	89.8	89.8

[a] The Stutt Huzpolar 2 basis set was used. The energy-minimized geometry was C_1. The atom labeling scheme corresponds to that used in Figure 8.10.[b] PBE1PBE.

Table A5.3. Calculated Geometrical Parameters for $[BrOF_2][AsF_6]\cdot XeF_2$

	PBE1PBE[a]	B3LYP[a]		PBE1PBE[a]	B3LYP[a]
		Bond Lengths (Å)			
Br(1)–O(1)	1.554	1.567	Xe(1)–F(4)	1.948	1.976
Br(1)–F(1)	1.730	1.753	As(1)–F(5)	1.762	1.770
Br(1)–F(2)	1.752	1.777	As(1)–F(6)	1.889	1.918
Br(1)---F(3)	2.369	2.397	As(1)–F(7)	1.705	1.719
Br(1)---F(5)	2.708	2.729	As(1)–F(8)	1.698	1.715
Br(1)---F(6)	2.162	2.178	As(1)–F(9)	1.695	1.707
Xe(1)–F(3)	2.068	2.083	As(1)–F(10)	1.727	1.744
		Bond Angles (deg)			
F(1)–Br(1)–F(2)	89.0	89.4	Br(1)---F(6)–As(1)	117.7	117.5
F(1)–Br(1)–O(1)	102.8	102.5	F(3)–Xe(1)–F(4)	177.8	176.8
F(1)–Br(1)---F(3)	165.1	165.2	F(5)–As(1)–F(6)	83.7	83.3
F(1)–Br(1)---F(5)	91.7	84.6	F(5)–As(1)–F(7)	88.7	89.1
F(1)–Br(1)---F(6)	85.2	86.9	F(5)–As(1)–F(8)	170.8	170.0
F(2)–Br(1)–O(1)	100.5	100.5	F(5)–As(1)–F(9)	92.9	93.5
F(2)–Br(1)---F(3)	86.1	86.4	F(5)–As(1)–F(10)	87.3	87.4
F(2)–Br(1)---F(5)	109.9	108.9	F(6)–As(1)–F(7)	86.6	86.7
F(2)–Br(1)---F(6)	167.0	167.4	F(6)–As(1)–F(8)	87.2	86.8
O(1)–Br(1)---F(3)	92.0	92.2	F(6)–As(1)–F(9)	176.4	176.6
O(1)–Br(1)---F(5)	146.6	149.9	F(6)–As(1)–F(10)	85.5	85.5
O(1)–Br(1)---F(6)	92.1	92.1	F(7)–As(1)–F(8)	92.0	91.8
F(3)---Br(1)---F(5)	76.8	83.3	F(7)–As(1)–F(9)	94.5	94.6
F(3)---Br(1)---F(6)	96.6	94.2	F(7)–As(1)–F(10)	171.5	171.7
F(5)---Br(1)---F(6)	58.8	58.8	F(8)–As(1)–F(9)	96.2	96.3
Br(1)---F(3)–Xe(1)	141.7	150.5	F(8)–As(1)–F(10)	90.8	90.4
Br(1)---F(5)–As(1)	99.7	100.2	F(9)–As(1)–F(10)	93.1	93.1

[a] The aug-cc-pVTZ(-PP) basis set was used. The energy-minimized geometry was C_1. The atom labeling scheme corresponds to that used in Figure 8.10.

Table A5.4. NBO Valencies, Bond Orders, and Charges (NPA) for $[BrOF_2][AsF_6]\cdot XeF_2$

	Charges [Valencies]			
	PBE1PBE		B3LYP	
Br(1)	2.397	[2.296]	2.371	[1.931]
O(1)	−0.709	[0.971]	−0.694	[0.862]
F(1)	−0.441	[0.467]	−0.439	[0.359]
F(2)	−0.476	[0.435]	−0.476	[0.337]
Xe(1)	1.268	[0.608]	1.258	[0.582]
F(3)	−0.655	[0.355]	−0.652	[0.329]
F(4)	−0.549	[0.374]	−0.545	[0.358]
As(1)	2.644	[3.207]	2.642	[3.136]
F(5)	−0.617	[0.484]	−0.607	[0.466]
F(6)	−0.596	[0.479]	−0.595	[0.436]
F(7)	−0.561	[0.518]	−0.558	[0.495]
F(8)	−0.553	[0.521]	−0.553	[0.504]
F(9)	−0.560	[0.533]	−0.559	[0.511]
F(10)	−0.590	[0.488]	−0.594	[0.470]
	Bond Orders			
Br(1)-O(1)	1.038		0.927	
Br(1)-F(1)	0.506		0.399	
Br(1)-F(2)	0.472		0.371	
Br(1)---F(3)	0.088		0.070	
Br(1)---F(5)	0.029		0.025	
Br(1)---F(6)	0.156		0.131	
Xe(1)-F(3)	0.242		0.234	
Xe(1)-F(4)	0.359		0.344	
As(1)-F(5)	0.509		0.504	
As(1)-F(6)	0.382		0.362	
As(1)-F(7)	0.579		0.570	
As(1)-F(8)	0.590		0.576	
As(1)-F(9)	0.591		0.581	
As(1)-F(10)	0.552		0.538	

Bonding in XeF_2. The QTAIM and ELF population analyses of XeF_2 are compared with those of KrF_2 in Table S14. The atomic populations of Xe and F indicate a net density transfer of 0.60 e from Xe towards each fluorine atom. The Kr-F and F-F delocalization indexes are 0.88 and 0.14, respectively. The Laplacian of the density at the XeF bond critical point is positive $(\nabla^2\rho(r_{bcp}) = 0.23\ e\ bohr^{-5})$. With respect to KrF_2, the charge transfer is larger by 0.13 e indicating more ionic character of the system, which is consistent with the larger value of the Laplacian calculated for XeF_2 than for KrF_2. The ELF reduction of localization diagram for XeF_2 (Scheme A5.1) is consistent with more ionic bonding than in KrF_2 because the bifurcation between V(F) and V(Xe) occurs for $\eta(\mathbf{r}) = 0.26$ instead of 0.42 in KrF_2. Figure A5.1 displays the ELF $\eta(\mathbf{r}) = 0.75$ localization domains of XeF_2 showing the absence of any disynaptic (bond) between Xe and F. The ELF population analysis, reported in Table A5.5, together with the QTAIM results suggest a bonding interpretation in terms of a large delocalization of the electron density between the Xe and F valence shells and transfer of electron density towards the fluorine center, 35% versus 27%. Weighted promolecular mesomeric forms can be proposed from the probabilities of finding n electrons in a given basin. It is worth noting that the weight of the totally ionic structure is significantly larger than in KrF_2.

$$\left\{\begin{array}{l} F\downarrow\ Xe\ F\uparrow \\ F\uparrow\ Xe\ F\downarrow \end{array}\right. \qquad 21\%$$

$$\left\{\begin{array}{l} F\downarrow\ Xe^{+}\uparrow\ F^{-} \\ F\uparrow\ Xe^{+}\downarrow\ F^{-} \\ F^{-}\ \ Xe^{+}\uparrow\ F\downarrow \\ F^{-}\ \ Xe^{+}\downarrow\ F\uparrow \end{array}\right. \qquad 44\%$$

$$F^{-}\ Xe^{2+}\ F^{-} \qquad 35\%$$

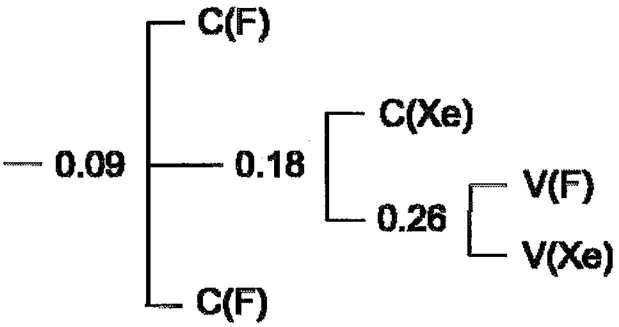

Scheme A5.1. Reduction of localization diagram for XeF_2 showing the ordering of localization nodes and the boundary isosurface value, $\eta(\mathbf{r})$, at which the reducible domains split.

Table A5.5: QTAIM Atomic Populations, Delocalization Indexes, ELF Basin Population and Covariance Matrix Elements of Free NgF_2 (Ng = Xe, Kr) NgF_2 Coordinated to the Bromine Atom in $[BrOF_2][AsF_6]{\cdot}2NgF_2$

	XeF_2	$[BrOF_2][AsF_6]{\cdot}2XeF_2$[a]	KrF_2[b]	$[BrOF_2][AsF_6]{\cdot}2KrF_2$[a,b]
$\bar{N}$(A)	52.80	52.70	35.03	34.96
$\bar{N}$ (F)	9.60	9.63	9.47	9.54
$\bar{N}$ (F')	9.60	9.55	9.47	9.39
$\bar{N}$ (Br)		32.60		32.66
δ(Ng,F)	0.88	0.68	0.86	0.68
δ(Ng,F')	0.88	0.96	0.86	0.98
δ(Br,F)		0.26		0.24
$\bar{N}$ [C(F)]	2.13	2.13	2.13	2.13
$\bar{N}$ [C(Ng)]	46.04	45.40	27.72	27.62
C [V(F)]	7.45	7.47	7.30	7.38
$\bar{N}$ [V(F')]	7.45	7.46	7.30	7.89
$\bar{N}$ [V(Ng)]	6.83	7.26	7.41	6.75
$\bar{N}$ [V(Br)]		3.04		3.11
⟨*cov*[V(Ng),V(F)]⟩	-0.39	-0.31	-0.40	-0.24
⟨*cov*[V(Ng),V(F')]⟩	-0.39	-0.42	-0.40	-0.84
⟨*cov*[V(F),V(F')]⟩	-0.06	-0.04	-0.10	-0.08

[a] In the adducts, F denotes the bridging fluorine atom and F' denotes the terminal fluorine atom. [b] From ref 232.

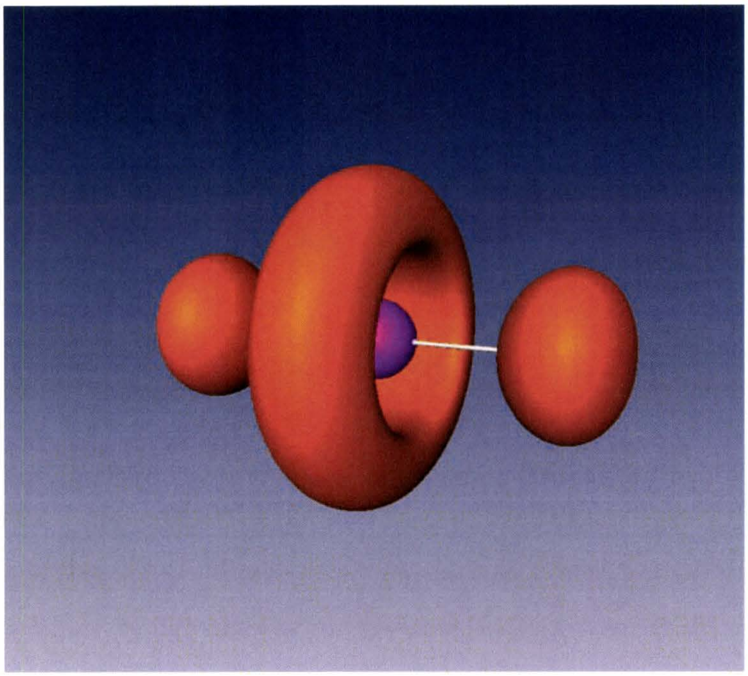

Figure A5.1. ELF localization domains for XeF_2. The isosurface value is $\eta(\mathbf{r}) = 0.75$. Color code: magenta = core, brick-red = monosynaptic basin.

Bonding in $[BrOF_2][AsF_6]_3^{2-}$. Figure A5.2. displays the $\eta(\mathbf{r}) = 0.75$ localization domains of the complex anion, $[BrOF_2][AsF_6]_3^{2-}$. The bonding between the cationic subunit and the surrounding anions is essentially ionic. However, the QTAIM analysis reveals a small electron density transfer of ca. 0.2 e from the two nearest AsF_6^- anions towards $BrOF_2^+$. The value of the Laplacian of the charge density at the bond critical points of the bond paths linking the bromine atom to fluorines of AsF_6^- is positive (0.17), in agreement with the ionic picture. Moreover, the corresponding delocalization index is small, δ(Br, F) = 0.22. The ELF analysis shows a bromine lone pair with a population of 3.0 e, that is 0.11 e lower than in the isolated $BrOF_2^+$ cation.

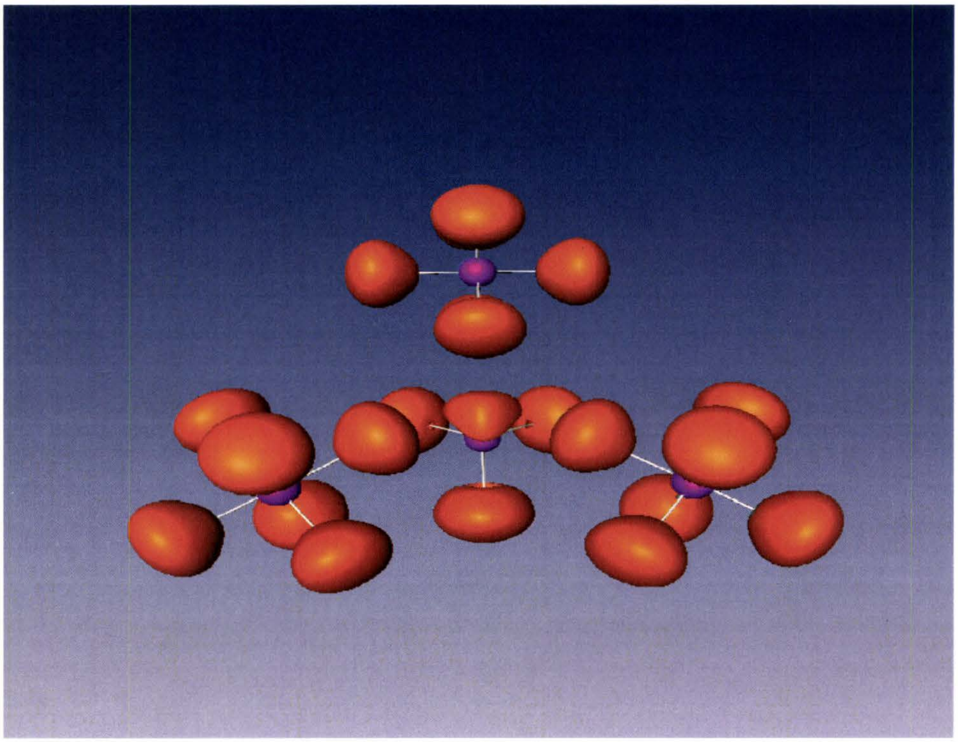

Figure A5.2. ELF localization domains for $[BrOF_2][AsF_6]_3^{2-}$. The isosurface value is $\eta(\mathbf{r}) = 0.75$. Color code: magenta = core, brick-red = monosynaptic basin, green = disynaptic basin.

APPENDIX 6

Solid State Thermochemistry. The standard enthalpies for the solid-state decomposition of $[XeONO_2][AsF_6]$ (eq A6.1) were evaluated from the lattice enthalpies of $[XeONO_2][AsF_6]$ and $[NO_2][AsF_6]$ according to eq A6.2. The lattice enthalpies were estimated by use of the volume-based method of Bartlett et al.[208,209] as generalized by Jenkins et al.[210,211] in eq 3, where R is the gas constant(8.314 J mol^{-1} K^{-1}), I is the ionicity

$$[XeONO_2][AsF_6]_{(s)} \longrightarrow [NO_2][AsF_6]_{(s)} + Xe_{(g)} + \tfrac{1}{2}\,O_{2(g)} \tag{A6.1}$$

$$\Delta H^{\circ}(A6.1) = \Delta H^{\circ}_{L}([XeONO_2][AsF_6]) - \Delta H^{\circ}_{L}([NO_2][AsF_6]) \tag{A6.2}$$

$$\Delta H^{\circ}_{L} = 2I\left(\frac{\alpha}{\sqrt[3]{V_m}} + \beta\right) + p\mathrm{RT} \tag{A6.3}$$

of the salt and the constants, α, β, and p, depend on the nature of the salt. For the salts under investigation, which are singly charged and the following values were used: $I = 1$, $\alpha = 117.3$ nm kJ mol^{-1}, $\beta = 51.9$ kJ mol^{-1}, and $p = 2$. In this formalism, ΔH°_{L} is the lattice enthalpy and is defined as the energy required to break the crystal lattice, and therefore has a positive value. This approach is generally accurate to ~4% for salts with ΔH°_{L} less than 5000 kJ mol^{-1},[211] and is particularly useful because the formula unit volume (V_m) of an unknown salt can be estimated with reasonable accuracy using several methods.[211] The value for $V([NO_2][AsF_6]) = 0.1330(2)$ nm^3 was determined directly from the X-ray crystal structure of $[NO_2][AsF_6]$[315] and that for $V([XeONO_2][AsF_6])$ was determined from eq A6.4. Where $V_m(FXeONO_2) = 0.096650(4)$ (this work), $V_{-}(F^{-}) = 0.025(10)$,[211] and $V_{-}(AsF_6^{-})$[211] $= 0.110(7)$ nm^3.

$$\begin{aligned} V_m([XeONO_2][AsF_6]) &= V_m(FXeONO_2) - V_{-}(F^{-}) + V_{-}(AsF_6^{-}) \\ &= 0.182(XX)\ \mathrm{nm}^3 \end{aligned} \tag{A6.4}$$

Application of eq A6.3 yields

$$\Delta H^{\circ}_{L}([XeONO_2][AsF_6]) = 523\ \mathrm{kJ\ mol^{-1}} \tag{A6.5}$$

$$\Delta H^{\circ}_{L}([NO_2][AsF_6]) = 568\ \mathrm{kJ\ mol^{-1}} \tag{A6.6}$$

$$\Delta H^{\circ}(A6.1) = -45\ \mathrm{kJ\ mol^{-1}} \tag{A6.7}$$

A method for estimating the absolute standard entropy of a salt from its unit volume has been reported by Jenkins and Glasser (eq A6.8) where $k = 1360$ J mol^{-1} K^{-1} (nm^{-3} formula unit^{-1}) and $c = 15$ J mol^{-1} K^{-1}.[30] The standard entropies of the salts under consideration are $S^{\circ}([XeONO_2][AsF_6]_{(s)}) =$

$$S^{\circ} = kV_m + c \tag{A6.8}$$

262 J mol^{-1} K^{-1} and $S^{\circ}([NO_2][AsF_6]_{(s)}) = 196$ J mol^{-1} K^{-1}. When coupled with the experimental standard entropies of $O_{2(g)}$ (206 J mol^{-1} K^{-1})[195] and $Xe_{(g)}$ (169.7 J mol^{-1} K^{-1}),[316] this method allows $\Delta S^{\circ}(A6.1)$ and $\Delta G^{\circ}(A6.1)$ to be calculated from eqs A6.9 and

A6.10, respectively, yielding $\Delta S°(\text{A6.1}) = 207$ J mol^{-1} K^{-1} and $\Delta G°(\text{A6.1}) = -107$ kJ mol^{-1}. As expected, the enthalpy and Gibbs free energy of the solid-state

$$\Delta S°(\text{A6.1}) = \tfrac{1}{2}S°(\text{O}_{2(g)}) + S°([\text{NO}_2][\text{AsF}_6]_{(s)}) + S°(\text{Xe}_{(g)}) - S°([\text{XeONO}_2][\text{AsF}_6]_{(s)}) \quad \text{(A6.9)}$$

$$\Delta G°(\text{A6.1}) = \Delta H°(\text{A6.1}) - \text{T}\Delta S°(\text{A6.1}) \quad \text{(A6.10)}$$

decomposition of $[\text{XeONO}_2][\text{AsF}_6]$ are significantly less exothermic and spontaneous than for the gas-phase decomposition of the XeONO_2^+ cation (eq A6.11 and Table 9.1).

Although the solid-state (eq A6.1) and gas-phase (eq A6.11) decompositions are spontaneous under standard conditions, the gas-phase reaction leading to the formation of XeONO_2^+ and AsF_6^- is highly endothermic (eq A6.12 and Table 9.1). In principle, the energetics of the fluoride ion abstraction reaction under standard conditions (eq A6.13) may be explored by construction of a Born-Fajans-Haber thermochemical cycle (eq

$$\text{XeONO}_2{}^+{}_{(g)} \longrightarrow \text{Xe}_{(g)} + \tfrac{1}{2}\text{O}_{2(g)} + \text{NO}_2{}^+{}_{(g)} \quad \text{(A6.11)}$$

$$\text{FXeONO}_{2(g)} + \text{AsF}_{5(g)} \longrightarrow \text{XeONO}_2{}^+{}_{(g)} + \text{AsF}_6{}^-{}_{(g)} \quad \text{(A6.12)}$$

$$\text{FXeONO}_{2(s)} + \text{AsF}_{5(g)} \longrightarrow [\text{XeONO}_2][\text{AsF}_6]_{(s)} \quad \text{(A6.13)}$$

A6.14), however, the absence of a value for the heat of sublimation/vaporization of FXeONO_2 precludes construction of a complete thermochemical cycle. Consideration of the incomplete thermochemical cycle (eq A6.14) establishes that, in the absence of a value for $\Delta H°(\text{sub/vap FXeONO}_2)$ and taking $\Delta H°(\text{vap AsF}_5) = 0$ for AsF_5 gas, eq A6.13

$$\begin{aligned}\Delta H°(\text{A6.13}) &= \Delta H°(\text{A6.12}) - \Delta H°(\text{sub/vap FXeONO}_2) - \Delta H°(\text{vap AsF}_5) - \Delta H°_{\text{L}}([\text{XeONO}_2][\text{AsF}_6]) \\ &= 359 - \Delta H°(\text{sub/vap FXeONO}_2) - 0 - 523 = -164 - \Delta H°(\text{sub/vap FXeONO}_2)\ \text{kJ mol}^{-1}\end{aligned} \quad \text{(A6.14)}$$

$$\Delta S°(\text{A6.13}) = S°([\text{XeONO}_2][\text{AsF}_6]_{(s)}) - S°(\text{AsF}_{5(g)}) - S°(\text{FXeONO}_{2(s)}) \quad \text{(A6.15)}$$

is expected to be exothermic ($\Delta H°(\text{A6.13}) < -164$ kJ mol^{-1}). The spontaneity of eq A6.13 is confirmed by an estimate of $\Delta S°(\text{A6.13})$ according to eq A6.15 where the experimental standard entropy value of (323.4 J mol^{-1} K^{-1})[317] is used for $\text{AsF}_{5(g)}$, that of $[\text{XeONO}_2][\text{AsF}_6]_{(s)}$ was estimated from eq A6.8 (262 J mol^{-1} K^{-1}), and that of $\text{FXeONO}_{2(s)}$ was estimated by the method of Latimer,[318,319] giving $S°(\text{FXeONO}_{2(s)}) = 197$ J mol^{-1} K^{-1}, so that $\Delta S°(\text{A6.13}) = -259$ J mol^{-1} K^{-1}. Reaction A6.13 is spontaneous under standard conditions based on the Gibbs free energy given by eq A6.16, with spontaneity increasing with decreasing temperature. Taking into account that the heat of vaporization

$$\Delta G°(\text{A6.13}) = \Delta H°(\text{A6.13}) - \text{T}\Delta S°(\text{A6.13}) = -66 - \Delta H°(\text{sub/vap FXeONO}_2)\ \text{kJ mol}^{-1} \quad \text{(A6.16)}$$

for $\text{AsF}_{5(l)}$ is unknown but is expected to be less than that of $\text{SbF}_{5(l)}$ (~27 kJ mol^{-1})[320] and the decrease in the magnitude of the negative TΔS term for low-temperature reactions in

$AsF_{5(l)}$, $[XeONO_2][AsF_6]_{(s)}$ is favored at lower temperatures but is unstable, decomposing according to eq A6.1 at lower temperatures (positive $T\Delta S$ term).

The thermochemistry for eq A6.1 was determined from the appropriate thermochemical cycle (eq A6.17) using the gas-phase standard enthalpy, ΔH°(A6.11)) (Table 9.1), and Gibbs free energy (ΔG°(A6.11)) according to eqs A6.18 and A6.19. The solid state decomposition of $[XeONO_2][AsF_6]$ (eq A6.1) is significantly more endothermic than for the gas phase decomposition of the $XeONO_2^+$ cation.

$$\begin{aligned}\Delta H^{\circ}(\text{A6.1}) &= \Delta H^{\circ}(\text{A6.11}) - \Delta H^{\circ}_{L}([NO_2][AsF_6]) + \Delta H^{\circ}_{L}([XeONO_2][AsF_6]) \\ &= -188 \text{ kJ mol}^{-1}\end{aligned} \quad \text{(A6.17)}$$

$$\begin{aligned}\Delta S^{\circ}(\text{A6.1}) &= S^{\circ}([NO_2][AsF_6]_{(s)}) + S^{\circ}(Xe_{(g)}) + \tfrac{1}{2}S^{\circ}(O_{2(g)}) - S^{\circ}([XeONO_2][AsF_6]_{(s)}) \\ &= 207 \text{ J mol}^{-1}\text{ K}^{-1}\end{aligned} \quad \text{(A6.18)}$$

$$\Delta G^{\circ}(\text{A6.1}) = \Delta H^{\circ}(\text{A6.1}) - T\Delta S^{\circ}(\text{A6.1}) = -250 \text{ kJ mol}^{-1} \quad \text{(A6.19)}$$

Table A6.1. Calculated[a] Vibrational Frequencies, Raman and Infrared Intensities for $FXe^{16}O^{14}N^{16}O_2$, $FXe^{18}O^{14}N^{16}O_2$, $FXe^{16}O^{14}N^{18}O_A{}^{16}O_S$, $FXe^{16}O^{14}N^{16}O_A{}^{18}O_S$, $FXe^{18}O^{14}N^{18}O_A{}^{16}O_S$, $FXe^{18}O^{14}N^{16}O_A{}^{18}O_S$ and $FXe^{16}O^{15}N^{16}O_2$[b]

PBE1PBE/aug-cc-pVTZ(-PP)														
$FXe^{16}ON^{16}O_2$	$FXe^{18}ON^{16}O_2$	$\Delta\nu^{16/18\,c}$	$FXe^{16}ON^{18}O_A{}^{16}O_S$	$\Delta\nu^{16/18A\,d}$	$FXe^{16}ON^{16}O_A{}^{18}O_S$	$\Delta\nu^{16/18S\,e}$	$FXe^{18}ON^{18}O_A{}^{16}O_S$	$\Delta\nu^{16/18\text{-}18A\,f}$	$FXe^{18}ON^{16}O_A{}^{18}O_S$	$\Delta\nu^{16/18\text{-}18S\,g}$	$FXeO^{15}NO_2$	$\Delta\nu^{14/15\,h}$	assgnt
1732.2(50)[362]	1732.0(50)[361]	–0.2	1714.0(45)[344]	–18.2	1721.7(52)[363]	–10.5	1713.7(45)[344]	–18.5	1721.4(51)[363]	–10.8	1692.5(48)[346]	–39.7	$\nu_1(A')$
1357.8(12)[386]	1357.6(12)[390]	–0.2	1336.5(12)[404]	–21.3	1330.1(9)[394]	–27.7	1336.3(12)[408]	–21.5	1329.8(9)[398]	–28.0	1341.5(12)[341]	–16.3	$\nu_2(A')$
929.8(3)[360]	919.2(3)[328]	–10.6	919.6(4)[345]	–10.2	918.5(3)[346]	–11.3	908.4(3)314]	–21.4	907.4(3)[314]	–22.4	916.2(3)[367]	–13.6	$\nu_3(A')$
811.1(<0.1)[10]	808.9(<0.1)[10]	–2.2	807.0(<0.1)[10]	–4.1	807.0(<0.1)[10]	–4.1	804.8(<0.1)[10]	–6.3	804.8(<0.1)[10]	–6.3	790.0(<1)[10]	–21.1	$\nu_{10}(A'')$
747.5(16)[23]	722.3(12)[18]	–25.2	740.9(15)[23]	–6.6	740.7(19)[29]	–6.8	715.4(10)[16]	–32.1	714.9(15)[25]	–32.6	746.1(17)[25]	–1.4	$\nu_4(A')$
708.7(14)[36]	685.2(14)[44]	–23.5	700.0(16)[36]	–8.7	699.1(12)[27]	–9.6	676.9(16)[45]	–31.8	676.5(12)[33]	–32.2	708.6(14)[35]	–0.1	$\nu_5(A')$
537.5(51)[255]	538.2(50)[259]	0.7	538.3(51)[255]	0.8	538.3(51)[257]	0.8	538.1(51)[257]	–0.1	538.1(50)[258]	0.6	538.3(50)[258]	0.8	$\nu_6(A')$
322.5(51)[37]	327.3(24)[36]	4.8	325.7(22)[35]	3.2	331.1(24)[37]	8.6	320.4(22)[35]	–2.1	325.6(24)[36]	3.1	331.9(23)[36]	9.4	$\nu_7(A')$
214.1(<1)[9]	209.5(<1)[9]	–4.6	214.3(<1)[9]	0.2	214.5(<1)[9]	0.4	209.2(<1)[9]	–4.9	209.4(<1)[9]	–4.7	214.5(<1)[9]	0.4	$\nu_{11}(A'')$
207.8(6)[7]	207.5(6)[7]	–0.3	208.1(6)[7]	0.3	204.8(5)[7]	–3.0	207.1(6)[7]	–0.7	203.9(5)[7]	–3.9	207.9(6)[7]	0.1	$\nu_8(A')$
123.3(2)[4]	123.1(2)[4]	–0.2	122.7(2)[4]	–0.6	121.7(2)[4]	–1.6	122.4(2)[4]	–0.9	121.4(2)[4]	–1.9	123.3(2)[4]	0.0	$\nu_9(A')$
75.3(<1)[2]	74.6(<1)[75]	–0.7	73.5(<1)[1]	–1.8	74.9(<1)[2]	–0.4	72.7(<1)[1]	–2.6	74:1(<1)[1]	–1.2	75.3(<1)[2]	0.0	$\nu_{12}(A'')$

MP2/aug-cc-pVTZ(-PP)													
$FXe^{16}ON^{16}O_2$	$FXe^{18}ON^{16}O_2$	$\Delta\nu^{16/18\,c}$	$FXe^{16}ON^{18}O_A{}^{16}O_S$	$\Delta\nu^{16/18A\,d}$	$FXe^{16}ON^{16}O_A{}^{18}O_S$	$\Delta\nu^{16/18S\,e}$	$FXe^{18}ON^{18}O_A{}^{16}O_S$	$\Delta\nu^{16/18\text{-}18A\,f}$	$FXe^{18}ON^{16}O_A{}^{18}O_S$	$\Delta\nu^{16/18\text{-}18S\,g}$	$FXeO^{15}NO_2$	$\Delta\nu^{14/15\,h}$	assgnt
1789.4(50)[200]	1789.4(50)[199]	0.0	1773.0(47)[191]	–16.4	1775.0(51)[200]	–14.4	1772.9(46)[191]	–16.5	1774.9(51)[200]	–14.5	1748.8(49)[192]	–40.6	$\nu_1(A')$
1269.4(17)[355]	1269.0(17)[363]	–0.4	1246.2(16)[371]	–23.2	1243.3(15)[366]	–26.1	1245.8(16)[379]	–23.6	1242.9(15)[375]	–26.5	1256.5(18)[311]	–12.9	$\nu_2(A')$
848.8(5)[457]	843.6(6)[409]	–5.2	839.1(5)[450]	–9.7	838.4(5)[453]	–10.4	832.8(6)[400]	–16.0	832.3(6)[402]	–16.5	835.7(4)[453]	–13.1	$\nu_3(A')$
769.5(<0.1)[6]	767.6(<0.1)[6]	–1.9	765.5(<0.1)[6]	–4.0	765.6(<0.1)[6]	–3.9	763.7(<0.1)[6]	–5.8	763.7(<0.1)[6]	–5.8	749.5(<1)[6]	–20.0	$\nu_{10}(A'')$
733.8(19)[51]	707.4(14)[44]	–26.4	727.7(19)[48]	–6.1	728.7(21)[60]	–5.1	700.8(13)[40]	–33.0	701.7(15)[54]	–32.1	732.5(19)[55]	–1.3	$\nu_4(A')$
680.0(10)[96]	654.9(10)[101]	–25.1	673.9(11)[90]	–6.1	671.8(9)[74]	–8.2	649.3(12)[99]	V30.7	647.5(9)[79]	–32.5	679.9(10)[96]	–0.1	$\nu_5(A')$
517.8(58)[320]	517.9(57)[328]	0.1	518.4(59)[319]	0.6	518.5(58)[321]	0.7	517.7(58)[325]	–0.1	517.8(57)[328]	–0.0	518.4(58)[323]	–0.4	$\nu_6(A')$
344.2(39)[27]	339.4(39)[26]	–4.8	336.6(36)[26]	–7.6	342.5(39)[27]	–1.7	331.8(36)[25]	–12.4	337.5(39)[27]	–6.7	343.4(38)[26]	–0.8	$\nu_7(A')$
217.3(<1)[9]	212.6(<1)[9]	–4.7	217.6(<1)[4]	0.3	217.8(<1)[10]	0.5	212.4(<1)[9]	–4.9	212.6(<1)[9]	–4.7	217.7(<1)[9]	0.4	$\nu_{11}(A'')$
217.2(5)[4]	216.9(5)[4]	–0.3	217.5(6)[4]	0.3	213.6(5)[4]	–3.6	216.5(5)[4]	–0.7	212.7(5)[4]	–4.5	217.2(6)[4]	0.0	$\nu_8(A')$
127.1(2)[4]	127.0(2)[4]	–0.1	126.5(2)[4]	–0.6	125.7(2)[4]	–1.4	126.2(2)[4]	–0.9	125.4(2)[4]	–1.7	127.1(2)[4]	0.0	$\nu_9(A')$
72.8(<1)[1]	72.1(<1)[1]	–0.7	71.0(<0.1)[1]	–1.8	72.3(<1)[1]	–0.5	70.2(<0.1)[1]	–2.6	71.6(<1)[1]	–1.2	72.8(<1)[1]	0.0	$\nu_{12}(A'')$

[a] aug-cc-pVTZ(-PP). Values in parentheses denote Raman intensities ($Å^4\ u^{-1}$). Values in square brackets denote infrared intensities (km mol^{-1}). [b] A denotes ^{18}O anti and S denotes ^{18}O syn with respect to the O–Xe–F group. [c] $\Delta\nu^{16/18} = \nu(FXe^{18}ON^{16}O_2) - \nu(FXe^{16}ON^{16}O_2)$. [d] $\Delta\nu^{16/18A} = \nu(FXe^{16}ON^{18}O_A{}^{16}O_S) - \nu(FXe^{16}ON^{16}O_2)$. [e] $\Delta\nu^{16/18S} = \nu(FXe^{16}ON^{16}O_A{}^{18}O_S) - \nu(FXe^{16}ON^{16}O_2)$. [f] $\Delta\nu^{16/18\text{-}18A} = \nu(FXe^{18}ON^{18}O_A{}^{16}O_S) - \nu(FXe^{16}ON^{16}O_2)$. [g] $\Delta\nu^{16/18\text{-}18S} = \nu(FXe^{18}ON^{16}O_A{}^{18}O_S) - \nu(FXe^{16}ON^{16}O_2)$. [h] $\Delta\nu^{14/15} = \nu(FXeO^{15}NO_2) - \nu(FXe^{16}ON^{16}O_2)$.

Table A6.2. Experimental and Calculated[a] Frequencies for $O(XeF)_2$

frequencies, cm^{-1}						
exptl[a]			calcd[b]			
$^{16}O^{c,d}$	$^{17}O^{c,d}$	$^{18}O^{c}$	^{16}O	^{17}O	^{18}O	assignts (C_{2v})[e]
558.5(4) 547.5(28)	532.3 sh	531.9(1) 519.2(36)	605.6(11)[327]	588.9(10)[317]	573.7(10)[306]	$\nu_7(B_2)$, $\nu_{as}(XeO)_2$
498.0 sh	n.o.	493.2(3)	539.3(41)[76]	538.9(46)[74]	537.8(50)[71]	$\nu_1(A_1)$, $\nu_s(XeO)_2 - \nu_s(XeF)_2$
437.7(7) 433.1(100)	427.4(100)	422.5(100) 418.3(14)	458.6(76)[6]	447.9(69)[8]	437.9(63)[9]	$\nu_2(A_1)$, $\nu_s(XeO)_2 + \nu_s(XeF)_2$
416.7(5) 406.6(20)		409.5(15) 403.2(58)	496.4(19)[448]	497.1(19)[444]	497.1(19)[440]	$\nu_8(B_2)$, $\nu_{as}(XeF)_2$
235.6(1)	228.9(5)	227.4(2)	233.5(<0.1)[25]	229.9(<0.1)[25]	226.3(<0.1)[25]	$\nu_6(B_1)$, $\delta(FXeO)$ o.o.p.
193.1(10)	193.0(72)	193.1(18)	181.8(6)[4]	183.0(6)[4]	183.1(6)[4]	$\nu_3(A_1)$, $\delta(FXeO + \delta(FXeO)$
173.7(2)	173.7(36)	173.7(3)	159.7(1)[0]	160.4(1)[0]	160.4(1)[0]	$\nu_5(A_2)$, $\rho_t(FXeO)$
159.3(6)	159.3(64)	159.3(11)	155.5(<1)[1]	156.2(<1)[1]	156.2(<1)[1]	$\nu_9(B_2)$, $\delta(FXeO - \delta(FXeO)$
62.4(2)	62.2(18)	62.4(4)	61.8(7)[3]	61.8(7)[3]	61.7(7)[3]	$\nu_4(A_1)$, $\delta(XeOXe)$

[a] PBE1PBE/aug-cc-pVTZ(-PP). [b]Values in parentheses denote Raman intensities (Å^4 u^{-1}). Values in square brackets denote infrared intensities (km mol^{-1}). [b] A denotes ^{18}O anti and S denotes ^{18}O syn with respect to the O–Xe–F group. [c] The abbreviations (sh) and n.o. denotes a shoulder and not observed, respectively. [d] The abbreviations denote stretch (ν), bend (δ), twist (ρ_t), and out-of-plane (o.o.p.). Bond elongations and angle openings are denoted by plus (+) signs and bond contractions and angle closings are denoted by minus (−) signs.

Table A6.3. Calculated[a] Vibrational Frequencies (cm^{-1}) for NO_2^+

$N^{16}O^{16}O^+$	$N^{16}O^{18}O^+$	$N^{18}O^{18}O^+$	assgnts
	B3LYP		
2437.9(0)[370]	2417.8(<0.1)[368]	2396.2(0)[367]	$\nu_3(\Sigma_u^+)$ $\nu_{as}(NO_2)$
1446.9(17)[0]	1405.0(16)[<1]	1364.0(15)[0]	$\nu_1(\Sigma_g^+)$ $\nu_s(NO_2)$
653.3(0)[10]	647.7(<0.1)[10]	642.1(0)[11]	$\nu_2(\Pi_u)$ $\delta(NO_2)$
	PBE1PBE		
2518.2(0)[394]	2497.4(<0.1)[392]	2475.1(0)[390]	$\nu_3(\Sigma_u^+)$ $\nu_{as}(NO_2)$
1490.7(16)[0]	1447.5(16)[<1]	1405.3(15)[0]	$\nu_1(\Sigma_g^+)$ $\nu_s(NO_2)$
673.6(0)[10]	667.9(<0.1)[11]	662.1(0)[12]	$\nu_2(\Pi_u)$ $\delta(NO_2)$

[a] The aug-cc-pVTZ basis set was used.